constant background pressure of 500 torr. In order to maintain minimum damage to the silicon and limit the effect of the microstructuring on the high gain performance of the APD, we minimized the size of the structures while still targeting enhanced absorption in the near-IR.

Following texturing, the APD wafers were either packaged with our standard processing techniques or they underwent thermal anneal in a laboratory oven in an N_2 atmosphere. Annealing ranged from 200 to 950 °C for up to 24 hours. Our standard packaging consisted of coating the APD with a passivation layer, attaching electrical contacts to both the anode and cathode, mounting on a supporting substrate and applying a polymer underfill.

Two 16-element detector arrays that were microstructured are shown in Figure 1. The effect of the microstructuring was evaluated across the array grooves and on individual pixels. One of the samples shown was divided into four different processing regions, each structured with a different number of laser pulses (0, 10, 100 and 300). The darkest region represents a greater number of laser pulses, while the shiny region is an unstructured region for comparison.

We investigated the effects of the processing conditions and thermal annealing on the performance of the APD detectors. We measured the current generated from each microstructured APD over a range of wavelengths emitted from a white light source dispersed through a monochromator. A 200 V bias was applied to each detector to ensure proper charge collection without internal gain. A NIST-traceable photodiode was used to calibrate the absolute response of the detector. In addition, a reference photodiode was used to monitor the output of the white-light source over time.

The gain profile of both structured and non-structured APDs was measured by employing a low-power, pulsed or CW diode laser source. When recording the CW signal, a picoammeter (Keithley model 619) was used to monitor the APD output with no additional amplification electronics. The pulsed setup used a 1 μs laser pulse, a charge-sensitive amplifier (Cremat model CR-110) and a spectroscopy amplifier (Canberra model 2020) was used to amplify the APD output. The minimum detectable energy was determined when the bias was set to unity gain. The bias was then increased and the photo-induced signal and dark current were recorded at each setting. Neutral density filters were used to reduce the laser power as necessary. Response to radiation from 635 nm and 1060 nm laser diodes was evaluated.

A passive Q-switched microchip laser (Uniphase model NG-10120-101) with output radiation at 1064 nm and 532 nm was used to estimate the bandwidth of the detector with and without microstructuring. The pulse width of the laser was monitored with a 1 GHz photodiode and compared to the APD output at various bias settings.

To help evaluate if the bandgap of silicon was altered following the microstructuring, the photocurrent generated from the detector was measured as a function of temperature. The devices were placed inside an aluminum enclosure that had optical and electrical feed-throughs. The enclosure was then placed in a heavily insulated liquid nitrogen bath for cooling below 100 K while a constant source of illumination at 1060 nm or 632 nm was incident upon the detectors. As the detector slowly warmed (< 1 °C/minute) to room temperature, the unity-gain response at a

SIONYX1403000036.0120

SAMSUNG EX. 1002 - 404/4148

reverse bias of 200 V was recorded. The response from microstructure and unstructured APDs were compared.

3. Experimental Results

Figure 2 shows the quantum efficiency of a single element APD with structured and unstructured regions as a function of wavelength. The data was collected with a 200 V bias across the APD junction to assist with the charge collection and ensure unity gain response. The response at wavelengths below 950 nm is dramatically reduced following the microstructuring while being enhanced at the near-IR wavelengths. The response was enhanced at energies below the bandgap by as much as a factor of ten, but the overall quantum efficiency was always relatively small (< than 0.01 % at 1300 nm). These results were fairly consistent for most processing conditions.

Table 1 provides the values for the measured QE at 1064 nm for several microstructured APD arrays or APD pixels as a function of various processing parameters. The equivalent unstructured devices exhibited a range of efficiencies that varied depending on the APD fabrication properties. The initial efficiencies following microstructuring were typically no more than 30% higher than the unstructured samples. However, the addition of a thermal annealing step increased the QE by over a factor of two. Consistent QE values at 1064 nm reached 40% or higher with low temperature annealing and as high as 58% with high temperature annealing. Thermal annealing did not affect the QE of the unstructured APDs that were used as reference.

We found that the most reliable microstructure processing used 100 laser pulses at 3.5 kJ/m^2 in an atmosphere of SF_6. While the processing atmosphere did not appear to affect the QE prior to annealing, the relative increase following annealing was greater for devices that were structured in atmospheres of SF_6 or H_2S.[23] Higher fluences or more laser pulses did not lead to higher QEs and were more damaging to the samples. Fewer laser pulses and a lower fluence were less reliable resulting in poor uniformity across the detector surface. Finally, microstructuring across the grooves between APD pixels did not produce a detrimental effect or limit the yield of functioning detectors. This promoted a means to structure an entire silicon wafer without limiting the existing planar processing capabilities.

The thermal annealing was also considered essential to obtain the enhanced near-IR response. The high temperatures (> 850 °C) also allowed us to drive in an additional surface doping to assist charge collection. In addition to the enhancement to the near-IR QE, high temperature thermal annealing improved the response in the visible. Figure 3 compares the response as a function of wavelength for a structured APD detector that was annealed at 950 °C with one that was annealed at 900 °C. Although we had limited sample numbers, the yield of working devices appeared to decrease following the annealing at temperatures above 900 °C, but the detectors that operated with low noise, maintained an enhanced QE in the near-IR.

The amount of light transmitted and reflected from the silicon at normal incidence was characterized with an unpackaged, partially structured APD wafer that was heated to 900 °C. Using a 1060 nm light source we found that the unstructured silicon had transmission and reflection of 42% and 33% respectively. These values are consistent with our APD thickness of ~ 250 μm. The structured detector, on the other hand, had transmission ranging from 4 to 7%

SIONYX1403000036.0121

SAMSUNG EX. 1002 - 405/4148

and reflection of < 3%, indicating that up to 50% of the electrons created during absorption are not collected at the electrode.

APD gain and noise performance were measured prior to and following the microstructuring. Figure 4 shows the typical gain response curves as a function of bias for a microstructured APD at two different wavelengths. The maximum gain at 1060 nm approached ~ 400, while the gain at 635 nm was > 1000. Interestingly, the gain and dark current dependence on bias was nearly identical to the detectors that were not microstructured.

Figure 5 shows the response of a microstructured and unstructured APD to sub-ns laser pulses at 532 and 1064 nm. The output from the APD was terminated with 50-Ohms at an oscilloscope to collect the data. No additional amplification electronics were used during this measurement. Again, there was very little difference between the two detectors, with a slightly faster fall time from the structured detector. While the response was faster at the higher bias, the difference between detectors did not change.

The unity gain response of a structured and unstructured APD was also compared as a function of temperature. Figure 6 shows the output signals normalized (to laboratory ambient) as a function of temperature. The decrease in QE as a function of temperature is expected because the bandgap energy increases with decreasing temperature.[1] The bandgap of silicon ranges from 1.12 eV (1120 nm) at 300 K to 1.16 eV (1070 nm) at 50 K. Again, there was a negligible difference between the microstructured and unstructured APD response as a function of temperature. This similar behavior also holds at 635 nm, where the QE for wavelengths far from the bandedge remains nearly constant with decreasing temperature.

4. Discussion

The most significant result of this work was the ability to fabricate a silicon-based APD with a QE of 58% at 1064 nm. With usable gains of 400 to 500, this translates to a responsivity of > 200 A/W. Equally important is the ability to integrate the microstructuring into a planar processing sequence without requiring additional labor-intensive steps.

Microstructuring in atmospheres of SF_6 or H_2S followed by thermal annealing produced an improvement in QE for every APD detector tested. Previous observations showed that irradiation of silicon with femtosecond laser pulses in a sulfur atmosphere resulted in a high concentration of sulfur (~ 1 %) in the disordered surface layer.[13,23] It is theorized that those sulfur atoms play a critical roll providing a mechanism for absorption beyond the bandgap.[24] However, based on the measurements at 1300 nm in this study, it is apparent that this IR absorption does not produce a high detector responsivity, suggesting that recombination at the surface hinders charge collection. The significant decrease in the QE for wavelengths below 950 nm is consistent with enhanced charge collection near the surface.

APDs structured in any background gas showed initial enhancement in their QE, but they did not exhibit a significant increase following a thermal annealing unless processed in a sulfur-containing atmosphere. This suggests that the microstructuring alone produced a slight advantage for the longer wavelength light due to surface scattering or photon trapping increasing the effective path length through the structured APD compared with an unstructured detector.

SIONYX1403000036.0122

SAMSUNG EX. 1002 - 406/4148

However, a second mechanism is needed to alter the dynamics of the trapping sites following thermal annealing. This secondary mechanism appears to be related to the sulfur content and annealing temperature. As the sample is thermally annealed, the charge collection increases although previous studies have shown that the total absorption decreases.[14] Simple reorganization of defect sites, reducing the trapping of electrons in the APD drift region is the most likely mechanism. Another possibility is an *n-type* silicon layer which, research has shown forms in the presence of a sulfur atmosphere during microtstructuring.[19] This induced doping will create a near-surface p-n junction on our APDs, decreasing the ability for the charges to reach the collection electrode. We suspect that the high temperature annealing may modify this layer and help compensate for this interference. However, further studies are required to validate this theory.

The detection of radiation with a long penetration depth is limited by lower achievable APD gains because some of the radiation is absorbed in the depletion region of the detector, limiting its path length through the amplification region. Shorter wavelengths, on the other hand, are absorbed closer to surface of the detector and achieve higher gain. This gain reduction was also observed in the structured detectors (Figure 6). If the enhancement were strictly due to greater absorption near the surface region of the detector we would have expected to measure a modification to the gain profile, including a larger maximum gain at 1060 nm. Because the gain dependence for the structured and unstructured APDs was nearly identical, we assume that the photons detected are absorbed at nearly identical depths. This suggests that we are still not taking advantage of the increased photon density absorbed near the APD surface.

Other intriguing pieces of data are from the APD temperature dependence and speed of response to 1064 nm radiation. If the enhancements were due to new bandgap states from the introduction of sulfur, we would have expected a more pronounced shift in the temperature dependence of the near-IR QE. In addition, if the structured APDs had a significant amount of absorption near the surface region, we would have expected the response speed to slow down, as a greater number of charge carries need to make their way through a drift region before amplification. However, neither of these effects was observed from our experimental arrangement further indicating that the microstructuring layer behaves as an antireflection coating increasing the total number of absorbed photons.

Although further studies are required to fully explain some of the experimental results, it is apparent that the increased absorption results in an increase number of charge carriers. The large number of defect sites created by the microstructuring limits the flow of charges from the near-surface region. Thermal annealing reduces or alters some of the sulfur-induced charge-trapping sites or limits the effect of a competing *n-type* layer formed following the structuring. Evidently, thermal annealing creates additional charge carriers near the depletion region, which are collected, resulting in improved QE in the near-IR.

5. Conclusion

Microstructuring of the surface layer of an APD with a femtosecond laser in an atmosphere of SF_6 has been shown to increase its responsivity in the near-IR to over 200 A/W at 1064 nm, without increasing the leakage current or slowing its speed-of-response. An additional annealing step is required following the microstructuring to achieve these high responsivities.

SIONYX1403000036.0123

SAMSUNG EX. 1002 - 407/4148

We have demonstrated this processing on the wafer scale without adding significant labor-intensive steps. We have seen no experimental evidence of changes to the band structure due to the introduction of sulfur. Reduction in the QE at wavelengths below 900 nm may be alleviated with additional high temperature annealing.

The mechanism leading to the enhanced response in the near-IR has not been fully explained. While the incorporation of sulfur appears to be essential for achieving the highest possible QE, results from experimental studies are not consistent with previous studies that indicate the potential introduction of new energy states. Further studies are required to answer some of the remaining questions about the mechanism.

Acknowledgements

The authors would like to acknowledge the support of the National Aeronautic and Space Administration (contracts NAS302187 and NNGO4CA27C) for the research reported in this paper.

6. References

1. S. M. Sze, *Physics of Semiconductor Devices*, 2nd ed. (Wiley Interscience, 1981).
2. L. T. Canham, T. I. Cox, A. Loni, and A. J. Simons, "Progress towards silicon optoelectronics using porous silicon technology," Appl. Surf. Sci. **102**, 436-441 (1996).
3. M. Okamura, and S. Suzuki, "Infrared photodetection using a A-SI-H photodiode," IEEE Photon. Tech. Lett. **6**, 412-414 (1994).
4. M. –K. Lee, C. –H. Chu, Y.-H. Wang, and S. M. Sze, "1.55- mm and infrared-band photoresponsivity of a Schottky barrier porous silicon photodetector," Opt. Lett. 26, 160-162 (2001).
5. M. Ghioni, A. Lacaita, G. Ripamonti, and S. Cova, "All-silicon photodiode sensitive at 1.3 micron with picosecond time resolution," IEEE J. Quantum Electron. **28** 2678-2681 (1992).
6. R. Farrell, R. H. Redus, J. S. Gordon, and P. Gothoskar, "High Gain APD Array for Photon Detection," in *Photodetectors and Power Meters II*, K. Muray; K. J. Kaufmann; eds. Proc. SPIE **2550**, 266-273 (1995).
7. M. K. Emsley, O. Dosunmu, and M. S. Ünlü, "High-speed resonant-cavity enhanced silicon photodetectors on reflecting silicon-on-insulator substrates," IEEE Photon, Tech. Lett. 14, 519-521 (2002).
8. A. Y. Loudon, P. A. Hiskett, G. S. Buller, R. T. Carline, D. C. Herbert, W. Y. Leong, and J. G. Rarity "Enhancement of the infrared detection efficiency of silicon photon-counting avalanche photodiodes by use of silicon germanium absorbing layers," Opt. Lett. **27**, 219-221 (2002).
9. S. –B. Ko, and H. T. Henderson, "The use of multiple internal reflection on extrinsic silicon infrared detection," IEEE Trans. Elect. Devices **ED-27**, 62-65 (1980).
10. T. -H. Her, R. J. Finlay, C. Wu, S. Deliwala, and E. Mazur, "Microstructuring of silicon with femtosecond laser pulses," Appl. Phys. Lett. **73**, 1673-1675 (1998).
11. C. Wu, C.H. Crouch, L. Zhao, J.E. Carey, R. Younkin, J.A. Levinson, E. Mazur, R.M. Farrell, P. Gothoskar, and A. Karger, "Near-unity Below-Band-gap Absorption by Microstructured Silicon," Appl. Phys. Lett. **78**, 1850-1852 (2001).

SIONYX1403000036.0124

SAMSUNG EX. 1002 - 408/4148

12. R. Younkin, J. E. Carey, E. Mazur, J. A. Levinson, and C. M. Friend, "Infrared absorption by conical silicon microstructures made in a variety of background gases using femtosecond-laser pulses," J. of Appl. Phys. **93**, 2626-2629 (2003).
13. C. H. Crouch, J. E. Carey, M. Shen, E. Mazur, and F. Y. Génin, "Infrared absorption by sulfur-doped silicon formed by femtosecond laser irradiation," Appl. Phys. A**79**, 1635-1641 (2004).
14. C. H. Crouch, J. E. Carey, J. M. Warrender, M. J. Aziz, E. Mazur, and F. Y. Génin, "Comparison of structure and properties of femtosecond and nanosecond laser-structured silicon," Appl. Phys. Lett. **84**, 1850-1852 (2004).
15. A. J. Pedraza, J. D. Fowlkes, and D. H. Lowndes, "Silicon microcolumn arrays grown by nanosecond pulsed-eximer laser irradiation," App. Phys. Lett. **74**, 2322-2324 (1999).
16. J. T. Zhu, Y. F. Shen, W. Li, X. Chen, G. Yin, D. Y. Chen, and Z. Li, "Effects of polarization on femtosecond laser pulses structuring silicon surfaces," Appl. Surf. Sci. **252**, 2752-2756 (2006).
17. J. T. Zhu, G. Yin, M. Zhao, D. Y. Chen, and L. Zhao, "Evolution of silicon surface microstructures by picosecond and femtosecond laser irradiations," Appl. Surf. Sci. **245**, 102-108 (2005).
18. J. Bonse, K. W. Brzezinka, and A. J. Meixner, "Modifying single-crystalline silicon by femtosecond laser pulses: an analysis by microraman spectroscopy, scanning laser microscopy and atomic force microscopy," Appl. Surf. Sci. **221**, 215-230 (2004).
19. J. E. Carey, C. H. Crouch, M. Shen, and E. Mazur, "Visible and near-infrared responsivity of femtosecond-laser microstructured silicon photodiodes," Optics Lett. **30**, 1773-1775 (2005).
20. R. Farrell, K. Vanderpuye, L. Cirignano, M. R. Squillante, and G. Entine, "Radiation Detection Performance of Very High Gain Avalanche Photodiodes," *Nucl. Inst. Meth.*, **A353**, 176-179, (1994).
21. R. Redus and R. Farrell, "Gain and Noise in Very High Gain Avalanche Photodiodes: Theory and Experiment," in *Hard X-Ray/Gamma Ray and Neutron Optic Sensors and Applications,* R. B. Hoover and F. P. Doty, eds., Proc. SPIE **2859**, 288-297 (1996).
22. R. Farrell, K. Shah, K. Vanderpuye, R. Grazioso, R. Myers, and G. Entine, "APD arrays and large area APDs via a new planar processing," Nucl. Instrum. Methods. A **442**, 171-178 (2000).
23. M. A. Sheehy, L. Winston, J. E. Carey, C. M. Friend, and E. Mazur, "Role of the background gas in the morphology and optical properties of laser-microstructured silicon," Chem. Mater. **17**, 3583-3586 (2005).
24. E. Janzén, R. Stedman, G. Grossman, and H. G. Grimmeiss, "High-resolution studies of sulfur- and selenium-related donor center in silicon," Phys. Rev. B **29**, 1907-1918 (1984).

SIONYX1403000036.0125

SAMSUNG EX. 1002 - 409/4148

Figure Captions

Figure 1. Picture of two microstructed APD arrays prior to packaging. Structuring was performed with an 800 nm fs laser operating at a fluence of 3.5 kJ/m^2 in an atmosphere of SF_6. The array on the right had four different structured regions, with pulse number ranging from 0 to 300. The shiny area is the bare silicon.

Figure 2. Quantum efficiency vs. wavelength for a single element APD that was partially microstructured. The structured region shows an enhanced signal in the near-IR but reduced responsivity below 950 nm. Data was recorded with a 200 V bias applied to the APD.

Figure 3. QE vs. wavelength for a unstructured APD and two APDs annealed at high temperatures. The thermal annealing further enhances the near-IR response, while annealing about 900 °C results in improved response in the visible.

Figure 4. APD gain as a function of applied bias for structured APD pixels. The gain dependence on bias was nearly identical to unstructured APDs for both 632 and 1060 nm.

Figure 5. Response of a microstructured and unstructured APD to a sub-ns pulse of radiation at (a) 532 nm and (b) 1064 nm. The response of the structured APD was nearly identical to the unstructured detector at all tested bias setting. No amplification electronics were used in this measurement.

Figure 6. APD signal strength due to 1060 nm illumination as a function of temperature. The unity gain signal (200 V bias) was recorded as the detector warmed from ~ 100 K. Both the microstructured and unstructured detectors had a similar dependence.

SIONYX1403000036.0126

SAMSUNG EX. 1002 - 410/4148

Figures

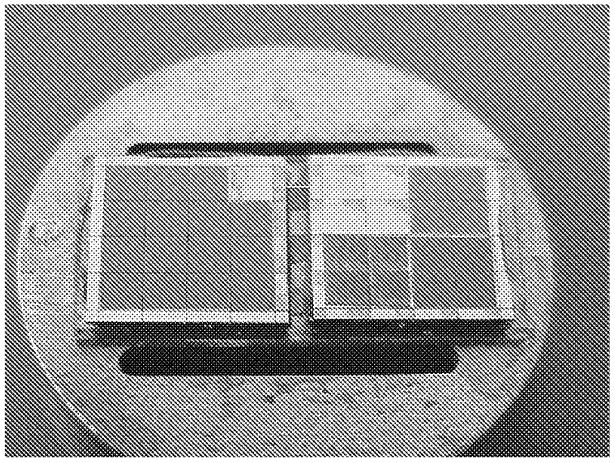


Figure 1. Picture of two microstructed APD arrays prior to packaging. Structuring was performed with an 800 nm fs laser operating at a fluence of 3.5 kJ/m^2 in an atmosphere of SF_6. The array on the right had four different structured regions, with pulse number ranging from 0 to 300. The shiny area is the bare silicon.

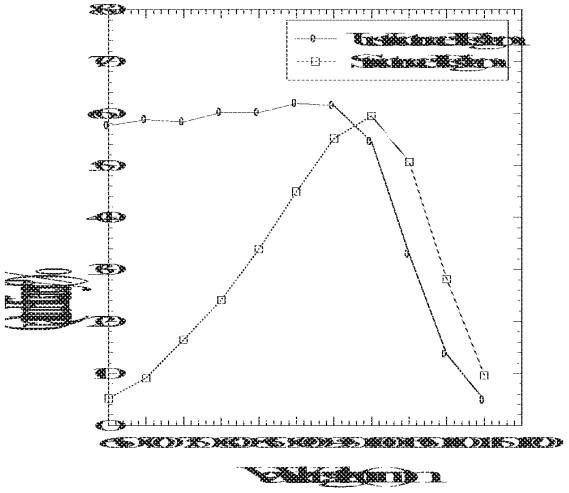


Figure 2. Quantum efficiency vs. wavelength for a single element APD that was partially microstructured. The structured region shows an enhanced signal in the near-IR but reduced responsivity below 950 nm. Data was recorded with a 200 V bias applied to the APD.

SIONYX1403000036.0127

SAMSUNG EX. 1002 - 411/4148

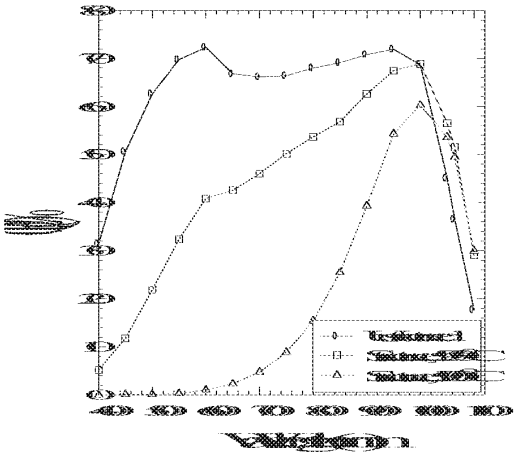


Figure 3. QE vs. wavelength for a unstructured APD and two APDs annealed at high temperatures. The thermal annealing further enhances the near-IR response, while annealing about 900 °C results in improved response in the visible.

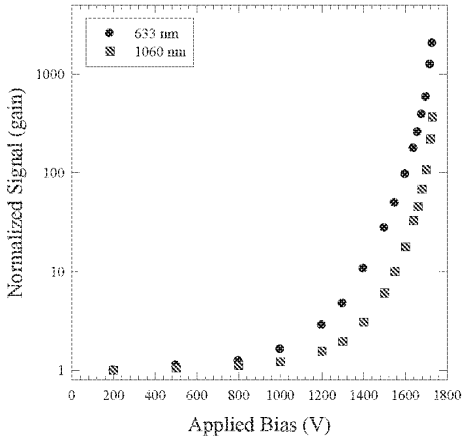


Figure 4. APD gain as a function of applied bias for structured APD pixels. The gain dependence on bias was nearly identical to unstructured APDs for both 632 and 1060 nm.

SIONYX1403000036.0128

SAMSUNG EX. 1002 - 412/4148

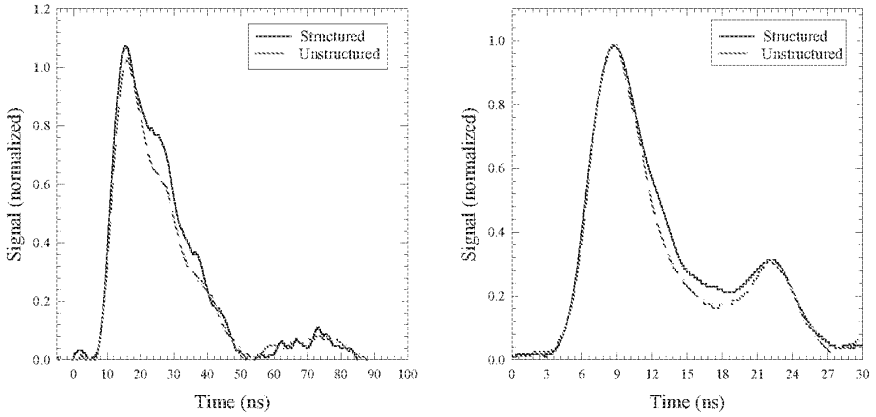


Figure 5. Response of a microstructured and unstructured APD to a sub-ns pulse of radiation at (a) 532 nm and (b) 1064 nm. The response of the structured APD was nearly identical to the unstructured detector at all tested bias setting. No amplification electronics were used in this measurement.

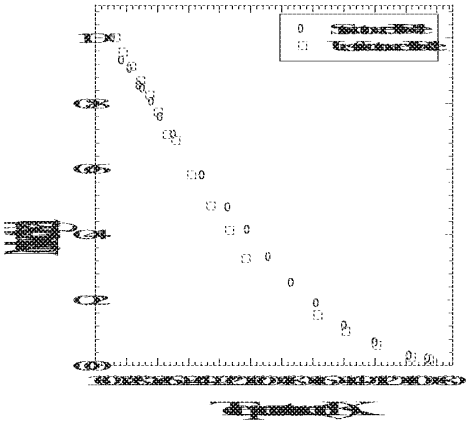


Figure 6. APD signal strength due to 1060 nm illumination as a function of temperature. The unity gain signal (200 V bias) was recorded as the detector warmed from ~ 100 K. Both the microstructured and unstructured detectors had a similar dependence.

SIONYX1403000036.0129

SAMSUNG EX. 1002 - 413/4148

Tables

Table 1. Effect of processing conditions on the QE at 1064 nm

APD Sample	Laser pulses	Laser fluence (kJ/m^2)	Gas	QE before annealing (% at 1064 nm)	Annealing temp (°C)/time (hrs.)	QE after annealing (% at 1064 nm)	Signal Ratio after/before annealing
1	0	0	SF_6	25	900/4	25	1
2	200	5	SF_6	15	400/2	34	2.3
3	200	5	SF_6	18	400/5	36	2.0
4	10	3.5	SF_6	28	400/2	41	1.5
5	100	3.5	SF_6	19	400/2	38	2.0
6	200	3.5	SF_6	21	400/2	38	1.8
7	400	3.5	SF_6	25	400/2	41	1.6
8	400	3.5	H_2S	27	400/3	42	1.6
9	200	3.5	Air	29	400/2	34	1.2
10	200	3.5	N_2	37	400/2	40	1.2
11	100	3.5	SF_6	NA	850/1*	48	NA
12	100	3.5	SF_6	NA	900/1*	58	NA
13	100	3.5	SF_6	NA	950/1*	54	NA

* A p^+-dopant was applied to the surface before annealing.

SIONYX1403000036.0130

SAMSUNG EX. 1002 - 414/4148

Intrinsic gettering in oxygen-free silicon

N. Nauka, J. Lagowski, H. C. Gatos, and C.-J. Li
Massachusetts Institute of Technology, Cambridge, Massachusetts 02139

(Received 5 November 1984; accepted for publication 15 January 1985)

We found that a three-step high-temperature annealing leads to intrinsic gettering in oxygen-lean Czochralski silicon grown in a magnetic field as well as in oxygen-free float zone silicon. Such thermal treatment has been used thus far for achieving intrinsic gettering only in oxygen-rich Czochralski silicon. We present experimental characteristics of this new intrinsic gettering process, and we propose a phenomenological explanation involving outdiffusion and precipitation of silicon interstitials rather than oxygen which is involved in the standard intrinsic gettering.

Thermal annealing leading to intrinsic gettering is commonly used in silicon very large scale integration technology in order to remove defects from the device-active region of the wafer.[1] Such gettering can be effectively realized by three-step annealing of Czochralski (CZ) grown Si containing interstitial oxygen at a concentration of about 10^{18} cm^{-3}.[2] It is generally believed that the first high-temperature (~1100–1200 °C) step (referred to as "denuding") leads to outdiffusion of oxygen, and it creates a denuded zone beneath the surface. Two subsequent lower temperature steps at 700–800 °C and 1000 °C cause nucleation and growth of oxygen precipitates. The final effect, i.e., removal of metallic contaminants from the denuded zone, is attributed to the gettering of oxygen precipitates. Thus, according to current modes, intrinsic gettering is intimately related to the presence of oxygen and the efficiency of the process to the concentration of oxygen.[3] The oxygen concentration must be high enough to cause supersaturation of the silicon lattice at elevated temperatures, and thus induce effective precipitation of oxygen. This condition is satisfied in standard CZ Si containing interstitial oxygen at a concentration ranging from 0.8 to 1.5×10^{18} cm^{-3}. In Si crystals grown by the float zone (FZ) method the oxygen concentration is about three orders of magnitude lower (10^{15} cm^{-3}) than in CZ Si. This concentration is well below the oxygen solubility limit in Si even at the lowest temperature (700 °C) used in three-step annealing.[4] It is thus apparent that oxygen precipitation and related intrinsic gettering cannot take place in FZ Si.

Surprisingly, we found that three-step annealing of FZ Si wafers does lead to very effective intrinsic gettering. In this work we present experimental characteristics of the new intrinsic gettering process, and we discuss a possible mechanism involving outdiffusion and precipitation of Si interstitials. In a comparative study of the effects of thermal annealing we have used three types of commercially grown dislocation-free Si crystals: (1) standard CZ Si containing interstitial oxygen at concentration $[O_i]$ of about 1×10^{18} cm^{-3} and substitutional carbon at concentration [C] of about 1×10^{16} cm^{-3} (determined by infrared spectroscopy employing the standards of Ref. 5), (2) CZ Si grown in a magnetic field (MCZ Si) with $[O_i]\simeq(1-1.5)\times10^{17}$ cm^{-3} and $[C]\lesssim5\times10^{15}$ cm^{-3}, and (3) swirl-free FZ Si with $[O_i]\lesssim1\times10^{15}$ cm^{-3}, i.e., virtually "oxygen free" and $[C]\lesssim5\times10^{15}$ cm^{-3}. We have studied both *n*-type and *p*-type crystals doped with P or B, respectively, at concentrations ranging from 8×10^{14} to 2×10^{15} cm^{-3}; no meaningful differences were observed between the behavior of *n*-type and *p*-type crystals, and no further reference to the conductivity type will be made.

The samples were subjected to three-step annealing in the following order: 1170 °C for 6 h, 700 °C for 20 h, and 1000 °C for 6 h. Four typical annealing ambients were used: chemically inert (N_2 and Ar) and oxidizing (O_2 and O_2 + 2% HCl) which inject Si interstitials and Si vacancies, respectively. Annealed samples were beveled at 4° angle and etched with the commonly used Secco or Wright etchants in order to reveal the distribution of defects. Typical results obtained using the chemically inert N_2 ambient are presented in Figs. 1 and 2. Photomicrographs of beveled surfaces are shown in Figs. 1(a), 1(b), and 1(c) for CZ Si, MCZ Si, and FZ Si, respectively. Very similar features are observed, i.e., a defect-free denuded zone beneath the surface and a large density of defects in the bulk is seen for all samples despite the pronounced differences in oxygen concentration.

In order to determine the excess carrier lifetime changes associated with gettering of metallic impurities we have carried out electron beam induced current (EBIC) measurements on the annealed samples. Schottky barriers were formed on the beveled surfaces by evaporation of Ti for *p*-type samples. Evaporated Pd briefly annealed at a low temperature to form a stabilizing layer of Pd_2Si was used for *n*-type Si. In EBIC measurements the beveled area was scanned by an electron beam normal to the Schottky barrier (i.e., passing through the metal).

Beam-induced current between the metal and a back contact was recorded as a function of the beam position. EBIC images and EBIC scans are shown in Figs. 2(a), 2(b), and 2(c) for CZ Si, MCZ Si, and FZ Si, respectively. Dark regions at the EBIC image and low current values in the EBIC scan correspond to the short lifetime of minority carriers, i.e., the high concentration of recombination centers; white regions and large current correspond to long lifetime, i.e., to a low concentration of recombination centers. It is evident from Fig. 2 that effective gettering of recombination centers was achieved for all three samples. Thus, the regions beneath the surface are white in EBIC images, and they exhibit large values of electron beam induced current. At the termination of denuded zones the current rapidly decreases (by as much as two orders of magnitude) and the corresponding bulk regions become black in the EBIC images.

It is important to note that the formation of a denuded zone is not equivalent to the removal of metallic impurities

 0003-6951/85/070673-03$01.00 © 1985 American Institute of Physics

Downloaded 27 May 2009 to 146.186.238.14. Redistribution subject to AIP license or copyright; see http://apl.aip.org/apl/copyright.jsp

SIONYX1403000036.0131

SAMSUNG EX. 1002 - 415/4148

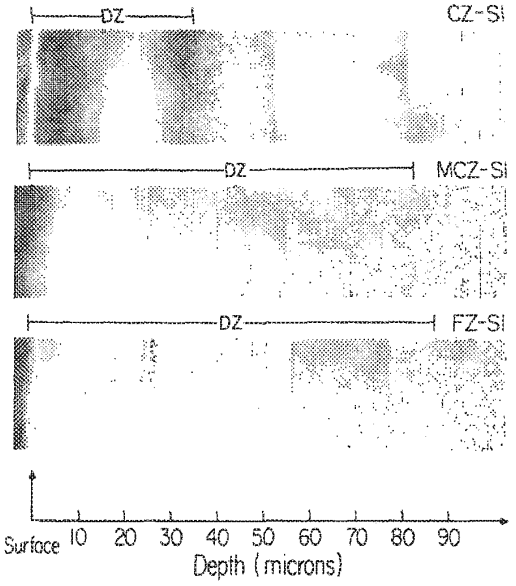


FIG. 1. Denuded zones and corresponding distribution of defects in Si crystals subjected to three-step annealing in chemically inert N_2 ambient.

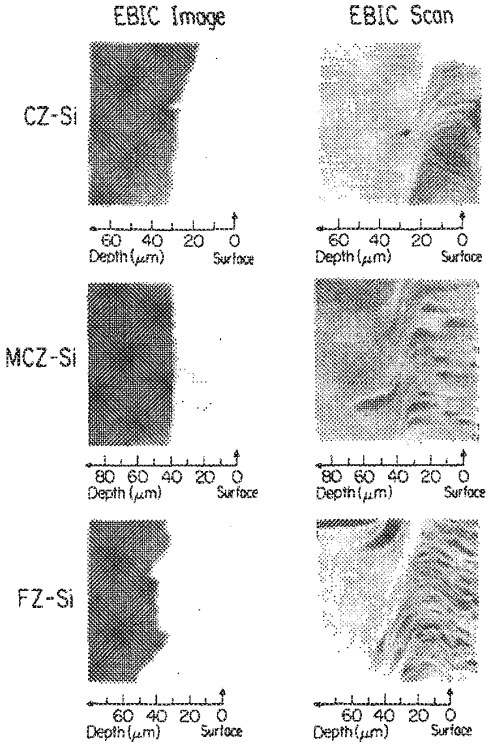


FIG. 2. Minority-carrier lifetime distribution in Si crystals subjected to three-step annealing in N_2 ambient. White region and high current observed within denuded zones beneath surfaces correspond to long lifetimes.

from the surface region and thus the defect distribution of Fig. 1 is not identical with the EBIC current profiles of Fig. 2. We have found that denuded zones are formed in all Si samples during the first annealing step (1170 °C). This annealing produced only minor changes in the lifetime. Significant lifetime enhancement was observed, however, after subsequent lower temperature annealing steps at 700 and 1000 °C. This behavior is summarized in Table I, which gives values of the lifetime, τ_G, determined from transient responses of MOS capacitors formed on the surface and along the level after different stages of thermal annealing.

The present results show that intrinsic gettering in oxygen-free silicon involves stages which are similar to those of gettering in Si with large oxygen concentration; namely, a high-temperature denuding stage and a subsequent, lower temperature, precipitation of defects. However in FZ Si the native defects (i.e., Si interstitials or Si vacancies) must be involved rather than oxygen impurities.

According to current models, the denuded zone in oxygen-rich CZ Si is formed as a result of oxygen outdiffusion toward the surface. The effects of oxidizing and inert ambients on the efficiency of intrinsic gettering, summarized in Table II, are consistent with this point of view. Thus, for CZ Si no significant differences were seen between O_2 and O_2 + HCl ambients; very efficient gettering took place in both cases. The beneficial effects of oxidizing ambients as compared with those of inert ambients could be associated with an enhancement of oxygen outdiffusion by injected defects, as suggested in Ref. 6.

In FZ Si the effect of O_2 is significantly different than that of O_2 + HCl. As seen in Table II, excellent getttering is realized in the O_2 + HCl ambient which leads to injection of vancancies. On the other hand, the process is hindered by injection of Si interstitials during annealing in O_2.[7–9] Accordingly, we speculate that the Si interstitials are the outdiffusing defects in oxygen-free Si. This outdiffusion process is rendered ineffective by injection of interstitials, and it is enhanced by injection of vacancies; thus very bad denuding is obtained in an O_2 ambient and excellent denuding in an

TABLE I. Effects of annealing on the generation lifetime τ_G.

Sample	Oxygen concentration $[O_i](cm^{-3})$	As grown	6 h at 1180 °C plus 20h at 700 °C plus 6 h at 1000 °C					
			Lifetime τ_G (μs)					
			B^a	D^b	B^a	D^b	B^a	D^b
CZ	1.0×10^{18}	40	70	100	30	980	15	1100
MCZ	1.5×10^{17}	70	70	210	40	750	35	920
FZ	1.0×10^{15}	110	100	480	20	1000	15	1050

[a] In the bulk.
[b] Within the denuded zone.

Downloaded 27 May 2009 to 146.186.238.14. Redistribution subject to AIP license or copyright; see http://apl.aip.org/apl/copyright.jsp

SIONYX1403000036.0132

SAMSUNG EX. 1002 - 416/4148

TABLE II. Effects of ambient on the denuded zone formation and the efficiency of instrinsic gettering.

		Ambient used during high-temperature (1170 °C annealing[a])			
		Oxidizing		Inert	
		O_2	O_2 + HCL	N_2	Ar
CZ Si (O-rich)	Denuded zone[b]	very good	very good	good	good
	Intrinsic gettering	very good	very good	good	good
	k[c]	~100	~100	~85	~85
FZ Si (O-free)	Denuded zone[b]	very bad	excellent	good	good
	Intrinsic gettering	very bad	excellent	good	good
	k[c]	~1.5	~100	~75	~70

[a] Subsequent annealing steps were carried out in Ar ambient.
[b] Quality judged by the width and the concentration of defects revealed by Secco etchant.
[c] k is the efficiency of the process assessed by the ratio of lifetime, τ_G, in the denuded zone and in the bulk.

O_2 + HCl ambient. Rough estimates show that the widths of the denuded zones are comparable to the diffusion length expected for Si interstitials. (Diffusivity of Si interstitials at 1200 °C is about 2.5×10^{-5} cm^2/s.[10])

The subsequent phases of intrinsic gettering in oxygen-free silicon, i.e., nucleation and precipitation in the bulk, can be explained in terms of precipitation of interstitials into dislocation loops. These extended defects can generate localized stress, which in turn can attract and immobilize metallic impurities.[11] The above hypothesis is consistent with the high density of Si interstitials expected to be present in swirl-free FZ Si crystals. These crystals are intentionally grown at rates high enough to prevent condensation of interstitials into swirl defects.[12]

In summary, we have shown for the first time that the formation of a denuded zone and intrinsic gettering can be effectively realized in Si crystals with both intermediate and with very low concentration of oxygen. Excellent gettering was obtained using O_2 + HCl as the ambient during annealing. A tentative explanation of these findings involved out-diffusion and precipitation of Si interstitials.

Quantitative modeling of the process and transmission electron microscopy study of the nature of gettering precipitates are in progress.

The authors are grateful to the Semiconductor Research Corporation for financial support.

[1] W. K. Tice and T. Y. Tan, Appl. Phys. Lett. **28**, 564 (1976).
[2] J. O. Borland, Electrochemical Society Meeting, San Francisco, May 1983, Ext. Abstr. No. 274 (Electrochem. Soc. Ext. Abstr. Vol. 83-1).
[3] R. A. Craven, in *Semiconductor Silicon 1981*, edited by H. R. Huff, R. J. Kriegler, and Y. Takeishi (Electrochemical Society Proc., NY, 1981), p. 254.
[4] J. C. Mikkelsen, Appl. Phys. Lett. **41**, 871 (1982).
[5] ASTM Standard: F121-80, F123-81.
[6] R. C. Newman, J. H. Tucker, and F. M. Livingston, J. Phys. C **16**, L151 (1983).
[7] H. Shiraki in, *Semiconductor Silicon 1977*, edited by H. R. Huff and E. Sirtl (Electrochemical Society Proc., NY 1977), p. 546.
[8] A. M. Lin, R. W. Dutton, D. A. Antoniadis, and W. A. Tiller, J. Electrochem. Soc. **128**, 1121 (1981).
[9] R. B. Fair, J. Electrochem. Soc. **128**, 1360 (1981).
[10] A. J. R. De Kock, P. J. Roksnoer, and P. G. T. Boonen, J. Cryst. Growth **30**, 279 (1975).
[11] J. R. Monkowski, Solid State Technol. **24**, No. 7, 44 (1981).
[12] A. J. R. de Kock, P. J. Roksnoer, and P. G. T. Boonen, J. Cryst. Growth **22**, 311 (1974).

Nonparabolic subband structure of $Ga_{0.47}In_{0.53}As$-InP quantum wells

Syoji Yamada, Akihito Taguchi, and Akira Sugimura
Musashino Electrical Communication Laboratories, Nippon Telephone and Telegraph Public Corporation, 3-9-11, Midoricho, Musashino-shi, Tokyo 180, Japan

(Received 29 October 1984; accepted for publication 27 December 1984)

Nonparabolic subband structure of GaInAs-InP quantum wells is studied theoretically. The dispersion relations for electron, light hole, and split-off hole subbands are obtained using the envelope function approximation taking into account band nonparabolicity. Reported experimental electron effective mass values and photoluminescence energies for wide quantum wells are reasonably explained by the present theory. The experimental photoluminescence energies, for the well width less than 50 Å, differ significantly from the calculated results.

Superlattices or heterojunctions have been recently attracting considerable attention because of their unique possibilities applicable for novel optical and electrical devices. The GaAs-GaAlAs[1] system has been very widely studied so far both theoretically and experimentally. An alternative system composed of GaInAs-InP has also been found to have good properties suitable for very fast devices, using fabrication technologies such as low-pressure metalorganic chemical vapor deposition[2,3] or chloride transport vapor phase epitaxy.[4] Quantitative understanding about the band structure of this material, however, is not sufficient. The theoretical analysis of superlattice band structure has been advanced by many authors.[5–7] Bastard[7] has successfully calculated the subband structures of GaAs-GaAlAs and InAs-

 0003-6951/85/070675-03$01.00 © 1985 American Institute of Physics

Downloaded 27 May 2009 to 146.186.238.14. Redistribution subject to AIP license or copyright; see http://apl.aip.org/apl/copyright.jsp

SIONYX1403000036.0133

SAMSUNG EX. 1002 - 417/4148

New intrinsic gettering process in silicon based on interactions of silicon interstitials

K. Nauka,[a] J. Lagowski, H. C. Gatos, and O. Ueda[b]
Massachusetts Institute of Technology, Cambridge, Massachusetts 02139

(Received 13 January 1986; accepted for publication 14 March 1986)

A new intrinsic gettering process was found in silicon crystals subjected to a three-step annealing sequence. The process involves native point defects (silicon interstitials) rather than residual oxygen impurity, and thus it can be realized in crystals with low or virtually zero oxygen concentration. The key characteristics of the process (i.e., denuding and gettering efficiency and the role of annealing ambient) are discussed in conjunction with a kinetic model involving diffusion of silicon interstitials. The identity of the intrinsic gettering centers was pursued by transmission electron microscopy.

I. INTRODUCTION

There has been considerable interest in recent years in defect gettering processes.[1] VLSI technology requires silicon material of a quality not commonly attainable by the present crystal growth techniques. In addition, defects introduced during device processing must be confined to regions away from the device active area. Intrinsic gettering has been developed[2] for effective defect control compatible with VLSI processing sequences. It is commonly achieved by a three-step annealing[3] (high-, low-, and medium-temperature sequence) employing silicon crystals grown by the Czochralski method (CZ-Si), which contain a high concentration of interstitial oxygen (about 10^{18} cm^{-3}). During the high-temperature annealing step, interstitial oxygen out-diffuses from the surface region. The subsequent annealing steps lead to the formation of bulk defects (oxide precipitates) acting as gettering sites just below the denuded surface region where the devices are fabricated.

We reported recently[4,5] on an intrinsic gettering process based on silicon self-interstitials rather than oxygen. This process was discovered in silicon crystals with low oxygen content (Czochralski silicon grown in a magnetic field, MCZ-Si), and also in virtually oxygen-free silicon grown by the float-zone technique (FZ-Si).

In this paper we present extensive experimental data on the new intrinsic gettering, and we discuss the relevant macroscopic and microscopic processes. The present results lay the basis for a phenomenological model describing the overall intrinsic gettering in silicon crystals grown by various techniques. The structure and composition of the intrinsic gettering centers are discussed in the accompanying paper.[5]

II. EXPERIMENT

Three types of commercially grown, dislocation-free, Si crystals were employed: (1) 3- or 4-in.-diam commercially grown, dislocation-free, Si crystals containing about 1.0–1.5×10^{18} cm^{-3} of the interstitial oxygen $[O_i]$; (2) 2-in.-diam MCZ-Si (grown in magnetic field) with $[O_i]$ of about 1×10^{17} cm^{-3}; and (3) virtually oxygen-free 2-in.-diam FZ-Si. The carbon concentration in these crystals ranged from 5×10^{15} to 1×10^{16} cm^{-3}. Experiments were carried out with both n (P-doped) and p (B-doped) crystals with a dopant concentration ranging from 10^{14} to 10^{15} cm^{-3}. No meaningful differences were observed between the dopants; no further reference to the conductivity type will be made. For some experiments, FZ-Si doped with nitrogen at a concentration of about 10^{15} cm^{-3} was employed. All three types of crystals employed in this study were obtained from at least two suppliers. The concentration of metallic contaminants was estimated from deep level transient spectroscopy (DLTS) measurements.[6] It was found that most of the crystals contained residual impurities, however, at low concentration, not exceeding 10^{11} cm^{-3}.

The samples were subjected to a three-step annealing, i.e., to 1170 °C for 6 h, then to 700 °C for 20 h, and finally to 1000 °C for 6 h. In standard intrinsic gettering these annealing steps correspond to out-diffusion, nucleation, and growth of the bulk gettering centers, respectively.[7] Various ambients were employed during the first, high-temperature annealing step: dry O_2, O_2 + HCl, N_2, Ar, and also dry O_2 followed by N_2 or N_2 followed by O_2 (O_2/N_2, N_2/O_2). In some experiments a protective film of SiO_2 (PYROX LPCVD SiO_2) was deposited on the samples. The second and third annealing steps were always carried out in an N_2 ambient.

The defect distribution was revealed by preferential etching.[8] Annealed samples were beveled at a 4° angle and etched with the commonly used Secco or Wright etchants. The defect density was obtained by counting etch pits on beveled and etched surfaces. Lifetime measurements were carried out empolying the Zerbst technique[9] or by measuring p–n junction recovery,[10] or photoconductivity decay.[11] All three techniques yielded similar values of the carrier lifetime. Devices (MOS or p–n junctions) used for lifetime measurements were fabricated on the beveled surface or directly on the surface of the wafer before and after removal of the defect-free denuded zone. Thus, denuded zone and bulk lifetimes were determined. The electron-beam-induced current (EBIC) mode of scanning electron microscopy was employed for imaging the spacial variations of lifetime. EBIC measurements were carried on Al Schottky barriers formed

[a] Present address: Hewlett-Packard Laboratories, 1501 Page Mill Rd., Palo Alto, California.
[b] On leave from Fujitsu Laboratories, Ltd., Atsugi, Japan.

 0021-8979/86/140615-07$02.40 © 1986 American Institute of Physics

Downloaded 26 May 2009 to 146.186.238.7. Redistribution subject to AIP license or copyright; see http://jap.aip.org/jap/copyright.jsp

SIONYX1403000036.0134

SAMSUNG EX. 1002 - 418/4148

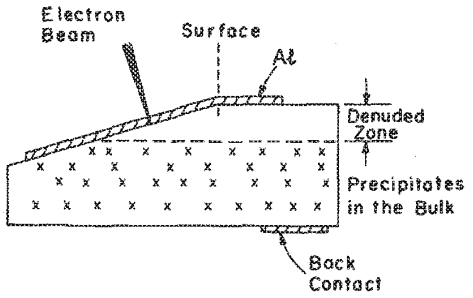


FIG. 1. Sample configuration employed for EBIC measurements.

on the beveled surface on the samples (Fig. 1) previously subjected to three-step annealing. The current signal collected between Al and the back contact to the sample was recorded versus electron beam position on the beveled surface.

III. RESULTS

Figure 2 shows beveled and preferentially etched surfaces of CZ-Si, MCZ-Si, and FZ-Si which were previously subjected to three-step annealing carried out entirely in an N_2 ambient. All three samples exhibit very similar features (despite pronounced differences in oxygen concentration): a defect-free layer (i.e., denuded zone) adjacent to the surface and defects in the bulk. EBIC studies demonstrated that the three-step annealing also resulted in a significant enhancement of the minority-carrier lifetime within the defect-free denuded zone region. Figure 3 shows EBIC results on the samples of Fig. 2. The dark regions in the EBIC images represent small lifetime values, while the white regions (regions of the large EBIC signal) represent large values. The lifetime values measured in these regions are given in Table I. It is evident from the above results that intrinsic gettering was achieved in all three types of Si crystals.

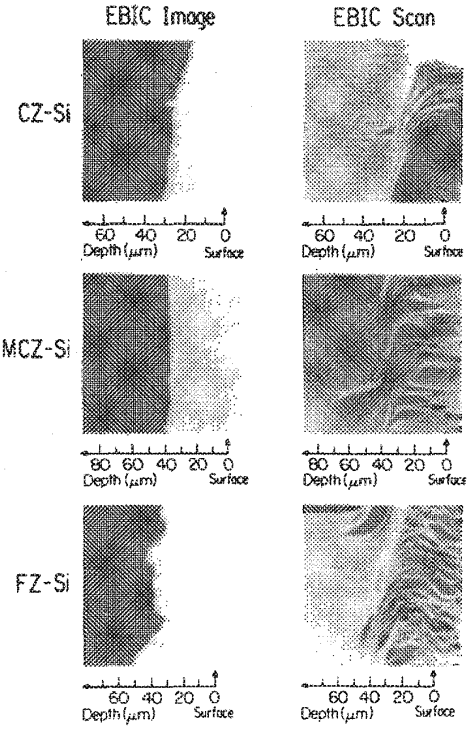


FIG. 2. Preferentially etched cross section of CZ-Si, MCZ-Si, and FZ-Si after three-step annealing.

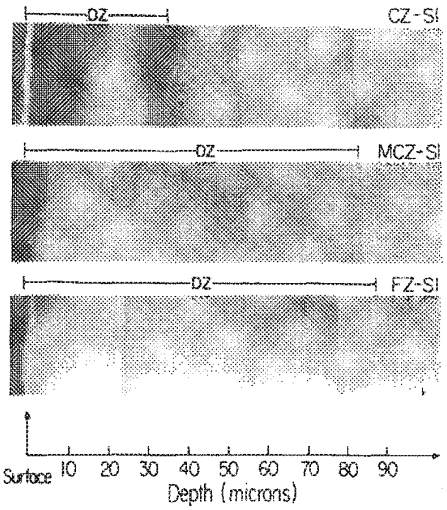


FIG. 3. EBIC signal measured in CZ-Si, MCZ-Si, and FZ-Si after three-step annealing. White regions and high EBIC signal in denuded zone correspond to long lifetime. Dark regions and low EBIC signal represent low lifetime values.

Subsequent studies of lifetime and etch pit profiles carried out after each annealing step revealed that for all three types of crystals the formation of a defect-free zone was not equivalent to the removal of the recombination centers from the surface region. The defect-free zone (adjacent to the surface) was formed during the first high-temperature annealing step; after this step, only minor changes in the lifetime were observed. The subsequent lower-temperature steps caused an increase in the bulk etch pit concentration and significantly enhanced the minority carrier lifetime within the denuded zone. The results are summarized in Tables II and III.

Comparison of data in Fig. 2 and Tables I and II shows that although the lifetime increase in the defect-free region is similar for all three types of samples, the defect patterns are different. Thus, the thickness of the defect-free region in CZ-Si is 2.5–3 times smaller than the one found in MCZ-Si and FZ-Si. Also, the bulk defect density in CZ-Si is about four orders of magnitude higher than in the crystals with low (MCZ-Si) or virtually zero (FZ-Si) oxygen content.

These differences became most pronounced when the high-temperature annealing was carried out in oxidizing ambients. Figure 4 presents a preferentially etched cross section of CZ-Si annealed: (A) in dry O_2, and (B) in $O_2 + HCl$. Pronounced denuded zones and similar defect patterns were obtained in both ambients. Figure 5 presents a preferentially

Downloaded 26 May 2009 to 146.186.238.7. Redistribution subject to AIP license or copyright; see http://jap.aip.org/jap/copyright.jsp

SIONYX1403000036.0135

SAMSUNG EX. 1002 - 419/4148

TABLE I. Minority carrier lifetime values in as-grown and annealed Si wafers.

Measuring technique	Lifetime (μs)								
	As-grown			Annealed					
				Surface			Bulk		
	CZ	MCZ	FZ	CZ	MCZ	FZ	CZ	MCZ	FZ
p–n junction recovery	35	58	90	1230	870	985	5	20	10
MOS capacitor transient	20	70	110	1180	920	1050	5	35	14
Photoconductivity decay	25	30	115	1250	850	1010	8	10	5

etched cross section of the FZ-Si annealed (A) in dry O_2 and (B) in O_2 + HCl. The behavior of MCZ-Si was very similar to that of FZ-Si. It is apparent that MCZ-Si and FZ-Si behave differently in oxidizing ambients than CZ-Si. Lifetime measurements showed that in FZ-Si the lifetime increase in the defect region took place in the case of O_2 + HCl, while no significant lifetime increase was observed in the dry O_2 ambient. It can be thus concluded that dry O_2 ambient suppressed the intrinsic gettering process in oxygen-free silicon crystals. On the other hand, annealing in O_2 + HCl ambient produced a well-defined denuded zone characterized by high values of lifetime in both oxygen-free FZ-Si and in oxygen-rich CZ-Si.

The effects of ambients on the denuded zone width and on the density of surface etch pits are summarized in Figs. 6 and 7, respectively. Surface defects were observed by preferential etching of the surface after stripping any layer of nitride or oxide grown during annealing. It is seen that the best results, i.e., the widest denuded zone and the lowest density of surface defects is obtained in an O_2 + HCl ambient. The largest differences between CZ-Si and FZ-Si in denuded zone widths were found after annealing in O_2, while the largest difference in surface defect density was observed in an N_2 ambient. The results of Figs. 6 and 7 indicate an interesting inverse relationship between denuded zone formation and surface defect concentration. The ambient which leads to the formation of a wide denuded zone simultaneously yields a high-quality surface with a low defect concentration.

During the course of the present studies it was found that the FZ-Si doped with nitrogen exhibited different properties than ordinary FZ-Si. Figure 8 presents preferentially etched cross sections of the FZ-Si(N) which was subjected to the three-step annealing. Various ambients were employed during the high-temperature annealing step. None of the cross sections shown in Fig. 8 reveals the characteristic pattern consisting of a denuded zone and bulk defects. Furthermore, the lifetime measurements did not reveal any lifetime enhancement in the vicinity of the surface. It was thus concluded that the presence of the nitrogen dopant suppressed the ability to achieve intrinsic gettering in float-zone silicon.

IV. DISCUSSION: KINETIC MODEL OF INTRINSIC GETTERING

An overall intrinsic gettering process involves two distinct stages: (1) the formation of defect complexes in the bulk together with the formation of a denuded zone (defect free) in the vicinity of the surface; and (2) the gettering of metal impurities (acting as recombination centers) by the defect complexes in the bulk. The driving force for stage (1) is the supersaturation of the crystal with point defects controlling intrinsic gettering [i.e., the difference, ΔC, between the actual concentration of the defects $C(x,t)$ and the equilibrium concentration C_0 at a given temperature]. In general, a certain critical defect supersaturation ΔC_{cr} may be required to initiate the precipitation. In the present treatment, we consider the simplest case of $\Delta C_{cr} \simeq 0$. At temperature high enough to ensure fast defect diffusion, the condition $\Delta C > 0$ (lattice supersaturated with defects) can lead to precipitation of defects or to growth of precipitates already present. On the other hand, if $\Delta C < 0$ (lattice undersaturated with defects) new precipitates will not be formed, and the existing ones will dissolve.

TABLE II. Bulk defects concentration in Si following each step.

Crystal	In as-grown state	Bulk etch pit concentration (cm^{-3}) after annealing		
		After 1st step	After 2nd step	After 3rd step
CZ-Si	0	1×10^4	$(3-5)\times10^{10}$	$(3–5)\times10^{10}$
MCZ-Si	0	5×10^5	5×10^6	1×10^7
FZ-Si	0	4×10^6	$(2–3)\times10^7$	3×10^7

TABLE III. Minority-carrier lifetime in Si following each annealing step.

Crystal	In as-grown state	Generation lifetime(μs) after annealing					
		After 1st step		After 2nd step		After 3rd step	
		Bulk	Surface	Bulk	Surface	Bulk	Surface
CZ-Si	25	70	100	20	980	10	1100
MCZ-Si	75	70	210	25	850	35	920
FZ-Si	110	100	280	15	1000	15	1050

Downloaded 26 May 2009 to 146.186.238.7. Redistribution subject to AIP license or copyright; see http://jap.aip.org/jap/copyright.jsp

SIONYX1403000036.0136

SAMSUNG EX. 1002 - 420/4148

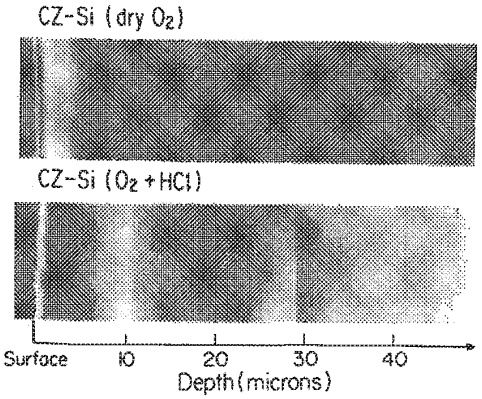


FIG. 4. Preferentially etched cross section of CZ-Si after three-step annealing with the high-temperature step carried out in dry O_2, and in O_2 + HCl, respectively.

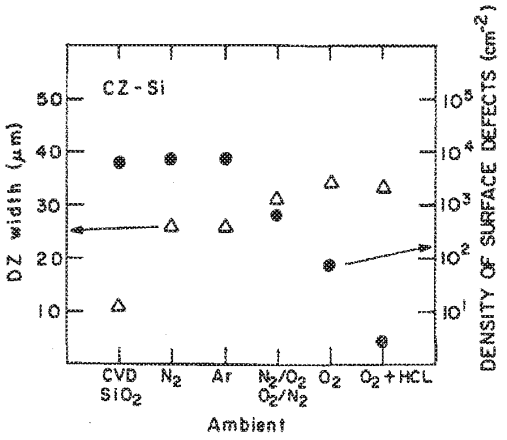


FIG. 6. Denuded zone width, surface defect density, and ambient in the case of CZ-Si.

For a denuded zone to form, ΔC must be negative in the region beneath the surface. On the other hand, ΔC should be positive in the bulk in order to achieve bulk complexes. A defect concentration profile satisfying these requirements is shown in Fig. 9. The corresponding defect transport processes are illustrated schematically in Fig. 10. These processes involve (1) extraction (or injection) of defects at the silicon surface (or interface): this process is controlled by the annealing ambient; (2) out-diffusion (or in-diffusion) of defects from (toward) the bulk; (3) dissolution of precipitates in the vicinity of the surface; (4) formation of precipitates in the bulk.

On the basis of the following experimental results it appears that silicon interstitials are the primary point defects involved in the intrinsic gettering process in oxygen-free silicon.

(a) Dry O_2 ambient present during high-temperature annealing inhibits the formation of a denuded zone in FZ-Si (and also in MCZ-Si). Dry oxidation is believed to cause injection of Si interstitials[12] thus preventing surface region depletion required for the denuded zone.

(b) O_2 + HCl ambient results in excellent surface region denuding in FZ-Si; this ambient is believed to cause extraction of Si interstitials (or injection of Si vacancies)[13] which is required for denuding.

(c) As seen in the accompanying paper,[5] the gettering centers in oxygen-free Si were found to involve silicon interstitials (interstitial type of dislocation loops and silicide precipitates). Our kinetic model is thus based on silicon interstitials and, unless otherwise stated, $C(x,t)$ will denote the concentration of silicon interstitials in the treatment that follows.

As pointed out above, the intrinsic gettering process is finalized when "lifetime killing" metallic impurities are removed from the denuded zone and form complexes with the immobile bulk gettering centers. Employing electron microscopy and dispersive x-ray spectroscopy studies, discussed in the accompanying paper,[5] "butterfly"-shaped intrinsic gettering centers were identified in FZ-Si consisting of interstitial-type dislocation loops (0.1–0.7 μm in diame-

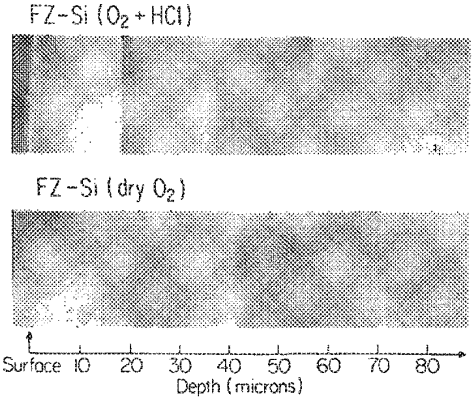


FIG. 5. Preferentially etched cross section of FZ-Si subjected to three-step annealing with the first, high-temperature step carried out in O_2 + HCl and in dry O_2, respectively.

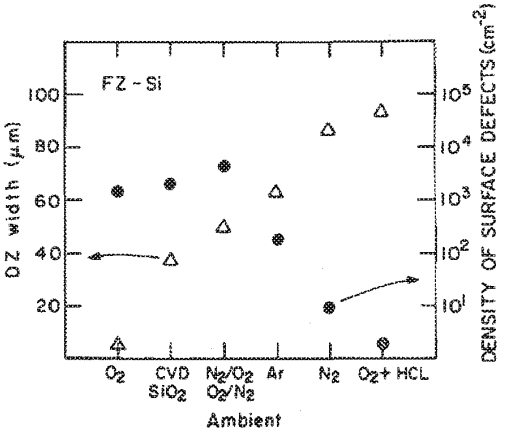


FIG. 7. Denuded zone width, surface defect density, and ambient in the case of FZ-Si.

Downloaded 26 May 2009 to 146.186.238.7. Redistribution subject to AIP license or copyright; see http://jap.aip.org/jap/copyright.jsp

SIONYX1403000036.0137

SAMSUNG EX. 1002 - 421/4148

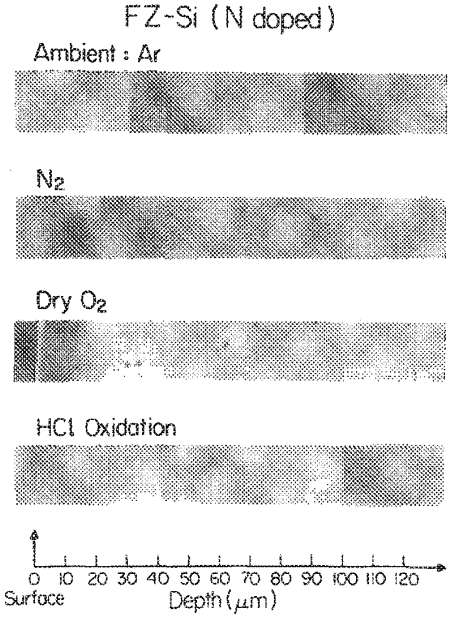


FIG. 8. Preferentially etched cross section of nitrogen-doped FZ-Si after three-step annealing. The high-temperature step was carried out in various ambients.

ter) with a high density of microprecipitates containing metallic constituents (primarily Cu and occasionally Ni) inside and/or on the dislocation cores. For the present discussion it is of key importance to point out that the gettering centers can be formed only in the regions where $\Delta C > 0$, i.e., where the lattice is supersaturated with silicon interstitials. Accordingly, the distribution of gettering centers will be determined by the processes outlined in conjunction with Fig. 10. The defects concentration profile of annealed samples can be found by solving the kinetic equation containing diffusion $D(\partial^2 C/\partial x^2)$ and precipitation $(\partial C/\partial t)p$ terms:

$$\frac{\partial C}{\partial t} = D\left(\frac{\partial^2 C}{\partial x^2}\right) - \left(\frac{\partial C}{\partial t}\right)p, \tag{1}$$

where D is the diffusivity of silicon interstitials. In treating the precipitation term $(\partial C/\partial t)p$ we consider two models presented in Refs. 14 and 15, respectively. The model of Ref.

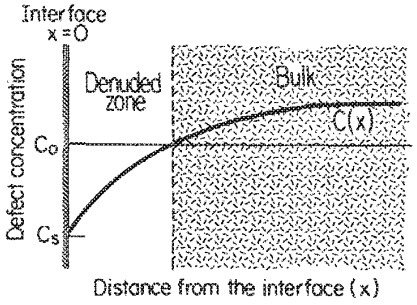


FIG. 9. Defect concentration profile in intrinsic gettering.

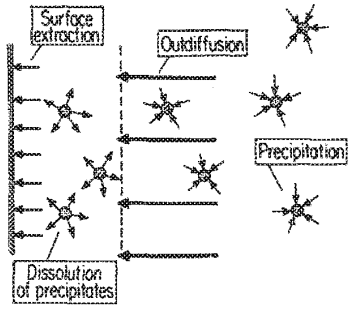


FIG. 10. Schematic representation of kinetic processes occurring in surface region when Si wafer is subjected to high-temperature annealing.

14 describes the capture of diffusing species by precipitates present at constant density. The excess defect concentration $C = C_i - C_0$ decays exponentially with a time constant τ. According to this model

$$\left(\frac{\partial C}{\partial t}\right)p = -(C_i - C_0)\tau^{-1}\exp\left(-\frac{t}{\tau}\right), \tag{2}$$

where C_i is constant and equal to the concentration of defects in the wafer prior to annealing. The other precipitation model, discussed in Ref. 15, assumes defect diffusion inside a sphere with its center located at the precipitate. This model yields

$$\left(\frac{\partial C}{\partial t}\right)p = -\frac{3}{2}\frac{[2D(C_i - C_0)]^{3/2}}{C_p^{1/2}r^3 t^{1/2}}, \tag{3}$$

where C_p is the defect concentration inside the precipitate with the shape of a sphere having a radius r.

We assume that, prior to annealing, interstitials are distributed uniformly in the wafer and that their concentration is C_i (after Refs. 16 and 17, we assume $C_i = 10^{16}$ cm^{-3}). The equilibrium concentration of interstitials at 1170 °C, $C_0 = 10^{14}$ cm^{-3} is adopted after Ref. 16. The diffusivity of silicon interstitials $D = 2\times10^{-5}$ cm^2/s at 1170 °C is taken from Ref. 17, where it was obtained under conditions similar to the present experiments. Injection or extraction of defects at the surface is treated as a process which maintains constant defect concentration at the interface $C(0,t) = C_s$. In an O_2 + HCl ambient extraction of interstitials takes place via injection of silicon vacancies; we thus approximate this process assuming $C_s \ll C_0$. On the other hand, annealing in dry O_2 causes injection of silicon interstitials. We assume after Refs. 18 and 19 that the corresponding C_s value is about 5×10^{14} cm^{-3}, i.e., it is larger than C_0.

As discussed in the Appendix, a distribution of defects in the initial stages of the annealing cycle is determined primarily by a diffusion process, with precipitation playing a secondary role. Thus, the solution of Eqs. (1) and (2) or Eqs. (1) and (3) can be approximated by a simple diffusion term:

$$C(x,t) = A\,\mathrm{erf}(x\sqrt{2DT}) + B\,\mathrm{erfc}(x\sqrt{2DT}), \tag{4}$$

where A and B are constants determined by values of C_s and C_i.

As pointed out above, the concentration profile $C(x,t)$ as given by Eq. (4) does not include complexing of defects

Downloaded 26 May 2009 to 146.186.238.7. Redistribution subject to AIP license or copyright; see http://jap.aip.org/jap/copyright.jsp

SIONYX1403000036.0138

SAMSUNG EX. 1002 - 422/4148

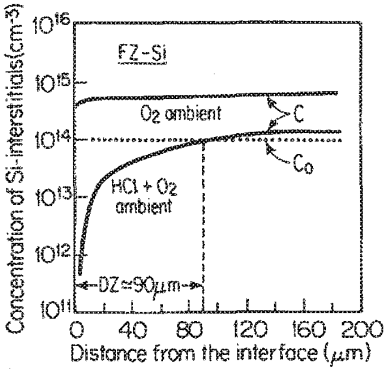


FIG. 11. Theoretical profile of Si interstitial concentration vs depth in FZ-Si annealed in various oxidizing ambients.

into precipitates. However, precipitation will not take place in the surface region depleted with defects, but it will occur in the bulk where $C(x,t)$ exceeds C_0. Accordingly, we can estimate the denuded zone width as the value of x corresponding to $\Delta C = 0$ (see Fig. 9).

The profiles of the interstitials shown in Fig. 11 were calculated for annealing in O_2 + HCl and in dry O_2, taking $C_s \to 0$ and $C_s = 5\times10^{14}$ cm^{-3}, respectively. It is seen that conditions corresponding to an O_2 + HCl ambient yield $C < C_0$ in a region extending about 90 μm beneath the surface. For dry O_2 the concentration of interstitials exceeds C_0 in the entire volume of the sample. Accordingly, precipitates will be formed in the entire sample, and a denuded zone will not be formed. It can be seen that there is a good agreement between the calculated defect profiles of Fig. 11 and the depth profiles of the etch pit density (EPD) of FZ-Si annealed in dry O_2 and in O_2 + HCl ambients shown in Fig. 12. (Figure 11 must also be compared with Fig. 5.) For the O_2 + HCl ambient the EDP is essentially zero within about 100 μm from the surface. On the other hand, high EPD is generated throughout the sample upon annealing of FZ-Si in dry O_2.

The present kinetic model was also applied to standard CZ-Si with high oxygen interstitial content. Equations (1)–(4) were used to calculate the concentration profile of interstitial oxygen employing the following parameters[20]: diffusivity of oxygen at 1170 °C, $D = 8\times10^{-9}$ cm^2/s; initial oxygen concentration, $C_i = 1.5\times10^{18}$ cm^{-3}; equilibrium oxygen concentration at 1170 °C, $C_0 = 7\times10^{17}$ cm^{-3}; it was assumed that an effective extraction of oxygen takes place at the interface, i.e., $C_s \ll C_0$. The calculated defect profile is shown in Fig. 13; the denuded zone width of about 30 μm agrees well with the typical width of the defect-free zone in CZ-Si (see Fig. 3).

The above results demonstrate the feasibility of predicting the denuded zone width in a rather straightforward manner, on the basis of rather simple assumptions. The concentration profiles obtained from these calculations depend on the boundary conditions employed, and particularly on the concentration of out-diffusing defects at the interface. In turn, this condition depends on the ambient employed. The discussed cases of dry O_2 and O_2 + HCl ambients during annealing of FZ-Si are extreme examples of such dependence. It can be expected that other ambients will also affect defect out-diffusion. They will, thus, affect the intrinsic gettering process, consistent with the results in Figs. 5 and 6.

The intrinsic gettering process discussed above depends in a critical way on the initial concentration of defects C_i. The exact relationship between the concentration of interstitials and the crystal growth parameters is not sufficiently understood. The quantitative control of C_i is thus a very difficult task. It can be, however, expected that commerical FZ-Si crystals grown under fast growth rate conditions (fast growth eliminates swirl defect formation) contain a rather large number of native point defects, and particularly silicon interstitials.[21–23] According to the present model, intrinsic gettering in oxygen-free Si is finalized with the capture of metal impurities by the precipitates of silicon interstitials. As a result, metal silicides are formed, surrounded by, and/or attached to interstitial-type dislocations (further details of this process are discussed in the accompanying paper).

The inhibition of intrinsic gettering and of the formation of a denuded zone in FZ-Si doped with nitrogen (see Fig. 8) is not understood at present. One can speculate that such behavior originates in a lower concentration of "as-grown" silicon interstitials, or in different heterogeneous, nitrogen-related precipitation mechanisms.

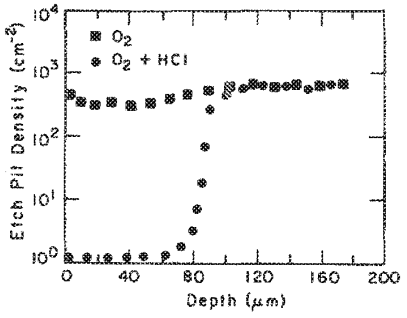


FIG. 12. Experimental data showing etch pit density vs depth profile in FZ-Si annealed in various oxidizing ambients.

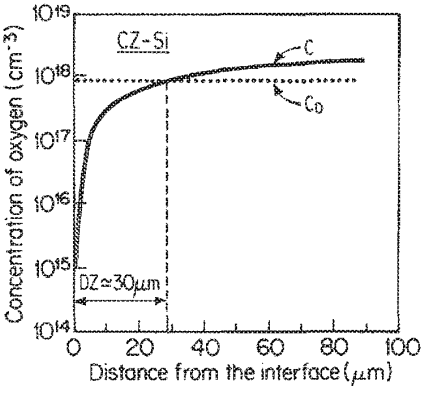


FIG. 13. Theoretical profile of oxygen interstitial concentration vs depth in CZ-Si subjected to three-step annealing.

Downloaded 26 May 2009 to 146.186.238.7. Redistribution subject to AIP license or copyright; see http://jap.aip.org/jap/copyright.jsp

SIONYX1403000041.0001

SAMSUNG EX. 1002 - 423/4148

V. SUMMARY

We present basic experimental characteristics of a new intrinsic gettering process which can be realized in Si crystals with virtually zero oxygen concentration. The process is driven by diffusion and precipitation of silicon interstitials. This new intrinsic gettering process involves Si interstitials and is markedly different from the standard oxygen-related gettering in CZ-Si. The new gettering mechanism depends critically on the surface reactions during high-temperature annealing, which can be effectively controlled by the ambient. The selection of the proper ambient assures effective intrinsic gettering, formation of a wide denuded zone, and a low density of surface defects.

A simple theoretical model describing the kinetics of the process is proposed. It is demonstrated that this model, based on a one-dimensional diffusion equation, accounts for the experimental results and makes possible calculations of the denuded zone width with satisfactory accuracy.

By means of electron microscopy and dispersive x-ray spectroscopy, we identified the intrinsic gettering centers in FZ-Si as "butterfly"-shaped defects consisting of interstitial-type dislocation loops and microprecipitates containing metal silicides. These findings are discussed in the accompanying paper.

ACKNOWLEDGMENT

The authors are grateful to the Semiconductor Research Corporation for financial support.

APPENDIX

In order to demonstrate that out-diffusion is the dominant kinetic process controlling the defect distribution, one must solve Eq. (1) with a realistically defined term $(\partial C/\partial t)p$. In the course of the study two different models describing $(\partial C/\partial t)p$ were employed:

Model A[14]:

$$\left(\frac{\partial C}{\partial t}\right)p = -(C_1 - C_0)\tau^{-1}\exp\left(\frac{-t}{\tau}\right), \tag{A1}$$

where C_1 and C_0 are constants describing initial defect concentration [$C_1 = C(x,t=0)$] and equilibrium defect concentration, respectively. τ is a time constant of the precipitation process.

Model B[15]:

$$\left(\frac{\partial C}{\partial t}\right)p = -\frac{3}{2}\left(\frac{2C_2}{3}\right)^{3/2} t^{1/2}, \tag{A2}$$

where C_2 is a constant which depends on diffusion coefficient, initial and equilibrium defect concentration, precipitate radii, and their density.

Equation (1) was solved for the boundary conditions:

$$C(x,t=0) = C_i = \text{const},$$
$$C(x=0,t) = C_s = \text{const}. \tag{A3}$$

The following solutions were obtained:

For the case A:

$$C(x,t) = A_1 + A_2 + A_3,$$
$$A_1 = (2C_i - C_0)\operatorname{erfc}(x2\sqrt{Dt}),$$
$$A_2 = (C_0 - C_i)\exp(-t/\tau), \tag{A4}$$
$$A_3 = \operatorname{Re}[(C_i - C_0)/2]\exp(-t/\tau) \times [\exp(-ix/\sqrt{Dt})]\operatorname{erfc}(x/2\sqrt{Dt} - ix\sqrt{Dt}) + \exp(ix\sqrt{Dt})\operatorname{erfc}(x/2\sqrt{Dt}).$$

For the case B:

$$C(x,t) = B_1 + B_2 + B_3,$$
$$B_1 = C_i - 3/2(2C_2/3)^{3/2}\operatorname{erfc}(x2\sqrt{Dt}),$$
$$B_2 = 3/2(2C_2/3)^{3/2}t^{1/2}, \tag{A5}$$
$$B_3 = 5/2(4t)^{3/2}i^3\operatorname{erfc}(x/2\sqrt{Dt}).$$

However, for the realistic boundary conditions such as (1) annealing time 6 h, annealing temperature 1170 °cm, (2) precipitate size less than 1 μm, (3) C_i of the order of 10^{14}–10^{18} cm^{-3}, (4) $C_s \sim 10^{-2} C_0$, (5) diffusion coefficient $D > 10^{-10}$ cm^{-2}/s, the following relationship holds:

$$A_1, B_1 > B_2 > A_3, B_3. \tag{A6}$$

Terms A_1 and B_1 describe pure out-diffusion.

[1] J. R. Monkowski, Solid State Technol. 24, 44 (1981).
[2] See, for example, Materials Research Society Symposia Proceedings, Vol. 36, *Impurity Diffusion and Gettering in Silicon*, edited by R. B. Fair, C. W. Pearce, and J. Washburn (Materials Research Society, Pittsburgh, PA, 1985).
[3] W. K. Tice and T. Y. Tan, Appl. Phys. Lett. 28, 564 (1976).
[4] K. Nauka, J. Lagowski, H. C. Gatos, and C.-J. Li, Appl. Phys. Lett. 46, 673 (1985).
[5] O. Ueda, K. Nauka, J. Lagowski, and H. C. Gatos, J. Appl. Phys. 60, 622 (1986).
[6] E. R. Weber, in Materials Research Society Symposia Proceedings, Vol. 36 *Impurity Diffusion and Gettering in Silicon*, edited by R. B. Fair, D. W. Pearce, and J. Washburn (Materials Research Society, Pittsburgh, PA, 1985), p. 3.
[7] J. O. Borland, *Electrochemical Society Extended Abstracts Series*, Vol. 83-1 (The Electrochemical Society, Pennington, NJ, 1983), p. 421.
[8] R. B. Heimann, in *Crystals* (Springer, Berlin, 1982), Vol. 8, p. 173.
[9] M. Zerbst, Z. Angew. Phys. 22, 30 (1966).
[10] H. J. Kuno, IEEE Trans. Electron Devices ED-11, 8 (1964).
[11] K. Seeger, *Semiconductor Physics* (Springer, Berlin, 1985).
[12] R. B. Fair, J. Electrochem. Soc. 128, 1360 (1981).
[13] H. Shirai, Jpn. J. Appl. Phys. 15, 1 (1976).
[14] F. S. Ham, J. Phys. Chem. Solids 6, 335 (1958).
[15] P. G. Shewmon, *Diffusion in Solids* (McGraw-Hill, New York, 1963), Chaps. 1–4.
[16] U. Gösele, *Electrochemical Society Proceedings Series*, Vol. 83-4 (The Electrochemical Society, Pennington, NJ, 1983), p. 17.
[17] A. J. R. de Kock, P. J. Roksnoer, and P. G. T. Boonen, J. Cryst. Growth 30, 279 (1975).
[18] A. M. R. Lin, R. D. Dutton, D. A. Antoniadis, and W. A. Tiller, J. Electrochem. Soc. 128, 1121 (1981).
[19] D. A. Antoniadis and I. Moskowitz, J. Appl. Phys. 53, 6788 (1982).
[20] J. C. Mikkelsen, in Materials Research Society Proceedings, Vol. 36, *Impurity Diffusion and Gettering in Silicon*, edited by R. B. Fair, C. W. Pearce, and J. Washburn (Materials Research Society, Pittsburgh, PA, 1985), p. 205.
[21] A. J. M. G. Van Run, J. Cryst. Growth 53, 441 (1981); 54, 195 (1981).
[22] R. J. Roksnoer and M. M. B. Van der Boom, J. Cryst. Growth 53, 563 (1981).
[23] N. H. Fletcher, J. Cryst. Growth 35, 39 (1976).
[24] T. Abe, H. Harada, and J. Chikawa, in Materials Research Society Proceedings, Vol. 14, *Defects in Semiconductors II*, edited by S. Mahajan and J. W. Corbett (Materials Research Society, Pennington, NJ, 1983), p. 1.

Downloaded 26 May 2009 to 146.186.238.7. Redistribution subject to AIP license or copyright; see http://jap.aip.org/jap/copyright.jsp

SIONYX1403000041.0002

SAMSUNG EX. 1002 - 424/4148

Semiconductor laser crystallization of a-Si:H

B. K. Nayak, J. McLeskey, A. Selvan, B. Eaton and M. C. Gupta[a)]
Applied Research Center, Old Dominion University, Newport News, Virginia 23606
R. Romero and G. Ganguly, BP Solar, Toano, Virginia 23168

ABSTRACT

Results of semiconductor laser crystallization of a-Si:H on transparent conducting fluoride doped tin oxide coated glass are discussed. A-Si:H films were prepared by plasma enhanced chemical vapor deposition. Laser crystallized films of a-Si:H were characterized by X-ray diffraction and optical microscopy. Semiconductor laser crystallization process as compared to well-established excimer laser offers low cost large area technology for solar cell, display and other applications. Longer wavelength of diode lasers (805 nm) allows light to penetrate deeper in the films for crystallization of thicker films required for enhanced light absorption.

Keywords: a-Si, a-Si:H, Laser crystallization, Diode laser, Solar cells, Semiconductor laser.

1. INTRODUCTION

Amorphous silicon is deposited on inexpensive substrates like glass or plastic for mass production of large area solar cells and display applications. For photovoltaic applications it is often desirable to produce cells with higher film thickness for better light trapping[1]. The requirement of low temperature deposition on these substrates results in amorphous films. However, due to the amorphous nature of the deposited films the device performance deteriorates due to carrier recombination. To avoid such recombination and at the same time keeping higher film thickness for significant light absorption necessitates a post processing. Large grain sizes are required, in case of thin film transistors (TFT's)[2] as well as for photovoltaic applications for improved performance[3]. Laser Crystallization is an attractive technique to produce device quality poly-silicon for photovoltaic and display applications[4]. Excimer laser crystallization is a well-established technology for producing poly-Si on glass. However, due to the very high absorption of excimer laser wavelength (248-316 nm) in a-Si:H, only a very thin layer (sub micron) could be crystallized. Although, some improvements in excimer laser technology have been reported to achieve crystallization of thicker films and/or large grain sizes, but they are not practical[5] due to their high processing cost.

Semiconductor lasers operating at near infrared wavelength (805 nm), on the other hand provide an opportunity to crystallize thicker films due to higher penetration of light in to the film at this wavelength. In addition to this, these lasers are very compact for large area robotic controlled applications and relatively lower cost.

2. EXPERIMENTAL

The amorphous silicon layers were deposited on plane glass and TCO (Fluoride doped tin oxide: SnO_2:F) coated glass, using low temperature Plasma Enhanced Chemical Vapor Deposition (PECVD) technique. The hydrogenated amorphous silicon (a-Si:H) films were deposited at a rate of 1 A°/s in hydrogen diluted silane environment at about 200° C. The samples were crystallized using a highly efficient laser diode bar from Nuvonyx (model PB-40) with maximum CW power of 50 Watts, conversion efficiency 50%, pulse width in the range of 100 µs – CW, pulse repetition rate of 0-2 KHz, operating at central wavelength of 805 nm. The laser was operated in pulse mode with repetition frequency of 1500 Hz and pulse width of 300 µs at the average power of 45 W. The samples were placed on a high precision computer controlled X-Y stage with a stepper resolution of 100 nm. The laser beam was focused on the sample through a plano-convex lens of 15 mm focal length. The spot size on the sample surface was approximately 1 mm x 80 µm. The photograph of experimental setup is shown in fig. 1. The sample was scanned at

[a)] Electronic mail: mgupta@odu.edu ; phone: 757-269-5645; fax: 757-269-5644

Photon Processing in Microelectronics and Photonics II, A. Piqué, K. Sugioka, P. R. Herman, J. Fieret, F. G. Bachmann, J. J. Dubowski, W. Hoving, K. Washio, D. B. Geohegan, F. Träger, K. Murakami, Editors, Proceedings of SPIE Vol. 4977 (2003) © 2003 SPIE · 0277-786X/03/$15.00

Downloaded from SPIE Digital Library on 18 Oct 2009 to 16.82.15.178. Terms of Use: http://spiedl.org/terms

SIONYX1403000041.0003

SAMSUNG EX. 1002 - 425/4148

a speed of 2.5 mm/s. The linear translation between two consecutive laser shots was approximately 1.67 μm. Crystallization was performed at room temperature and in air. The laser fluence was ~17 J/cm^2. Note here that there was a necessity to have very high input laser fluence because of relatively lower absorption at 805 nm. A 2.54 × 2.54 cm^2 area of a-Si:H film was crystallized by scanning the sample under the laser beam.

3. RESULTS

The optical microscope picture of laser-crystallized surface is shown in Fig. 2. A clear distinction between laser treated to untreated region is apparent from the figure. X-Ray diffraction (XRD) was carried out on the laser treated/untreated samples to study the structural modification induced by laser treatment. The Rigaku Miniflex 2005 X-ray diffractometer with Cr target was used for our experiment. Fig. 3. Shows the X-ray diffraction results, before and after laser treatment of the sample. Fig. 3 (a) shows the X-ray diffraction result for a-Si:H film (2 μm thick) deposited on glass substrate. An expected broad amorphous peak was observed. However, after laser treatment, three peaks corresponding to (111), (311) and a (331) could be observed in Fig. 3 (b), confirming the crystallization of a-Si:H on glass. The (111) orientation was observed to be predominant peak over both (311) and (331) crystal orientations. Some samples of a-Si:H of 0.5 μm thickness were deposited on SnO2:F coated glass for laser crystallization. After crystallization (220) peak was observed in addition to (111) and (311) peaks. However, (331) peak was absent. The light absorption of the sample at 805 nm wavelength was estimated from spectrophotometeric measurements and was compared with already published literature values for both SnO2:F glass[6] and a-Si[7]. It was found that there was not a very significant amount of absorption at this wavelength. The measurements for 500 nm a-Si:H film on 950 nm SnO_2:F coated glass substrate showed reflection value of 43.5% and, transmission as 36 %. So absorption and scattering, amounts to only 20.5%. With average power of 45 watt laser output no crystallization was observed when tried to crystallize 500 nm thick a-Si:H film deposited on glass. So SnO_2:F layer play a critical role in crystallization process. In order to estimate the grain size of the sample after laser treatment, Secco etching (solution: 3 parts of H_2O, 2 parts of HF 50%, 1 part 0.15 mol solution of $K_2Cr_2O_7$ in H_2O) was applied to the samples. Grains of the order of 5 μm in size were observed from AFM images taken on Secco etched samples[8]. Raman back scattering experiments were carried out on laser treated samples and a sharp peak at 522 cm-1 further confirmed the crystallization.. From the Raman spectrum the crystalline fraction of the laser treated sample were calculated to be 87 %[8].

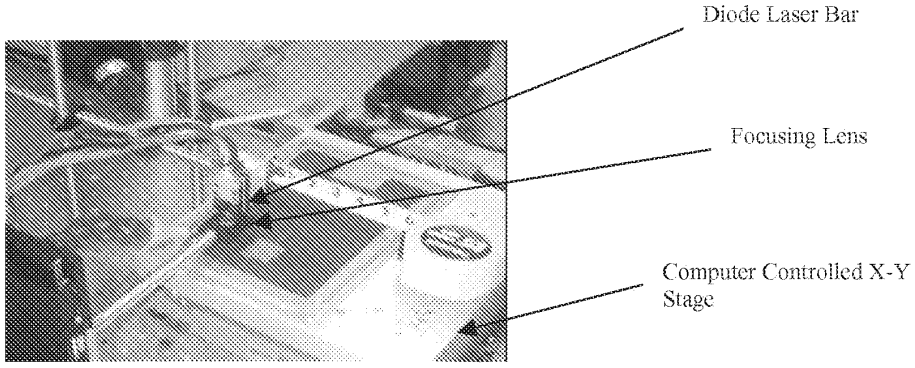


Fig. 1. Photograph showing diode laser crystallization set up

Downloaded from SPIE Digital Library on 15 Oct 2009 to 16.82.15.178. Terms of Use: http://spiedl.org/terms

SIONYX1403000041.0004

SAMSUNG EX. 1002 - 426/4148

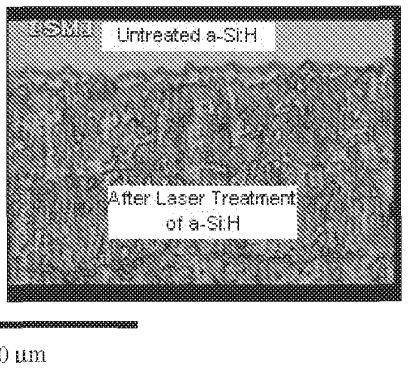


Fig. 2. The optical micrograph of diode laser crystallized a-Si:H on SnO_2:F coated glass

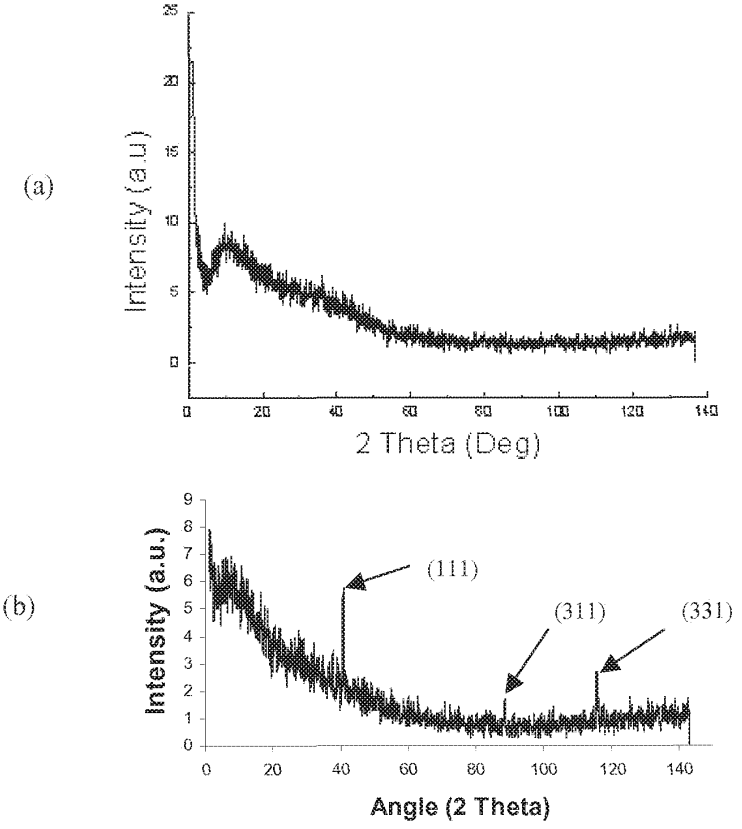


Fig. 3. The X-Ray diffraction results for (a) a-Si:H film (2 µm thick) deposited on glass substrate (b) after laser treatment. (111), (311) and (331) peaks emerged because of laser treatment.

Downloaded from SPIE Digital Library on 16 Oct 2009 to 16.82.15.178 Terms of Use: http://spiedl.org/terms

SIONYX1403000041.0005

SAMSUNG EX. 1002 - 427/4148

4. CONCLUSIONS

a-Si:H film on conducting tin oxide coated glass and uncoated glass substrate was crystallized using 805 nm wavelength from a compact, low cost semiconductor laser. X-ray diffraction and Raman measurements confirm the crystallization of films. Films as thick as 2 μm have been successfully crystallized. The electrical properties of the film and effect of dopants on crystallization process are being investigated.

ACKNOWLEDGEMENTS

We gratefully acknowledge the financial support from the National Science Foundation under the grant ECS-0100243 for this work. We thank James Brok and Brandt Robertson for their help.

REFERENCES

1. G. Andra, J. Bergmann, F. Falk, E. Ose, Thin Solid Films **318**, 42-45 (1998).
2. S. D. Brotherton, J. R. Ayres, M. J. Edwards, C. A. Fisher, C. Glaister, J. P. Gowers, D. J. McCulloch, and M. Trainor, Thin Solid Films **337**, 188 (1999).
3. R. B. Bergmann, Appl. Phys. A **69**, 187 (1999)
4. S. D. Brotherton, D. J. McCulloch, J. B. Clegg, and J. P. Gowers, IEEE Trans. Electron Devices **40**, 407 (1993).
5. M. Matsumura, Chang-Ho Oh, Thin Solid Films **337**, 123, (1999).
6. K. Von Rottkay, M. Rubin, Mater. Res. Soc. Symp. Proc., **426**, 449 (1996).
7. St. Kanev, Z. Nenova, K. Ivanova, S. Koynov, Solar Energy Materials and Solar Cells, **36**, 277-187, (1995).
8. B. K. Nayak, B. Eaton, J. A. Anna Selvan, J. McLeskey, R. Romero, G. Ganguly and M. C. Gupta[a], Submitted to Appl. Phys. Lett.

[a] Electronic mail: mgupta@odu.edu

Downloaded from SPIE Digital Library on 15 Oct 2009 to 16.82.15.178. Terms of Use: http://spiedl.org/terms

SIONYX1403000041.0006

SAMSUNG EX. 1002 - 428/4148

Appl. Phys. A 80, 1077–1080 (2005)
DOI: 10.1007/s00339-003-2352-9

Applied Physics A
Materials Science & Processing

B.K. NAYAK[1]
B. EATON[1]
J.A.A. SELVAN[1]
J. MCLESKEY[1]
M.C. GUPTA[1,✉]
R. ROMERO[2]
G. GANGULY[2]

Semiconductor laser crystallization of a-Si : H on conducting tin-oxide-coated glass for solar cell and display applications

[1] Applied Research Center, Old Dominion University, Newport News, VA 23606, USA
[2] BP Solar, Toano, VA 23168, USA

Received: 4 March 2003/Accepted: 11 August 2003
Published online: 21 November 2003 • © Springer-Verlag 2003

ABSTRACT Semiconductor laser ($\lambda = 805$ nm) crystallization of hydrogenated amorphous silicon (a-Si : H) deposited on a low-cost fluoride-doped tin-oxide-coated glass substrate is demonstrated. X-ray diffraction confirms that the structure of the polycrystalline silicon thus formed shows (111), (220), and (311) peaks. A sharp Raman peak at 520 cm^{-1} further confirms the crystallization. Atomic force microscope images of a Secco-etched laser-treated sample reveal the granular structure of the poly-Si. Grains as big as ~ 10 times the film thickness are readily obtained and sample as thick as 5000 Å is easily crystallized. The method can be extended to films with a thickness of several microns.

PACS 42.55.Px; 42.62.Cf; 81.05.Ge

1 Introduction

Polycrystalline silicon (poly-Si) is regarded as an attractive material for use in thin film transistors (TFT's) in active-matrix liquid-crystal displays (AMLCD's) [1] and in high-efficiency low-cost thin-film solar cells [2]. However, the requirement of inexpensive large-area amorphous substrates (such as glass) for the fabrication of these devices restricts the deposition to temperatures below 500 °C, at which amorphous films are formed. Amorphous Si-based devices show light-induced instabilities. The majority and minority carrier properties of large-grained silicon films are close to those of monocrystalline silicon [2]. It is thus logical to think of a post-processing technique to convert a-Si to poly-Si. Laser crystallization is considered as an attractive technique for producing large-grained poly-Si through the crystallization of hydrogenated amorphous silicon (a-Si : H) [3]. Solar cell applications require silicon films with a thickness of several microns, in order to have significant solar light absorption [4]. Solar cell applications also require laser techniques that are low cost and suitable for large-area crystallization. Currently, excimer laser crystallization is a well-established technology for producing poly-Si on glass. However, due to the very high absorption of excimer laser wavelengths (248–316 nm) in silicon, only very thin (sub-micron) layers have been crystallized using excimer laser technology. Some improvements in the excimer laser technique have been reported, such as substrate heating [5] and the multiple-shot [6], dual-beam [7], double-pulse [8], super-lateral-growth (SLG) [9], double-pulse and dual-beam [10], bridge [11], and sequential-lateral-crystallization [12] methods. Although larger grains have been grown by the latter three methods, they do not appear to be practical, due to their high processing cost, complicated structure, and time-consuming growth sequence [13].

The longer wavelength of semiconductor lasers ($\lambda = 805$ nm) offers an excellent opportunity to crystallize the several-micron-thick films needed for photovoltaic applications. Also, diode lasers are compact, as required by large-area robotic-controlled applications, and of low cost. However, at the longer wavelengths from diode lasers, absorption in a-Si : H films is smaller than that of excimer lasers. In this paper, successful new results of semiconductor laser crystallization of a-Si : H deposited on fluoride-doped tin oxide (SnO_2 : F)-coated glass are presented. The films were deposited by plasma-enhanced chemical vapor deposition (PECVD). Since a-Si : H thin film solar cells with large film thickness show poor performance because of the high recombination of photo-generated charge carriers, diode laser crystallization technology could be a cost-effective solution for the fabrication of efficient solar cells.

2 Experimental

Amorphous silicon layers of 500-nm thickness were deposited on TCO (fluoride-doped tin oxide: SnO_2 : F)-coated glass, using low-temperature plasma-enhanced chemical vapor deposition (PECVD). The a-Si : H films were deposited at a rate of 1 Å/s in a hydrogen-diluted silane environment at about 200 °C. The samples were crystallized using a highly efficient laser diode bar from Nuvonyx (model PB-40) with a maximum cw power of 50 W, conversion efficiency of 50%, pulse width in the vicinity of 100 µs, pulse repetition rate of 0–2 kHz, and central wavelength of 805 nm. The laser was operated in pulse mode with a repetition frequency of 1500 Hz and a pulse width of 300 µs at an average power of 45 W. The sample was placed on a high-precision computer-controlled x–y stage with a stepper resolution of 100 nm. The laser beam was focused on the sam-

✉ Fax: +1-757-269-5644, E-mail: mgupta@odu.edu

SIONYX1403000041.0007

SAMSUNG EX. 1002 - 429/4148

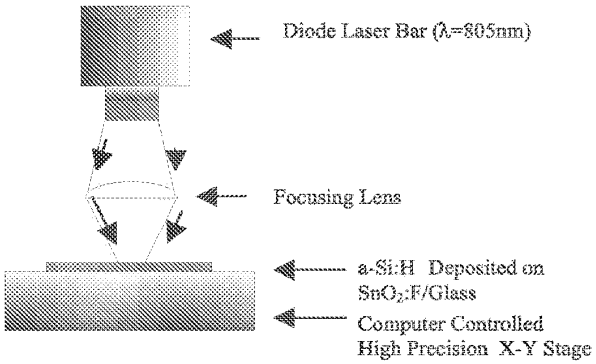


FIGURE 1 Schematic showing diode laser crystallization set up

ple through a plano-convex lens of 15-mm focal length. The spot size on the sample surface was approximately 1 mm × 80 μm. A schematic of the experimental setup is given in Fig. 1. The sample was scanned at a speed of 2.5 mm/s. The linear translation between two consecutive laser shots was approximately 1.67 μm. Crystallization was performed at room temperature and in air. The laser fluence was ~ 17 J/cm^2. A very high input laser fluence was necessary because of the relatively low absorption at 805 nm. Usually, large areas of the sample were crystallized by scanning the sample beneath the laser beam.

X-ray diffraction (XRD) was carried out on the laser-treated/untreated samples to study the structural modifications induced by the laser treatment. A Rigaku Miniflex 2005 X-ray diffractometer with a Cr target was used for our experiment. Raman characterization was performed on the laser-treated samples using a Bio Rad FT Raman instrument in the back-scattering configuration. The light absorption of the sample at 805 nm was estimated from spectrophotometric measurements and was compared with already published literature values for both SnO_2 : F glass [14] and a-Si [15]. The surface morphology was characterized by use of an atomic force microscope (AFM) (Dimension 3100) operating in the tapping mode. In order to reveal the granular structure of the crystallized layer, Secco etching [16] was applied (solution: 3 parts H_2O, 2 parts HF 50%, 1 part 0.15-mol solution of $K_2Cr_2O_7$ in H_2O) for 18 s. By using this treatment, the thin oxide layer formed on top of the treated sample and any fine-grained Si were oxidized by potassium dichromate and etched away, leaving behind only large-grained material. Optical micrographs and scanning electron micrographs were taken for further characterization of the surface morphology. An optical microscope picture of a laser-crystallized surface is shown in Fig. 2. A clear distinction between the laser-treated and untreated regions is apparent. The untreated surface is smooth and does not show any morphological changes. However, after laser crystallization, a highly textured region is observed. The results indicate that the laser-crystallized region may have a mixed phase. The observed changes in the morphology appear to be in the range of a few microns.

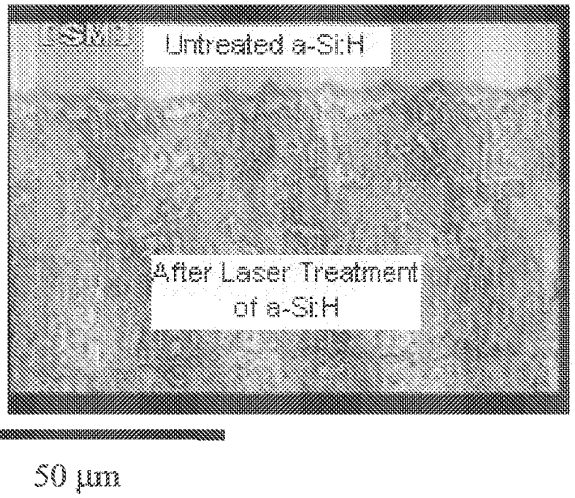


FIGURE 2 Optical micrograph of diode-laser-crystallized a-Si : H on SnO_2 : F-coated glass

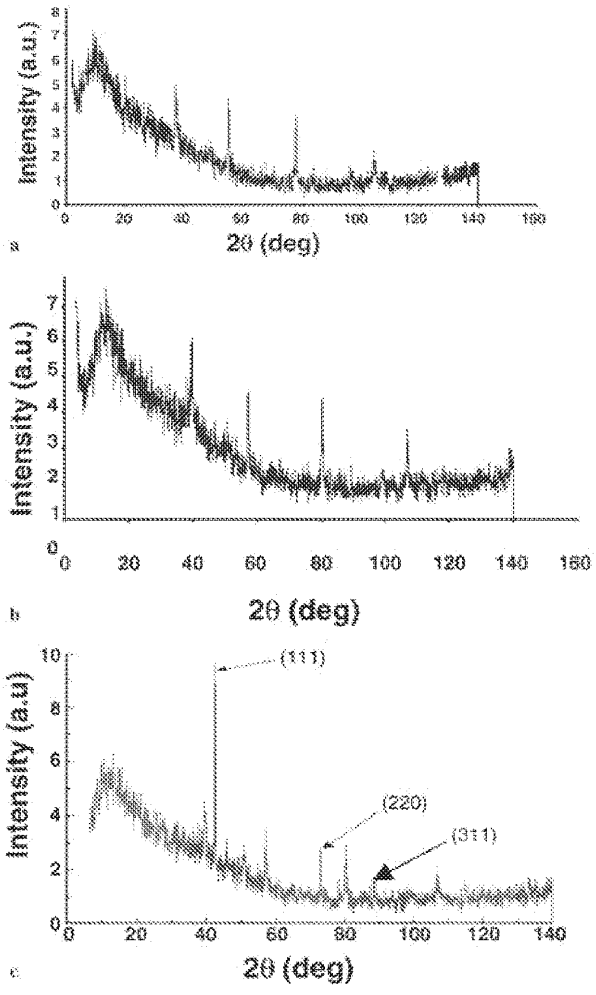


FIGURE 3 X-ray diffraction results for **a** SnO_2 : F glass, **b** a-Si : H deposited on SnO_2 : F glass, and **c** laser-crystallized a-Si : H deposited on SnO_2 : F glass

SIONYX1403000041.0008

SAMSUNG EX. 1002 - 430/4148

3 Results and discussion

Figure 3 shows the X-ray diffraction results, before and after laser treatment of the sample. Figure 3a is the X-ray diffraction spectrum for SnO_2 : F-coated glass. SnO_2 : F is a transparent conductor and serves as an electrical contact for solar cells. The observed X-ray diffraction peaks are due to the polycrystalline nature of SnO_2 : F. Figure 3b is the X-ray diffraction spectrum for a-Si : H deposited on SnO_2 : F glass. The X-ray diffraction spectrum for a-Si : H does not show any peaks. However, after laser treatment, two sharp peaks corresponding to the (111) and (220) orientations, and a very weak peak due to the (311) orientation, were observed (as shown in Fig. 3c), confirming the crystallization of a-Si : H on SnO_2 : F glass. The (111) orientation is the predominant peak, over both the (220) and (311) crystal orientations, which agrees with the well-known Si powder diffraction pattern. For grain-size determination, AFM images were taken. Figure 4a shows the AFM image of an untreated sample and Fig. 4b the image of a treated sample after Secco etching. Grains as big as 5 μm in size were observed.

The absorption in the thin a-Si : H films was determined from spectrophotometric measurements. Absorption was not significant at the wavelength employed. The measurements for a 5000-Å-thick a-Si : H film on a 9500-Å-thick SnO_2 : F-coated glass substrate showed a reflection value of 43.5% and a transmission of 36%. So absorption and scattering amounted to only 20.5%. It is important to mention here that it was only possible to crystallize a-Si : H when deposited on SnO_2 : F-coated glass. With a laser output of 45 W, no crystallization was observed with a-Si : H deposited on glass. Therefore, the SnO_2 : F layer plays a critical role in the crystallization process. The absorptivity at 805 nm for fluoride-doped tin oxide is higher than that for a-Si : H [14]. Also, the strong tempera-

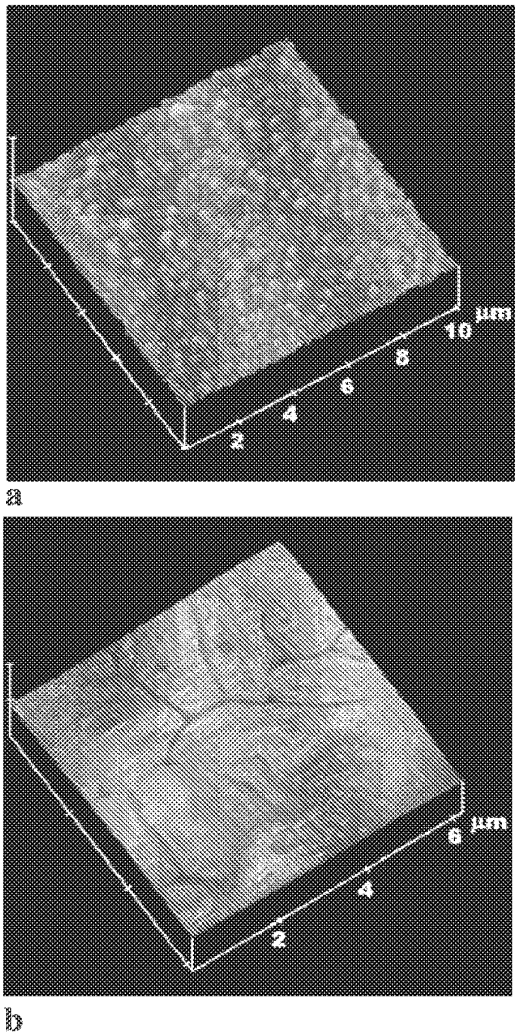


FIGURE 4 AFM image of **a** a-Si : H before laser treatment and **b** laser-crystallized films treated subsequently with Secco etching. A grain size of ~ 5 μm is clearly seen in **b**

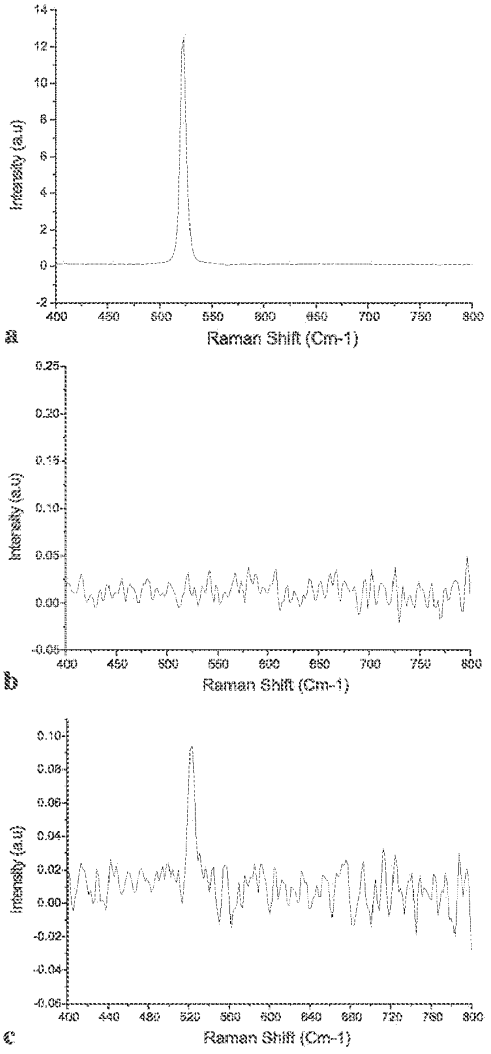


FIGURE 5 Raman spectrum of **a** single-crystal Si, **b** amorphous Si (a-Si : H), and **c** laser-crystallized films

SIONYX1403000041.0009

SAMSUNG EX. 1002 - 431/4148

ture dependence of the Si absorption coefficient enhances the absorption of the diode laser light.

From the optical transmission and reflection measurements, it was found that the absorption coefficient of a-Si : H at 805 nm is about 300 cm^{-1}, which corresponds to a penetration depth of about 33 μm. Since the a-Si : H film thickness was only about 0.5 μm, it is reasonable to assume that a large fraction of the energy was deposited in the thick (~1 μm) SnO_2 : F layer. According to results reported by Rottkay et al. [14], the imaginary part of the refractive index k is 0.02 for SnO_2 : F at 805 nm. This value corresponds to an absorption coefficient ($4\pi k/\lambda$) of 3122 cm^{-1}, about an order of magnitude higher than that of a-Si : H at 805 nm. Since the melting point of SnO_2 : F (~1630 °C) is higher than that of a-Si : H, the former remains solid, whereas a-Si : H reaches its melting point. It was further observed that when the substrate was heated to about 200 °C, we were able to crystallize the a-Si : H film on glass substrate, which was otherwise not possible. We conclude that with a higher laser power, it would be possible to crystallize films of higher thickness even without the presence of the SnO_2 : F layer.

Figure 5 shows a Raman spectrum of a laser-treated sample, along with those for untreated and single-crystal silicon. The spectrum was taken using the BIO RAD FT Raman system with 1.06-μm laser excitation in the back-scattering (180°) mode. The laser spot at the sample was about 1 mm × 1 mm and the power was about 400 mW. The system was calibrated with c-Si, which has a peak at around 521 cm^{-1}, as shown in Fig. 5a. Figure 5b shows the Raman spectrum of a-Si : H. No peak was obtained. However, according to theory, a very broad peak is expected for the untreated sample. The peak appears to have been suppressed by noise at the large wavelength of the excitation laser. Figure 5c shows the Raman spectrum of the laser-treated sample. The occurrence of a very sharp and narrow peak at around 520 cm^{-1} for the laser-treated sample further confirms the crystallization demonstrated by the XRD measurements. The intensity of the Raman peak increased with increasing pulse energy of the laser used for crystallization. For the single-crystal Si wafer, the Raman signal was higher due to the larger penetration depth of the 1.06-μm Nd : YAG laser used for the Raman measurements.

In summary, we have successfully demonstrated the crystallization of a-Si : H films on glass using low-cost and compact semiconductor laser technology. Crystallization was confirmed by X-ray diffraction and Raman measurements and the achieved grain size of several microns was confirmed by AFM techniques.

ACKNOWLEDGEMENTS We gratefully acknowledge financial support for this work from the National Science Foundation under Grant No. ECS-0100243. We thank James Brock and Brandt Robertson for their help.

REFERENCES

1 S.D. Brotherton, J.R. Ayres, M.J. Edwards, C.A. Fisher, C. Glaister, J.P. Gowers, D.J. McCulloch, M. Trainor: Thin Solid Films **337**, 188 (1999)
2 R.B. Bergmann: Appl. Phys. A **69**, 187 (1999)
3 S.D. Brotherton, D.J. McCulloch, J.B. Clegg, J.P. Gowers: IEEE Trans. Electron Devices **40**, 407 (1993)
4 G. Andra, J. Bergmann, F. Falk, E. Ose: Thin Solid Films **318**, 42 (1998)
5 H. Kuriyama, S. Kiyama, S. Noguchi, Y. Kuwano: Jpn. J. Appl. Phys. **30**, 3700 (1991)
6 H. Kuriyama, K. Sano, S. Ishida, Y. Aya, T. Kuwahara, S. Noguchi, S. Kiyama, S. Tsuda, S. Nakano: Mater. Res. Soc. Symp. Proc. **321**, 657 (1994)
7 K. Shimizu, O. Sugiura, M. Matsumura: IEEE Trans. Electron Devices **40**, 112 (1993)
8 R. Ishihara, W.-C. Yeh, T. Hattori, M. Matsumura: Jpn. J. Appl. Phys. **34**, 1759 (1995)
9 J.S. Im, R.S. Sposili: Mater. Res. Soc. Bull. **21**, 39 (1996)
10 R. Ishihara, M. Matsumura: Electron. Lett. **31**, 1956 (1995)
11 D.H. Choi, E. Sadayuki, O. Sugiura, M. Matsumura: Jpn. J. Appl. Phys. **33**, 70 (1994)
12 H.J. Kim, J.S. Im: Mater. Res. Soc. Symp. Proc. **358**, 903 (1995)
13 M. Matsumura, C.-H. Oh: Thin Solid Films **337**, 123, (1999)
14 K. Von Rottkay, M. Rubin: Mater. Res. Soc. Symp. Proc. **426**, 449 (1996)
15 S. Kanev, Z. Nenova, K. Ivanova, S. Koynov: Sol. Energy Mater. Sol. Cells **36**, 277 (1995)
16 F. Secco d'Aragano: J. Electrochem. Soc. **119**, 948 (1972)

SIONYX1403000041.0010

SAMSUNG EX. 1002 - 432/4148

Available online at www.sciencedirect.com
ScienceDirect
Applied Surface Science 253 (2007) 6580–6583
applied surface science
www.elsevier.com/locate/apsusc

Ultrafast-laser-assisted chemical restructuring of silicon and germanium surfaces

Barada K. Nayak [a], Mool C. Gupta [a,*], Kurt W. Kolasinski [b]

[a] Department of Electrical & Computer Engineering, University of Virginia, Charlottesville, VA 22904, United States
[b] Department of Chemistry, West Chester University, West Chester, PA 19383, United States

Available online 30 January 2007

Abstract

This article reports a comparative study on texturing in silicon and germanium surfaces after exposure to femtosecond laser irradiation in the gaseous environments of sulfur hexafluoride (SF_6) and hydrogen chloride (HCl). The surface texturing results from the combined effect of laser-assisted chemical etching and laser ablation. Optimized processing conditions have produced features on the order of nanometers in size. We demonstrate for the first time that regular conical pillars can be formed in Ge and that HCl can be used to form regular conical pillars in Si.
© 2007 Elsevier B.V. All rights reserved.

Keywords: Femtosecond laser; Surface texturing; Ultrafast lasers; Chemical restructuring; Silicon and germanium surfaces

1. Introduction

Silicon and germanium are two of the most important electronic materials used in the semiconductor industry. Restructuring the surface of silicon has been an active area of research due to several reasons including: (1) it enhances the surface area and hence the effective active area of a device increases, (2) it can effectively trap more light for fabrication of high efficiency optoelectronic devices, (3) it increases catalytic actions due to large surface area, and (4) it can have possible biomedical applications.

Surface texturing by porosification of silicon has been extensively studied over decades and recently ultrafast laser-assisted surface texturing [1–8] has become progressively more popular due to several advantages: (1) unlike porous structures, regular sharp pillars can be formed in which the entire surface area is exposed as *exterior* surface, (2) the structural, optical and electronic properties can be well tailored by controlling the processing conditions, and (3) large area samples can be processed with automation. Nonetheless, the formation of regular conical pillars has only been demonstrated previously in silicon. Furthermore, while it is known unambiguously that the initial stages (i.e. during the first few laser shots) of surface texturing exhibit virtually no dependence on the presence and nature of the process gas, it is equally well known that the ultimate structures formed after hundreds of laser shots depend sensitively on the presence and nature (i.e. comparing vacuum to air to He to SF_6) of the process gas. The specific role of the chemical interactions that lead to structure formation are shrouded in mystery. In this study we report the laser texturing of silicon and germanium surfaces and compare their surface morphologies.

2. Experimental procedure

The Si(1 0 0) (B doped) and undoped Ge(1 0 0) wafers were cleaved into small chips and cleaned with acetone and methanol. Silicon and germanium chips were put successively on a stage inside a vacuum chamber (with base pressure ~1 mbar) mounted on a high precision computer controlled *X*–*Y* stage. The chamber was backfilled with 400 mbar SF_6 or HCl after rinsing several times with the process gas. The samples were then exposed to 1.4 mJ pulses of 800 nm/130 fs light at a repetition rate of 1 kHz from a regeneratively amplified Spectra Physics Ti-sapphire laser system. The laser beam was focused by a 1 m focal length coated lens and incident normal to the sample surface. The laser fluence was controlled by using a calcite Glan-laser polarizer.

* Corresponding author. Tel.: +1 434 924 6167; fax: +1 434 924 8818.
E-mail address: mgupta@virginia.edu (M.C. Gupta).

0169-4332/$ – see front matter © 2007 Elsevier B.V. All rights reserved.
doi:10.1016/j.apsusc.2007.01.079

SIONYX1403000041.0011

SAMSUNG EX. 1002 - 433/4148

The spatial profile of the laser pulse was nearly Gaussian, though elongated in one axis compared to the other creating an elliptical profile, and the fluence was calculated using the spot size determined by exposing a small area on the sample surface to thousands of shots. In order to scan an area bigger than the laser spot size, the samples were translated using a motorized X–Y stage. Scanning also assists to make more uniform surface structures by smoothing out any shot-to-shot irregularities in the beam profile. By varying the scanning speed of the X–Y stage, the number of laser pulses impinging on the sample surface at a particular spot was controlled. The spot size was 0.3 mm along the minor axis and 0.6 mm along the major axis. Scanning was performed parallel to the minor axis. Samples were produced either with isolated single line scans or with large areas created by overlapping several line scans. The step size between scan lines was chosen to be sufficiently small (generally 0.38 mm) such that successive lines overlapped substantially, improving homogeneity. Homogeneity is further enhanced by performing two overlapping scans in orthogonal directions rather than one overlapping scan with an exposure of the same total number of shots. After laser processing, the samples were analyzed with a field emission scanning electron microscope (Zeiss SUPRA 40).

3. Results and discussion

Fig. 1. shows the SEM images of sharp conical pillars formed on the silicon surface produced with 240 shots of 130 fs laser pulses at a fluence of 0.6 J cm^{-2} in 400 mbar of SF_6 (Fig. 1a) and HCl (Fig. 1b), viewed 45° from the surface normal. The pillar size varies across the scanned laser line indicating the intensity variation of the laser fluence across the spatial profile of the laser pulse. We overlapped the scan lines to minimize height variation over a large area on the sample surface. The spikes that are obtained in SF_6 are ~ 15 μm tall and around 5 μm at the base.

On the other hand, under similar conditions, the structures formed in the presence of HCl are composed of taller pillars (~ 20 μm height) with a base dimension around 7 μm. It is evident from Fig. 1a and b that the pillars which are formed in SF_6 are narrower towards the tips compared to pillars formed in HCl. Although the pillar density is comparable in both cases, the pillars formed in HCl look stronger and relatively blunt towards the tip indicating that differences in the etch chemistry in the F/Si system relative to that of Cl/Si system are responsible for significant structural differences. The role of chemistry in structure formation is not well understood and it is not a trivial result that regular conical pillars are formed during fs irradiation in SF_6 as well as HCl. For example, regular conical pillars can be formed during ns irradiation of Si in the presence of SF_6 but they are not formed for ns irradiation in the presence of HCl [9]. During ns pulsed irradiation of Si, HCl produces significantly blunter tips, the pillars are much taller (>50 μm) and they are porous rather than solid core [9]. This is a further indication that the mechanisms of pillar formation are not the same for fs and ns irradiation. This result is also significant because chemical impurities, namely sulfur,

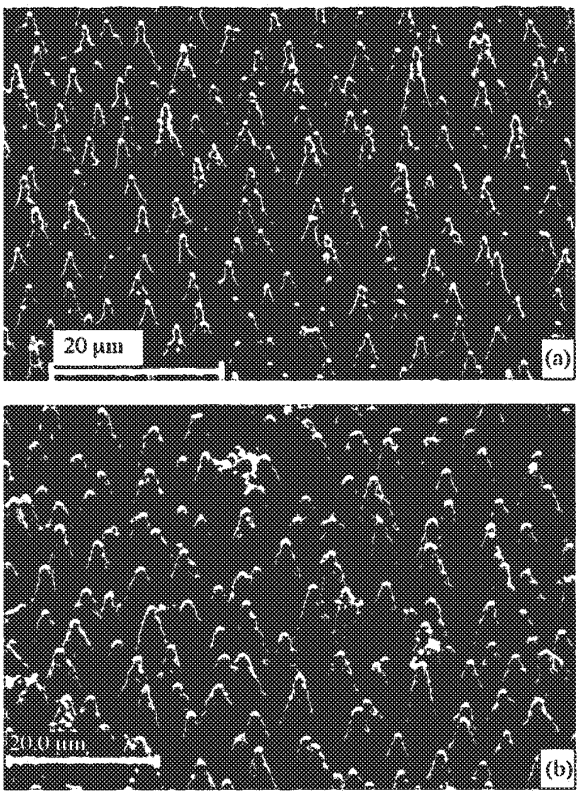


Fig. 1. SEM images of pillars, viewed 45° from the surface normal, formed in silicon surface by 240 laser pulses of 130 fs duration, 0.6 J cm^{-2} fluence in the gaseous environment of 400 mbar of (a) SF_6 and (b) HCl.

incorporated during laser processing have been implicated in changing the optical and electronic properties of the textured surfaces [10]. By expanding the range of gases in which pillar formation is possible, we should be able to disentangle the effects on optical and electronic properties of geometric parameters from chemical parameters.

Fig. 2 displays SEM images taken for germanium samples treated under similar laser and gaseous conditions as in the case of silicon described above. A very different surface texturing was observed in germanium as is clear from Fig. 2. In the case of germanium processed in SF_6, we noticed two distinct features not observed under conditions that are similar to those used for silicon: (a) conical pillar formation with higher cone angle up to a neck and (b) atop these pillars very sharp spikes up to ~ 2 μm in length with ~ 100 nm tip radius. Nanoclusters formed during laser ablation are more abundant in germanium compared to silicon under similar laser conditions, which might be due to the lower melting temperature of the former. On the other hand, the germanium structures formed in the presence of HCl (Fig. 1b) are less densely populated, shorter, high cone angle, wider base, and exhibit greater variations in pillar height compared to silicon (Fig. 1a). It is interesting to note that gas phase silicon etching is anisotropic in HCl and the etch rate is ~ 20 μm min^{-1} for the Si(1 0 0) plane at temperatures in the

SIONYX1403000041.0012

SAMSUNG EX. 1002 - 434/4148

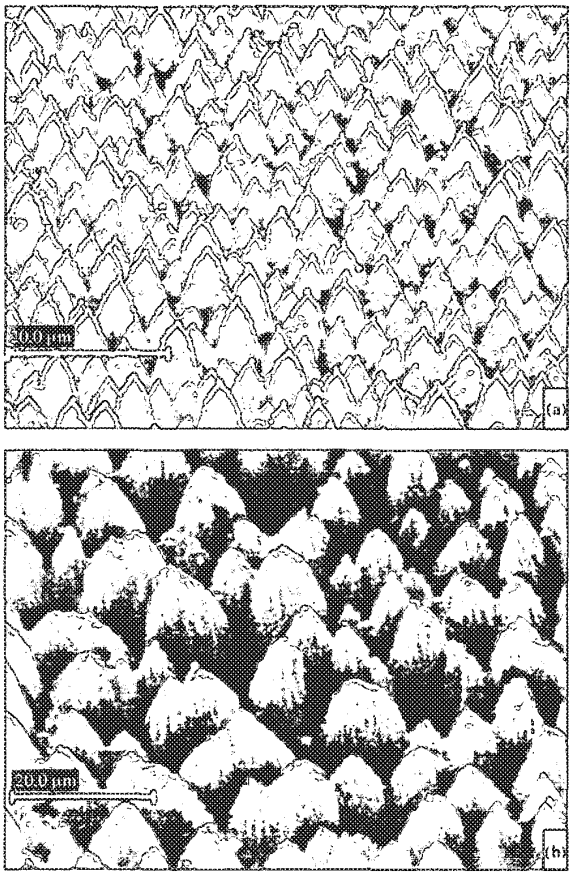


Fig. 2. SEM images of pillars, viewed 45° from the surface normal, formed in germanium surface by 240 laser pulses of 130 fs duration, 0.6 J cm^{-2} fluence in the gaseous environment of 400 mbar of (a) SF_6 and (b) HCl.

range of 1050–1250 °C [11], whereas in germanium the etch rate is around 3 μm min^{-1}, the etch rate is independent of temperature beyond 800 °C, and it leads to the development of square pits for Ge(1 0 0) [12]. The associated differences in etch chemistry are involved in determining the different structure formation dynamics that result in more regular spike formation in silicon compared to germanium in HCl. The details of how these differences affect structure formation will form the basis of future investigations.

Laser induced surface texturing that produces regular structures on materials in the presence of reactive species is a complex process involving: (1) plume/process gas and plume/surface interactions (decomposition of reactive gas, chemical etching enhanced by laser heating of the material and the formation of radicals, deposition out of the plume, etc.), (2) laser ablation of material, and (3) optical phenomena that initiate the formation of regular structures. The laser parameters, gaseous environment and the nature of the substrate, all play a role in the final outcome of the surface morphology. Structure formation is ultimately a convoluted dynamical process involving all three factors. The dimensions and character of the pillars formed in silicon have been observed to depend critically on the temporal pulse width of the laser beam. Whereas pillar production with pulse durations in the range of 100 fs - 20 ns has been demonstrated with much smaller pillars being formed in the case of fs irradiation [10,13], we were unable to produce pillars with a 300 ns Nd:VO_4 laser. It appears that pulses significantly shorter than the melt lifetime (~ 250 ns) are a requisite characteristic of the laser for sharp pillar formation.

4. Conclusion

We have for the first time demonstrated ultrafast laser induced pillar formation in Ge using SF_6 and HCl gaseous environments. We have also demonstrated that ultrafast laser induced pillar formation is not limited to SF_6 but other gases such as HCl can be used. In this article we have also reported a comparative study of ultrafast laser induced pillar formation between Ge and Si.

Based on our observations, we make the following points regarding structure formation in silicon and germanium: (a) under similar laser and gas conditions the aspect ratios (height to base ratio) of silicon pillars is higher compared to germanium in both SF_6 and HCl environments, (b) there is a spike formation atop pillars that occurs in germanium, whereas a bulb like structure forms atop silicon pillars when processed in SF_6, (c) silicon pillars formed in HCl are taller and sturdier compared to SF_6, (d) in germanium the structures formed in SF_6 are more regular, sharp, well defined features compared to structures formed in HCl, (e) for the formation of regular conical pillars, the pulse length of the laser must be significantly shorter than the melt lifetime.

Acknowledgements

We gratefully acknowledge the financial support of the National Science Foundation under grant ECS-0100243, NSF I/UCRC center grant, IGERT Program Grant 9972790 and CREST supplement Program Grant 0520208. This work was also supported by the University of Virginia and West Chester University.

References

[1] T.-H. Her, R.J. Finlay, C. Wu, S. Deliwala, E. Mazur, Appl. Phys. Lett. 73 (1998) 1673.
[2] A.J. Pedraza, J.D. Fowlkes, D.H. Lowndes, Appl. Phys. Lett. 74 (1999) 2322.
[3] T.-H. Her, R.J. Finlay, C. Wu, E. Mazur, Appl. Phys. A 70 (2000) 388.
[4] J. Bonse, S. Baudach, J. Kruger, W. Kautek, M. Lenzner, Appl. Phys. A 74 (2002) 19.
[5] M.Y. Shen, C.H. Crouch, J.E. Carey, R. Younkin, E. Mazur, M. Sheehy, C.M. Friend, Appl. Phys. Lett. 82 (2003) 1715.
[6] D. Riedel, J.L. Hernandez-Pozos, R.E. Palmer, K.W. Kolasinski, Appl. Phys. A 78 (2004) 381.
[7] B.K. Nayak, M.C. Gupta, Mater. Res. Soc. Symp. Proc. 850 (2005) (MM1.8.1).
[8] D. Mills, K.W. Kolasinski, J. Phys. D: Appl. Phys. 38 (2005) 1.

SIONYX1403000041.0013

SAMSUNG EX. 1002 - 435/4148

[9] K.W. Kolasinski, D. Mills, M. Nahidi, J. Vac. Sci. Technol. A 24 (2006) 1474.
[10] C.H. Crouch, J.E. Carey, J.M. Warrender, M.J. Aziz, E. Mazur, F.Y. Génin, Appl. Phys. Lett. 2004 (1850) 84.
[11] M. Druminski, R. Gessner, J. Cryst. Growth 31 (1975) 312.
[12] J.A. Amick, E.A. Roth, H. Gossenberger, RCA Rev. 24 (1963) 473.
[13] K.W. Kolasinski, in: S.G. Pandalai (Ed.), Recent Research Advances in Applied Physics, vol. 7, Transworld Research Network, Kerala, India, 2004, p. 267.

SIONYX1403000041.0014

SAMSUNG EX. 1002 - 436/4148

Mater. Res. Soc. Symp. Proc. Vol. 1123 © 2009 Materials Research Society 1123-P07-09

Ultrafast Laser Textured Silicon Solar Cells

Barada K. Nayak, Vikram Iyengar and Mool C. Gupta[1]

Charles L. Brown Department of Electrical and Computer Engineering, University of Virginia, Charlottesville, VA 22904

ABSTRACT

A novel ultrafast laser texturing method has been developed to produce arrays of nano/micro surface textures in silicon. Laser processing conditions have been optimized for achieving appropriate optical and electronic properties for photovoltaic applications. The textured silicon surfaces absorb greater than 99% of incident light over the entire solar spectrum and the material appears complete black to bare eye. Textured silicon surfaces are characterized for surface morphology and optical properties. Chemical etching and thermal annealing steps have been performed to remove laser slag and induced defects. Finally, we report the total and external quantum efficiency results on photovoltaic devices fabricated on the textured silicon wafers, which can be further improved.

INTRODUCTION

Efficient light energy absorption to cause carrier generation in a photoactive material is one of the most important requirements for enhancing photovoltaic energy conversion in solar cells. Therefore, high efficiency solar cell devices require good reflection control to minimize optical loss at the front surface. This is typically achieved with a combination of surface texturing (using wet chemical process) and anti-reflection coating (by deposition of Si_3N_4 layer using PECVD method). Usually industry uses two types of texturing procedure:
(a) Anisotropic etching for mono-crystalline silicon using alkaline solutions like NaOH and KOH at 70-80 ° C with addition of isopropanol [1]. This etching process produces randomly distributed pyramids and suffers from following shortcomings: lack of pyramid size control, poor reproducibility, presence of untextured regions, need for adequate surface preparation, and requirement of accurate control of temperature and isopropanol concentration. While this method is applicable for mono-crystalline materials, it could not be applied to multi-crystalline materials due to the anisotropic nature of the etchant.
(b) Isotropic texturing for multi-crystalline silicon using acidic mixture of HF and HNO_3 and organic additives [2]. This method relies on the residual saw damage that causes uneven etching of the surface that result in the texture formation. However, acidic texturing has several issues for multi-crystalline wafers due to: requirement of saw damage for effective texturing; accurate surface preparation, etc. Other methods of texturing like reactive ion etching, mechanical texturing and photolithography and wet

[1] Corresponding author E-mail: mgupta@virginia.edu

SIONYX1403000041.0015

SAMSUNG EX. 1002 - 437/4148

etchings has been proposed but are not cost effective. On the other hand, lasers are unique energy sources that could texture surface by selectively removing material by ablation process. Since laser ablation is an isotropic process, texturing could be achieved irrespective of the crystallographic orientation of material surface. Several groups have demonstrated that laser could be used to texture the surface by creating grooves [3,4] or pits [5]. Previously we have reported that an ultrafast laser could be used to create arrays of self-assembled nano/micro surface textures on various materials [6-9]. These nano/micro textures trap light very efficiently (over 99 % from UV to IR) irrespective of the angle of incidence and state of polarization. Also lasers are increasingly used for photovoltaic manufacturing. Here for the first time we report photovoltaic device results fabricated on the ultrafast laser textured silicon surfaces, where further improvements in efficiency are possible.

EXPERIMENT

Boron doped FZ silicon (100) of resistivity 2 Ω cm is diced into small square chips of size 2 cm x 2 cm. One of the chips is put on a stage inside a vacuum chamber (with base pressure ~ 1 mbar) mounted on a computer controlled X-Y stage. The chamber is rinsed with SF_6 at least twice and then backfilled with 400 mbar SF_6. The samples are exposed to 0.6 mJ pulses of 800 nm wavelength and 130 fs pulse duration at a repetition rate of 1 kHz from a regeneratively amplified Spectra Physics Ti-sapphire laser system. The laser beam is focused along the normal onto the sample surface by a 200 mm focal length lens and the laser fluence is adjusted by using a Glan laser calcite polarizer. In order to expose an area bigger than the laser spot size, the samples are raster scanned under the laser beam using the motorized X-Y stage. Scanning is adjusted such that laser lines overlap suitably to generate a uniform surface texture over the silicon surface.

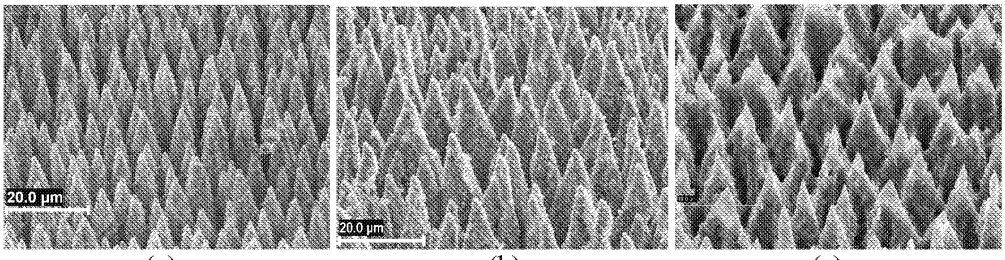
Laser textured wafers are first cleaned using a chemical etching procedure (NaOH solution rinse followed by Isotropic etching (HNO_3:CH_3COOH: HF: 30: 10:4)) to remove laser slag and smoothen the textured cones. The textured wafers are further cleaned by IMEC process [10] for removal of organic and metal contamination. Wafers are then annealed at 900 C for 30 minutes in an inert (90% Ar + 10% H_2) environment to passivate any laser induced defects. In order to form an n+p junction, commercially available phosphorus doped oxide (P509 from Filmtronics) solution is spun on the texture surface. After spin coating, the wafers are baked at 200 °C for 15 minutes before they are inserted into a diffusion furnace. Doping is carried out in a N_2:O_2:3:1 ambient at 900 °C for 15 minutes. The spin on dopant film is retained after diffusion and front electrode area is patterned using photolithography. Aluminum (700 nm) is sputtered on to the back of the device (p-side) and Ti/Ag (50 nm/700 nm) is e-beam evaporated onto the front side of the device (n+ side) for the ohmic contact. The front electrode shadowing is around 6% of the device surface area. Lastly, the samples undergo a forming gas anneal at 450 °C for 30 minutes. Devices are then edge isolated before further characterization.

Surface morphology of the textured surfaces are analyzed using a scanning electron microscope (SEM) (Zeiss SUPRA 40), reflectance measurements are carried out using a spectrophotometer, I-V measurements are carried out using a class B solar simulator from

PV Measurements and photovoltaic efficiency is calibrated using a commercial solar cell calibrated by NREL for 1.5 SUN (100 mW/cm^2) illumination.

RESULTS AND DISCUSSION

Fig. 1 shows the SEM image of as-laser textured (a) single crystalline and (b) multicrystalline (c) textured and chemically etched silicon surface. It is evident from the image that the size of the conical microstructures are ~ 10 μm tall with base diameter of ~ 5 μm tapering down to ~ 100 nm and separated by ~ 6 μm from each other. Figure 1 (a) and (b) indicate the laser slag that is produced by redeposition of ablated material. A thin disordered layer over the conical structures is also produced during rapid laser melting and resolidification process [11]. Figure 1 (c) demonstrate that most of the laser slag and amorphous layer are successfully removed by employing a chemical cleaning followed by thermal annealing mentioned in the experimental section. The blackness of the textured material is retained even after the chemical etch (see the inset picture of a solar cell of size 1 cm x 1 cm fabricated on a textured surface in figure 2).



(a) (b) (c)

Figure 1: SEM images of (a) as-laser textured CZ silicon (b) as-laser textured multi-crystalline silicon (c) after NaOH and isotropic etching. Scale bar for all the images is 20 μm.

Figure 2 demonstrates the impact of surface texturing on the reflectivity of silicon. It is clear that the laser textured surface absorb the entire visible spectrum of the electromagnetic radiation compared to its un-textured counter part. We have also observed that reflectivity turns out to be less than 10 % up to 15 μm wavelength in the IR region of the spectrum [9]. The total scattering from the textured surface is less than 1% measured using an integrating sphere.

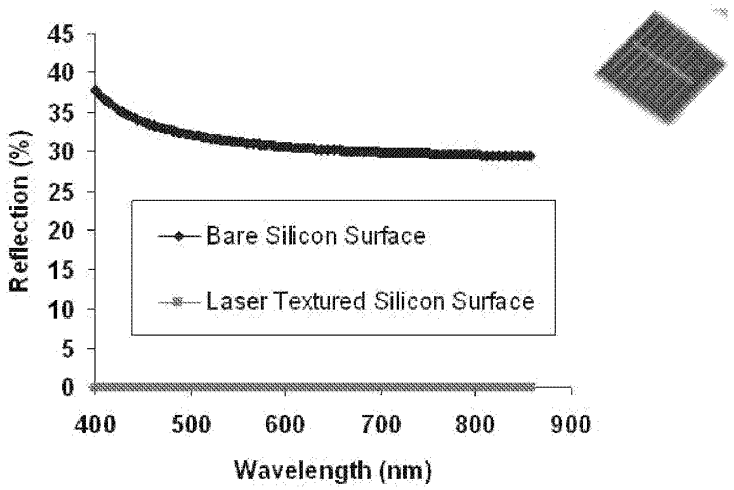


Figure 2: Light reflection from polished bare silicon and laser textured silicon surfaces after chemical etching and thermal annealing process. Inset shows the photograph of a diced device fabricated on textured silicon wafer.

Figure 3 (a) and (b) show the dark and 1 SUN illuminated I-V data for the fabricated device. It is evident from the short circuit current value that the textured surface has efficiently trapped incident light. However, the low open-circuit voltage and fill factor have caused the reduction in the over all efficiency. The low open-circuit voltage can be attributed to high reverse saturation current as seen in figure 3 (a). The high recombination current could result from high doping levels for the emitter region and/or residual laser induced defects. We believe that optimization of doping and appropriate etching for this textured material could reduce the recombination current.

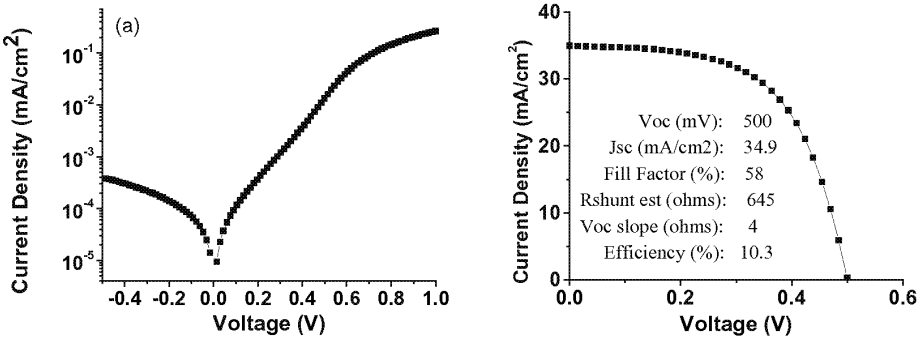


Figure 3: Current-voltage characteristics of textured silicon solar cell at 1 SUN illumination. Left side curve indicates dark I-V characteristics.

Another possibility for poor fill factor could be attributed to high series resistance. Scanning electron microscope images (figure 4) clearly indicate the porosity in the front metal film deposited for electrical contact. The devices showed external quantum efficiency (EQE) at an average of 75 % over the entire visible spectrum. In spite of the

SAMSUNG EX. 1002 - 440/4148

high absorption in this material, the reduction in overall EQE could be due to the porosity and/or non-uniformity of the metal layer leading to poor charge collection.

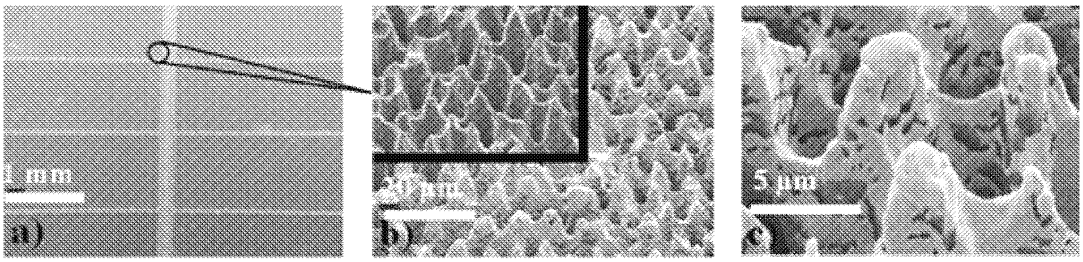


Figure 4: SEM images of (a) device showing front finger electrodes (b) a higher magnification region of (a) indicating an area at the crossing of bus bar and finger. The dark line separates the metallized region (white area) from the unmetallized region (c) Higher magnification image of metallized region of (b) showing the porosity/discontinuity in the metal film deposited for ohmic contact.

CONCLUSIONS

In conclusion, we have demonstrated for the first time that solar cell devices of over 10% efficiency could be fabricated using ultrafast laser textured silicon substrates. It should also be noted that the fabricated devices are not optimized for best surface passivation, doping profile and do not have a back surface field. So further improvements in device efficiency could be realized with optimization of fabrication process. The laser texturing process is unique due to the following reasons: (a) textured surfaces absorb around 99 % of incident radiation over the entire solar spectrum (b) process is highly reproducible and is relatively fast (c) the process produces same micro textures on multi-crystalline silicon wafers.

Post chemical and thermal treatments on as-textured surfaces seem to have removed most of the laser induced defects that is evident from the high photocurrent. Thick metallization is required to overcome the observed porosity in the deposited metal film. With appropriate finger grid geometry, surface passivation, back surface field and better charge collection, ultra fast laser texturing can yield high efficiency photovoltaic cells.

ACKNOWLEDGEMENTS

We thank NSF and NASA-Langley for their financial support for this project.

REFERENCES

[1] D. L. King and M. E. Buck, "Experimental Optimisation of an Anisotropic Etching Process for Random Texturisation of Silicon Solar Cells", Proc. 22nd IEEE Photovoltaic Specialists Conf., pp. 303-308 (1991).

[2] D. Sarti, Q. N. Le, S. Bastide, G. Goaer, and D. Ferry, "Thin industrial multicrystalline solar cells and improved optical absorption", Proceedings of the 13th European PV Solar Energy Conference, pp. 25–28, 1995.

[3] J. C. Zolper, S. Narayanan, S. R. Wenham and M. A. Green, "16.7 % efficient, laser

textured, buried contact polycrystalline silicon solar cell", Appl. Phys. Letts., 55 (22), 2363 (1989).
[4] L. Pirozzi, G. Arabito, F. Artuso, V. Barbarossa, U. Besi-Vetrella, S. Loreti, P. Mangiapane, E. Salza, Selective emitters in buried contact silicon solar cells: Some low-cost solutions", Solar Energy Materials & Solar Cells 65, 287-295 (2001).
[5] Malcolm Abbott, and Jeffrey Cotter, "Optical and Electrical Properties of Laser Texturing for High-efficiency Solar Cells", Prog. Photovolt: Res. Appl. ; 14:225–235, (2006).
[6] Barada K. Nayak, Mool C. Gupta and Kurt W. Kolasinski, "Spontaneous formation of nano-spiked microstructures in germanium by femtosecond laser irradiation", Nanotechnology, 18, 195302. (2007).
[7] Barada K. Nayak, Mool C. Gupta and Kurt W. Kolasinski, "Ultrafast-laser-assisted chemical restructuring of silicon and germanium surfaces", Applied Surface Science, 253, 6580, (2007).
[8] Kurt W. Kolasinski, Margaret E. Dudley, Barada K. Nayak, and Mool C. Gupta, "Pillars formed by laser ablation and modified by wet etching", Invited Paper – Proceedings of SPIE, The International Society for Optical Engineering, Vol. 6586, Prague, Czech Republic, (2007).
[9] Mool C. Gupta and Barada K. Nayak, "Systems and methods of laser texturing and crystallization of material surfaces", International Patent Application Serial No. PCT /US2006/049065), filed on December 21, 2006 in the U.S. Patent and Trademark Office.
[10] M. M. Heyns, T. Bearda, I. Cornelissen, S. De Gendt, R. Degraeve, G. Groeseneken, C. Kenens, D. M. Knotter, L. M. Loewenstein, P. Mertens, S. Mertens, M. Meuris, T. Nigam, M. Schaekers, I. Teerlinck,W. Vandervorst, R. Vos, and K.Wolke, "Cost-effective cleaning and high-quality thin gate oxides," IBM J. Res. Develop., vol. 43, no. 3, p. 339, May 1999.
[11] C. H. Crouch, J. E. Carey, M. Shen, E. Mazur, F. Y. Genin, " Infrared absorption by sulfer-doped silicon formed by femtosecond laser radiation, " Appl. Phys. A, 79, 1635 (2004).

PROGRESS IN PHOTOVOLTAICS: RESEARCH AND APPLICATIONS
Prog. Photovolt: Res. Appl. (2011)
Published online in Wiley Online Library (wileyonlinelibrary.com). DOI: 10.1002/pip.1067

RESEARCH ARTICLE

Efficient light trapping in silicon solar cells by ultrafast-laser-induced self-assembled micro/nano structures

Barada K. Nayak, Vikram V. Iyengar and Mool C. Gupta*

Charles L. Brown Department of Electrical and Computer Engineering, University of Virginia, Charlottesville, VA 22904, USA

ABSTRACT

A novel ultrafast laser processing technique is used to create self-assembled micro/nano structures on a silicon surface for efficient light trapping. Under appropriate experimental conditions, light reflection (including scattering) of the Si surface has been reduced to less than 3% for the entire solar spectrum and the material appears completely black to the naked eye. A post-chemical cleaning is applied to remove laser-redeposited material and induced defects. Optical, morphological, and structural characterizations have been carried out on as-laser-treated and post-chemically cleaned surfaces. Finally, we report for the first time the total efficiency of over 14% and high external quantum efficiency (EQE) results on photovoltaic devices fabricated on the ultrafast-laser-induced micro/nano structured silicon wafer, which can be further improved upon process optimization. Copyright © 2011 John Wiley & Sons, Ltd.

KEYWORDS

solar cells; light trapping; ultrafast laser; micro/nano structure; texturing; silicon; self-assembled

***Correspondence**

Mool C. Gupta, Charles L. Brown Department of Electrical and Computer Engineering, University of Virginia, Charlottesville, VA 22904, USA.

E-mail: mgupta@virginia.edu

Received 24 January 2010, Revised 3 September 2010

1. INTRODUCTION

Efficient light energy absorption over the entire solar spectrum causing carrier generation in a photovoltaic material is one of the most important requirements for enhancing power conversion. This is becoming an important issue as we are moving towards thinning the wafers for cost saving while enhancing manufactured cell efficiency closer to laboratory results and reducing bulk recombination. Also, a cell structure design that could trap light efficiently irrespective of the angle of incidence of solar radiation is desirable. Most of the commercial solar cells use surface texturing to achieve reduction in front surface reflection to enhance light trapping. This is most commonly achieved with a combination of surface texturing (using wet chemical process) and anti-reflection coating [by deposition of Si_3N_4 layer using Plasma Enhanced Chemical Vapor Deposition (PECVD) method]. Usually industry uses two types of texturing procedures:

(1) Anisotropic chemical etching for mono-crystalline silicon (c-Si) using alkaline solutions, such as NaOH and KOH, at 70–80°C with addition of isopropanol [1–3]. Although, this etching process produces randomly distributed pyramids, the process suffers from following shortcomings: lack of pyramid size control, poor reproducibility, presence of untextured regions, need for adequate surface preparation, and requirement of accurate control of temperature and isopropanol concentration. Thus, it is very difficult to reduce reflection to less than 10% with anisotropic etching. While this method is applicable for c-Si materials, it could not be applied to multi-crystalline materials due to the anisotropic nature of the chemical etchant.
(2) Isotropic chemical texturing for multi-crystalline silicon (mc-Si) uses acidic mixture of HF and HNO_3 and organic additives [4,5]. This method relies on the residual saw damage that causes uneven etching of the surface that results in the texture formation.

Copyright © 2011 John Wiley & Sons, Ltd

SIONYX1403000041.0021

SAMSUNG EX. 1002 - 443/4148

Table I. Various texturing methods and reflectivity values reported for mono-crystalline (c-Si) and multi-crystalline (mc-Si) wafers.

Author	Year	Technique	Substrate used	Applicable to	Approx. R (%) @ 550 nm (as textured)
Gangopadhyay *et al.*	2007	Isotropic acidic texturing	mc-Si	mc-Si	15
Zechner *et al.*	1997	Mechanical grooving	mc-Si	c-Si & mc-Si	>15
Inomata *et al.*	1997	RIE	mc-Si	c-Si & mc-Si	<2
Vazsonyi *et al.*	1999	NaOH + IPA	c-Si	c-Si	10
Nishimoto *et al.*	2000	Na_2CO_3	c-Si	c-Si	10
Abbott *et al.*	2006	Laser texture	c-Si	c-Si & mc-Si	<5
Nishioka *et al.*	2009	Ag nanoparticle	c-Si	c-Si & mc-Si	<5
Branz *et al.*	2009	Au nanoparticle	c-Si	c-Si & mc-Si	<2
Younkin *et al.*	2003	Femtosecond laser-induced microstructure	c-Si	c-Si & mc-Si	<3
This work	2010	Ultrafast laser micro/nano structure	c-Si	c-Si, mc-Si, and thin a-Si	<3

However, acidic texturing causes several problems with multi-crystalline wafers due to the requirement of saw damage for effective texturing and of accurate surface preparation. It is difficult to reduce reflectance below 15% for multi-crystalline substrates. To reduce reflectance to lower values, other methods of texturing, such as reactive ion etching [6], mechanical texturing [7,8], nanoparticle-based nanoporous surfaces [9–11] photolithography, and wet etchings [12], have also been proposed. Table I compares various texturing methods and reflectivity values reported for c-Si and mc-Si wafers.

On the other hand, lasers are unique energy sources that could texture surfaces by selectively removing materials by ablation process. Since laser ablation is an isotropic process, texturing could be achieved irrespective of the crystallographic orientation of material surface. Several groups have demonstrated that lasers could be used to texture the surface by creating grooves [13] or pits [14]. To create such types of textures, usually lasers with pulse widths of tens of nanoseconds are used. These tightly focused longer pulses sculpt the silicon surface to create grooves or pits that effectively trap light through multiple reflections. However, under shorter pulse regimes a (few nanoseconds to femtoseconds), a very different types of self-assembled micro/nano structures are formed (see Figure 1). Over the past decade, several groups have investigated the formation of such structures in various semiconductors, such as Si [15–18], Ge [19], metals [20,21], and thin films [22], under various experimental conditions. These micro/nano structures reduce reflectivity very efficiently over a broad spectrum from ultraviolet (UV) to infrared (IR) [23–25]. Under ultrafast laser irradiation, micro/nano structures are self-assembled as compared to point by point scanning used with nanosecond pulse lasers. One of the unique features of these self-assembled structures is that efficient light trapping occurs irrespective of the angle of incidence and state of polarization of incident radiation. Other important advantages of ultrafast-laser-textured surfaces are (a) high reproducibility; (b) good uniformity of micro/nano-structures; (c) applicability to c-Si, mc-Si, as well as thin films. Since lasers are increasingly adopted in PV industry at various process steps, such as edge isolation, groove formation, soldering, etc. [26], this technology could have a promising future for fabricating high efficiency cells. Previously, we have reported the feasibility of fabricating solar cell devices on ultrafast-laser-structured surfaces [27]. Here for the first time we report photovoltaic device results (measured efficiency 14.2%) fabricated on the ultrafast laser micro/nano structured silicon surfaces, where further improvements in efficiency are possible through optimized texturing and device fabrication processes.

2. EXPERIMENTAL

2.1. Laser micro/nano structuring

Boron-doped FZ c-Si (100) of resistivity 2 Ω cm, undoped c-Si, and mc-Si wafers are diced into small square chips of size 2 cm × 2 cm. One of the chips is put on a stage inside a vacuum chamber (with base pressure ~1 mbar) which is mounted on a computer controlled X-Y stage. The chamber is rinsed with SF_6 at least twice and then backfilled with 400 mbar SF_6. The samples are exposed to 0.6 mJ pulses of 800 nm wavelength and 130 fs pulse duration at a repetition rate of 1 kHz from a regeneratively amplified Spectra Physics Ti-sapphire laser system. The laser beam is focused along the normal onto the sample surface by a 200 mm focal length lens and the laser fluence is adjusted by using a Glan laser calcite polarizer. In order to expose an area bigger than the laser spot size, the samples are raster scanned under the laser beam using a motorized X-Y stage. Scanning is adjusted such that laser lines overlap suitably to generate a uniform surface texture over the silicon surface.

SIONYX1403000041.0022

SAMSUNG EX. 1002 - 444/4148

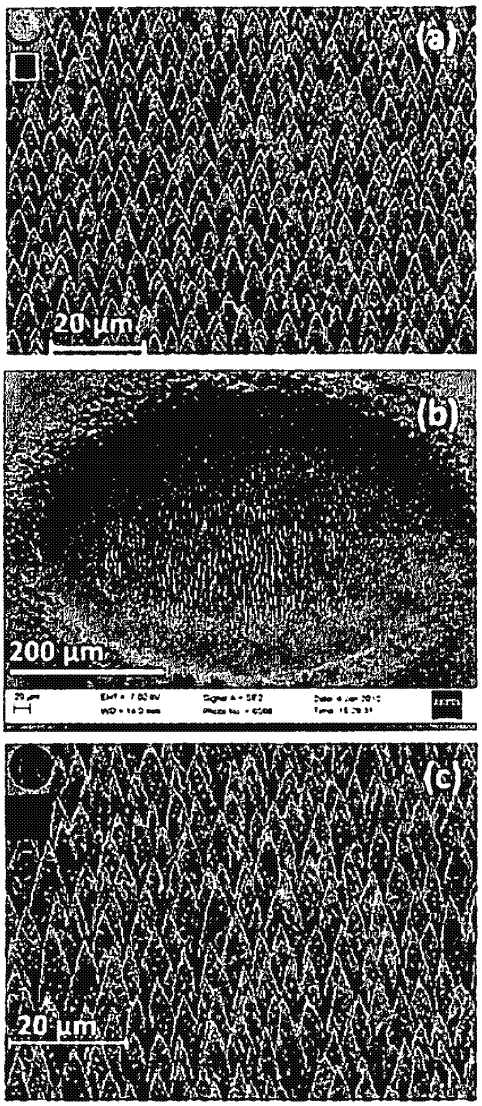


Figure 1. SEM images of ultrafast-laser-induced micro/nano structured silicon surface. Laser fluence (F) = 0.9 J/cm^2 (a) mono-crystalline Si surface exposed to about 300 laser shots, (b) single spot on Si surface exposed to 1000 laser shots, (c) multi-crystalline Si surface exposed to about 300 laser shots. Inset in both (a) and (c) shows optical photograph of laser-treated silicon surface that looks black.

2.2. Solar cell device fabrication

Ultrafast-laser-textured FZ c-Si (100) (p-type with resistivity 2 Ω cm) wafer is used for the solar cell device fabrication. To remove laser-redeposited material and induced defects, laser-micro/nano-structured wafers are first cleaned using a chemical etching procedure (NaOH solution rinse followed by isotropic etching (HNO_3:CH_3. COOH: HF: 30: 10:4)). The etching process also smoothens the conical micro/nano structures to some extent. The micro/nano-structured wafers are further cleaned by the IMEC process [28] for the removal of organic and metal contamination. In order to form an n^+p junction, commercially available phosphorus doped oxide (P509 from Filmtronics) spin-on-dopant (SOD) solution is spun on the laser-structured surface. After spin coating, the wafers are baked at 200°C for 15 min before they are inserted into a diffusion furnace. Doping is carried out in a N_2:O_2:3:1 ambient at 925°C for 15 min. After diffusion, the SOD film is etched away in dilute HF solution. The wafers are oxidized at 800°C for 30 min followed by a deposition of 70 nm SiN_x layer by PECVD (silane and ammonia gases are used) for surface passivation and further reduction of surface reflection. Back contact is formed by firing Al paste [from Ferro Corp.] and front contact is made by lithographically pattering front surface and evaporating Ti/Pd/Ag (100 nm/50 nm/500 nm) by e-beam. Thicker photoresist is used in lithography to avoid problems of punching by sharp-tips through the resist during lithography step. Finally, electroplating is performed for front electrode followed by forming gas annealing and edge isolation by mechanical dicing.

2.3. Material and device characterization

Surface morphology and elemental incorporation in the micro/nano structured surfaces are analyzed using a scanning electron microscope (SEM) (Zeiss SUPRA 40) and energy dispersive X-ray spectroscopy system (EDS) (INCA x-Sight, model 7426). Transmission, reflection, and scattering studies are carried out on the laser-textured samples using a Mattson Fourier transform infrared (FTIR) and a Nicolet Protégé infrared spectrophotometer with integrating sphere attachment. Measurements are conducted at a resolution of 16 cm^{-1} and averaged over 250 scans. The specular reflectivity in the visible region is estimated at different angles by placing the sample on a rotating stage and directing a He–Ne laser (632 nm) and a green solid state laser (530 nm) beam and then measuring the reflected light intensities at different angles. Reflected light is measured by a silicon detector of active region of around 4 cm^2 and the total reflectivity (specular plus scattering) due to the micro/nano structures is estimated by integrating the measured results for total solid angles for each measurement taken for each steps of angles. Quantum efficiency measurements are carried out using an I–V setup and a tungsten halogen lamp. Individual wavelengths are obtained by passing the white light from halogen lamp through a 270 M Jobin Yvon spectrometer and the power for each wavelength is measured using a Newport 842-P power meter. Total efficiency measurements are carried out using an I–V setup and a class B solar

SIONYX1403000041.0023

SAMSUNG EX. 1002 - 445/4148

simulator from PV Measurements Inc. The device efficiency results are verified against a commercial solar cell calibrated by NREL for 1.5 SUN (100 mW/cm^2) illumination.

3. RESULTS AND DISCUSSION

Figure 1 shows the micro/nano surface structures on Si surface after ultrafast laser treatment. Figure 1(a) shows the formation of micro/nano structures on a c-Si surface. These structures are conical in shape; around 5–7 μm in base diameter, 8–10 μm in height, tapering down to about 100 nm at the tip and separated by ~6 μm from each other. Laser fluence is maintained at 0.9 J/cm^2 and average number of laser shots used to create these structures are about 300. Figure 1(b) shows a laser spot irradiated with 1000 shots at the same fluence. It is apparent from Figure 1(b) that these structures are self-assembled on Si surface upon ultrafast laser irradiation. When the Si surface is raster scanned under the laser beam, a large area covered with micro/nano structures is generated. The surface appears completely black to the naked eye after laser treatment. Figure 1(c) shows the SEM image of a mc-Si surface after ultrafast laser treatment. Micro/nano structures, similar to that of c-Si, are formed in mc-Si indicating that laser-texturing process produces same surface features for grains of different orientations. Inset in Figure 1(a) and (c) shows the optical images of c-Si and mc-Si chips, respectively, where ultrafast-laser-treated areas look completely black. This is confirmed by the results, shown in Figure 2, which shows that the specular reflection is virtually negligible in the visible range from an as-ultrafast-laser-treated Si surface. Figure 3 indicates the reflectivity of these surfaces at various angles of incidence for P and S polarization states of incident radiation at wavelengths of 530 and 632 nm. It is clear from the figure that the surface reflectivity is negligible

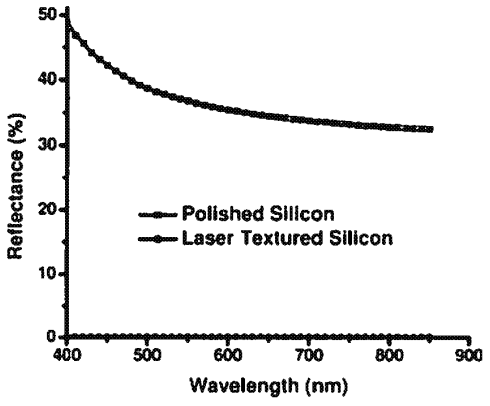


Figure 2. Specular light reflection from polished bare silicon and laser micro/nano structured silicon surface of Figure 1(a).

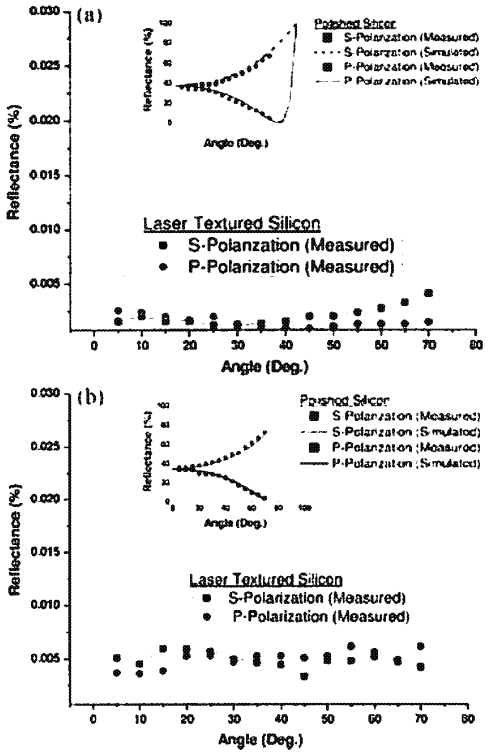


Figure 3. Reflectance from the control and micro/nano structured Si as a function of angle. (a) Reflectance at 532 nm for laser-textured sample and inset is the reflectance for polished Si. (b) Reflectance at 633 nm for laser-textured sample and inset is the reflectance for polished Si

compared to polished Si surfaces for both 530 and 632 nm wavelengths and for both polarization states. Since any arbitrary polarization state could be considered as combination of P and S polarized light, we can safely say that these surfaces would remain highly non-reflective for a wide range of incidence angles, polarization states of incident radiation, and wavelength.

Si surfaces reflect over 35% of incident light over the visible spectrum. The remaining light is absorbed and can partly transmit depending on the wafer thickness and wavelength. As the absorption coefficient of c-Si decreases significantly for the wavelengths closer to the band edge (1.12 eV), transmission values will be high for thin wafers and for longer wavelengths. Hence, light absorption becomes an issue for longer wavelengths and in particular for thin wafers. For example, silicon absorption coefficient at 1000 nm wavelength is 6.4 cm^{-1} [29]. In order to trap most of the incident light at this wavelength, the wafer thickness has to be more than 1.5 mm. This is unacceptable for photovoltaics where Si wafer thickness is in the range of 250 μm. Ultrafast-laser-induced micro/nano-structures

SIONYX1403000041.0024

SAMSUNG EX. 1002 - 446/4148

trap light very efficiently through multiple reflections where a few microns high surface structures could trap most of the light without much transmission due to larger effective thickness.

As mentioned in the Section 2, laser-structuring process is carried out in SF_6 environment which leads to the incorporation of sulfur in silicon. It has been reported that sulfur incorporation in Si can cause absorption of photons whose energy is less than Si band gap [30]. We have also reported previously that ultrafast-laser-treated surfaces show very low total reflection [25] as well as transmission over the IR region up to 20 μm. This indicates that absorption is enhanced for longer wavelengths (beyond band gap) by sulfur incorporation in addition to multiple reflection. Factors such as laser-induced structural and chemical modifications (defects, dislocations, a-Si layer formation, impurities, and compound formation) could also contribute to light absorption.

It is evident from Figure 1(b) that there is a significant amount of redeposited particles on the laser-treated area. Also, the surface of the conical structures is rougher due to rapid laser melting and resolidification. In order to study the laser-induced defects and elemental incorporation, Raman and EDS analysis is carried out. The presence of foreign atoms in a crystal can alter the lattice periodicity and, thus, can create absorbing states in the band gap. Since the laser processing is performed in the presence of different gases, we carried out the EDS spectra measurements on ultrafast-laser-treated undoped Si samples processed under SF_6 gaseous conditions. Table II gives the atomic percentage of different elements found in the treated Si material. It is clear from the table that a sufficient amount of sulfur is incorporated into the structures. It is worth mentioning here that the samples are not annealed or cleaned prior to EDS analysis. Therefore, much of the C and O may arise from contamination on the surface. Also, no effort is made to remove the surface layer of oxide and this account for most of the O presence.

Figure 4 shows the micro Raman spectrum obtained from control as well as textured samples using 632.8 nm excitation from a He–Ne laser source. The Raman signal is collected in a back-scattering configuration with resolution in the range of 1–3 cm^{-1} depending on the gratings chosen. The calibration is done using a standard c-Si sample. It is clear from Figure 4 that the treated sample shows (a) a slight broadening of the LO–TO phonon peak; (b) an asymmetry around 521 cm^{-1}; and (c) an observed blue shift. These observations indicate that there is some amorphous material in the sample and a change in the electronic properties. The asymmetric broadening of the LO–TO phonon mode are observed in the silicon

Table II. EDS results of laser micro/nano structured undoped Si surfaces treated in SF_6 gaseous conditions.

Element	C	O	Si	S	F
Atomic %	8.3	5.5	85.9	0.14	0.26

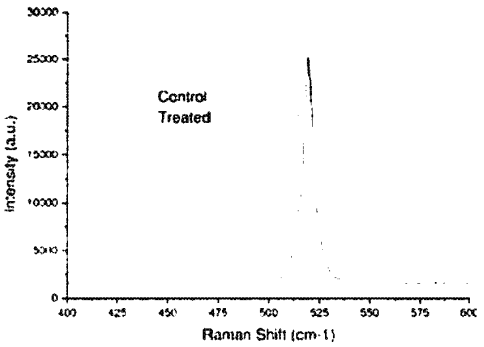


Figure 4. Raman spectra from control and treated sample. Control sample shows a typical symmetric Raman line peaked at 521 cm^{-1}, where as the treated sample shows a slight blue shift and asymmetry in the signal.

due to phosphorus doping [31]. With increasing phosphorous concentration, a broad low-energy tail extending from 400 to 500 cm^{-1} develops. In undoped micro-crystalline silicon, this broadening is commonly attributed to the presence of a residual amorphous and/or nano-crystalline phase. Since EDS and Raman experiments are carried out with undoped Si, from Raman study it is apparent that there might be a small skin of amorphous and/or nano-crystalline material covering the pillars and sulfur incorporation contributing to the broadening of the Raman peak resulting from laser processing.

In order to remove the laser-redeposited particles, a post-chemical cleaning of laser-treated surfaces is carried out. Figure 5 shows the SEM images of micro/nano-structured surfaces after removal of redeposited particles using the chemical procedure described in the Section 2. From Figure 5(d) it is clear that the micro cones look clean and free of debris. While it is possible to etch away debris by longer chemical etchings, doing so is not advantageous because it enhances the surface reflectivity due to smoothening of micro/nano structures. We have fabricated solar cell devices on laser-treated surfaces that have been chemically cleaned under different conditions: (a) highly cleaned (about 60 s cleaning in isotropic etchant), (b) moderately cleaned (about 40 s cleaning in isotropic etchant), and (c) moderately cleaned and annealed at 1000 °C for 30 min in forming gas. The device results for all three types of devices are given in Table III.

Ultrafast-laser-induced micro/nano-structures have conical shapes with a steeper slope compared to the pyramidal structure formed using chemical etching. During laser processing, the pillar cone angles vary within the range of 30–60° depending on the processing condition and random height variation. However, due to smaller cone angles compared to chemical etching, incoming light gets trapped with multiples reflections with higher fraction. Total reflection of as-laser-treated samples is very low and increases by a few more percentages after post-chemical

SIONYX1403000041.0025

SAMSUNG EX. 1002 - 447/4148

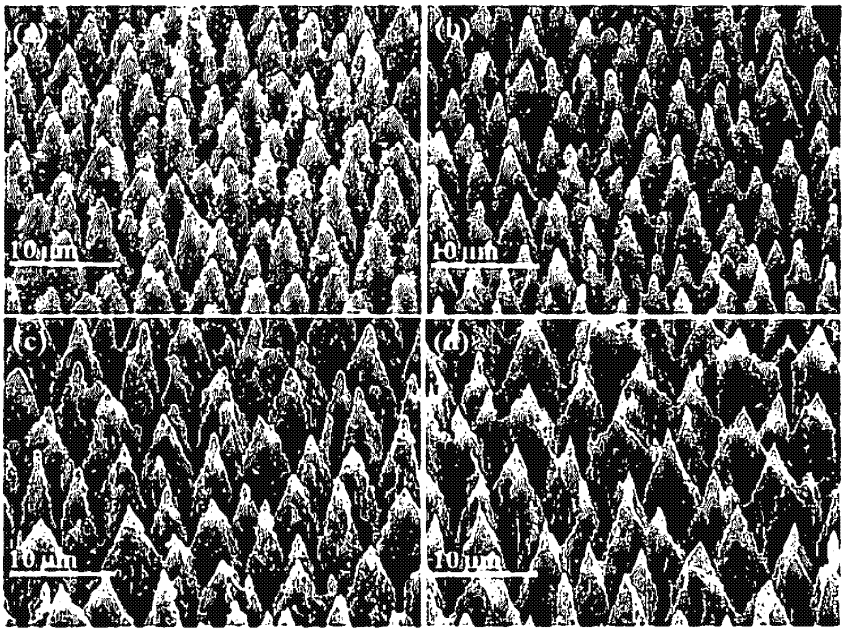


Figure 5. SEM images of laser-structured surface: (a) as-laser-treated; 40 s NaOH etch followed by isotropic etch for (b) 5 s, (c) 10 s, (d) 20 s.

cleaning. For instance, at 550 nm wavelength, an as-treated surface has a total surface reflectivity of 2.5% and that rises to 5.1% after chemical etching and reduces back to 1.4% after a thin oxide (~10 nm) and SiN_x layer (~70 nm) is deposited (see Figure 6 and Table III). We have carried out simulations for our laser-treated surface using the PV Optics program from NREL [32]. Figure 7 shows the simulated reflectance values with respect to texture angle at 550 nm wavelength. It is clear from Figure 7 that reflectance increases with cone angle. Initially 8–10 μm texture height was chosen knowing that post-chemical etching would reduce the texture height to 4–5 μm. Since silicon is etched uniformly by post-chemical processing, cone angle does not change significantly by it. Therefore, micro/nano-structures of a few micron heights are able to trap light efficiently (which is consistent with simulation). For texture angles between 30–60°, the reflectance is below 5%. For 550 nm wavelength, as-laser-treated surface has a measured total surface reflectivity of 2.5%, which is very close to the simulation result of 1.8%, assuming that the average texture angle is 45°. According to the simulation, after the thin oxide (10 nm) and SiN_x layer (70 nm) deposition, the reflectivity should go to zero at 550 nm, whereas we measure a very low value of around 1.4%. This slight variation could be due to the variation in micro/nano-structure heights of laser-treated surfaces and minor changes in the refractive indices (n & k) between amorphous and crystalline phases. Total reflectivity of a highly cleaned sample measured using an integrating sphere at different processing stages is shown in the Figure 6 and Table III which contains the total reflectivity data for surfaces that have undergone different chemical etching.

Figure 8(a) shows the 1 SUN illuminated *I–V* curve for the device fabricated on a laser-textured Si surface. Currently, a total efficiency of 14.2% is achieved for ultrafast-laser-treated devices compared to 14% for a control device (which has no surface texturing but has an antireflection layer of 10 nm of oxide plus 70 nm of SiN_x) and to 16.4% [33] for a chemically textured device with similar antireflection layer as in the case of control device. The efficiency of laser-textured devices can be further improved, since a higher short-circuit current value for the laser-textured devices is indicative of efficient light trapping. However, for laser-textured devices, the low open-circuit voltage (V_{oc}) and fill factor have caused the reduction in the overall efficiency. The low V_{oc} can be partly attributed to a high saturation current as seen in Table III. The saturation current density is extracted from the dark *I–V* curves using the two diode model assuming two non-ideal diodes. Nonlinear regression analysis is performed using a program provided by MTR Software. It is evident from Table III that the recombination current (J_{02}) for all laser-textured samples is higher compared to reference cells. This increase in the recombination current can be attributed to the presence of laser-induced defects, impurity incorporation, and high surface area. This can partly explain the lower open-circuit voltage. It is also

SIONYX1403000041.0026

SAMSUNG EX. 1002 - 448/4148

Table III. Photovoltaic device results for laser-structured samples under various post-processing conditions along with a control sample. (R is reflectivity, R_s is series resistance, V_{oc} is open-circuit voltage, FF is fill factor and η is total efficiency). Control sample has not gone through any surface texturing or post-chemical etching. It has 10 nm of thermal oxide and 70 nm of SiN_x. Chemical textured control sample has undergone same steps as control sample with no texture.

Device processing condition	R (%) @ 550 nm (after laser structured)	R (%) @ 550 nm (after chemical etching)	R (%) @ 550 nm (after SiO_2 + SiN_x)	Saturation current density (A/cm^2)		R_s (Ω)	V_{oc} (mV)	I_{sc} (mA/cm^2)	FF (%)	η (%)
				J_{01}	J_{02}					
High post-chemical cleaning	2.5	5.1	1.4	3.13E-10	1.15E-5	2.49	507	39.2	71.4	14.2
Moderate post-chemical cleaning	2.5	4.9	1.9	6.1E-8	1.87E-5	2.48	482	34.6	66.6	11.2
Moderate post-chemical cleaning + annealing	2.5	5.6	2.1	1.0E-8	1.46E-5	2.54	426	33.0	64.8	9.1
Control sample	36.7	36.7	3.9	3.23E-11	5.31E-6	2.40	618	34.6	65.3	14.0
Control sample with chemical texture	15.6	15.6	3	5.8E-12	5.13E-6	1.3	590	37	75	16.4

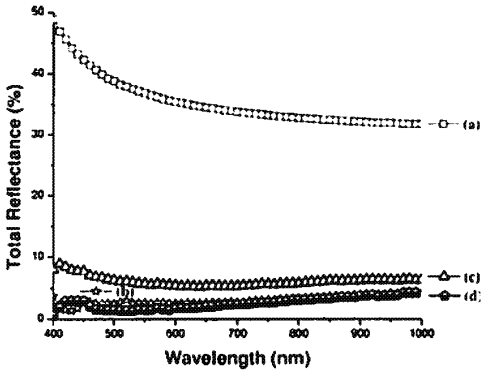


Figure 6. Total reflection measured using an integrating sphere. (a) Polished Si, (b) as laser structured, (c) post-chemically cleaned laser-treated surface, (d) after thin oxide growth (10 nm oxide for passivation) followed by PECVD silicon nitride (70 nm) on sample prepared in (c).

observed in Table III that post-chemical etching and thermal annealing improve the V_{oc} and I_{sc}.

Figure 8(b) shows the external quantum efficiency (EQE) results for a laser-treated device. Ideally, quantum efficiency values should be higher owing to the increased absorption due to multiple reflections in laser-treated surfaces. A textured surface can be expected to show increased current density due to higher light absorption and at the same time decrease in current density due to surface recombination. However, the textured samples were chemically etched to remove laser-induced damage. We have observed EQE values of around 90% ($\lambda = 700$ nm) which is closer to the measured value for our reference sample (untextured). Overall EQE could be further improved by minimizing the laser-induced defects and adopting suitable passivation schemes such as coating a

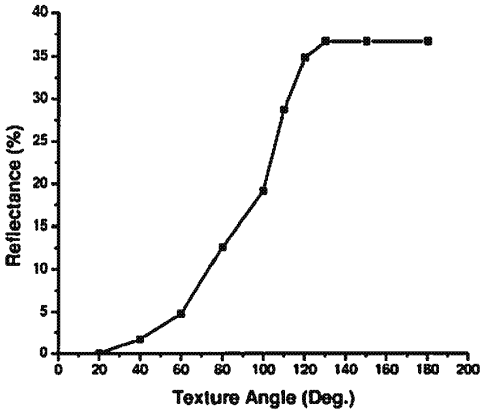


Figure 7. Effect of cone angle on reflectance calculation using PV Optics program.

SIONYX1403000041.0027

SAMSUNG EX. 1002 - 449/4148

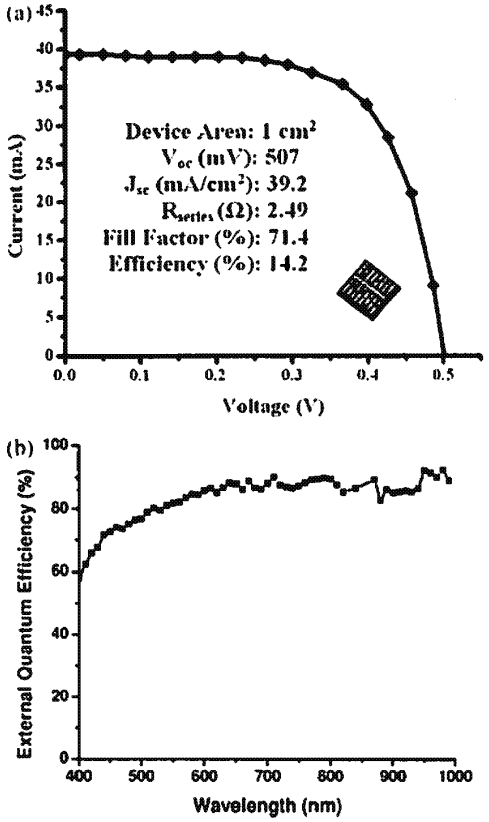


Figure 8. (a) Current–voltage characteristics of micro/nano structured silicon solar cell at 1 SUN illumination. Inset shows the photograph of a diced device fabricated on a micro/nano structured silicon chip. (b) External quantum efficiency result for a device fabricated on ultrafast laser micro/nano structured surface.

thin layer of a-Si:H. High dark current is also indicative of this fact (see Table III).

While the post-chemical etching process needs further improvements, it is possible to carry out laser-surface structuring in the presence of other gases such as HCl, where sulfur incorporation could be avoided. We have demonstrated that it is possible to create self-assembled micro/nano structures in HCl environments [17]. The laser-treated samples used in this study are prepared in a chamber filled with SF_6 gas at 400 mbar without maintaining a constant flow of gas. By maintaining a constant gas flow while the laser processing is going on, redeposition of ablated particles could be minimized. Appropriate post-chemical processing and the use of HCl gas during the laser treatment combined with a proper passivation scheme could result in a much higher open-circuit voltage. This study shows that with very high short-circuit current (39 mA/cm^2) resulting from extra-ordinary light trapping properties of ultrafast-laser-treated surfaces, an improvement in open-circuit voltage could lead towards the fabrication of very high efficiency silicon solar cells.

4. CONCLUSIONS

In conclusion, we have demonstrated for the first time that solar cell devices of total efficiency of 14.2% can be fabricated using self-assembled micro/nano structures by ultrafast laser processing of silicon substrates. It should also be noted that the fabricated devices are not optimized for defect removal, sulfur incorporation, best surface passivation, doping profile, and front electrical contact. Further improvements in device efficiency could be realized with optimization of the fabrication processes. The ultrafast-laser micro/nano-structuring process is unique due to (a) textured surfaces reducing surface reflectivity to less than few percent of the incident radiation over the entire solar spectrum irrespective of the angle of incidence and state of polarization of the incident radiation; (b) process is highly reproducible and produces uniformity of micro/nanostructures; and (c) the process produces similar micro/nano surface structures on mc-Si wafers as effectively as on mono-crystalline wafers.

ACKNOWLEDGEMENTS

The authors thank NSF I/UCRC program and NASA-Langley/NIA Professor grant for the financial support for this work. They also thanks Dr Keith Williams for Raman measurements.

REFERENCES

1. King DL, Buck ME. Experimental optimisation of an anisotropic etching process for random texturisation of silicon solar cells. *Proceedings of 22nd IEEE Photovoltaic Specialists Conference*, 1991; 303–308.
2. Vazsonyi E, De Clercq K, Einhaus R, Van Kerschaver E, Said K, Poortmans J, Szlufcik J, Nijs J. Improved anisotropic etching process for industrial texturing of silicon solar cells. *Solar Energy Materials and Solar Cells* 1999; **57**: 179.
3. Nishimoto Y, Namba K. Investigation of texturization for crystalline silicon solar cells with sodium carbonate solutions. *Solar Energy Materials and Solar Cells* 2000; **61**: 393.
4. Sarti D, Le QN, Bastide S, Goaer G, Ferry D. Thin industrial multi-crystalline solar cells and improved optical absorption. *Proceedings of the 13th European PV Solar Energy Conference*, 1995; 25–28.
5. Gangopadhyay U, Dhungel SK, Basu PK, Dutta SK, Saha H, Yi J, Comparative study of different approaches of multicrystalline silicon texturing for solar cell fabrication. *Solar Energy Materials and Solar Cells* 2007; **91**: 285.

SIONYX1403000041.0028

SAMSUNG EX. 1002 - 450/4148

6. Inomata Y, Fukui K, Shirasawa K. Surface texturing of large area multicrystalline silicon solar cells using reactive ion etching method. *Solar Energy Materials and Solar Cells* 1997; **48**: 237.
7. Bender H, Szlufcik J, Nussbaumer H, Nijs J, Mertens R, Willeke G, Bucher E. Polycrystalline silicon solar cells with a mechanically formed texturization. *Applied Physics Letters* 1993; **62**: 2941.
8. Zechner C, Hahn G, Jooss W, Wibral M, Bitnar B, Keller S, Spiegel M, Fath P, Willeke G, Bucher E. Systematic study towards high efficiency multicrystalline silicon solar cells with mechanical surface texturization. *Proceedings of the 26th IEEE Photovoltaic Specialists Conference*, 1997; 243.
9. Yuan H, Yost VE, Page MR, Stradins P, Meier DL, Branz HM. Efficient black silicon solar cell with a density-graded nanoporous surface: optical properties, performance limitations, and design rules. *Applied Physics Letters* 2009; **95**: 123501.
10. Branz HM, Yost VE, Ward S, Jones KM, To B, Stradins P. Nanostructured black silicon and the optical reflectance of graded-density surfaces. *Applied Physics Letters* 2009; **94**: 231121.
11. Nishioka K, Sueto T, Saito N. Formation of antireflection nanostructure for silicon solar cells using catalysis of single nano-sized silver particle. *Applied Surface Science* 2009; **255**: 9504.
12. Zhao J, Wang A, Green MA. 19.8% efficient "honeycomb" textured multicrystalline and 24.4% monocrystalline silicon solar cells. *Applied Physics Letters* 1998; **73**: 1991.
13. Zolper JC, Narayanan S, Wenham SR, Green MA. 16.7% efficient, laser textured, buried contact polycrystalline silicon solar cell. *Applied Physics Letters* 1989; **55**(22): 2363.
14. Abbott M, Cotter J. Optical and electrical properties of laser texturing for high-efficiency solar cells. *Progress in Photovoltaics: Research Applications* 2006; **14**: 225–235.
15. Her T-H, Finlay RJ, Wu C, Deliwala S, Mazur E. Microstructuring of silicon with femtosecond laser pulses. *Applied Physics Letters* 1998; **73**: 1673.
16. Pedraza AJ, Fowlkes JD, Lowndes DH. Silicon microcolumn arrays grown by nanosecond pulsed-excimer laser irradiation. *Applied Physics Letters* 1999; **74**: 2322.
17. Nayak BK, Gupta MC, Kolasinski KW. Ultrafast-laser-assisted chemical restructuring of silicon and germanium surfaces. *Applied Surface Science* 2007; **253**: 6580.
18. Halbwax M, Sarnet T, Delaporte P, Sentis M, Etienne H, Torregrosa F, Vervisch V, Perichaud I, Martinuzzi S. Micro and nano-structuration of silicon by femtosecond laser: application to silicon photovoltaic cells fabrication. *Thin Solid Films* 2008; **516**: 6791.
19. Nayak BK, Gupta MC, Kolasinski KW. Spontaneous formation of nano-spiked microstructures in germanium by femtosecond laser irradiation. *Nanotechnology* 2007; **18**: 195302.
20. Nayak BK, Gupta MC, Kolasinski KW. Formation of nano-textured conical microstructures in titanium metal surface by femtosecond laser irradiation. *Applied Physics A* 2008; **90**: 399.
21. Gupta MC, Nayak BK. Systems and methods of laser texturing and crystallization of material surfaces, International. Patent Application Serial No. PCT / US2006/049065, filed on 21 December 2006 in the U.S. Patent and Trademark Office.
22. Nayak BK, Gupta MC. Femtosecond-laser-induced-crystallization and simultaneous formation of light trapping microstructures in thin a-Si:H films. *Applied Physics A* 2007; **89**: 663–666.
23. Younkin R, Carey JE, Mazur E, Levinson JA, Friend CM. Infrared absorption by conical silicon microstructures made in a variety of background gases using femtosecond laser pulses. *Applied Physics Letters* 2003; **93**: 2626.
24. Iyengar VV, Nayak BK, Gupta MC. Optical properties of light trapping structures for photovoltaics. *Solar Energy Materials and Solar Cells* 2010; **94**(12): 2251.
25. Kolasinski KW, Dudley ME, Nayak BK, Gupta MC. Pillars formed by laser ablation and modified by wet etching. *Invited Paper—Proceedings of SPIE, The International Society for Optical Engineering*, 2007; **6586**: 65860H-1.
26. Grohe A, Preu R, Glunz SW, Willeke G. Laser application in crystalline silicon solar cell production. *Proceedings of SPIE, The International Society for Optical Engineering*, 2006; **6197**: 619717.
27. Nayak BK, Iyengar VV, Gupta MC. Ultrafast laser textured silicon solar cells. *Material Research Society Symposia Proceedings*, 2009; **1123**: 1123-P07-09.
28. Heyns MM, Bearda T, Cornelissen I, De Gendt S, Degraeve R, Groeseneken G, Kenens C, Knotter DM, Loewenstein LM, Mertens P, Mertens S, Meuris M, Nigam T, Schaekers M, Teerlinck I, Vandervorst W, Vos R, Wolke K. Cost-effective cleaning and high-quality thin gate oxides. *IBM Journal of Research and Development* 1999; **43**(3): 339.
29. Green MA, Keevers M. Optical properties of intrinsic silicon at 300 K. *Progress in Photovoltaics: Research and Applications* 1995; **3**: 189.
30. Sheehy M, Winston L, Carey JE, Friend CM, Mazur E. Role of the background gas in the morphology and optical properties of laser-microstructured silicon. *Chemistry of Materials* 2005; **17**: 3582.
31. Nickel NH, Lengsfeld P, Sieber I. Raman spectroscopy of heavily doped polycrystalline silicon thin films. *Physical Review B* 2000; **61**: 15558.
32. Sopori B, Madjdpour J, Zhang Y, Chen W. PV optics: an optical modeling tool for solar cell and module design. *Electrochemical Society Proceedings*, 1999; **99**: 138.
33. Iyengar VV, Nayak BK, Gupta MC. Performance of silicon PV devices based on a single step for doping, antireflection and surface passivation. *Solar energy materials and solar cells* 2010; **94**(12): 2205.

Prog Photovolt: Res Appl (2011) © 2011 John Wiley & Sons, Ltd
DOI: 10.1002/pip

SIONYX1403000041.0029

SAMSUNG EX. 1002 - 451/4148

Optical and Infrared Detection Using Microcantilevers

P. I. Oden, E. A. Wachter, P. G. Datskos, T. Thundat and R. J. Warmack
Oak Ridge National Laboratory, P.O. Box 2008, Oak Ridge, Tennessee, 37831-6123
Department of Physics, University of Tennessee, Knoxville, TN 37996-1200 (P.I.O., P.G.D., R.J.W.)

ABSTRACT

The feasibility of micromechanical optical and infrared (IR) detection using microcantilevers is demonstrated. Microcantilevers provide a simple means for developing single- and multi-element sensors for visible and infrared radiation that are smaller, more sensitive and lower in cost than quantum or thermal detectors. Microcantilevers coated with a heat absorbing layer undergo bending due to the differential stress originating from the bimetallic effect. Bending is proportional to the amount of heat absorbed and can be detected using optical or electrical methods such as resistance changes in piezoresistive cantilevers. The microcantilever sensors exhibit two distinct thermal responses: a fast one ($\tau_1^{thermal} < ms$) and a slower one ($\tau_2^{thermal} \sim 10ms$). A noise equivalent temperature difference, NEDT = 90 mK was measured. When uncoated microcantilevers were irradiated by a low-power diode laser ($\lambda = 786nm$) the noise equivalent power, NEP, was found to be $3.5nW/\sqrt{Hz}$ which corresponds to a specific detectivity, D^*, of $3.6\times10^7 cm\cdot\sqrt{Hz}/W$ at a modulation frequency of $20Hz$.

2. INTRODUCTION

Because infrared is the second most intense radiation band in our environment, its detection and imaging has extensive industrial, military, and commercial applications, including remote monitoring of facilities and equipment, process control, surveillance, night-vision, collision avoidance, and medical imaging. Presently, there are several families of commercially available infrared detectors, including thermopiles, pyroelectrics, bolometers, and various solid state detectors[1,2]. Thermopile detectors typically have a large thermal mass and long response times ($>10ms$). Bolometers using micromachined, suspended foils have much better rise times due to their reduced mass. Both thermopiles and bolometers offer broad spectral response when coated with suitable optically absorbing materials. Solid state detectors for the infrared region, such as quantum well devices, must generally be operated at reduced temperatures due to inherently high thermal noise. Additionally, the spectral response of these semiconductor devices is limited by the intrinsic properties of the composing materials. These infrared detectors can be classifies either as quantum - such as the pyroelectrics; or thermal detectors - such as bolometers and thermopiles. For the former type, incident infrared radiation is converted into an electronic response while with thermal detectors, IR radiation is converted into heat which is subsequently detected through temperature changes in the detector. Depending on the operational demands, one type of detection device may be favored over another. As a general rule, when the photon energy of the infrared radiation $h\upsilon > k_B T$, photon detectors offer better performance and when $h\upsilon < k_B T$, thermal detectors are generally favored.

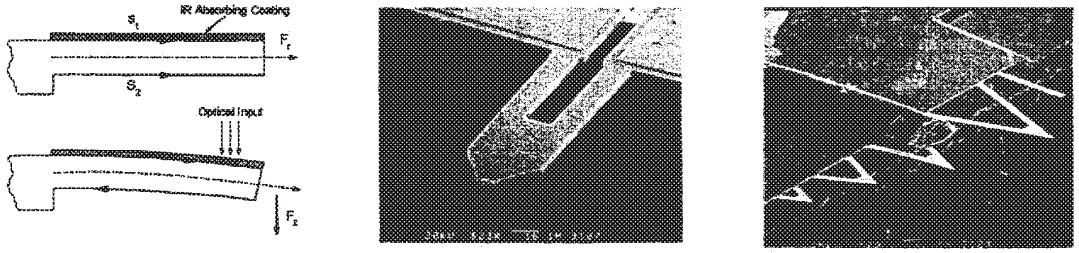


Figure 1. Left drawing is a cross-sectional schematic showing the bending response of a bimetallic cantilever with an IR adsorbing coating. Surface stresses S_1 and S_2 are balanced at equilibrium, generating a radial force F_r along the medial plane of the microcantilever. These stresses become unequal upon exposure to IR radiation producing a bending force, F_z, that displaces the tip of the microcantilever. Middle - is a scanning electron micrograph of one of the piezoelectric IR sensors used (calibration bar is $16\mu m$). Right - is another scanning electron micrograph of the Si_3N_4 microcantilevers used for the experiments compared to a human hair (calibration bar is $62.5\mu m$).

0-8194-2125-1/96/$6.00

Downloaded from SPIE Digital Library on 13 Oct 2018 to 151.207.242.4. Terms of Use: http://spiedl.org/terms

SIONYX1403000041.0030

SAMSUNG EX. 1002 - 452/4148

A new approach for producing compact, light-weight, highly-sensitive micromechanical infrared detectors is provided by microcantilever technology which is based on the bending of a microcantilever resulting from absorption of optical energy. When a microcantilever is exposed to infrared radiation, the temperature of the cantilever increases due to absorption of this optical energy[3,4]. If these microcantilevers are constructed from materials exhibiting dissimilar thermal expansion properties (such as silicon nitride coated with a thin gold film), the bimetallic effect will cause the microcantilever to bend in response to this temperature variation[3-14] (such a response is shown in the left image of Figure 1). The extent of bending is directly proportional, in first order, to the rate of energy absorption, which in turn is proportional to the radiation intensity. Previous work has shown that microcantilever bending can be detected with extremely high sensitivity[15-17]. For example, the metal-coated microcantilevers that are commonly employed in atomic force microscopy (AFM) allow sub-Angstrom ($< 10^{-10} m$) sensitivity to be routinely obtained. Recent studies have reported[9,14] the use of microcantilever bending for calorimetric detection of chemical reactions with energies as low as a few pJ. It was demonstrated[3] that the detector had an observed sensitivity of $100\,pW$ corresponding to an energy of $150\,fJ$ and proposed using the sensor as a femtojoule calorimeter. An estimate of the minimum detectable power level was of the order of $10\,pW$, corresponding to a detectable energy of $20\,fJ$ and a temperature sensitivity $10^{-5} K$[9]. However, using an optimally designed cantilever, the sensitivity may be improved even further[10-13]. Hence, for applications in optical radiation detection, microcantilevers can be coated with appropriate absorptive materials such that they undergo bending upon exposure to radiation (such as infrared or near infrared radiation). IR sensing cantilevers are typically $100-200\,\mu m$ long, $0.3-4\,\mu m$ thick and $10-50\,\mu m$ wide, and made out of materials such as silicon nitride, silicon or other types of semiconducting materials[18]. Due to the monolithic nature of these devices, they can easily be produced in one- and two-dimensional arrays with hundreds of levers on a single wafer. This type of fabrication scheme possesses obvious advantages when considering the production of infrared imaging systems with these cantilever devices.

When considering the bending of the lever, a proportionality between bending and the absorbed energy by the microcantilever is obtained by assuming a spatially uniform incident power, dQ/dt, onto a bimetallic microcantilever. Therefore, the maximum deflection, z_{max}, due to differential stress is given by[3,11,13,19]:

$$z_{max} = \frac{5}{4}\frac{(t_1+t_2)l^3}{(\lambda_1 t_1+\lambda_2 t_2)wt_2^2}\cdot\frac{\eta(\alpha_1-\alpha_2)(dQ/dt)}{4\left(1+t_1^2/t_2^2\right)+1/t_1t_2\left(6t_1^2+E_1t_2^2/E_2\right)+E_1t_1^3/E_2t_2^3} \qquad (1)$$

where l and w are, the length and width of the microcantilever, respectively, t_1 and t_2 are the thicknesses of the two layers, λ_1, λ_2; α_1, α_2; E_1, E_2 are the thermal conductivities; thermal expansion coefficients and Young's moduli of elasticity of the two layers; η is the fraction of the radiation power absorbed.

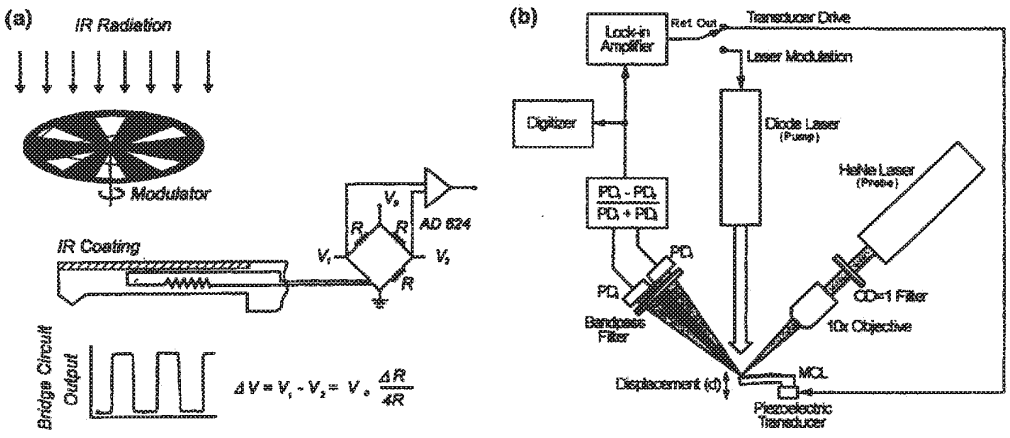


Figure 2. (a) Schematic representation of the piezoresistive IR detection experiment. The piezolever is part of a Wheatstone bridge, one of the legs connected to ground, the other to a metal film resistor with approximately the same resistance $R \sim 2000\Omega$. The other two outputs are connected to the input of a differential instrumentation amplifier. (b) Schematic diagram of the optical read-out method for IR detection.

Downloaded from SPIE Digital Library on 13 Oct 2010 to 151.207.242.4. Terms of Use: http://spiedl.org/terms

SIONYX1403000041.0031

SAMSUNG EX. 1002 - 453/4148

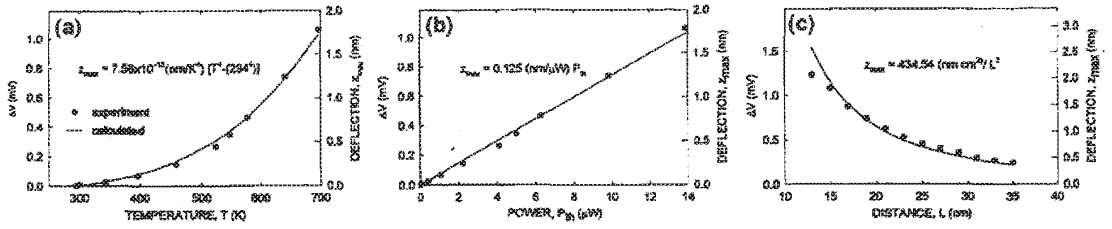


Figure 3. (a) Response of the Wheatstone bridge detection circuit, ΔV, and deflection, z_{max}, of the piezolever as a function of the source temperature. (b) Response as a function of the absorbed thermal power and (c) as a function of IR source distance, L.

3. EXPERIMENTAL

3.1. Piezoresistive Deflection Monitoring

A schematic diagram of the piezoresistive cantilever deflection detection technique is given in Figure 2(a). In this example, surface doped silicon microcantilevers were used in which the piezoresistance across the cantilever varied when it bent due to thermal stimulation. The design and construction of these cantilevers is described in detail elsewhere[20,21]. The total resistance of the cantilever was approximately $2000\,\Omega$, which was electrically connected across one arm of a dc-biased Wheatstone bridge circuit. The change in the total resistance is directly proportional to the maximum deflection of the cantilever[20]:

$$\Delta R(T) = 3R z_{max}(T) \times 10^{-6} \tag{2}$$

where $z_{max}(T)$ is expressed in nm.

The thermally induced deflection of the cantilever is caused by the bimetallic effect which arises due to the difference in the thermal properties of the IR coating, the metal layer, and the native silicon body of the cantilever. A reference voltage V_0 (equal to 9 volts in these experiments) was applied across the circuit and the voltage difference, $\Delta V(T)$, across the Wheatstone bridge circuit was digitized using a Tektronix TDS 544A digital oscilloscope or fed into a Stanford Research Systems SR850 lock-in amplifier. The measured voltage ΔV is related to the deflection of the cantilever by

$$\Delta V(T) = \frac{3V_0}{4} z_{max}(T) \times 10^{6} \tag{3}$$

The experimental measurements were performed using piezoresistive microcantilevers as temperature sensors in the configuration shown in Figure 2(a). The commercially available piezolever[18] was coated with $\sim 50\,nm$ of gold black which served as the IR absorbing material. IR radiation was then focused onto the sensor using a $2.54\,cm$ diameter IR lens with a focal length of $3.5\,cm$ and a wavelength transmission range between $0.6-15\,\mu m$[22]. A Stanford Research Systems SR-540 chopper was used to modulate the IR radiation upon the detector. The sensor assembly was positioned $15\,cm$ from a soldering iron which served as the IR source. A calibrated thermocouple was attached to the IR source so that its temperature could be recorded.

The thermal power absorbed by the detector can be described as:

$$P_{thermal} = \eta \frac{dQ}{dt} = \eta t_L \left(\frac{A_D'}{2\pi L^2} \right) A_S \varepsilon \sigma_{S-B} \left(T_S^4 - T_R^4 \right) \tag{4}$$

where t_L is the transmission of the lens, A_D' is the effective area of the sensor, L is the distance of the detector from the source, A_S is the area of the target (IR source), ε is the target's emissivity, σ_{S-B} is the Stefan-Boltzmann constant

Downloaded from SPIE Digital Library on 13 Oct 2019 to 151.207.242.4. Terms of Use: http://spiedl.org/terms

SIONYX1403000041.0032

SAMSUNG EX. 1002 - 454/4148

$(\sim 5.67\times10^{-12}\,W\cdot cm^{-2}\cdot K^{-4})$, T_S is the temperature of the target, and T_R is the background temperature. In the present studies $t_L \sim 0.7$, $A_D = 6.2\times10^{-4}\,cm^2$, $L \sim 15\,cm$, $A_S \sim 90\,cm^2$, and $T_R = 294\,K$. Using these values in Eq. (4), the absorbed thermal power (in Watts) is $P_{thermal} \sim 6.064\times10^{-17}\left[T_S^4 - (294)^4\right]$ (assuming that $\eta \sim 0.9$ and a measured $\varepsilon \sim 0.43$ for the hot iron IR source).

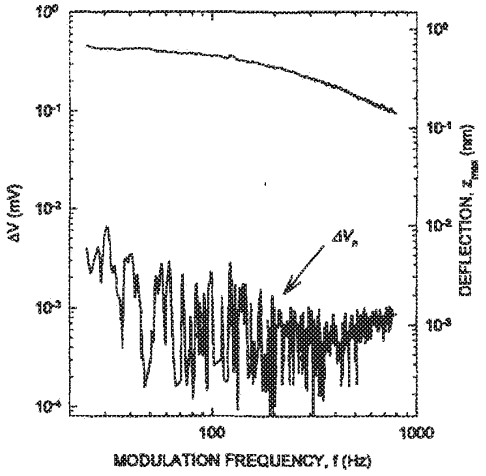


Figure 4. Response of the Wheatstone bridge detection circuit, ΔV, deflection, z_{max} and noise ΔV_n of the piezolever as a function of the modulation frequency.

The response ΔV was measured as a function of the temperature, T, of the IR source. This is plotted in Figure 3(a) along with the deflection, z_{max}, of the piezolever and can be seen to be a monotonically increasing function of temperature. In Figure 3(b) a plot of the response of Wheatstone bridge circuit, ΔV, and the deflection, z_{max}, of the piezolever detector as a function of the total power absorbed by the detector and it can be seen that it increases linearly with increasing power. From the slope of this line, a deflection sensitivity of $0.125\,nm/\mu W$ is obtained. At a modulation frequency of $30\,Hz$, a noise equivalent power (NEP) of $\sim 70\,nW/Hz^{1/2}$ was also obtained, where $NEP = (\Delta V_n/\Delta V)\times P_{thermal}$; ΔV_n is the background noise level $(\Delta V_n \sim 10^{-6}\,V)$.

The response of the detector was also measured as a function of the distance from an IR source. This is shown in Figure 3(c) where ΔV and z_{max} are plotted as a function of the distance, L, between the detector and the surface of the soldering iron (IR source); L was varied from $14\,cm$ to $35\,cm$. The ambient temperature was $\sim 294\,K$ and the temperature of the IR source was held at $693\,K$. The measured ΔV and calculated z_{max} were found to decrease with increasing distance and followed closely an inverse square relationship with distance [see Eq. (4)] for distances larger than $15\,cm$.

Since the response of any thermal sensor depends on both the amount of heat falling onto the detector and the length of time it is exposed to the incoming IR radiation we measured the response of the Wheatstone bridge circuit, ΔV, and the deflection, z_{max}, as a function of modulation frequency of the IR radiation (Figure 4). It can be seen that the detector response (and the deflection of the cantilever) decreases with increasing modulation frequency. The temporal response of the temperature sensor was also determined by measuring ΔV as a function of time. The microcantilever was found to exhibit two thermal response times due to the incoming IR radiation; a time $\tau_1^{thermal} < 1\,ms$ and a time $\tau_2^{thermal}$ that is somewhat longer $(\sim 10\,ms)$.

These findings demonstrate that small changes in temperature induce deflections of the microcantilever correspond to measurable changes in the piezocantilever resistance. It should be noted that these commercially available piezolevers have

Downloaded from SPIE Digital Library on 13 Oct 2016 to 151.207.242.4. Terms of Use: http://spiedl.org/terms

SIONYX1403000041.0033

SAMSUNG EX. 1002 - 455/4148

been designed to be minimally sensitive to changes in temperature so as to reduce the noise and interference in scanning probe microscopy applications. Therefore, the temperature sensitivity of the piezolever could be further improved by optimizing its shape, IR absorbing coating and thermal isolation.

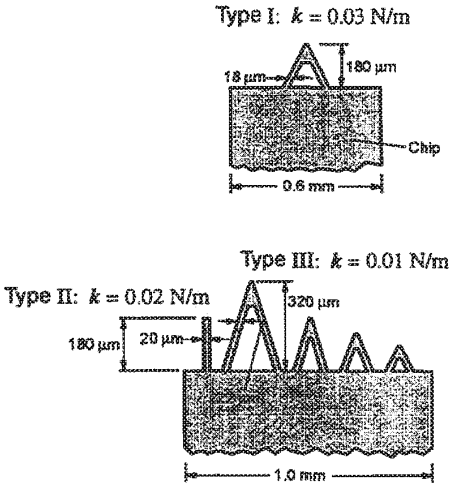


Figure 5. Schematic view of the $0.6\mu m$ thick Si_3N_4 microcantilevers used for evaluation of thermal response. Note that results from only the two left-most microcantilevers (out of five total) on the lower chip are presented.

3.2. Optical Deflection Monitoring

Bending of microcantilevers can readily be determined by a number of means, including optical, capacitive, tunneling, and, as shown before, piezoresistive. The optical deflection approach used was adapted from standard atomic force microscopy imaging systems, and is shown in Figure 2(b). Microcantilevers were mounted in a holder (from Digital Instruments) designed for tapping mode AFM, which secured the base of the microcantilever against a small piezoelectric transducer; this chip holder was then mounted on a three-axis translation stage to facilitate fine adjustment of the microcantilever relative to the rest of the experimental apparatus. Collimated optical radiation from a diode laser was used to evenly illuminate the mounted microcantilever (pump wavelength of $786\,nm$, beam diameter of $6\,mm$, centered on the tip of cantilevers $180-320\,\mu m$ in length). Output of this excitation source was modulated sinusoidally at frequencies ranging from DC to $100\,kHz$, with peak powers ranging from 0 to $18.5\,mW$ (0 to $65\,mW/cm^2$). This configuration provided a flexible, easily controlled test system for quantifying microcantilever response to optical energy. All measurements were conducted at ambient temperature and atmospheric conditions.

A second laser was used in a probe configuration to monitor bending. A helium-neon laser (or HeNe, delivering $3\,mW$ at $633\,nm$) was focused onto the tip of the microcantilever using a 10X microscope objective; to minimize heating of the tip by the probe laser, optical power was reduced by placing a neutral density filter with an optical density of 1.0 between the probe laser and the objective. A dual element photodiode displacement detector was used to collect the reflected probe beam [position detectors PD_1 and PD_2 in Figure 2(b)]; a $1\,nm$ bandpass filter centered at $633\,nm$ was placed in front of the detector to block scattered light from the pump laser. The difference signal from the detector pair as the cantilever tip changed position $\left([PD_1 - PD_2]/[PD_1 + PD_2]\right)$ was used to measure the displacement, d. This signal was directly digitized and stored, or sent to a lock-in amplifier (SR850, Stanford Research Systems) for signal extraction and averaging. The lock-in amplifier was also used to control modulation frequency and output level of the pump laser.

Downloaded from SPIE Digital Library on 13 Oct 2010 to 151.207.242.4. Terms of Use: http://spiedl.org/terms

SIONYX1403000041.0034

SAMSUNG EX. 1002 - 456/4148

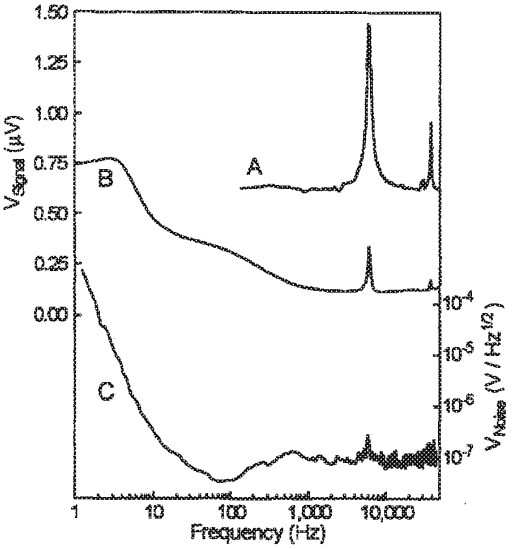


Figure 6. Mechanical and optical excitation spectra for a Type III microcantilever. Response to frequency swept mechanical excitation is given in spectrum 'A'; similar results for optical excitation are shown in spectrum 'B'. Optical excitation was effected using a sinusoidally modulated pump laser at $786\,nm$. Spectrum 'C' shows noise response when the pump laser is operated in a dc mode. Fundamental mechanical resonance at $6.2\,kHz$ and higher-order resonance at $37\,kHz$ are evident for both optical and mechanical excitation.

Optical response characteristics of three different types of commercially available AFM probe tips were evaluated. These microcantilevers are shown schematically in Figure 5 as well as in the scanning electron micrograph of Figure 1. Microcantilevers typically come from the manufacturer attached to a large rectangular chip (ca. $1\,mm$ wide x $3\,mm$ long x $1\,mm$ thick) that is used to facilitate manipulation and mounting, and all those evaluated in this work were used as received. The microcantilevers used were: a triangular silicon nitride Si_3N_4 microcantilever (labeled "I" in Figure 5, with a length of $180\,\mu m$, a width of $18\,\mu m$ and a bending force constant $k \sim 0.3\,N/m$, from Park Scientific); a rectangular silicon nitride microcantilever (labeled "II", $200\,\mu m$ in length and $20\,\mu m$ in width, bending force constant $k \sim 0.2\,N/m$, Park Scientific); and a triangular silicon nitride cantilever (labeled "III", which was $320\,\mu m$ long and $22\,\mu m$ wide, with a bending force constant $k \sim 0.1\,N/m$, Park Scientific). Each was $0.6\,\mu m$ thick. The Type I cantilever was coated with aluminum on one side to see how this would affect its optical response characteristics; Types II and III were used as received from the manufacturer, with a gold/chromium film uniformly covering one side.

An essential aspect of any scheme for micromechanical optical detection is the ability to sensitively detect physical changes resulting from thermal stress, since this directly affects the sensitivity and precision in measurement of temperature change or thermal flux. As an initial evaluation of the ability to detect optically-induced bending of a microcantilever, each of the three types of microcantilever were subjected to both mechanical and optical excitation, and their response measured as a function of excitation frequency. Mechanical excitation was achieved by driving the piezoelectric element in the AFM chip holder with the reference signal from the lock-in amplifier; such mechanical excitation spectra are helpful in locating resonance frequencies for allowed microcantilever bending modes. Optical excitation spectra were obtained by modulating the pump laser with the lock-in reference signal. Typical response spectra for a triangular microcantilever (Type III) are shown in Figure 6. The mechanical spectrum (curve "A") shows two resonances, at $6\,kHz$ and $38\,kHz$, attributable to the fundamental transverse resonance and a higher-order resonance (possibly torsional bending), respectively. The optical spectrum (curve "B") shows similar resonance features, although with somewhat different relative intensities; a large, broadband response is also noted at low frequencies. No synchronous oscillatory response was noted when the microcantilever was excited with constant dc laser power (curve "C"). Similar response was noted under these conditions for the other two microcantilevers.

Downloaded from SPIE Digital Library on 13 Oct 2010 to 151.207.242.4. Terms of Use: http://spiedl.org/terms

SIONYX1403000041.0035

SAMSUNG EX. 1002 - 457/4148

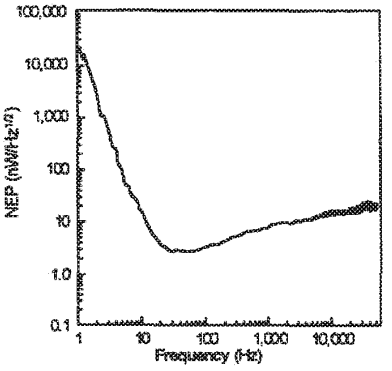


Figure 7. Noise equivalent power (NEP) as a function of modulation frequency for a Type III Si_3N_4 microcantilever. Optical excitation at $785nm$, utilizing bimetallic bending induced in a gold/chromium film.

Figure 6(B) shows that microcantilever response to optical input decreases rapidly for frequencies above $10\,Hz$, but that mechanical resonance is still observed even at frequencies well above $10\,kHz$. In fact, the Type I and II microcantilevers exhibited strong optical resonance at frequencies of $17\,kHz$ and $14\,kHz$, respectively; these modes correspond to the fundamental transverse resonances for the microcantilevers. Such resonant response demonstrates that reversible heating and bending of the cantilever occurs as a result of optical excitation, producing mechanical vibration. These resonances also have quality factors that are identical to their mechanically-driven counterparts, confirming that optically-pumped mechanical vibration is occurring.

The rapid roll-off in response observed in Figure 6(B) is attributed to thermal equilibration of the cantilever at high modulation frequencies. Because the cantilever must dissipate heat between laser pulses, the finite thermal conductivity of its legs limits the rate at which heat from these thermal impulses can be transferred out of the microcantilever and into the support structure (the chip); thus, as modulation frequency is increased and the microcantilever approaches thermal equilibrium, changes in thermal stress as a function of time approach zero. Comparison of the response of the Type II and Type III cantilevers showed that the rectangular Type II microcantilever had a higher relative response at frequencies above $7.5\,kHz$. We believe this is due to more effective thermal transfer for the rectangular geometry. Since the rectangular microcantilever does not have a geometric restriction between the cantilever and the chip, transfer of thermal energy absorbed at the tip should be more rapid than that for the triangular microcantilever, which has a large area tip suspended on relatively narrow legs. The direct route of thermal transfer in the rectangular microcantilever appears to allow it to maintain a thermal differential at higher optical modulation frequencies, and hence to continue responding to the time varying optical stimulus at frequencies well above those practical with the triangular geometry.

In order to evaluate the role of optical reflectivity (or thermal absorptivity) on microcantilever response, a silicon nitride microcantilever (the Type I specimen) was coated on one side with a thin layer of aluminum; note that the manufacturer's gold/chromium film was removed prior to aluminum deposition. This produced a microcantilever that had a nearly transparent body that was highly reflective to the pump laser on the aluminum coated side (reflectivity, $R \sim 0.95$ at $786\,nm$), but slightly less reflective on the uncoated side (due to absorption of the pump radiation upon transmission through the Si_3N_4 cantilever body). As expected, the resonant frequency of this cantilever was found to be $17\,kHz$. However, when the uncoated side of the microcantilever was illuminated (reverse geometry), the magnitude of bending response at all frequencies increased by about 20% in comparison to normal illumination on the reflective side. We believe this difference is attributable to increased absorption of the pump beam upon transmission through the Si_3N_4 material, resulting in more effective transduction of optical energy into thermal heating of the microcantilever. While this simple experiment demonstrates that sensitivity can be improved by increasing absorption of impinging optical radiation, it is obvious that to optimize the method further suitable optically absorbing coatings are needed (such as carbon black, gold black, or other broadband absorbers). Unfortunately, such materials were not available for this study.

Downloaded from SPIE Digital Library on 13 Oct 2019 to 151.207.242.4. Terms of Use: http://spiedl.org/terms

SIONYX1403000041.0036

SAMSUNG EX. 1002 - 458/4148

Photometric response was further characterized by measuring microcantilever response at various modulation frequencies and optical pump levels (Figures 6 and 7, and Table I). For the Type III Si_3N_4 microcantilever, we estimate a

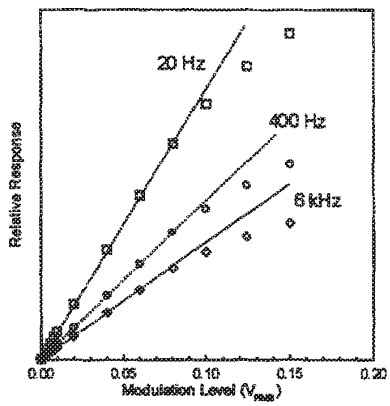


Figure 8. Photometric response for a typical microcantilever (Type III) at various optical pump levels using excitation at 20Hz, 400Hz and 6kHz.

noise equivalent power (NEP) of $3.5 nW/Hz$ at $20 Hz$, where $NEP = (V_{noise}/B)(P/V_{signal})$, V_{noise} is the background noise level on the cantilever over a lock-in amplifier bandwidth, B, of $0.26 Hz$, and P is the incident optical power producing an observed signal, V_{signal}. Specific detectivity, D^*, is equal to $3.6\times10^7\ cm\cdot Hz^{1/2}/W$ under these conditions, where $D^* = (A^{1/2}V_{signal})/(V_{noise}P)$, and A is the area of the detector element. Note that the characteristics of this initial, unoptimized microcantilever compare quite favorably with some room temperature technologies currently under development, including indium antimonide photoconductors ($NEP = 5nW$ at $500 Hz$)[23], but are not yet competitive with silicon microbolometers ($NEP = 5pW/Hz$, $NETD = 40mK$ at $30 Hz$)[24] or pyroelectric devices ($NEP = 8pW/Hz$, $D^* = 3.5\times10^8\ cm\cdot Hz^{1/2}/W$)[25]. However, in contrast to these highly optimized examples, several simple improvements to our microcantilever system are obvious that could improve performance dramatically. For instance, since the metal coating on

Table I. Photometric response at 785nm for a gold/chromium coated Si_3N_4 microcantilever (Type III). Data at 6.02kHz was obtained at the mechanical of the microcantilever.

Optical Modulation Frequency (Hz)	Detector Time Constant (ms)	V_{signal} (μV)	V_{noise} (μV)	NEP (nw/√Hz)	D* (cm·Hz$^{1/2}$/W)
6020	300	307.1	0.585	13.1	9.48 x 10^6
	30	305.3	1.76	12.5	9.91 x 10^6
	1	305.5	9.46	12.3	1.01 x 10^7
400	300	223.2	0.196	6.03	2.06 x 10^7
	30	221.1	0.691	6.78	1.83 x 10^7
	10	226.3	1.19	6.59	1.88 x 10^7
20	300	528.2	0.266	3.46	3.59 x 10^7

the tested cantilevers is highly reflective at the pump wavelength (for gold, $R > 98\%$ at $785 nm$), use of an improved absorptive coating (such as gold black, $R < 2\%$) could improve NEP in this example to $< 75 pW$. Furthermore, the observed

Downloaded from SPIE Digital Library on 13 Oct 2019 to 151.207.242.4. Terms of Use: http://spiedl.org/terms

SIONYX1403000041.0037

SAMSUNG EX. 1002 - 459/4148

detection limits appear to be determined by readout noise in our optical detection circuit. We believe that with careful design of this circuitry, performance could be substantially improved. Finally, response of the microcantilevers was extremely linear (with a correlation coefficients, $r_2 > 0.99995$) for all but the highest test levels; roll-off in measured response for very high laser modulation levels is an artifact of our method for modulating the pump laser, which exhibited a reduced depth of modulation at high drive levels.

4. CONCLUSIONS

We have demonstrated that microcantilevers represent an important development in room temperature infrared detector technology, and can be expected to provide the basis for considerable further development. For example, while the microcantilevers employed here were optimized for standard AFM applications (and were in fact designed to minimize thermal sensitivity), vastly improved detectors could be produced by making relatively simple changes in the materials and geometries used in microcantilever fabrication. It is possible to design microcantilevers with much smaller force constants by varying the geometry of the cantilever, and in contrast to the devices used in this study, cantilevers with force constants as small as $0.006\,N/m$ are now commercially available. Since the fundamental mechanical resonance frequency of a microcantilever is proportional to $\sqrt{k}$, reductions in force constant can be used to bring resonance into ranges compatible with mechanical chopping frequencies. It is also clear that the coatings applied to the cantilever are at least as important as the composition of the cantilever itself. For example, high thermal expansion bimetallic coatings (such as films of Al, Zn, Pb, or In) could be used to increase the thermally-induced bending of the cantilever. Coating the surface of the cantilever with high emissivity materials (such as gold black) can also enhance IR response.

Since microcantilever spectral response can be easily tailored through the application of specific absorptive coatings, choice of material for fabrication of the microcantilever can be determined primarily by the requirements of the manufacturing process. This means that microcantilevers can be fabricated using standard semiconductor methods and materials, and as a consequence could be mass produced at very low cost. Hence, two-dimensional cantilever arrays based on the technology described here could become very competitive with existing technologies due to their inherent simplicity, high sensitivity, and rapid response to optical radiation. While the optical readout method is useful with single element designs, practical implementation of microcantilever arrays may require the use of other readout methods, such as piezoresistance. Fortunately, the microcantilever technology's compatibility with a variety of readout methods also affords tremendous flexibility to potential system designers.

5. ACKNOWLEDGEMENTS

Research sponsored by U.S. Department of Energy under contract DE-AC05-96OR22464 with Lockheed Martin Energy Research Corp. The authors wish to acknowledge the support of the ORNL Seed Money Program. The efforts of P.I. Oden were supported, in part, by an appointment to the Alexander Hollaender Distinguished Postdoctoral Fellowship Program sponsored by the U.S. Department of Energy, Office of Health and Environmental Research, and administered by the Oak Ridge Institute for Science and Education. P.G. Datskos wishes to acknowledge the support of the National Science Foundation under the SBIR award DM2-9460929 to Consultec Scientific, Inc.

6. REFERENCES

1. R.J. Kayes, Editor "Optical and Infrared Detectors," *Topics in Applied Physics*, Volume 19, Springer Verlag Berlin (1977).
2. P. Howard, J. Stevens, C. Rau, R.J. Herrring, and R.A. Wood, *Infrared Technology XXI*, SPIE Vol. 2552-60, July 1995.
3. J.R. Barnes, R.J. Stephenson, C.N. Woodburn, and M.E. Welland, *Rev. Sci. Instum.* , **65**, 3793 (1994).
4. O. Nakabeppu, M. Chandrachood, Y. Wu, J. Lia, and A. Majumdar, *Appl. Phys. Lett.* , **66**, 694 (1995).
5. N. Umeda, S. Ishizaki, and H. Uwai, *J. Vac. Sci. Technol.* , **B9**, 1318 (1991).
6. M. Allegrini, C. Astoli, P. Baschieri, F. Dinneli, C. Frediani, A. Lio, and T. Mariani, *Ultramicroscopy*, **42-44**, 371 (1992).
7. O. Marti, A. Ruf, M. Hipp, B. Bielefeldt, J. Colchero, and J. Mlynek, *Ultramicroscopy*, **42-44**, 345 (1992).
8. J. Mertz, O. Marti, and J. Mylnek, *Appl. Phys. Lett.*, **62**, 2344 (1993).
9. J. K. Gimzewski, Ch. Gerber, E. Meyer, and R. R. Schlitter, *Chem. Phys. Lett.*, **217**, 589-594 (1994).
10. T. Thundat, R. J. Warmack, G. Y. Chen, and D. P. Allison, *Appl. Phys. Lett.*, **64**, 2894-2896 (1994).

Downloaded from SPIE Digital Library on 13 Oct 2019 to 151.207.242.4. Terms of Use: http://spiedl.org/terms

SIONYX1403000041.0038

SAMSUNG EX. 1002 - 460/4148

11. E. A. Wachter, T. Thundat, P. G. Datskos, P. I. Oden, S. L. Sharp, and R. J. Warmack, "Remote Infrared Detection Using Microcantilevers", *Rev. Sci. Instrum.* (submitted).
12. G. Y. Chen, T. Thundat, E. A. Wachter, R. J. Warmack, "Adsorption-Induced Surface Stress and Its Effect on Resonance Frequency of Microcantilevers," *J. Appl. Phys.*, 77, 1 (1995).
13. P.G. Datskos, P.I. Oden, T. Thundat, E.A. Wachter, R.J. Warmack and S.R. Hunter, "A Micromechanical Temperature Sensor", *Appl. Phys. Lett.* (submitted).
14. J. K. Gimzewski, Ch. Gerber, E. Meyer, and R. R. Schlitter, "Micromechanical Heat Sensor: Observation of a Chemical Reaction, Photon and Electrical Heat Pulses", in *Forces in Scanning Probe Methods*, Proceeding of the Nato ASI, H.-J. Güntherodt, D. Anselmetti, and E. Mayer (eds.) p. 123-131 (1995).
15. D. Sarid, *Scanning Force Microscopy*, Oxford University Press, New York, (1991).
16. *"Investigations of the Reconstructed Gold Surface with Electrochemical Scanning Probe Microscopy"* - PhD. dissertation, Patrick Ian Oden, Arizona State Univesity Physics Department (1993).
17. P.I. Oden, N.J. Tao and S.M. Lindsay, *J. Vac. Sci. Technol.* **B11**(2), 137 (1993).
18. Commercial versions available through Digital Instruments, Santa Barbara, CA and Park Scientific, Sunnyvale, CA.
19. W. C. Young, *Roark's Formulas for Stress and Strain*, Sixth ed., McGraw Hill, New York, pp. 118 (1989).
20. M. Tortonese, R. C. Barrett, and C. F. Quate, *Appl. Phys. Lett.*, **62**, 834 (1993).
21. F. J. Giessibl and B. M. Trafas, *Rev. Sci. Instrum.*, **65**, 1923 (1994).
22. Oriel Co., Model 43402 AMTIR-1 lens.
23. R. Anton, E.L Dereniak, and J. Garcia, *Infrared Technology XXI*, SPIE Vol. 2552, 592, July 1995.
24. N. Butler, R. Blackwell, R. Murphy, R. Silva, and C. Marshall, *Infrared Technology XXI*, SPIE Vol. 2552, 583, July 1995.
25. S. Fujii, T. Kamada, S. Hayashi, Y. Tomita, R. Takayama, T. Hirao, T. Nakayama, and T. Deguchi, *Infrared Technology XXI*, SPIE Vol. 2552, 612, July 1995.

Downloaded from SPIE Digital Library on 13 Oct 2018 to 151.207.242.4. Terms of Use: http://spiedl.org/terms

SIONYX1403000041.0039

SAMSUNG EX. 1002 - 461/4148

A BACK-ILLUMINATED MEGAPIXEL CMOS IMAGE SENSOR

Bedabrata Pain, Thomas Cunningham, Shouleh Nikzad,
Michael Hoenk, Todd Jones, Bruce Hancock, Chris Wrigley
Jet Propulsion Laboratory
California Institute of Technology
4800 Oak Grove Drive, Pasadena, CA 91109
Phone: 818-354-8765; Fax: 818-393-0045; Email: bpain@jpl.nasa.gov

Imaging with a back-illuminated CMOS imager provides a number of advantages, especially as the pixel size is reduced. These advantages include high (100%) fill-factor and increased quantum efficiency, efficient implementation of antireflection coatings, improved angular response, availability of the traditional "frontside" of the pixel to incorporate in-pixel processing circuits, and increased compatibility with the next generation metals (e.g Cu) and low-k dielectrics.

In this paper, we present the test and characterization results for a back-illuminated megapixel CMOS imager. The imager pixel consists of a standard junction photodiode coupled to a three transistor-per-pixel switched source-follower readout [1]. The imager also consists of integrated timing and control and bias generation circuits, and provides analog output. The analog column-scan circuits were implemented in such a way that the imager could be configured to run in off-chip correlated double-sampling (CDS) mode. The imager was originally designed for normal front-illuminated operation, and was fabricated in a commercially available 0.5 μm triple-metal CMOS-imager compatible process. For backside illumination, the imager was thinned by etching away the substrate was etched away in a post-fabrication processing step.

Figure 1 shows the schematic cross-section of the back-illuminated CMOS APS. The device structure consists of a low-doped (~ $3x10^{14}/cm^3$) epitaxial p-type silicon, with the photo-detecting junction formed by a front-implanted n-well and the p-type epitaxial silicon. Photons enter the detector from the backside, and the resultant photo-electrons are collected in the front-side p-nwell junction.

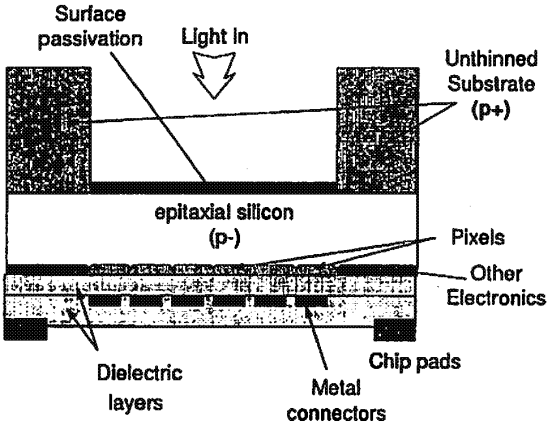


Figure 1: Schematic cross-section of the back-illuminated imager

The imager was thinned at an individual die level using a frame-thinning approach. Only the pixel area was thinned down to ~ 7-10 μm thickness (corresponding to epitaxial silicon thickness), leaving a thick peripheral region (~ 1 mm wide). A surface passivation step was then applied to the thinned silicon layer.

The resultant structure provides increased mechanical stability, a significant ease of die handling, and protection against wrinkling of the thinned die. This approach is well-suited for a CMOS imager, since the imager consists not only of the pixels, but the support and signal chain electronics along the periphery of the pixel array.

Backside thinning was carried out as follows. First, the front-side of the die is attached to a protective wax. Then a protective frame on the backside was created through deposition and patterning of a Si_3N_4 mask. The unmasked p^+ silicon substrate (with doping ~ $1x10^{19}/cm^3$) was then etched using hot KOH down to within ~ 10 μm of the final silicon thickness. The remainder of the etching was carried out in $HF:HNO_3:CH_3COOH$ solution (HNA etch) [2]. HNA etches silicon through a redox reaction where the silicon oxidation rate is dependent on the doping concentration. Due to its doping concentration dependence, the etch-rate significantly slows down when the silicon substrate is etched, leaving an optically flat thin (~ 10 μm thick) epitaxial silicon layer. Following thinning, the front-side wax was removed, and the die was packaged in a standard pin-grid array (PGA) package (with its central portion removed to let light in) using a standard wire-bonding technique.

SAMSUNG EX. 1002 - 462/4148

Passivation of the etched silicon presents a unique challenge. After thinning, the interface trap density at the unterminated silicon surface is unacceptably high, while a naturally formed native oxide (~20 °A thickness) causes the surface to become positively charged. Unwanted band-bending and the presence of dangling bonds result in a loss of QE and abnormally high dark currents, necessitating the use of post-metallization surface-passivation steps. Unfortunately, any post-metallization process step is challenging, since due to the presence of front-side metal with low melting point (~ 400°C), no high temperature step can be used. Thus, boron implantation and high-temperature furnace anneal is ruled out.



Figure 2: Photograph of the thinned megapixel imager

Self-passivation can achieved by controlling the HF concentration during the final stages of etching that leaves behind a 30-50°A oxide. However, the lack of a well-defined end-point of the etching process makes it difficult to carry out reliable self-passivation of the etched silicon surface. To get around this problem, some CCDs have used alternate passivation techniques that include UV-flooding, flash gates (MBE deposited mono-layer of metal), boron-doping followed by high-energy pulsed-laser anneal, and low-pressure oxide deposition [3,4,5,6].

We have used a delta-doping technique for surface passivation [7]. The technique consists of a low-temperature molecular beam epitaxy (MBE) that places an extremely high density of dopant atoms (> 10^{14} Boron/cm^2) within a few atomic layers of the surface with no observable crystal defects and no requirement for post-growth annealing, making it compatible with post-metallization processing. Delta-doping is carried out under ultra-high vacuum conditions (10^{-10} torr) using electron-beam evaporation of elemental silicon and thermal evaporation of elemental boron. The process steps are as follows. A 1 nm-thick p+ silicon layer was grown first, followed by depositing ~30% of a monolayer of boron atoms. 1.5 nm-thick capping layer of epitaxial silicon was then grown. After removal from the MBE system, oxidation of the silicon capping layer protects the buried delta-doped layer. Finally, the resultant optically flat surface allows easy deposition of anti-reflection coating using deposited oxides and plasma-enhanced silicon nitrides.

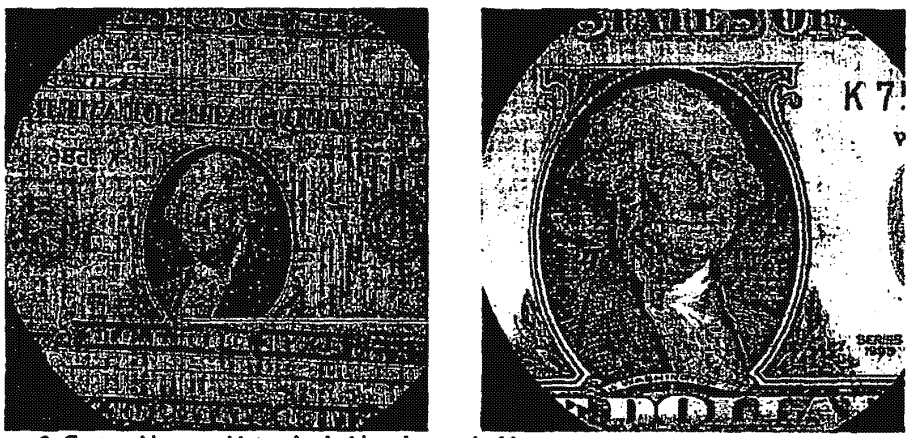


Figure 3: Captured image with two back-thinned megapixel imagers

Figure 2 shows the die level picture of the back-thinned imager. The unthinned frame is clearly visible in the picture. One of the advantages of the thinning approach described above is that the back-illuminated imager is packaged using conventional packaging techniques only.

Figure 3 shows captured images with two back-illuminated CMOS imagers. The problem with the first imager is clearly visible in figure 3 (left). Following thinning, the imager developed crystallographic defects resulting in the loss of one column and multiple imager rows. The second imager showed no such problems, resulting in an excellent quality image as shown in figure 3 (right). The circular aperture shown in the images correspond to the opening that was cut in the PGA package to let light in.

Without delta-doping, the imager showed very high dark currents, and was virtually inoperable. After delta-

SAMSUNG EX. 1002 - 463/4148

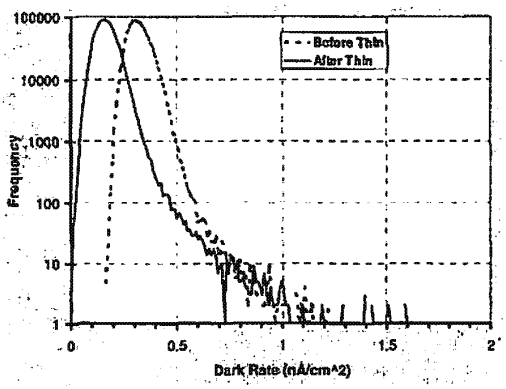


Figure 4: Dark current distribution of the megapixel imager before and after thinning

doping, however, the dark current was reduced to normal levels. In fact, as shown in figure 4, the modal dark current dropped below its original value. The modal dark rate before thinning was 294 pA/cm^2, and was reduced below 153 pA/cm^2, indicating the efficacy of delta-doping for trap interface trap passivation.

Figure 5 shows the measured quantum efficiency (QE) of the CMOS imager, before and after thinning. QE for the back-illuminated CMOS imager is shown as square dots, while the QEs for the same imager measured from the front-side - before (triangles) and after thinning (diamonds) - are shown in the same figure for comparison. Figure 5 clearly indicates the benefits of 100% fill-factor. Without any anti-reflection coating added to the backside, QE increased by a factor 2.6x in blue, 2.5x in green, and 2.7x in red.

We have compared the measured back-illuminated QE against existing back-illuminated imager QE models [8,9]. Figure 6 shows the measured QE before and after the application of anti-reflection coating. The measured data is shown in dots, and the modeled QE is shown as dashed lines. The data fits the model with a surface recombination velocity of 6x10^4 cm/s and an epitaxial silicon thickness of 7 µm. With reflection losses limiting the QE, it can be seen from figure 6 that, except at shorter wavelengths, the QE data without AR coating agrees with the modeled QE very well. Figure 6 also shows that with AR coating, QE increased to ~ 90% in green, although the variance from the model is larger, possibly indicating the need for improved AR coating design.

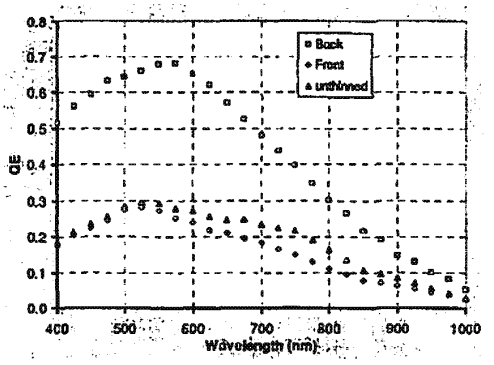


Figure 5: Measured QE of the megapixel imager – comparison between back and front illumination

A relatively fast drop off of the QE with increasing wavelength is indicative of the limited silicon thickness (~ 7 um) in the imaging area. In addition, since the imager was not originally designed for back-illumination, it did not have sufficient metal covering over the front-side of the pixel. As a result, the imager shows reduced red response due to a diminished optical collection of longer wavelength light. However, the QE in the red region is sufficient for consumer imaging applications.

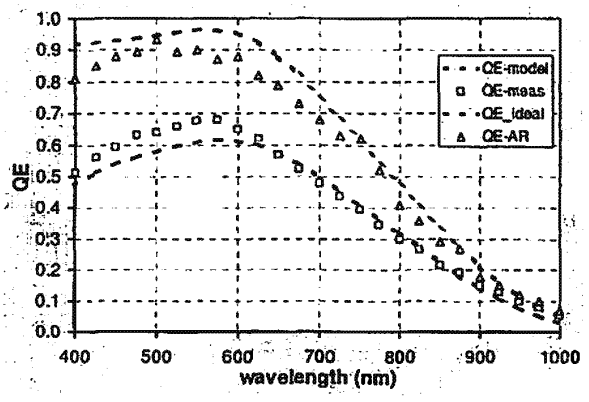


Figure 6: Modeled QE – before and after AR coating

While modulation transfer function (MTF) has not been measured yet, certain observations about the diffusion cross-talk between pixels can be made. Figure 7 shows that the modeled 1-D dopant concentration from the backside surface (origin) to the frontside nwell area. The p-substrate doping is ~ 1x10^7/µm^3, the epi-doping is 3x10^2/µm^3, and the n-well doping is ~ 6x10^4/µm^3.

SAMSUNG EX. 1002 - 464/4148

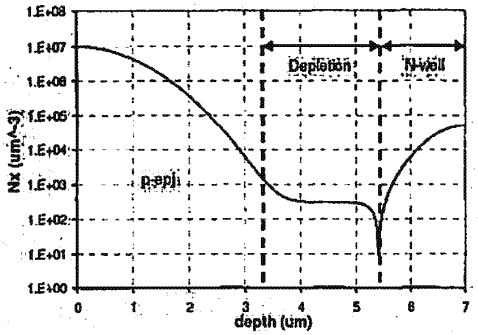


Figure 7: 1-D model of doping concentration variation from the backside surface to the front

As a result of high-temperature steps that a wafer undergoes during a typical CMOS fabrication process, an abrupt boundary between the p^+-substrate and the p-epitaxial region no longer exists. It can be seen from figure 7 that the doping concentration gradient extends as much as 4 μm into the epitaxial region from the backside. On the other hand, the depletion region between the n-well and the p-epitaxial region extends ~ 2 μm below the n-well junction. The presence of the depletion region and the doping gradient creates an electric field to drive the electrons from the backside to the collecting n-well junction. Therefore, the imager is be expected to provide low diffusion cross-talk even to photoelectrons created by short wavelength (blue) light.

For measuring noise, the megapixel imager was operated in CDS mode. Off-chip CDS was implemented by using a 4-point sampling method, where both reset and signal levels were acquired differentially. A low modal noise of ~ 8 electrons was measured at room temperature, both before and after thinning, with no noticeable degradation in the spatial distribution of noise.

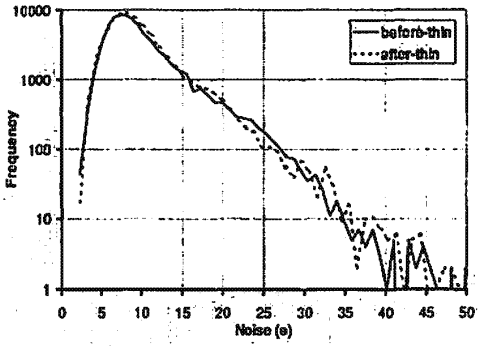


Figure 8: Measured noise histogram

Table 1 shows the summary of performance for the megapixel imager operated both under front- and back-illumination. It indicates that thinning and back-illumination has expectedly increased the QE without introducing any unwanted performance degradation.

In conclusion, we have demonstrated a back-illuminated CMOS imager with high QE by using a successful backside thinning and MBE-based surface passivation process. The main disadvantages of the thinning process are the absence of proper etch-stop required for accurate and reliable thinning, and the use of MBE for surface passivation, posing problems for wafer-level thinning and manufacturable back-illuminated imager implementation. Our on-going work will solve these two problems soon.

Table 1: Performance comparison

Characteristics	Front-illum. (no thinning)	Back-illumination
Format	1024x1024	1024x1024
Pixel Pitch	8 μm	8 μm
QE @ 550 nm	25%	80%
Mean dark rate @ 296K	294 pA/cm^2	153 pA/cm^2
Modal read noise @ 2 MHz	7.6 e$^-$	8.2 e$^-$
PRNU @ 1/3 full-well	< 1%	< 1%
Signal handling capacity	200 ke$^-$	200 ke$^-$

Acknowledgments:

This research was carried out at the Jet Propulsion Laboratory, California Institute of Technology, under a contract with the National Aeronautics and Space Administration.

References:

1. E.R.Fossum, *IEEE Trans. on Electron Devices*, vol. ED-44, pp. 1689-1698, 1997
2. S. Nikzad et al., *Proc. of SPIE*, vol. 2198, pp. 907, 1994
3. R. A. Stern, *Proc. SPIE*, vol. 1071, pp. 43–57, 1989
4. M. Lesser, *Proc. SPIE*, vol. 1447, pp. 177-183, 1991
5. P.A. Levine, *Proc. SPIE*, vol. 2172, pp. 100–114, 1994
6. B. E. Burke, *1995 IEEE Workshop on charge coupled devices and advanced image sensors*
7. M.E. Hoenk et al. *Appl. Phys. Lett.*, vol. 61, 1084 1992
8. M. Blouke et al., *Proc. SPIE*, vol.1447, pp. 142-155, 1991
9. C.M. Huang et al. *Proc. SPIE*, vol. 1447, pp. 156-164, 1991

SAMSUNG EX. 1002 - 465/4148

Backside Illumination Technology For SOI-CMOS Image Sensors

Bedabrata Pain
Edict Inc
bpain@sbcglobal.net
310-666-6749

2009 IISW Symposium on
Backside Illumination of Solid-State Image Sensors
June 25th 2009
Bergen, Norway

ACKNOWLEDGMENT

My ex-colleagues at JPL, specially Tom Cunningham, Chao Sun, Chris Wrigley, Suresh Seshadri, Xinyu Zheng, Victor White, Risaku Toda

Magnachip Semiconductor

Avago Technologies

Tom Joy

Homayoon Haddad

Prof. Durga Misra at New Jersey Institute of Technology

Indian Institute of Technology, Kharagpur

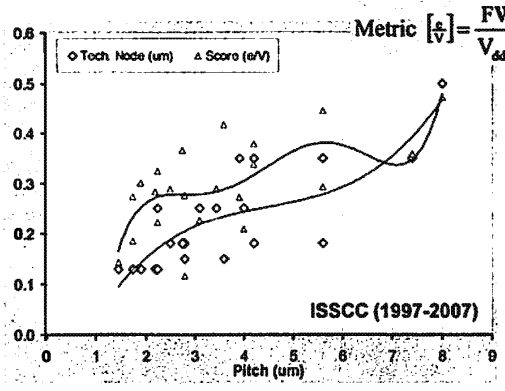
SIONYX1403000041.0044

SAMSUNG EX. 1002 - 466/4148

PROBLEMS of SMALL PIXEL

PIXEL SCALING TRENDS

$$\text{Metric } \left[\frac{e}{V}\right] = \frac{FW(e) \cdot Tech(\mu m)}{V_{dd}(V) \cdot Pitch(\mu m)}$$

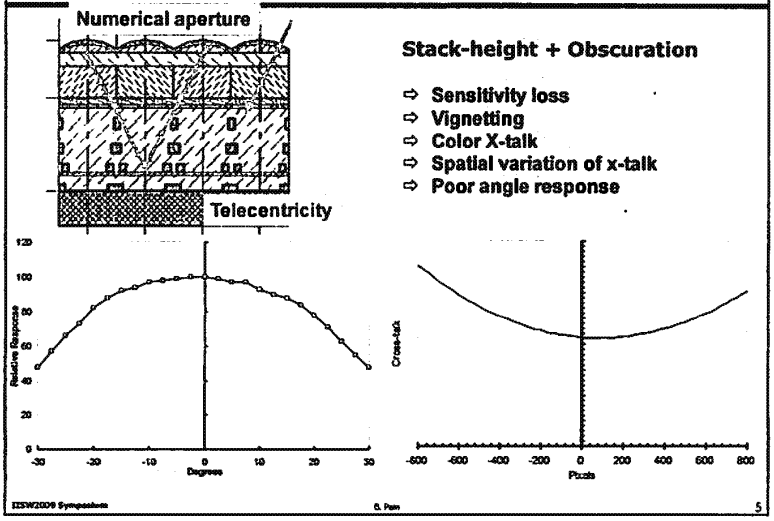


Continuous Technology "Breakthrough"
Needed to Keep up with the Scaling Trend

SIONYX1403000041.0045

SAMSUNG EX. 1002 - 467/4148

ANGULAR RESPONSE

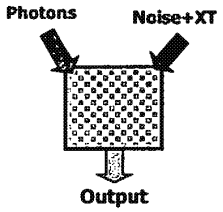


Stack-height + Obscuration

- ⇨ Sensitivity loss
- ⇨ Vignetting
- ⇨ Color X-talk
- ⇨ Spatial variation of x-talk
- ⇨ Poor angle response

IISW2009 Symposium — S. Pain — 5

DETECTIVE QE (MODIFIED)

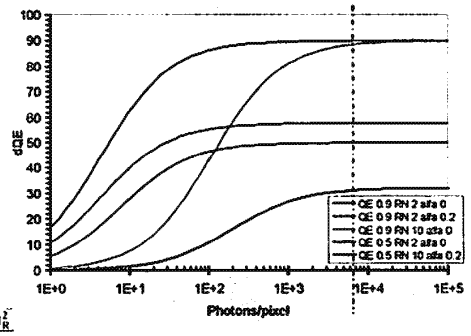


How well does it transfer power?

$$dQE = \frac{SNR_{out}^2}{SNR_{in}^2} = \frac{\frac{QE^2(1-\alpha)^2 P^2}{QE[P(1-\alpha)+P'\alpha]+N_R^2}}{P}$$

$$= QE \cdot \left[\frac{(1-\alpha)^2}{(1-\alpha)+\frac{P'}{P}\alpha+\frac{N_R^2}{QE \cdot P}} \right]$$

[1, 2]



Increase QE (QE >= 100)

Reduce Noise (N_R=0)

Eliminate X-talk (α=0)

IISW2009 Symposium — S. Pain — 6

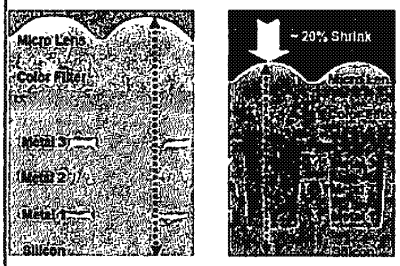
SIONYX1403000041.0046

SAMSUNG EX. 1002 - 468/4148

FRONT-SIDE ILD MODIFICATION

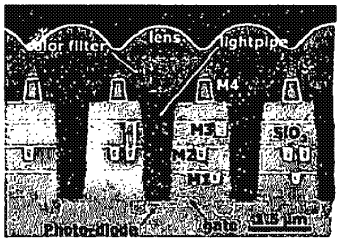
THINNER FRONT-END [3]

Al Process | Cu Process



Process Complexities
Basic Problems remain

LIGHTPIPE APPROACH [4]



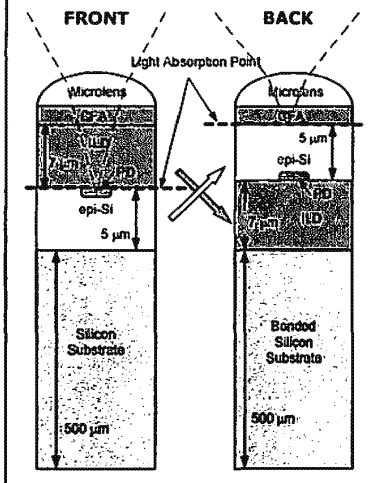
Difficulties in material selection

BACK-ILLUMINATION

SIONYX1403000041.0047

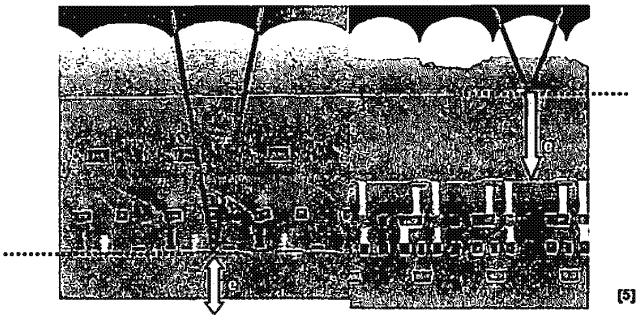
SAMSUNG EX. 1002 - 469/4148

BACK-ILLUMINATION: A SOLUTION



- **High Sensitivity and quantum efficiency**
  - 100 % fill-factor
- **Excellent X-talk and Angular Response**
  - "Canyon" effect eliminated
  - No obscuration
  - Spurious reflections eliminated
- **Efficient microlens and anti-reflection coating**
  - Planar surface
- **Advanced pixel processing**
  - Dynamic range expansion
  - Global shutter
  - Gain ranging
  - Low noise
- **Compatibility with next generation dielectrics and metals**

CROSS-SECTION



[5]

- **Collection much closer to microlens**
- **No Obscuration**
- **Supports larger numerical aperture**

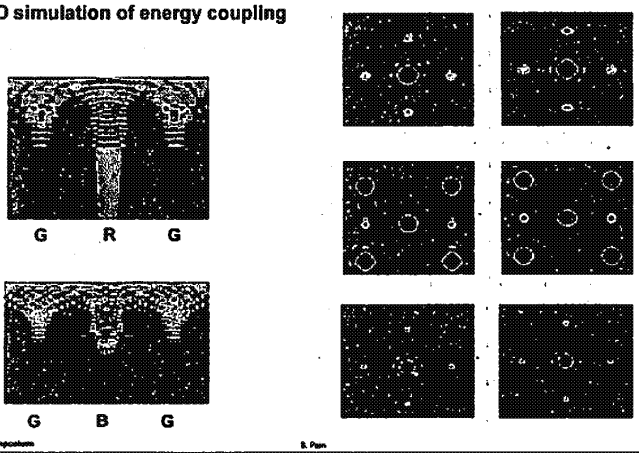
SIONYX1403000041.0048

SAMSUNG EX. 1002 - 470/4148

BACK TO MAXWELL

Plenty of optical energy leakage due to pixel dimension, wave-effects, CFA

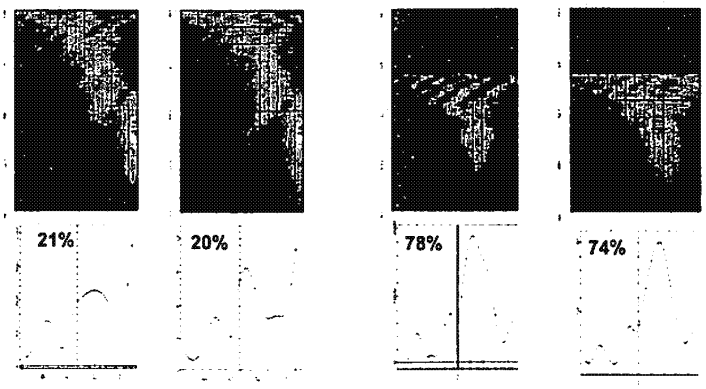
FDTD simulation of energy coupling



OPTICAL ADVANTAGE

Optical Coupling into Silicon for 1.75 µm pixel

Front Illumination (TE/TM) **Back Illumination (TE/TM)**

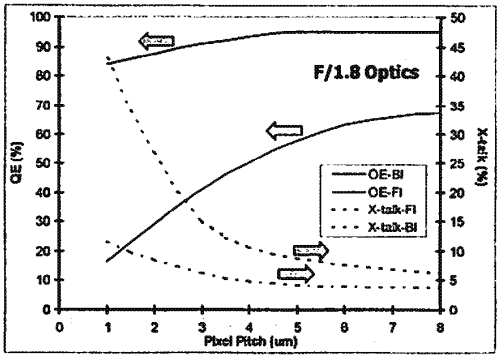


Almost 3x improvement at F 2.0

SIONYX1403000041.0049

SAMSUNG EX. 1002 - 471/4148

QE & OPTICAL CROSS-TALK



- QE goes down and Cross-talk goes up
- QE loss due energy spread via E-M field propagation
- Front-side QE also limited by imperfect AR coating

BACK-THINNING ISSUES

Manufacturable + Wafer-level Processing + Good device performance

- **Accurately thinning 700 μm substrate with <50 A⁰ surface roughness**
  - ⇨ Appropriate etch-stop
- **Backside passivation**
  - ⇨ Hold exposed surface in accumulation
- **Device support (during and after thinning)**
  - ⇨ Attachment of support wafers – must allow post-processing
- **Packaging**
  - ⇨ Where do pads come out from? Wire-bond or CSP?
- **AR coating, Color, Microlens**
  - ⇨ Alignment key
  - ⇨ Stack issues
- **Diffusion Cross-talk Control**
  - ⇨ Field-shaping implants
  - ⇨ Back-surface gradients

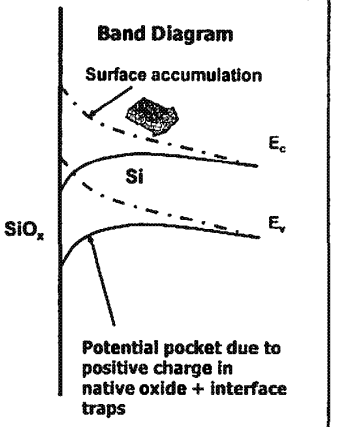
SIONYX1403000041.0050

SAMSUNG EX. 1002 - 472/4148

PASSIVATION OF EXPOSED SURFACE

PASSIVATION PROBLEM:

- Exposed Si-SiO_2 interface quality is poor
  - high trap density, potential pocket due to band-bending
  - loss of blue QE and high dark current



BACKSIDE TREATMENT

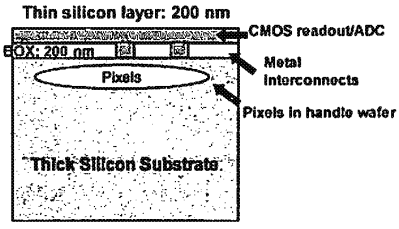
- **Implant + RTA Anneal**
  - **Cannot be used due to the presence of metals**
- **Implant + Laser Anneal** [6, 7]
  - **PRNU, Dark current**
- **Delta-doping: few monolayers of boron added by MBE to the back surface** [8]
  - **Excellent results, but non-standard process**
- **Flash gate: deposited oxide + UV flooding** [9, 10]
  - **Outgassing, Long-term stability**
- **Back-gate: deposited oxide + Silver capping** [11]
  - **Non-desirable metal; AR coating issues**
- **Back-gate: deposited oxide + ITO gate**
  - **Process Control; AR coating issues**

SIONYX1403000041.0051

SAMSUNG EX. 1002 - 473/4148

FABRICATION STEPS

SOI TO THE RESCUE



NIR enhanced Imager [12]

Small Pixels [13]



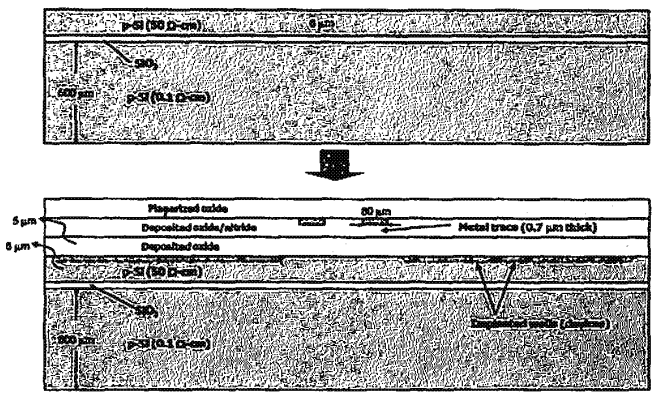
SIONYX1403000041.0052

SAMSUNG EX. 1002 - 474/4148

SOI IMAGER FABRICATION

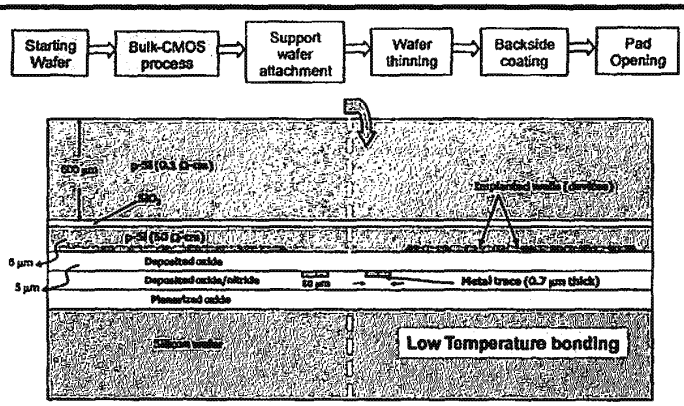
- SOI wafer with thick device layer (~ 2-10 μm)
- Imager-compatible bulk-CMOS process

[13, 14]



IISW2009 Symposium B. Pain 19

SOI IMAGER FABRICATION



- Provides mechanical support
- Bonding process/material must be back-end compatible

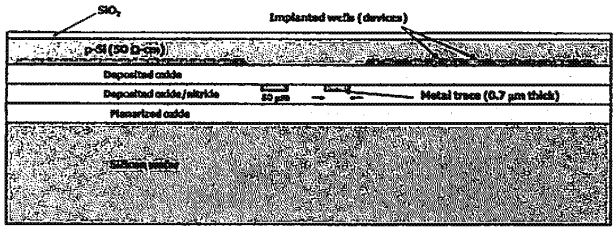
[15]

IISW2009 Symposium B. Pain 20

SIONYX1403000041.0053

SAMSUNG EX. 1002 - 475/4148

THINNING



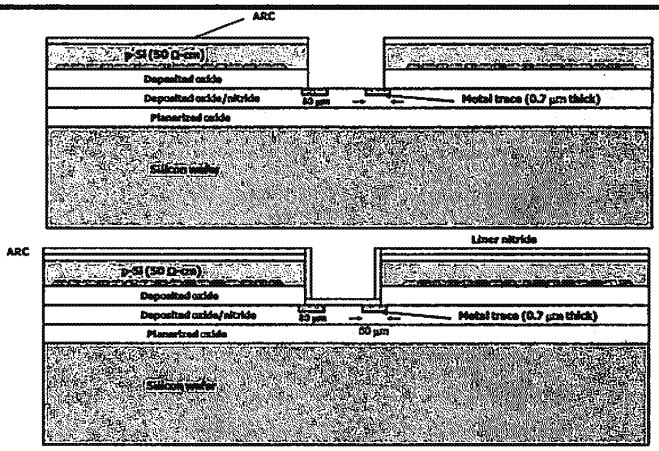
THINNING
- Wafer-level thinning
- Natural high-selectivity (Si-SiO_2) etch-stop

PASSIVATION
- Buried oxide made by thermal oxidation
- Pre-implanted region for passivation
- Self-passivation: surface never exposed

Chemical Etch
- Hot KOH/TMAH wet-etch
- RIE with SF_6
- XeF_2 vapor-phase

	KOH	SF_6	XeF_2
Local	<20 A	<500A	<20A
Global	<200A	3000A	<40

BACK-to-FRONT ALIGNMENT

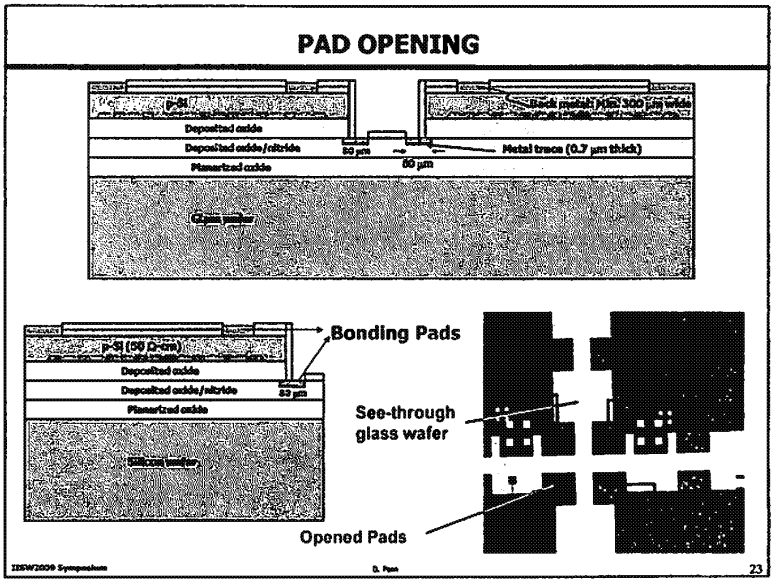


Exposed metal holds alignment keys

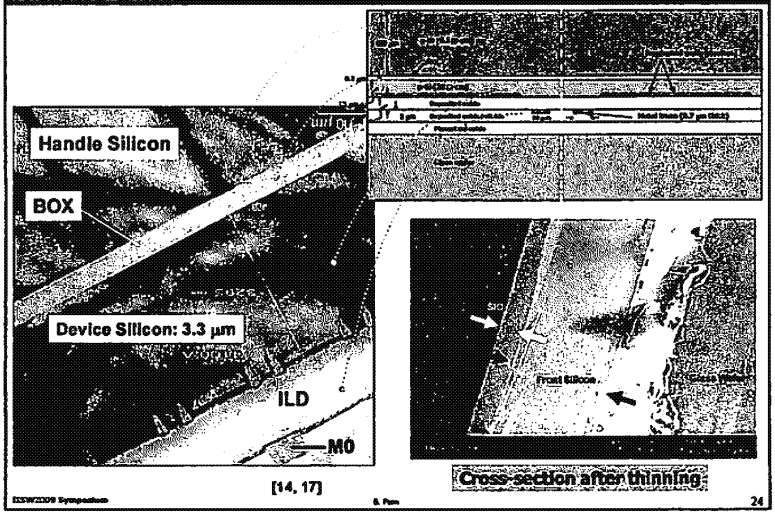
SIONYX1403000041.0054

SAMSUNG EX. 1002 - 476/4148

PAD OPENING



THE CROSS-SECTION

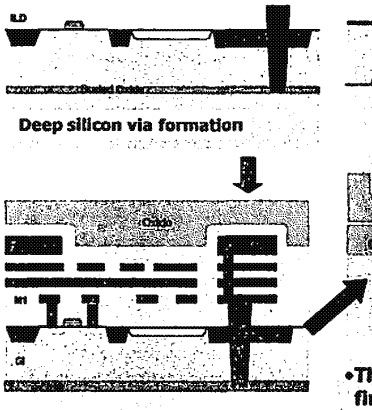


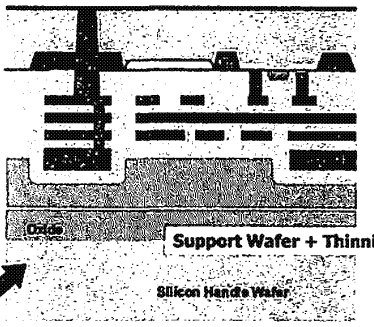
[14, 17]

SIONYX1403000041.0055

SAMSUNG EX. 1002 - 477/4148

ALTERNATE INTEGRATION SCHEME

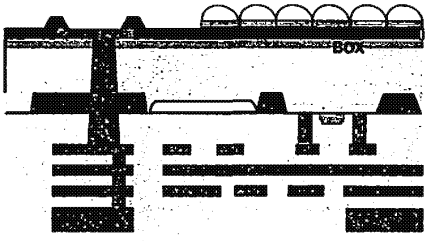


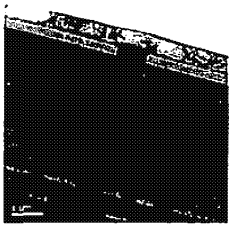


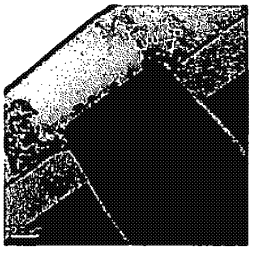
- Through silicon via is formed at the first metallization step
- Liner oxide for isolation
- Serves as alignment key for CFA/ML

[17, 18]

ALTERNATE INTEGRATION SCHEME







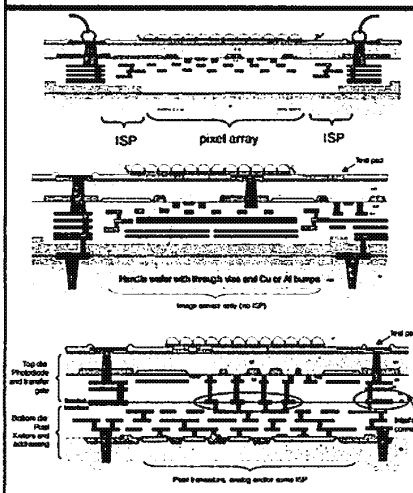
Silicon Handle Wafer

Final Cross-section

SIONYX1403000041.0056

SAMSUNG EX. 1002 - 478/4148

POSSIBLE EVOLUTION



1st Generation
Through Silicon Contacts for wirebonds
Pixel optimization

2nd Generation
Higher Dynamic Range – In-pixel Cap
Better Z-height - WLCSP

3rd Generation
Only pixel in wafer – best peformance
SOC integration

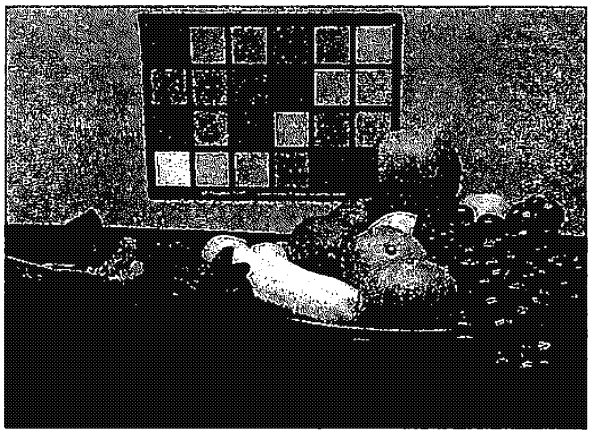
[16]

PERFORMANCE

SIONYX1403000041.0057

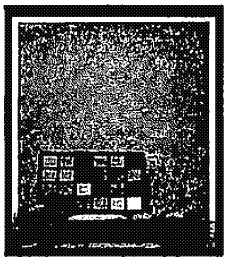
SAMSUNG EX. 1002 - 479/4148

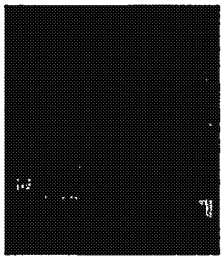
COLOR BIS IMAGER

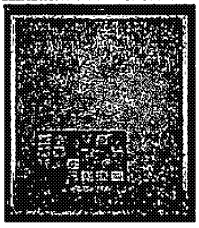


Back-illuminated 1.75 μm Color Picture [17]

PERFORMANCE IMPROVEMENT



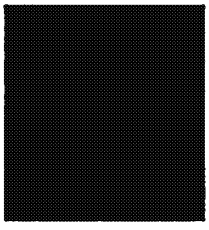




Median luminance = 3 lux

Median luminance = 690 lux for D65

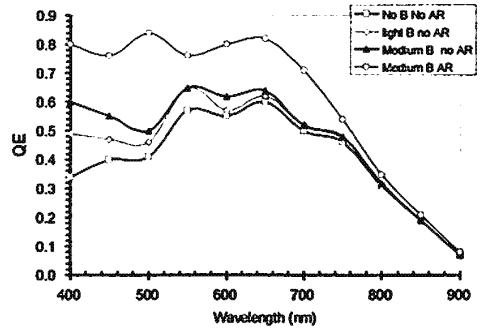
- ↑ 2.5x increase in Sensitivity for 2.2 μm pixel
- ↑ Dark current & Full-well about the same
- ↑ Angular response improves by 5x
- ↓ Electrical cross-talk worse



SIONYX1403000041.0058

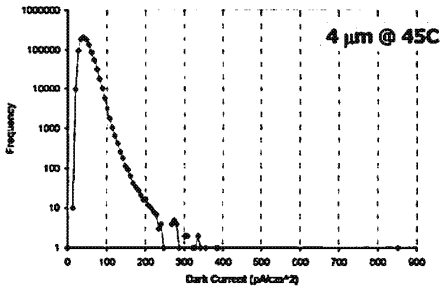
SAMSUNG EX. 1002 - 480/4148

QUANTUM EFFICIENCY



- **Surface Boron is an effective tool to improve QE**
- **Blue QE affected by boron content at the surface** [14]
- **For color Imager: 20% loss going through CFA and OCL**

WELL BEHAVED DARK CURRENT



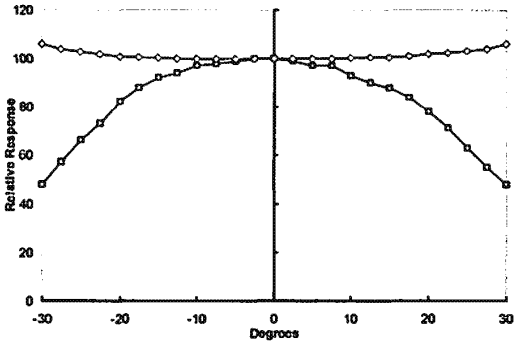
Front Illuminated	Nitride cover	53
Back surface Boron	Nitride + H_2 anneal	Dark Current (e/sec)
Minimum	None	8000
Small	None	419
Small	Yes	133
Medium	Yes	57
High	Yes	76

[14]

SIONYX1403000041.0059

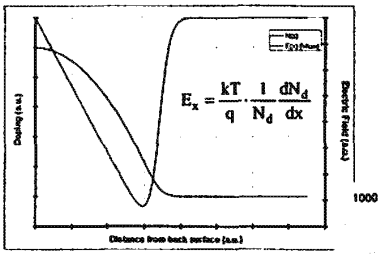
SAMSUNG EX. 1002 - 481/4148

ANGULAR RESPONSE



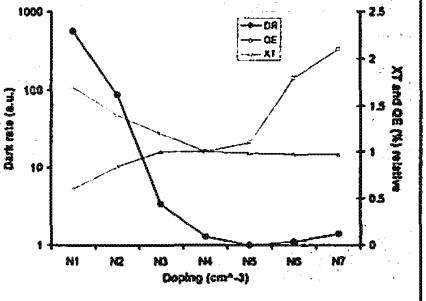
Slight increase in relative angular response is due to optical path difference

BACK FIELD



- Simulated Nominal Back doping gradient and electric field
- Back-field drives minority carriers towards front
- Back-field suppresses Cross-talk
- Proper doping gradient is extremely important

Doping Trade-offs

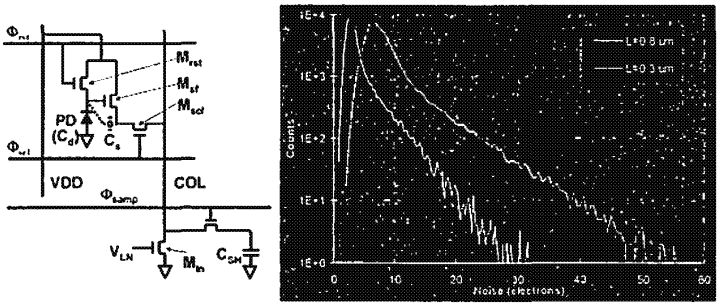


SIONYX1403000041.0060

SAMSUNG EX. 1002 - 482/4148

RTS NOISE REDUCTION

C_{SH} = 1.5 pF; G_{cp} ~ 45 µV/e; I_{bias} = 3 µA



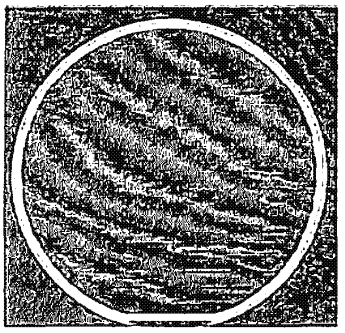
- Source follower as the main source of RTS
- Both modal noise and noise spread is reduced by length increase

MANUFACTURABILITY ISSUES

SIONYX1403000041.0061

SAMSUNG EX. 1002 - 483/4148

SUPPORT WAFER BONDING



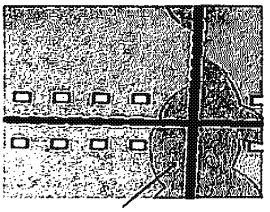
Acoustic micrograph of low-temperature oxide-oxide bonded support wafer (courtesy Ziptronix, Inc.): No voids

Passes die-level thermo-mechanical tests (thermal shocks and temperature cycles)

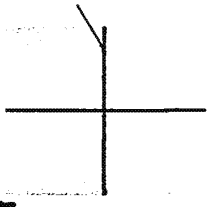
Alternate schemes? [17]

"PEEL OFF"

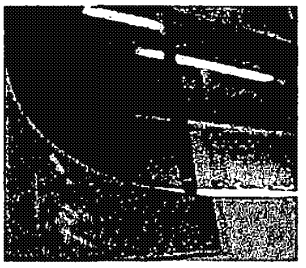
DELAMINATION



Sawing Process optimization to prevent delamination



EDGE EXCLUSION

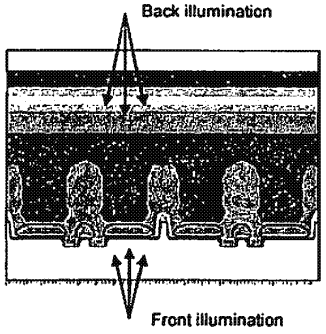


Optimization of bonding and grinding process to eliminate edge-cracking during subsequent processing

SIONYX1403000041.0062

SAMSUNG EX. 1002 - 484/4148

THE THREE THINGS ...

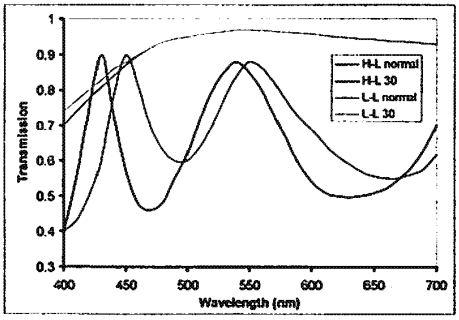


Electrical Cross-talk
- Separated generation and collection area
- Back surface field
- Deeper Junction

QE
- Integration of AR stack on the BOX

Dark Current
- Back surface passivation with integrated AR stack

AR STACK OPTIMIZATION

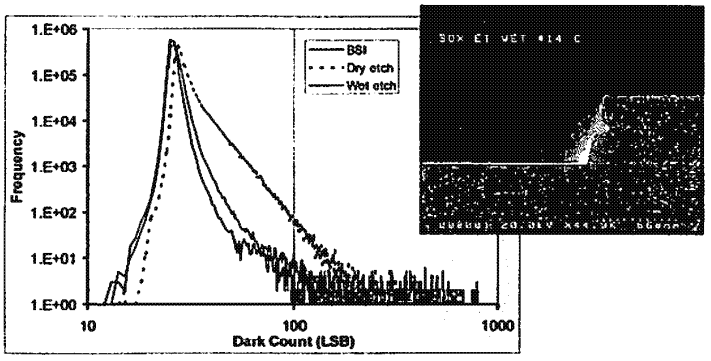


- **Excellent AR stack can be achieved with SiN/SiO layers**
- **Need to ensure that angular response is acceptable**
- **BOX not the ideal-choice for 1st AR layer**

SIONYX1403000041.0063

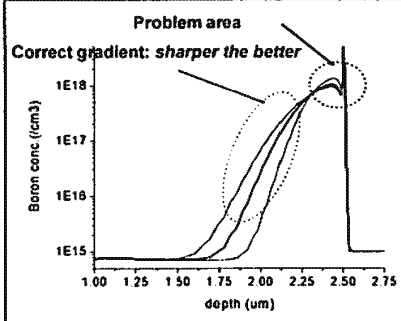
SAMSUNG EX. 1002 - 485/4148

DARK CURRENT with AR STACK

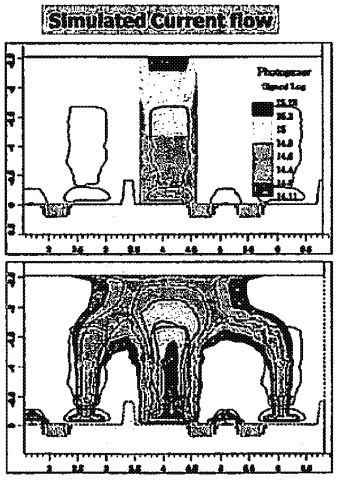


BOX etching does not increase dark current, if done right!

CROSS-TALK



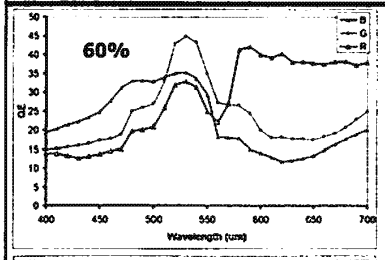
- Boron needed to passivate interface states
- Boron gradient needs to be optimized
- Boron segregation is the source of problems
- N-type substrate is preferable

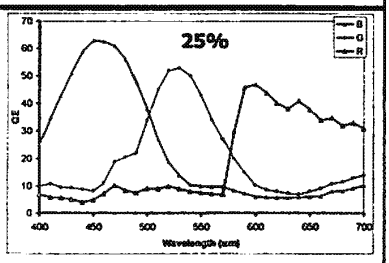


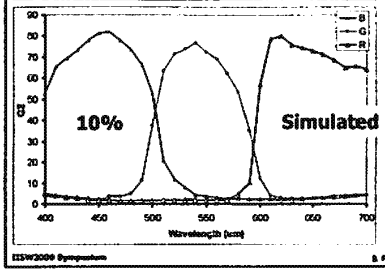
SIONYX1403000041.0064

SAMSUNG EX. 1002 - 486/4148

CROSS-TALK TRADE-OFF







- Diode doping profile engineering for deeper field penetration
- Optimize silicon thickness
- "Clean-up" back surface: Boron segregation could be a problem
- Modify CFA?
- Modify microlens
- Optimize AR stack

IISW2009 Symposium B. Pain 43

MOVING FORWARD (in lieu of conclusion)

Cost - how low can you go?
- Special SOI wafer needed?
- Will SOI wafer become cheaper and have shorter turn-around time?
- Where are the yield and reliability "gotchas"?

Performance
- SOI wafer quality? Will lack of gettering be an issue?

Alternate Support Wafer Attachment
- Need for an alternative to LT-bonding? Alternate support materials?

Appropriate Optical Stack
- What materials for AR stack?
- Alternate CFA?

Improving Cross-talk
- Boron segregation - N-type material?
- Alternate diode profiles and barrier implants? Deep trenches?
- Alternate dielectric for improved passivation? ITO?

Packaging
- Chip-on-board (COB) or Chip-scale-packaging (CSP) or wafer scale (WSP)?

IISW2009 Symposium B. Pain 44

SIONYX1403000041.0065

SAMSUNG EX. 1002 - 487/4148

REFERENCES

1. A. Rose, J. Soc. Motion Picture Engrs. 47 (1946) 273.
2. G. Zanella, R. Zannoni, "The role of the quantum efficiency on the DQE of an imaging detector", Nuclear Instruments and Methods in Physics Research A 331, 157-160, 1956.
3. Y-C Kim et al., "1/2 inch 7.2 Mega-Pixel CMOS Image Sensor with 2.25μm Pixels using 4-Shared Pixel Structure for Pixel-Level Summation", Proc. ISSCC 2006, paper 27.2, San Francisco, CA, USA, 2006.
4. J. Gambino et al. "CMOS Imager with Copper Wiring and Lightpipe," Proc. IEEE IEDM, pp. 131-134, San Francisco, CA, USA, 2006.
5. S. Iwatsuchi, et al, "A Back-Illuminated High-Sensitivity Small-Pixel Color CMOS Image Sensor with Flexible Layout of Metal Wiring", Proc. ISSCC 2006, paper 16.8, San Francisco, CA, USA, 2006.
6. B. Burke et al., "640x480 Back-Illuminated CCD Imager with Improved Blooming Control for Night Vision," Proc. IEEE IEDM, pp. 33-36, San Francisco, CA, USA, 1998.
7. C. Huang et al., "A New Process for Thinned, Back-Illuminated CCD Image Devices," Proc. IEEE VLSI Technology Systems and Applications, pp. 98-101, Taipei, Taiwan, 1989.
8. S. Nikzad et al., "Delta-doped CCDs: High QE with long-term stability at 1W and visible wavelengths" Proc. SPIE 2198, pp. 907-918, 1994.
9. J. Janesick, et al., "Flash Technology for Charge-Coupled Device Imaging in the Ultraviolet", Optical Engineering, vol. 28, pp 852-861, 1987.
10. B. Burke et al., "CCD Soft-X-Ray Detectors With Improved High- and Low-Energy Performance," IEEE Trans. Nuclear Science, vol. 51, pp. 2222-2227, vol. 51, 2004.
11. M. Lesser, "Improving CCD Quantum Efficiency," Proc. SPIE 2198, pp. 782-791, 1994.
12. B. Pain, et al, "SOI-based Monolithic Imaging for Scientific Applications," Proc. International Image Sensor Workshop 2007, pp. 192-195, Ogunquit, ME, USA, 2007.
13. B. Pain et al, "Wafer-Level Thinned CMOS Imagers Implemented in a Bulk-CMOS Technology," Proc. International Image Sensor Workshop 2007, pp. 158-161, Ogunquit, ME, USA, 2007.
14. B. Pain, "Fabrication and Initial Results for a Back-Illuminated Monolithic APS in a mixed SOI/Bulk CMOS Technology", Proc. IEEE CCD/AIS Workshop, 2005, Nagano, Japan, 2005.
15. J. A. Burns et al., "A Wafer-Scale 3-D Circuit Integration Technology," IEEE Trans. Elect. Dev., vol. 53, pp. 2507-2516, 2006.
16. V. Suntharalingam et al., "Megapixel CMOS Image Sensor Fabricated in Three-Dimensional Integrated Circuit Technology," Proc. ISSCC, pp. 356-357, San Francisco, CA, 2005.
17. T. Joy et al, "Development of Production-Ready, Back-Illuminated CMOS Image Sensor with Small Pixels," Proc. IEEE IEDM, pp. 1007-1010, Washington DC, USA, 2007.
18. J. Prima et al., "A 3 Mega-pixel Back-Illuminated Image Sensor with 1T5 Architecture with 1.45 μm Pixel Pitch," Proc. International Image Sensor Workshop 2007, pp. 5-8, Ogunquit, ME, USA, 2007.

SIONYX1403000041.0066

SAMSUNG EX. 1002 - 488/4148

Available online at www.sciencedirect.com
SCIENCE DIRECT®
Thin Solid Films 451–452 (2004) 544–551
thin solid films
www.elsevier.com/locate/tsf

CIGSSe thin film PV modules: from fundamental investigations to advanced performance and stability

J. Palm*, V. Probst, W. Stetter, R. Toelle, S. Visbeck, H. Calwer, T. Niesen, H. Vogt, O. Hernández, M. Wendl, F.H. Karg

Shell Solar GmbH, Otto Hahn Ring 6, D-81739 Munich, Germany

Abstract

A process for high efficiency large area $Cu(In,Ga)(Se,S)_2$ (CIGSSe) thin film solar modules is developed applying rapid thermal processing and controlled sodium doping. Continuous optimization aims at sufficient process maturity for a successful transfer into cost-effective mass production. The pilot line yields aperture area efficiencies of 11% (average) for 30×30 cm^2 modules and a certified champion efficiency of 13.1% for the first 60×90 cm^2 demonstrator module (unencapsulated). First Cd-free 30×30 cm^2 circuits yield up to 11.9% efficiency applying CBD-Zn(S,OH)-buffer layers. Investigations on the absorber formation by structural, compositional and electrical characterization will be given. Models for the Ga and S distribution will be discussed and experimentally verified. A favorable double band gap grading structure is accomplished by controlled sulfur profiling and by a process induced gallium accumulation towards the back electrode. The stability of the frameless low-cost packaged pilot line modules against humidity is confirmed externally by passing the damp heat test sequence according to IEC 61646.
© 2003 Elsevier B.V. All rights reserved.

Keywords: $Cu(In,Ga)(Se,S)_2$; $Cu(In,Ga)Se_2$; Sulfurization; Cd-free buffer; Damp heat stability

1. Introduction

Thin film solar cells based on chalcopyrite semiconductors have reached a high level of performance over the last few years both for laboratory scale cells and commercial products [1]. Since 1998, a first generation of CIS modules is commercialized by Siemens Solar (now Shell Solar). Over the past years we have also developed a second generation process for CIS formation based on a rapid two-step process: deposition of Na-enriched precursor materials at room temperature on barrier-coated float glass substrates is followed by rapid thermal processing (SEL-RTP, stacked elemental layer rapid thermal processing). Three critical issues are properly addressed by this concept: First, by conducting the deposition process at room temperature, proven standard processes such as magnetron sputtering can be applied. Second, Na doping is controlled independently on glass properties or crystal growth temperatures by using a diffusion barrier and adding a dopant compound to the precursor layer. Sodium control is critical for the overall device performance, for lateral homogeneity and for film adhesion. Third, by minimizing the thermal budget for CIS formation at high temperature the processing cycle times are strongly reduced allowing for true inline concepts and high throughput. The feasibility of this concept has been demonstrated in the past on a laboratory scale by high efficiency mini modules with 14.7% champion conversion efficiency [2]. The up-scaling from 10×10 to 60×90 cm^2 substrate size has been successfully accomplished in the past 2 years by demonstrating average efficiencies of 11% on 30×30 cm^2 modules with CIGSSe absorbers selenized and sulfurized on 60×90 cm^2 substrates [3,4]. Now the development efforts focus on improving the module efficiency, demanding a detailed understanding of the absorber formation and of the impact of significant processing parameters. Alloying the $CuInSe_2$ chalcopyrite with Ga and S is known to increase the efficiency by widening the band gap towards the optimum values of 1.4 eV [5]. The incorporation of Ga and S in the SEL-RTP process and its impact on device performance is investigated in this publication. The optimized process results in

*Corresponding author. Tel.: +49-89-636-58726; fax. +49-89-636-58702.
E-mail address: joerg.palm@shell.com (J. Palm).

0040-6090/04/$ - see front matter © 2003 Elsevier B.V. All rights reserved.
doi:10.1016/j.tsf.2003.10.160

SIONYX1403000041.0067

SAMSUNG EX. 1002 - 489/4148

increased module efficiency due to improved open circuit voltage and fill factor. Excellent I–V-characteristics for the first 60×90 cm^2 large demonstrator modules have been obtained. Product oriented PV development demands high starting efficiencies *and* long-term module stability to ensure a cost-effective product at a long lifetime. The results of module stabilization improvements are documented by standard accelerated stress testing. Accounting for the importance of environmental aspects and for strong customer acceptance, the first Cd-free 30×30 cm^2 modules were developed yielding efficiencies comparable to the CdS-containing devices.

2. Experimental details

2.1. Pilot line process

The SEL-RTP pilot line process (Fig. 1) has been presented previously in detail [3,4]. In order to achieve low-cost thin film modules float glass substrates are used. For reproducibility in substrate surface conditions and in alkali doping, silicon nitride is deposited as an alkali-barrier layer on top of the float glass surface. Controlled sodium doping is a key feature of the SEL-RTP-process: the application of a barrier layer enables a well-defined Na dosage prior to the absorber formation process [4,6]. The deposition of all precursor layers is performed in a modified vertical in-line sputter coater. The back electrode (Mo), the Na dopant compound and several alternating layers of Cu (85%)+Ga (15%) and In are deposited by DC magnetron sputtering. The Se layer is deposited on top by thermal evaporation through a linear source. Selenization and sulfurization is performed in a custom built large area RTP reactor [2,3]. The total IR-power density of the furnace is sufficient to allow heating rates of 10 °C/s on 3-mm-thick glass substrates. No cracking or warping of substrates has been observed. Sulfurization is performed by adding a sulfur containing gas into the reaction chamber. The reaction chamber has a minimized volume to ensure high Se- and S-partial pressure. The CdS buffer layer is deposited by a chemical bath deposition (CBD) process using the decomposition of thiourea. The ZnO deposition is performed in a commercial glass coater using magnetron sputtering from ceramic targets. A thin layer (~75 nm) of i-ZnO is deposited by r.f.-magnetron sputtering from an undoped ceramic target. Subsequently, a 600–800-nm-thick n-type ZnO layer is deposited by DC magnetron sputtering from a ZnO–Al_2O_3 target. The patterning of Mo (P1) uses a pulsed laser operating in the near-infrared. Mechanical scribing is applied for patterning of absorber (P2) and ZnO (P3). All process steps from substrate wash to absorber formation are performed on 60×90 cm^2 substrates. The subsequent module processing steps from CdS to contacting and encapsulation are usually performed on 30×30 cm^2 format. The Munich pilot line is also capable of 60×90 cm^2 demonstrator module processing on a limited volume. Exception is the ZnO-frontelectrode—which is deposited at the Camarillo production site using a metalorganic chemical vapour deposition (MO-CVD) process.

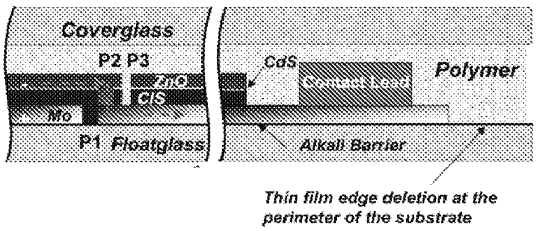


Fig. 2. Schematic cross-section of the module.

A schematic cross-section of the module is given in Fig. 2, displaying layer sequence, integrated series connection and packaging. A low-cost frameless glass–glass package is used. Before lamination of a coverglass to the circuit substrate, thin film edge deletion and contacting are performed.

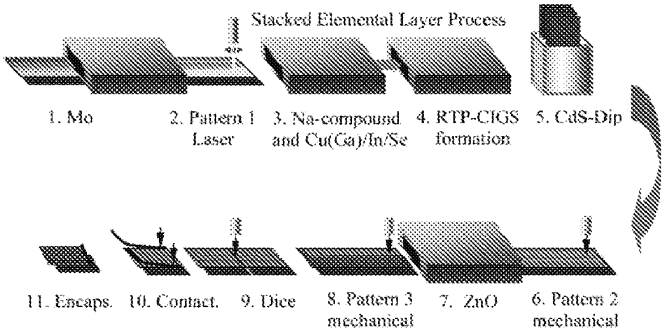


Fig. 1. Process scheme for CIGS-modules with monolithic integration of series connected cells.

SIONYX1403000041.0068

SAMSUNG EX. 1002 - 490/4148

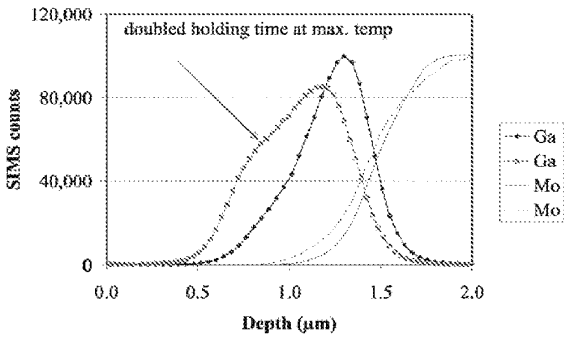


Fig. 3. SIMS profile of Ga and Mo for an SEL-RTP CIGSSe absorber for two different process times at maximum temperature.

2.2. Experiments

For investigation purposes the RTP process was modified using different temperature/time and gas profiles. The processed CIGSSe absorbers were analyzed by several techniques. X-ray fluorescence (XRFA) was carried out using a wavelength dispersive spectrometer. For the analysis of our multi-layer structures a fit program was used that takes into account the re-absorption of emitted X-rays. X-ray photoelectron spectroscopy (XPS) was done using Al Kα excitation and an argon ion sputter beam. Secondary ion mass spectroscopy (SIMS) was carried out using a Cs-ion sputter beam detecting the CsX molecules (X=Mo, Ga, Cu, S, Se). Current–voltage (I–V) measurements were performed on a constant light source solar simulator at standard test conditions (25 °C, AM1.5).

3. Results and discussion

3.1. Gallium depth profile

Fig. 3 shows a SIMS depth profile of Ga and Mo: at the front no Ga is observed. The profile rises in the second half of the absorber peaking at the onset of the Mo signal. The second Ga profile was obtained by extending the phase of maximum temperature of the RTP process. The profile is broadened and the half-maximum-value has shifted towards the top. The accumulation of Ga is typically observed for the two-step process absorbers [2,7,8].

Applying the results of recent work on in situ investigations of the selenization of Cu–In–Ga precursors [9,10], the Ga distribution can now be well understood. Using in situ XRD, Brummer et al. [9] identified the following synthesis route for CIGS: beside In and $CuIn_2$ the precursor contains mostly $Cu_{11}(In,Ga)_9$ when prepared by magnetron sputtering. Above the Se melting point (220 °C) $Cu_{11}(In,Ga)_9$ decomposes forming In_4Se_3, $Cu_{2-x}Se$ and CuSe. The rest of $Cu_{11}(In,Ga)_9$ converts at approximately 310 °C into $Cu_{16}(In,Ga)_9$. When $Cu_{16}(In,Ga)_9$ is consumed, rapid decomposition of CuSe and In_4Se_3 occurs and InSe and $Cu_{2-x}Se$ form. InSe and $Cu_{2-x}Se$ are the direct binary precursor phases from which $CuInSe_2$ forms above 370 °C. With respect to Ga, the following observations were made: (1) No gallium selenide phases are observed by in situ X-ray diffraction. Ga selenization is kinetically impeded (see also Ref. [11]). (2) The lattice parameters of the direct precursors $Cu_{2-x}Se$ and InSe of the CIS formation give no indication that significant amounts of gallium are located within these structures. (3) After formation of the quaternary precursors a separate gallium rich phase of composition $CuIn_{0.4}Ga_{0.6}Se_2$ is located below the pure CIS-phase.

Apparently Ga is driven towards the back during fast formation of Cu- and In-selenides. Ga is consumed only in the crystallization of a second Ga-rich CIGS phase. The crystallization front progresses from the top of the precursor that is in direct contact to Se towards the back electrode [10]. This process results in the double layer structure of well crystallized CIS on top of a Ga rich fine-grained CIGS layer in contact with the back electrode [2]. Extended annealing at elevated temperatures (Fig. 3) leads to Ga diffusion from the bottom to the top (as in Ref. [8]): the initial—kinetically induced distribution—changes to a thermodynamically preferred one.

3.2. Sulfur profile controlling

Fig. 4 shows SIMS profiles of sulfur in the first 0.5 µm of the absorber thickness for three different processes: (I) sulfur was present during the ramp phase to a maximum temperature of below 550 °C and during the maximum temperature plateau (process 'R&P'); (II) sulfur was present only at the T_{max}-plateau (process 'P'); (III) the sulfur containing process ambient gas was present during the ramp phase, but diluted after reaching the plateau (process 'R'). Processes 'R&P' and 'P' result in a high surface concentration of sulfur. XPS depth profiles of the ratio of the S 2s and Se 3d line intensities confirm the relative differences, see Fig. 5.

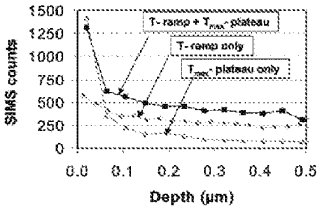


Fig. 4. SIMS profile of sulfur in CIGSSe absorbers as a result of sulfur containing process gas introduced at different states of RTP selenization/sulfurization.

SIONYX1403000041.0069

SAMSUNG EX. 1002 - 491/4148

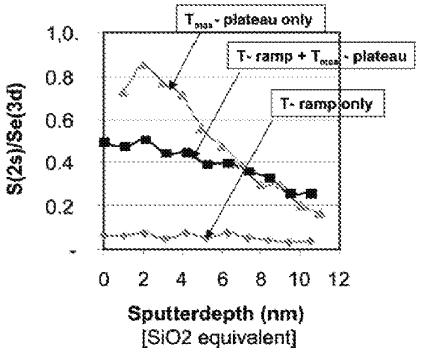


Fig. 5. XPS-profiles of the S(2s)/Se(3d) intensity ratio from the CIGSSe-surfaces for the same processes as in Fig. 4

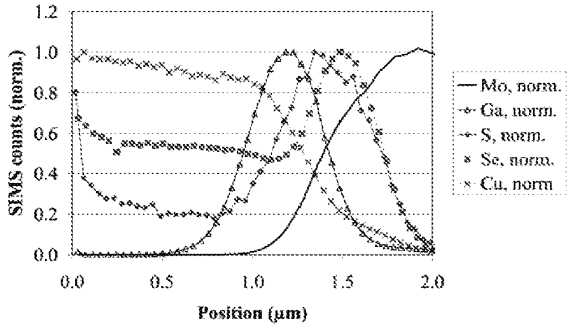


Fig. 7. SIMS profile of Mo, Ga, S, Se and Cu, normalized to the maximum values (process 'R&P').

Processes 'R&P' and 'R', on the other hand, result in higher bulk concentrations. The ramp phase, hence, is critical for an efficient sulfurization of the bulk, whereas the plateau phase is critical for a high surface concentration. Fig. 6 shows that in processes 'R&P' the total S and Se concentrations increase with the CIG ratio Cu/(In+Ga).

The increased S incorporation for stoichiometric or Cu-rich CIGS absorbers was observed previously [12,13]. Basol et al. [12] assume enhanced diffusion in the presence of liquid Cu–(SeS) phases. Titus et al. [13] explain the increased S incorporation with fast diffusion of S in Cu_2Se. Brummer et al. [9] observe by in situ-XRD that the Cu_2Se phase transforms with InSe into $Cu(In,Ga)Se_2$ above 380 °C. The fraction of remaining Cu_2Se hence depends on the state of selenization. Accordingly, Tanaka et al. [14] have observed that the S content can be optimized with increasing temperature difference between selenization (by H_2Se) and sulfurization (by H_2S). Hence, all results are in agreement with the model that S incorporation is more efficient in the ramp phase because sulfur can rapidly diffuse through residual $Cu_{2-x}Se$ phases. The incorporation and diffusion through the selenized CIGS chalcopyrite appears to be slower. Engelmann et al. [15] presented a model that takes into account the formation of a sulfur-rich surface layer through exchange of Se with S and the diffusion into the bulk. The profiles for 'R&P' and 'P' can be superposed by subtracting a constant offset from profile 'R&P'.

Fig. 7 presents SIMS profiles of Mo, Cu, Ga, S and Se from top to bottom, normalized to their maximum values each. The intensities of S and Se rise towards the Mo back electrode, peaking at the half of maximum value of Mo. The profiles indicate that Mo, S and Se form a Mo-sulfoselenide intermediate layer between Mo and CIGSSe. SEM [4], SEM-EDX [3] and XRD [16] prove the existence of $Mo(S,Se)_2$. Fig. 8 shows the sulfur and selenium SIMS profiles in a semilogarithmic plot for two different CIG ratios: the excess Se+S > 50% measured by XRFA for higher CIG ratios obviously is incorporated within this layer.

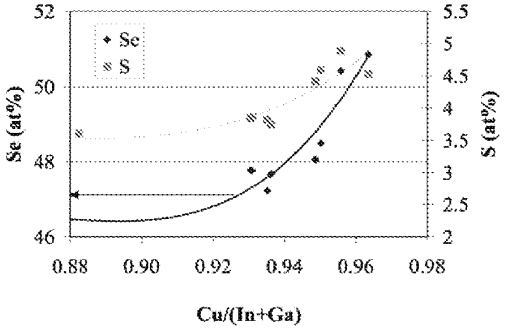


Fig. 6. Atomic concentration of Se (left axis) and S (right axis) for process 'R&P' as obtained from XRFA.

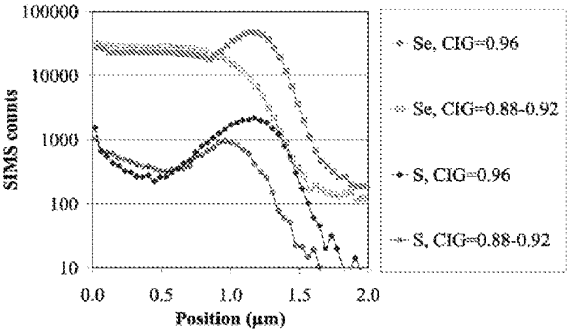


Fig. 8. SIMS profile of S and Se (semilogarithmic scale) for two different CIG ratios (process 'R&P').

SIONYX1403000041.0070

SAMSUNG EX. 1002 - 492/4148

Table 1
I–V data of 30×30 cm² circuits with absorbers from different RTP processes

Process type	η (%)	V_{oc} (mV)	J_{sc} (mA/cm²)	FF (%)
S in *T*-ramp and T_{max}-plateau ('R&P')	11.0	531	31.9	65
S in T_{max}-plateau ('P')	11.0	509	33.3	65
S in *T*-ramp ('R')	9.2	488	32.2	59
Current optimum	11.9	543	32.8	67

3.3. Impact of S- and Ga-profiles on I–V-characteristics

Band gap widening through alloying with Ga and S is known to improve the efficiency of CIS based solar cells and modules [5]. In the SEL-RTP process Ga improves V_{oc}, but no Ga is found in the depletion region at the front. The Ga accumulation in the back acts as a back surface field. Sulfur is present at the interface and in the depletion region (Fig. 7). The comparison of *I–V* data (Table 1) of process 'R&P' and 'R' reveals a strong improvement of fill factor and open circuit voltage with increased sulfur concentration at the front contact, in agreement with previous results [2,14], through the increase of band gap in the depletion region and the passivation of defects. The comparison of process 'P' and 'R&P' reveals that a slightly lower sulfur concentration within the depletion region (process 'P') results in a decrease of voltage (20 mV). The lower sulfur concentration in the bulk increases absorption and results in an increase of short circuit current (1.4 mA/cm²). The SEL-RTP process results in double band gap grading. Further optimization of the process is in progress. The current state of the art is 11.9% (best value) and 11.4±0.4% (average) across six modules 30×30 cm² of the same RTP run (60×90 cm²).

3.4. Pilot line circuits: performance

The pilot line circuit efficiency on 30×30 cm² large substrates is shown in Fig. 9 yielding an average efficiency of close to 11%. A CBD-CdS/sputter i-ZnO/ZnO:Al window layer was applied. Fig. 10 illustrates the efficiencies of the six 30×30 cm² modules of a single selenization and sulfurization run (recent optimization, not included in Fig. 9). The average efficiency is 11.4% with a champion value of 11.9%.

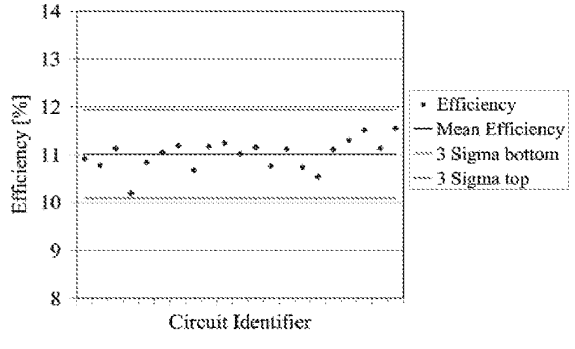


Fig. 9. Pilot line efficiency process control chart of 30×30 cm² large unencapsulated modules: average aperture area efficiency at 11%.

3.5. Pilot line glass–glass packaged modules: damp heat stability

In view of a future module qualification according to IEC 61646 accelerated stress testing is being performed. As it is well known that thin film circuits without packaging may be susceptible to humidity at elevated temperature the main focus is put on damp heat stability of frameless glass–glass packaged modules from the pilot line. Internal damp heat test results of those 30×30 cm² modules (Fig. 11) demonstrate power losses significantly less than the accepted 5% over 1000 h at 85 °C, 85% relative humidity.

In addition to the internal climate test another two 30×30 cm² sized pilot line modules were tested at the external test center TÜV Immissionsschutz und Energiesysteme GmbH. These tests as well as the internal tests were performed according to the damp heat part of the international standard IEC 61646 as far as this qualification norm for thin film modules is applicable to CIS modules.

Beforehand the modules were power stabilized by two successive annealing cycles (subject to the regulations of IEC 61646, test 10.19). No test sample showed major visual defects after the test. After 1000 h of damp heat according to test 10.13 of TEC 61646 and after 1

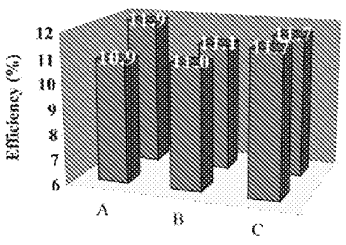


Fig. 10. Efficiencies of six 30×30 cm² circuits of a single RTP run.

SIONYX1403000041.0071

SAMSUNG EX. 1002 - 493/4148

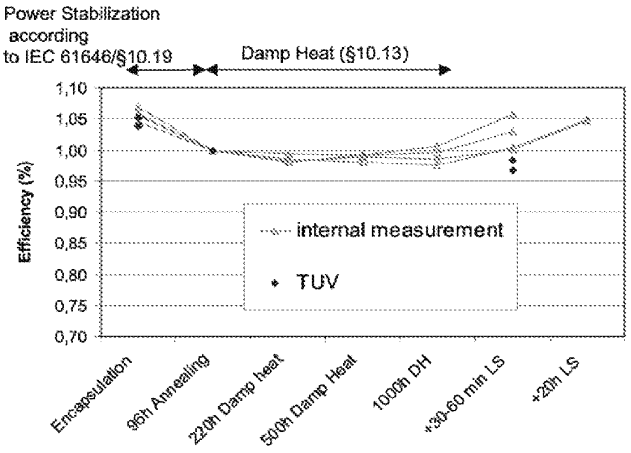


Fig. 11. SEL-RTP-processed CIGSSe 30×30 cm² large modules pass damp heat test according to IEC 61646 with low-cost glass–glass package.

h of additional light soaking at 1 sun the power loss compared to the initial stabilized values amounted to −3.2 and −1.7%. These values are within the acceptance limit of −5% given by IEC 61646 and hence it is confirmed by TÜV that the damp heat test sequence is passed successfully with the low-cost glass–glass package as described above.

3.6. Cd-free 30×30 cm² circuits

In order to replace the toxic CdS buffer layer by an alternative buffer, free of heavy metals, Zn(S,OH) compound buffer layers were applied to the device structure. Such buffer layers were fabricated by CBD, as previously demonstrated by other research groups [17–19]. We used a chemical bath formed by zinc acetate and ammonia and thiourea as sulfide source. The depositions were performed in our custom made CBD equipment at 70 °C, while continuously filtering the solution and applying ultrasonic agitation 4 of the bath [20]. Such processing is necessary to prevent Zn(S,OH) agglomerates—formed inevitably during the deposition process—from incorporation in or onto the growing film, so that uniform coatings of the CIGSSe absorbers are reached. The CBD process was followed by vacuum annealing of the devices, to completely dry the film and to transform zinc hydroxide species into oxide [21]. The device structure was completed by MO-CVD of the ZnO front electrode.

Table 2
I–V data of CIGSSe-based circuits measured at AM1.5 at 25 °C with a constant light solar simulator after 30 min light soaking

Buffer	η (%)	V_{oc} (mV)	I_{sc} (mA/cm²)	FF (%)
Zn(S,OH) best module	11.9	519	35.1	65.4
Zn(S,OH) average of 4	11.7	523	34.6	64.8
CdS reference*	12.3	537	34.5	66.3

The *I–V* data of the 30×30 cm² unencapsulated modules with Zn(S,OH) and CdS buffer layer are given in Table 2. Note that all samples belong to the same 60×90 cm² mother plate (same RTP run). Fig. 12 shows the *I–V* characteristics of the best circuit. Efficiency data with and without light soaking prior to the measurement differ just by 1% relative, indicating low transient effects. The results already demonstrate that the Zn(S,OH) compound layer is indeed a promising alternative buffer for CdS replacement.

3.7. First demonstrator modules on 60×90 cm²

Recently, the very first unencapsulated modules based on 60×90 cm² processed SEL-RTP CIGSSe absorbers were processed. For that purpose the 30×30 cm² proc-

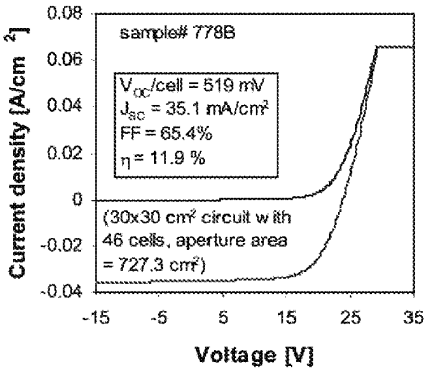


Fig. 12. *I–V* characteristic of the best CIGSSe-based circuit with Zn(S,OH) buffer layer.

SIONYX1403000041.0072

SAMSUNG EX. 1002 - 494/4148

Table 3
Certified *I–V*-characteristics of the champion 60×90 cm² circuit processed by SEL-RTP

Parameter	Value
Maximum output power (W)	64.8
Maximum power voltage (V)	41.2
Maximum power current (A)	1.57
Open circuit voltage (V)	54.6
Short circuit current (A)	1.78
Fill factor (%)	66.7
Module aperture efficiency (%)	13.1
Aperture area (cm²)	4938
Number of cells	98

essing capability of the CBD-CdS dip was extended by a single plate thin liquid film CBD processor for horizontally oriented processing of the 60×90 cm² substrates. A continuous flow of a filtered CBD solution and an additional substrate heating from the bottom was included. For the transparent front electrode a MO-CVD ZnO layer was deposited at the Shell Solar production site in Camarillo, CA. The circuits were finished in Munich by insulation cut P3, edge deletion and contacting. Table 3 summarizes the best circuit (unencapsulated) certified performance data at standard test conditions (25 °C cell temperature, 1000 W/cm² irradiance, spectral irradiance distribution according to IEC 60904-3). The certified measurement was performed also by TÜV Immissionsschutz und Energiesysteme GmbH (Cologne, Germany).

4. Summary and conclusions

The pilot line yields aperture area efficiencies of 11% (average) for 30×30 cm² modules and a certified champion efficiency of 13.1% for the first 60×90 cm² demonstrator module (unencapsulated). This improvement would not have been possible without further understanding of the absorber formation process: a favorable double band gap grading structure is accomplished by controlled sulfur profiling and by natural gallium accumulation towards the back electrode, which is typical for all stacked elemental layer processes. Based upon our previously published model obtained by in situ XRD analysis the Ga profile can be explained by the strongly inhibited formation of binary gallium-selenides. By introducing the sulfur containing process gas at certain stages of the selenization process piling up of the sulfur profile towards the surface and increased sulfur bulk incorporation is achieved.

Following our route of cost reduction a frameless glass–glass package was applied and tested successfully: the stability of the pilot line modules against humidity is confirmed externally by passing the damp heat test sequence according to IEC 61646.

For a future product the importance of environmental aspects is taken into account by developing Cd-free modules. The first 30×30 cm² circuits yield up to 11.9% efficiency when the CBD-CdS film was replaced by a CBD-Zn(S,OH)-buffer layer.

From fundamental investigations to product oriented development the given results are a strong confirmation of the technology concept based on the SEL-RTP-process, extended by controlled Na-incorporation and sulfur profiling. Beside further process and stability optimization to exploit the full potential of SEL-RTP future activities will focus on high throughput equipment engineering in preparation for a successful transfer to mass production.

Acknowledgments

Shell Solar greatly acknowledges funding from the German Ministry of Economics and the Bavarian Research Foundation and the Ministry of Economics, Traffic and Technology.

References

[1] M.A. Green, K. Emery, D.L. King, S. Igari, W. Warta, Prog. Photovolt.: Res. Appl. 11 (2003) 39.
[2] V. Probst, W. Stetter, W. Riedl, H. Vogt, M. Wendl, H. Calwer, S. Zweigart, K.-D. Ufert, B. Freienstein, H. Cerva, F. Karg, Thin Solid Films 387 (2001) 262–267.
[3] V. Probst, W. Stetter, J. Palm, S. Zweigart, M. Wendl, H. Vogt, K.-D. Ufert, H. Calwer, B. Freienstein, F.H. Karg, Proceedings of the 17th EC PVSEC (2001) 1005.
[4] J. Palm, V. Probst, A. Brummer, W. Stetter, R. Tölle, T.P. Niesen, S. Visbeck, O. Hemandez, M. Wendl, H. Vogt, H. Calwer, B. Freienstein, F. Karg, Thin Solid Films 431–432 (2003) 514.
[5] D. Tarrant, J. Ermer, Proceeding of the 23rd IEEE PVSC (1993) 357.
[6] V. Probst, F. Karg, J. Rimmasch, W. Riedl, W. Stetter, H. Harms, O. Eibl, Mater. Res. Soc. Symp. Proc. 426 (1996) 165.
[7] C.L. Jensen, D.E. Tarrant, J.H. Ermer, G.A. Pollock, Proceedings of the 23rd IEEE PVSC (1993) 577.
[8] M. Marudachalam, R.W. Birkmire, H. Hichiri, J.M. Schultz, A. Swartzlander, M.M. Al-Jassim, J. Appl. Phys. 82 (1997) 2896.
[9] A. Brummer, V. Honkimäki, P. Berwian, V. Probst, J. Palm, R. Hock, Thin Solid Films, 437 (2003) 297–307.
[10] P. Berwian, J. Hirmke, G. Müller, Proceedings of the ICTMC 2002, Paris, 14.10.2003–18.10.2003.
[11] H. Dittrich, U. Prinz, J. Szot, H.W. Schock, Proceedings of the Ninth EC PVSEC (1988) 163.
[12] B.M. Basol, A. Halani, C. Leidholm, G. Norsworthy, V. Kapur, A. Swartzlander, R. Matson, Prog. Photovolt.: Res. Appl. 8 (2000) 227.
[13] J. Titus, H.W. Schock, R.W. Birkmire, W. Shafarman, U.P. Singh, Mater. Res. Proc. 668 (2001) H1.5.1.
[14] Y. Tanaka, N. Akema, T. Morishita, D. Okumura, K. Kushiya, Proceedings of the 17th EC PVSEC (2001).
[15] M. Engelmann, B.E. McCandless, R.W. Birkmire, Thin Solid Films 387 (2001) 14.
[16] A. Brummer, R. Hock, unpublished.

SIONYX1403000041.0073

SAMSUNG EX. 1002 - 495/4148

[17] K. Kushiya, M. Ohshita, I. Hara, Y. Tanaka, B. Sang, Y. Nagoya, M. Tachiyuki, O. Yamase, Sol. Energ. Mater. Sol. Cells 75 (2003) 171.
[18] A. Ennaoui, S. Siebentritt, M.C. Lux-Steiner, W. Riedl, F. Karg, Sol. Energ. Mater. Sol. Cells 67 (2001) 31.
[19] T. Nakada, M. Mizutani, Jap. J. Appl. Phys. 41 (2002) L165.
[20] T.P. Niesen, H. Calwer, W. Stetter, V. Probst, Presented at 203rd Meeting of the Electrochemical Society, Paris (2003).
[21] K. Kushiya, O. Yamase, Jap. J. Appl. Phys. 39 (2000) 2577.

SIONYX1403000041.0074

SAMSUNG EX. 1002 - 496/4148

CHARACTERIZATION OF EXPERIMENTAL TEXTURED ZnO:Al FILMS FOR THIN FILM SOLAR CELL APPLICATIONS AND COMPARISON WITH COMMERCIAL AND PLASMONIC ALTERNATIVES

David N. R. Payne[1], Stuart A. Boden[1], Owain D. Clark[1], Alan E. Delahoy[2] and Darren M. Bagnall[1]
[1]Nano Research Group, Electronics and Computer Science, University of Southampton, SO17 1BJ, UK
[2]EPV Solar, Inc., 8 Marlen Dr., Robbinsville, NJ 08691, USA

ABSTRACT

We present the comprehensive characterization of several experimental ZnO:Al films for thin film solar cell applications. The morphological and optical properties of these films are determined using traditional and new, experimental measurement techniques and results are compared to those of the commercial Asahi U-type TCO as well as samples of planar TCOs coated in silver nanoparticles. Results show that the textured ZnO:Al films provide far superior scattering to the commercial alternatives studied. Nanoparticle coated planar TCOs also show scattering enhancement with results suggesting that nanoparticle layers could be tuned to predominantly scatter light within a chosen wavelength range.

INTRODUCTION

Thin film amorphous silicon (a-Si) solar cells are one of the most important photovoltaic technologies; they are cheap and lightweight, they can be deposited at low temperature on either rigid or flexible substrates and silicon is abundant within the Earth's crust. However, short diffusion lengths necessitate thin active regions and this, combined with low absorption ensures an absolute requirement for effective light-trapping, otherwise a significant amount of light reflected from the back of the cell escapes through the front of the device.

One proven method for improving total absorption in a thin a-Si solar cell is to texture the top transparent conducting oxide (TCO). This works by scattering light into the plane of the semiconductor and increasing the effective optical path length for light within the silicon layer. To enable optimal scattering within low cost cells a suitable TCO must be used which exhibits excellent electrical and optical properties and can be fabricated and textured economically. Most successful commercial TCOs are based on tin oxides deposited on glass, with Asahi U-type being one of the most successful as it is highly optimized for a-Si solar cells [1]. However, in recent years it has become apparent that ZnO:Al films are capable of providing improved transparency with superior haze characteristics in comparison to tin oxides [2].

Although heavily textured TCOs can demonstrate very high scattering, growing thin film solar cells on an extremely rough superstrate can be exceptionally troublesome and a compromise between scattering and device quality must be sought. A promising alternative to complete reliance on texturing is the use of metal nanoparticles. These nanoparticles are relatively smooth and are therefore likely to cause fewer fabrication issues whilst their plasmonic properties could significantly enhance scattering [3].

In this work, we present the extensive characterization of a series of experimental ZnO:Al films, each with uniquely textured surfaces created by varying fabrication parameters. These films are an extension of previous efforts in this area [2, 4]. The morphological and optical properties of these films are compared to the popular commercial TCO, Asahi U-type, as well as experimental samples of planar TCOs coated with silver nanoparticles.

EXPERIMENTAL TECHNIQUES

Sample Fabrication

Textured ZnO:Al films were prepared on soda-lime glass substrates by reactive hollow cathode sputtering using metallic Zn targets [4]. The deposition pressure was 260 mTorr and the substrate temperature was approximately 230°C. Both static and dynamic depositions were performed and films of different thickness were prepared in order to vary the feature size.

Metal nanoparticle coated planar TCOs were fabricated using the metal island film approach. Each sample consists of a thin (~40 nm) layer of planar ITO on glass, the ITO layer is then coated with nanoparticles by using electron beam evaporation to deposit Ag films of specific thicknesses and annealing for 2 hours at 200°C. Several different film thicknesses were used in order to vary the shape and size of the resulting metal nanoparticles.

Characterization

We have employed various methods to characterize the physical and optical properties of all samples as well as the electrical properties of each of the TCO samples. Surface topography was determined from a combination of scanning electron microscopy (SEM) and atomic force microscopy (AFM). AFM analysis was used to accurately determine the surface profile and extract roughness parameters. SEM was used to image the sample surface

978-1-4244-5892-9/10/$26.00 ©2010 IEEE

SIONYX1403000041.0075

SAMSUNG EX. 1002 - 497/4148

at various magnifications. A Focused Ion Beam (FIB) system was also employed to prepare cross-sections through the samples, allowing measurement of layer thicknesses. Initial electrical characterization has been carried out via standard four point probe measurements used to determine sheet resistance. The four point probe system used was a Jandel RM3-AR capable of measuring sheet resistance to an accuracy of ~0.3%.

The basic optical transmission properties of all samples have been determined using standard haze measurements. These measurements have been carried out using a Fianium white light laser source along with a integrating sphere (IS) and BWTEK spectrometer with a wavelength range of 450 to 900 nm. The IS was set up in double beam mode in order to obtain high accuracy results [5]. Haze measurements provide a relatively rapid and simple means of quantifying the overall scattering caused by a surface, however, in the case of photovoltaic devices, the angle of scatter is crucial to device performance and therefore more sophisticated measurements are also required in addition to haze.

To determine the angular distribution of scattered light, angle resolved scattering measurements are typically used. We have enhanced this measurement technique to include wavelength dependent detail, resulting in wavelength and angle resolved scattering measurements (WARS). These measurements are carried out using a Fianium white light laser source together with a custom built motorized goniometer system and BWTEK spectrometer (wavelength range of 450 nm to 900 nm). The goniometer system consists of 7 highly accurate computer controlled motorized stages, allowing for extremely precise sample alignment. Once a sample has been mounted and aligned within the system the white light laser is directed through the sample and detected by a spectrometer through a fiber initially positioned at 0° (detecting specular transmission). The sample and laser are then kept stationary as the fiber is rotated around the angle θ. Spectrometer measurements are taken between the angles of 0° and 80° at 1° intervals. An annotated 3D rendering of the custom built WARS measurement system is shown in Figure 1.

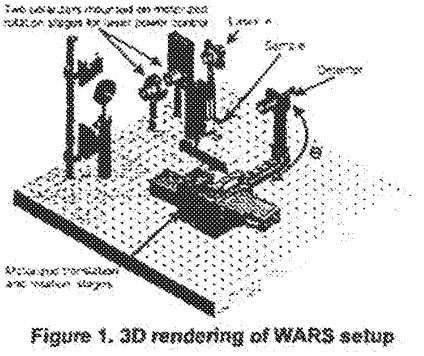


Figure 1. 3D rendering of WARS setup

The WARS measurement process has been fully automated and is controlled by a LabVIEW™ software interface which has been developed in house. The measurement data is then automatically processed by a custom built Matlab® program which normalizes all measurements of scattered light with respect to the specular transmission and then outputs various 2D and 3D graphical representations of the results. For an accurate representation of the total scattering at an angle θ, the distribution of the scattered light around the azimuthal angle φ must also be considered. This is important because light scattered at larger angles of θ is distributed over a wider area and therefore the in plane measurement must be scaled accordingly to give approximate results for the solid angle θ revolved around φ, see Figure 2. The Matlab® post processing code carries out this conversion using a sin(θ) based relationship which can be calculated using simple geometry with the assumption that the scattering is isotropic around φ.

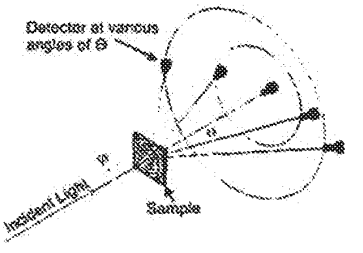


Figure 2. 3D illustration of the distribution of scattered light

RESULTS AND DISCUSSION

Textured TCO Samples

AFM and SEM analysis of the surface topography of the experimental ZnO:Al samples shows vast differences between samples in terms of feature size, shape and overall surface RMS roughness, with the majority of films having a highly faceted surface structure. SEM images of the commercial Asahi U-type TCO and two of the ZnO:Al samples are shown in Figure 3. Some of the experimental ZnO:Al samples appear to have very similar shaped surface features to the Asahi U-type although in general the features of the experimental ZnO:Al films are considerably larger than those of the commercial TCO alternative. Many of the ZnO:Al films consist of very high aspect ratio surface features, therefore it was necessary to use special purpose high aspect ratio AFM probes in order to accurately determine the surface topography and roughness parameters. The specific probe used was a TESP-HAR probe from Veeco. Asahi U-type was found to have an RMS roughness of around 40 nm; this value agrees well with literature [6]. The ZnO:Al samples range in RMS roughness from ~80 nm to around ~130 nm, considerably rougher than Asahi U-type.

978-1-4244-5892-9/10/$26.00 ©2010 IEEE

SIONYX1403000041.0076

SAMSUNG EX. 1002 - 498/4148

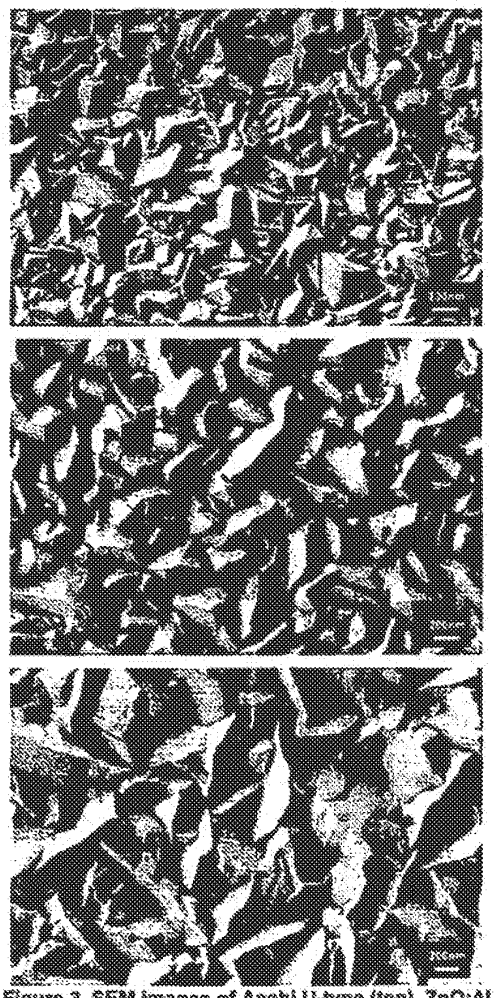


Figure 3. SEM images of Asahi U-type (top), ZnO:Al #751 (middle) and ZnO:Al #757 (bottom)

To determine an approximate value for the film thickness of a TCO, it is conventional to use ellipsometry measurements which are capable of providing highly accurate results. However, in the case of some of the very rough ZnO:Al samples analysed here, fitting ellipsometry data proved to be extremely troublesome. Therefore a focused ion beam (FIB) was used to create cross sections within the samples, enabling approximate values for film thickness to be measured from SEM images. An example SEM image of a cross section in the ZnO film #751 is shown in Figure 4. Asahi U-type was found to be around 970 nm thick, the ZnO:Al films were found to range between 642 nm and 3.1 μm in thickness.

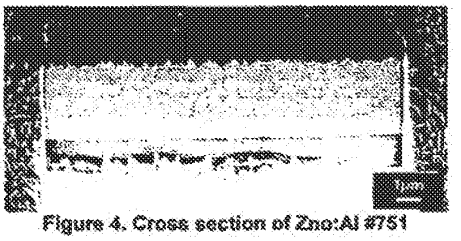


Figure 4. Cross section of Zno:Al #751

Four point probe measurements show that all of the ZnO:Al samples have a low sheet resistance of between 2 and 7 Ω/□; this is significantly lower than the commercial Asahi U-type with a sheet resistance of 9-11 Ω/□. The measured sheet resistance for several of the TCO samples is shown in Table 1 along with calculated resistivity values. For photovoltaic device applications a sheet resistance of around 10 Ω/□ or less is considered to be good. Thus the ZnO:Al samples exhibit excellent resistance values.

Sample	Sheet Resistance (Ω/□)	Resistivity ($\times 10^{-4}$ Ω cm)
Asahi U-type	9-11	8.7-10.6
ZnO:Al #386	6.57	4.22
ZnO:Al #751	2.81	6.41
ZnO:Al #757	2.01	6.26

Table 1. Sheet resistance values for all textured TCOs

Haze measurements show that the ZnO:Al films provide extremely high haze, far superior to that of Asahi U-type, see Figure 5. As expected, results show a reduction in haze at longer wavelengths for all samples. Corresponding total transmittance measurements show that on average over the wavelength range, the majority of the ZnO:Al samples transmit around ~75% of the light, slightly less than Asahi U-type transmission at ~80%. However, these measurements were made without use of an index-matching fluid, which probably underestimates the transmittance of the more heavily textured samples to a greater degree than the less textured samples.

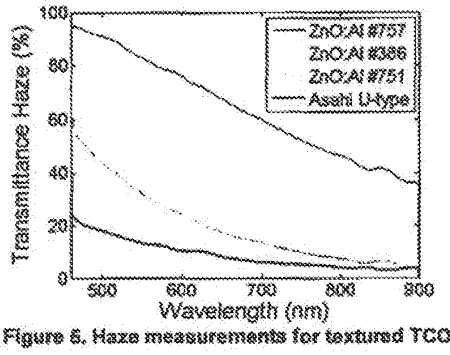


Figure 6. Haze measurements for textured TCOs

SIONYX1403000041.0077

SAMSUNG EX. 1002 - 499/4148

Results from WARS measurements show very clear differences between the angles and wavelengths of scattering for the commercial and experimental TCO samples. A sample of the WARS results for Asahi U-type and ZnO:Al films #751 and #757 is shown in Figure 6.

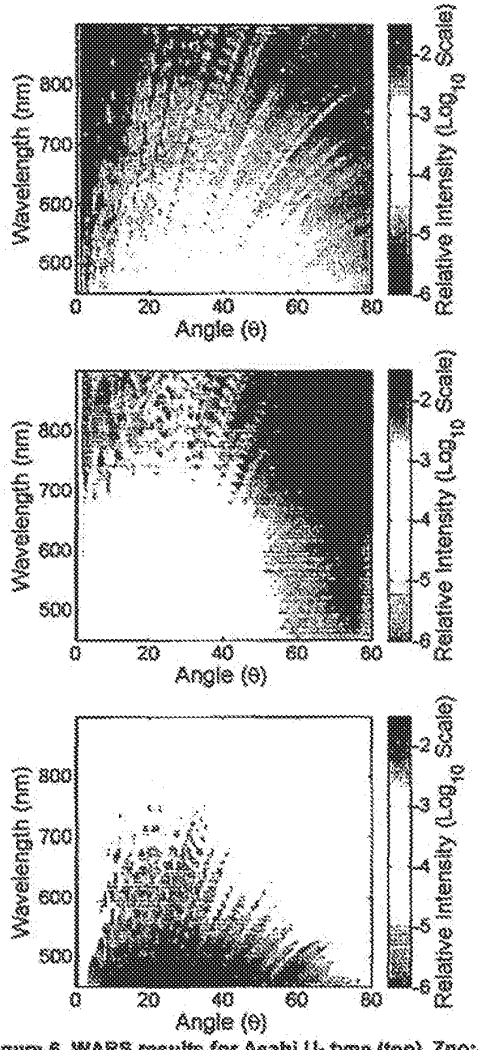


Figure 6. WARS results for Asahi U- type (top), Zno:Al #751 (middle) and ZnO:Al #757 (bottom)

The WARS results clearly show that the ZnO:Al films exhibit superior high angle scattering when compared to the commercial Asahi U-type. As expected, Asahi U-type appears to provide a reasonably high scattering intensity over a broad distribution of angles at shorter wavelengths (600 nm). The rougher ZnO:Al films generally show an even higher intensity of scattering and the angular distribution of scattered light varies significantly per sample, with the best sample being ZnO:Al #757 which shows intense scattering over a broad angular range up to wavelengths of ~800 nm.

Metal Nanoparticle Coated Samples

The surface topography of the metal nanoparticle coated samples has been determined using SEM images. Various initial silver layer thicknesses ranging between 2.5 nm to 20 nm were deposited, resulting in a range of samples with different sizes, shapes and distributions of nanoparticles. Example SEM images of the 7.5 nm and the 20 nm annealed samples are shown in Figure 7.

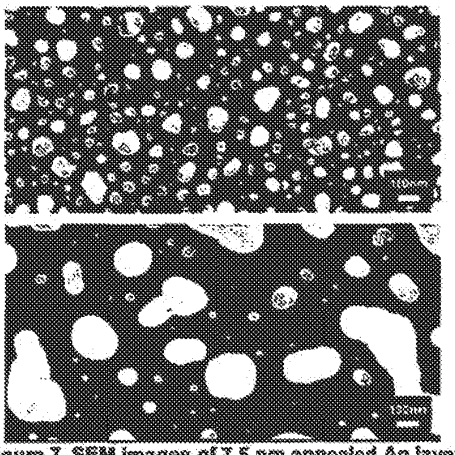


Figure 7. SEM images of 7.5 nm annealed Ag layer (top) and 20 nm annealed Ag layer (bottom).

Haze measurements for the nanoparticle coated samples are shown in Figure 8. These results show a dramatic increase in haze as particle size increases; however, increases in absorption and reflection were also present causing the arrays of larger nanoparticles to have an average overall transmission of only around 45%.

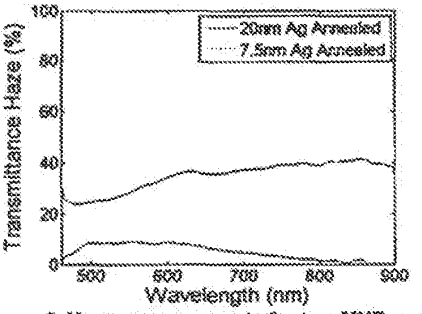


Figure 8. Haze measurements for two MNP coated samples

SIONYX1403000041.0078

SAMSUNG EX. 1002 - 500/4148

Finally, WARS results for two of the MNP coated planar TCO samples are shown in Figure 9. As with the textured TCO WARS measurements, these results are for the scattering in transmission. Thus they provide information on scattering enhancement for MNPs used at the front interface of a thin film device structure.

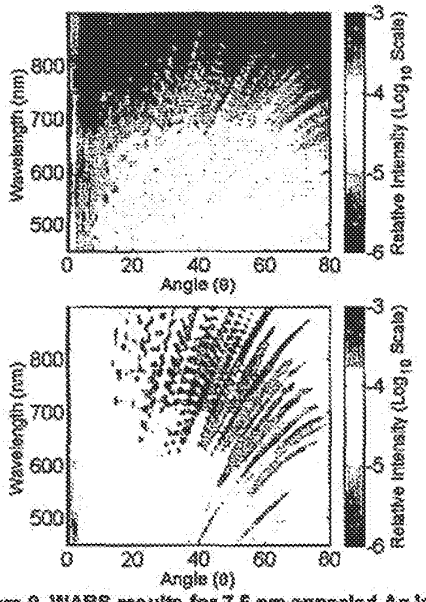


Figure 9. WARS results for 7.5 nm annealed Ag layer (top) and 20 nm annealed Ag layer (bottom)

The WARS results show a significant increase in scattering in comparison to a standard planar TCO. Interestingly, it can be observed that by varying the size and distribution of the Ag nanoparticles, the scattering peak can be tuned to particular wavelengths. This may be partially due to the change in surface texture but it is likely that plasmonic effects are also involved, and this trend agrees well with plasmonic theory [3]. In general, annealing thicker layers of Ag leads to larger nanoparticles which form more ellipsoidal shapes as opposed to smaller spherical nanoparticles. These larger, ellipsoidal nanoparticles have a red-shifted resonant frequency [3], therefore the peak wavelength of scattering also red-shifts.

CONCLUSIONS

Experimental textured ZnO:Al films have been physically, electrically and optically characterized and it is clear from the results that these TCOs are superior to the commercial Asahi U-type in several ways. Experimental ZnO:Al samples exhibit sheet resistances that are typically ~60% lower than Asahi U-type, whilst optically they provide excellent haze. However, whilst the haze of the ZnO:Al films is very good, the overall transmission of the films may be lower than that of Asahi U-type. WARS results for the ZnO:Al samples show that some of the samples scatter intensely over an excellent angular distribution and often scattering is still high at wavelengths of above 800 nm. This indicates that some of the ZnO:Al films could be particularly suitable for lower band gap µc-Si or micromorph solar cells. However, in general the best ZnO:Al films were also the roughest and the high aspect ratio of the surface features of these samples is likely to be problematic for silicon deposition.

The MNP coated TCO samples do not exhibit scattering intensities as high as the textured ZnO:Al samples but they do generally scatter to higher angles and the peak wavelength of scattering varies with MNP size and distribution. This suggests that MNP layers could be tuned to provide optimal scattering for a particular semiconductor absorber layer. However, the application of MNPs also has an effect on the reflection and absorption of light. It is therefore likely that layers such as these will be more beneficial when incorporated into the back reflector of the device, where the increased reflection becomes a useful property.

Future work includes further optimization of the experimental textured ZnO:Al films, followed by their use as superstrates for the growth of a-Si and µc-Si solar cells. Further analysis of the effects of MNPs should also be carried out, particularly for the application of long wavelength scattering within µc-Si solar cells.

ACKNOWLEDGEMENTS

The authors would like to thank Rajesh Kappera for deposition of the ZnO:Al films and Tristan L. Temple for providing the metal nanoparticle coated samples.

REFERENCES

[1] K. Sato et al., "Highly Textured SnO2:F TCO Films for a-Si Solar Cells", *Reports Res. Asahi Glass Co.* **42**, 1992.

[2] A. E. Delahoy et al., "Influence of TCO Type on the Performance of Amorphous Silicon Solar Cells", *SPIE Proceedings* **7045**, 2008, pp. 704506.

[3] S. Pillai, K. R. Catchpole, T. Trupke and M. A. Green, "Surface Plasmon Enhanced Silicon Solar Cells", *Journal of Applied Physics* **101**, 2007, pp. 093105.

[4] S. Y. Guo, L. Sahoo, G. Scoale and A. E. Delahoy, "Textured, Doped, ZnO Thin Films Produced by a new Process for a-Si and CIGS Solar Cell Applications", *SPIE Proceedings* **6651**, 2007, pp. 665108.1-665108.10.

[5] H. Tu and C. Hsaio, "Comparison of Different Measurement Methods for Transmittance Haze", *Metrologia* **46**, 2009, pp. S233-S237.

[6] J. Krc et al. "Optical Modeling of a-Si:H Solar cells Deposited on Textured Glass/SnO_2 Substrates", *Journal of Applied Physics* **92**, 2002, pp. 749-755.

C15

Appl. Phys. A 77, 277–284 (2003)
DOI: 10.1007/s00339-003-2113-9

Applied Physics A
Materials Science & Processing

Surface nanostructuring of silicon

A.J. PEDRAZA✉
J.D. FOWLKES
Y.-F. GUAN

Department of Materials Science and Engineering, The University of Tennessee, Knoxville, TN 37996-2200, USA

Received: 16 December 2002/Accepted: 20 January 2003
Published online: 28 May 2003 • © Springer-Verlag 2003

ABSTRACT Irradiation with polarized laser light of 248-nm wavelength induces the formation of periodic undulations ~ 10-nm-high on flat silicon substrates. The wavelength of these periodic structures is a function of the light wavelength and the angle of incidence of the laser beam. Linear arrays of silicon nanoparticles with fairly uniform size that extended up to a millimeter were formed if the irradiation was performed using polarized light. When non-polarized laser light with the same fluence was used to illuminate an initially flat surface, non-aligned nanoparticle strings were obtained. However, if part of the irradiated area was microstructured, nanoparticle linear arrays resulted in the vicinity of the microstructured region. An analysis on the evolution of these nanostructures is presented. Nanocolumns could be grown on top of every cone of a microstructured surface upon cumulative laser irradiation with non-polarized light, reaching a height of ~ 3 μm and a diameter of 100–200 nm. The mechanisms of nanocolumn origin and growth are analyzed.

PACS 61.46. +w; 61.80.Ba; 61.82.Fk; 68.35.Bs

1 Introduction

Laser-induced surface microstructuring of silicon has been extensively studied [1–8], and has been found to be a function of fluence and of the composition and pressure of the background atmosphere present in the irradiation chamber [5, 6]. At a fluence between 2 and 3 J/cm^2 two distinct processes can take place sequentially as a result of cumulative laser irradiation. Shallow depressions evolve and can reach a depth of a few micrometers and a separation distance of 20 to 30 μm [7]. These depressions are initially sparsely distributed on the surface, but new ones form and progressively cover the entire irradiated area. At the same time, the depressions continuously deepen with the number of laser pulses. For irradiation in non-reactive environments such as vacuum or Ar, this surface relief continuously builds up with the number of laser pulses, up to 10 000 pulses [8].

In a reactive atmosphere like SF_6, the same evolution is initially observed in the same fluence range, but more dramatic changes occur after 600 pulses. Additional irradiation in SF_6 produces a drastic change both in the surface-roughening rate and in the morphology, establishing the signature of a second, different process. The change to this second process, which produces a characteristic microhole–microcone microstructure, is preceded by a transition stage in the morphology. Figure 1 shows the three stages of microstructure evolution just outlined. After ~ 400 laser pulses, the surface relief depends only on the crystallographic orientation of the laser-exposed surface. The optical image acquired with Nomarski contrast shown in Fig. 1a illustrates the first stage in the process of a surface relief production. Shallow depressions and elevations that have the appearance of a cube structure can be seen. The orientation of the surface is very close to (111) and the characteristic three-fold symmetry is clearly revealed by the surface traces. The same relief is produced under reactive and non-reactive atmospheres. The second stage, shown in Fig. 1b, has been observed only under a reactive (SF_6) irradiation atmosphere and after a higher number of pulses. Intense etching takes place at the bottom of the depressions formed during stage 1. Multiple reflections focus the beam at these depressions, enhancing the decomposition of SF_6 and thus the etching activity [8]. The third stage (Fig. 1c) is characterized by a synergistic process involving hole deepening by etching- assisted ablation and cone growth by re-deposition of ablated species on top and to the sides of the laser-melted regions. Since ablation also takes place in these regions, growth can occur only when re-deposition occurs in excess of ablation.

A reduction of the laser energy to $\leq$ 1 J/cm^2 drastically changes the scale of the surface relief, promoting the formation of nanostructures. Three different phenomena will be described and analyzed: (1) the production of periodic nanochannels; (2) the formation of an organized array of nanoparticles; and (3) the growth of nanocolumns. The processing characteristics could be of interest for some technologies, since long-range ordering of nanostructures is a key issue, central to the utilization of nanostructures in electronic materials applications.

2 Experimental procedure

Boron-doped silicon substrates were irradiated using a Lambda Physik LPX–305i KrF excimer laser (248-nm wavelength), with a pulse duration of 25 ns. Unless otherwise

✉ Fax: +1-865/974-4115, E-mail: apedraza@utk.edu

SIONYX1403000041.0080

SAMSUNG EX. 1002 - 502/4148

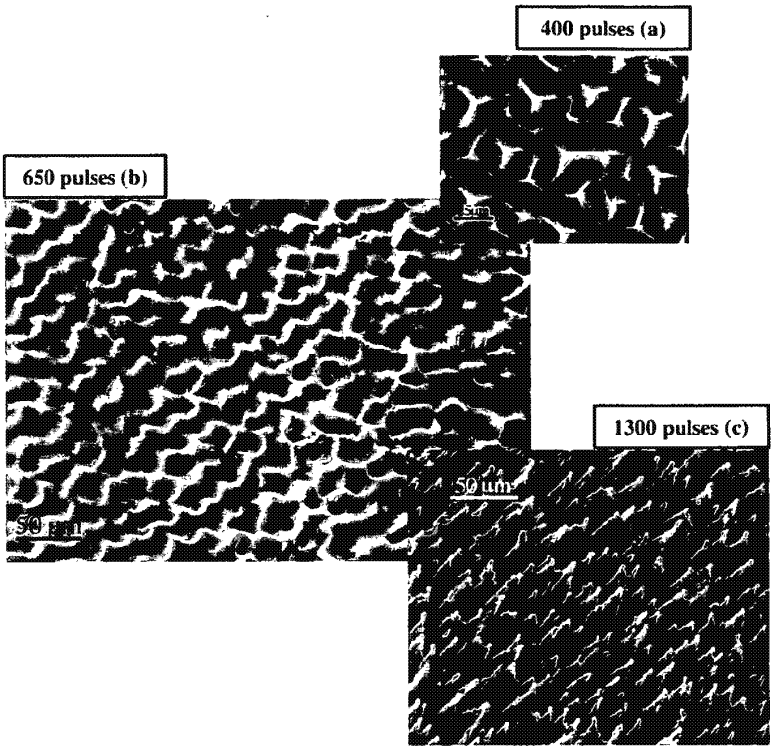


FIGURE 1 The three stages of cone formation in silicon under an SF_6 atmosphere. **a** Optical micrograph with Nomarski contrast; **b** and **c** SEM images with sample tilted 40°

indicated, all laser treatments were carried out at normal incidence. The beam emerging from the laser cavity was directed to an optic bench using a MgF_2-coated fused-silica mirror. The optic bench contained an aperture, a fused-silica lens array, and the irradiation chamber. The rectangular aperture partly removed the low energy tails of the trapezoidal laser beam. The laser fluence was varied by adjusting the position of the fused-silica lens array relative to the sample holder in the irradiation chamber.

All of the experiments were conducted using helium as background gas. For each laser irradiation cycle, the irradiation chamber was pumped to a base pressure of 1×10^{-7} Torr He prior to introducing 99.999% pure helium gas at a selected pressure. For some experiments, the substrates were first laser-microstructured in an SF_6 atmosphere, to produce a cone relief.

Native oxide layer removal was done by immersing the specimens in a 10 : 1 HF aqueous solution for 5 min, washing, drying and quickly transferring them to a vacuum chamber. Table 1 summarizes the experimental conditions used for the examples shown in the figures.

Ex situ characterization studies were conducted using scanning electron microscopy (SEM), atomic force microscopy (AFM), and Auger emission spectroscopy (AES).

Figure number	Laser fluence (J/cm^2) and polarization (p,np)[a]	Number of pulses	Composition and pressure (Torr) of irradiation atmosphere	Initial surface topography	Final surface structure
2	0.8 p	400	Vacuum 1×10^{-6}	Smooth[b]	Nanochannels
3	0.6 np	450	He 100	Smooth[c]	Nanoparticles
4a	0.6 np	500	He 100	Smooth[c]	Nanoparticles
4b	0.6 np	700	He 100	Smooth[c]	Nanoparticles
5	1 np	200	He 100	Smooth[c]+ Cones	Nanoparticle clusters and ordered nanoparticle array
6	1 np	200	He 0.5	Smooth[c]+ Cones	Ordered nanoparticle array
7	0.5 np	2000	He 10	Microcones	Nanocolumn (Start)
8	0.5 np	0–10000	He 10	Microcones	Nanocolumn on top of cone
9	0.5 np	15000	He 10	Microcones	Nanocolumn on top of cone

[a] p: polarized; np: non-polarized
[b] native oxide present in surface
[c] native oxide removed

TABLE 1 Summary of experimental conditions related to figures

SIONYX1403000041.0081

SAMSUNG EX. 1002 - 503/4148

3 Formation of nanochannels by laser irradiation

The formation of nanochannels was observed only when using polarized light to irradiate silicon specimens and when the surface had its native oxide. In order to examine the effect of the presence of this oxide layer, two types of experiment were first performed, using the same conditions: 2000 pulses of polarized laser light at an angle of incidence of 14°, a fluence of 0.7 J/cm^2 and a vacuum pressure of 5×10^{-6} Torr. In one of the experiment types, the native oxide was removed from the surface of the silicon targets prior to the irradiation, while for the other type, specimens with the native oxide were irradiated without any surface conditioning. These experiments consistently showed that the oxide layer stabilizes the ripples. All the experiments described in this section were performed on silicon with the native oxide film using polarized light.

Formation of 6–10-nm-deep nanochannels was induced by laser irradiation of an initially flat silicon substrate, in a background pressure of 1×10^{-6} Torr, at a laser fluence of 0.8 J/cm^2. These channels were produced using linearly p-polarized light (for which the electric field lies in the plane of incidence) and were aligned normal to the polarization direction. At normal laser beam incidence, the spacing between channels, Λ, equaled the laser wavelength, λ. The channels were not featureless, as can be seen in Fig. 2. The overall structure could be described as two periodic structures or waves of the same wavelength displaced from each other by half a wavelength. The amplitude of one of the waves was ~6 nm – significantly larger than the amplitude of the other wave.

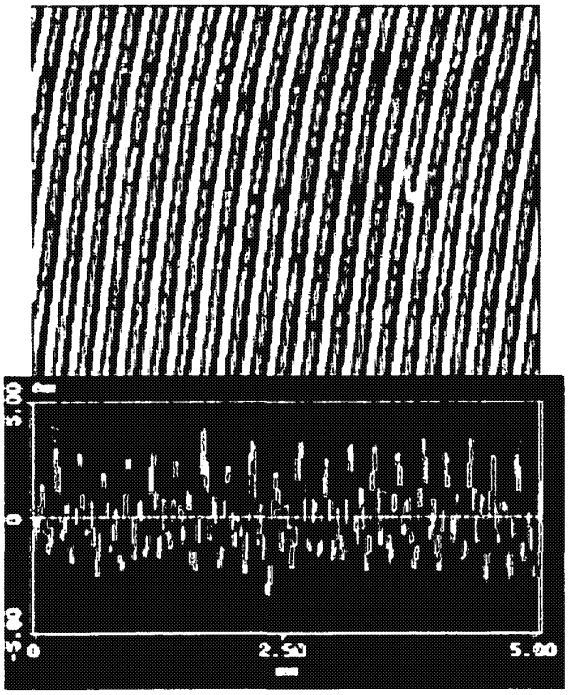


FIGURE 2 AFM image of LIPSS formed in silicon under vacuum. Linearly polarized laser light at normal incidence. Laser wavelength: 248 nm; fluence: 0.8 J/cm^2; 400 pulses. Note: y-scale in nm; x-scale in μm

Several experiments were done with an angle of incidence of the beam $\theta > 0$. In this case, two line-spacings were found in the same specimen in some instances. For example, for a sample irradiated with 2000 pulses at a fluence of 1 J/cm^2 in a 10 Torr background pressure of He and for $\theta = 15°$, the two spacings given in the first column of Table 2 were measured.

The spontaneous formation of periodic ripples on the surface of a material illuminated with polarized pulsed laser light has been reported in many different materials [9–23] at fluences close to the melting threshold, spanning a wavelength range of 10.6 to 0.193 μm. The period and orientation of these surface ripples, known in the literature as laser-induced periodic surface structures (LIPSS), mainly depend on the following aspects of the laser beam: angle of incidence, polarization, frequency, and energy. However, the occurrence of LIPSS in a given material appears to be a strong function of the specific response of this material to inhomogeneous energy deposition. For instance, for a given set of the main laser parameters just listed, some fringe patterns observed in Ge have not been detected in Si or Al [12]. Excluding the studies in polymers, all of the previous reports refer to LIPSS spacings on the order of microns. This is the first time that nano-LIPSS have been demonstrated in silicon.

The most often encountered periodic structures are those whose wave vector is parallel to the projection of the electric field on the surface plane [12]. These ripples or fringes were found mostly when the electromagnetic field was linearly polarized, whether the electric field lay in the plane of incidence (p-polarized) or perpendicular to it (s-polarized). LIPSS could be very simply interpreted as being produced by the interference between the refracted radiation and two scattered waves parallel to the surface propagating in opposite directions, giving the following dependence of fringe spacings, Λ_+ and Λ_-, on the angle of incidence θ and the laser wavelength λ:

$$\Lambda_{\pm} = \frac{\lambda}{1 \pm \sin\theta} . \tag{1}$$

As can be seen from Table 2, the line-spacings calculated using (1) for the case of $\theta = 15°$ and $\lambda = 248$ nm are in good agreement with the two values reported above of 204 nm and 331 nm. In addition, in some cases a spacing following a different law,

$$\Lambda = \frac{\lambda}{\cos\theta} , \tag{2}$$

was found for fringes running parallel to the polarization vector of incident p-polarized light, in contrast with those whose spacing was described by the sine law, which run perpendicular to it [14, 15].

$\Lambda_{\text{measured}}$ (nm)	$\Lambda = \frac{\lambda}{1+\sin\theta}$	$\Lambda = \frac{\lambda}{1-\sin\theta}$
204	197	–
335	–	331

TABLE 2 Measured and calculated line-spacing of LIPSS

SIONYX1403000041.0082

SAMSUNG EX. 1002 - 504/4148

Several groups have developed theories to explain the production of LIPSS [11, 13, 14, 23]. The key factor to explain LIPSS evolution in all of the models is the occurrence of an inhomogeneous light intensity distribution on the surface. The inhomogeneity in the light distribution arises from the interaction between the light scattered by surface roughness and the refracted laser light. There are several ways whereby the material can respond to the temperature modulation due to this energy inhomogeneity [13, 14]. It has also been recognized that a positive feedback is necessary for the ripples to be produced. Concurrent with this concept, we have observed in our studies that nanoripple formation always requires multiple laser pulses, also indicating that the interaction between roughness and light evolves with an increasing number of pulses. The difficulty in stabilizing this nanostructure is highlighted by two factors, possibly interrelated: the large number of pulses needed to form them, as just emphasized, and the apparent requirement that there must be a native oxide layer present.

4 Self-organized linear arrays of laser-induced silicon nanoparticles

All the experiments in this section, with one exception, were performed using non-polarized light. The native oxide was removed in all the specimens, flat and microstructured, prior to laser irradiation to minimize oxide contamination of the nanoparticles. At laser fluences close to 1 J/cm^2 and using a background atmosphere of ultra high purity (UHP) He rather than vacuum, a film was deposited on the surface of a silicon substrate [24]. The background gas backscattered atoms and probably very small clusters were also deposited on the substrate. The film detected by AFM using a tapping mode scan, after 200 pulses at 1 J/cm^2 and 10 Torr of He background pressure, was very porous with some areas a few nanometers thick and other areas with a much thinner film or no film at all. The average film thickness observed over all the measured specimens was of the order of 1 nm. However the film thickness did not increase very significantly after the first 50 pulses, giving an average deposition rate of $\sim 2 \times 10^{-2}$ nm/pulse. From this deposition rate, it is difficult to evaluate the average ablation rate during irradiation because in some regions of the specimen ablation was taking place, while in others there was material accumulation.

It is clear from the extensive work done on ripple formation that a non-uniform deposition of energy is produced during laser irradiation of a surface with micro- or nano-roughness. In our case, AFM images recorded very significant nano-roughness in all specimens, with some regions as high as 8 nm. Light scattering from this random nano-roughness will produce a random interference pattern with the refracted light that will generate a non-uniform energy deposition. For this reason, it is difficult to establish a meaningful correlation between the ablation rate and laser fluence. The fact that a film was formed at the same time as ablation was taking place indicates that the laser fluence used in these experiments was very close to the ablation threshold. The film did not seem to increase significantly with the number of pulses, probably due to continuous ablation and clustering. Auger emission spectroscopy revealed that beyond the first nanometer the film was at least 90% silicon, with no silicon bound to an oxide or carbide.

SEM and AFM images indicate that the film clusters and forms nanoparticles as it is being irradiated with non-polarized laser light [24]. We have observed film-denuded zones, 1 to 2 μm in diameter, containing nanoparticles that had apparently consumed the film originally in the zone. The distance between nanoparticles in these small regions was close to the wavelength of the incident light, indicating a process controlled by a non-homogeneous distribution of energy similar to what happens during ripple formation.

As nanoparticle formation proceeded with additional irradiation, the particles tended to aggregate into curvilinear strings and became stabilized at $\sim$ 30 nm-diameter, as measured in SEM images (Fig. 3). This behavior resulted in a fairly uniform size distribution. The evolution of this nanostructure with additional irradiation was followed using a high-precision SEM stage positioning mechanism. The nanoparticles kept their identity and shape; however, they experienced displacements, as illustrated in Fig. 4. They tended to align in short curvilinear strings like pearls in a necklace, and some ordering can be appreciated in the micrographs. At a certain point the strings became locked and further movement or ordering did not occur. At higher laser fluence, e.g., 1.3 J/cm^2, they flattened and tended to fuse with the substrate.

A very dramatic change in the nanoparticle spatial distribution occurred when the irradiation was done on a surface partly covered with a well-developed cone microstructure. The microcones were grown by laser irradiation in a 0.5 bar SF_6 atmosphere, using 1200–2000 pulses at a laser energy of $\sim$3 J/cm^2; they had a height of 20–30 μm and tips of a few micrometers in diameter [6–8]. A typical microstructure is shown in Fig. 1c.

The irradiation in He resulted in film deposition and the formation of linear arrays in the regions of the irradiated sub-

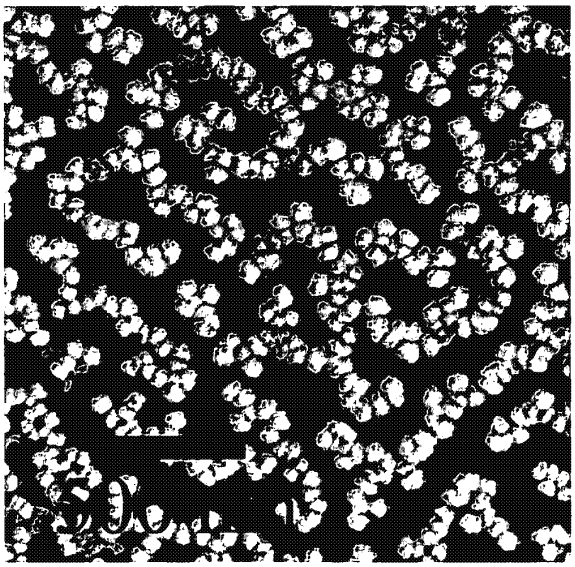


FIGURE 3 Nanoparticles formed under 100 Torr He, after 450 pulses at 0.6 J/cm^2

SIONYX1403000041.0083

SAMSUNG EX. 1002 - 505/4148

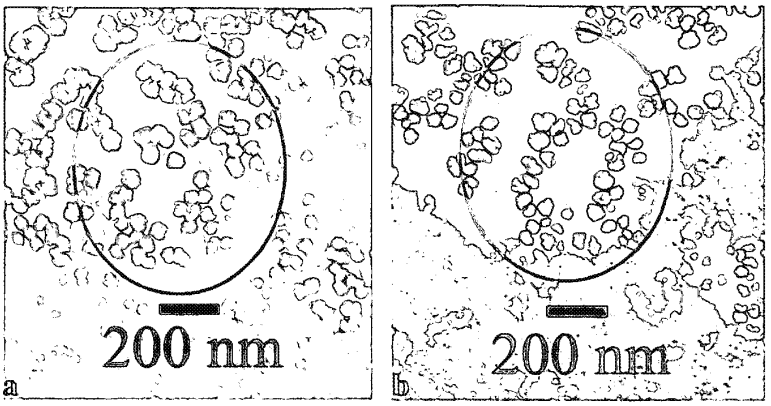


FIGURE 4 Motion of nanoparticles followed inside *encircled region*. **a** 500 pulses; **b** 700 pulses. Fluence: 0.6 J/cm^2; He pressure: 100 Torr

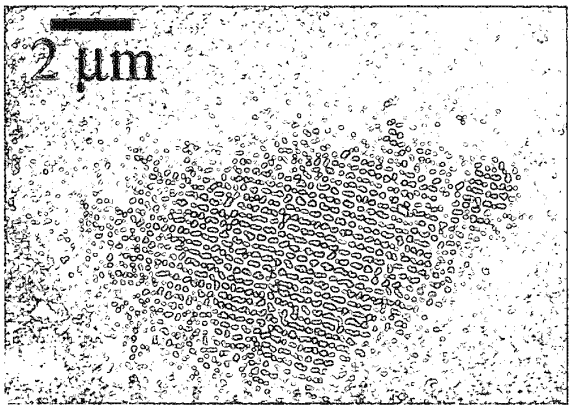


FIGURE 5 SEM image showing film clustering, and nanoparticle formation and ordering. Specimen irradiated with 200 pulses at 1 J/cm^2 under 100 Torr He

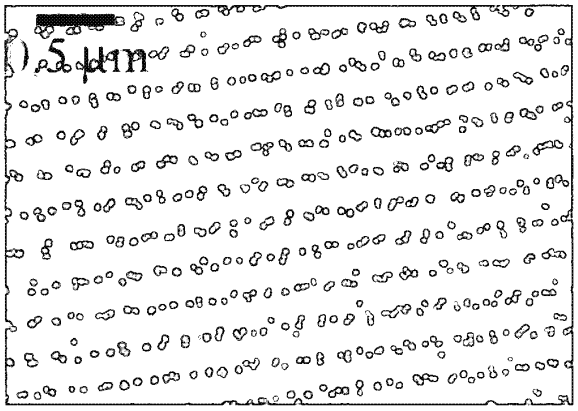


FIGURE 6 Laser-induced nanoparticle linear array in the vicinity of a microstructured region of the surface. Fluence: 1 J/cm^2; 0.5 Torr He; 200 pulses

strate surface adjacent to the microstructured zone. Figure 5 illustrates the evolution of the film, demonstrating that the nanoparticles grew in the substrate, consuming the film, and became aligned as they were being irradiated.

The nanoparticle ordered array shown in Fig. 6, has a line-spacing close to 248 nm and extends over microscopic regions with few perturbations in the alignment. This array developed in the immediate vicinity of the cone microstructure region. Characterization of the nanocrystals by using Auger electron spectroscopy demonstrated that the nanoparticle consisted of silicon cores covered with a very thin sheath of oxide.

Certain aspects of the nanoparticle alignment phenomenon suggest that it could be associated with the LIPSS phenomenon. Similar to the conditions reported for LIPSS development, the alignment was initially observed just above the melting threshold, and occurred in a narrow laser fluence range above this threshold. In almost every case, although not in all of them, for normal incidence, the particles aligned along the rectangular beam short axis, which corresponded to the direction where the E field was at a maximum. In a second set of experiments, in which a fine wire (100 μm) crossing the beam was imaged on a flat Si substrate surface, a linear alignment of nanoclusters occurred within the interference fringe pattern resulting from the diffraction of light by the wire. An AFM image taken from the same specimen shown in Fig. 6 reveals that nanoparticles were located on the valleys of LIPSS (Fig. 7). Lack of contrast prevented observation of the smooth undulations of LIPSS by SEM.

At variance with the LIPSS experiments described in the preceding section, the alignment of nanoparticles did not require polarized light; the presence of an extended defective region was sufficient. Next, we used p-polarized light, and aligned nanoparticles were produced on a flat surface, without the need for an initial microcone structure. Nanoparticle arrays aligned normal to the direction of the electric field. An experiment that illustrates well the process of nanoparticle production and alignment with size selection was done by irradiating the silicon surface with polarized light at an average energy density higher than 1 J/cm^2. The irradiated area was rectangular and we utilized a beam size of approximately 7 mm x 3 mm. All over the edges, where the beam energy tapered off and within a width of ~ 0.4 mm, an aligned array of ~ 30-nm-diameter nanoparticles was generated. A microstructure consisting of long surface waves was produced in the central portion of the irradiated region where the energy was too high for particle formation. The production of this microstructure indicates that very significant ablation could have taken place in the central region of the spot. AFM scans reveal an abrupt change in the spatial and size distribution of nanoparticles at the sides of the edges of the laser shot, into

SIONYX1403000041.0084

SAMSUNG EX. 1002 - 506/4148

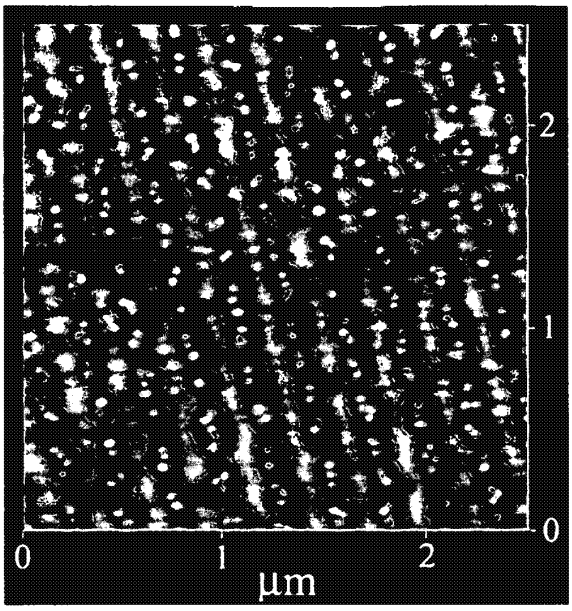


FIGURE 7 AFM image of the same surface as in Fig. 6

the unirradiated region. Instead of the highly organized array of small, fairly uniformly sized nanoparticles detected inside the irradiated edge, a completely random distribution of much larger nanoparticles with a wide size distribution was found to cover the adjacent unirradiated area.

Using p-polarized light, the angle of incidence of the laser beam was changed and it was found that the nanoparticle line spacing followed (1) with the minus sign in the denominator, i.e., the line-spacing increased as the angle of incidence was increased. This result strongly suggests that similar mechanisms are responsible for the formation of nanochannels and for nanoparticle alignment.

The results just described, whereby spontaneous alignment of silicon nanoparticles form regular arrays as a result of pulsed-laser irradiation of a silicon substrate, opens the possibility of using UV lasers as manipulators of nanoparticles on a large scale, on the order of millimeters.

5 Silicon nanostructuring atop a laser-produced microcone template

The formation of microcones has been explained by a mechanism similar to that used to explain the formation of whiskers in silicon [6–8]. The cone microstructure appears first to present a natural limit – as far as a minimum dimension is concerned – for laser-induced structuring of a surface with self-organized tips. This limitation arises from the formation and growth mechanisms of the cone and the fact that it starts at a surface that is melted throughout. Once a cone is formed, and its subsequent growth is accomplished by preferential re-deposition of material at its laser-melted tip, continuing irradiation under the same conditions will produce a rise in the cone first and result in its fall at later stages. However, we have found that a change in processing conditions could benefit from a well developed microcone structure, using it as a template for a finer structure.

A silicon target, microstructured as shown in Fig. 1c, was irradiated at 0.5 J/cm^2 in a He atmosphere at 10 Torr. It was first noticed that 2000 pulses produced the emergence at the microcone tips of small protrusions ~ 100 nm in diameter and a few nanometers in height (Fig. 8). The sequence of images presented in Fig. 9 shows the growth of one nanocolumn as a function of the number of laser pulses. Figure 9a shows the cone tip of the initial microstructured surface for which the nanocolumn evolution has been followed. We always observed a small tip at the top of the microcones, and as we continued the irradiation at low energy, the protrusion grew and a flat depression was formed around it (Fig. 9b and c). A careful examination of the images shows that the low-energy irradiation only produced melting at the very top of the cone tip. The fluence used in these experiments (referred to a flat surface) was very close to the melting threshold and it decreased from the center of the cone tip towards the sides due to the tip curvature. Thus, these irradiation conditions explain the highly localized melting. As the irradiation was continued, the depression around the protrusion disappeared (Figs. 9d–f), and the protrusion developed into a nanocolumn, while a multitude of very small protrusions appeared at its base (Fig. 9e). Finally, after 10000 pulses the nanocolumn had a height of 3.1 μm and a diameter of 200 nm, giving an aspect ratio of 15. Due to the nanosecond pulse duration, silicon transport to the top could only have taken place in the liquid or gas phase. The liquid could only be removed from the immediate vicinity where melting took place. The small and flat depression around the nanocolumn cannot account for the extra mass of silicon from the nanocolumn and the protrusions that mushroomed around it.

The chemical composition of the nanocolumns grown in He was measured using the electron beam of a SEM at normal incidence, focused at the center of the nanocolumn in a spot of 150-nm-diameter. Only the chemical composition of the nanocolumn was measured, because the probe region extends to ~ 1.5 μm in depth, which is significantly less than the column height. It was found that the nanocolumns were made of silicon with less than 2 at. % of oxygen, while the amount of oxygen measured in the substrate was less than 1%. The error



FIGURE 8 Nanocolumns growing on microcone tips. Fluence: 0.5 J/cm^2, 2000 pulses, He pressure: 10 Torr

SIONYX1403000041.0085

SAMSUNG EX. 1002 - 507/4148

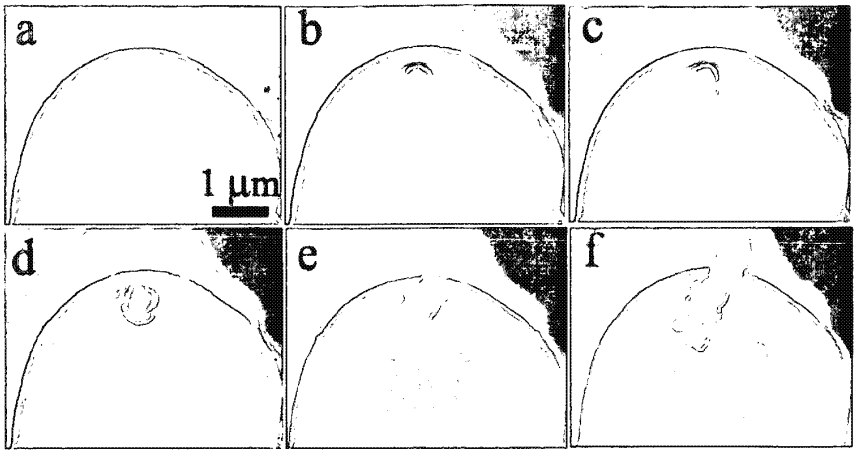


FIGURE 9 Nanocolumn evolution upon laser irradiation at 0.5 J/cm^2 in 10 Torr He. **a** initial cone tip; **b** 1000 pulses; **c** 2500 pulses; **d** 5000 pulses; **e** 8000 pulses; **f** 10000 pulses

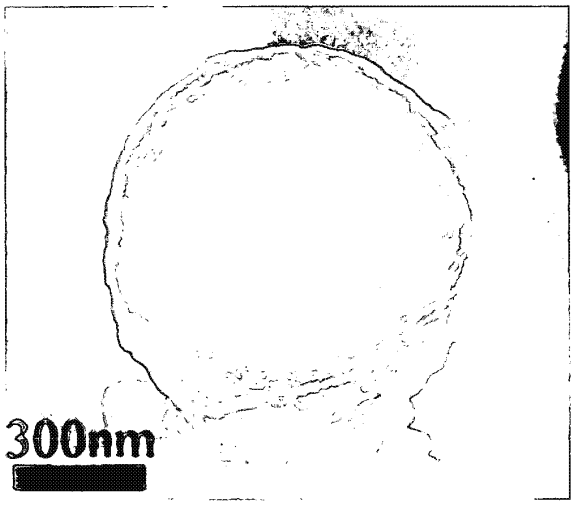


FIGURE 10 Tip of same nanocolumn as shown in Fig. 8, after 15000 pulses

in the electron dispersion X-ray spectroscopy measurements was on the order of 1%.

The laser fluence at the bottom of the microcones is enhanced by multiple reflections promoting ablation, and due to the background pressure, ablated material is partly backscattered and can be trapped at the melted nanocolumn tip. It has been calculated that the intensity at the bottom of the microcones, tens of micrometers below the surface, is increased over 4-fold [8]. The process of deposition is clearly visible after 15000 pulses because a film covers a large portion of the substrate. Also, after 15000 pulses the top of the nanocolumns become significantly enlarged and the deposition process is further revealed by the multiple small protrusions that cover the tip (Fig. 10). The low ablation rate is reflected in the extremely low growth rate of nanocolumns, 0.2 nm per pulse.

Irradiation in vacuum, for which the trapping of ablated material is more difficult because there is no buffer gas atmosphere, shows that after 2500 pulses small protrusions similar to those shown in Fig. 9c are formed at the top of the microcones. However, in vacuum these protrusions do not grow additionally and after 10000 pulses they tend to flatten.

These experimental observations suggest that the initial protrusion at the top of the microcones (Fig. 9b and c) is most likely a result of the solidification process of the laser-melted pool. When the nano-protrusions reach a certain size, deposition of silicon strongly increases their length by continuing irradiation under helium, keeping the diameter approximately constant (Fig. 9e and f). This last process appears to be similar to that described for microcolumn growth [4].

ACKNOWLEDGEMENTS This research was sponsored by the National Science Foundation Grant No. DMR-9901238.

REFERENCES

1 F. Sanchez, J.L. Morenza, R. Aguiar, J.C. Delgado, M. Varela: Appl. Phys. Lett. **69**, 620 (1996); F. Sanchez, J.L. Morenza, R. Aguiar, J.C. Delgado, M. Varela: Appl. Phys. A **66**, 83 (1998); F. Sanchez, J.L. Morenza, V. Trtik: Appl. Phys. Lett. **75**, 3302 (1999)
2 T.-H. Her, R.J. Finlay, C. Wu, S. Deliwala, E. Mazur: Appl. Phys. Lett. **73**, 1673 (1998); T.-H. Her, R.J. Finlay, C. Wu, E. Mazur: Appl. Phys. A **70**, 383 (2000)
3 V.V. Voronov, S.I. Dolgaev, S.V. Lavrishchev, A.A. Lyalin, A.V. Simakin, G.A. Shafeev: Phys. Vib. **7**, 131 (1999); S.I. Dolgaev, S.V. Lavrishchev, A.A. Lyalin, A.V. Simakin V.V. Voronov, G.A. Shafeev: Appl. Phys. A **73**, 177 (2001)
4 A.J. Pedraza, J. Fowlkes, D.H. Lowndes: Appl. Phys. Lett. **74**, 2322 (1999)
5 J. Pedraza, J.D. Fowlkes, D.H. Lowndes: Appl. Phys. Lett. **77**, 3018 (2000)
6 J.D. Fowlkes, A.J. Pedraza, D.H. Lowndes: Appl. Phys. Lett. **77**, 1629 (2000)
7 J. Pedraza, S. Jesse, Y. Guan, J.D. Fowlkes: J. Mater. Res. **16**, 3599 (2001)
8 S. Jesse, A.J. Pedraza, J.D. Fowlkes, J.D. Budai: J. Mater. Res. **17**, 1002 (2002)
9 P.A. Temple, M.J. Soileau: IEEE J. Quantum Electron. **QE-17**, 2067 (1981)
10 P.M. Fauchet, E. Siegman: Appl. Phys. Lett. **40**, 824 (1982)
11 Z. Guosheng, P.M. Fauchet, E. Siegman: Phys. Rev. **B 26**, 5366 (1982)
12 J.F. Young, J.S. Preston, H.M. van Driel, J.E. Sipe: Phys. Rev. B **27**, 1155 (1982)
13 S.R.J. Brueck, D.J. Ehrlich: Phys. Rev. Lett. **48**, 1678 (1982)
14 S.A. Akhmanov, V.I. Emel'yanov, N.I. Koroteev, V.N. Seminogov: Sov. Phys. Usp. **28**, 1084 (1986)

SIONYX1403000041.0086

SAMSUNG EX. 1002 - 508/4148

15 D. Bäuerle: *Laser Processing and Chemistry*, 3rd edn. (Springer-Verlag, Berlin 2000) p. 571
16 F. Keilmann, Y.H. Bai: Appl. Phys. A **29**, 9 (1982)
17 J.F. Figueira, S.J. Thomas: Appl. Phys. B **28**, 267 (1982)
18 F. Keilmann: Phys. Rev. Lett. **51**, 2097 (1983)
19 J.F. Young, J.E. Sipe, H.M. van Driel: Phys. Rev. B **30**, 2001 (1984)
20 M. Bolle, S. Lazare: J. Appl. Phys. **73**, 3516 (1993)
21 P.E. Dyer, R.J. Farley, R. Giedl, D.M. Karnakis: Appl. Surf. Sci. **96–98**, 537 (1996)
22 M. Csete, Z. Bor: Appl. Surf. Sci. **133**, 5 (1998)
23 J.E. Sipe, J.F. Young, J.S. Preston, H.M. van Driel: Phys. Rev. B **27**, 1141 (1982)
24 J.D. Fowlkes, A.J. Pedraza, D.A. Blom, H.M. Meyer III: Appl. Phys. Lett. **80**, 3799 (2002); Virtual J. Nanoscale Sci. Technol. May 27, (2002)

SIONYX1403000041.0087

SAMSUNG EX. 1002 - 509/4148

C15

Appl. Phys. A 77, 277–284 (2003)
DOI: 10.1007/s00339-003-2113-9

Applied Physics A
Materials Science & Processing

Surface nanostructuring of silicon

A.J. PEDRAZA✉
J.D. FOWLKES
Y.-F. GUAN

Department of Materials Science and Engineering, The University of Tennessee, Knoxville, TN 37996-2200, USA

Received: 16 December 2002/Accepted: 20 January 2003
Published online: 28 May 2003 • © Springer-Verlag 2003

ABSTRACT Irradiation with polarized laser light of 248-nm wavelength induces the formation of periodic undulations ~ 10-nm-high on flat silicon substrates. The wavelength of these periodic structures is a function of the light wavelength and the angle of incidence of the laser beam. Linear arrays of silicon nanoparticles with fairly uniform size that extended up to a millimeter were formed if the irradiation was performed using polarized light. When non-polarized laser light with the same fluence was used to illuminate an initially flat surface, non-aligned nanoparticle strings were obtained. However, if part of the irradiated area was microstructured, nanoparticle linear arrays resulted in the vicinity of the microstructured region. An analysis on the evolution of these nanostructures is presented. Nanocolumns could be grown on top of every cone of a microstructured surface upon cumulative laser irradiation with non-polarized light, reaching a height of ~ 3 μm and a diameter of 100–200 nm. The mechanisms of nanocolumn origin and growth are analyzed.

PACS 61.46. +w; 61.80.Ba; 61.82.Fk; 68.35.Bs

1 Introduction

Laser-induced surface microstructuring of silicon has been extensively studied [1–8], and has been found to be a function of fluence and of the composition and pressure of the background atmosphere present in the irradiation chamber [5, 6]. At a fluence between 2 and 3 J/cm^2 two distinct processes can take place sequentially as a result of cumulative laser irradiation. Shallow depressions evolve and can reach a depth of a few micrometers and a separation distance of 20 to 30 μm [7]. These depressions are initially sparsely distributed on the surface, but new ones form and progressively cover the entire irradiated area. At the same time, the depressions continuously deepen with the number of laser pulses. For irradiation in non-reactive environments such as vacuum or Ar, this surface relief continuously builds up with the number of laser pulses, up to 10 000 pulses [8].

In a reactive atmosphere like SF_6, the same evolution is initially observed in the same fluence range, but more dramatic changes occur after 600 pulses. Additional irradiation in SF_6 produces a drastic change both in the surface-roughening rate and in the morphology, establishing the signature of a second, different process. The change to this second process, which produces a characteristic microhole–microcone microstructure, is preceded by a transition stage in the morphology. Figure 1 shows the three stages of microstructure evolution just outlined. After ~ 400 laser pulses, the surface relief depends only on the crystallographic orientation of the laser-exposed surface. The optical image acquired with Nomarski contrast shown in Fig. 1a illustrates the first stage in the process of a surface relief production. Shallow depressions and elevations that have the appearance of a cube structure can be seen. The orientation of the surface is very close to (111) and the characteristic three-fold symmetry is clearly revealed by the surface traces. The same relief is produced under reactive and non-reactive atmospheres. The second stage, shown in Fig. 1b, has been observed only under a reactive (SF_6) irradiation atmosphere and after a higher number of pulses. Intense etching takes place at the bottom of the depressions formed during stage 1. Multiple reflections focus the beam at these depressions, enhancing the decomposition of SF_6 and thus the etching activity [8]. The third stage (Fig. 1c) is characterized by a synergistic process involving hole deepening by etching- assisted ablation and cone growth by re-deposition of ablated species on top and to the sides of the laser-melted regions. Since ablation also takes place in these regions, growth can occur only when re-deposition occurs in excess of ablation.

A reduction of the laser energy to $\leq$ 1 J/cm^2 drastically changes the scale of the surface relief, promoting the formation of nanostructures. Three different phenomena will be described and analyzed: (1) the production of periodic nanochannels; (2) the formation of an organized array of nanoparticles; and (3) the growth of nanocolumns. The processing characteristics could be of interest for some technologies, since long-range ordering of nanostructures is a key issue, central to the utilization of nanostructures in electronic materials applications.

2 Experimental procedure

Boron-doped silicon substrates were irradiated using a Lambda Physik LPX–305i KrF excimer laser (248-nm wavelength), with a pulse duration of 25 ns. Unless otherwise

✉ Fax: +1-865/974-4115, E-mail: apedraza@utk.edu

SIONYX1403000041.0088

SAMSUNG EX. 1002 - 510/4148

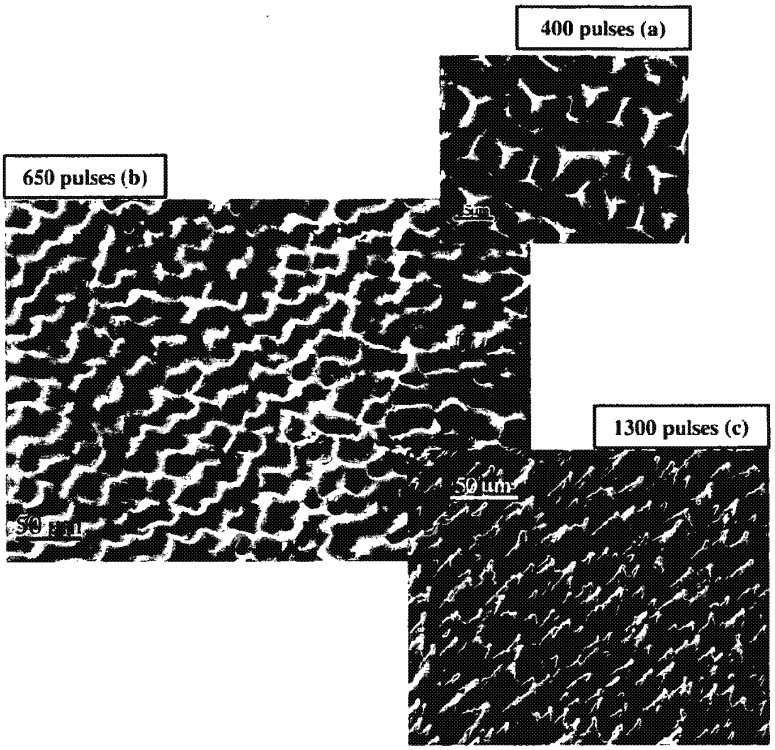


FIGURE 1 The three stages of cone formation in silicon under an SF_6 atmosphere. **a** Optical micrograph with Nomarski contrast; **b** and **c** SEM images with sample tilted 40°

indicated, all laser treatments were carried out at normal incidence. The beam emerging from the laser cavity was directed to an optic bench using a MgF_2-coated fused-silica mirror. The optic bench contained an aperture, a fused-silica lens array, and the irradiation chamber. The rectangular aperture partly removed the low energy tails of the trapezoidal laser beam. The laser fluence was varied by adjusting the position of the fused-silica lens array relative to the sample holder in the irradiation chamber.

All of the experiments were conducted using helium as background gas. For each laser irradiation cycle, the irradiation chamber was pumped to a base pressure of 1×10^{-7} Torr He prior to introducing 99.999% pure helium gas at a selected pressure. For some experiments, the substrates were first laser-microstructured in an SF_6 atmosphere, to produce a cone relief.

Native oxide layer removal was done by immersing the specimens in a 10 : 1 HF aqueous solution for 5 min, washing, drying and quickly transferring them to a vacuum chamber. Table 1 summarizes the experimental conditions used for the examples shown in the figures.

Ex situ characterization studies were conducted using scanning electron microscopy (SEM), atomic force microscopy (AFM), and Auger emission spectroscopy (AES).

Figure number	Laser fluence (J/cm^2) and polarization (p,np)[a]	Number of pulses	Composition and pressure (Torr) of irradiation atmosphere	Initial surface topography	Final surface structure
2	0.8 p	400	Vacuum 1×10^{-6}	Smooth[b]	Nanochannels
3	0.6 np	450	He 100	Smooth[c]	Nanoparticles
4a	0.6 np	500	He 100	Smooth[c]	Nanoparticles
4b	0.6 np	700	He 100	Smooth[c]	Nanoparticles
5	1 np	200	He 100	Smooth[c]+ Cones	Nanoparticle clusters and ordered nanoparticle array
6	1 np	200	He 0.5	Smooth[c]+ Cones	Ordered nanoparticle array
7	0.5 np	2000	He 10	Microcones	Nanocolumn (Start)
8	0.5 np	0–10000	He 10	Microcones	Nanocolumn on top of cone
9	0.5 np	15000	He 10	Microcones	Nanocolumn on top of cone

[a] p: polarized; np: non-polarized
[b] native oxide present in surface
[c] native oxide removed

TABLE 1 Summary of experimental conditions related to figures

SIONYX1403000041.0089

SAMSUNG EX. 1002 - 511/4148

3 Formation of nanochannels by laser irradiation

The formation of nanochannels was observed only when using polarized light to irradiate silicon specimens and when the surface had its native oxide. In order to examine the effect of the presence of this oxide layer, two types of experiment were first performed, using the same conditions: 2000 pulses of polarized laser light at an angle of incidence of 14°, a fluence of 0.7 J/cm^2 and a vacuum pressure of 5×10^{-6} Torr. In one of the experiment types, the native oxide was removed from the surface of the silicon targets prior to the irradiation, while for the other type, specimens with the native oxide were irradiated without any surface conditioning. These experiments consistently showed that the oxide layer stabilizes the ripples. All the experiments described in this section were performed on silicon with the native oxide film using polarized light.

Formation of 6–10-nm-deep nanochannels was induced by laser irradiation of an initially flat silicon substrate, in a background pressure of 1×10^{-6} Torr, at a laser fluence of 0.8 J/cm^2. These channels were produced using linearly p-polarized light (for which the electric field lies in the plane of incidence) and were aligned normal to the polarization direction. At normal laser beam incidence, the spacing between channels, Λ, equaled the laser wavelength, λ. The channels were not featureless, as can be seen in Fig. 2. The overall structure could be described as two periodic structures or waves of the same wavelength displaced from each other by half a wavelength. The amplitude of one of the waves was ~6 nm – significantly larger than the amplitude of the other wave.

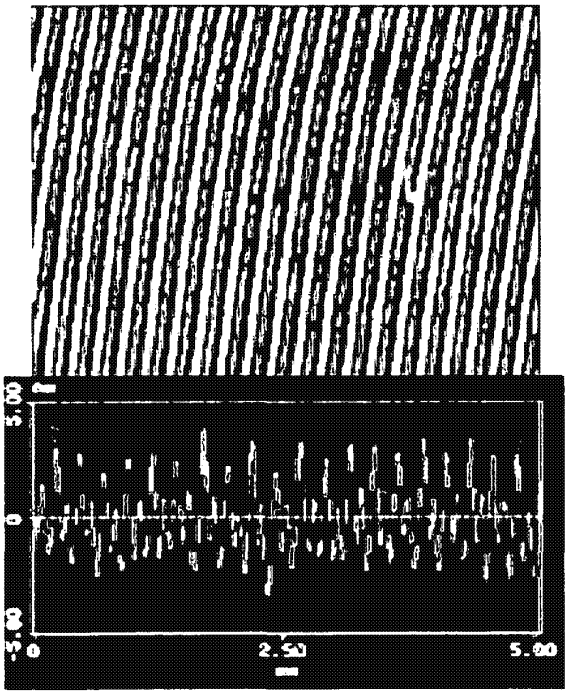


FIGURE 2 AFM image of LIPSS formed in silicon under vacuum. Linearly polarized laser light at normal incidence. Laser wavelength: 248 nm; fluence: 0.8 J/cm^2; 400 pulses. Note: y-scale in nm; x-scale in μm

Several experiments were done with an angle of incidence of the beam $\theta > 0$. In this case, two line-spacings were found in the same specimen in some instances. For example, for a sample irradiated with 2000 pulses at a fluence of 1 J/cm^2 in a 10 Torr background pressure of He and for $\theta = 15°$, the two spacings given in the first column of Table 2 were measured.

The spontaneous formation of periodic ripples on the surface of a material illuminated with polarized pulsed laser light has been reported in many different materials [9–23] at fluences close to the melting threshold, spanning a wavelength range of 10.6 to 0.193 μm. The period and orientation of these surface ripples, known in the literature as laser-induced periodic surface structures (LIPSS), mainly depend on the following aspects of the laser beam: angle of incidence, polarization, frequency, and energy. However, the occurrence of LIPSS in a given material appears to be a strong function of the specific response of this material to inhomogeneous energy deposition. For instance, for a given set of the main laser parameters just listed, some fringe patterns observed in Ge have not been detected in Si or Al [12]. Excluding the studies in polymers, all of the previous reports refer to LIPSS spacings on the order of microns. This is the first time that nano-LIPSS have been demonstrated in silicon.

The most often encountered periodic structures are those whose wave vector is parallel to the projection of the electric field on the surface plane [12]. These ripples or fringes were found mostly when the electromagnetic field was linearly polarized, whether the electric field lay in the plane of incidence (p-polarized) or perpendicular to it (s-polarized). LIPSS could be very simply interpreted as being produced by the interference between the refracted radiation and two scattered waves parallel to the surface propagating in opposite directions, giving the following dependence of fringe spacings, Λ_+ and Λ_-, on the angle of incidence θ and the laser wavelength λ:

$$\Lambda_{\pm} = \frac{\lambda}{1 \pm \sin\theta} . \tag{1}$$

As can be seen from Table 2, the line-spacings calculated using (1) for the case of $\theta = 15°$ and $\lambda = 248$ nm are in good agreement with the two values reported above of 204 nm and 331 nm. In addition, in some cases a spacing following a different law,

$$\Lambda = \frac{\lambda}{\cos\theta} , \tag{2}$$

was found for fringes running parallel to the polarization vector of incident p-polarized light, in contrast with those whose spacing was described by the sine law, which run perpendicular to it [14, 15].

$\Lambda_{\text{measured}}$ (nm)	$\Lambda = \frac{\lambda}{1+\sin\theta}$	$\Lambda = \frac{\lambda}{1-\sin\theta}$
204	197	–
335	–	331

TABLE 2 Measured and calculated line-spacing of LIPSS

SIONYX1403000041.0090

SAMSUNG EX. 1002 - 512/4148

Several groups have developed theories to explain the production of LIPSS [11, 13, 14, 23]. The key factor to explain LIPSS evolution in all of the models is the occurrence of an inhomogeneous light intensity distribution on the surface. The inhomogeneity in the light distribution arises from the interaction between the light scattered by surface roughness and the refracted laser light. There are several ways whereby the material can respond to the temperature modulation due to this energy inhomogeneity [13, 14]. It has also been recognized that a positive feedback is necessary for the ripples to be produced. Concurrent with this concept, we have observed in our studies that nanoripple formation always requires multiple laser pulses, also indicating that the interaction between roughness and light evolves with an increasing number of pulses. The difficulty in stabilizing this nanostructure is highlighted by two factors, possibly interrelated: the large number of pulses needed to form them, as just emphasized, and the apparent requirement that there must be a native oxide layer present.

4 Self-organized linear arrays of laser-induced silicon nanoparticles

All the experiments in this section, with one exception, were performed using non-polarized light. The native oxide was removed in all the specimens, flat and microstructured, prior to laser irradiation to minimize oxide contamination of the nanoparticles. At laser fluences close to 1 J/cm^2 and using a background atmosphere of ultra high purity (UHP) He rather than vacuum, a film was deposited on the surface of a silicon substrate [24]. The background gas backscattered atoms and probably very small clusters were also deposited on the substrate. The film detected by AFM using a tapping mode scan, after 200 pulses at 1 J/cm^2 and 10 Torr of He background pressure, was very porous with some areas a few nanometers thick and other areas with a much thinner film or no film at all. The average film thickness observed over all the measured specimens was of the order of 1 nm. However the film thickness did not increase very significantly after the first 50 pulses, giving an average deposition rate of $\sim 2 \times 10^{-2}$ nm/pulse. From this deposition rate, it is difficult to evaluate the average ablation rate during irradiation because in some regions of the specimen ablation was taking place, while in others there was material accumulation.

It is clear from the extensive work done on ripple formation that a non-uniform deposition of energy is produced during laser irradiation of a surface with micro- or nano-roughness. In our case, AFM images recorded very significant nano-roughness in all specimens, with some regions as high as 8 nm. Light scattering from this random nano-roughness will produce a random interference pattern with the refracted light that will generate a non-uniform energy deposition. For this reason, it is difficult to establish a meaningful correlation between the ablation rate and laser fluence. The fact that a film was formed at the same time as ablation was taking place indicates that the laser fluence used in these experiments was very close to the ablation threshold. The film did not seem to increase significantly with the number of pulses, probably due to continuous ablation and clustering. Auger emission spectroscopy revealed that beyond the first nanometer the film was at least 90% silicon, with no silicon bound to an oxide or carbide.

SEM and AFM images indicate that the film clusters and forms nanoparticles as it is being irradiated with non-polarized laser light [24]. We have observed film-denuded zones, 1 to 2 μm in diameter, containing nanoparticles that had apparently consumed the film originally in the zone. The distance between nanoparticles in these small regions was close to the wavelength of the incident light, indicating a process controlled by a non-homogeneous distribution of energy similar to what happens during ripple formation.

As nanoparticle formation proceeded with additional irradiation, the particles tended to aggregate into curvilinear strings and became stabilized at $\sim$ 30 nm-diameter, as measured in SEM images (Fig. 3). This behavior resulted in a fairly uniform size distribution. The evolution of this nanostructure with additional irradiation was followed using a high-precision SEM stage positioning mechanism. The nanoparticles kept their identity and shape; however, they experienced displacements, as illustrated in Fig. 4. They tended to align in short curvilinear strings like pearls in a necklace, and some ordering can be appreciated in the micrographs. At a certain point the strings became locked and further movement or ordering did not occur. At higher laser fluence, e.g., 1.3 J/cm^2, they flattened and tended to fuse with the substrate.

A very dramatic change in the nanoparticle spatial distribution occurred when the irradiation was done on a surface partly covered with a well-developed cone microstructure. The microcones were grown by laser irradiation in a 0.5 bar SF_6 atmosphere, using 1200–2000 pulses at a laser energy of $\sim$3 J/cm^2; they had a height of 20–30 μm and tips of a few micrometers in diameter [6–8]. A typical microstructure is shown in Fig. 1c.

The irradiation in He resulted in film deposition and the formation of linear arrays in the regions of the irradiated sub-

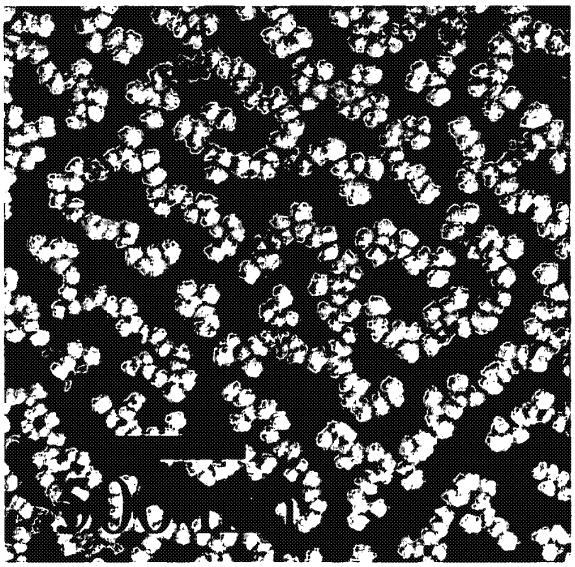


FIGURE 3 Nanoparticles formed under 100 Torr He, after 450 pulses at 0.6 J/cm^2

SIONYX1403000041.0091

SAMSUNG EX. 1002 - 513/4148

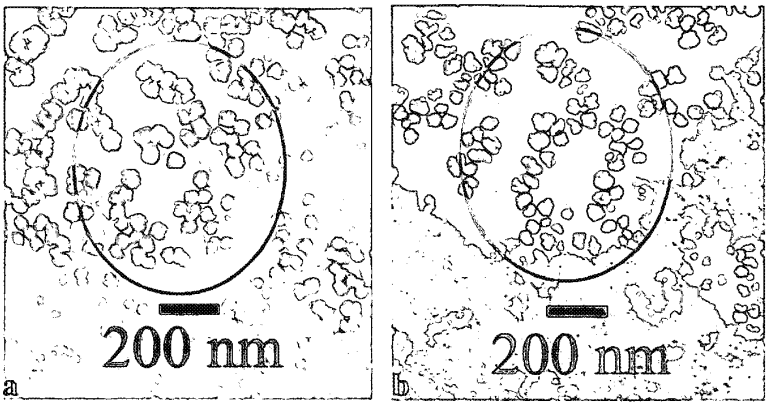


FIGURE 4 Motion of nanoparticles followed inside *encircled region*. **a** 500 pulses; **b** 700 pulses. Fluence: 0.6 J/cm^2; He pressure: 100 Torr

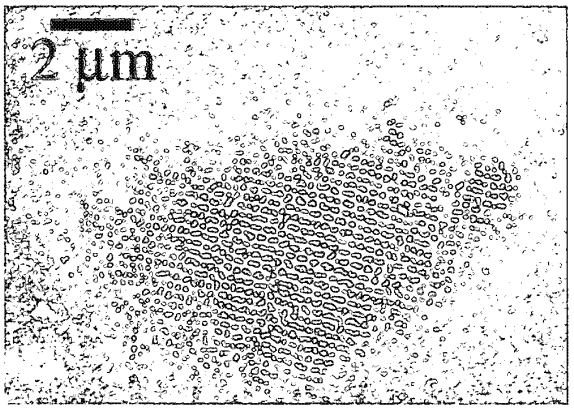


FIGURE 5 SEM image showing film clustering, and nanoparticle formation and ordering. Specimen irradiated with 200 pulses at 1 J/cm^2 under 100 Torr He

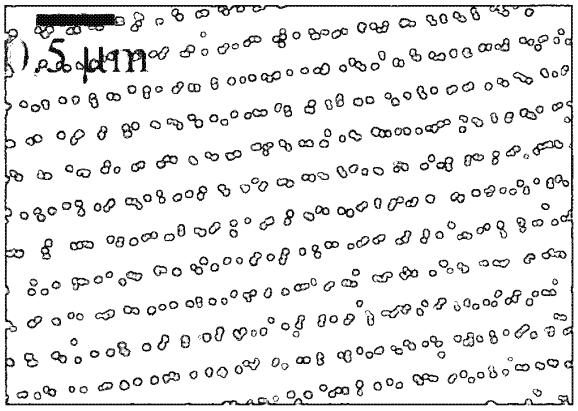


FIGURE 6 Laser-induced nanoparticle linear array in the vicinity of a microstructured region of the surface. Fluence: 1 J/cm^2; 0.5 Torr He; 200 pulses

strate surface adjacent to the microstructured zone. Figure 5 illustrates the evolution of the film, demonstrating that the nanoparticles grew in the substrate, consuming the film, and became aligned as they were being irradiated.

The nanoparticle ordered array shown in Fig. 6, has a line-spacing close to 248 nm and extends over microscopic regions with few perturbations in the alignment. This array developed in the immediate vicinity of the cone microstructure region. Characterization of the nanocrystals by using Auger electron spectroscopy demonstrated that the nanoparticle consisted of silicon cores covered with a very thin sheath of oxide.

Certain aspects of the nanoparticle alignment phenomenon suggest that it could be associated with the LIPSS phenomenon. Similar to the conditions reported for LIPSS development, the alignment was initially observed just above the melting threshold, and occurred in a narrow laser fluence range above this threshold. In almost every case, although not in all of them, for normal incidence, the particles aligned along the rectangular beam short axis, which corresponded to the direction where the E field was at a maximum. In a second set of experiments, in which a fine wire (100 μm) crossing the beam was imaged on a flat Si substrate surface, a linear alignment of nanoclusters occurred within the interference fringe pattern resulting from the diffraction of light by the wire. An AFM image taken from the same specimen shown in Fig. 6 reveals that nanoparticles were located on the valleys of LIPSS (Fig. 7). Lack of contrast prevented observation of the smooth undulations of LIPSS by SEM.

At variance with the LIPSS experiments described in the preceding section, the alignment of nanoparticles did not require polarized light; the presence of an extended defective region was sufficient. Next, we used p-polarized light, and aligned nanoparticles were produced on a flat surface, without the need for an initial microcone structure. Nanoparticle arrays aligned normal to the direction of the electric field. An experiment that illustrates well the process of nanoparticle production and alignment with size selection was done by irradiating the silicon surface with polarized light at an average energy density higher than 1 J/cm^2. The irradiated area was rectangular and we utilized a beam size of approximately 7 mm x 3 mm. All over the edges, where the beam energy tapered off and within a width of ~ 0.4 mm, an aligned array of ~ 30-nm-diameter nanoparticles was generated. A microstructure consisting of long surface waves was produced in the central portion of the irradiated region where the energy was too high for particle formation. The production of this microstructure indicates that very significant ablation could have taken place in the central region of the spot. AFM scans reveal an abrupt change in the spatial and size distribution of nanoparticles at the sides of the edges of the laser shot, into

SIONYX1403000041.0092

SAMSUNG EX. 1002 - 514/4148

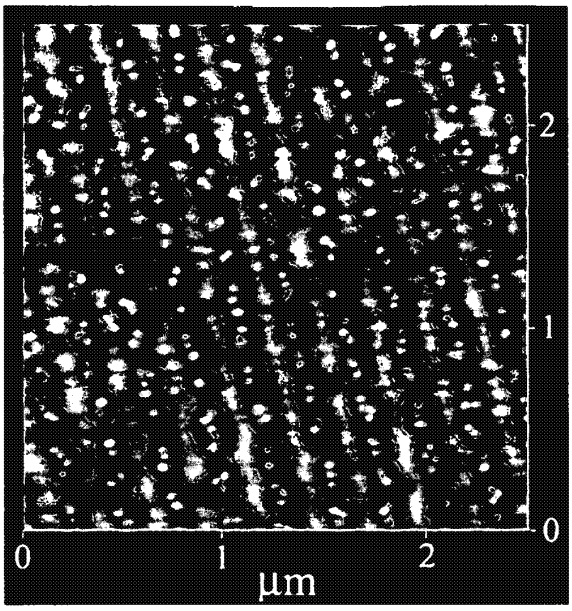


FIGURE 7 AFM image of the same surface as in Fig. 6

the unirradiated region. Instead of the highly organized array of small, fairly uniformly sized nanoparticles detected inside the irradiated edge, a completely random distribution of much larger nanoparticles with a wide size distribution was found to cover the adjacent unirradiated area.

Using p-polarized light, the angle of incidence of the laser beam was changed and it was found that the nanoparticle line spacing followed (1) with the minus sign in the denominator, i.e., the line-spacing increased as the angle of incidence was increased. This result strongly suggests that similar mechanisms are responsible for the formation of nanochannels and for nanoparticle alignment.

The results just described, whereby spontaneous alignment of silicon nanoparticles form regular arrays as a result of pulsed-laser irradiation of a silicon substrate, opens the possibility of using UV lasers as manipulators of nanoparticles on a large scale, on the order of millimeters.

5 Silicon nanostructuring atop a laser-produced microcone template

The formation of microcones has been explained by a mechanism similar to that used to explain the formation of whiskers in silicon [6–8]. The cone microstructure appears first to present a natural limit – as far as a minimum dimension is concerned – for laser-induced structuring of a surface with self-organized tips. This limitation arises from the formation and growth mechanisms of the cone and the fact that it starts at a surface that is melted throughout. Once a cone is formed, and its subsequent growth is accomplished by preferential re-deposition of material at its laser-melted tip, continuing irradiation under the same conditions will produce a rise in the cone first and result in its fall at later stages. However, we have found that a change in processing conditions could benefit from a well developed microcone structure, using it as a template for a finer structure.

A silicon target, microstructured as shown in Fig. 1c, was irradiated at 0.5 J/cm^2 in a He atmosphere at 10 Torr. It was first noticed that 2000 pulses produced the emergence at the microcone tips of small protrusions ~ 100 nm in diameter and a few nanometers in height (Fig. 8). The sequence of images presented in Fig. 9 shows the growth of one nanocolumn as a function of the number of laser pulses. Figure 9a shows the cone tip of the initial microstructured surface for which the nanocolumn evolution has been followed. We always observed a small tip at the top of the microcones, and as we continued the irradiation at low energy, the protrusion grew and a flat depression was formed around it (Fig. 9b and c). A careful examination of the images shows that the low-energy irradiation only produced melting at the very top of the cone tip. The fluence used in these experiments (referred to a flat surface) was very close to the melting threshold and it decreased from the center of the cone tip towards the sides due to the tip curvature. Thus, these irradiation conditions explain the highly localized melting. As the irradiation was continued, the depression around the protrusion disappeared (Figs. 9d–f), and the protrusion developed into a nanocolumn, while a multitude of very small protrusions appeared at its base (Fig. 9e). Finally, after 10000 pulses the nanocolumn had a height of 3.1 μm and a diameter of 200 nm, giving an aspect ratio of 15. Due to the nanosecond pulse duration, silicon transport to the top could only have taken place in the liquid or gas phase. The liquid could only be removed from the immediate vicinity where melting took place. The small and flat depression around the nanocolumn cannot account for the extra mass of silicon from the nanocolumn and the protrusions that mushroomed around it.

The chemical composition of the nanocolumns grown in He was measured using the electron beam of a SEM at normal incidence, focused at the center of the nanocolumn in a spot of 150-nm-diameter. Only the chemical composition of the nanocolumn was measured, because the probe region extends to ~ 1.5 μm in depth, which is significantly less than the column height. It was found that the nanocolumns were made of silicon with less than 2 at. % of oxygen, while the amount of oxygen measured in the substrate was less than 1%. The error



FIGURE 8 Nanocolumns growing on microcone tips. Fluence: 0.5 J/cm^2, 2000 pulses, He pressure: 10 Torr

SIONYX1403000041.0093

SAMSUNG EX. 1002 - 515/4148

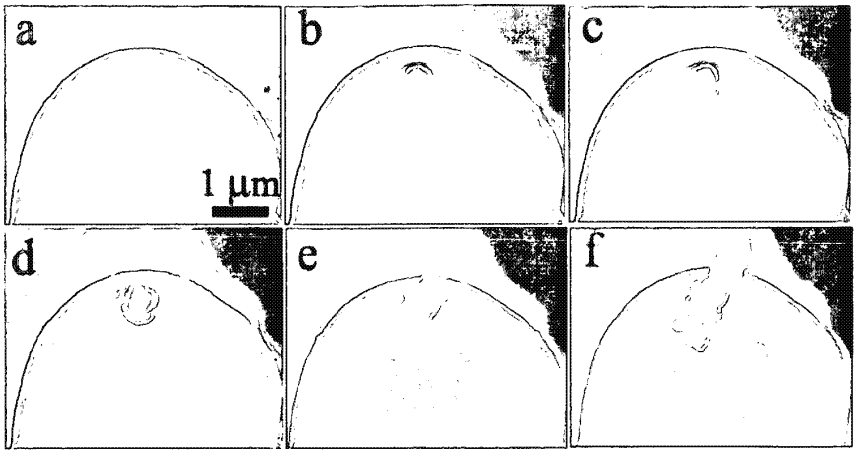


FIGURE 9 Nanocolumn evolution upon laser irradiation at 0.5 J/cm^2 in 10 Torr He. **a** initial cone tip; **b** 1000 pulses; **c** 2500 pulses; **d** 5000 pulses; **e** 8000 pulses; **f** 10 000 pulses

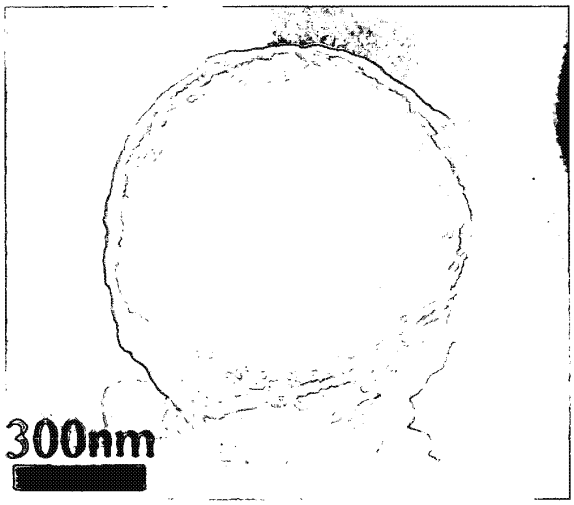


FIGURE 10 Tip of same nanocolumn as shown in Fig. 8, after 15 000 pulses

in the electron dispersion X-ray spectroscopy measurements was on the order of 1%.

The laser fluence at the bottom of the microcones is enhanced by multiple reflections promoting ablation, and due to the background pressure, ablated material is partly backscattered and can be trapped at the melted nanocolumn tip. It has been calculated that the intensity at the bottom of the microcones, tens of micrometers below the surface, is increased over 4-fold [8]. The process of deposition is clearly visible after 15 000 pulses because a film covers a large portion of the substrate. Also, after 15 000 pulses the top of the nanocolumns become significantly enlarged and the deposition process is further revealed by the multiple small protrusions that cover the tip (Fig. 10). The low ablation rate is reflected in the extremely low growth rate of nanocolumns, 0.2 nm per pulse.

Irradiation in vacuum, for which the trapping of ablated material is more difficult because there is no buffer gas atmosphere, shows that after 2500 pulses small protrusions similar to those shown in Fig. 9c are formed at the top of the microcones. However, in vacuum these protrusions do not grow additionally and after 10 000 pulses they tend to flatten.

These experimental observations suggest that the initial protrusion at the top of the microcones (Fig. 9b and c) is most likely a result of the solidification process of the laser-melted pool. When the nano-protrusions reach a certain size, deposition of silicon strongly increases their length by continuing irradiation under helium, keeping the diameter approximately constant (Fig. 9e and f). This last process appears to be similar to that described for microcolumn growth [4].

ACKNOWLEDGEMENTS This research was sponsored by the National Science Foundation Grant No. DMR-9901238.

REFERENCES

1 F. Sanchez, J.L. Morenza, R. Aguiar, J.C. Delgado, M. Varela: Appl. Phys. Lett. **69**, 620 (1996); F. Sanchez, J.L. Morenza, R. Aguiar, J.C. Delgado, M. Varela: Appl. Phys. A **66**, 83 (1998); F. Sanchez, J.L. Morenza, V. Trtik: Appl. Phys. Lett. **75**, 3302 (1999)
2 T.-H. Her, R.J. Finlay, C. Wu, S. Deliwala, E. Mazur: Appl. Phys. Lett. **73**, 1673 (1998); T.-H. Her, R.J. Finlay, C. Wu, E. Mazur: Appl. Phys. A **70**, 383 (2000)
3 V.V. Voronov, S.I. Dolgaev, S.V. Lavrishchev, A.A. Lyalin, A.V. Simakin, G.A. Shafeev: Phys. Vib. **7**, 131 (1999); S.I. Dolgaev, S.V. Lavrishchev, A.A. Lyalin, A.V. Simakin V.V. Voronov, G.A. Shafeev: Appl. Phys. A **73**, 177 (2001)
4 A.J. Pedraza, J. Fowlkes, D.H. Lowndes: Appl. Phys. Lett. **74**, 2322 (1999)
5 J. Pedraza, J.D. Fowlkes, D.H. Lowndes: Appl. Phys. Lett. **77**, 3018 (2000)
6 J.D. Fowlkes, A.J. Pedraza, D.H. Lowndes: Appl. Phys. Lett. **77**, 1629 (2000)
7 J. Pedraza, S. Jesse, Y. Guan, J.D. Fowlkes: J. Mater. Res. **16**, 3599 (2001)
8 S. Jesse, A.J. Pedraza, J.D. Fowlkes, J.D. Budai: J. Mater. Res. **17**, 1002 (2002)
9 P.A. Temple, M.J. Soileau: IEEE J. Quantum Electron. **QE-17**, 2067 (1981)
10 P.M. Fauchet, E. Siegman: Appl. Phys. Lett. **40**, 824 (1982)
11 Z. Guosheng, P.M. Fauchet, E. Siegman: Phys. Rev. **B 26**, 5366 (1982)
12 J.F. Young, J.S. Preston, H.M. van Driel, J.E. Sipe: Phys. Rev. B **27**, 1155 (1982)
13 S.R.J. Brueck, D.J. Ehrlich: Phys. Rev. Lett. **48**, 1678 (1982)
14 S.A. Akhmanov, V.I. Emel'yanov, N.I. Koroteev, V.N. Seminogov: Sov. Phys. Usp. **28**, 1084 (1986)

SIONYX1403000041.0094

SAMSUNG EX. 1002 - 516/4148

15 D. Bäuerle: *Laser Processing and Chemistry*, 3rd edn. (Springer-Verlag, Berlin 2000) p. 571
16 F. Keilmann, Y.H. Bai: Appl. Phys. A **29**, 9 (1982)
17 J.F. Figueira, S.J. Thomas: Appl. Phys. B **28**, 267 (1982)
18 F. Keilmann: Phys. Rev. Lett. **51**, 2097 (1983)
19 J.F. Young, J.E. Sipe, H.M. van Driel: Phys. Rev. B **30**, 2001 (1984)
20 M. Bolle, S. Lazare: J. Appl. Phys. **73**, 3516 (1993)
21 P.E. Dyer, R.J. Farley, R. Giedl, D.M. Karnakis: Appl. Surf. Sci. **96–98**, 537 (1996)
22 M. Csete, Z. Bor: Appl. Surf. Sci. **133**, 5 (1998)
23 J.E. Sipe, J.F. Young, J.S. Preston, H.M. van Driel: Phys. Rev. B **27**, 1141 (1982)
24 J.D. Fowlkes, A.J. Pedraza, D.A. Blom, H.M. Meyer III: Appl. Phys. Lett. **80**, 3799 (2002); Virtual J. Nanoscale Sci. Technol. May 27, (2002)

SIONYX1403000041.0095

SAMSUNG EX. 1002 - 517/4148

Hydrogen passivation and activation of oxygen complexes in silicon

S. N. Rashkeev,[a] M. Di Ventra,[b] and S. T. Pantelides
Department of Physics and Astronomy, Vanderbilt University, Nashville, Tennessee 37235

(Received 1 December 2000; accepted for publication 19 January 2001)

We report first-principles calculations in terms of which we describe the role of hydrogen in passivating or activating oxygen complexes in Si. In particular we find that attaching H to a pre-existing oxygen cluster can change the electric activity of the cluster. Furthermore, the addition of a hydrogen atom in the core structure of thermal donors can account for the NL10 electron-paramagnetic-resonance signal. The interaction of H with the thermal-donor-like defects at the Si–SiO_2 is also discussed. © *2001 American Institute of Physics.* [DOI: 10.1063/1.1355297]

Electrically active oxygen complexes in Si (double-donor defects), known as shallow "thermal donors" (TDs), appear after annealing Si crystals at temperatures of 400–500 °C. Since their discovery a few decades ago,[1] extensive experimental[2–7] and theoretical[8–11] studies have been done, but many questions about TDs remain unsettled. For example, deep-level-transient-spectroscopy measurements show that TDs can be passivated by hydrogen incorporation only partially, i.e., a sizeable number of electrically active defects still remains in the sample after hydrogenation.[12,13] This effect is contrary to the established behavior of hydrogen in Si as a passivator of dopant impurities.[14] Also, electron-paramagnetic-resonance (EPR) measurements have provided evidence that hydrogen plays a prominent role in the formation of the Si–NL10 centers with orthorhombic symmetry.[4] These centers have been related to the TDs.[5] Hydrogen is believed to passivate one of the two electrons of the oxygen complexes and convert them into shallow single donors. Recent infrared measurements[6] also show that the spectral features that correspond to shallow single donor levels are correlated to the concentration of the Si–NL10 centers.

The earlier experimental data clearly show that hydrogen can be incorporated into the core of TDs. In this letter we present first-principles calculations that reveal several possible mechanisms of passivation of oxygen complexes in silicon. We find that hydrogen can attach to the TD complex and transform double shallow donors into single donors. Also, the attachment of a hydrogen atom can stabilize a symmetric core structure of TD, accounting for the orthorhombic NL10 EPR signal. Finally, we find that H can actually activate electrically inactive oxygen complexes, converting them into TDs, which accounts for the observed partial passivation.

The calculations were carried out in the framework of density functional theory and the local density approximation.[15] We used a plane wave basis set, ultrasoft pseudopotentials[16] and periodic supercells of 32 and 64 atoms. Oxygen pseudopotentials have a history of difficulties.[10,17] The ones used for the present study have been thoroughly tested in earlier work on a variety of Si–O–H systems.[18,19] The energy cutoff for the basis set was 24 Ry, and only one special **k** point was used for the evaluation of the self-consistent electron density.[20] Tests with larger number of **k** points indicate that formation energies are converged to better than 0.2 eV.

Theoretical calculations[10,11,17,18] have already established that for an oxygen trimer the staggered-chain configuration [Fig. 1(a)] has the lowest energy and has no states in the band gap. There exists, however, a metastable configuration, electrically active structure that has been identified as the smallest thermal donor[11,18] [Fig. 1(b)]. The symmetric configuration of Fig. 1(c) originally proposed in Ref. 9 as the core of thermal donors, is actually unstable[10] against a distortion that leads to the configuration of Fig. 1(b).[18] Addition

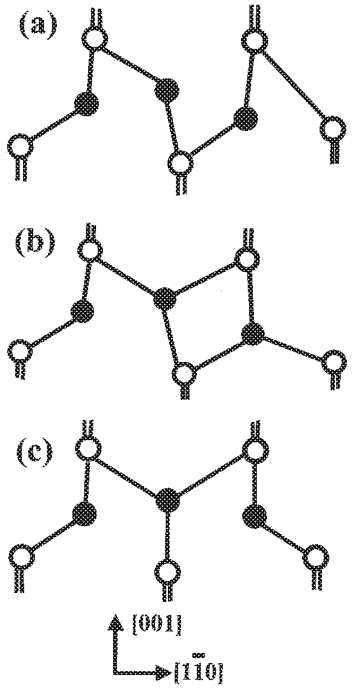


FIG. 1. The stable electrically inactive state of oxygen trimer in bulk silicon-staggered chain (a), the TD from Ref. 18(b), and the symmetric TD structure considered in Ref. 10(c). Empty circles correspond to the silicon atoms, filled to the oxygen atoms.

[a]Electronic mail: sergery.rashkeev@vanderbilt.edu
[b]Present address: Department of Physics, Virginia Polytechnic Institute and State University, Blacksburg, VA 24061-0435.

 © 2001 American Institute of Physics
Downloaded 28 May 2008 to 148.168.238.18. Redistribution subject to AIP license or copyright; see http://apl.aip.org/apl/copyright.jsp

SIONYX1403000041.0096

SAMSUNG EX. 1002 - 518/4148

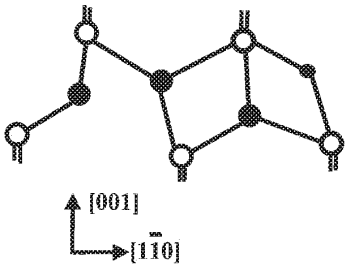


FIG. 2. H interaction with the TD structure. Hydrogen atoms are shown by small black circles.

of more O atoms in adjacent Si–Si bonds in some cases causes emission of Si interstitial and formation of SiO_2 precipitates[18] and in some cases simply makes the TDs shallower (see later).

In the present calculations, we investigated interactions of atomic H with oxygen complexes. In each of the cases, we used total energy calculations to identify low-energy stable configurations that can occur experimentally over long times (thermodynamic limit). In most of the cases we also estimated reaction pathways and barriers because some reactions can be prohibited by kinetic constraints.

Now let us consider the interaction of a single H atom with O complexes. At hydrogenation regimes corresponding to Ref. 13 ($T<200\,^{\circ}C$) oxygen cannot be kicked out by H because the barrier for O atom to move away, i.e., the migration activation energy is very high (2.5 eV).[18] In that case H can only attach to oxygen complexes.

Attaching to electrically active double shallow donor H can transform the defect into a single shallow donor. An example of such a "partially passivated" single donor structure is shown in Fig. 2 (the result is valid for all of the cases when H attaches between the two Si atoms that have bonds with the three-coordinated oxygens). These single-donor structures can contribute to the infrared optical measurements of Ref. 6. Here we considered the complexes with three oxygen atoms. Addition of extra oxygen staggered-chain links along the (1$\bar{1}$0) axis makes both the double-donor and single-donor structures shallower, in accord with observation that there is a whole range of shallow levels in a family of TDs.[21]

In some cases, H can activate electrically inactive oxygen complexes. In Si, a single H atom prefers to stay in the middle of Si–Si bond. In the presence of O one can expect a formation of combined staggered chains which involve both O and H atoms. The electric activity of such chains depends on the sequence of O and H atoms involved. For example, the O–O–H chain [Fig. 3(a)] is a single shallow donor (addition of hydrogen activates the inactive O–O complex). At the same time, the H–O–H chain [Fig. 3(b)] is completely inactive.

We also tried to identify the Si–NL10 complex with orthorhombic symmetry observed in EPR experiments.[4] A good candidate is the symmetric structure shown in Fig. 4 (single donor) which was obtained by attaching a H atom to the symmetric TD structure of Fig. 1(c). The H atom stabilizes the symmetric structure (without H it transforms into asymmetric configuration), probably because H is located

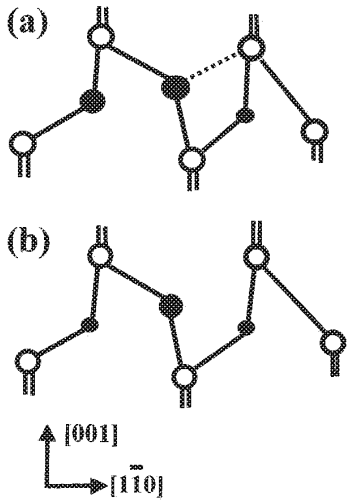


FIG. 3. The O–O–H cluster (a), and H–O–H staggered chain (b).

close to the so-called C position of the Si crystal[22] that has a high electron density and is attractive for neutral hydrogen.

The most important fact is that for H involved in all of the O complexes considered earlier, the binding energies (0.5–0.7 eV) and the barriers to move H atom to nearest interstitial (0.6–0.8 eV) are quite low. They are comparable with the diffusion barrier ($\sim$0.4 eV) for neutral H in Si.[22] This means that H atoms can be easily activated and removed from the complex. The structure immediately regains its original electric activity, i.e., the processes of H passivation and activation of oxygen complexes are reversible. This is in agreement with measurements[12,13] which show that the H passivation of TDs is imcomplete, and a sizeable number of electrically active defects still remains in the sample after hydrogenation.

At higher temperatures (400–500 °C), the oxygen atoms become mobile and can travel between interstitials. In such a case H can kick off and replace an oxygen atom. When hydrogen atom replaces one oxygen atom from the TD, the total energy of the final configuration is 0.1–0.3 eV lower than the energy of the initial configuration. However, the probability of such a reaction depends on too many factors and cannot be easily estimated.

In the earlier work by Ramamoorthy and Pantelides[18] it was shown that addition of a "fourth" O atom to the core of a TD [e.g., Fig. 1(b)] pushes the central Si atom into an interstitial position. This Si emission eliminates the electrical

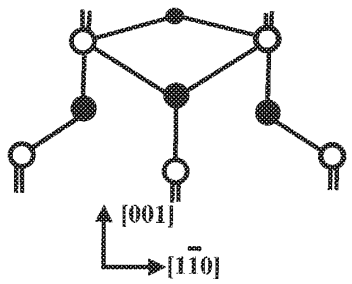


FIG. 4. The symmetric (orthorhombic) TD structure stabilized by an attached H atom.

Downloaded 28 May 2008 to 148.168.238.18. Redistribution subject to AIP license or copyright; see http://apl.aip.org/apl/copyright.jsp

SIONYX1403000041.0097

SAMSUNG EX. 1002 - 519/4148

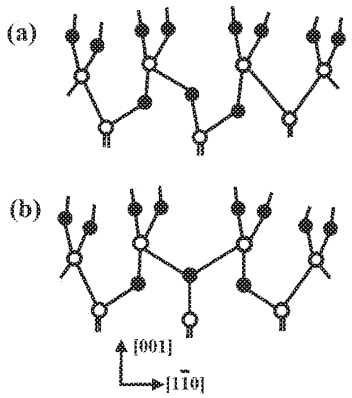


FIG. 5. SiO_2 protrusions into the Si side of a Si–SiO_2 interface: staggered chain (a), thermal donor complex (b).

activity as the system is left only with normal Si–O–Si and Si–Si bonds. It was proposed that the same process can account for the observed emission of Si atoms during thin-film oxidation. In other words, new O atoms arriving at the Si–SiO_2 interface can lead to the formation of TD-like defects. We have now performed such calculations using the model interface of Buczko *et al.*[19] and indeed found that TD-like defects form as protrusions (Fig. 5). As in the bulk Si, the TD structure is metastable. Hydrogen can attach to these structures but the binding energy is lower than 1 eV. At the temperatures at which oxidation occurs (and O is mobile), H can kick out and replace oxygen. The reaction energy for this process is 0.3–0.5 eV, but the binding energy of H in the new position is also lower than 1 eV. Thus, we conclude that H can also eliminate the "frustrated O bonds" (remove three-coordinated O) at the interface, in addition to the process of the emission of Si interstitials described in Ref. 18. However, the interaction between H and Si–SiO_2 interfaces has many other aspects that are reported elsewhere.[23]

This work was supported in part by AFOSR Grant No. F-49620-99-1-0289, NSF Grant No. DMR-9803768, and by the William A. and Nancy F. McMinn Endowment at Vanderbilt University.

[1] C. S. Fuller, J. W. Ditzenberger, N. B. Hannay, and E. Buehler, Phys. Rev. **96**, 833 (1954).
[2] B. J. Heijmink Liesert, T. Gregorkiewicz, and C. A. J. Ammerlaan, Phys. Rev. B **47**, 7005 (1993).
[3] M. Stavola, K. M. Lee, J. C. Nabity, P. E. Freelans, and L. C. Kimmerling, Phys. Rev. Lett. **54**, 2639 (1985).
[4] Yu. V. Martynov, T. Gregorkiewicz, and C. A. J. Ammerlaan, Phys. Rev. Lett. **74**, 2030 (1995).
[5] T. Gregorkiewicz, D. A. van Wezep, H. H. P. Th. Bekman, and C. A. J. Ammerlaan, Phys. Rev. B **35**, 3810 (1987).
[6] R. C. Newman, J. H. Tucker, N. G. Semaltianos, E. C. Lightowlers, T. Gregorkiewicz, I. S. Zevenbergen, and C. A. J. Ammerlaan, Phys. Rev. B **54**, R6803 (1996).
[7] W. Götz, G. Pensl, and W. Zulehner, Phys. Rev. B **46**, 4312 (1992).
[8] A. Ourmazd, W. Schröter, and A. Bourret, J. Appl. Phys. **56**, 1670 (1984).
[9] L. C. Snyder and J. W. Corbett, Mater. Res. Soc. Symp. Proc. **59**, 207 (1985).
[10] D. J. Chadi, Phys. Rev. Lett. **77**, 861 (1996).
[11] M. Pesola, Y. J. Lee, J. von Boehm, M. Kaukonen, and R. M. Nieminen, Phys. Rev. Lett. **84**, 5343 (2000).
[12] N. M. Johnson and S. K. Hahn, Appl. Phys. Lett. **48**, 709 (1986).
[13] A. Chantre, S. J. Pearton, L. C. Kimerling, K. D. Cummings, and W. C. Dautremont-Smith, Appl. Phys. Lett. **50**, 513 (1987).
[14] *Hydrogen in Semiconductors*, edited by J. I. Pankove and N. M. Johnson (Academic, Boston, 1991).
[15] P. Hohenberg and W. Kohn, Phys. Rev. **136**, B864 (1964); W. Kohn and L. J. Sham, *ibid.* **140**, A1133 (1965).
[16] D. Vanderbilt, Phys. Rev. B **41**, 7892 (1990).
[17] M. Needels, J. D. Joannopoulos, Y. Bar-Yam, and S. T. Pantelides, Phys. Rev. B **43**, 4208 (1991).
[18] M. Ramamoorthy and S. T. Pantelides, Appl. Phys. Lett. **75**, 115 (1999); S. T. Pantelides and M. Ramamoorthy, Mater. Res. Soc. Symp. Proc. **490**, 59 (1998).
[19] R. Buczko, S. J. Pennycook, and S. T. Pantelides, Phys. Rev. Lett. **84**, 943 (2000).
[20] D. J. Chadi and M. L. Cohen, Phys. Rev. B **8**, 5747 (1973).
[21] B. Pajot, H. Compain, J. Lerouille, and B. Clerjaud, Physica B **117/118**, 110 (1983).
[22] C. G. Van de Walle, P. J. H. Denteneer, Y. Bar-Yam, and S. T. Pantelides, Phys. Rev. B **39**, 10791 (1989).
[23] S. T. Pantelides, S. N. Rashkeev, R. Buczko, D. M. Fleetwood, and R. D. Schrimpf, IEEE Trans. Nucl. Sci. (in press).

Downloaded 28 May 2009 to 146.186.238.18. Redistribution subject to AIP license or copyright; see http://apl.aip.org/apl/copyright.jsp

SIONYX1403000041.0098

SAMSUNG EX. 1002 - 520/4148

6 pg

Nanosecond Excimer Laser Processing for Novel Microelectronic Fabrication

Stephen D. Russell, Ayax D. Ramirez, and Eugene P. Kelley
SSC San Diego

ABSTRACT

This paper summarizes progress in using nanosecond excimer laser processing in the fabrication of novel microelectronic devices such as backside-illuminated charge-coupled devices and self-aligned silicon carbide field-effect transistors. This technology enables spatially localized thermal processing and ultra-shallow junctions amenable with next-generation, deeply scaled microelectronic devices.

INTRODUCTION

As microelectronic devices continue to shrink in lateral dimensions, there is a concomitant requirement to similarly scale the vertical dimensions of the devices. Manufacturing techniques to form ultra-shallow material junctions have not kept pace with the advances with lithography for forming deeply scaled (less than 0.25 micron) dimensions. Excimer laser processing is a novel technique for microelectronic materials processing because it offers spatially localized thermal processing and a very small thermal budget (on the order of tens of nanoseconds). This technique has been used to anneal ion-implanted dopants and to incorporate dopants from a gaseous ambient into the semiconductor device to form electrical junctions. It has also been used to control laser-assisted etching processes to locally remove material from the semiconductor layer.

This paper summarizes progress in using nanosecond excimer laser pulses in the fabrication of novel microelectronic devices such as backside-illuminated charge coupled devices (CCDs) and silicon carbide field-effect transistors. The SSC San Diego laser-processing laboratory employs an excimer laser beam directed into an optical path that homogenizes and shapes the intensity profile to provide uniform illumination across the area to be processed without scanning the beam. This is required because the intensity profile emitted by the excimer laser exhibits both spatial and temporal (pulse-to-pulse) non-uniformities and must be correctly shaped. The subsequent shaped and homogenized intensity profile is directed into a processing chamber and then onto a semiconductor wafer or device to be processed. The laser-processing system includes in-situ characterization of the laser process using a reflectivity monitor to measure the melt duration of the material, which is an important process control parameter. Additional process controls include mass flow controllers for process and purge gases, evacuation systems, and alignment systems. Details of these subsystems have been described elsewhere [1].

LASER PROCESSING OF CCDS

CCDs are solid-state electronic imaging devices that read out image charges from wells in an array of pixels. CCDs designed for solid-state cameras, such as camcorders, are in great demand and are widely available. They have been designed to provide adequate performance when viewing brightly illuminated scenes. However, in astronomical, scientific,

SIONYX1403000041.0099

SAMSUNG EX. 1002 - 521/4148

and military applications their spectral response, dark current, and other characteristics are not satisfactory. The gate electrodes of a CCD are used for clocking the read-out from the imaging array in a "bucket brigade" architecture. These electrodes may be fabricated with thin layers of aluminum or polysilicon, but constitute an obstacle for high-performance CCDs, which detect the image light after passing through or around the metal structure. This conventional design exhibits limitations for low-light-level detection, high-resolution imaging, uniform responsivity, and short wavelength response. To eliminate these problems, backside-illuminated CCDs are fabricated with analogous circuitry on the front-side, but with a thinned area above the pixel array, allowing detection of the image light by photo-generated charges traversing from the backside to the front-side collection electrodes. The benefits of the backside-illuminated CCD design, however, come with substantial added complexity in the fabrication process. For example, the backside illumination design requires forming a thin membrane (about 10 μm thick) across the active area of the array by wet etching the (100)-oriented silicon wafer with a potassium hydroxide (KOH) solution. The KOH anisotropically etches to the (111) crystallographic plane, thereby forming sidewalls at an angle of 54.7 degrees with respect to the image plane. These sidewalls are smooth and highly reflective and allow stray light to be reflected onto the image plane, causing spurious images.

A three-dimensional plot of the optical response (i.e., responsivity) of a typical backside-illuminated CCD under constant background illumination is shown in Figure 1, where the x and y coordinates correspond to the pixels in the imaging array, and the z-axis is the responsivity. Two imaging problems correlated to the reflective sidewalls are apparent: non-uniformity characterized by a cruciform (or cross) pattern and a relatively high background level. The application of conventional etching techniques to eliminate this scattering would require complex masking and handling of thin membranes, which have proven to be low in yield and reproducibility and therefore costly. Alternative system configurations for illumination of the imaging detector increase overall system complexity, cost, and weight. Furthermore, manufacturability is greatly diminished because of the need for accurate alignment tolerances during assembly. Therefore, a novel laser-assisted etching process has been demonstrated to avoid sidewall scattering on backside-illuminated CCDs.

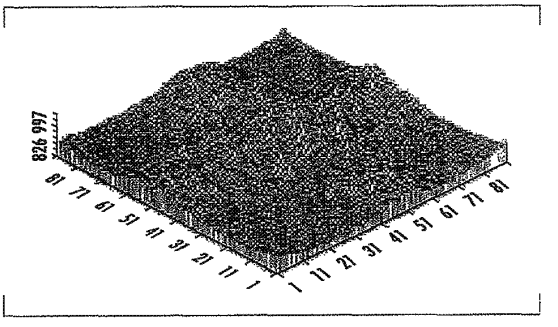


FIGURE 1. CCD responsivity.

LASER-ASSISTED ETCHING

The laser-assisted etching process requires introduction of an ambient into a chamber with the device to be etched and illumination of the CCD sidewall in the presence of the ambient. The process starts with adsorption of the ambient onto the silicon; laser illumination of the device to locally melt the silicon, causing a pyrolytic or photolytic decomposition of the adsorbed gas; subsequent formation of halogen radicals that react with the silicon forming volatile byproducts; desorption of the byproducts, thereby etching about one monolayer of the silicon; and re-adsorption of the ambient and repetition of the cycle. This cycle is

SIONYX1403000041.0100

SAMSUNG EX. 1002 - 522/4148

typically repeated thousands or tens of thousands of times to achieve the required etch depth. Details of the etching process have been described in detail elsewhere [2]. Chloropentafluoroethane (C_2ClF_5) was chosen as the etching ambient because it is non-corrosive, has a high etch rate, and results in a roughened (textured) surface. The non-corrosive nature (except in the presence of laser illumination) enables localized processing of fully fabricated CCDs without damage to any portion. A step-and-repeat process was employed to illuminate regions of the CCD sidewall with about 5000 laser pulses at each position, resulting in an etch depth of about 0.5 mm that produced the desired mat (non-reflective) texture. Figure 2 shows a scanning electron microscope (SEM) cross section of the microscopically etched features that serve as a trap to scattered light. The CCD received a total of about 100,000 laser pulses, corresponding to less than 5 minutes of processing per device (at 400 Hz). The responsivity of a laser-textured backside-illuminated CCD is shown in Figure 3. This exhibits less than 1% responsivity uniformities and a 10 times lower background level than unprocessed devices, showing the benefit of the laser-etching process [3].

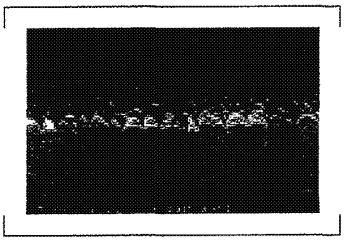


FIGURE 2. SEM of laser-etched surface.

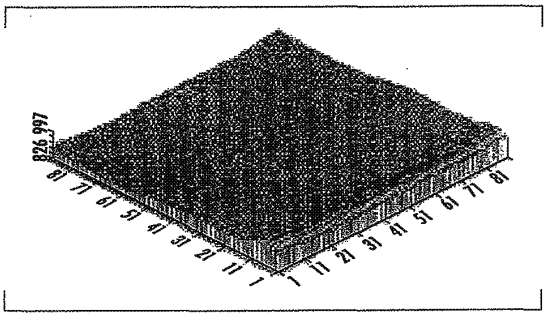


FIGURE 3. Laser-etched CCD responsivity.

LASER-ANNEALING AND ACTIVATION OF ION-IMPLANTED DOPANTS

High-performance, low-light-detecting CCDs are also susceptible to dark current, i.e., the thermally generated charge carriers under zero illumination. Excessive dark current will destroy the dynamic range of the imager, thereby masking low-light-level signals. In addition, variations across the array will degrade image quality and can be misinterpreted by subsequent signal processing circuitry. Dark current effects in CCDs range from individual pixels with excessive dark current to high average dark current and variations in dark current across the imaging array. While dark current is normally associated with front-side circuitry, crystalline damage arising from un-annealed ion-implanted dopants can lead to generation sites for dark current. Therefore, fabrication techniques to improve the dark current of CCDs are highly desirable. Backside-illuminated CCDs containing a 90-pixel x 90-pixel array were fabricated and used as a test vehicle for a laser-annealing process. The CCDs were conventional four-phase buried-channel devices. In addition to the dark current reported in this paper, the CCDs were fully tested for functionality before and after laser processing to ensure no damage to either the imaging area or the associated electronics. Devices were selected that exhibited dark current defects, i.e., excessive average dark current, non-uniformities, and/or individual pixels with excessive dark current. The test devices were then laser processed in accordance with the parameters in Table 1 and retested [4].

Results of a typical (not best case) laser-annealed sample are discussed here. This sample was chosen because of the unique spiral defect structure that was "repaired" by laser processing. Figure 4 shows a map of the dark current for this 90-pixel x 90-pixel array before laser processing, with colors corresponding to dark currents ranging from less than 7 to greater than 11 nA/cm^2. Numerous defective pixels (designated in red),

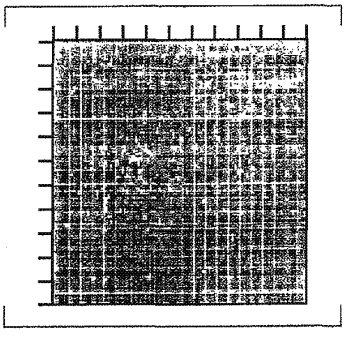


FIGURE 4. CCD dark current.

SAMSUNG EX. 1002 - 523/4148

with dark currents exceeding 11 nA/cm^2 are present. Figure 5 shows the dark current map following the laser process. Note that all defective pixels were improved. The mean dark current of the 8100 pixels in the array decreased from 9.958 nA/cm^2 to 9.658 nA/cm^2. The standard deviation of the dark current, which is representative of the uniformity in the array, decreased from 4.826 nA/cm^2 to 0.812 nA/cm^2. Note, because the front-side metal is already formed on the CCD, conventional furnace anneals are restricted below 400° C and therefore prevent the elimination of the cited defects using conventional furnace annealing.

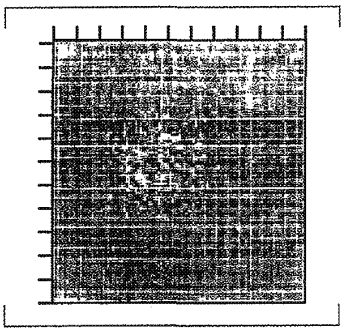


FIGURE 5. Laser-annealed CCD dark current.

TABLE 1. Laser Processing Parameters.

Parameter	Typical Value	Range
implant dose and species	5x10^{13} ions/cm^2 boron	1x10^{13} to 1x10^{15} ions/cm^2 boron or boron difluoride
implant depth	120 nm	5 to 150 nm
process ambient	helium	inert or dopant gases
sample temperature	23°C	< 400°C (restricted by device)
laser fluence	1.0 J/cm^2	0.7 to 2.0 J/cm^2
laser wavelength	248 nm	157 to 351 nm
laser intensity profile	tophat, < 5% nonuniformity	< 10% nonuniformity
laser temporal profile	23 ns	10 to 30 ns
number of laser pulses	10	1 to 10

GAS IMMERSION LASER DOPING (GILD) IN SILICON CARBIDE

Silicon carbide (SiC) is a semiconductor of wide interest because of its applicability in high-temperature, high-power, and photonic devices and circuits. However, difficulties in fabrication, as compared to silicon, have prevented the full realization of its capabilities in these areas. The high melting point and limited diffusion of impurities have greatly limited the use of ion implantation and furnace annealing commonly employed in the silicon microelectronics industry as a means of incorporating and activating dopants. Such fabrication processes are desirable to produce self-aligned field-effect transistor structures for use in discrete power devices or digital logic. Limited success with ion implanting n-type dopants in SiC, such as arsenic, has been obtained but requires furnace anneals of greater than 1300° C for activation. However, ion implantation and furnace annealing of p-type dopants has demonstrated only about 5% activation, insufficient for practical device fabrication. Alternative techniques are therefore desired to obtain dopant activation, in particular p-type impurities, in SiC.

6H-SiC samples were placed in a processing chamber that was evacuated to <10^{-7} Torr and back-filled with a 10 psi ^{11}B-enriched boron trifluoride atmosphere. The samples were illuminated at 1.3 J/cm^2 with between 1 and 10 laser pulses with the sample in the doping ambient. This process, called gas immersion laser doping (GILD), enables the dissociation of the dopant ambient and simultaneous incorporation of the dopant atoms into

SIONYX1403000041.0102

SAMSUNG EX. 1002 - 524/4148

the semiconductor, thereby eliminating ion implantation. Point-contact current-voltage measurements (PCIV) were performed in the laser-illuminated region. PCIV, a technique analogous to spreading resistance profilometry, is used to determine the concentration of electrically activated carriers in compound semiconductors using a two-point current-voltage probe along a polished bevel. Figure 6 shows the electrically active carrier concentration vs. depth obtained from the PCIV voltage profiling for one pulse. Boron activation is observed with a maximum carrier concentration of 3.4 x 10^{18} cm^{-3} with a junction depth of ~90 nm. The abruptness of the pn junction edge is characteristic of a laser-formed junction where enhanced diffusion occurs during the molten phase. Given the nearly uniform distribution throughout the melted region, a boron diffusion coefficient of ~2.3 x 10^{-3} cm^2/sec was calculated, which is an order of magnitude greater than that reported for boron in silicon. Little change in carrier concentration is observed with increasing pulses, and demonstrates that a single laser pulse can incorporate and simultaneously activate dopants in SiC [5]. This technique may be applied to the fabrication of low-resistance contacts or shallow junctions in the source and drain regions of SiC field-effect devices.

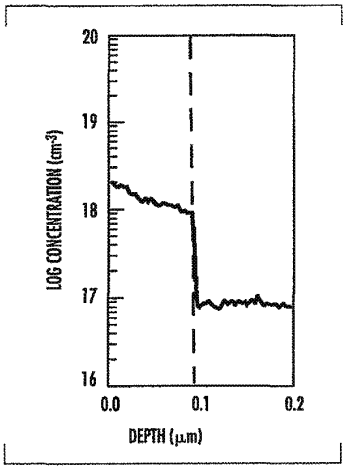


FIGURE 6. GILD pn junction in SiC.

SUMMARY

The localized, nanosecond thermal processing offered by an excimer laser has demonstrated the ability to perform localized etching of silicon and to anneal ion implanted dopants in a backside-illuminated CCD. These techniques have improved the optical performance (responsivity uniformity) and their electrical performance (reduced dark current and pixel defects). The excimer laser has also demonstrated the ability to incorporate dopants from a gaseous ambient into SiC to form electrical junctions. This advanced processing technique will enable advances in deeply scaled integrated circuit processing.

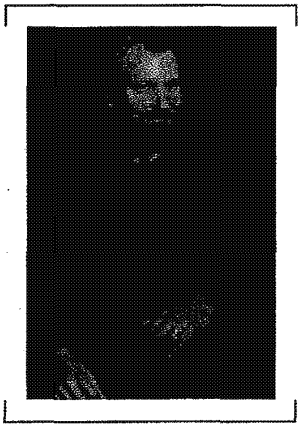
REFERENCES

1. Russell, S. D. and D. A. Sexton. 1989. "Excimer Laser Thinning of Backside Illuminated CCDs," NOSC TD 1697 (November), Naval Ocean Systems Center (now SSC San Diego), San Diego, CA.
2. Russell, S. D. and D. A. Sexton. 1990. "Excimer Laser-Assisted Etching of Silicon Using Chloropentafluoroethane," in R. Rosenberg, A. F. Bernhardt and J. G. Black, eds., *In-Situ Patterning: Selective Area Deposition and Etching*, (Materials Research Society Proceedings, vol. 158, Pittsburgh, PA, 1990), pp. 325–303.
3. Russell, S. D. and D. A. Sexton. 1991. "Responsively Uniformity Enhancements for Backside-Illuminated Charge-Coupled Devices (BICCDs) by Excimer Laser-Assisted Etching," NOSC TD 2103 (May), Naval Ocean Systems Center (now SSC San Diego), San Diego, CA.
4. Russell, S. D. 2002. "Excimer Laser Processing of Backside-Illuminated CCDs," *Technology 2002 Conference Proceedings*, NASA Conference Publication 3189, vol. 2, 1993, pp. 296–303.
5. Russell, S. D. and A. D. Ramirez. 1999. "In-Situ Boron Incorporation and Activation in Silicon Carbide Using Excimer Laser Recrystallization," *Applied Physics Letters*, vol. 74, no. 22, pp. 3368–3370.

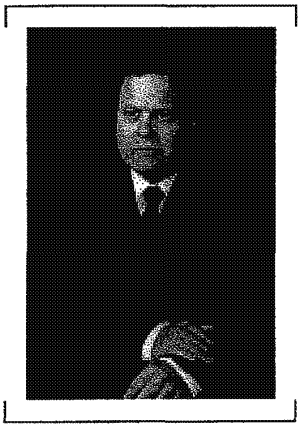
SIONYX1403000041.0103

SAMSUNG EX. 1002 - 525/4148

This technology is the subject of one or more patents assignable to the U.S. Government, including U.S. Patent Numbers 6,204,160; 5,840,592; 5,688,715; 5,385,633; 5,348,609; and 5,266,532. Licensing inquiries may be directed to: Office of Patent Counsel, (Code 20012), SSC San Diego, 53510 Silvergate Avenue, Room 103, San Diego, CA 92151–5765; (619) 553–3001.



Stephen D. Russell
Ph.D., Physics, University of Michigan, 1986
Current Research: Microsensors; photonic devices; optoelectronics; microelectromechanical systems (MEMS); laser applications.



Ayax D. Ramirez
MS, Physics, San Diego State University, 1991
Current Research: Microsensors; photonic devices; optoelectronics; microelectromechanical systems (MEMS); laser applications.

Eugene P. Kelley
BS, Electrical Engineering, San Diego State University, 1971
Current Research: Microelectronics; silicon-on-insulator devices and circuits; laser processing of semiconductors.

SIONYX1403000041.0104

SAMSUNG EX. 1002 - 526/4148

6 pg

Nanosecond Excimer Laser Processing for Novel Microelectronic Fabrication

Stephen D. Russell, Ayax D. Ramirez, and Eugene P. Kelley
SSC San Diego

ABSTRACT

This paper summarizes progress in using nanosecond excimer laser processing in the fabrication of novel microelectronic devices such as backside-illuminated charge-coupled devices and self-aligned silicon carbide field-effect transistors. This technology enables spatially localized thermal processing and ultra-shallow junctions amenable with next-generation, deeply scaled microelectronic devices.

INTRODUCTION

As microelectronic devices continue to shrink in lateral dimensions, there is a concomitant requirement to similarly scale the vertical dimensions of the devices. Manufacturing techniques to form ultra-shallow material junctions have not kept pace with the advances with lithography for forming deeply scaled (less than 0.25 micron) dimensions. Excimer laser processing is a novel technique for microelectronic materials processing because it offers spatially localized thermal processing and a very small thermal budget (on the order of tens of nanoseconds). This technique has been used to anneal ion-implanted dopants and to incorporate dopants from a gaseous ambient into the semiconductor device to form electrical junctions. It has also been used to control laser-assisted etching processes to locally remove material from the semiconductor layer.

This paper summarizes progress in using nanosecond excimer laser pulses in the fabrication of novel microelectronic devices such as backside-illuminated charge coupled devices (CCDs) and silicon carbide field-effect transistors. The SSC San Diego laser-processing laboratory employs an excimer laser beam directed into an optical path that homogenizes and shapes the intensity profile to provide uniform illumination across the area to be processed without scanning the beam. This is required because the intensity profile emitted by the excimer laser exhibits both spatial and temporal (pulse-to-pulse) non-uniformities and must be correctly shaped. The subsequent shaped and homogenized intensity profile is directed into a processing chamber and then onto a semiconductor wafer or device to be processed. The laser-processing system includes in-situ characterization of the laser process using a reflectivity monitor to measure the melt duration of the material, which is an important process control parameter. Additional process controls include mass flow controllers for process and purge gases, evacuation systems, and alignment systems. Details of these subsystems have been described elsewhere [1].

LASER PROCESSING OF CCDS

CCDs are solid-state electronic imaging devices that read out image charges from wells in an array of pixels. CCDs designed for solid-state cameras, such as camcorders, are in great demand and are widely available. They have been designed to provide adequate performance when viewing brightly illuminated scenes. However, in astronomical, scientific,

SIONYX1403000041.0105

SAMSUNG EX. 1002 - 527/4148

and military applications their spectral response, dark current, and other characteristics are not satisfactory. The gate electrodes of a CCD are used for clocking the read-out from the imaging array in a "bucket brigade" architecture. These electrodes may be fabricated with thin layers of aluminum or polysilicon, but constitute an obstacle for high-performance CCDs, which detect the image light after passing through or around the metal structure. This conventional design exhibits limitations for low-light-level detection, high-resolution imaging, uniform responsivity, and short wavelength response. To eliminate these problems, backside-illuminated CCDs are fabricated with analogous circuitry on the front-side, but with a thinned area above the pixel array, allowing detection of the image light by photo-generated charges traversing from the backside to the front-side collection electrodes. The benefits of the backside-illuminated CCD design, however, come with substantial added complexity in the fabrication process. For example, the backside illumination design requires forming a thin membrane (about 10 μm thick) across the active area of the array by wet etching the (100)-oriented silicon wafer with a potassium hydroxide (KOH) solution. The KOH anisotropically etches to the (111) crystallographic plane, thereby forming sidewalls at an angle of 54.7 degrees with respect to the image plane. These sidewalls are smooth and highly reflective and allow stray light to be reflected onto the image plane, causing spurious images.

A three-dimensional plot of the optical response (i.e., responsivity) of a typical backside-illuminated CCD under constant background illumination is shown in Figure 1, where the x and y coordinates correspond to the pixels in the imaging array, and the z-axis is the responsivity. Two imaging problems correlated to the reflective sidewalls are apparent: non-uniformity characterized by a cruciform (or cross) pattern and a relatively high background level. The application of conventional etching techniques to eliminate this scattering would require complex masking and handling of thin membranes, which have proven to be low in yield and reproducibility and therefore costly. Alternative system configurations for illumination of the imaging detector increase overall system complexity, cost, and weight. Furthermore, manufacturability is greatly diminished because of the need for accurate alignment tolerances during assembly. Therefore, a novel laser-assisted etching process has been demonstrated to avoid sidewall scattering on backside-illuminated CCDs.

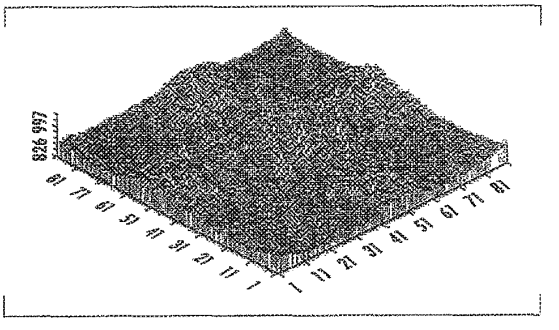


FIGURE 1. CCD responsivity.

LASER-ASSISTED ETCHING

The laser-assisted etching process requires introduction of an ambient into a chamber with the device to be etched and illumination of the CCD sidewall in the presence of the ambient. The process starts with adsorption of the ambient onto the silicon; laser illumination of the device to locally melt the silicon, causing a pyrolytic or photolytic decomposition of the adsorbed gas; subsequent formation of halogen radicals that react with the silicon forming volatile byproducts; desorption of the byproducts, thereby etching about one monolayer of the silicon; and re-adsorption of the ambient and repetition of the cycle. This cycle is

SIONYX1403000041.0106

SAMSUNG EX. 1002 - 528/4148

typically repeated thousands or tens of thousands of times to achieve the required etch depth. Details of the etching process have been described in detail elsewhere [2]. Chloropentafluoroethane (C_2ClF_5) was chosen as the etching ambient because it is non-corrosive, has a high etch rate, and results in a roughened (textured) surface. The non-corrosive nature (except in the presence of laser illumination) enables localized processing of fully fabricated CCDs without damage to any portion. A step-and-repeat process was employed to illuminate regions of the CCD sidewall with about 5000 laser pulses at each position, resulting in an etch depth of about 0.5 mm that produced the desired mat (non-reflective) texture. Figure 2 shows a scanning electron microscope (SEM) cross section of the microscopically etched features that serve as a trap to scattered light. The CCD received a total of about 100,000 laser pulses, corresponding to less than 5 minutes of processing per device (at 400 Hz). The responsivity of a laser-textured backside-illuminated CCD is shown in Figure 3. This exhibits less than 1% responsivity uniformities and a 10 times lower background level than unprocessed devices, showing the benefit of the laser-etching process [3].

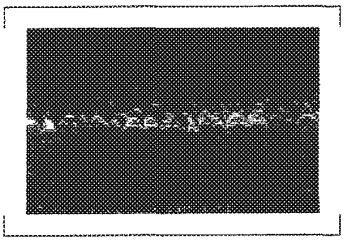


FIGURE 2. SEM of laser-etched surface.

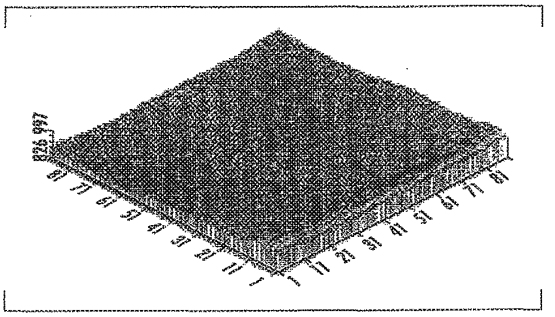


FIGURE 3. Laser-etched CCD responsivity.

LASER-ANNEALING AND ACTIVATION OF ION-IMPLANTED DOPANTS

High-performance, low-light-detecting CCDs are also susceptible to dark current, i.e., the thermally generated charge carriers under zero illumination. Excessive dark current will destroy the dynamic range of the imager, thereby masking low-light-level signals. In addition, variations across the array will degrade image quality and can be misinterpreted by subsequent signal processing circuitry. Dark current effects in CCDs range from individual pixels with excessive dark current to high average dark current and variations in dark current across the imaging array. While dark current is normally associated with front-side circuitry, crystalline damage arising from un-annealed ion-implanted dopants can lead to generation sites for dark current. Therefore, fabrication techniques to improve the dark current of CCDs are highly desirable. Backside-illuminated CCDs containing a 90-pixel x 90-pixel array were fabricated and used as a test vehicle for a laser-annealing process. The CCDs were conventional four-phase buried-channel devices. In addition to the dark current reported in this paper, the CCDs were fully tested for functionality before and after laser processing to ensure no damage to either the imaging area or the associated electronics. Devices were selected that exhibited dark current defects, i.e., excessive average dark current, non-uniformities, and/or individual pixels with excessive dark current. The test devices were then laser processed in accordance with the parameters in Table 1 and retested [4].

Results of a typical (not best case) laser-annealed sample are discussed here. This sample was chosen because of the unique spiral defect structure that was "repaired" by laser processing. Figure 4 shows a map of the dark current for this 90-pixel x 90-pixel array before laser processing, with colors corresponding to dark currents ranging from less than 7 to greater than 11 nA/cm^2. Numerous defective pixels (designated in red),

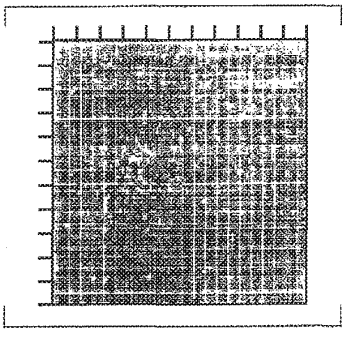


FIGURE 4. CCD dark current.

SIONYX1403000041.0107

SAMSUNG EX. 1002 - 529/4148

with dark currents exceeding 11 nA/cm^2 are present. Figure 5 shows the dark current map following the laser process. Note that all defective pixels were improved. The mean dark current of the 8100 pixels in the array decreased from 9.958 nA/cm^2 to 9.658 nA/cm^2. The standard deviation of the dark current, which is representative of the uniformity in the array, decreased from 4.826 nA/cm^2 to 0.812 nA/cm^2. Note, because the front-side metal is already formed on the CCD, conventional furnace anneals are restricted below 400° C and therefore prevent the elimination of the cited defects using conventional furnace annealing.

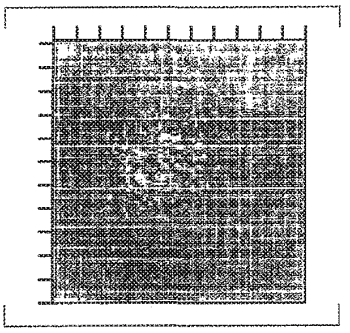


FIGURE 5. Laser-annealed CCD dark current.

TABLE 1. Laser Processing Parameters.

Parameter	Typical Value	Range
implant dose and species	5x10^{13} ions/cm^2 boron	1x10^{13} to 1x10^{15} ions/cm^2 boron or boron difluoride
implant depth	120 nm	5 to 150 nm
process ambient	helium	inert or dopant gases
sample temperature	23°C	< 400°C (restricted by device)
laser fluence	1.0 J/cm^2	0.7 to 2.0 J/cm^2
laser wavelength	248 nm	157 to 351 nm
laser intensity profile	tophat, < 5% nonuniformity	< 10% nonuniformity
laser temporal profile	23 ns	10 to 30 ns
number of laser pulses	10	1 to 10

GAS IMMERSION LASER DOPING (GILD) IN SILICON CARBIDE

Silicon carbide (SiC) is a semiconductor of wide interest because of its applicability in high-temperature, high-power, and photonic devices and circuits. However, difficulties in fabrication, as compared to silicon, have prevented the full realization of its capabilities in these areas. The high melting point and limited diffusion of impurities have greatly limited the use of ion implantation and furnace annealing commonly employed in the silicon microelectronics industry as a means of incorporating and activating dopants. Such fabrication processes are desirable to produce self-aligned field-effect transistor structures for use in discrete power devices or digital logic. Limited success with ion implanting n-type dopants in SiC, such as arsenic, has been obtained but requires furnace anneals of greater than 1300° C for activation. However, ion implantation and furnace annealing of p-type dopants has demonstrated only about 5% activation, insufficient for practical device fabrication. Alternative techniques are therefore desired to obtain dopant activation, in particular p-type impurities, in SiC.

6H-SiC samples were placed in a processing chamber that was evacuated to <10^{-7} Torr and back-filled with a 10 psi ^{11}B-enriched boron trifluoride atmosphere. The samples were illuminated at 1.3 J/cm^2 with between 1 and 10 laser pulses with the sample in the doping ambient. This process, called gas immersion laser doping (GILD), enables the dissociation of the dopant ambient and simultaneous incorporation of the dopant atoms into

SIONYX1403000041.0108

SAMSUNG EX. 1002 - 530/4148

the semiconductor, thereby eliminating ion implantation. Point-contact current-voltage measurements (PCIV) were performed in the laser-illuminated region. PCIV, a technique analogous to spreading resistance profilometry, is used to determine the concentration of electrically activated carriers in compound semiconductors using a two-point current-voltage probe along a polished bevel. Figure 6 shows the electrically active carrier concentration vs. depth obtained from the PCIV voltage profiling for one pulse. Boron activation is observed with a maximum carrier concentration of 3.4×10^{18} cm^{-3} with a junction depth of ~90 nm. The abruptness of the pn junction edge is characteristic of a laser-formed junction where enhanced diffusion occurs during the molten phase. Given the nearly uniform distribution throughout the melted region, a boron diffusion coefficient of $\sim 2.3 \times 10^{-3}$ cm^2/sec was calculated, which is an order of magnitude greater than that reported for boron in silicon. Little change in carrier concentration is observed with increasing pulses, and demonstrates that a single laser pulse can incorporate and simultaneously activate dopants in SiC [5]. This technique may be applied to the fabrication of low-resistance contacts or shallow junctions in the source and drain regions of SiC field-effect devices.

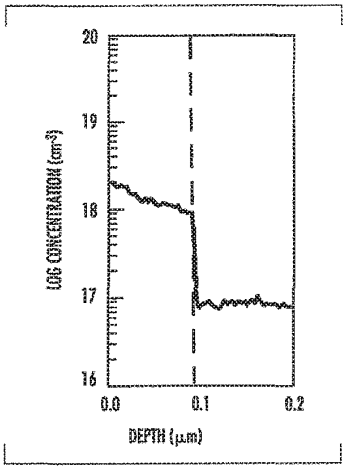


FIGURE 6. GILD pn junction in SiC.

SUMMARY

The localized, nanosecond thermal processing offered by an excimer laser has demonstrated the ability to perform localized etching of silicon and to anneal ion implanted dopants in a backside-illuminated CCD. These techniques have improved the optical performance (responsivity uniformity) and their electrical performance (reduced dark current and pixel defects). The excimer laser has also demonstrated the ability to incorporate dopants from a gaseous ambient into SiC to form electrical junctions. This advanced processing technique will enable advances in deeply scaled integrated circuit processing.

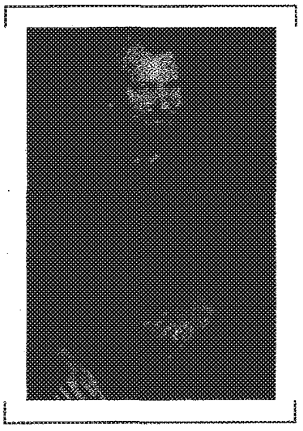
REFERENCES

1. Russell, S. D. and D. A. Sexton. 1989. "Excimer Laser Thinning of Backside Illuminated CCDs," NOSC TD 1697 (November), Naval Ocean Systems Center (now SSC San Diego), San Diego, CA.
2. Russell, S. D. and D. A. Sexton. 1990. "Excimer Laser-Assisted Etching of Silicon Using Chloropentafluoroethane," in R. Rosenberg, A. F. Bernhardt and J. G. Black, eds., *In-Situ Patterning: Selective Area Deposition and Etching*, (Materials Research Society Proceedings, vol. 158, Pittsburgh, PA, 1990), pp. 325–303.
3. Russell, S. D. and D. A. Sexton. 1991. "Responsively Uniformity Enhancements for Backside-Illuminated Charge-Coupled Devices (BICCDs) by Excimer Laser-Assisted Etching," NOSC TD 2103 (May), Naval Ocean Systems Center (now SSC San Diego), San Diego, CA.
4. Russell, S. D. 2002. "Excimer Laser Processing of Backside-Illuminated CCDs," *Technology 2002 Conference Proceedings*, NASA Conference Publication 3189, vol. 2, 1993, pp. 296–303.
5. Russell, S. D. and A. D. Ramirez. 1999. "In-Situ Boron Incorporation and Activation in Silicon Carbide Using Excimer Laser Recrystallization," *Applied Physics Letters*, vol. 74, no. 22, pp. 3368–3370.

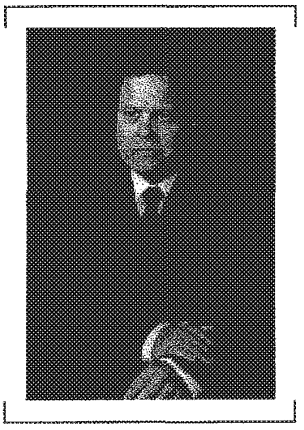
SIONYX1403000041.0109

SAMSUNG EX. 1002 - 531/4148

This technology is the subject of one or more patents assignable to the U.S. Government, including U.S. Patent Numbers 6,204,160; 5,840,592; 5,688,715; 5,385,633; 5,348,609; and 5,266,532. Licensing inquiries may be directed to: Office of Patent Counsel, (Code 20012), SSC San Diego, 53510 Silvergate Avenue, Room 103, San Diego, CA 92151–5765; (619) 553–3001.



Stephen D. Russell
Ph.D., Physics, University of Michigan, 1986
Current Research: Microsensors; photonic devices; optoelectronics; microelectromechanical systems (MEMS); laser applications.



Ayax D. Ramirez
MS, Physics, San Diego State University, 1991
Current Research: Microsensors; photonic devices; optoelectronics; microelectromechanical systems (MEMS); laser applications.

Eugene P. Kelley
BS, Electrical Engineering, San Diego State University, 1971
Current Research: Microelectronics; silicon-on-insulator devices and circuits; laser processing of semiconductors.

SIONYX1403000041.0110

SAMSUNG EX. 1002 - 532/4148

Enhancement of light trapping in thin-film hydrogenated microcrystalline Si solar cells using back reflectors with self-ordered dimple pattern

Hitoshi Sai,[1,a] Hiroyuki Fujiwara,[1] Michio Kondo,[1] and Yoshiaki Kanamori[2]
[1]*Research Center for Photovoltaics, National Institute of Advanced Industrial Science and Technology (AIST), Central 2, Umezono 1-1-1, Tsukuba, Ibaraki 305-8568, Japan*
[2]*Graduate School of Engineering, Tohoku University, Aoba 6-6-01, Aramaki, Aoba-ku, Sendai 980-8579, Japan*

(Received 8 August 2008; accepted 12 September 2008; published online 8 October 2008)

In this article, the light-trapping effect of textured back surface reflectors in thin-film Si solar cells is investigated. A unique substrate with a periodic dimple pattern has been developed by utilizing anodic oxidation of Al as a self-ordering process. *n-i-p* hydrogenated microcrystalline Si (μc-Si:H) cells fabricated on the Al substrate with a period of 0.9 μm show an improved infrared response compared to those fabricated on randomly textured substrates. A high short circuit current density of 24.3 mA/cm^2 has been achieved in a 1-μm-thick μc-Si:H cell by adopting the patterned Al substrate. © *2008 American Institute of Physics*. [DOI: 10.1063/1.2993351]

Thin-film Si solar cells with tandem structures are promising candidates for future low-cost and high-efficiency solar cells.[1–3] In the high-efficiency tandem cells, hydrogenated microcrystalline Si (μc-Si:H) plays a key role as an absorber material in the bottom or middle cell. For μc-Si:H cells, light trapping is crucial to obtain a high current density, as the absorption coefficient of μc-Si:H is small in the near infrared (NIR) region. To date, to enhance the light trapping, various randomly textured substrates have been fabricated including SnO_2,[4,5] and ZnO.[6–8] When incorporated into μc-Si:H solar cells, such textured surfaces significantly increase the optical path length of the incident light due to (i) light scattering on textured surface at oblique angles and (ii) enhanced total internal reflection at the interface within the cells. However, for μc-Si:H solar cells, more efficient light trapping is required to maximize the current density, which is of importance to obtain high efficiencies. To surpass the limitation of conventional random textures, optically functional periodic structures, such as surface gratings[8,9] and photonic crystals,[10] have been applied to thin-film Si solar cells. Nevertheless, the advantage of periodic structures over random textures has remained rather ambiguous. The purpose of our work is to develop back surface reflectors (BSRs) with grating structures that exhibit improved light trapping properties and to demonstrate their effectiveness in actual μc-Si:H solar cells. In this work, we utilize anodic oxidation of Al as a self-ordering process to prepare BSRs with grating structures. The anodic oxidation allows systematic control of the grating period and height by simply changing the wet processing conditions.[11,12] Using this approach, self-ordered dimple patterns with submicron sizes are prepared on Al substrates with high uniformity as well as large substrate sizes.

According to grating theories, a surface grating structure with a period of $\Lambda > 0.3$ μm is required to generate diffracted light inside μc-Si:H in the NIR region. This means that BSRs with a grating structure with $\Lambda > 0.3$ μm can reflect the incident light obliquely, resulting in a longer optical path length in the μc-Si:H cells. To estimate the diffraction behavior of BSRs with grating structures quantitatively, we have performed numerical simulations based on rigorous coupled-wave analysis[13] using the optical constants of Ag[14] and crystalline Si.[15] Figure 1 shows the calculated diffraction behaviors of Ag BSRs with periods of (a) $\Lambda = 0.3$ μm and (b) $\Lambda = 0.9$ μm embedded in Si as schematically shown in the inset. For simplicity, here we assume that the gratings have a two-dimensionally (2D) symmetrical pyramid structure with a constant aspect ratio $h/\Lambda = 0.25$, where h denotes the grating height. In this figure, the gray scale indicates the light intensity reflected at each angle. The pairs of integers in the brackets denote the corresponding diffraction orders for 2D gratings (m,n), where m and n denote the diffraction orders for the x- and y-directions. As shown in Fig. 1(a), the grating with $\Lambda = 0.3$ μm generates the first order diffraction at relatively large angles in a wavelength range of λ

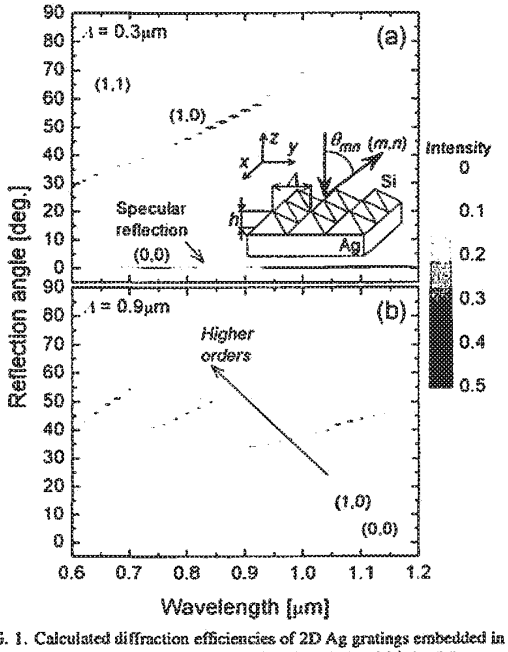


FIG. 1. Calculated diffraction efficiencies of 2D Ag gratings embedded in Si as functions of wavelengths for two different periods of (a) $\Lambda = 0.3$ μm and (b) $\Lambda = 0.9$ μm. In this calculation, normal incidence is assumed.

[a]Electronic mail: hitoshi-sai@aist.gov.jp.

 © 2008 American Institute of Physics

SIONYX1403000041.0111

SAMSUNG EX. 1002 - 533/4148

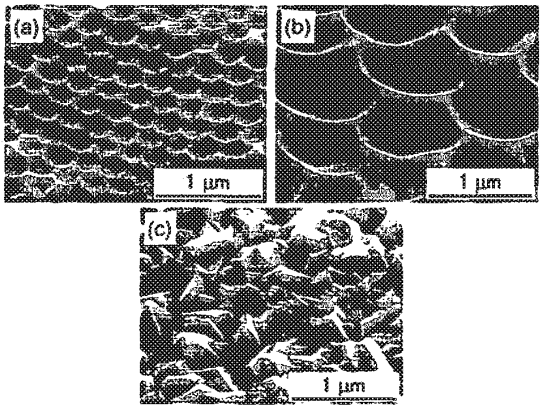


FIG. 2. SEM images of patterned Al substrates fabricated by anodic oxidation process with average periods of (a) $\Lambda=0.3$ μm and (b) $\Lambda=0.9$ μm and (c) Asahi-U-type textured SnO_2 on glass.

$=0.6-1.1$ μm, which can contribute to an increase in the optical path length. However, almost a half of incident light is specularly reflected. Alternatively, as shown in Fig. 1(b), the grating with $\Lambda=0.9$ μm shows multiple lines in the NIR region because this periodicity can satisfy a number of diffraction conditions. This behavior indicates that a BSR with $\Lambda=0.9$ μm can effectively diffract incident light at larger angles not only for normal incidence but also for obliquely incident light. In addition, it suppresses specular reflection almost perfectly in the wavelength range shown in this figure. From these results, gratings with $\Lambda=0.9$ μm are more preferable than those with $\Lambda=0.3$ μm for light trapping in thin-film Si solar cells.

BSRs with grating structures were fabricated by the following procedure. Electrochemically polished Al sheets are first anodically oxidized at a constant voltage in an electrolyte solution.[11,12] By the anodization, an Al_2O_3 film with pore arrays is formed on the Al surfaces. During the oxidation, a self-ordered dimple pattern is simultaneously formed on the Al surface beneath the Al_2O_3 film. The Al_2O_3 film is easily etched off with a mixture of chromium and phosphoric acid solutions, leaving a bare patterned Al substrate. In this work, patterned Al substrates with average dimple sizes, i.e., periods of $\Lambda=0.3$ and 0.9 μm, were prepared by anodization in a 2.6 wt % oxalic acid solution at 120 V[11] and in a 4 wt % citric acid solution at 370 V,[12] respectively.

n-i-p substrate-type μc-Si:H cells with an active area of 1 cm^2 were fabricated on the patterned Al substrates coated with a Ag/ZnO stacked film by conventional plasma-enhanced chemical vapor deposition. The structure of the solar cell consists of Al substrate/Ag(100 nm)/ZnO(40 nm)/μc-Si:H *n-i-p* layers/In_2O_3:Sn(75 nm)/Ag grid. The μc-Si:H *i*-layers with thicknesses of $t_i=0.5-4$ μm were deposited on the substrates using a SiH_4 and H_2 gas mixture ($SiH_4/H_2=10.5/380$ SCCM) (SCCM denotes cubic centimeter per minute at STP) at a substrate temperature of 170 °C, a pressure of 1.5 torr, and a rf power density of 0.04 W/cm^2. For comparison, *n-i-p* μc-Si:H cells were also fabricated on flat-glass/Ag/ZnO and textured-SnO_2(Asahi-U)/Ag/ZnO substrates in the same manner.

Figure 2 shows scanning electron microscope (SEM) images of Al surfaces obtained after the anodic oxidation process at (a) 120 and (b) 370 V and (c) Asahi-U type textured SnO_2 substrate. It can be seen in Figs. 2(a) and 2(b) that self-ordered dimple patterns with $\Lambda\sim0.3$ and 0.9 μm are uniformly formed on Al sheets by the anodic oxidation process. The average depths of the dimple patterns with $\Lambda\sim0.3$ and 0.9 μm are 0.05 and 0.2 μm, respectively.

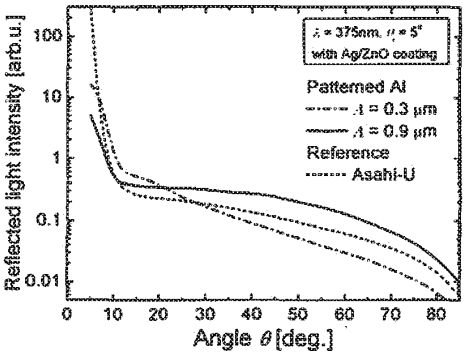


FIG. 3. Angular distribution of the reflected light from the patterned Al and Asahi-U substrates coated with a Ag/ZnO film stack at $\theta_i=5°$ and $\lambda=375$ nm.

Figure 3 shows the angular distribution of the reflected light intensities from the patterned Al and Asahi-U substrates with a Ag/ZnO coating. In this experiment, a laser beam with $\lambda=375$ nm was used as a light source and the incident angle was set near the normal ($\theta_i=5°$). It should be noted that the wavelength of $\lambda=375$ nm corresponds to NIR light ($\lambda\sim1.3$ μm) when propagating in μc-Si:H films because the refractive index is ~3.5. It can be seen from Fig. 3 that the patterned Al substrate with $\Lambda=0.9$ μm reflects the incident light at larger angles more effectively than that with $\Lambda=0.3$ μm. This result qualitatively agrees with Fig. 1, although any clear diffraction peaks are not observed due to insufficient long-range periodicity. The patterned Al substrate with $\Lambda=0.9$ μm also exhibits stronger reflection at larger angles compared to the Asahi-U substrate. This property is useful to increase the optical path length within the *i*-layer of μc-Si:H solar cells and enhance the total internal reflection at the interface between the μc-Si:H film and the transparent conductive oxide top electrode.

Figure 4 shows the external quantum efficiency (EQE) spectra of the μc-Si:H cells with $t_i=1.0$ μm fabricated on the flat, Asahi-U, and patterned Al substrates with $\Lambda=0.3$ and 0.9 μm. It can be seen in Fig. 4 that the patterned Al substrates enhance the EQE in the wavelength range from 0.6 to 1.1 μm compared to the flat substrate. In addition, this EQE gain is significantly improved by increasing Λ, as expected from Fig. 3. The patterned Al substrate with $\Lambda=0.9$ μm shows higher EQE than Asahi-U-type randomly textured substrate. The corresponding short circuit current densities J_{SC} of the flat, Asahi-U, and patterned Al with $\Lambda=0.3$ and 0.9 μm are 18.6, 22.5, 21.0, and 24.3 mA/cm^2, respectively.

Figure 5 shows the EQE ratios of the *n-i-p* μc-Si:H solar cells fabricated on the patterned Al substrate with $\Lambda=0.9$ μm to the Asahi-U substrate for *i*-layer thicknesses of $t_i=0.5-4$ μm. The EQE ratio increases almost monotonically with increasing wavelength in the NIR region. However, the EQE gain over the Asahi-U substrate becomes

SIONYX1403000041.0112

SAMSUNG EX. 1002 - 534/4148

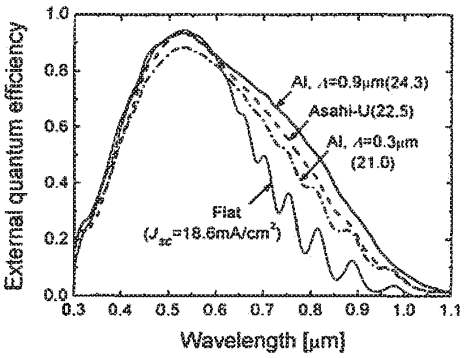


FIG. 4. EQE spectra of the *n-i-p* μc-Si:H solar cells with t_i=1 μm fabricated on a flat, Asahi-U, and the patterned Al substrates with Λ=0.3 and 0.9 μm measured under white bias light. The values in the brackets show the corresponding short circuit current densities.

smaller with increasing t_i because less of the incident light reaches the BSR of the cells. Nevertheless, as confirmed by Fig. 5, the patterned Al substrate clearly enhances the spectral response in the NIR region, even for the thickest cell with t_i=4 μm.

It is well known that textured substrates often deteriorate the open circuit voltage V_{OC} and the fill factor (FF) of thin-film Si solar cells. The characteristics of the several *n-i-p* μc-Si:H solar cells fabricated in this study are listed in Table I. In the case of t_i=0.5 μm, the cell on the Al substrate with Λ=0.9 μm shows the almost same V_{OC} and FF as the cell on the Asahi-U in spite of the large gain in J_{SC}. As a result, the cell efficiency is improved by using the patterned Al substrate. According to the previous report,[11] U-shaped texture is advantageous to avoid defect formation in the *i*-layer and deterioration of V_{OC} and FF in thin-film Si solar cells. The better performance of the 0.5-μm-thick cell on the Al substrate is attributable to this effect since the dimples on the Al substrate also have a quite smooth U-shape as shown in Fig. 1(b). Alternatively, in the case of t_i=2 μm, a larger decrease in V_{OC} and FF is observed for the cell fabricated on the Al substrate. This result suggests that defect formation occurs during the growth of thick *i*-layer. Further improvement of the overall cell performance can be realized by the optimization of the period, depth, and shape of the patterned

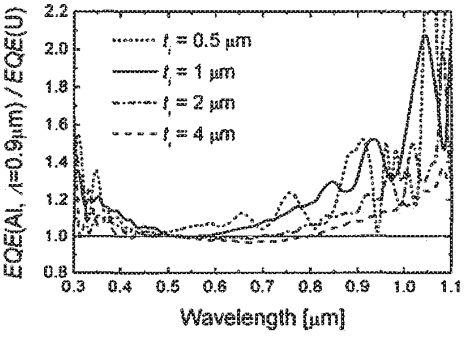


FIG. 5. EQE ratios of the *n-i-p* μc-Si:H solar cells fabricated on the patterned Al substrate with Λ=0.9 μm to the Asahi-U substrate for *i*-layer thicknesses of t_i=0.5–4 μm.

TABLE I. Characteristics of *n-i-p* μc-Si:H solar cells fabricated on the patterned Al with Λ=0.9 μm and Asahi-U substrates measured under AM 1.5 100 mW/cm² illumination.

Substrate	t_i (μm)	V_{OC} (V)	J_{SC} (mA/cm²)	FF	Efficiency (%)
Patterned Al	0.5	0.522	20.6	0.751	8.1
(Λ=0.9 μm)	2	0.491	26.2	0.670	8.6
	0.5	0.525	18.8	0.744	7.3
Asahi-U	2	0.518	25.2	0.697	9.1

Al substrates. In addition, modification of μc-Si:H deposition condition can be beneficial, although we used a constant deposition condition optimized for Asahi-U substrates in this study.

In summary, we have investigated the light trapping effect of periodically structured BSRs in thin-film Si solar cells. Numerical calculations quantitatively show that Ag gratings with Λ=0.9 μm can reflect NIR light at oblique angles efficiently. To demonstrate this effect, we have developed a BSR with a unique periodic dimple pattern by utilizing anodic oxidation of Al. It is found that *n-i-p* μc-Si:H cells fabricated on patterned Al substrates with Λ=0.9 μm exhibit an improved spectral response in the NIR region compared to those fabricated on randomly textured substrates. As a result, a high J_{SC} of 24.3 mA/cm² has been achieved in a 1-μm-thick μc-Si:H cell. In this study, we did not investigate the effect of the shape and depth of BSR structures in detail. Therefore we expect that there is a plenty of room to improve the light-trapping effect in thin-film Si solar cells.

The authors thank Dr. Koida and Dr. Turkevych of RCPVs in AIST for their help and advice in this work. This work was supported by New Energy and Industrial Technology Development Organization (NEDO) under Ministry of Economy, Trade and Industry (METI), Japan.

[1]J. Meier, S. Dubail, R. Platz, P. Torres, U. Kroll, J. A. Anna Selvan, N. Pellaton Vaucher Ch. Hof, D. Fischer, H. Keppner, R. Flückiger, A. Shah, V. Shklover, and K.-D. Ufert, Sol. Energy Mater. Sol. Cells **49**, 35 (1997).
[2]K. Yamamoto, T. Suzuki, M. Yoshimi, and A. Nakajima, Jpn. J. Appl. Phys., Part 2 **36**, L569 (1997).
[3]K. Sato, Y. Gotoh, Y. Wakayama, Y. Hayashi, K. Adachi, and H. Nishimura, Rep. Res. Lab. Asahi Glass Co., Ltd. **42**, 129 (1992).
[4]T. Matsui, M. Tsukiji, H. Saika, T. Toyama, and H. Okamoto, J. Non-Cryst. Solids **299**, 1152 (2002).
[5]M. Berginski, J. Hüpkes, M. Schulte, G. Schöpe, H. Stiebig, B. Rech, and M. Wuttig, J. Appl. Phys. **101**, 074903 (2007).
[6]T. Söderström, F.-J. Haug, V. Terrazzoni-Daudrix, and C. Ballif, J. Appl. Phys. **103**, 114509 (2008).
[7]N. Toyoma, R. Hayashi, Y. Sonoda, M. Iwata, Y. Yamamoto, H. Otoshi, K. Saito, and K. Ogawa, Proceedings of the Third World Conference on Photovoltaic Energy Conversion (IEEE, New York, 2003), p. 1601.
[8]C. Heine and R. H. Morf, Appl. Opt. **34**, 2476 (1995).
[9]H. Stiebig, N. Senoussaoui, C. Zahren, C. Hesse, and J. Müller, Prog. Photovoltaics **14**, 13 (2006).
[10]L. Zeng, Y. Yi, C. Hong, J. Liu, N. Feng, X. Duan, L. C. Kimerling, and B. A. Aramaria, Appl. Phys. Lett. **89**, 111111 (2006).
[11]W. Lee, R. Ji, U. Gösele, and K. Nielsch, Nat. Mater. **5**, 741 (2006).
[12]S. Z. Chu, K. Wada, S. Inoue, M. Isogai, Y. Katsuta, and A. Yasumori, J. Electrochem. Soc. **153**, B384 (2006).
[13]M. G. Moharam, Proc. SPIE **883**, 8 (1988).
[14]D. W. Lynch and D. W. Hunter, in *Optical Constants of Solids*, edited by E. D. Palik (Academic, Boston, 1985), pp. 350–357.
[15]D. E. Asnes, in *Properties of Crystalline Silicon*, edited by R. Hull (INSPEC, London, 1999), pp. 683–690.

SIONYX1403000041.0113

SAMSUNG EX. 1002 - 535/4148

C18

Whiskerlike structure growth on silicon exposed to ArF excimer laser irradiation

F. Sánchez,[a] J. L. Morenza, R. Aguiar, J. C. Delgado, and M. Varela
Universitat de Barcelona, Departament de Física Aplicada i Electrònica, Avda. Diagonal 647, E-08028 Barcelona, Spain

(Received 12 April 1996; accepted for publication 20 May 1996)

The effects of ArF excimer laser irradiation on silicon single crystals in air have been studied. The etch rate versus fluence curve shows three well defined zones, with very different etch rates and dependences. In the intermediate zone (from 1.5 to 2.5 J/cm^2), narrow (1–2 μm diameter) and tall columns (3–30 μm) start to grow after irradiation with some hundreds of laser pulses. These whiskerlike columns, with height between one and two orders of magnitude higher than the depth of the crater, have not been formed by preferential etching of the surrounding material, but through hydrodynamical processes. © *1996 American Institute of Physics.* [S0003-6951(96)01431-3]

Matter irradiation with a laser beam has been extensively studied because of its many useful applications. In the low laser fluence regime, material emission is limited, but surface target properties can be substantially altered. Applications in this regime include recrystallization, oxidation, doping, hardening, and smoothing. At high laser fluence levels, the target is ablated and a considerable amount of material is removed. Targets can be cut, patterned according to complicated geometries, and high quality films can be deposited from the ejected material.

After irradiation of a solid with a large number of laser pulses, surface is not usually flat, but important roughness can be found due to the formation of a distribution of cones. It is generally thought that there are microscopical local areas (impurities, different chemical composition) more resistant to ablation, and they are ablated more slowly than the surrounding material.[1] It is important to minimize cone formation when laser ablation is used as deposition technique because otherwise droplet emission is higher and deposition rate is lower.

Silicon is a material of great interest because of its important role in microelectronics. It has very high ultraviolet absorption coefficient and thermal conductivity. Its melting by laser radiation has been extensively studied.[2] However, information about surface modification and ablation at higher fluence levels is limited to a short number of papers.[3–5]

In this work we study the surface modification of silicon single crystals in air by ArF excimer laser irradiation. The laser generated 23 ns pulses at 193 nm. An 8×4 mm^2 mask was used in order to select the most homogeneous part of the beam. The mask was imaged with a lens system on Si(100) along the normal direction. The Si(100) targets were glued to a copper holder and vertically placed in an XYZ manipulator. Spots with dimensions around 0.5 mm were obtained. Laser fluences in the range 0.7–6 J/cm^2 were used in this study. The repetition rate was 5 Hz and the number of shots was changed between 1 and 4000. The energy was measured with a pyroelectric energy meter. Crater depth and roughness were determined by stylus profilometry, and surface morphology by scanning electron microscopy (SEM).

The etch rate per pulse has been calculated for craters formed by 200 laser pulses. Its dependence versus fluence has been plotted in Fig. 1. Three different zones can be distinguished, defined by two fluence thresholds of $F_1 \approx 1.5$ J/cm^2 and $F_2 \approx 2.5$ J/cm^2. In the first one, the etch depth is not measurable. In the intermediate one (fluences between F_1 and F_2) the etch rate is very low (below 2 nm/pulse), and an Arrhenius-type dependence is observed. In the third one the etch rate increases rapidly (at 2.8 J/cm^2 is already 20 nm/pulse) and follows the Beer–Lambert law.

Surface morphology in the irradiated area is clearly different in the three fluence ranges defined by F_1 and F_2. Although no etch depth is measured for $F < F_1$, the surface is noticeably modified after cumulative irradiation. In fact, the melting threshold[6] at 193 nm and 20 ns pulses is ≈0.4 J/cm^2, well below F_1. We observe clear melting signs after irradiation with some thousands of pulses at 0.7 J/cm^2, and ripples develop for fluences near F_1.

A deep crater is formed at fluences higher than F_2. The V shape profile and the accumulation of solidified material at the edges reveal the importance of melt flow in the process. Moreover, evaporation also occurs, as revealed by the debris

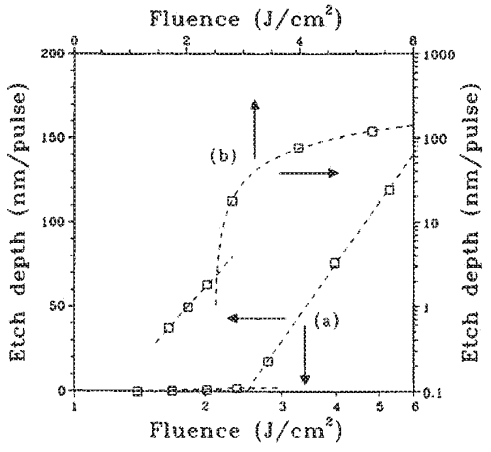


FIG. 1. Etch depth per pulse as a function of the laser fluence. (a) Linear-logarithmic plot, (b) logarithmic-linear plot.

[a]Electronic mail: fsanchez@electra.fae.ub.es

 0003-6951/96/69(5)/620/3/$10.00 © 1996 American Institute of Physics
Downloaded 11 May 2004 to 128.103.60.225. Redistribution subject to AIP license or copyright, see http://apl.aip.org/apl/copyright.jsp

SIONYX1403000042.0001

SAMSUNG EX. 1002 - 536/4148

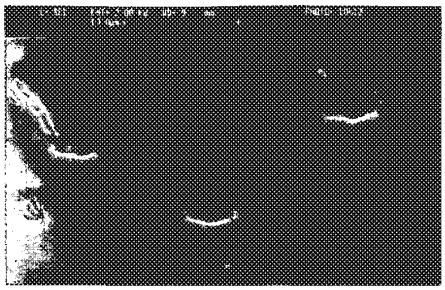


FIG. 2. SEM microphotograph of silicon irradiated at 1.7 J/cm^2 with 200 laser pulses (45° view).

around the crater formed by recondensation of evaporated material. Its spatial distribution on the surface is the same as that reported and modeled by Kelly *et al.* on the ablation of polymers.[7,8]

The most noticeable morphology modification occurs, however, at fluences between F_1 and F_2. The effect of the first 200–400 pulses is an increase of crater depth and roughness. Figure 2, which corresponds to the morphology of the silicon surface after irradiation with 200 pulses at 1.7 J/cm^2 shows the beginning of the roughening process. After roughness is high enough, columns start to grow on the surface. The resulting whiskerlike structure is shown in Fig. 3, which corresponds to a sample irradiated with 500 pulses at 1.7 J/cm^2. These columns, typically 1–2 μm in diameter and never below 1 μm, present an important dispersion in height and some of them are as high as 20–30 μm in a 0.3-μm-deep crater. Most of the columns have cylindrical or slightly conical shape. Some columns have more or less spherical drops on their tops, whose diameters are greater than the column one. They are mainly found on the shortest columns. There are also broken columns. In some cases this could be due to manipulation of the sample after irradiation, but in other cases clear signs of melt in the broken tip indicate that breaking was produced during irradiation. In contrast to cones and related structures extensively described in the literature, they have not been formed by preferential etching of the surrounding material, but have grown at the expense of the rest of material in the bottom of the crater.

Reported works including details of laser ablation of silicon have been carried out in vacuum. Van de Riet *et al.*[3] irradiated silicon with 308 nm and 3 and 6 J/cm^2. At the highest fluence a crater was formed, and resolidified silicon was accumulated at the edges. At the lowest fluence, the whole crater presented a dense cone structure and it was risen over to the nonirradiated area. Rothenberg and Kelly[4] irradiated silicon at 248 nm and found similar conical structures, which were attributed to cumulative thermal expansion. Silicon melt flow is the most important effect in these works as well as in our results, but there are important differences. We present narrow and tall columns, similar to whiskers, growing on isolated places of the irradiated area, instead of the dense cone structure in the globally elevated topography of the reported works.

According to Kelly and co-workers[4,9,10] the primary mechanisms which allow material removal when a target is

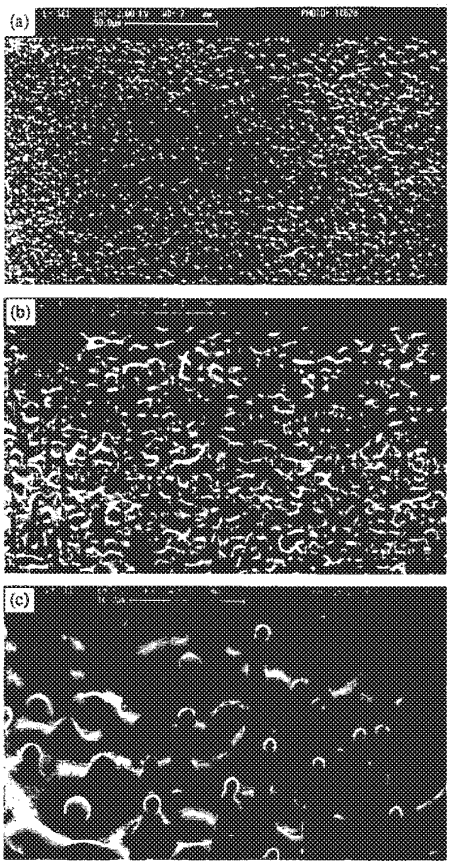


FIG. 3. SEM microphotographs of silicon irradiated at 1.7 J/cm^2 with 500 laser pulses. (a) A 10° view, (b) 45° view, (c) magnified view of (b).

irradiated with a pulsed laser can be divided into four groups: collisional, thermal, electronic, and thermomechanical (exfoliational, condensational and hydrodynamic). Hydrodynamical sputtering refers to the formation of asperities in the surface when the melting point is achieved, which evolve to droplets that are expelled.[10] These authors modeled the process and determined that only from a minimum radius could asperities develop and be expelled as droplets. The columns shown here seem to have been formed according to this mechanism, but it is important to remark that in contrast to other materials where asperities are expelled as droplets, silicon asperities keep on growing and even become columns. Direct application of hydrodynamical sputtering based models to our case is not easy, because we do not know the precise density of resolidified silicon and it is difficult to evaluate the temperature of a rough surface. However, qualitative agreement is found as far as only columns of diameter higher than a minimum value are observed.

As we pointed before, an interesting feature is the drop that most of the shortest columns have in their tops. Tall columns have a rounded top, but no drops with larger diameter than the column one. Therefore, drops have to be detached or progressively diffused in the columns with cumulative irradiation, in a similar way as cones produced by

Downloaded 11 May 2004 to 128.103.60.225. Redistribution subject to AIP license or copyright, see http://apl.aip.org/apl/copyright.jsp

SIONYX1403000042.0002

SAMSUNG EX. 1002 - 537/4148

ion-beam sputtering become columns by surface diffusion after annealing.[11] It should be noted that a pulse cannot melt the whole protuberance. The thermal diffusion length for a 23 ns pulse is ≈ 1 μm and the surface temperature will not be extremely high because fluence is moderate. According to modelization of Unamuno and Fogarassy,[2] melt depth can be estimated to be about 0.5 μm for fluences between 1.5 and 2 J/cm^2. Silicon flow will occur when the end of the column or the drop is melted after every pulse. As far as the walls are concerned, absorbed radiation is low. Only reflected radiation can reach the walls of cylindrical columns. If they have conical shape, direct radiation will also arrive, but in this case fluence will be diluted[12] to a very low value.

We have observed that the whiskerlike structure grows in air and only appears in relatively narrow ranges of fluence and number of pulses. There are no reported works about silicon laser irradiation in vacuum with a complete study of the effects of fluence and number of pulses, but in our preliminary studies on irradiation in vacuum we have only found results similar to the previously reported ones.[3–5] A comparative study of irradiation in air, vacuum, and nonreactive atmospheres is in progress in order to elucidate the possible influence of silicon oxide in the column growth process.

In summary, a laser induced whiskerlike structure on silicon has been found. To our knowledge, this kind of structure has not been reported after laser irradiation of any material. The columns appear in a well defined fluence range in the etch rate versus fluence curve, and they only start to develop after irradiation with some hundreds of laser pulses. Contrary to the well-known laser induced cones, these columns are not formed by preferential etching, but they grow and their height is between one and two orders of magnitude higher than the depth of the crater. Its formation is due to a hydrodynamical process, while evaporation is an effect of smaller order.

The authors acknowledge the collaboration of the Scientific and Technical Services of Universitat de Barcelona. We thank Dr. R. Fontarnau for his help in the SEM characterization. This work is a part of a research program financed by CICYT of the Spanish Government (Project No. MAT93-297) and Generalitat de Catalunya.

[1] S. R. Foltyn, in *Pulsed Laser Deposition of Thin Films*, edited by D. B. Chrisey and G. K. Hubler (Wiley, New York, 1994), pp. 89–113.
[2] S. Unamuno and E. Fogarassy, Appl. Surf. Sci. **36**, 1 (1989), and references therein.
[3] E. van de Riet, C. J. C. M. Nillesen, and J. Dieleman, J. Appl. Phys. **74**, 2008 (1983).
[4] J. E. Rothenberg and R. Kelly Nucl. Instrum. Methods B **1**, 291 (1985).
[5] G. B. Shinn, F. Steigerwald, H. Stiegler, F. K. Tittel, and W. L. Wilson, J. Vac. Sci. Technol. B **4**, 1273 (1986).
[6] F. Foulon, E. Fogarassy, A. Slaoui, C. Fuchs, S. Unamuno, and P. Siffert, Appl. Phys. A **45**, 361 (1988).
[7] R. Kelly, A. Miotello, B. Braren, and C. E. Otis, Appl. Phys. Lett. **60**, 2980 (1992).
[8] A. Miotello, R. Kelly, B. Braren, and C. E. Otis, Appl. Phys. Lett. **61**, 2784 (1992).
[9] R. Kelly, J. Cuomo, P. A. Leary, J. E. Rothenberg, B. E. Braren, and C. F. Aliotta, Nucl. Instrum. Methods B **9**, 329 (1985).
[10] R. Kelly and J. E. Rothenberg, Nucl. Instrum. Methods B **7/8**, 755 (1985).
[11] I. H. Wilson, J. Belson, and O. Auciello, in *Ion Bombardment Modification of Surfaces*, edited by O. Auciello and R. Kelly (Elsevier, Amsterdam, 1984), pp. 225–297.
[12] P. E. Dyer, S. D. Jenkins, and J. Sidhu, Appl. Phys. Lett. **49**, 453 (1986).

Downloaded¬11¬May¬2004¬to¬128.103.60.225.¬Redistribution¬subject¬to¬AIP¬license¬or¬copyright,¬see¬http://apl.aip.org/apl/copyright.jsp

SIONYX1403000042.0003

SAMSUNG EX. 1002 - 538/4148

C17

Appl. Phys. A 66, 83–86 (1998)

Applied Physics A
Materials
Science & Processing
© Springer-Verlag 1998

Dynamics of the hydrodynamical growth of columns on silicon exposed to ArF excimer-laser irradiation

F. Sánchez, J.L. Morenza, R. Aguiar, J.C. Delgado, M. Varela

Universitat de Barcelona, Departament de Física Aplicada i Electrònica, Avda. Diagonal 647, E-08028 Barcelona, Spain
(Fax: +34-3/402-1138, E-mail: fsanchez@electra.fae.ub.es)

Received: 6 January 1997/Accepted: 8 July 1997

Abstract. We present new results about the development of the whiskerlike structures that grow on silicon single crystals exposed in air to ArF excimer-laser irradiation. Small depressions appear on the surface after 100–200 laser pulses. With the next pulses, the size of these depressions increases, without change in depth, and new depressions are formed. At the end of this step the non-depressed regions are constricted and form a reticular network with a mesh size of some μm. With more pulses the material of the network tends to desert the branches and accumulate in the nodes, and discrete hillocks result. The hillocks progressively change their shape until tall columns are formed. Independent of this process, small protuberances appear on flat areas of the irradiated spot, initially in regions far from the center of the spot. These protuberances evolve to mushroom-type shapes, which remain much shorter than the columns.

PACS: 81.40 Z; 81.60 Z; 68.70

We have recently reported the development of a new type of whiskerlike columns formed on silicon single crystals upon pulsed laser irradiation in air at 193 nm [1]. The columns are tall and narrow, between 1 and 2 orders of magnitude taller than the depth of the crater, and are not formed by preferential etching as are the well-known cone structures that develop on ion- and laser-bombarded surfaces [2] but through an hydrodynamical growth process. The structure only appears in a narrow range of laser fluence, from 1.5 to 2.5 J/cm^2, and after irradiation with some hundreds of laser pulses. In order to investigate the evolution of the surface morphology that leads to the formation of the columns, we have prepared a new series of samples by changing the number of laser pulses. We report in this paper the obtained results showing the dynamics of the hydrodynamical growth leading to the formation of the columns.

1 Experimental

A Si(100) single crystal wafer was irradiated in air with a normally incident ArF excimer-laser beam. The laser generated 23 ns pulses at 193 nm. A mask was used in order to select the most homogeneous part of the beam. The Si(100) targets were mounted on a copper block with heat conducting glue and placed vertically in an XYZ manipulator. Rectangular spots with dimensions of 0.5 by 1.0 mm were obtained by imaging the mask with a lens system. The laser fluence was around 2 J/cm^2 in all experiments and the repetition rate was 5 Hz. The energy was measured with a pyroelectric energy meter. Spots were obtained with different numbers of pulses, between 25 and 1000. Crater depth was determined by stylus profilometry and surface morphology by scanning electron microscopy (SEM).

2 Results and discussion

After irradiation with up to 100 pulses, the whole area inside the spot is very flat. A crater is being formed, but etching rate is as low as ~ 1 nm per pulse. However, material is accumulated in the borders and frozen waves can be observed there (Fig. 1). The motion of silicon in radial direction is presumably produced by thermocapillarity as a consequence of differences in temperature and then in surface tension [3, 4]. Surface modification is mainly by melt flow. Although there is evaporation, as is indicated by debris outside the spot, its importance under this near-threshold irradiation is notably lower than at high fluences. Therefore, recoil vapour pressure from evaporating material is not expected to produce the very important effects on the liquid that could be produced at high fluences.

A target irradiated with 200 pulses maintains the same flatness in the central region of the spot, but around it micrometer-size depressions are clearly visible (Fig. 2a). The spatial distribution is not a consequence of the laser beam inhomogeneity but of the flow of melted silicon from the center

SIONYX1403000042.0004

SAMSUNG EX. 1002 - 539/4148

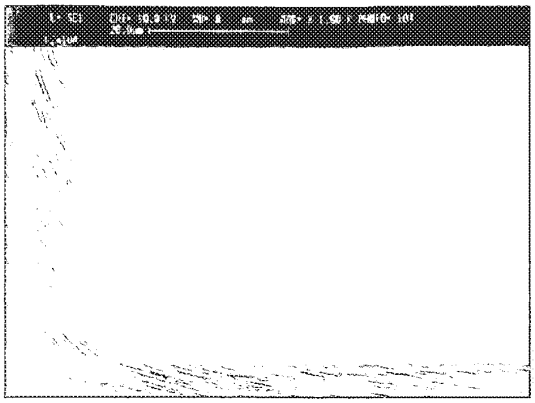


Fig. 1. SEM view (45°) of the corner of a spot originated by irradiation at 2 J/cm^2 with 25 pulses

to the borders of the spot after each pulse [5]. Morphology is very different after irradiation with 350 pulses (Fig. 2b), although the surface non-uniformity is maintained. From the center to the borders, we find successively some non-depressed areas with small depressions, broad depressions delimited by narrow non-depressed areas, which form a reticular network, then a network with broken branches, followed by isolated hillocks, and finally columns. After 500 pulses the target is fully covered with columns, as was shown in our previous work [1].

The appearance of the depressions only beyond the central region in Fig. 2a and the non-uniform morphology also observed in Fig. 2b suggests that the space evolution of the structure from the center toward the borders corresponds to the successive steps in the time evolution of the structure from the initial depressions until the final columns. Then we present in Fig. 3 a selection of localized SEM views ordered to show the growth process of the columns. At first, small micrometer-size depressions (Fig. 3a) on the flat surface appear after more than 100 hundred pulses. With more pulses, the depressions that were formed increase in area (Fig. 3b) but not significantly in depth. Simultaneously, other depressions appear and the result is the constriction of the non-depressed area and the formation of an elevated reticular network with a mesh size of some micrometers (Fig. 3c). The original surface is no longer identifiable and a quite flat new one is present in the inner part of the polygons defined by the network (Fig. 3c). With additional pulses, the material of the network tends to desert the branches and accumulate in the nodes. As a consequence of this process the branches become slim and break, and isolated hillocks are formed (Fig. 3d). When irradiation continues, material in these hillocks goes up and the structure becomes columnar (Fig. 3e). This process is gradual and the initial conical shape evolves to a cylindrical one after more pulses (Fig. 3f). Tall columns result with diameters between 1 and 2 μm, whose height can increase as fast as 15 μm in 100 pulses. If the sample is further irradiated these columns gather liquid silicon and they grow to as much as 50 μm, but some of them are tilted or show no well-defined cylindrical shapes. Simultaneously, the roughness of the surface around the columns increases.

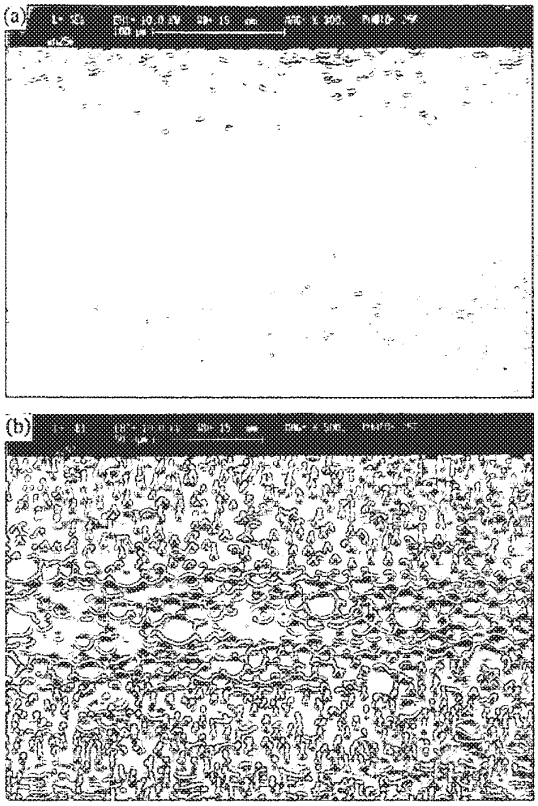


Fig. 2a,b. Low magnification SEM views (45°) of surface morphology after irradiation at 2 J/cm^2 with (a) 200 pulses, and (b) 350 pulses

It is to be noted that depressions start to appear only after more than 100 pulses. The physical processes originated by these first pulses that will lead to the final morphology are determined by the optical and thermal parameters of silicon, and by the fact that irradiation is done in air. The absorption coefficient of silicon is very high at 193 nm (higher than 10^6 cm^{-1}) [6]. Radiation is absorbed in a thin layer of less than 10 nm and heat diffuses toward the bulk (thermal diffusion length for a 23 ns pulse is ≈ 1 μm) [7]. Melting of silicon by pulsed lasers has been widely studied, and the melting depth and melting duration are estimated to be 0.4–0.7 μm and 100–200 ns, respectively, for a laser beam of wavelength, pulse duration, and fluence as we used [7]. Liquid silicon is more dense (2.52 g/cm^3) than solid silicon (2.32 g/cm^3), so the liquid will go up as the solid-liquid interface advances during solidification (the volume of the solidified layer is bigger and the volume expansion during the short time of the solidification will result in an ascendent force on the not yet solidified liquid top layer). A possible explanation for the existence of the depressions is that the solid-liquid interface would not be flat, but the liquid layer will be thinner in small areas than in the rest. When solidification takes place, the solid-liquid interface would reach the surface first in these small areas. The later solidification and expansion of the surrounding region would lead to its raising over the firstly so-

SIONYX1403000042.0005

SAMSUNG EX. 1002 - 540/4148

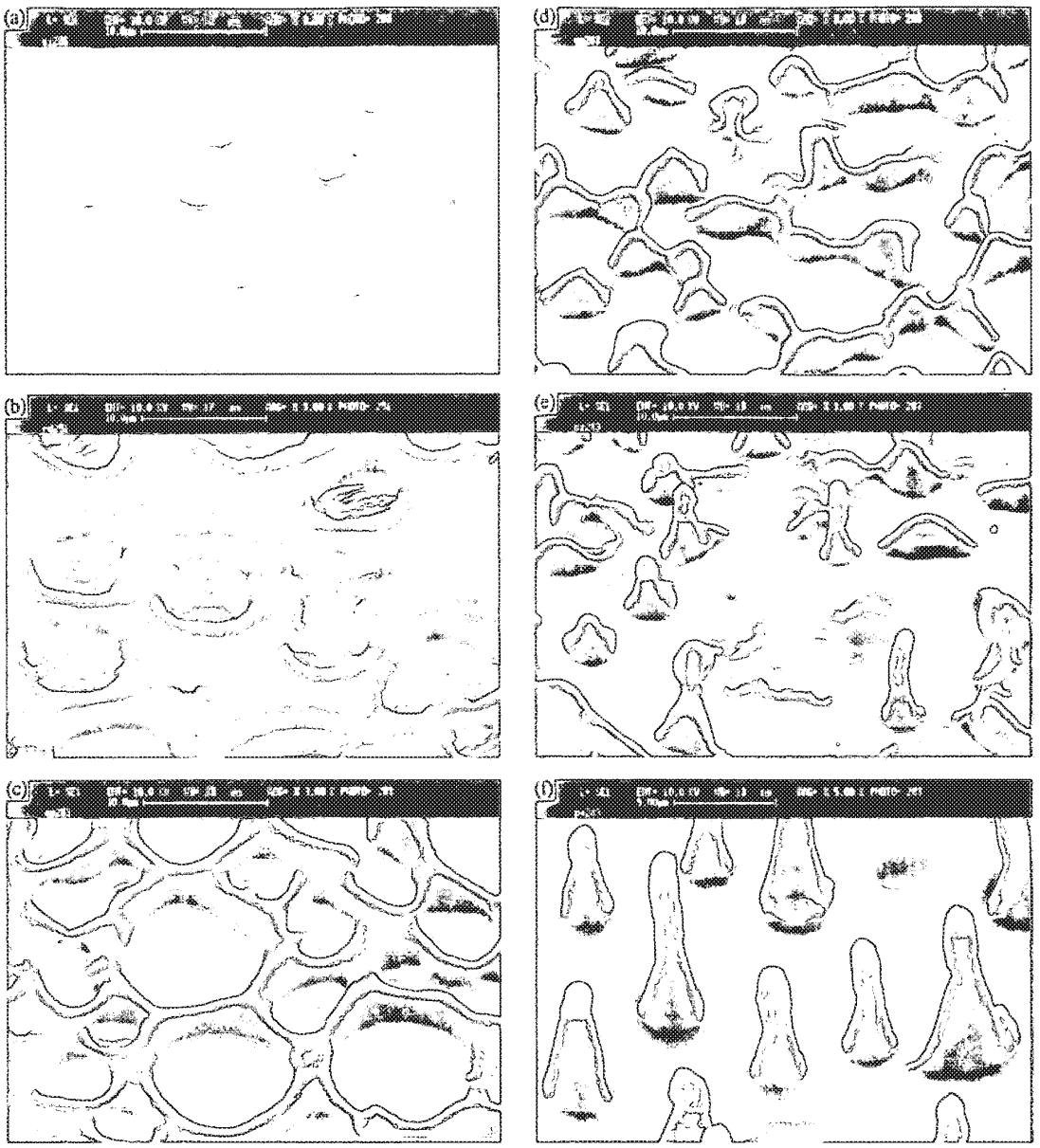


Fig. 3. Selection of localized SEM views (45°) showing the evolution of the surface from the initial depressions (a) to the final columns (f) (note that magnification of (f) is higher). Fluence was 2 J/cm^2

lidified area and would also explain the convex shape of the depression borders. A schema of the process is displayed in Fig. 4. The nonflat solid-liquid horizontal interface has not a clear origin at this moment but is consistent with the time-resolved reflectivity results reported by others authors [8, 9], which conclude that, close to the melting threshold, melting is inhomogeneous and solid and liquid phases coexist in the surface. In our experiments, the fluences at which the depressions appear are twice or more the melting threshold, so a liquid layer with a non-flat solid-liquid interface is to be expected more than locally melted zones. Local melting and then material expansion during solidification due to the density decrease has been involved by several authors [10, 11] to explain the formation of emergent structures in laser-

SIONYX1403000042.0006

SAMSUNG EX. 1002 - 541/4148

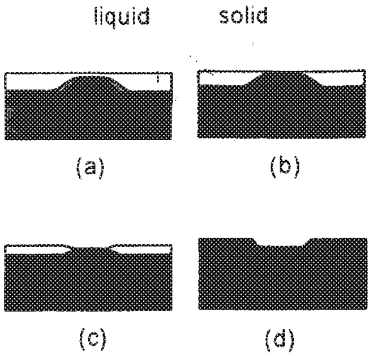


Fig. 4. Schema of the solidification process supposing a non-flat liquid-solid interface

irradiated germanium (liquid is denser than solid, as with silicon). In a similar way, if we would consider local unmelting (i.e., the existence of local areas in which melting did not occur), and/or that the solid-liquid interface was locally shallower, the analogous processes would lead to depressions, as we have observed. With additional pulses, the depressions would solidify first because the solid-liquid interface is deeper there than in the rest of the spot, and the depression borders are less efficiently heated. In addition to the initial depression formation, the later evolution from the reticular network to hillocks first and, finally, to tall columns is also noticeable. In these steps, thermocapillary flow toward the hillocks and columns, due to the non-uniform temperature in the modified surface, and ascendent forces led by the expansion of the material during solidification will determine the growth of the columns. A detailed analysis of these processes is beyond the scope of this paper.

Besides the described columns, a second kind of structure grows out from the surface (Fig. 5). This structure has a shape similar to that found by Kelly et al. [12] after laser irradiation of gold. It starts not as depressions but as small protuberances (Fig. 5a), which appear on flat places of the spot and go up, leading to mushroom-type shapes (Fig. 5b). "Mushrooms" appear first near the spot border after 50–100 pulses, and they can be found in the whole spot area after about 1000 pulses. "Mushrooms" have a shape similar to that of columns that start to develop, but "mushrooms" appear with less pulses and in a different zone of the irradiated spot that columns. They appear from emerging material in isolated points. They progressively increase in number, but their height scarcely increases, and they do not evolve into columns. "Mushrooms" are thus different than columns and have a different formation process, but more work will be necessary to have a better knowledge of them.

3 Conclusion

The new whiskerlike columns structure on silicon originated upon ArF excimer-laser irradiation in air is formed through hydrodynamic processes, and material expansion during solidification is at the origin of the process that leads to the final shapes. The evolution with progressive irradiation successively shows small depressions, broad depressions, which constitute the meshes of a reticular network, a broken network, isolated hillocks, and tall columns. In addition to this process, small protuberances appear on flat areas and they evolve to have a mushroom shape.

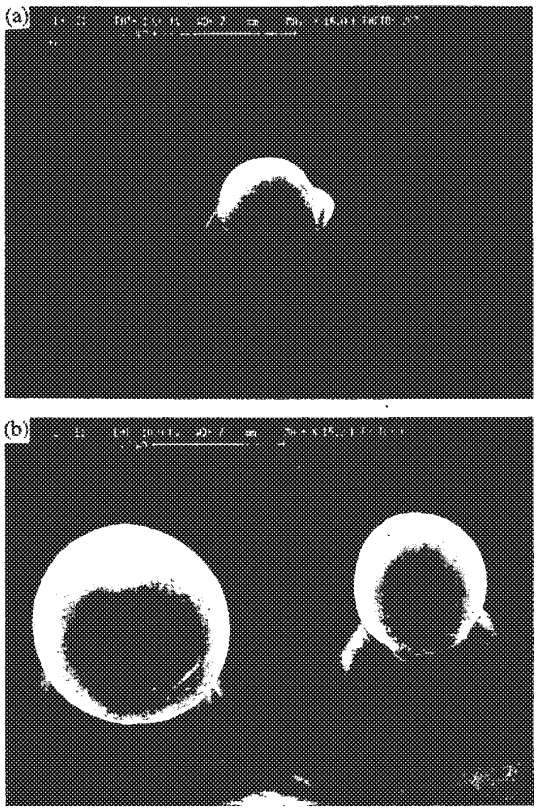


Fig. 5. Mushroom-type structures in different stages of formation after irradiation at 2 J/cm^2 (SEM view 45°)

Acknowledgements. The authors acknowledge the collaboration of the Scientific and Technical Services of Universitat de Barcelona. This work is a part of a research program financed by CICYT of the Spanish Government (Project MAT96-91 1) and DGR of the Catalan Government.

References

1. F. Sánchez, J.L. Morenza, R. Aguiar, J.C. Delgado, M. Varela: Appl. Phys. Lett. 69, 620 (1996)
2. R. Kelly, A. Miotello: In *Pulsed Laser Deposition of Thin Films*, D.B. Chrisey, G.K. Hubler, eds. (Wiley, New York 1994), pp. 55–88
3. M. von Allmen: *Laser-Beam Interactions with Materials*, (Springer, Berlin 1987)
4. V. Yu. Baladin, D. Otte, O. Bostanjoglo: J. Appl. Phys. 78, 2037 (1995)
5. F. Sánchez et al., (unpublished)
6. H.R. Phillip, H. Ehrenheit: Phys. Rev. 129, 1550 (1963)
7. S. Unamuno, E. Fogarassy: Appl. Surf. Sci. 36, 1 (1989)
8. G.E. Jellison, D.H. Lowndes, D.N. Mashburn, R.F. Wolf, Phys. Rev. B 34, 2407 (1986)
9. J. Solis, C.N. Afonso: J. Appl. Phys. 69, 2105 (1991)
10. L.J. Willis, D.C. Emmony: Opt. Laser Technol. 7, 222 (1975)
11. J.F. Young, J.E. Sipe, H.M. van Driel: Phys. Rev. B 30, 2001 (1984)
12. R. Kelly, J.J. Cuomo, P.A. Leary, J.E. Rothenberg, B.E. Braren, C.F. Aliotta: Nucl. Instrum. Methods B 9, 329 (1985)

SIONYX1403000042.0007

SAMSUNG EX. 1002 - 542/4148

Invited Paper

Femtosecond laser for black silicon and photovoltaic cells

T. Sarnet*[a], M. Halbwax[d], R. Torres[a], P. Delaporte[a], M. Sentis[a], S. Martinuzzi[c],
V. Vervisch[b], F. Torregrosa[b], H. Etienne[b], L. Roux[b], S. Bastide[d]
[a]LP3 CNRS UMR 6182 Luminy, Case 917, 13009 Marseille, France
[b]IBS, ZI Peynier Rousset - Rue Gaston Imbert Prolongée - 13790 Peynier, France
[c]TECSEN CNRS UMR 6122, Av. Esc. Normandie Niemen, 13397 Marseille CEDEX 20, France
[d]ICMPE, CNRS UMR 7182, 2-8 rue Henri Dunant, 94320 Thiais, France

ABSTRACT

We have prepared absorbing structures for photovoltaic cells with different nano-texturization, obtained by means of a femtosecond laser, without the use of corrosive gas (i.e. under vacuum). To take in account the 3D structured front surface, the emitter doping has been realized by using Plasma Immersion Ion Implantation (so-called PULSION). The results show a photocurrent increase up to 60 % in the laser texturized zones.

Keywords: nanotexturization, black silicon, photovoltaics, photocurrent, femtosecond laser, plasma immersion doping

1. INTRODUCTION

In order to increase the efficiency of actual solar cells many different ways are currently being developed by researchers. They include the nano and micro-structuration of the surface [1-8], the use of antireflection (AR) coatings [9], rear totally diffused structures [10], or the use of absorbing nanoparticles [11].

It has been recently shown (Mazur *et al*) [1-7] that a simple way to improve the silicon-based solar cell efficiency is to irradiate the silicon surface with a series of femtosecond laser pulses, in the presence of a sulfur containing gas [1-7]. This produces micro-spikes on the silicon surface that strongly reduces the incident solar light reflection (Black Silicon). We have in this study created a photovoltaic structure in a silicon wafer, which the illuminated surface was locally nanostructured (squares of $1mm^2$) using a femtosecond laser, before the formation of p-n junction. Various parameters, like polarization, spot size, energy density, number of shots, scanning parameters were chosen to make an appropriate nanotexturization without SF_6, i.e. the laser treatment was performed under vacuum (10^{-5} mbar).

Once the optical properties have been optimized it is important to realize an efficient p-n junction. Therefore a counterdoping of the wafer surface has been obtained by means of the Plasma Immersion Technique (PULSION tool, developed by IBS [11]) followed by Rapid Thermal Annealing (RTA). This new doping technique has been compared to a more traditional ion implantation followed by thermal annealing. The results show the consequence of the junction quality on the final photocurrent.

It will be shown that the photocurrent can be increased up to 60 % in the texturized areas.

2. EXPERIMENTS

2.1 Processing steps

Samples were n-type silicon doped phosphorus to 10^{15} cm^{-3} (5-20 ohms.cm), cleaned by means of the conventional RCA treatment. The surfaces were first phosphorus diffused from a $POCl_3$ source in order to create a n+ layer which helps the formation of a back ohmic contact , while the n+ front layer was chemically removed (CP_4 etch) before the laser treatment.

*sarnet@lp3.univ-mrs.fr ; phone +(33) 4 91 82 95 12; fax +(33) 4 91 82 92 89; http://www.lp3.univ-mrs.fr

Commercial and Biomedical Applications of Ultrafast Lasers VIII, edited by Joseph Neev, Stefan Nolte, Alexander Heisterkamp, Christopher B. Schaffer, Proc. of SPIE Vol. 6881, 688119, (2008) · 0277-786X/08/$18 · doi: 10.1117/12.768516

SIONYX1403000042.0008

SAMSUNG EX. 1002 - 543/4148

After the laser structuring of the surface, the samples have been boron implanted by Plasma Immersion (PULSION, BF_3, 2 kV, 900 °C, 30 mn) and RTA annealed. The junction depth in that case should be about 150 nm, which is much shallower than the 3D laser structures: therefore the junction follows the topography of the structures.

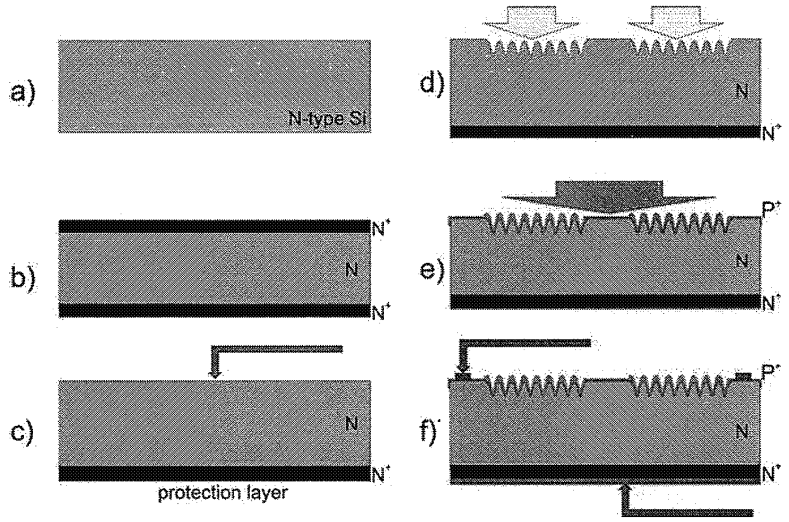


Fig. 1: Processing steps of the photocell: a) RCA cleaning, b) creation of n + layer by diffusion, c) removal of the front n+ layer, d) femtosecond laser structuring, e) plasma immersion implantation (PIII) + rapid thermal annealing (RTA), f) metallization of contact

After realizing the p-n junction, the electrical contacts have been deposited by electron gun evaporation: a silver layer on the back side and one aluminum pad on the front non texturized surface, as shown in Fig. 1. A light-beam induced current LBIC mapping tool is used to detect the increase of the photocurrent in the texturized areas by comparison with the standard surface. This mapping tool was conceived to detect a photocurrent contrast in polycrystalline silicon between defect containing and defect free regions, giving rise to electrical image of defects [12]. In our samples it indicates directly if the photocurrent is increased below the nanotexturized areas. The photocurrent produced by a light spot (λ>800 nm), 20µm in diameter, is measured outside and inside the texturized regions, in order to evaluate the enhancement really due to the increase of the light transmission in the wafer bulk. Some samples have also been prepared using a more traditional technique using an ion implantation followed by thermal annealing, in order to highlight the influence of the junction quality on the final photocurrent.

2.2 Laser experimental set-up

The laser engraving of Si (001) was carried out in a vacuum system with a pressure of $5x10^{-5}$ to $1x10^{-5}$ mbar. This low pressure considerably reduces the redeposition of unwanted debris from the laser ablation process.

The optical set-up that was used to deliver the laser beam to the sample surface is presented in Fig. 2. The micromachining experiments was performed using a Ti:sapphire laser (Hurricane model, Spectra-Physics) at 800 nm, 500 µJ energy, 1 kHz repetition rate and a laser pulse duration of 100 fs. To get a more uniform laser energy distribution, only the center part of the gaussian laser beam was selected using a square mask (D) of 2 x 2 mm^2. A spot of about 30 x 30 μm^2 area was obtained by projecting the mask image onto the sample surface with a planoconvex lens (f' 50 mm). The laser beam was perpendicular to the sample surface. A computer-controlled XY-stage (for the sample) and Z-stage (for the objective lens) has allowed precise positioning of the spot on the surface sample. The laser energy that was delivered to the sample surface could be attenuated by using a combination of analyzer (A) and polarizer (P) and completed by a set of neutral density filters (NDF). A PC controlled the analyzer rotation, the opening and closing of

SIONYX1403000042.0009

SAMSUNG EX. 1002 - 544/4148

shutter (S) placed in front of the polarizer, and the XYZ stages. The engraving results are *in situ* monitored by a CCD camera.

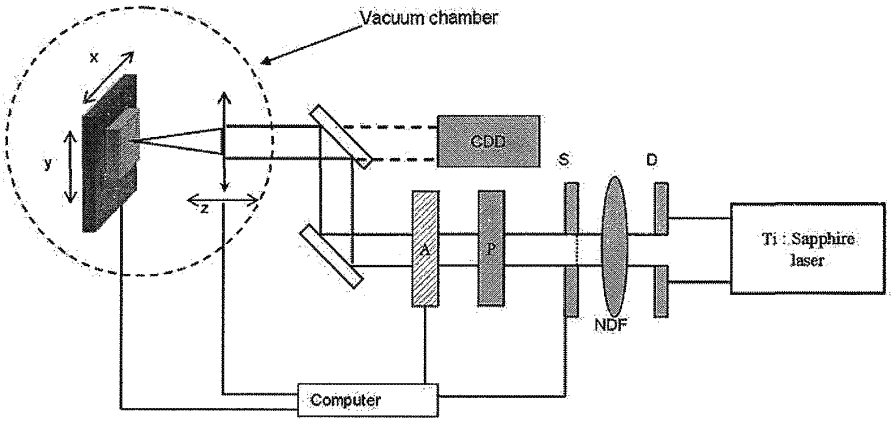


Fig. 2 : diagram of the femtosecond laser experimental set-up.

Different square surfaces have been irradiated, ranging from 100x100 μm^2 to 1x1 mm^2. The laser-induced structuring of the sample surfaces was produced by scanning a simple straight line (30 µm width) at a speed-velocity of 150 µm/s (maximum speed of our stages), with a d shift between the parallel scans to treat the whole surface. The role of the beam overlaps on the formed structures was analyzed by varying the distance d between the scans. The d value was changed between 1 and 15 µm. The experiments were carried out at different laser fluences: between 140 and 850 mJ/cm^2.

The laser spot displacement was perpendicular to the polarization. When scanning a single square spot (size a) using a laser frequency (f) and a scanning speed (V), with a displacement (D) between the parallel scan, the number of shots (N) received anywhere on the surface (except on the edges) can be defined as:

$$N = \frac{a^2 \cdot f}{V.D}$$

In our experimental conditions (f=1 kHz, a=30 µm, V=150 µm/s) the different displacements we used D = 1, 2, 5, 10 and 15 µm correspond to N= 6000, 3000, 1200, 600 and 400 shots respectively.

2.3 Experimental Results

Nano and microstructuring of a silicon surface with a pulsed laser (from nanosecond to femtosecond) generally induces the formation of typical wave-like structures (LIPSS, capillary waves, ripples etc...) which have been studied for decades [13]. In this study, the surface topography of these structures was characterized using Scanning Electron Microscopy (SEM) and Optical Microscopy (OM) in dark field mode.

Figure 3 shows different types of structures: the left part is the original Si surface, the center part is formed by capillary waves and the right part features "beads" that are formed with higher number of pulses and energy density. The periodicity of the capillary waves (center) is usually close to the laser wavelength (800 nm), they are formed by the interference between the incident beam and the light scattered by minor surface defects. Ablation and melt formation occur at non-uniform depths: after resolidification, the ripple structure is frozen in place and acts as a precursor for the formation of beads, cones and spikes.

SIONYX1403000042.0010

SAMSUNG EX. 1002 - 545/4148

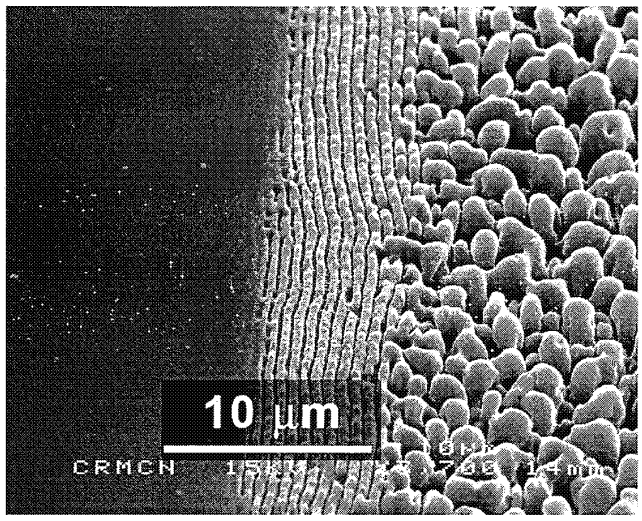


Fig. 3: SEM photo of Laser Induded Periodic Surface Structures (LIPSS): capillary waves (periodicity 800 nm, center) and beads (about 2 µm, right).

For higher energy densities and number of pulses those capillary waves tend to collapse to form a more hydrodynamically stable structure, like the beads observed in Figure 3 (right part). The absorption of light on these beads is not uniform: the ablation is maximized in the valley between the beads which tends to amplify the phenomena and creates more erected structures ("penguin-like" structures), when increasing the energy density and the number of laser pulses.

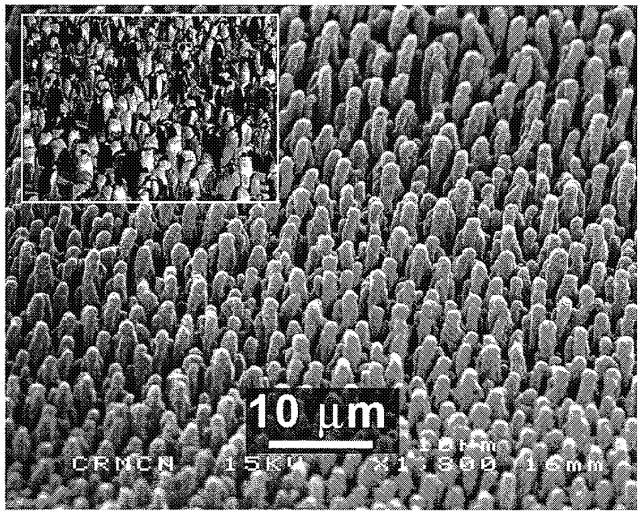


Fig. 4: SEM photo of penguin-like structures created by femtosecond laser (top left corner is a picture of a real penguin colony in Antartica) .

Without using SF_6 gas we did not observe spikes, but rather rounded structures, like those shown in Figure 4: these "penguin-like" structures have been named from their similarity with colonies of penguins *(Aptenodytes forsteri)* when

SIONYX1403000042.0011

SAMSUNG EX. 1002 - 546/4148

they spread over the antarctic ice, standing next to each other. The height of these structures is approximately 10 μm, with a spacing of 2 to 5 μm, as measured by SEM. These structures tend to trap the incident light by decreasing the amount of specular (mirror-like) and diffuse reflections. Simple optical simulations of the surface properties have been performed using a commercial ray-tracing renderer (Autodesk 3ds Max).

Computer-Generated Images (CGI) are usually used for visual effects (movies, videogames, architecture, simulation...): although they are not always accurate but they include many user-defined physical parameters (optical, particles...) that lead to photorealistic images. For instance, this simulation takes into account the multiple reflections on the silicon structures, as well as the transmission and absorption as a function of the incident wavelength. The resulting images allow to observe the amount of light reflection on the structured surfaces in the visible spectral range.

We have 3D modeled different types of structures like spikes, penguin-like structures and pyramids like the one obtained by KOH anisotropic etching. After the optical simulation, the best structures seem to be the spikes, immediately followed by the penguin-like structures, in terms of light absorption: they look darker than the other structures on the simulation (Figures 5 and 6).

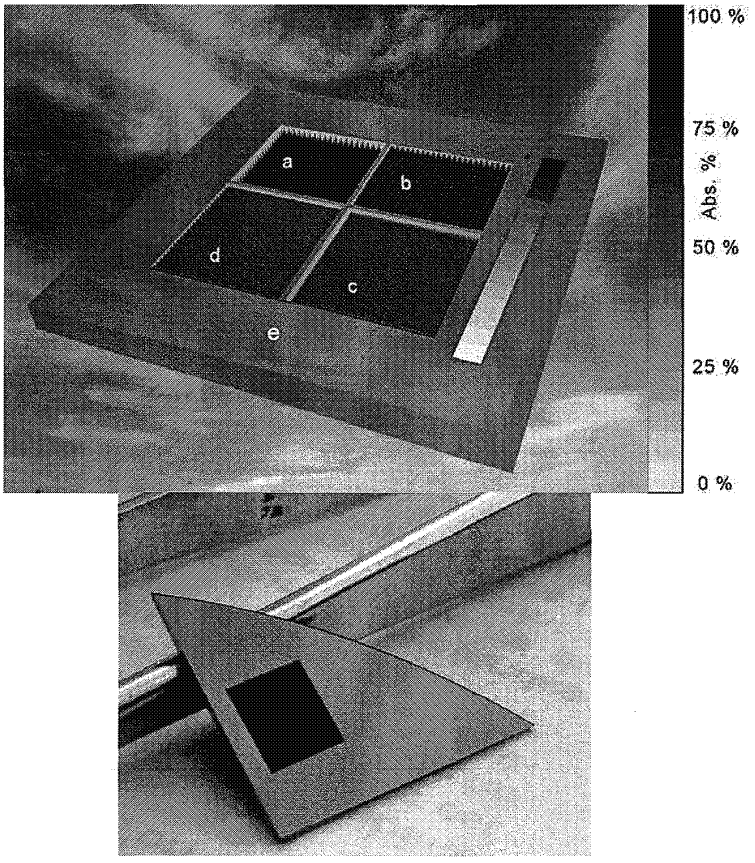


Fig. 5: **top:** 3D optical simulation of the optical absorption/reflectivity of a silicon surface with different texturizations: spikes b) "penguin-like" texturization c) pillars d) KOH pyramids e) flat;

bottom : real sample of a laser structured silicon (penguin-like).

The pyramids like the one created by anisotropic etching, which are used nowadays on "high efficient" commercial photocells do not appear to be as absorbent as spikes or penguin-like structures. Moreover, these structures need to be

SIONYX1403000042.0012

SAMSUNG EX. 1002 - 547/4148

coated (ARC) and are very dependent of the crystal orientation, which is a disadvantage on multi-crystalline silicon, in comparison with the laser structuration which is not sensitive to the different grains orientation.

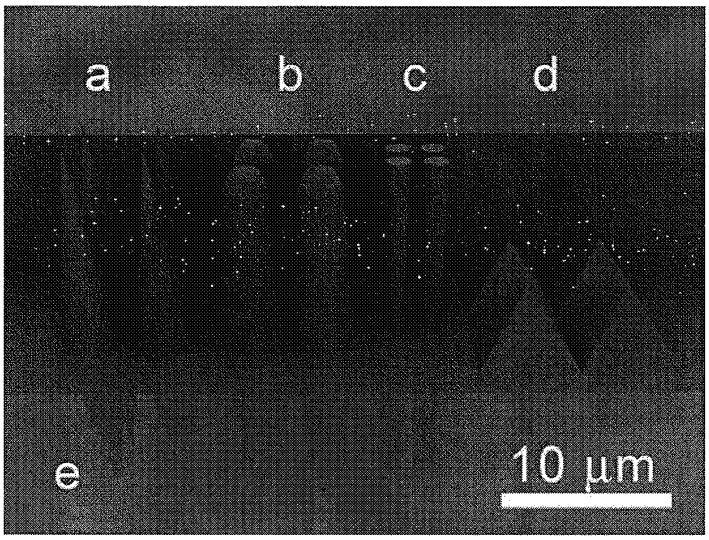


Fig. 6: Detail of the structures used for the 3D optical simulation:

a) spikes b) "penguin-like" texturization c) pillars d) KOH pyramids e) flat.

The different structures used for the simulation are described in Table 1 and shown in Figure 6.

Table 1 : properties of the structures used for the optical simulation (see also Fig. 6).

Structure	height (µm)	FWHM diameter (µm)	spacing (µm)	Reflectivity R (%) Visible	Absorption A (%) Vis.
Spikes (a)	10	2.5	4	6	94
Penguin-like (b)	10	2.5	4	9	91
Pillars (c)	10	1.5	2	21	79
Pyramids (d)	5	2.5	4	27	73
Flat (e)	-	-	-	35	65

Experimental characterization of the real spectral absorption of the laser created structures has been performed inside an integrating sphere and compared to other texturizations. The reflected (R) and transmitted (T) light from a monochromator has been collected: the effective absorption (or absorptance A=1-R-T) was determined from these values and confirms the optical simulation: absorption is very high (90 % +) and quite flat in a wide spectral range (350-1000 nm).

Figure 7 shows the absorptance of a reference silicon surface after polishing and after different texturizations (acidic, alkaline and laser). Compared to the other techniques the laser texturization is obviously much more efficient and seems to be even better when going to the short wavelength (visible below 600 nm and down to the UV range), which can be an advantage for space applications.

SIONYX1403000042.0013

SAMSUNG EX. 1002 - 548/4148

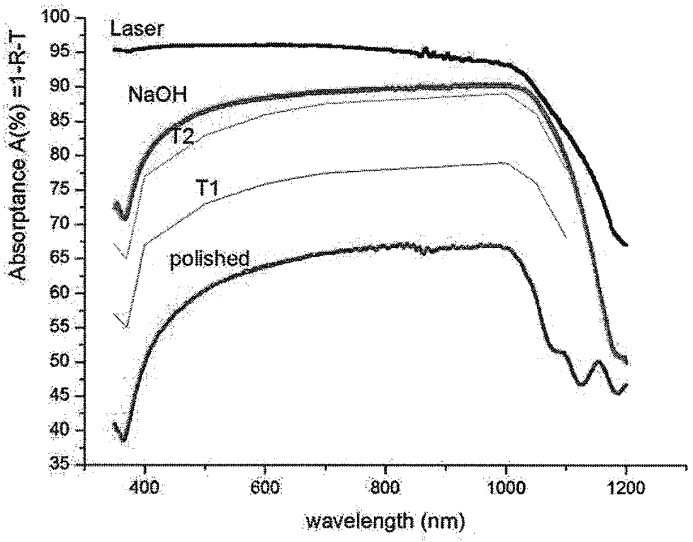


Fig. 7: Absorptance of a silicon surface for different texturizations: laser texturing (850 mJ/cm^2, black silicon), alkaline texturing (NaOH), acidic etching (T1 is an industrial process and T2 is from reference [15]), compared to a Si polished sample.

Figure 8 shows the topography obtained with a commercial alkaline texturization ("high-efficiency" 18 % solar cell) compared to the laser created topography: the pyramids created by the chemical etching are smaller (less erected) than the black silicon which explain the smaller absorptance on the surface.

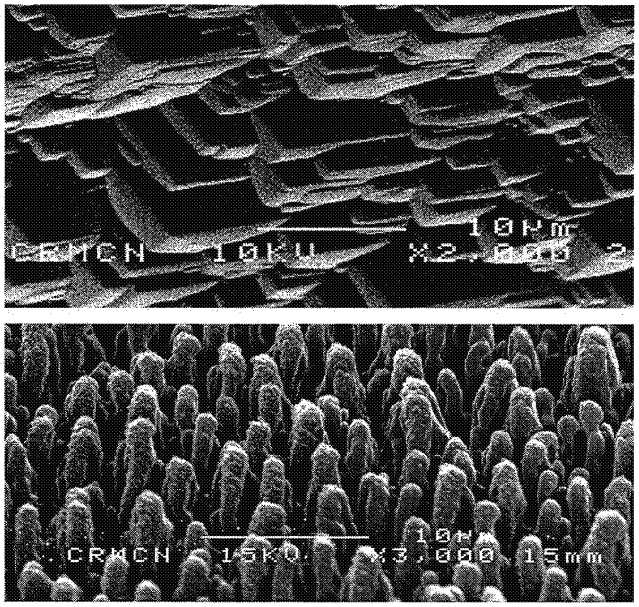


Fig. 8: SEM photo of an alkaline texturization (top) showing pyramids and a laser texturization (bottom) with erected structures, tilt 50 °, same magnification.

SIONYX1403000042.0014

SAMSUNG EX. 1002 - 549/4148

Moreover the alkaline chemical etching is usually highly anisotropic and therefore depends on the crystal orientation. When working with multi-crystalline silicon (mc-Si) it creates different type and size of structures for each grain which leads to different optical absorption: this disadvantage is illustrated in Figure 9.

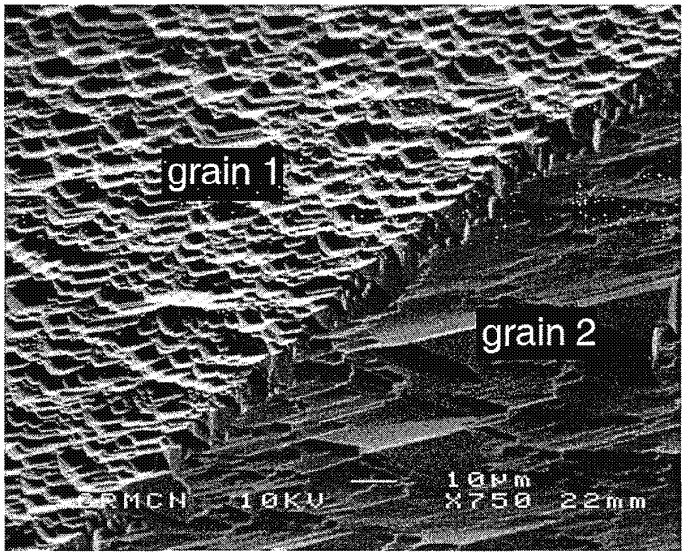


Fig. 9 : Anisotropic etching of a mc-Si surface: different structure for each grain

Figure 10 is a general view of a laser structured area (SEM) which shows a good homogeneity of the topography, for F= 185 mJ/cm^2 and D = 1µm. When increasing D to higher values (D>15 µm) the homogeneity is not as good: the lack of overlaps (i.e. number of pulses) tends to create a mixture of capillary waves and beads. Also, working with smaller fluence or number of pulses advantages the formation of capillary waves instead of beads and cones.

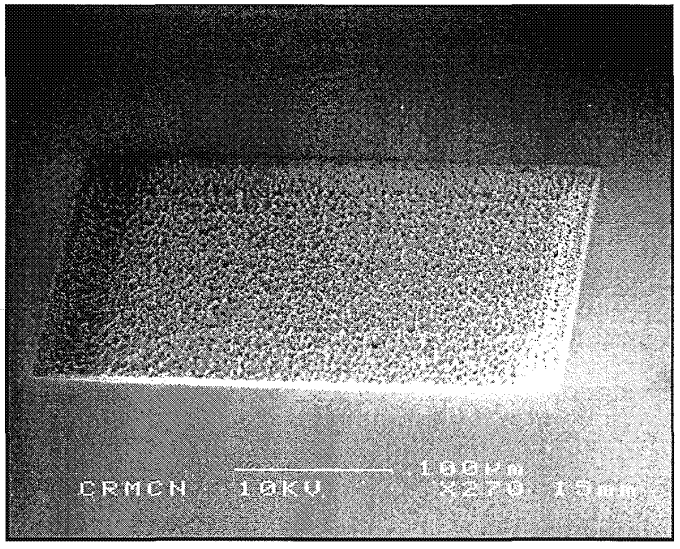


Fig. 10: SEM photo of a laser micro-structured area of a photo cell. Size of the treated zone is 300 µm^2, spot size a= 30 µm, F= 185 mJ/cm^2, D= 1µm, scanning speed V= 150 µm/s.

SIONYX1403000042.0015

SAMSUNG EX. 1002 - 550/4148

The influence of the laser fluence is shown in Figure 11: different samples have been laser treated with fluences F between 250 and 850 mJ/cm^2, the other parameters were kept constant (f= 1 kHz, a= 30 μm, V= 150 μm/s, D= 10 μm). We observed an increase in the absorptance from 65 % to 80 % at 250 mJ/cm^2, up to 96 % when working at higher energy density (F=850 mJ/cm^2).

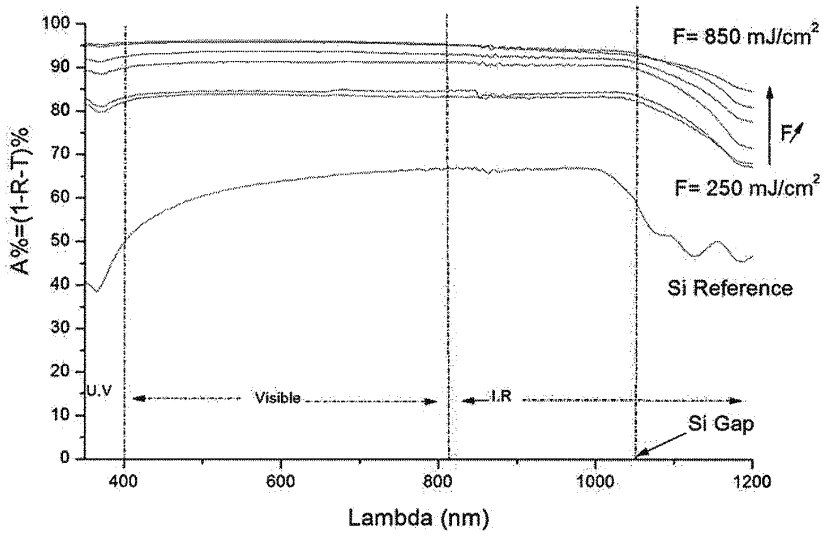


Fig. 11: Absorptance of a silicon surface for different laser fluences: from 250 mJ/cm^2 to 850 mJ/cm^2, compared to a Si polished sample.

This increase in the absorptance is clearly related to the change of topography in terms of structure size, diameter and spacing between the erected structures. The evolution of the topography with different fluences is shown by the SEM photos in Figure 12.

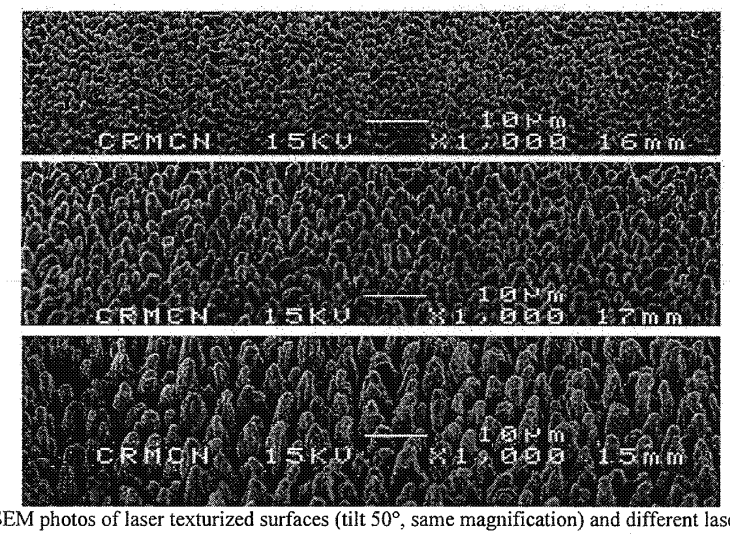


Fig. 12: SEM photos of laser texturized surfaces (tilt 50°, same magnification) and different laser fluences: Top: 250 mJ/cm^2, center : 400 mJ/cm^2, down : 850 mJ/cm^2

SIONYX1403000042.0016

SAMSUNG EX. 1002 - 551/4148

From these SEM photos we can easily measure the diameters and the spacings between the structures. The height is more difficult to estimate (high density of the structures and 50 ° tilt), therefore we have measured the average "apparent" height of the structures. This "apparent" height usually underestimates the real size of the structures but give the general tendency of the evolution. For instance a structure with a 7 μm apparent height is in reality closer to 10 μm, as observed by SEM on cross-sectioned structures. The different obtained sizes tend to increase when increasing the laser energy density, as plotted in Figure 13.

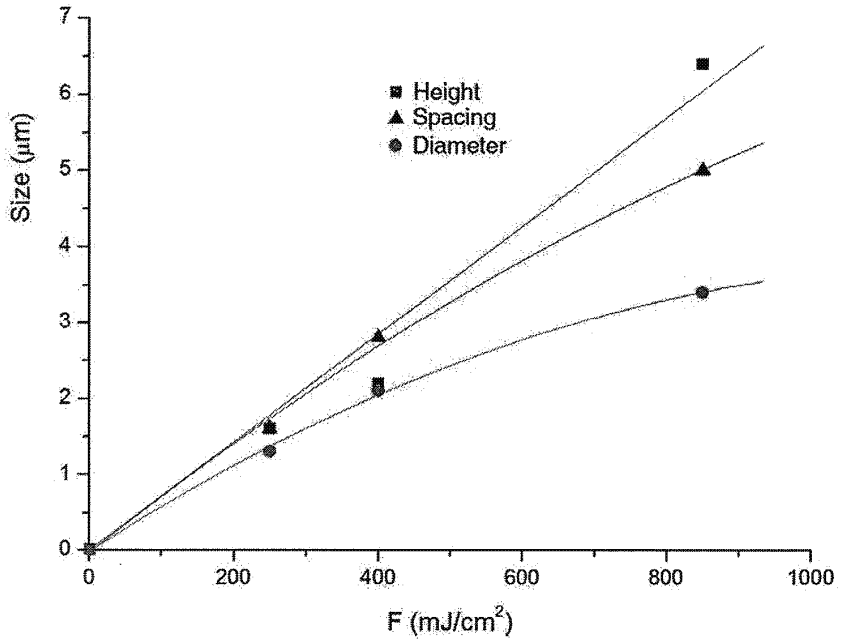


Fig. 13: Size of the laser-created structures (apparent height, spacing and diameter) as a function of the laser fluence, number of shots N=600, SEM tilt 50°.

We used the 3D optical simulation to observe the optical absorption as a function of the structure size (height, diameter and spacing) and verify and explain the phenomena. We have 3D modeled four types of structures with different sizes (S, M, L and XL), the specification of the different structures are given in Table 2, along with the Reflectivity and Absorption obtained by the simulation. The metallic teapot and the USB mouse in Figure 14 are only displayed for ray-tracing verification purpose (sun lighting, multi-reflection, direct and diffuse shadows…).

Table 2 : Properties of the structures used for the optical simulation (Fig. 14) and results for reflectivity and absorption:

Structure size	Height (μm)	FWHM diameter (μm)	Spacing (μm)	Reflectivity R (%) Visible	Absorption A (%) Vis.
Small (S)	1	0.75	1.5	22	78
Medium (M)	2.5	1.75	2.75	17	83
Large (L)	5	2.5	3.5	12	88
X-Large (XL)	10	3	5	5	95

The 3D optical simulation shows a better absorption when working with large structures (10 μm height) and a decrease of this absorption for smaller structures (down to 1μm height). The simulation does not take into account any diffraction effect, therefore, the absorption of smaller structures (like nanoparticles) was not simulated but it has been observed [15]

SIONYX1403000042.0017

SAMSUNG EX. 1002 - 552/4148

that they do contribute in a small amount, to the global absorption on the structures. However, in order to obtain a nice black silicon surface, it is not recommended to decrease the size of the structures below 5 µm. This has been confirmed by experimental results: we obtained better optical absorption and better photocurrent with larger structures, and also can explain the relatively poor absorption of commercial texturization (Figure 7).

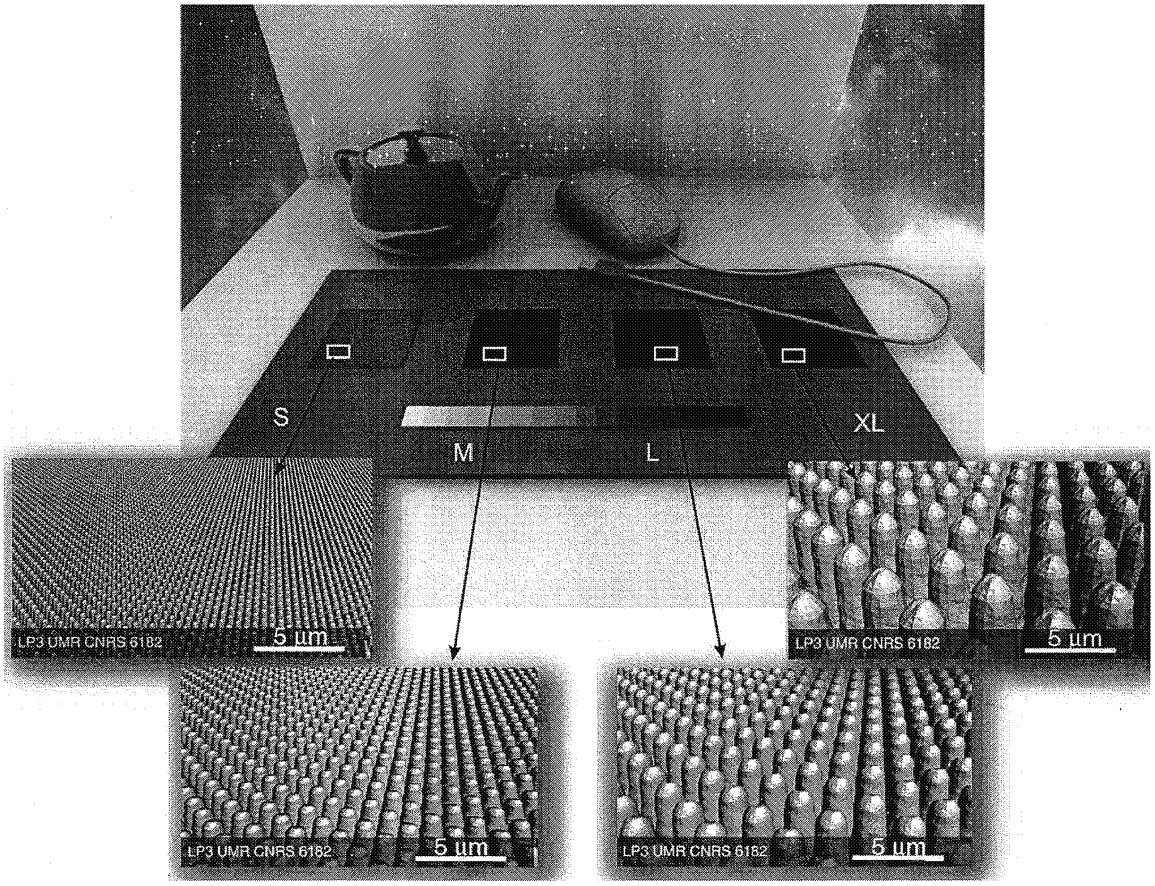


Fig. 14: 3D optical simulation of the optical absorption/reflectivity of a silicon surface with different texturizations: influence of the structure size: large structures (L and XL) induce a better light absorption (black spot) than smaller structures (S and M), characteristics of S, M, L and XL structures are given in table 2.

The absorptance gain (%) has been measured in the integrating sphere and plotted (Fig. 15) as a function of the structure size (height, diameter and spacing): this absorptance improves from 49% for small structures (size S) to 56% for large structures (size XL). This relative gain corresponds to absorption of 80 to 95 %, at 350 nm.

This absorptance gain (%) has also been measured in different spectral regions (UV-VIS-IR): the absorption improvement reaches 37 % both in the visible (600 nm) and in the near-IR region (1100 nm) and up to 56% in the UV (350 nm), close to the direct gap of the silicon (Fig. 16).

SIONYX1403000042.0018

SAMSUNG EX. 1002 - 553/4148

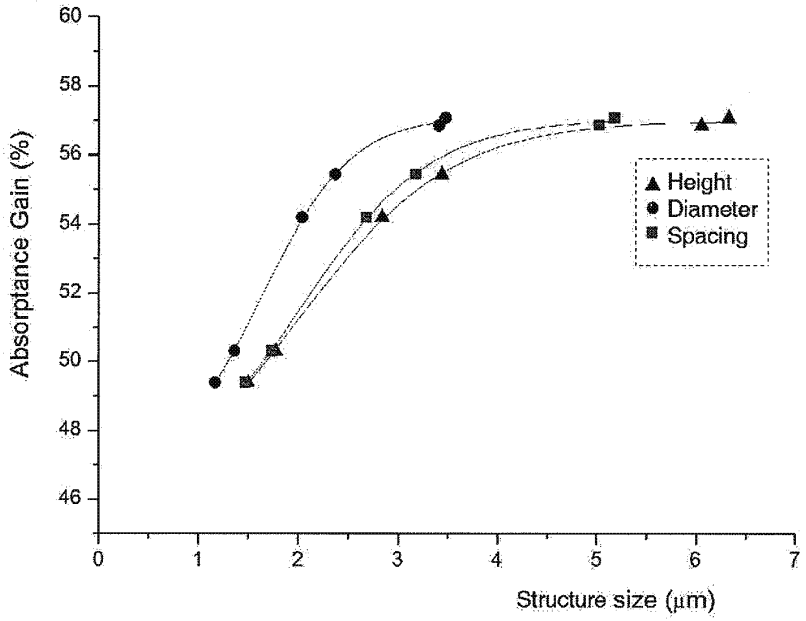


Fig. 15: Measured absorptance gain (%) as a function of height, diameter and spacing of the laser created structure.

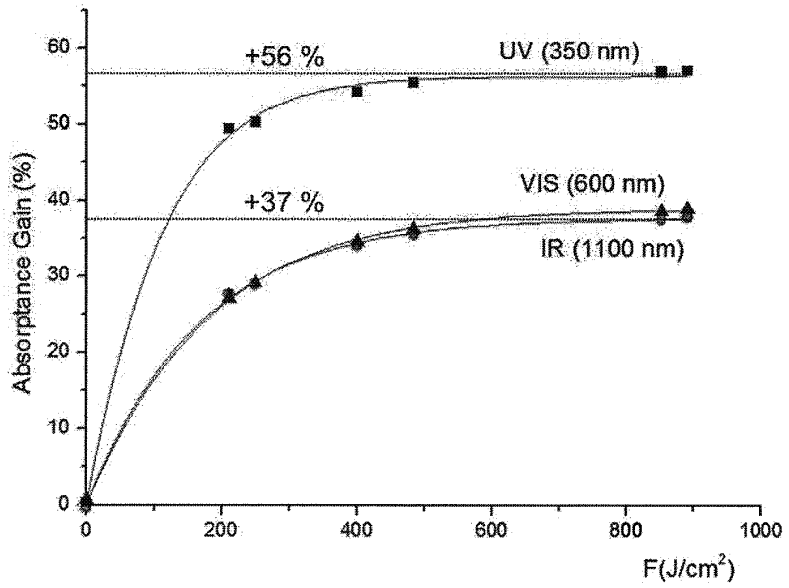


Fig. 16: Measured absorptance gain (%) as a function of laser energy density for different spectral region (UV-VIS-IR).

SIONYX1403000042.0019

SAMSUNG EX. 1002 - 554/4148

It is interesting to notice that the nanoparticles that are redeposited during the laser ablation also contribute in a small amount (5 %) to the improvement of the absorption. They have been measured by FEG-SEM: they range in size from 10 to 100 nm, they are also clearly visible outside the laser treated area using dark field optical microscopy (Fig. 17).

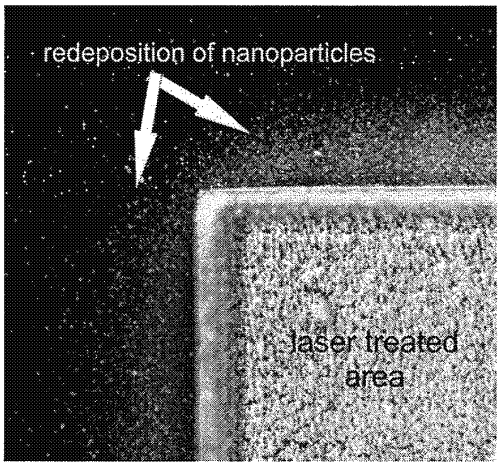


Fig. 17: Optical microscope view (Dark Field) of a laser treated area showing the nanoparticle redeposition outside the spot. F= 185 mJ/cm2, v=150 μm/s.

After laser texturing the surface, we have used two different ways of doping the material: ion implantation followed by thermal annealing and PIII + RTA (Fig. 1). The Figure 18 shows a photocurrent map (LBIC scan) of a surface that has been treated with different laser scan parameters, ion implanted and annealed. This figure shows that the LBIC signal related to the photocurrent intensity is clearly increased in the laser treated regions For these experimental conditions, the best results have been obtained on highly structured areas (high fluence and number of pulses): we observed a 40 % increase of the photocurrent, compared to the flat surface. At low fluence (F=185 mJ/cm^2) and low number of pulses (D = 15, 10 μm) the surface structure is poorly texturized (small-size structures, see Fig.13) and lead to a decrease in the photocurrent.

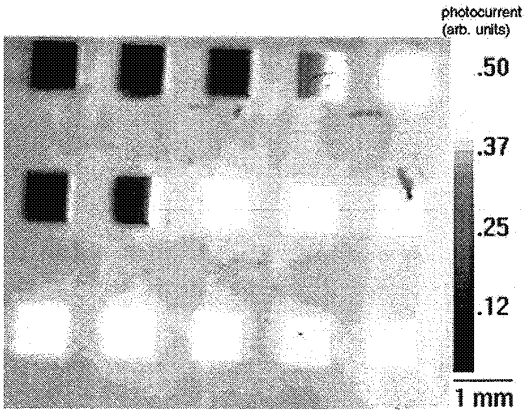


Fig. 18: LBIC scan maps showing the increase in the photocurrent in the different laser treated zones. 1st row (top) : F = 185 mJ/cm^2, d=15, 10, 5, 2 and 1 μm, 2nd row (center) : F= 250 mJ/cm^2, D=15, 10, 5, 2 and 1 μm, 3st row (down): F= 400 mJ/cm^2, D=15, 10, 5, 2 and 1 μm. Laser texturization + ion implantation + annealing.

SIONYX1403000042.0020

SAMSUNG EX. 1002 - 555/4148

The Figure 19 presents a photocurrent map (LBIC scan) of a surface that has also been treated with different laser scan parameters, but in that case the doping has been realized by plasma immersion (PIII). The measured photocurrent corresponding to a, b, c and d are 40, 42, 44 and 46 nA. The photocurrent without texturization (measured outside the spot) is 30 nA, therefore the corresponding increase in the photocurrent is 33 %, 40 %, 46% and 53 %, which is higher than the values obtained with traditional doping.

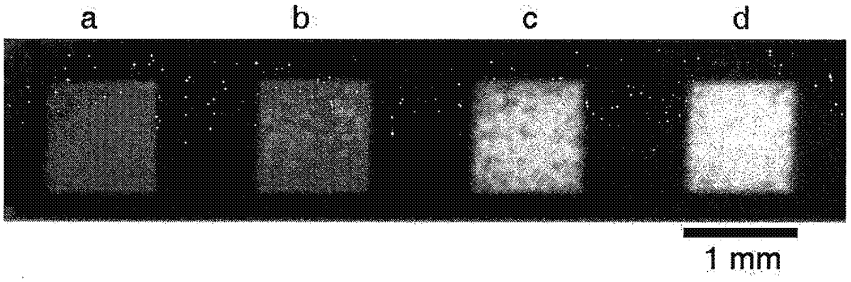


Fig. 19: LBIC scan maps showing the increase in the photocurrent in the laser treated zones, 1 x 1 mm2, 30 μm spot size, v=150 μm/s, laser fluence F= 185 mJ/cm^2·with a) d=10 μm, N = 600 shots; b) d=5 μm, N = 1200 shots; c) d=2μm, N = 3000 shots; d) d=1μm, N = 6000 shots.

As seen before with the conventional doping, the improvement is even better at high fluence/number of pulses: we have already observed a photocurrent gain of 60%, at F= 400 mJ/cm2 and 6000 shots. These first experimental data are plotted in Fig. 20 and will be completed soon:

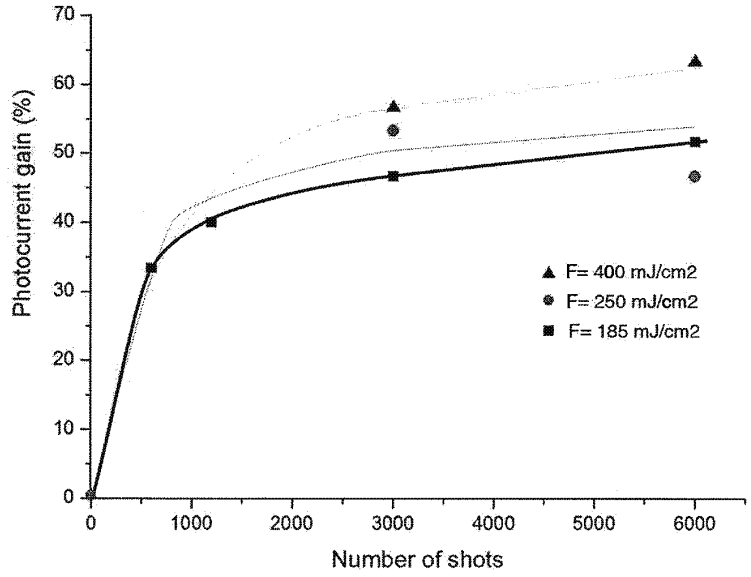


Fig. 20: Photocurrent gain (%) measured by LBIC for different laser irradiation conditions followed by PIII doping showing a photocurrent increase up to 60%.

SIONYX1403000042.0021

SAMSUNG EX. 1002 - 556/4148

3. CONCLUSIONS

We have prepared laser-microtexturized Si structures which reduce the reflection of a silicon surface (black silicon) without using corrosive gases (under vacuum). Millimeter size cells were structured on n-type silicon. The experimental results show the influence of our laser irradiation parameters on the topography of the black silicon. The topography of the texturized surface directly changes the optical properties. The 3D optical simulation and the experimental data show the evolution of the optical absorption: up to 96 % absorption can be obtained in a wide spectral range by optimizing the laser parameters.

After the laser texturization, the doped junctions have been obtained using both traditional doping (ion implantation + thermal annealing) and Plasma Ion Immersion technique.

The resulting photocurrent has been analyzed by LBIC and shows improvements of 40 % using the laser treatment followed by traditional doping and up to 60 % with the laser treatment+Plasma Ion Immersion technique.

REFERENCES

[1] C. H. Crouch, J. E. Carey, J. M. Warrender, M. J. Aziz, and E. Mazur, Appl. Phys. Lett. 84, 1850 (2004).
[2] M. Y. Shen, C. H. Crouch, J. E. Carey, and E. Mazur, Appl. Phys. Lett. 85, 5694 (2004).
[3] J. E. Carey, C. H. Crouch, M. Shen, and E. Mazur, Opt. Lett. 30, 1773 (2005).
[4] J. E. Carey, Ph.D. dissertation, Harvard Univ., (2004).
[5] C. H. Crouch, J. Carey, M. Shen, E. Mazur, and F. Y. Genin, Appl. Phys. Lett. 79, 1635 (2004).
[6] R. J. Younkin, J. E. Carey, E. Mazur, J. A. Levinson, and C. M. Friend, J. Appl. Phys. 93, 2626, (2003).
[7] B. R. Tull, J. E. Carey, E. Mazur, J. P. McDonald, and S. M. Yalisove, MRS Bulletin, Vol. 31, 626-633 (2006).
[8] J. Zhao and A. Wang, Appl. Phys. Lett. 88, 242102 (2006).
[9] A.E Mann,."Optical Coatings For Solar Cells", Spectrolab Sylmar Calif. Report AD0271358 (1960).
[10] M Law et al,. "Nanowire dye-sensitized solar cells" Nature Materials 4:455-459 (2005).
[11] F.Torregrosa, H.Etienne, G.Matthieu, L.Roux, Proceedings of the 16th Int'. Conf. Ion Impl. Tech. 609-613 (2006).
[12] M. Stemmer, Appl. Surf. Sci., 63, 213 (1993).
[13] M. Birnbaum, Journal of Applied Physics, 36, 3688 (1965).
[14] C.J.J. Tool, G. Coletti, F.J. Granek, J. Hoornstra, M. Koppes, E.J. Kossen, H.C. Rieffe, I.G. Romijn, A.W. Weeber, "17% mc-Si SOLAR CELL EFFICIENCY USING FULL IN-LINE PROCESSING WITH IMPROVED TEXTURING AND SCREEN-PRINTED CONTACTS ON HIGH-OHMIC EMITTERS" Proceedings of the 20th European Photovoltaic Solar Energy Conference and Exhibition, Barcelona, Spain, 6-10 June 2005
[15] Micro and nano-structuration of silicon by femtosecond laser: application to silicon photovoltaic cells fabrication M. Halbwax, T. Sarnet, Ph. Delaporte, M. Sentis, H. Etienne, F. Torregrosa, V. Vervisch, I. Perichaud, S. Martinuzzi, Thin Solid Films (2007), doi:10.1016/j.tsf.2007.12.117

SIONYX1403000042.0022

SAMSUNG EX. 1002 - 557/4148

Available online at www.sciencedirect.com
SCIENCE DIRECT®
Thin Solid Films 451–452 (2004) 397–401
Thin Solid Films
www.elsevier.com/locate/tsf

Thin-film solar cells with periodic grating coupler

N. Senoussaoui*, M. Krause, J. Müller, E. Bunte, T. Brammer, H. Stiebig

Institute of Photovoltaics, Forschungszentrum Jülich, D-52425 Jülich, Germany

Abstract

The application of periodic light grating couplers as an alternative to randomly textured transparent conductive oxides was investigated by using patterned aluminium doped zinc oxide (ZnO:Al) as a front contact. The periods and groove depths of the gratings were adjusted independently from each other and vary between 1–4 μm and 100–600 nm, respectively. We have analysed the optical properties of the gratings and the optoelectronic properties of microcrystalline silicon thin-film solar cells with integrated grating couplers. To benchmark the achieved results, the performance of the solar cells is discussed in comparison to the cells deposited on flat and randomly textured substrates.
© 2003 Elsevier B.V. All rights reserved.

Keywords: Grating coupler; Solar cells; Microcrystalline silicon; Light trapping

1. Introduction

Amorphous and microcrystalline (μc-Si:H) silicon thin-film solar cells require effective light trapping schemes to achieve efficient absorption. Hence, textured transparent conductive oxides (TCO) with a randomly distributed surface morphology are widely employed. As an alternative to a randomly textured substrates the effect of periodic light grating couplers on solar cell performance was discussed by different groups [1–3]. The integration of an one-dimensional grating in thin-film solar cells should be the simplest device structures, which leads to a prolonged absorption path in the absorption region compared to structures with flat interfaces. For a detailed investigation of the effect of such a modified front contact design on the cell performance, the period and the groove depth of the grating has to be varied independently from each other. This can be fulfilled when the grooves of the gratings are realized using photolithography. On the basis of a detailed investigation of the grating parameters we will evaluate the applicability of periodic light couplers in solar cells.

2. Experiment

The ZnO grating couplers were prepared using photolithography including a lift-off process. First, an approximately 500 nm thick ZnO_1 layer was r.f.-magnetron sputtered on a glass substrate at high temperature to achieve a highly conductive and transparent front contact. Afterwards photoresist was applied and developed using a standard exposure and chromium masks for patterning. Then, the undeveloped photoresist was removed and on the whole substrate a ZnO_{II} layer was deposited at room temperature to avoid combustion of the photoresist. The thickness of this ZnO_{II} layer determines the groove depth of the grating coupler. Next, the undesired regions of the ZnO material were removed by a lift-off step. The period of the grating coupler depends on the design of the mask for patterning. Thus, the periods and groove depths (h_{gb}) were adjusted independently from each other and were varied between 1–4 μm and 100–600 nm, respectively. The masks were designed in a way so that the width of the grooves is half the length of the period. Some deviation is caused by the lift-off process. For more details concerning the ZnO sputtering process see Ref. [4]. Fig. 1 shows selected scanning electron microscopy (SEM) images of processed ZnO gratings with a period of 1.2 μm (a) and 4 μm (b) for a groove depth of 400 nm.

On top of these couplers state-of-the-art μc-Si:H p-i-n-solar cells with an absorber layer thickness of 1 μm were deposited by plasma enhanced chemical vapor deposition [5]. The fill factors (FFs) of the p-i-n-diodes were above 68%. The high FFs demonstrate that diodes

*Corresponding author. Tel.: +49-2461-61-2069; fax: +49-2461-61-3735.
E-mail address: n.senoussaoui@fz-juelich.de (N. Senoussaoui).

0040-6090/04/$ - see front matter © 2003 Elsevier B.V. All rights reserved.
doi:10.1016/j.tsf.2003.10.142

SIONYX1403000042.0023

SAMSUNG EX. 1002 - 558/4148

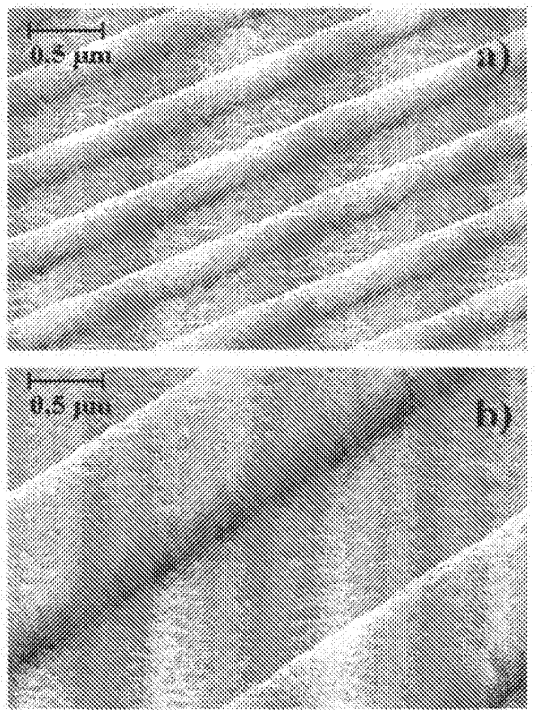


Fig. 1. SEM images of gratings with a period of 1.2 µm (a) and 4 µm (b). The groove depth is 400 nm (the plotted scale is only valid along the horizontal due to the oblique perspective).

with a good device performance were realized on different substrates. The I/V characteristics of the cells under illumination were determined using an AM 1.5 spectrum (100 mW/cm^2), blue light (filtered AM1.5 spectrum using a BG 7 filter) and red light (applying an OG 590 filter).

3. Results

3.1. Optical properties of the grating coupler

The gratings consisting of a glass/patterned TCO layer system are characterised by optical spectroscopy. The measured diffraction angles (Φ_m) of the rectangular grating (not shown) exhibit a wavelength (λ) dependence in accordance to the grating formula:

$$\sin(\Phi_m) = \frac{m\lambda}{P}, \tag{1}$$

where m is the diffraction order and P is the grating period. The light intensity of the different diffraction orders of the transparent gratings depends strongly on P and h_{gh}. The effect of P on the specular transmission (T_{spec}) of the grating with a groove depth of 400 nm is depicted in Fig. 2. Only the total transmittance (T_{total}) of the grating with $P = 1.2$ µm is shown for clarity since T_{total} proved to be nearly independent of P. For gratings with a large period ($P = 3$ and 4 µm) a distinct minimum in T_{spec} can be observed at $\lambda = 600$–700 nm. In this case the light is mainly diffracted into higher orders ($m > 0$). The erasement of T_{spec} is caused by a destructive interference due to different phasing of waves propagating through the TCO and air (groove) regions. If the optical retardation in the TCO is equal to an uneven-numbered multiple of $\lambda/2$ in comparison to the wave front that passes through air, a destructive interference occurs. This leads to

$$(2k-1)\frac{\lambda}{2} = h_{gh}(n_{TCO} - n_{Air}) \tag{2}$$

where $n_{TCO} \approx 2$ is the refractive index of the TCO and k an arbitrary integer. Eq. (2) shows that for a groove depth of 400 nm and $k = 1$ a destructive interference occurs for $\lambda = 800$ nm. This value nearly fits with the measured minimum of T_{spec} for a grating with $P = 4$ µm. For gratings with small P this interference effect is not observed. However, the difference between the T_{spec} and T_{total} of the grating with a period of 1.2 µm in the short wavelength range indicates that a certain amount of light is scattered.

The influence of h_{gh} on T_{spec} of a grating with a period of 4 µm is shown in Fig. 3. For a groove depth of 600 nm a minimum of T_{spec} at approximately 1200 nm for $k = 1$ and at 400 nm for $k = 2$ is expected using Eq. (2). Both minima can also be observed in the experiment even if the wavelength of the minima is slightly shifted. For $h_{gh} = 200$ nm a minimum in T_{spec} is calculated at 400 nm. This minimum is not observed, because the transmittance of the grating in this wave-

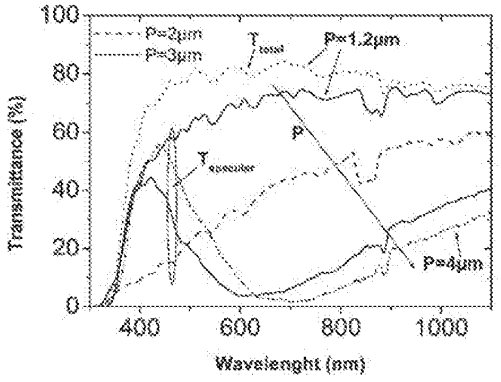


Fig. 2. Specular transmission of gratings (air/glass/ZnO) with different periods and a groove depth of 400 nm. Additionally, the total transmission of the grating with a period of 1.2 µm is plotted.

SIONYX1403000042.0024

SAMSUNG EX. 1002 - 559/4148

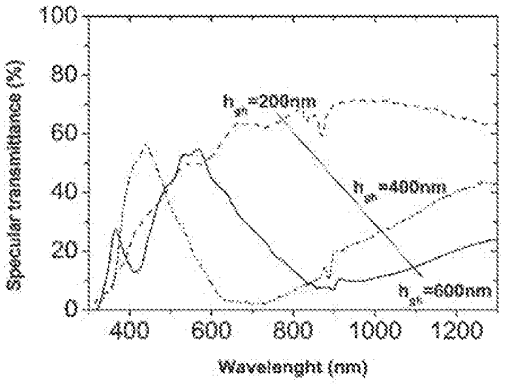


Fig. 3. Specular transmission of gratings with a period of 4 μm and different groove depths.

lengths region is covered by the influence of the absorption within the TCO material.

3.2. Optoelectronic properties of thin-film silicon solar cells with integrated grating couplers

The grating couplers were integrated into μc-Si:H solar cells. The external quantum efficiency (EQE) of cells with couplers with a groove depth of 400 nm and different periods is shown in Fig. 4. Additionally, the EQE of a μc-Si:H solar cell deposited on a flat and a randomly textured substrate is plotted. In the whole wavelength range the EQE of cells with integrated gratings exceeds the values of a diode deposited on flat substrates. The EQEs show no significant dependence on P. The strong variation in $T_{sp,\infty}$ as a function of P (as shown in Fig. 2) is not reflected in the spectral response data. On the other hand, the EQE of the cell fabricated on randomly textured substrates exhibits a higher red response. The shown EQE of the μc-Si:H diode with a randomly textured substrate exhibits a typical spectral sensitivity. Previous investigations have shown that the EQE exhibits no significant dependence on the correlation length of the texture, when the correlation length varied between 400 nm and 1 μm and the texture is achieved by a HCl etching step [6]. The comparison of EQE of structures with a randomly textured and a periodically textured TCOs shows that light trapping in structures with randomly textured substrates is more pronounced.

One important criterion for effective light trapping schemes is that the light is totally trapped due to total reflection. This condition is not fulfilled for the gratings investigated here, since the diffraction orders are totally reflected back into the solar cell in the case that

$$\lambda > \frac{P}{m}. \qquad (3)$$

Note, Eq. (3) does not depend on the refractive index of the employed materials. Since P is above the corresponding wavelength of the band gap of the absorber material, this structure should not lead to effective multiple reflections in the wavelength range shorter than 1.2 μm. This can be one reason for the lower red response of the diodes with integrated couplers.

However, also diodes with a randomly textured TCO with a correlation length of 1 μm—a correlation length which is close to the smallest period of the gratings investigated here—exhibit a high red response (600 nm < λ < 1000 nm). As mentioned above, the EQE in the long wavelength region is equal to structures with lower correlation length (shown in [6]). Thus, a straight forward discussion of data derived from far field measurements and their application for the explanation of near field phenomena (status within solar cells) is more complex.

Surprisingly, the blue response of cells with couplers is comparable to cells deposited on textured substrates although the reflectance (R) of the diodes match well with the spectrum from a flat diode (Fig. 5). Due to the large period of the gratings investigated here (up to 4 μm), no effective refractive index matching is expected between the TCO and the silicon layer. Consequently, the reflectance of cells on gratings and on flat substrates should be similar. Thus, the gain in the blue response for cells with integrated couplers can not be attributed to a better light in-coupling. The blue response of the cells will be discussed later on. In contrast, R of the structure with randomly textured substrates is significantly reduced in the whole wavelength region mainly due to a better light in-coupling (effective refractive index matching) and also due to a more effective light trapping in the long wavelength range.

Next, the influence of the groove depth on the short-circuit current (I_{sc}) under different illumination conditions is studied. Figs. 6 and 7 show the measured I_{sc}

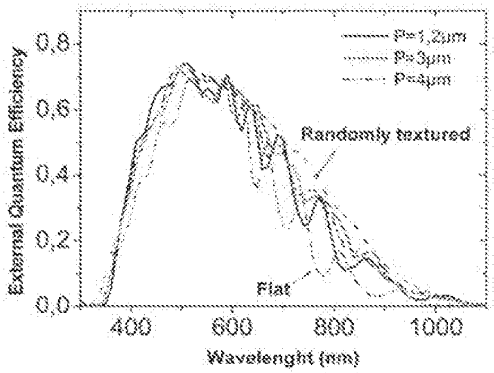


Fig. 4. Quantum efficiency of μc-Si:H solar cells deposited on flat, randomly textured and periodically textured (h_{gr} = 400 nm) substrate.

SIONYX1403000042.0025

SAMSUNG EX. 1002 - 560/4148

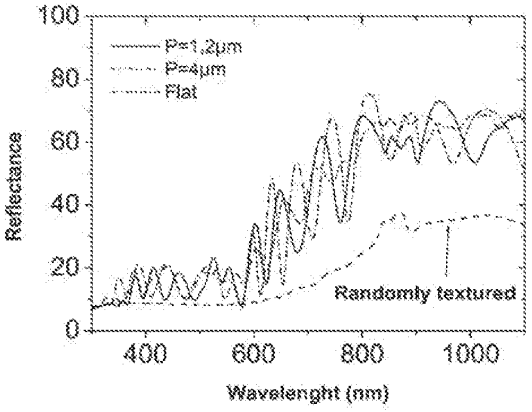


Fig. 5. Reflectance of μc-Si:H solar cells deposited on flat, randomly textured and periodically textured (h_{gb}=400 nm) substrate.

(symbols) as a function of P for different groove depths under red and blue illumination. The lines are guides for the eye. For comparison, the values for cells on randomly textured and flat substrates are plotted. For these, co-domains are defined which take into account the scattering of the data. In general, I_{sc} shows no significant dependence on P.

Under red illumination I_{sc} increases with increased h_{gb} (Fig. 6). A further increase in I_{sc} with higher groove depth is not observed since the absorption losses within the low temperature ZnO_B also increases. For samples with a groove of 600 nm (not shown) the current decreases. I_{sc} vs. h_{gb} can be explained by the increasing diffraction efficiency of light into higher orders with increasing h_{gb}. However, I_{sc} of cells with gratings is smaller than I_{sc} of cells deposited on randomly textured substrates. This can be explained by the higher reflectance (Fig. 5) caused by less effective light in-coupling and light trapping.

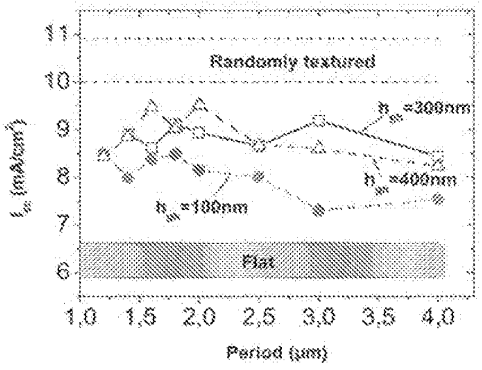


Fig. 6. Short circuit current of μc-Si:H solar cells deposited on flat, randomly textured and periodically textured substrate measured under red illumination.

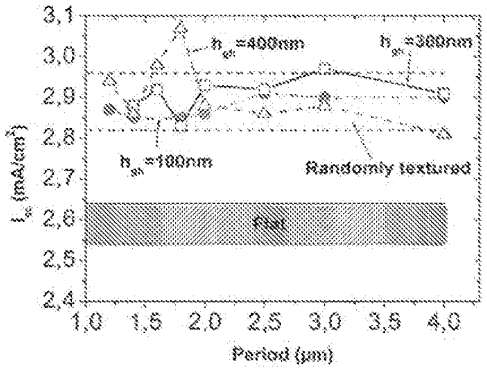


Fig. 7. Short circuit current of μc-Si:H solar cells deposited on flat, randomly textured and periodically textured substrate measured under blue illumination.

Under blue light I_{sc} shows no dependence on h_{gb} and the measured values are equal to I_{sc} of cells with randomly textured substrates (Fig. 7). Thus, under AM1.5 illumination I_{sc} as a function of h_{gb} is determined by the red response. The current from diodes with periodic textured substrates under blue illumination the current of solar cells with gratings is significantly higher than that of solar cells deposited on flat substrates even though R is similar (Fig. 5). Since, also for h_{gb} of only 100 nm a significant enhancement of the blue response is observed, an explanation due to reduced absorption losses within a decreasing p-layer thickness as a consequence of an effective larger surface of the substrate and a constant deposition time of the p-layer can be excluded for the blue response behavior. Thus, the high 'blue current' can be likely attributed to a better extraction of carriers photo-generated in the p-layer.

4. Conclusions

The optical properties of gratings as a function of the period and groove depth and their integration in silicon thin-film solar cells were studied. The red response of the diodes increases with groove depth but is lower than the red response of cells deposited on optimised randomly textured substrates. The blue response is significantly higher than that expected from the reflectance indicating that the extraction efficiency of charge carriers generated in the doped regions has to be taken into account for an accurate device analysis.

Acknowledgments

The authors thank O. Kluth, B. Rech and W. Reetz for helpful discussions. N. Senoussaoui thanks Deutscher Akademischer Austauschdienst (DAAD) for funding of her stay at Forschungszentrum Jülich.

SIONYX1403000042.0026

SAMSUNG EX. 1002 - 561/4148

References

[1] J. Tinnen, F. Wyrowski, Diffraction Optics, Akademie Verlag, Berlin, 1997, p. 361.
[2] J. Zimmer, H. Stiebig, H. Wagner, Proceedings of the Second World Conference and Exhibition on Photovoltaic Solar Energy Conversion, Vienna, Austria, 1998, 944.
[3] C. Eisele, C.E. Nebel, M. Stutzmann, J. Appl. Phys. 89 (2001) 7722.
[4] O. Kluth, A. Löffl, S. Wieder, C. Beneking, L. Houben, B. Rech, H. Wagner, S. Waser, J.A. Selvan, H. Keppner, Proceedings of the Twenty Sixth IEEE Photovoltaic Specialist Conference, IEEE, Anaheim, CA, USA, 1997, 715.
[5] B. Rech, T. Roschek, T. Repmann, J. Müller, R. Schmitz, W. Appenzeller, Thin Solid Films 427 (2003) 157.
[6] H. Stiebig, T. Brammer, T. Repmann, O. Kluth, N. Senoussaoui, A. Lambertz, H. Wagner, Proceedings of the Sixteenth European Photovoltaic Solar Energy Conference, James and James, Glasgow, UK, 2000, 549.

SIONYX1403000042.0027

SAMSUNG EX. 1002 - 562/4148

Temperature dependence of photoluminescence in non-crystalline silicon

Ali Serpengüzel,* Temel Bilici,† Ibrahim Inanç,‡ and Adnan Kurt
Koç University, Microphotonics Research Laboratory, Department of Physics,
Rumeli Feneri Yolu, Sariyer, Istanbul 34450 Turkey

Jim Carey and Eric Mazur
Harvard University, Department of Physics and Division of Engineering and Applied Sciences,
29 Oxford Street, Cambridge, Massachusetts 02138 USA

ABSTRACT

Crystalline silicon being ubiquitous throughout the microelectronics industry has an indirect bandgap, and therefore is incapable of light emission. However, strong room temperature visible and near-IR luminescence from non-crystalline silicon, e.g., amorphous silicon, porous silicon, and black silicon, has been observed. These silicon based materials are morphologically similar to each other, and have similar luminescence properties. We have studied the temperature dependence of the photoluminescence from these non-crystalline silicons to fully characterize and optimize these materials in the pursuit of obtaining novel optoelectronic devices.

Keywords: amorphous silicon, black silicon, non-crystalline silicon, porous silicon, plasma enhanced chemical vapor deposition, photoluminescence..

1. INTRODUCTION

Interest in silicon (Si) as a material for optoelectronics has increased recently. With modern process techniques, it will be possible to integrate lasers, photodetectors, and waveguides into optoelectronic silicon motherboards to route and modulate optical signals within such silicon motherboards. Integrated silicon optoelectronics is a rapidly developing field [1]. Discrete and integrated devices such as photodetectors, modulators, light emitters, resonant cavity enhanced (RCE) photodetectors, waveguides, photonic bandgap filters, optical amplifiers, optical interconnects, and optoelectronic integrated circuits are already being realized. However, most of these devices, with the exception of light emitters, are fabricated using crystalline silicon. Light emission requires the use of amorphous silicon, since crystalline silicon can not emit light due to its indirect bandgap. With modern process techniques, it will be possible to integrate lasers, photodetectors, and waveguides into Si motherboards [2,3] for wavelength division multiplexing (WDM) applications [4].

2. EXPERIMENTAL PHOTOLUMINESCENCE SETUP

The room temperature PL setup consists of a pump laser, a spectrometer, a lock-in amplifier, and a digital oscilloscope. The collected PL signal is imaged to the entrance slit of the spectrometer, whose output is fed to a sensitive photomultiplier tube (PMT). A lock-in-amplifier is providing the necessary electronic gain to the PMT output gain in phase with the laser pulse. The digital oscilloscope is used for monitoring and optimizing the PMT signal. All of the

* aserpenguzel@ku.edu.tr; phone: + 90 (212) 338-1312; fax: + 90 (212) 338-1547; http://home.ku.edu.tr/~aserpenguzel, http://microphotonics.ku.edu.tr; Koç University, Microphotonics Research Laboratory, Department of Physics, Rumeli Feneri Yolu, Sariyer, Istanbul 34450 Turkey. Ibrahim Inanç and Adnan Kurt are with Koç University, Microphotonics Research Laboratory, Department of Physics, Rumeli Feneri Yolu, Sariyer, Istanbul 34450 Turkey. † Temel Bilici is currently at Boston University, Department of Electrical and Computer Engineering, 8 St. Mary's Street, Boston, Massachusetts 02215 USA. ‡ Ibrahim Inanç is also with the Bogaziçi University, Physics Department, Bebek, Istanbul 34342 Turkey. Jim Carey and Eric Mazur are with Harvard University, Department of Physics, Cambridge, Massachusetts 02138 USA.

SAMSUNG EX. 1002 - 563/4148

measurement and test devices are computer controlled and the data is acquired digitally. For the room temperature measurements at 300 K the samples are attached to a holder. For low temperature measurements the samples are placed in a closed cycle cryostat system. The closed cycle cryostat system is used to control the sample temperature from 10 K to 300 K.

3. AMORPHOUS SILICON

In the optoelectronics and microelectronics industry silicon is the most widely used semiconductor, not only in its crystalline, but also in its amorphous form. Being a direct band-gap material, [5] unlike crystalline silicon,[6] amorphous silicon is unmatched as a photoreceptor for laser printing, for switching elements in large area liquid crystal displays, for large photovoltaic panels, and any other application that calls for a high quality semiconductor that can be processed on large areas or on curved or flexible substrates. It is generally agreed that the terms amorphous solid, non-crystalline solid, disordered solid, glass, or liquid have no precise structural meaning beyond the description that, the structure is not crystalline on any significant scale. The principal structural order present is imposed by the approximately constant separation of nearest-neighbor atoms or molecules. Until the early 1970's, amorphous silicon prepared by evaporation or sputtering was not considered as one of the valuable semiconductor materials, because of high density of electronic states in the band gap related to a large density of structural defects. [7] The discovery of an amorphous silicon material prepared by the glow discharge deposition of silane, which can be doped and whose conductivity can be changed by ten orders of magnitude marked a turning point and opened a new research area. Most interest focused on hydrogenated amorphous silicon and its alloys, since hydrogen by removing dangling bonds eliminates non-radiative recombination centers, that are responsible for reduced luminescence efficiency (and reduced photovoltaic efficiency) and allows doping. [8] Hydrogenated amorphous silicon (a-Si:H) is already an established material in semiconductor technology [9]. The major application of a-Si:H is photovoltaics, color detectors, and active matrix displays. The primary attribute of the technology is its large area capability, which is unavailable with other technologies. Another advantage of the hydrogenated amorphous silicon is that, it can be deposited by plasma enhanced chemical vapor deposition (PECVD) onto almost any substrate at temperatures below 500 K, which makes it compatible with the microelectronic technology. This property justifies the interest in a-Si:H as a potential optoelectronic material. Planar waveguides are already being realized from a-Si:H [10]. The advantage of a-Si:H, as well as porous silicon (π-Si), is that, they attract interest as a potential optical gain medium, because of their room temperature visible electroluminescence (EL) and photoluminescence (PL). Recently, we have observed visible PL from a-Si:H, as well as its oxides (a-SiO_X:H) and nitrides (a-SiN_X:H) grown by low temperature PECVD. [11] While the exact mechanism of the occurrence of the PL in bulk a-SiN_X:H is still under discussion, the quantum confinement model is a widely accepted [12] In the quantum confinement model the material consist of small a-Si clusters in a matrix of a-SiN_X:H. The regions with Si-H and Si-N, having larger energy gaps due to strong Si-H and Si-N bonds, isolate these a-Si clusters, and form barrier regions around them. The PL originates from the a-Si clusters. A-SiN_X:H can be grown both with and without ammonia (NH_3). The samples grown without NH_3 are referred to as the Si rich samples. The luminescence of these samples is in the red-near-infrared part of the optical spectrum. The samples grown with NH_3 and annealed at 800° C are referred to as the nitrogen rich samples. The luminescence of these samples is in the blue-green part of the optical spectrum [13].

3.1. Temperature dependence of the amorphous silicon photoluminescence

Figure 3.1 shows the PL spectra of the a-SiN_X:H measured in the 550 - 900 nm wavelength and in the 12 – 298 K temperature range at a constant excitation laser intensity of 0.1 W cm^{-2}. A broad PL band centered at 710 nm (E_p = 1.746 eV) at 12 K is observed. The PL spectra have approximately a Gaussian lineshape modulated slightly by Fabry-Perot resonances. These resonances are due to the Fresnel reflections from the a-SiN_X:H film surfaces. The PL intensity decreases with increasing temperature. This feature is typical of the PL, which is due to donor-acceptor pair transitions observed in semiconductors. The variation of the PL peak with respect to temperature is plotted in the figure 3.2. In the 12 - 170 K range, the PL intensity decreases slowly. Above 170 K, however, the PL intensity decreases at a larger rate due to a thermal quenching process. The activation energy ΔE for this thermal quenching process can be derived in the 170 - 298 K temperature range using a nonlinear least squares fit to the following equation, $I = I_o \exp(\Delta E/k_B T)$, where I is the PL intensity, I_o a proportionality constant, and k_B the Boltzmann's constant. The semilog plot of the emission band intensity as a function of the reciprocal temperature gives a straight line in the 170 - 298 K region. An activation energy of E_a = 0.027 eV for the emission band is derived from the slope of the straight line fit. This activation energy is associated with a shallow level located at 0.027 eV from the band. This shallow level in undoped a-SiN_X:H may be associated with the presence of defects and unintentional impurities.

SAMSUNG EX. 1002 - 564/4148

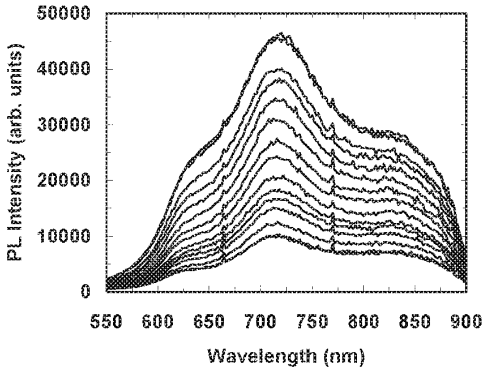


Figure 3.1. PL spectra of a-SiNx:H in the 12 - 298 K temperature range.

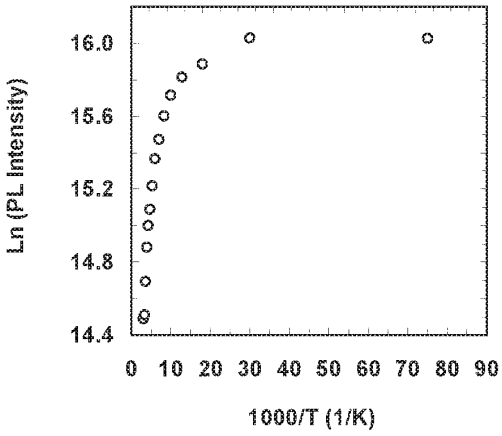


Figure 3.2. Temperature dependence of a-SiN_x:H PL intensity at the emission band maximum. Intensive quenching starts at 170 K.

3.2. Surface morphology of the amorphous silicon

Atomic force microscopy (AFM) has been performed the on the a-SiN_x:H samples to characterize the morphology of the surface and to analyze origin of the luminescence. The surface of the a-SiN_x:H is optically flat and thus amenable for the growth of multiple layers. This is necessary condition for the realization of the one-dimensional PBG microcavity. The surface morphology of the a-SiNx:H is quite uniform. The bulk of the material is composed of globules of a-SiNx:H and is similar to π-Si. Figure 3.3 shows the medium resolution AFM picture of the silicon rich a-SiNx:H surface. Additionally, although the surface is flat optically, it is quite rough in the 100 nm range, which corresponds to the average globule size.

SAMSUNG EX. 1002 - 565/4148

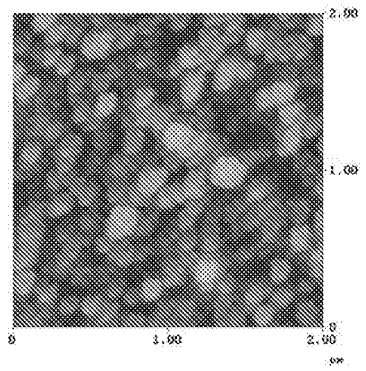


Figure 3.3. Medium resolution AFM of the silicon rich a-SiNx:H surface.

4. POROUS SILICON

Similar to hydrogenated amorphous silicon (a-Si:H), porous silicon (π-Si) also exhibits room temperature visible PL [14]. Semiconductor microcavity effects have been applied to π-Si, after the observation of room temperature visible PL)[15] made π-Si a potential optical gain medium.[16] Steady state [17, 18, 19] and temporally resolved, [20] single and multiple[21] microcavity controlled PL in π-Si has been observed experimentally [22, 23, 24] and calculated theoretically [25]. The possibility of using π-Si microcavities as chemical sensors has been investigated [26]. In addition, microcavity controlled PL has been observed in π-Si inorganic-organic structures, [27] as well as Si/SiO_x superlattices. [28,29,30] SiO_y/TiO_2 microcavities,[31] SiO_x/WO_y, and SiO_x/MO_y multilayers[32] have been fabricated. Microcavity controlled electroluminescence (EL) of π-Si has been reported.[33, 34] Interference filters [35] and optical waveguides [36] have also formed from π-Si. Two-dimensional (2-D) photonic crystals have been fabricated in π-Si [37] and silicon nitride (Si_3N_4) [38] waveguides.

4.1. Temperature dependence of the porous silicon photoluminescence

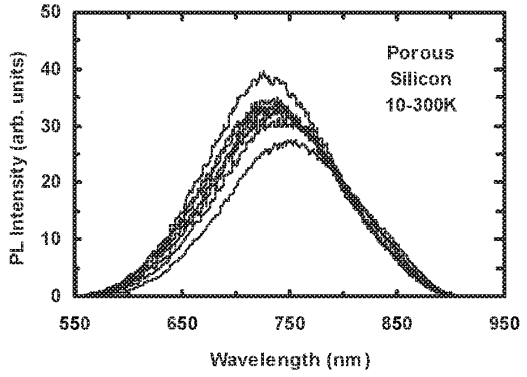


Figure 4.1. PL spectra of porous silicon in the 10 - 300 K temperature range.

SAMSUNG EX. 1002 - 566/4148

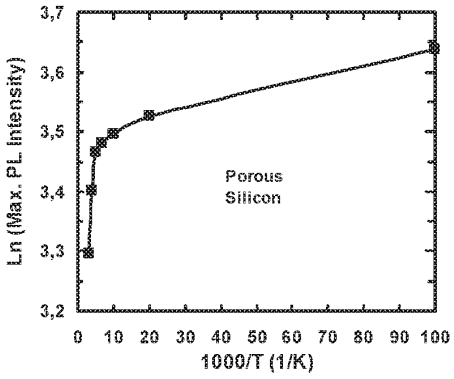


Figure 4.2. Temperature dependence of porous silicon PL intensity at the emission band maximum. Intensive quenching starts at 200 K.

Figure 4.1 shows the PL spectra of the porous silicon measured in the 550 - 900 nm wavelength and in the 10 – 300 K temperature range at a constant excitation laser intensity of 0.005 W cm^{-2}. A broad PL band centered at 750 nm (E_p = 1.698 eV) at 10 K is observed. The PL spectra have approximately a Gaussian lineshape. The PL intensity decreases with increasing temperature. This feature is typical of the PL, which is due to donor-acceptor pair transitions observed in semiconductors. The variation of the PL peak with respect to temperature is plotted in the figure 4.2. In the 10 - 150 K range, the PL intensity decreases slowly. Above 200 K, however, the PL intensity decreases at a larger rate due to a thermal quenching process. The activation energy ΔE for this thermal quenching process can be derived in the 200 - 300 K temperature range using a nonlinear least squares fit to the following equation, $I = I_o \exp(\Delta E/k_B T)$, where I is the PL intensity, I_o a proportionality constant, and k_B the Boltzmann's constant. The semilog plot of the emission band intensity as a function of the reciprocal temperature gives a straight line in the 200 - 300 K region. An activation energy of E_a = 0.009 eV for the emission band is derived from the slope of the straight line fit. This activation energy is associated with a shallow level located at 0.009 eV from the band. This shallow level in porous silicon may be associated with the presence of defects and unintentional impurities.

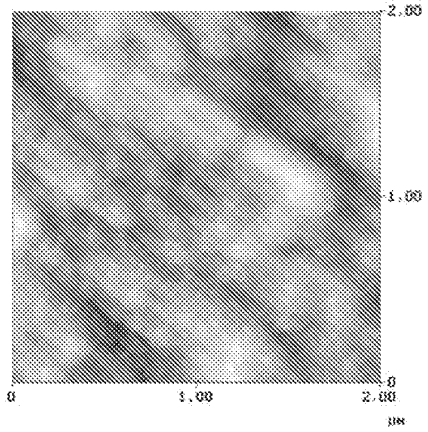


Figure 4.3. Medium resolution AFM of the porous silicon surface.

SAMSUNG EX. 1002 - 567/4148

4.2. Surface morphology of the porous silicon

Atomic force microscopy (AFM) has been performed the on the porous silicon samples to characterize the morphology of the surface and to analyze origin of the luminescence. The surface of the porous silicon is rather rough. The bulk of the material is composed of globules of as we have seen in porous silicon. Figure 4.3 shows the medium resolution AFM picture of the porous silicon surface.

5. BLACK SILICON

Ordinarily, silicon absorbs a moderate amount of visible light, but a substantial amount of visible light is reflected as well, and infrared and ultraviolet light are transmitted through silicon or reflected from it with very little absorption. Spiked silicon surfaces, in contrast, absorb nearly all light at wavelengths ranging from the ultraviolet to the infrared. This suggests it may be very useful in improving the performance of existing silicon devices, such as photodetectors and photovoltaics. Mazur group recently discovered that irradiation of silicon surfaces with femtosecond laser pulses in the presence of a halogen containing gas transforms the flat, mirror-like surface of a silicon wafer into a forest of microscopic spikes.[39,40] The spiked surface is strongly light-absorbing: the surface of silicon, normally gray and shiny, turns deep black; hence the name black silicon.

5.1. Temperature dependence of the PL from the black silicon

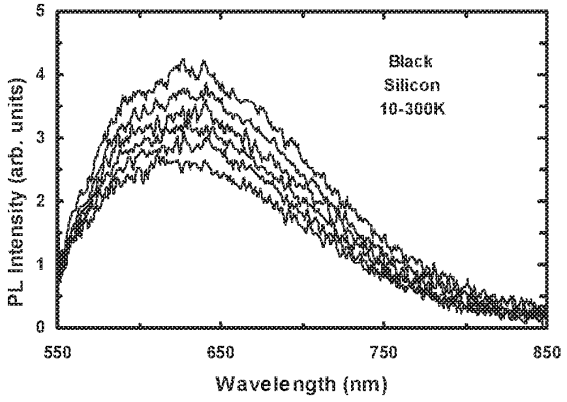


Figure 5.1. PL spectra of black silicon in the 10 - 300 K temperature range.

Figure 5.1 shows the PL spectra of the black silicon measured in the 550 - 850 nm wavelength and in the 10 – 300 K temperature range at a constant excitation laser intensity of 0.1 W cm^{-2}. A broad PL band centered at 630 nm (E_p = 1.968 eV) at 10 K is observed. The PL spectra have approximately Gaussian lineshape. The PL intensity decreases with increasing temperature. The variation of the PL peak with respect to temperature is plotted in the figure 2. In the 10 - 120 K range, the PL intensity decreases slowly. Above 120 K, however, the PL intensity decreases at a larger rate due to a thermal quenching process. The activation energy ΔE for this thermal quenching process can be derived in the 120 - 300 K temperature range using a nonlinear least squares fit to the following equation, $I = I_o \exp(\Delta E/k_B T)$, where I is the PL intensity, I_o a proportionality constant, and k_B the Boltzmann's constant. The semilog plot of the emission band intensity as a function of the reciprocal temperature gives a straight line in the 120 - 300 K region. An activation energy of E_a = 0.006 eV for the emission band is derived from the slope of the straight line fit. This activation energy is associated with a shallow level located at 0.006 eV from the band. This shallow level in black silicon may be associated with the presence of defects and unintentional impurities.

SAMSUNG EX. 1002 - 568/4148

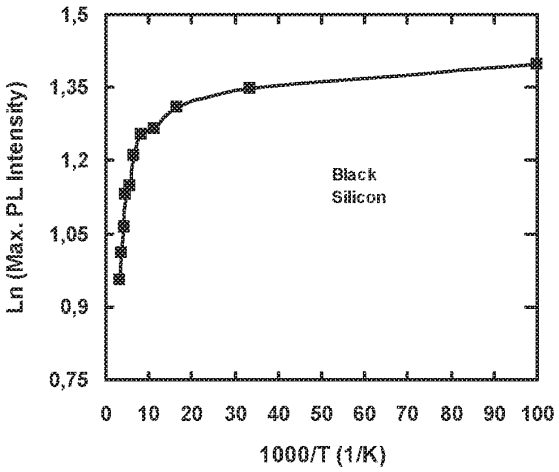


Figure 5.2. Temperature dependence of black silicon PL intensity at the emission band maximum. Intensive quenching starts at 120 K.

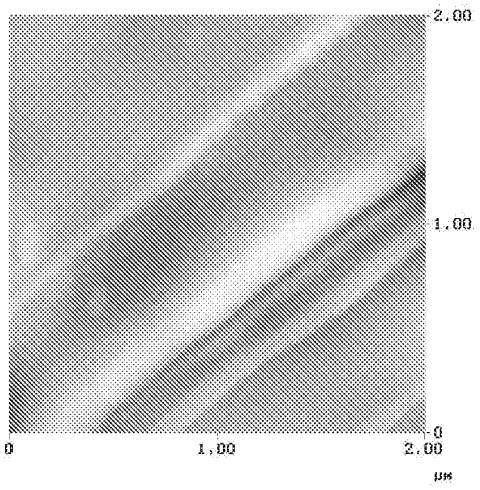


Figure 5.3. Medium resolution AFM of the black silicon surface.

SAMSUNG EX. 1002 - 569/4148

5.2. Surface morphology of the black silicon

Atomic force microscopy (AFM) has been performed the on the black silicon samples to characterize the morphology of the surface and to analyze origin of the luminescence. The surface of the black silicon is optically black and consists of conical layers. The bulk of the material is composed of globules of black silicon and is similar to π-Si. Figure 5.3 shows the medium resolution AFM picture of the black silicon surface.

6. CONCLUSIONS

Bulk luminescence properties of hydrogenated amorphous silicon nitride (a-SiN_x:H), porous silicon, and black silicon were studied at room temperature and at low temperatures. The PL emission intensity increases at low temperatures due to the lack of thermally excited phonons. The emission spectrum stays broad even at low temperatures. The broad luminescence spectrum even at low temperatures is a results of the heterogenous size distribution of the amorphous silicon quantum dots. This heterogenous size distribution is further confirmed by atomic force microscopy (AFM) measurements of the sample surface. The broad PL spectrum of the a-SiN_x:H, porous, and black silicon makes them suitable sources for wavelength division multiplexing (WDM) applications.

7. ACKNOWLEDGMENTS

We would like to acknowledge the partial support of this research by the Scientific and Technical Research Council of Turkey (TUBITAK) Grant No: TBAG-1952 and the European Office of Aerospace Research and Development (EOARD) Grants No: F61775-01-WE062 and FA8655-02-M-4086.

8. REFERENCES

1 H. Zimmermann, "Integrated Silicon Optoelectronics," (Springer Verlag, Berlin, 2000) pp. 1-352.
2 B. Jalali, S. Yegnanarayanan, T. Yoon, T. Yoshimoto, I. Rendina, and F. Coppinger, "Advances in Silicon on insulator Optoelectronics," IEEE J. Select. Topics in Quantum Electron. **4**, 938 (1998).
3 A. Kaneko, T. Goh, H. Yamada, T. Tanaka, and I. Ogawa "Design and applications of silica-based planar lightwave circuits," IEEE J. Select. Topics in Quantum Electron. **5**, 1227 (1999).
4 B. J. Offrein, R. Germann, F. Horst, H.W.M. Salemink, R. Beyerl, and G. L. Bona, "Resonant coupler-based tunable add-after-drop filter in silicon–oxynitride technology for WDM networks," IEEE J. Select. Topics in Quantum Electron. **5**, 1400 (1999).
5 J.D. Joannopoulos and G. Lucovsky, "The physics of hydrogenated amorphous silicon," (Springer Verlag, Berlin, 1984).
6 S. Perkowitz, "Optical Characterization of Semiconductors," (Academic Press, London, 1993), p.27.
7 P. Shaoqi and D. Xiaoning, "Properties of Sputtered Amorphous Silicon without Hydrogen", in *"Proceedings of the International Workshop on Amorphous Semiconductors,"* H. Fritzsche, D. Han, C. C. Tsai, Eds. (World Scientific, Singapore, 1987).
8 J. I. Panvoke, "Luminescence in Hydrogenated Amorphous Silicon", in *"Proceedings of the International Workshop on Amorphous Semiconductors,"* H. Fritzsche, D. Han, C. C. Tsai, Eds., (World Scientific, Singapore, 1987).
9 R. A. Street, Ed., "Technology and Applications of Amorphous Silicon," (Springer Verlag, Berlin, 2000), pp. 1-403.
10 A. M. Agarwal, L. Liao, J. S. Foresi, M. R. Black, X. Duan, and L.C. Kimerling, "Low-loss Polycrystalline Silicon Waveguides for Silicon Photonics," J. Appl. Phys. **80**, 6120 (1996).
11 A. Serpengüzel, A. Aydinli, and A. Bek, "Enhancement and inhibition of photoluminescence in hydrogenated amorphous silicon nitride microcavities," Optics Express **1**, 108 (1997).
12 M. H. Brodsky, "Quantum Well Model of the Hydrogenated Amorphous Silicon," Solid State Commun. **36**, 55 - 59 (1980).
13 A. Serpengüzel, A. Aydinli, A. Bek, and M. Güre, "Visible photoluminescence from planar amorphous silicon nitride microcavities, " J. Opt. Soc. Am. B. **15**, 2706 (1998).
14 D. J. Wolford, B. A. Scoot, J. A. Reimer and J. A. Bradley, "Efficient visible luminescence from hydrogenated amorphous silicon," Physica **B 117**, 920 (1983).
15 T. Canham, "Silicon Quantum Wire Array Fabrication by Electrochemical and Chemical Dissolution of Wafers," Appl. Phys. Lett. **57**, 1046 (1990).
16 D. J. Lockwood, "Optical Properties of Porous Silicon," Solid State Commun. **92**, 101 (1994).
17 L. Pavesi, C. Mazolleni, A. Tredicucci, and V. Pellegrini, "Controlled photon emission in porous silicon microcavities," Appl. Phys. Lett. **67**, 3280 (1995).

SAMSUNG EX. 1002 - 570/4148

18 L. Pavesi and V. Mulloni, "All porous silicon microcavities: growth and physics," J. Lumin. **80**, 43 (1999).
19 M. Araki, H. Koyama, and N. Koshida, "Precisely tuned emission from porous silicon vertical optical cavity in the visible region," J. Appl. Phys. **80**, 4841 (1996).
20 M. Cazzanelli and L. Pavesi, "Time-resolved photoluminescence of all porous silicon microcavities," Phys. Rev. B **56**, 15264 (1997).
21 E. K. Squire, P. A. Snow, P. St. J. Russell, L. T. Canham, A. J. Simmons, and C. L. Reeves, "Light emission from porous silicon single and multiple cavities," J. Lumin. **80**, 125 (1999).
22 M. Takahashi, Y. Toriumi, T. Matsumoto, Y. Masumoto, N. Koshida, "Significant photorefractive index change observed in porous silicon Fabry-Perot resonators," Appl. Phys. Lett. **76**, 1990 (2000).
23 S. Setzu, S. Letant, P. Solsona, R. Romestain, and J. C. Vial, " Improvement of luminescence in p-type as-prepared or dye impregnated porous silicon microcavities," J. Lumin. **80**, 129 (1999).
24 Z. H. Xiong, S. Yuan, Z. M. Jiang, J. Qin, C. W. Pei L. S. Liao, X. M. Ding, X. Y. Hou, and X. Wang, "Photoluminescence studies of porous silicon microcavities," J. Lumin. **80**, 137 (1999).
25 E. K. Squire, P. St. J. Russell, and P. A. Snow, "Optimized light emission from layered porous silicon structures," Appl. Opt. **37**, 7107 (1998).
26 V. Mulloni and L. Pavesi, "Porous silicon microcavities as optical chemical sensors," Appl. Phys. Lett. **76**, 2523 (1999).
27 A. Arena, S. Patane, G. Saitta, S. Savasta, R. Girlanda, and R. Rinaldi, "Silicon based organic-inorganic microcavity and its dispersion curve from angle resolved photoluminescence," Appl. Phys. Lett. **72**, 2571 (1998).
28 B. T. Sullivan, D. J. Lockwood, H. J. Labbe, and Z.-H. Lu, "Photoluminescence in Amorphous Si/SiOx Superlattices Fabricated by Magnetron Sputtering," Appl. Phys. Lett. **69**, 3149 (1996).
29 D. J. Lockwood, J.M. Baribeau, and B. T. Sullivan, "Visible light from Si/SiOx superlattices in planar microcavities," J. Vac. Sci. Technol. B **16**, 1707 (1998).
30 D. J. Lockwood, B. T. Sullivan, and H. J. Labbe, "Visible light emission from Si/SiOx superlattices in optical microcavities," J. Lumin **80**, 75 (1999).
31 K. M. Cheng, A. W. Sparks, H.-C. Luan, D. R. Lim, K. Wada, and L. C. Kimerling, "SiO2/TiO2 omnidirectional reflector and resonator with sol-gel method," Appl. Phys. Lett. **75**, 3805 (1999).
32 F. Hamelmann, G. Haindl, J. Schmalhorst, A. Aschentrup, E. Majkova, U. Kleineberg, U. Heinzmann, A. Klipp, P. Jutzi, A. Anopchenko, M. Jergel, and S. Luby, "Metal oxide / silicon oxide multilayer with smooth interfaces produced by in situ controlled plasma enhanced MOCVD," Thin Solid Films **358**, 90 (2000).
33 L. Pavesi, R. Guardini, and C. Mazzoleni, "Porous Silicon Resonant Cavity Light Emitting Diodes," Solid State Commun. **97**, 1051 (1996).
34 M. Araki, H. Koyama, and N. Koshida, "Controlled electroluminescence spectra of porous silicon diodes with vertical optical cavity," Appl. Phys. Lett. **69**, 2956 (1996).
35 D. Hunkel, R. Butz, R. Ares-Fisher, M. Marso, and H. Lüth, "Interference filters from porous silicon with laterally varying wavelength of reflection," J. Lumin. **80**, 133 (1999).
36 H. F. Arrand, T. M. Benson, P. Sewell, and A. Loni, "Optical waveguides in porous silicon pre-patterned by localized nitrogen implantation," J. Lumin. **80**, 199 (1999).
37 S. W. Leonard, H. M. van Driel, K. Busch, S. John, A. Birner, A.-P. Li, F. Müller, U Gösele, and V. Lehmann, "Attenuation of optical transmission within the band gap of thin two-dimensional macroporous silicon photonic crystals," Appl. Phys. Lett. **75**, 3063 (1999).
38 M. C. Netti, M. D. B. Charlton, G. J. Parker, and J. J. Baumberg, "Visible photonic band gap engineering in silicon nitride waveguides," Appl. Phys. Lett. **76**, 991 (2000).
39 Tsing-Hua Her, Richard J. Finlay, Claudia Wu, and Eric Mazur, "Femtosecond laser-induced formation of spikes on silicon", Appl. Phys. A 70, 383-385 (2000);
40 Tsing-Hua Her, Richard J. Finlay, Claudia Wu, Shrenik Deliwala, and Eric Mazur, "Microstructuring of silicon with femtosecond laser pulses", Appl. Phys. Lett. 73, 1673-1675 (1998).

SAMSUNG EX. 1002 - 571/4148

C 20

Formation of regular arrays of silicon microspikes by femtosecond laser irradiation through a mask

M. Y. Shen,[a] C. H. Crouch, J. E. Carey, R. Younkin, and E. Mazur
Department of Physics and Division of Engineering and Applied Sciences, Harvard University, Cambridge, Massachusetts 02138

M. Sheehy and C. M. Friend
Department of Chemistry, Harvard University, Cambridge, Massachusetts 02138

(Received 3 October 2002; accepted 22 January 2003)

We report fabrication of regular arrays of silicon microspikes by femtosecond laser irradiation of a silicon wafer covered with a periodic mask. Without a mask, microspikes form, but they are less ordered. We believe that the mask imposes order by diffracting the laser beam and providing boundary conditions for capillary waves in the laser-melted silicon. © *2003 American Institute of Physics.* [DOI: 10.1063/1.1561162]

A variety of micrometer-scale surface patterns have been observed on silicon surfaces after pulsed laser irradiation.[1–6] When irradiated by nanosecond laser pulses at a fluence close to the melting threshold, silicon surfaces develop ripples with submicrometer periodicity (often called laser-induced periodic surface structures, or LIPSS).[1,7] By irradiating surfaces with femtosecond laser pulses above the ablation threshold in SF_6, we previously created silicon surfaces covered with a semi-ordered pattern of sharp conical microspikes.[3,4] Others have also reported laser-induced formation of larger conical microstructures using high-intensity nanosecond pulses.[2,5,6]

While the mechanism responsible for LIPSS formation is now well understood, the mechanism of microspike formation is not. To better understand this mechanism, we imposed boundary conditions on the excited silicon surface and the incident laser light by irradiating the silicon surface through a periodic mask. The resulting microspikes are arranged in regular arrays with the same symmetry as the mask apertures. The arrangement and separation of the microspikes indicate that capillary waves in the molten silicon may play a role in microspike formation; ordering may arise from confinement of the region of laser-melted silicon at the surface combined with diffraction of the laser light.

We masked silicon chips [float zone Si(111)] by affixing 2-μm-thick copper transmission electron microscope (TEM) grids to the sample surface with conductive carbon tape. The carbon tape causes a gap between the silicon surface and the TEM grid, varying from a few micrometers to tens of micrometers. We used square grids of width 10, 20, 30, 40, 50, and 200 μm, and hexagonal grids of width 30 μm. The sample is mounted normal to the laser beam on a three-axis translation stage in a vacuum chamber with a base pressure of less than 10^{-2} Pa. During sample irradiation, the chamber is backfilled with 6.7×10^4 Pa SF_6. The laser pulses (800 nm, 100 fs, 0.3 mJ) are focused to a beam waist of 200 μm at the sample surface; the spatial profile of the beam is Gaussian, and the fluence per pulse at the sample surface is 6 kJ/m^2, which is well above the thresholds for both ablation and plasma formation. The sample is translated at 200 μm/s in the plane perpendicular to the laser beam, and a fast shutter is used to vary the repetition rate of the laser pulse train between 5 and 50 Hz, thereby controlling the average number of laser pulses per unit area.[8] After irradiation, the masks are removed and the resulting structures imaged with a scanning electron microscope.

Figures 1(a) and 1(b) are electron micrographs of the surfaces obtained using a mask with 30-μm hexagonal openings; Figs. 1(c) and 1(d) show surfaces obtained using a mask with 20-μm square openings. The microspikes are arranged in regular arrays with the same symmetry as the mask. The gray bars above Figs. 1(a) and 1(b) show the spatial intensity profile of the laser beam; the density of the microspikes depends on the laser fluence, with a higher density of microspikes forming where the fluence is less. Along a constant-fluence line perpendicular to the laser intensity profile, the density and arrangement of microspikes is nearly uniform. Using a mask with 10-μm or 30-μm square openings also produces ordered microspikes of the same number density as the 20-μm square openings; using a mask with larger openings produces ordered microspikes at the edges, but the microspikes in the center of the opening are quasi-ordered, like the microspikes produced without a mask.

Figures 2(a)–2(e) show the development of the microspikes as the number of laser pulses increases, using a mask with square openings, and with the laser polarization parallel to the vertical axis of the mask. After five laser pulses, periodic ripples form with the same wavelength as the laser light (800 nm), oriented perpendicular to the polarization of the laser light. Between 10 and 50 pulses, a coarser periodic structure appears on top of the ripples, consisting of ridges parallel to the polarization of the light and perpendicular to the underlying ripple structure. In the absence of a mask, periodic ripples also form perpendicular to the laser polarization, but the subsequent coarser structure lacks the order of the structures shown in Fig. 2.[9] Between 100 and 200 pulses, the underlying ripples vanish, and the coarsened structure evolves into an ordered array of microspikes. If the laser polarization is rotated 45° relative to the sides of the

[a]On leave from Tohoku University, Sendai, Japan; electronic mail: mshen@deas.harvard.edu

 © 2003 American Institute of Physics

SIONYX1403000042.0037

SAMSUNG EX. 1002 - 572/4148

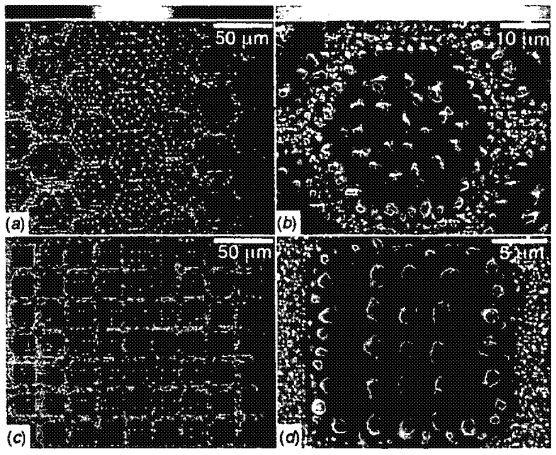


FIG. 1. Scanning electron micrographs of ordered silicon spikes formed by masking the irradiated sample with (a), (b) a 30-μm hexagonal grid and (c), (d) a 20-μm square grid. The nearly Gaussian spatial intensity profile of the laser pulse is shown at the top in grayscale (white corresponds to maximum intensity).

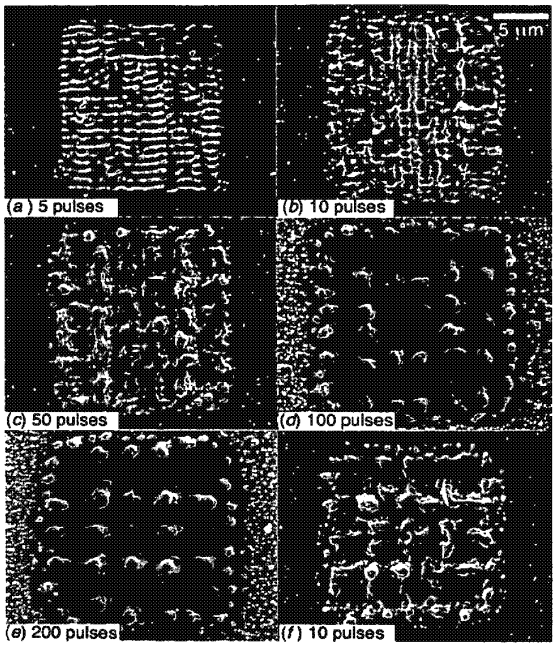


FIG. 2. Scanning electron micrographs of (a)–(e) silicon spikes formed with a square grid after increasing number of laser pulses. The direction of the electric field is vertical in (a)–(e). (f) Spikes formed with the grid rotated 45° relative to the grids in (a)–(e).

mask openings, as in Fig. 2(f), the coarsened structure that exists after 10 pulses no longer consists of ridges parallel to the polarization, as in Fig. 2(b). Instead, the coarsened structure is fragmented into smaller structures, and those structures fall roughly on a square array with axes parallel to the sides of the mask openings.

We identify three stages in the process of spike formation from the images presented in Fig. 2. First, ripples form on the silicon surface, then a coarsened layer forms on top of the ripples, and finally the coarsened layer fragments into beads which subsequently are etched into microspikes. In the remainder of this letter, we will discuss possible mechanisms for this process.

Periodic ripple formation upon laser irradiation of solids with nanosecond pulses below the ablation threshold has been previously reported, and was attributed to periodic melting of strips on the surface (at low fluence) or capillary wave formation in a uniformly melted area (at high fluence).[7] Under the conditions we use, with each laser pulse, a plasma forms; after the plasma expands, a molten silicon layer is left behind on the surface, which solidifies before the next laser pulse arrives. The ripples we observe [Fig. 2(a)] have the same wavelength as the laser wavelength; we therefore expect that as in the nanosecond case, ripple formation is due to capillary waves excited in the molten silicon by interference between the incident and scattered laser light.[7]

Formation of the coarsened layer and subsequent fragmentation into microspikes could either involve plasma oscillations[10] or capillary waves in the molten silicon.[6] In addition, Fresnel diffraction of the incident light from the edges of the mask openings[11] should produce a modulated temperature profile in the plasma or the liquid; temperature variations may play a role in exciting or sustaining the oscillations.

Let us first consider the possibility of a plasma oscillation induced by the trailing edge of the light pulse. By analyzing the radiation backscattered from a laser-produced plasma, Jannitti and coworkers[10] observed a resonant interaction between the plasma and laser pulse light when the plasma frequency equals the laser light frequency. This resonance occurs because the electron density of the plasma increases with increasing laser fluence; the corresponding plasma frequency can therefore increase until the plasma frequency is resonant with the laser light frequency, and the electromagnetic field couples directly to the plasma oscillation. However, we find that increasing the fluence increases both the typical separation of the microspikes [Figs. 1(a) and 1(c)] and the wavelength of the coarsened layer. If the microspike separation was determined by the plasmon wavelength, increasing the plasma density, and therefore the plasma frequency, should instead decrease the typical separation of the microspikes and the wavelength of the coarsened layer. Therefore plasma oscillations cannot be responsible for the arrangement of the microspikes.

Let us next consider capillary waves in the molten silicon as a mechanism for forming the coarsened layer. Diffraction of the laser light from the mask apertures causes inhomogeneous energy deposition into the substrate; as a result, the temperature in the molten surface layer is periodically modulated. The surface tension of the molten silicon decreases with increasing temperature, so the hot liquid flows toward cooler regions, deforming the surface. Relaxation of the deformation as the molten silicon cools can then excite capillary waves in the molten liquid; these capillary waves are most likely the instability that drives both the formation of the coarsened layer and its subsequent breakup.

We can estimate the characteristic length scale of the coarsened layer from the dispersion relation for capillary waves in a shallow liquid layer:[6,12]

SIONYX1403000042.0038

SAMSUNG EX. 1002 - 573/4148

$$\lambda = \left[\frac{\sigma d}{\rho}\right]^{1/4} (2\pi\tau)^{1/2}, \quad (1)$$

where λ and τ are the wavelength and period of the capillary waves, respectively and σ, d, and ρ are the surface tension coefficient, depth, and mass density of the liquid layer, respectively. Note that the capillary wave period cannot exceed the lifetime of the liquid layer τ_{liq}, and therefore the average spike separation λ_{spike} cannot exceed the wavelength corresponding to τ_{liq}. We estimate τ_{liq} to be between 75 ns (a value measured by others with somewhat lower fluence at a shorter wavelength[13]) and 600 ns (calculated from a simple model that ignores the effect of ablation[14]). The penetration depth α^{-1} of 800-nm light into silicon is roughly 10 μm,[15] and others have determined that the liquid layer formed at lower fluence and shorter wavelength is roughly 100 nm deep;[13] we therefore expect the liquid layer depth d to lie between these two limits. Using these ranges of values for τ_{liq} and d and literature values for σ and ρ[16,17] in Eq. (1), we estimate the longest allowed wavelength to be between 2 and 20 μm. The observed λ_{spike} of 5 μm (Figs. 1 and 2) falls nicely in this range of values.

The observed increase of the average spike separation with increasing fluence is also consistent with capillary wave-driven formation. Increasing the fluence deposits more energy in the silicon substrate, melting more silicon and therefore increasing the liquid layer depth and lifetime. The dispersion relation given above indicates that increased depth and lifetime should correspond to a longer wavelength.

When the melted silicon layer is confined rather than infinite in extent, the size of the melted area constrains the allowed capillary wavelengths, and standing waves form. In a melted square with side a, allowed standing wave vectors are given by $k = \pi m/a$ ($m = 1,2,3,...$). As we observe only a single wavelength in all the squares irradiated with a given fluence, some additional mechanism must be at work to select a particular wavelength. Fresnel diffraction from the edges of the mask opening cannot on its own determine the arrangement of the microspikes, as the spatial period of a diffraction pattern is independent of laser fluence and therefore cannot produce a fluence-dependent arrangement of microspikes. However, the diffraction pattern may help select a particular capillary wavelength. We calculated the power spectrum of the diffracted light intensity on the silicon surface, and find that the peak amplitude decreases with increasing m.[18] Consequently, diffraction should promote formation of the longest wavelength capillary wave that can exist given the lifetime of the melted layer. When the grid opening is larger than 30 μm, the diffraction pattern is only significant near the edges of the openings, and so ordering only occurs there.

The dependence of the structures on laser polarization is also consistent with a formation mechanism involving both capillary wave excitation and Fresnel diffraction. Because the mask is conducting, the tangential electrical field at the edges of the mask must be zero. When the polarization is parallel to one pair of sides of the square aperture, as shown in Fig. 2(b) the intensity of the electric field is zero along the parallel sides and nonzero along the perpendicular sides, which may promote formation of wavefronts parallel to one pair of parallel sides. When the polarization can be decomposed into roughly equal components along both pairs of sides, as in Fig. 2(f), standing waves form parallel to both pairs of sides.

In conclusion, we form micrometer-scale regions containing ordered arrays of silicon microspikes by femtosecond laser-assisted etching of silicon with periodic masks. We attribute this ordering to the selection of particular capillary waves in the molten silicon by Fresnel diffraction of light from the mask aperture. These ordered arrays of microspikes could find application as pixels of microspikes for field-emission devices and detectors.

This work was supported by the Harvard MRSEC (NSF/DMR-98-09363) and the Department of Energy. The authors thank J. Ashcom for experimental assistance, and Profs. H. Stone and M. Brenner for helpful discussions.

[1] P. M. Fauchet and A. E. Siegman, Appl. Phys. Lett. **40**, 824 (1982).
[2] J. E. Rothenberg and R. Kelly, Nucl. Instrum. Methods Phys. Res. B **1**, 291 (1984).
[3] T.-H. Her, R. J. Finlay, C. Wu, S. Deliwala, and E. Mazur, Appl. Phys. Lett. **73**, 1673 (1998).
[4] T.-H. Her, R. J. Finlay, C. Wu, and E. Mazur, Appl. Phys. A: Mater. Sci. Process. **70**, 383 (2000).
[5] A. J. Pedraza, J. D. Fowlkes, and D. H. Lowndes, Appl. Phys. Lett. **74**, 2322 (1999).
[6] S. I. Dolgaev, S. V. Lavrishev, A. A. Lyalin, A. V. Simakin, V. V. Voronov, and G. A. Shafeev, Appl. Phys. A: Mater. Sci. Process. **73**, 177 (2001).
[7] J. E. Sipe, J. F. Young, J. S. Preston, and H. M. van Driel, Phys. Rev. B **27**, 1141 (1983).
[8] We find that the spike formation is almost independent of the laser pulse train frequency when the laser repetition rate is slower than 100 Hz and the translation velocity is 200 μm/s. Thus we simply vary the repetition rate (determined by the shutter) to control the average number of light pulses incident on the silicon surface.
[9] C. H. Crouch, M. Y. Shen, J. E. Carey, and E. Mazur (unpublished).
[10] E. Jannitti, A. M. Malvezzi, and G. Tondello, J. Appl. Phys. **46**, 3096 (1975).
[11] M. Born and E. Wolf, *Principles of Optics*, 7th ed. (Cambridge University Press, Cambridge, UK, 1999), p. 481.
[12] L. D. Landau and E. M. Lifshitz, *Hydrodynamics* (Nauka, Moscow, 1988).
[13] K. Sokolowski-Tinten, J. Bialkowski, A. Cavalleri, D. von der Linde, A. Oparin, J. Meyer-ter-Vehn, and S. I. Anisimov, Phys. Rev. Lett. **81**, 224 (1998).
[14] $\tau_{liq} \sim (2D)^{-1}\alpha^{-2}$, where D is the thermal diffusivity and α^{-1} the penetration depth; from N. Bloembergen, AIP Conf. Proc. **50**, 1 (1979).
[15] $\alpha^{-1} = \lambda/(4\pi\kappa)$, with $\lambda = 800$ nm and $\kappa = 0.007$; κ is obtained from Palik, *Handbook of Optical Constants of Solids* (Academic, Chestnut Hill, MA, 1998), Vol. 1.
[16] *CRC Handbook of Chemistry and Physics*, 66th ed. (CRC Press, Boca Raton, FL, 1985–1986) p. F-25.
[17] C. Kittel, *Introduction to Solid State Physics*, 5th ed. (Wiley, New York, 1976), p. 32.
[18] The power spectrum shows that the component with wave vector k depends on the gap between the silicon surface and the TEM grid. The amplitude decreases as m increases, except that the component with $m = 2$ has near-zero amplitude for the range of gap values corresponding to our experiment. As we observe structures only with $m \geq 3$, we expect that $m = 1$ corresponds to a lifetime too great to be observed.

SIONYX1403000042.0039

SAMSUNG EX. 1002 - 574/4148

C21

SCIENTIFIC LIBRARY
FEB 11 1985
PAT. & T.M. OFFICE

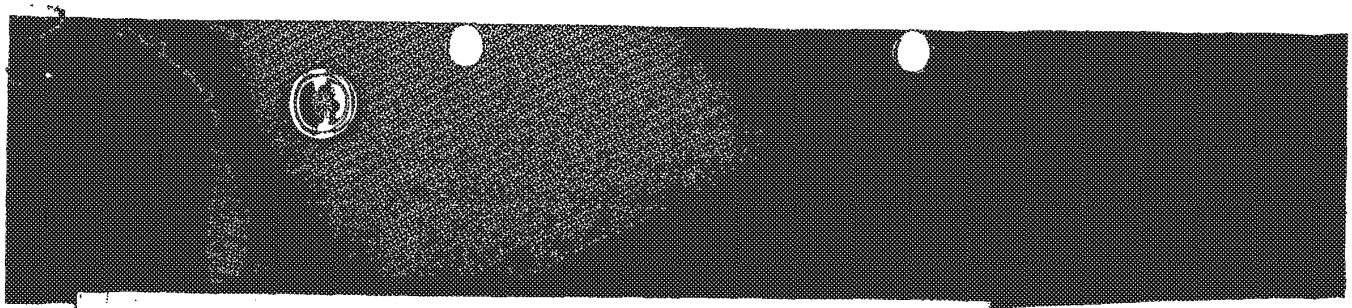
BASIC PHOTOVOLTAIC PRINCIPLES AND METHODS

Solar Energy Research Institute

VNR VAN NOSTRAND REINHOLD COMPANY

SIONYX1403000042.0040

SAMSUNG EX. 1002 - 575/4148



ASSIGN
A. Ullal Weststuck
TK
2960
Z9
1984

Copyright © 1984 by Van Nostrand Reinhold Company Inc.

Library of Congress Catalog Card Number: 83-21853
ISBN: 0-442-28126-9

All rights reserved. No part of this work covered by the copyright hereon may be reproduced or used in any form or by any means—graphic, electronic, or mechanical, including photocopying, recording, taping, or information storage and retrieval systems—without permission of the publisher.

Manufactured in the United States of America

Published by Van Nostrand Reinhold Company Inc.
135 West 50th Street
New York, New York 10020

Van Nostrand Reinhold Company Limited
Molly Millars Lane
Wokingham, Berkshire RG11 2PY, England

Van Nostrand Reinhold
480 Latrobe Street
Melbourne, Victoria 3000, Australia

Macmillan of Canada
Division of Gage Publishing Limited
164 Commander Boulevard
Agincourt, Ontario MIS 3C7, Canada

15 14 13 12 11 10 9 8 7 6 5 4 3 2 1

Library of Congress Cataloging in Publication Data

Zweibel, Kenneth
Basic photovoltaic principles and methods.

"The principal authors of this document are Kenneth Zweibel, PV Program Office, and Paul Hersch, Technical Information Branch.

Includes bibliographies and index.
1. Solar cells. I. Hersch, Paul. II. Solar Energy Research Institute. III. Title.
TK2960.H47 1984 621.31'244 83-21853
ISBN 0-442-28126-9

We are all very familia
utilizes sunlight to bioch
plants. However, there a
with matter, from simpl
atomic structure to pro
which occurs in certain
so-called photovoltaic e
produce a low voltage (

The purpose of this
voltaics, discuss the un
development status, an
tions for such systems. T
the engineer unfamiliar
ager looking looking fo
engineering student cor

The book is libera
and figures to allow on
place. This greatly enha
the abstract quantum
visualized voltage differ
which limit the efficienc
illuminates the necessi
obtain satisfactory perf

If we look back fo
key pioneering work c
Laboratories, with th
solar cell. Until the e
research programs and
vide "market quantitie
However, in the mid-1
research and developn
velopment, with photo

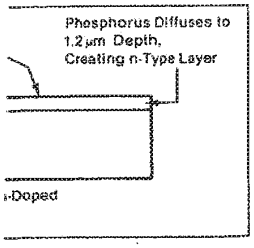
SIONYX1403000042.0041

SAMSUNG EX. 1002 - 576/4148

to diffuse into the
te of diffusion drop-
orus penetrates be-
type layer is a very
ant dopant switches
pe acceptor)—this is
terial is unchanged,

phosphorus varies as
: 950°C. The concen-
10^{16} atoms per cubic
he surface to have a
ıtimeter there. Heat-
oms to penetrate the
rops off with depth.
centimeter at a depth
rs of magnitude more
Thus the n-type char-
rs. Below 1.2 micro-
cell, the base material

phorus at the surface.
ut a hundredth of the
the phosphorus atoms



of phosphorus into silicon.
oduce the right amount and
atoms/cm^3. The model cell
ere the top-layer doping and

no longer assume places in the silicon crystal—there are just too many phosphorus atoms present for this simple structure. Instead, the phosphorus and silicon form an alloy, eliminating the donor-type electrical behavior of the phosphorus atoms. Because of this, the heavily doped surface shows little resemblance to n-type silicon: It is highly resistive and causes much recombination. Called the "dead layer," it is the subject of much work to minimize its negative effects.

The thickness of the top collector layer is of some importance. Solar cell efficiency is aided when light generates electrons and holes near the junction because then there is more likelihood that these charge carriers will be separated by the junction. As an illustration, consider this possibility: If the top surface is too thin almost all the light will pass through it and be absorbed below the junction. On the other hand, if the front surface is properly designed, it can be made the right thickness to absorb about half the light, while the remaining light can be absorbed on the other side of the junction: this would minimize the average distance from the junction of the light-generated charge carriers.* All of this is oversimplified but suggests the parameters involved in designing a cell's front layer. In silicon, light absorption depends on wavelength (shorter wavelengths are absorbed more easily): Over 50% of the sunlight incident on silicon is absorbed within 3 micrometers of the surface, but it takes almost 300 micrometers in total to absorb all the rest of the sunlight. This would suggest a cell with a shallow junction (less than 3 micrometers), a thick base, and a high mobility of charge carriers in the base (because light-generated carriers may be formed far from the junction).

ANTIREFLECTIVE COATINGS AND ELECTRICAL CONTACTS

A surface through which light passes has to be treated so that it reflects minimally, and electrical contacts have to be attached to a cell to collect charges. Untreated silicon reflects more than 30% of the light incident on it. However, a measured layer of silicon mon-

*Each incremental thickness of silicon has a certain constant probability of absorbing light and having an electron-hole pair generated. The thicker the substance, the more likely light will be absorbed.

SIONYX1403000042.0042

SAMSUNG EX. 1002 - 577/4148

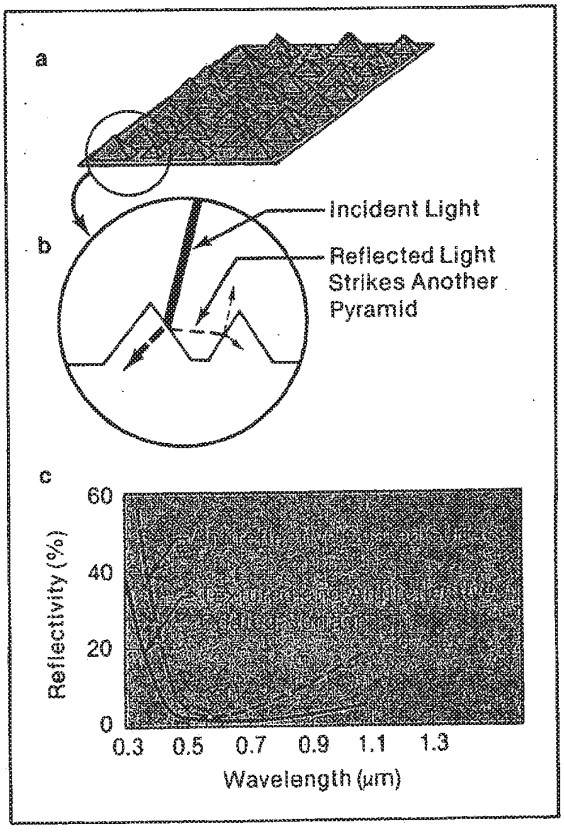


Figure 4-7. Texturing a cell exposes the tetrahedral surfaces of the silicon crystal lattice *(a)*. Light that strikes the cell nearly perpendicularly *(b)* can either be absorbed or reflected; if it is reflected, it will strike another surface and have another chance to be absorbed. Note also that light that is absorbed is bent at the treated surface, so that it penetrates the cell obliquely. Because light travels through the cell at an angle, the cell need not be as thick to absorb as much light. The lower reflectivity *(c)* and the longer length the light travels through the cell give about a 15% improvement in cell efficiency over smooth, uncoated cells. (After Jonston, 1980, p. 68.)

oxide (SiO), a very go
on a silicon cell. A sing
reflection to about 10
stance) can reduce it t

A further means t
of a cell (Figure 4-7).
second surface before
absorption. For exam
absorbed on one bo
reflected) has a probal
= 0.04; i.e., its probal
to 96% by the texture

Electrical contacts
placed in an electrical
are similar to those as
would be best to comp
with contacts; this wc
riers experience. But,
metallic contact wou
tradeoff must be ma
effects. It is usual to d
thin conductive finger
The grid fingers mus
enough not to block l
ficiently low, while sha
be expensive to fabric
make top-surface gric
through a mask, or t
method. Attaching th
not as complex: the c
new cell designs (for
that light enter the ce
the cell has to be tre
also.

Experiments are
(such as putting them
transparent grid mat
examined in Chapter

SIONYX1403000042.0043

SAMSUNG EX. 1002 - 578/4148

oxide (SiO), a very good *antireflective coating,* can easily be formed on a silicon cell. A single layer of SiO reduces a silicon cell's surface reflection to about 10%, while a double layer (with another substance) can reduce it to below 3%.

A further means to reduce reflection is to *texture* the top surface of a cell (Figure 4-7). Texturing causes reflected light to strike a second surface before it can escape, increasing the probability of absorption. For example, light with an 80% probability of being absorbed on one bounce (and therefore a 20% chance being reflected) has a probability of being reflected *twice* of $(0.2) \times (0.2) = 0.04$; i.e., its probability of absorption has been raised from 80% to 96% by the textured layer.

Electrical contacts must be attached to a cell for the cell to be placed in an electrical circuit. Design issues associated with contacts are similar to those associated with coated and textured surfaces. It would be best to completely cover the cell surfaces, back and front, with contacts; this would minimize the resistance that charge carriers experience. But, obviously, covering a cell with an opaque, metallic contact would completely block out the light. Thus a tradeoff must be made between resistance losses and shading effects. It is usual to design top-surface contacts as grids, with many thin conductive fingers spreading to every part of the cell's surface. The grid fingers must be thick enough to conduct well but thin enough not to block light. Such a grid keeps resistance losses sufficiently low, while shading only about 10% of the surface. Grids can be expensive to fabricate and can cause dependability problems. To make top-surface grids, metallic vapors can be deposited on a cell through a mask, or they can be painted on via a screen printing method. Attaching the back-surface contact to a cell is frequently not as complex: the contact simply can be a metal sheet. However, new cell designs (for concentrated light, for instance) may require that light enter the cell from the front and back, so that the back of the cell has to be treated antireflectively and have grid contacts, also.

Experiments are being conducted on alternative grid designs (such as putting them only on the cell's back surface) and on finding transparent grid materials, both of which are among the options examined in Chapter 5 on advanced silicon cells.

Light

d Light
nother

Surface
Receiver

1.3

faces of the silicon crystal
b) can either be absorbed or
l have another chance to be
he treated surface, so that it
the cell at an angle, the cell
effectivity *(c)* and the longer
provement in cell efficiency

SIONYX1403000042.0044

SAMSUNG EX. 1002 - 579/4148

The output from an array is tied to a collecting conductor, called a bus. Sometimes the electrical connectors are called on for double duty—such as conducting heat as well as electricity.

The designer, in addition to arranging a needed number of cells, must make sure that the voltage within a group of cells cannot cause electric arcing (akin to a lightning flash) to another group of cells should voltage imbalances develop within the array. Arcing is prevented by providing sufficient inter-module electric insulation. Safely switches must also be provided for repair work.

PLACING THE CELLS

The way in which individual cells are placed in the array and the cell's shape have to be considered by the PV panel designer. Areas within the array where there are no cells are areas that cannot produce electricity. Overall panel efficiency, as measured by wattage per unit area, drops as the space between cells increases.

Early in the development of PV panels, the designer mostly used the round wafer cells that resulted from pulling Czochralski crystals. Also, early crystals were considerably smaller in diameter than those grown today, aggravating the designer's packing problem (i.e., the need for a maximum cell-to-panel-area ratio). The designer, however, is not always interested in the use of large cells to boost packing efficiency. Cell sizing is an important aspect in creating modules with desired electrical characteristics. The current available from a cell grows with the size of the cell: the voltage remains constant (depending only on the potential existing at the cell junction, which is invariant). To build modules providing large voltage outputs requires many small cells connected in series.

Nevertheless, were packing a particular consideration, the designer could make use of round cells that had been cut in half and then placed into an array in an offset pattern to get more of them into a unit area, or the designer could have the disks specially cut into hexagons or squares to increase the packing density of the cells even more. But such specially shaped cells are considerably more costly than the round cells from which they are prepared (Figure 9-4). Hexagonal and square-shaped cells also invariably are smaller than round cells from which they are cut. Being smaller, more cells are

Figure 9-4. There ar
cells are used. In *(b)*,
halving circular cells
of the module's are
expansion or contra

SIONYX1403000042.0045

SAMSUNG EX. 1002 - 580/4148

ollecting conductor,
ors are called on for
is electricity.
needed number of
group of cells cannot
to another group of
the array. Arcing is
electric insulation.
r work.

the array and the
nel designer. Areas
areas that cannot
measured by watt-
ells increases.
he designer mostly
oulling Czochralski
maller in diameter
's packing problem
ratio). The design-
e of large cells to
ant aspect in creat-
stics. The current
e cell: the voltage
tial existing at the
les providing large
ted in series.
onsideration, the
een cut in half and
get more of them
disks specially cut
lensity of the cells
onsiderably more
prepared (Figure
riably are smaller
ller, more cells are

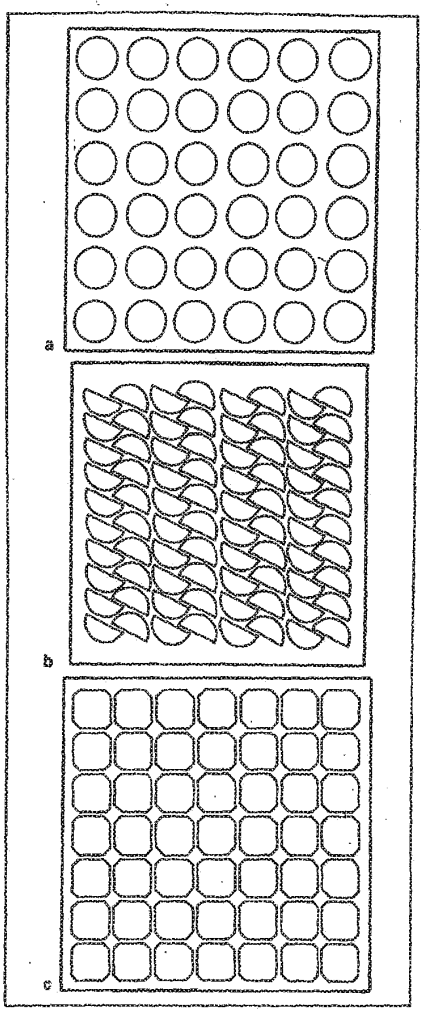


Figure 9-4. There are several ways to fill a module with PV cells. In *(a)*, standard round cells are used. In *(b)*, the amount of dead space (unusable by the cells) is diminished by halving circular cells to obtain a better fit. In (*c*), the square cells allow almost total use of the module's area. (Some space always must be provided to allow for thermal expansion or contraction of the module).

SIONYX1403000042.0046

SAMSUNG EX. 1002 - 581/4148

needed and this contributes to electrical connection complications (in joining increased numbers of cells). More recently, designers have had the option of choosing cells with areal shapes determined by the method of growth (see previous chapters covering cell design). But cells made from, say, ribbon material, are smaller and often produce electricity less efficiently than round cells from Czochralski-drawn material: Thus, depending on a particular array design, square cells cut from ribbon may or may not be preferred.

Although the designer's aim is to place cells as closely together as possible, cells cannot be allowed to touch or they will short out electrically. In fact, extra space must be allowed between cells to accommodate thermal expansion. The best packing of an array, therefore, usually is about 90%.

ARRAY SUPPORT

There is more to array building than simply resolving electrical needs. Individual solar cells are fragile. Groups of them can be equally fragile, if not more so. Each module must be able to hold up to the rigors of assembly and disassembly (during maintenance). Terrestrial arrays must be able to withstand wind loads and mechanical movement. Earthbound and space arrays must stand up to stresses induced by temperature changes. The array must be structurally self-supporting and/or have a supporting frame (Figure 9-5).

Weight, per se, of the array support structure is not much of a consideration for terrestrial arrays. The cost of the support structure is, however, quite meaningful. The situation is quite reversed for PV satellite applications, where every ounce of weight is at a premium, and the price for saving ounces is not an overriding consideration.

MODULE COVERS

Part of a module's support is in the form of the transparent cover applied to it, particularly if glass is used. The primary application of the cover, however, is to protect the PV module. For terrestrial arrays, for example, protection is afforded against such conditions as oxygen, humidity, dust, and precipitation. An earthbound array

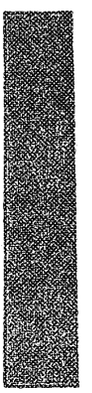


Figure 9-5. Amon
module must take
frame, and the fur

cover, inciden
terrestrial mod
array the indiv
integral cover
earth-array cel
encountered in

Since moc
sunlight that e
usually materi
spectrum and t

Some mod
so that light ca
increasing phot
required for ar
10).

Cover mat
rately or in con
plastics. In ge
elements that t
space applicati

SIONYX1403000042.0047

SAMSUNG EX. 1002 - 582/4148

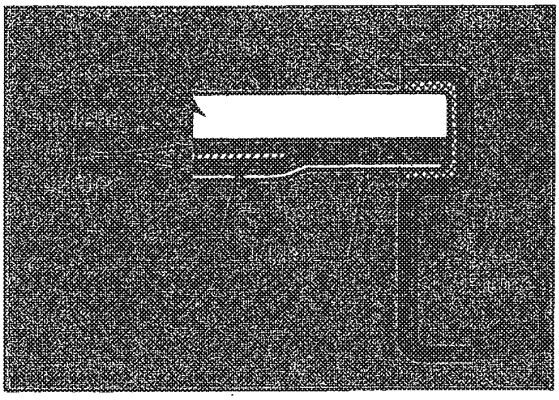


Figure 9-5. Among other things a standard design for encapsulating an earthbound PV module must take into consideration the transmissivity of the cover, the integrity of the frame, and the functionability (ability to stay in place) of the gasket and/or sealants.

cover, incidentally, differs from that for a spaceflight array. The terrestrial module is overlayed with an integral cover. In the space array the individual solar cell is protected. Part of the reason for an integral cover is that it is thus easier to protect a large number of earth-array cells from humidity and oxygen seepage—elements not encountered in space.

Since module covers must be transparent to the part of the sunlight that excites the PV cells, covers made for silicon cells are usually materials that admit light in the violet to the far-infrared spectrum and beyond (0.3–3 micrometer wavelength region).

Some modules have transparent covers at their front and back so that light can enter the solar cells from two directions, thereby increasing photocurrent output from the cells. (Special mounts are required for arrays of this nature, and they are covered in Chapter 10).

Cover materials that have been employed to date, either separately or in combination, include glasses and both rigid and flexible plastics. In general, glass is more resistant than plastics to the elements that the cover is intended to protect against. However, for space applications, where weight is a big factor, use of plastics is

SIONYX1403000042.0048

SAMSUNG EX. 1002 - 583/4148

more likely than glass. For terrestrial applications, glass usually is preferred for its low cost, high performance, and retention of clarity. For example, if the glass is regularly washed, the amount of light transmitted through the glass can be expected to remain for 20 or more years within 5% of that at the time of manufacture. (Of course, glass may be more susceptible to breakage than is plastic, and care must be taken to provide glasses that are appropriate to the applications). Even the best plastics will lose 25% and more transmissivity within several years.

The covers, which are usually cemented in place using silicones, must be made as thin as possible, not neccessarily for purposes of keeping transmissivity high, but for aiding in the cooling of the module. As discussed in previous chapters, the performance of a silicon PV cell degrades if it heats much above 25°C. It is therefore usually expedient to provide for cooling of the arrays.

MODULE COOLING

In space, the only cooling option is to radiate away excess heat. For earthbound arrays, the designer can rely on radiation, convection, and conduction to keep the array from working at temperatures that appreciably degrade operation. (The cooling design for one compact module is shown in Figure 9-6).

For earthbound arrays not subject to concentrated rays of the sun, cooling can usually be achieved without elaborately designing for it. Natural radiation and convective air currents do all the cooling needed so long as the array is not installed in a way that impedes air circulation. For many applications (and particularly in space), black heat sinks and radiative fins (passive system) must be provided at the back of the panel to help radiate the heat. For terrestrial applications, it also is possible to provide coolants, such as water and fluorocarbons, pumped through tubes embedded in a panel's support structure in order to conduct heat from the panel (active system). Passive cooling systems are basic to satellite arrays. They are also generally preferred for earthbound arrays. Only when large optics are used to magnify the sun's light, by perhaps a hundredfold or more, are active systems made part of an array cooling design.

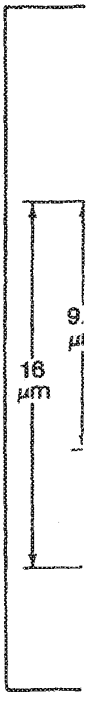


Figure 9-6. High ter
Many modules can b
used with sunlight t
trator cell, cannot. I
temperatures within

HYBRID DESIGN

Photovoltaic sy
squeeze the ma
ployment of tra
ter 10).

The most e
the sun's energ
More practical

SIONYX1403000042.0049

SAMSUNG EX. 1002 - 584/4148

A 1280x960 3.75um pixel CMOS imager with Triple Exposure HDR

Johannes Solhusvik[1], Sohrab Yaghmai[1], Arthur Kimmels[1], Christian Stephansen[1], Alf Storm[1], Jenny Olsson[1], Anders Rosnes[1], Tore Martinussen[1], Trygve Willassen[1], Per Olaf Pahr[1], Siri Eikedal[1], Steve Shaw[2], Ranjit Bhamra[2], Sergey Velichko[3], Dan Pates[3], Sachin Datar[3], Scott Smith[3], Lingtao Jiang[3], Dave Wing[3] , Ajaya Chilumula[3]
[1]Aptina Imaging, Oslo, Norway,
[2]Aptina Imaging, Bracknell, UK
[3]Aptina Imaging, San Jose, CA, USA

A triple exposure 20-bit output high dynamic range (HDR) CMOS imager with sub 2e- rms noise floor is presented. The array consists of 1280x960 pinned photodiode pixels with 3.75um pitch and programmable (high or low) conversion gain (Fig.1). A two-way row sharing architecture is utilized after weighing fill factor (i.e. QE and crosstalk) against conversion gain (reduced with sharing). The dual conversion gain (CG) feature allows CG adjustment globally across all pixels to match the overall light level in the scene. This is controlled by turning the DCG gate ON or OFF to connect or disconnect the in-pixel capacitor C to the floating diffusion (FD) node. CG is equal to 147uV/e- in High CG (HCG) mode and 37uV/e- in Low CG (LCG) mode. The timing diagram in Fig.2 illustrates the pixel readout process in LCG mode. The DCG gate is turned on when ROW is active, as well as during the extra pixel reset operation. The latter is done to avoid long duty cycle high voltage stress on node A when the sensor is running in LCG mode.

The 'triple exposure' HDR method yields two knee-points and is essentially an extension of the HDR scheme presented by Yadid-Pecht et al (JPL) at this Workshop in 1997. It benefits from inherent signal-to-noise advantages compared to other HDR schemes (e.g. lateral overflow), namely (i) no added pixel circuitry, (ii) no reduction in full-well capacity and (iii) supports regular CDS readout. This comes at a cost of 3x faster readout electronics and on-chip line buffer memory, both of which increases die size and power.

In this device we have implemented 42+3 rows of line memory based on a target to keep SNR above 20dB (in LCG mode) at the knee-points where SNR is at its lowest. The term 'triple exposure' signifies three captures per frame, each with different integration time (T1, T2 and T3). This is achieved by sampling and digitizing three pixel rows per row-time (nominal 22.2usec) as illustrated in (Fig.3). Two of the rows (T1 and T2) are stored in memory for later use and the third (T3) is combined with previously sampled T1 and T2 data to generate the output value. T1 is the longest integration time. Its' maximum value is equal to 1/(Tframe-T2-T3) which is the case illustrated in Fig.3. The T3 row represents the shortest integration time, and it is also the output row. The other two are 'pushed' onto their corresponding line memory stacks (one for T1 and one for T2). At the opposite end of these stacks one finds the T1 and T2 pixel values corresponding to the output (T3) row. By combining these three values (T1, T2, and T3) one obtains a 20bit linear response pixel value suitable for post processing in the ISP (color processing, tone mapping, etc.).

Fig.4 shows the chip block diagram. One-time-programmable-memory (OTPM) is used to store trimming values and pixel defect correction table. The auto-exposure module sets integration time and exposure ratios depending on the scene dynamics. After linearization to 20bits in the signal processing data path, output values can be compressed to 14bits or 12bits (parallel or serial SLVS) in the output data path. A more detailed view of the analog readout architecture is given in Fig.5. Triple exposure HDR imposes three times faster row sampling and A/D conversion compared to a regular linear sensor. Both serial readout (one ADC) and group parallel readout were considered, but a column-parallel architecture was chosen primarily due to lower power consumption. Every column-pair has its own 2:1 multiplexer (MUX), a 20dB programmable gain amplifier and a 12-bit successive approximation (SA) ADC. Even and odd columns are sampled at the top and bottom depending on the row number being odd or even. This gives better layout efficiency (twice the pixel pitch per column layout) and reduced green channel offsets (since neighboring Gr and Gb pixels are read out through the same column mux+amp+ADC). The SA-ADCs are capable of running up to 750kpix/sec. The Correlated Double-Sampling (CDS) and A/D conversion process for one row lasts approximately 5.5us.

The chip floorplan (Fig.6) illustrates the positioning of the various modules. Both serial (1-4 lane SLVS at 450Mbps) and 12-bit parallel output is supported. In the latter case a 20-to-12 bit companding scheme with its knee-points close to the actual T1/T2/T3 knee-points is utilized to minimize compression losses.

At present time, first silicon has emerged from the fab and available measurement data confirms projected performance. Fig. 7 illustrates HDR 20bit output mode signal and noise performance. Measured dynamic range is >110dB. Fig. 8 illustrates signal-to-noise ratio as a function of light level. It confirms that SNR keeps well above 20dB at the knee-points. Fig. 9 shows SNR performance in linear mode. By selecting LCG or HCG upon light level a dynamic range of >72dB is achieved. Low readout noise <2e- enables image capture with Navitar (F#2.8) lens below 0.05lux at 5 frames per second. Bare die quantum efficiency (QE) is shown in Fig. 10. Maximum QE reaches 60% for green. A captured HDR scene is shown in Fig.11, and some basic performance parameters are listed in Table 1.

SAMSUNG EX. 1002 - 585/4148

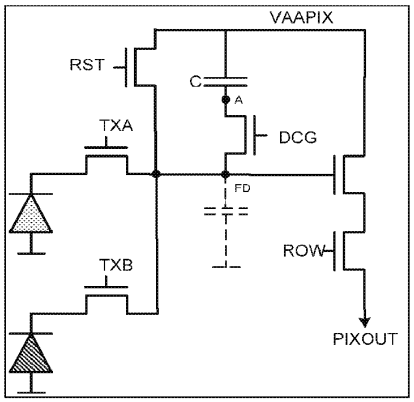


Figure 1

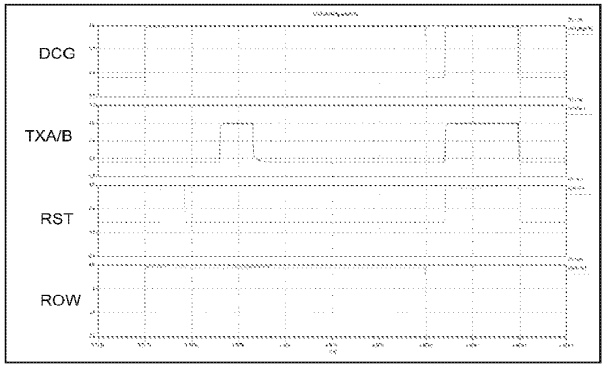


Figure 2

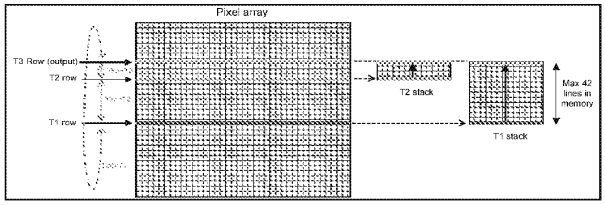


Figure 3

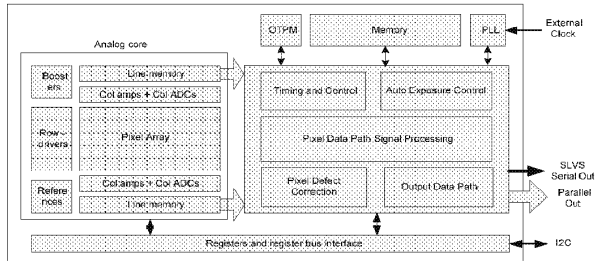


Figure 4

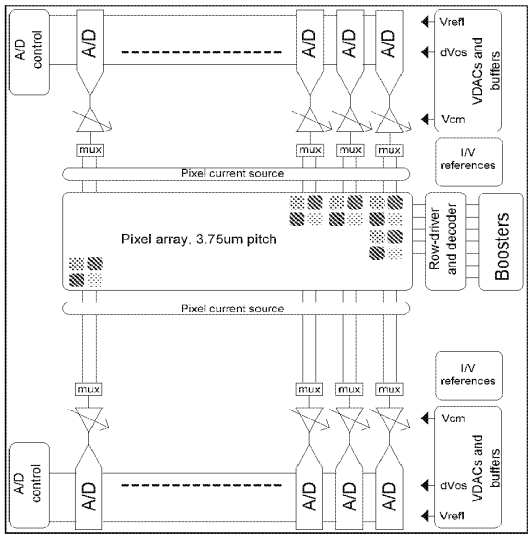


Figure 5

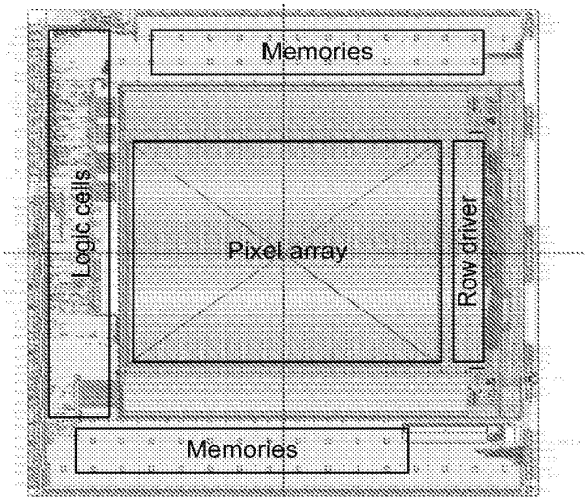


Figure 6

Parameter	Value	Comments
Power consumption	340mW	720p60 mode, Vaa=2.8, Vdd=1.8
High CG	147uV/e-	Measured on 1st silicon
Low CG	37uV/e-	Measured on 1st silicon
Source follower gain	0.92	Measured on 1st silicon
Readnoise @ Low CG	< 7e- rms	10x gain, 74.25Mpix/sec
Readnoise @ High CG	< 2e- rms	10x gain, 74.25Mpix/sec
Dynamic range @1x gain	112dB	CGL, T1/T2=T2/T3=16/1
Dynamic range @8x gain	106dB	CGH, T1/T2=T2/T3=16/1
T1/T2=T2/T3 ratios	4x, 8x, 16x, 32x	Programmable
Output data	12b, 14b, 20b	Parallel or serial (SLVS)
Chip die size	7.9mmx7.9mm	

Table 1

SAMSUNG EX. 1002 - 586/4148

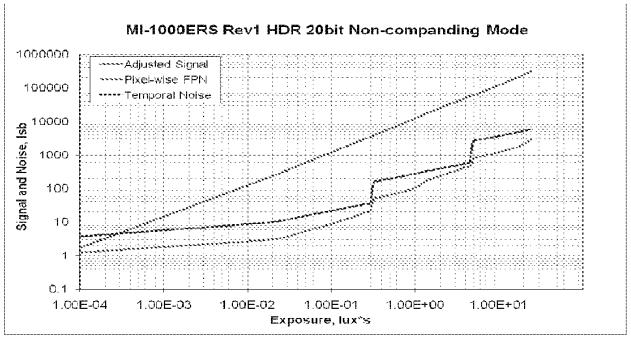


Figure 7

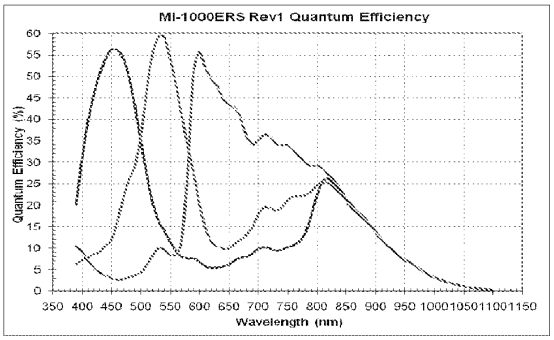


Figure 10

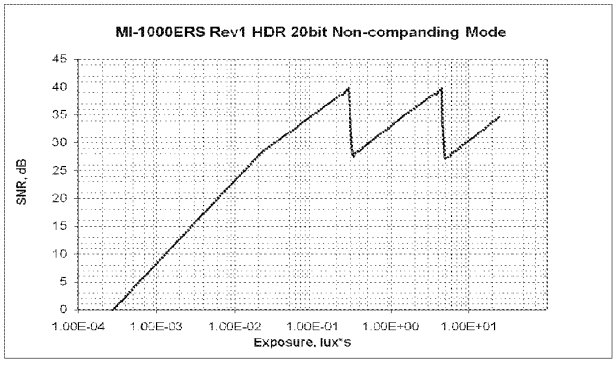


Figure 8

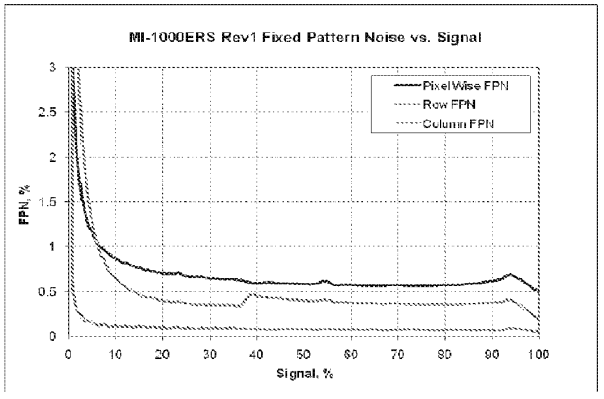


Figure 11

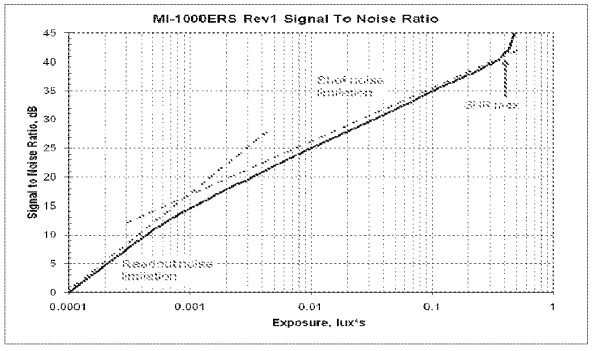


Figure 9



Figure 12

The x-ray sensitivity of amorphous selenium for mammography

Mary F. Stone
Department of Physics and Astronomy, State University of New York at Stony Brook, Stony Brook, New York 11794-3800

Wei Zhao[a)]
Department of Radiology, L-4, 120 Health Science Center, State University of New York at Stony Brook, Stony Brook, New York 11794-8460

Barbara V. Jacak
Department of Physics and Astronomy, State University of New York at Stony Brook, Stony Brook, New York 11794-3800

Paul O'Connor, Bo Yu, and Pavel Rehak
Instrumentation Division, Brookhaven National Laboratory, Upton, New York 11973

(Received 4 September 2001; accepted for publication 18 December 2001; published 19 February 2002)

A study of the x-ray sensitivity of amorphous selenium (a-Se) for digital mammography has been performed. A uniform layer of a-Se was deposited on a glass substrate with electrodes on both surfaces. The deposition procedure was identical to that used for a-Se flat-panel detectors. A high voltage was applied to the top surface of the a-Se layer in order to establish an electric field E_{Se}. Then the sample was exposed to x rays with 27 kVp spectra generated from an x-ray tube with a molybdenum (Mo) target. The mean x-ray energy of the spectrum used was ~16.6 keV. The x-ray current generated by the a-Se layer was measured as a function of E_{Se}. From the current measurement and the estimation of total x-ray energy absorbed in the a-Se, the energy required to create one electron-hole pair (EHP), W, was determined as a function of E_{Se}. It was found that at the most commonly used E_{Se} of 10 V/μm, W was measured as 64 eV. This is considerably higher than the widely accepted typical value of $W=50$ eV measured at higher x-ray photon energies (e.g., 50 keV). The dependence of W as a function of E_{Se} can be best fitted using the empirical expression of $E_{Se}^{-\gamma}$. This relationship is consistent with the results obtained at higher x-ray energies. This article provides an accurate measurement of x-ray sensitivity of a-Se at mammographic energies independent of detector operation, such as the most recently developed flat-panel detectors. The results will be a useful tool for investigation and optimization of a-Se-based x-ray imaging detectors, such as determination of pixel fill-factor and optimal E_{Se} during operation. © *2002 American Association of Physicists in Medicine.* [DOI: 10.1118/1.1449874]

Key words: amorphous selenium, x-ray sensitivity, mammography

I. INTRODUCTION

Digital mammography has been under investigation for over a decade to overcome the limitations of traditional screen-film mammography. Currently, three different types of digital mammography systems with instantaneous image readout have been developed commercially.[1] They all use a column-structured, thallium-doped cesium iodide [CsI(Tl)] scintillator as the x-ray detector, which absorbs the incident radiation and converts the energy to light photons. The light photons are then converted to electrons by an optical sensor, which is either an array of photodiodes or charge coupled devices (CCD). This method of x-ray detection using a phosphor is often referred to as the *indirect* approach. The column structure of the CsI(Tl) helps channel light to the surface. However, due to imperfections in the columns, there is still significant image blurring in the system, and the problem worsens as the thickness of CsI(Tl) increases. The blurring is also depth dependent, which results in a detective quantum efficiency (DQE) that decreases at high spatial frequencies.[2,3] Methods for improving the high spatial frequency DQE of digital mammography detectors are desirable, and one method is to use photoconductors for *direct* x-ray detection.[1] In photoconductors, such as amorphous selenium (a-Se), the absorbed x rays are converted directly to charge, which is then drawn to the surfaces by an applied electric field without significant image blurring. High-resolution images have been produced with an a-Se detector using a laser readout method.[4] Other photoconductors such as silicon (Si) and cadmium zinc telluride (CZT) have also been proposed for a direct conversion slot-scan digital mammography detector.[5]

Recently, flat-panel digital detectors based on amorphous silicon (a-Si) active matrix technology have become a clinical reality in radiographic applications, and their attractive features include compact size and rapid image readout. Both the direct[6–9] and indirect[10–13] methods have been implemented. For mammography, so far only indirect flat-panel detectors (with 100 μm pixels) have been commercialized.[14,15] However direct a-Se flat-panel mammographic detectors (85 and 70 μm pixels) are under development.[16,17] Efforts have also been made on the devel-

SIONYX1403000042.0053

SAMSUNG EX. 1002 - 588/4148

opment of small area a-Se flat-panel detectors based on the more cost effective and lower noise CMOS technology for application in interventional mammographic procedures such as needle biopsy.[18] With the increasing interests in the development of a-Se-based digital mammography detectors, it is important to understand and optimize the fundamental properties of a-Se layers for the imaging conditions and x-ray energies used for mammography. One important factor is the x-ray sensitivity.

The x-ray sensitivity of a-Se has been studied previously using different experimental methods and samples and for different x-ray photon energies. The data published in the 1970s for the values of W are highly variable,[19] and it is not clear whether this is due to experimental error or differences in a-Se samples. With the renewed interest in the use of a-Se for digital x-ray imaging detectors,[20] especially the flat-panel detectors,[21] there have been several recent studies on the x-ray sensitivity of a-Se for photon energies used in diagnostic radiology. Aiyah *et al.* measured W for an x-ray spectrum of 60 kVp using the radiographic discharge method, where the surface of an a-Se sample was charged to a preset voltage by a corotron, then exposed to a known amount of radiation and the residual surface potential was measured with an electrostatic voltmeter.[22] The difference in surface potentials allows the estimation of the total amount of EHPs generated, together with a calculation of the total amount of x-ray energy absorbed, the value for W can be determined. The radiographic discharge method was also used in a more recent study of W for three different x-ray spectra in the range of 40–140 kVp.[23] Haugen *et al.* measured W for a 45 kVp x-ray spectrum using the integrated current method, where an a-Se sample under a constant E_{Se} was exposed to a known amount of radiation, the current across the a-Se during irradiation was measured, and it was integrated to obtain the total EHPs generated, from which W was determined.[24] Both the radiographic and the integrated current methods require the calculation of the total amount of energy, E_{ab}, absorbed in the a-Se layer, which is subject to error in the determination of the spectrum. Rowlands *et al.* developed a more direct method for measuring W based on pulse height spectroscopy, where a small sample of a-Se was used as the radiation sensor for monoenergetic x rays ranging from 39.9 to 58 keV.[19] A more recent study by the same group improved the experimental apparatus and extended the energy range to 40–140 keV.[25] These recent studies of W reported more consistent values, e.g., a nominal value of $W=50$ eV at $E_{Se}=10$ V/μm with incident x-ray energy E of ~50 keV. Moreover, recent studies of W have also revealed an energy dependence, i.e., W decreases as incident x-ray energy E increases,[23,25] the mechanism for which is not yet fully understood with the continuing debate between columnar and Onsager recombination models for a-Se. Because of the energy dependence of W and the lack of published data for W at typical mammographic energies, where the mean incident x-ray energy is often <20 keV, we conducted the present study for the a-Se layers used in ongoing development of a-Se flat-panel digital mammography detectors. Our study will provide complementary data in a different x-ray energy range for the continuing investigation of x-ray sensitivity of a-Se. Because our study is performed independently from any image sensor, the results can be used in the investigation of imaging performance of a-Se flat-panel digital mammography detectors, such as the determination of pixel fill factor. The results will also be useful in optimizing the x-ray sensitivity of a-Se based image sensors.

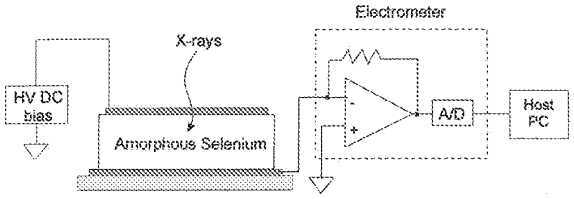


FIG. 1. Schematic diagram showing the experimental setup.

Because of the lower x-ray energy used in mammography, the number of EHPs generated by each x ray is 300–400. This makes it difficult to use the more accurate PHS method because the electronic noise of the apparatus limits the energy resolution. For our present study, we used the integrated current method, and made careful determination of the incident x-ray spectrum.

II. METHODS

A. Experimental apparatus and procedure

Figure 1 shows the experimental apparatus for the present work. The a-Se layer used in our experiments was prepared by Anrad Corporation using the same procedure as that used in small area a-Se flat-panel digital mammography detectors.[16] The a-Se layer was deposited on a glass substrate, and has bias electrodes on both surfaces, with indium tin oxide (ITO) on the bottom and aluminum on top. The thickness of the a-Se layer is 240 μm and the active area of the sample is determined by the size of the top electrode, which is 87×87 mm^2. The a-Se sample was biased using a negative potential on the top bias electrode, and the current in the sample before, during and after x-ray exposure was measured using an electrometer (Keithley model 6517). The current signal is taken from the bottom electrode of the a-Se sample and fed to the input of the electrometer, where the potential is kept at virtual ground. The electrometer is equipped with an A/D converter and storage memory so that the measured data for each exposure can be stored and transferred to a host PC through GPIB interface after the exposure is completed. Then the current measurement was integrated over the period of x-ray exposure to obtain the total charge generated by the a-Se.

A Senographe 600T Senix HF x-ray mammography system (General Electric) was used for the production of x rays during the experiments. The x-ray tube has a molybdenum (Mo) anode and added filters of Al or Mo. The x-ray tube has two focal spot sizes, 100 and 300 μm. During our measurement, we chose 27 kVp, the Mo filter (30 μm), and the small focal spot. The x-ray exposure was set at 32 mAs. The a-Se sample was placed along the chest-wall side of a cassette tray

SIONYX1403000042.0054

SAMSUNG EX. 1002 - 589/4148

and centered. Since the size of the sample is only 87 $\times$ 87 mm^2, a diaphragm was placed in the beam to reduce the radiation field (to 171 $\times$ 110 mm^2) in order to minimize the amount of backscatter. The x-ray exposure to the a-Se sample was measured with an ion chamber designed specifically for mammography (Radical Corporation Model 1015). The dosimeter has the ability to measure the total exposure and duration of each x-ray pulse.

B. Dark current

The dark current is the current produced in a biased a-Se sample when it is not exposed to x rays. It originates from either thermal excitation of charge carriers in the bulk of the a-Se sample, or from injected charge carriers from the bias electrodes. Our a-Se layer is equipped with blocking layers at both electrode interfaces, and the purpose of these blocking layers is to minimize charge injection from the electrodes. In order to accurately determine the x-ray photocurrent in the sample during an exposure, the dark current must be measured before each exposure and subtracted from the total measurement. The temporal behavior of the dark current needs to be investigated so that we can allow sufficient time between exposures for the dark current to stabilize.

C. Sensitivity

1. X-ray energy absorbed by a-Se

In order to measure the x-ray sensitivity of a-Se, i.e., the W value, we must first determine the energy absorbed in the a-Se sample for a given x-ray exposure. Since the x-ray spectrum from an x-ray tube is not monochromatic, the shape of the spectrum must be determined. Previous studies of W using wide x-ray spectra often used a monoenergetic approximation of the incident beam for calculation of absorbed energy, which can lead to significant systematic error. In the present work, we used the parametrization model developed by Boone *et al.* for mammographic spectra[26] to calculate the absorbed energy. In order to ensure that the modeled spectrum closely matches that generated by the x-ray tube, the half-value-layer, HVL, of the modeled spectrum was calculated, and compared to the measurement of the HVL under our experimental conditions. In the event of discrepancy between the calculated and measured HVL, additional aluminum (Al) filtration can be added to the spectral model to obtain a spectrum that best matches that used in the experiments.[26]

Once the x-ray spectrum was determined, the energy absorbed in the a-Se layer was calculated using the method described by Chen and Doi, which includes the energy absorbed due to k-fluorescence reabsorption.[27] In this method, the fraction of energy absorbed for each incident x-ray photon due to primary interaction is given by

$$P_E = \frac{(\mu_a/\rho)_E}{(\mu/\rho)_E}[1-\exp(-\mu L)], \tag{1}$$

where μ_a/ρ and μ/ρ are the mass energy absorption and mass attenuation coefficients of a-Se, respectively, and μ and L are the linear attenuation coefficient and the thickness of a-Se, respectively. The P_E value given in Eq. (1) does not include energy deposited due to k-fluorescence reabsorption, hence the total energy deposited by an incident photon of energy E is given by

$$E_T = EP_E + E_\alpha P_\alpha + E_\beta P_\beta, \tag{2}$$

where E_α and E_β are the energy of the k_α and k_β fluorescent x rays, and P_α and P_β are the probability of reabsorption of k_α and k_β x rays. The values of P_α and P_β of a-Se can be numerically calculated by dividing the a-Se layer into many thin sublayers.[28] Then the total energy absorbed by the a-Se layer can be calculated using

$$E_{ab} = \sum_E q_0(E)E_T(E), \tag{3}$$

where q_0(E) is the number of x-ray photons per mm^2 per mR with energy E for the given x-ray spectrum. The E_{ab} given in Eq. (3) has a unit of eV/mm^2/mR.

2. Experimental determination of W

The total charge generated by a-Se, q_{Se}, for a given x-ray exposure X was obtained by integrating the measured current of the a-Se layer during the exposure. Then the value for W can be determined using

$$W = \frac{E_{ab} X A_{Se} q_e}{q_{Se}}, \tag{4}$$

where q_e is the charge for an electron and A_{Se} is the active area of the a-Se sample.

For the present investigation, we measured W values as a function of the electric field across the a-Se layer, E_{Se}, which ranged from 2 to 20 V/μm. Under each bias condition, the measurement of x-ray-generated current in a-Se was repeated three times. For each current measurement, the result was integrated and used to derive a separate value of W using Eq. (4). These W values were then averaged to obtain a single value of W for each bias condition, and used to estimate the experimental error.[29]

III. RESULTS AND DISCUSSION

A. Dark current

Shown in Fig. 2 is a typical measurement of dark current of the a-Se sample as a function of time after the high voltage bias was turned on. The measurement shown was with a bias voltage of 2000 V, which corresponds to E_{Se} = 8.33 V/μm. It shows that the dark current decreases almost exponentially as a function of time after the high voltage was applied, and the value stabilizes after ~20 min. This behavior was observed for all E_{Se} values used in our experiment. Our hypothesis is that the blocking layers of the a-Se sample function by trapping charge injected from the electrodes, as shown in the diagram of Fig. 3, and reducing the electric field at the interface between the bias electrodes and the a-Se layer. When the high voltage is first turned on, there is no buildup of charge in the blocking layer, hence the

SIONYX1403000042.0055

SAMSUNG EX. 1002 - 590/4148

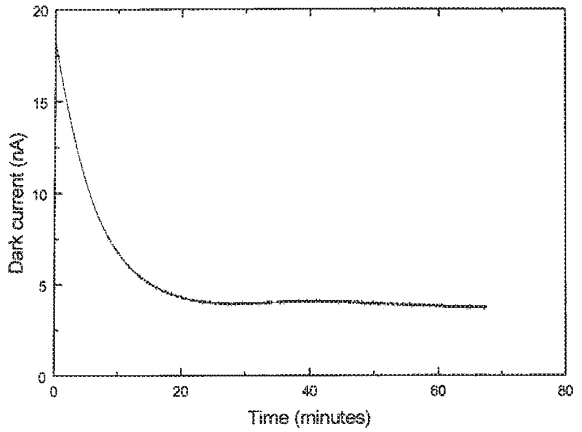


FIG. 2. Dark current measurement for the a-Se sample with bias voltage =2000 V, i.e., $E_{Se}=8.33$ V/μm.

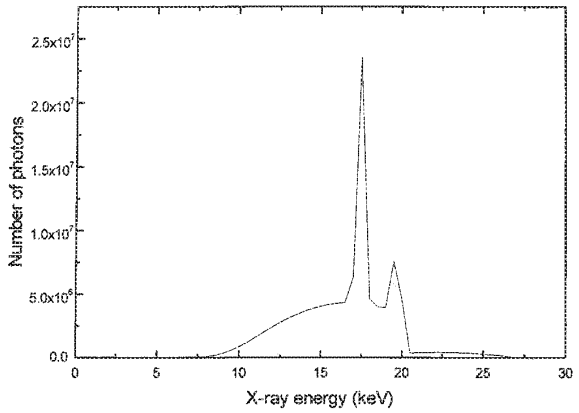


FIG. 4. Modeled x-ray spectrum for 27 kVp beam with Mo target and 30 μm thick Mo filtration.

charge injection and dark current is high. As the injected charge starts being trapped in the blocking layer, the electric field at the interface decreases, which in turn reduces further charge injection from the bias electrodes. Because this process of minimizing dark current takes a certain amount of time to reach equilibrium, during our experiments we allowed at least 20 min after the application of high voltage and between subsequent x-ray exposures for the dark current to stabilize.

B. Sensitivity

1. X-ray energy absorbed by a-Se

The modeled spectrum for the x-ray beam used in our measurement (27 kVp with Mo target and Mo filtration) is shown in Fig. 4. Its HVL was calculated to be 309 μm. The mean incident x-ray photon energy of this spectrum was calculated to be 16.6 keV. The result of experimental measurement of HVL is shown Fig. 5, which is a plot of measured x-ray exposure as a function of thickness of Al filtration in the beam. The Al filters used in the experiments were of type 1145 with 99.45% purity. The HVL was determined by logarithmic interpolation of the measured data, and yielded a result of HVL=305 μm. Since the HVL of the modeled spectrum closely matches that generated by the x-ray tube during experiments, the modeled spectrum was used directly for the calculation of energy absorption in a-Se. Using Eq. (3), the total energy absorbed in the a-Se sample is 3.69×10^{12} eV/mm^2/mR.

2. Determination of W

Figure 6 shows the result of the x-ray current measurement as a function of time with $E_{Se}=10$ V/μm. The slow rising of current after the x-ray was turned on is mainly due to the slow rising of the x-ray exposure from the x-ray generator. Lag is evident in the current measurement at the falling edge of the x-ray pulse; it is usually due to release of trapped charge in the bulk of a-Se. The mechanism and characteristics of lag in a-Se will not be the subject of discussion for this article and will be investigated and reported in future publications. However, in order to minimize the effect of lag and ensure that all x-ray-generated charge was included in the determination of W, the integration of x-ray-generated current was performed until 200 ms after the x-ray is turned

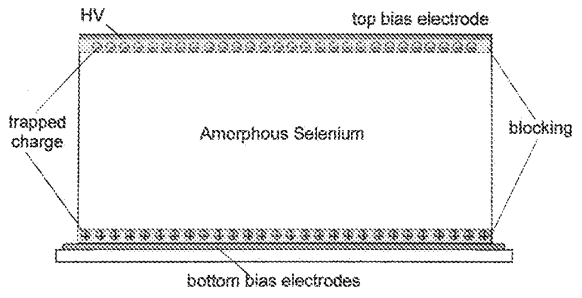


FIG. 3. Schematic diagram showing the trapping of charge carriers in the blocking layers of the a-Se sample, which reduces the electric field at the interface between the bias electrodes and a-Se, and minimizes dark current.

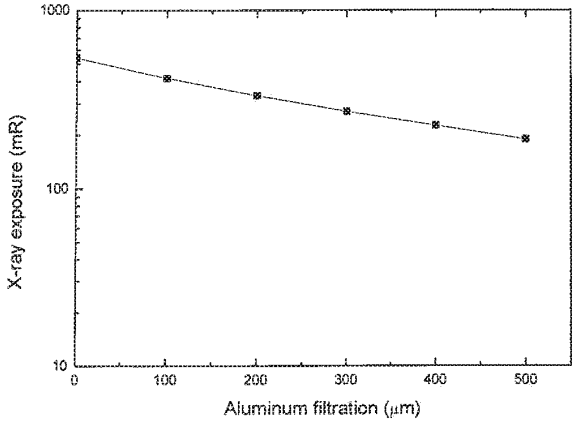


FIG. 5. X-ray exposure measured as a function of Al filtration for the determination of HVL for the x-ray spectrum used in the experiments.

SIONYX1403000042.0056

SAMSUNG EX. 1002 - 591/4148

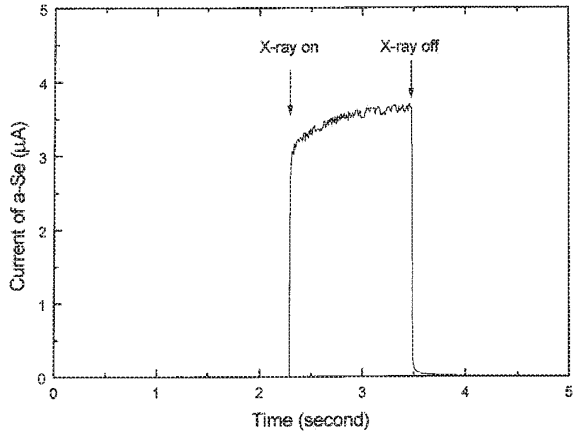


FIG. 6. Plot of x-ray induced current in the a-Se sample as a function of time with $E_{Se}=10$ V/μm.

off (when lag is less than 3%). Once the x-ray-generated charge was obtained, the value for W was calculated using Eq. (4) and the results are plotted as a function of E_{Se} in Fig. 7. It shows that W decreases as a function of E_{Se}, and the dependence can be best fitted by a power law. This field dependence of W has been seen previously by Rowlands *et al.*,[19] Haugen *et al.*,[24] Blevis *et al.*,[25] Donovan,[30] and Aiyah *et al.*[22] It was found that with an empirical fitting of $W \sim E_{Se}^{-\gamma}$, the typical value of γ ranged from 0.7 to 1. The fit from the data obtained in our investigation results in $\gamma = 0.70 \pm 0.01$, which is within the range of values from previous studies.

A widely accepted typical value of W at $E_{Se}=10$ V/μm is ~50 eV for a 50 keV incident x-ray photon.[21] This is to be compared with our result of $W=64$ eV under the same E_{Se} with mammographic x-ray energies. The mean x-ray energy

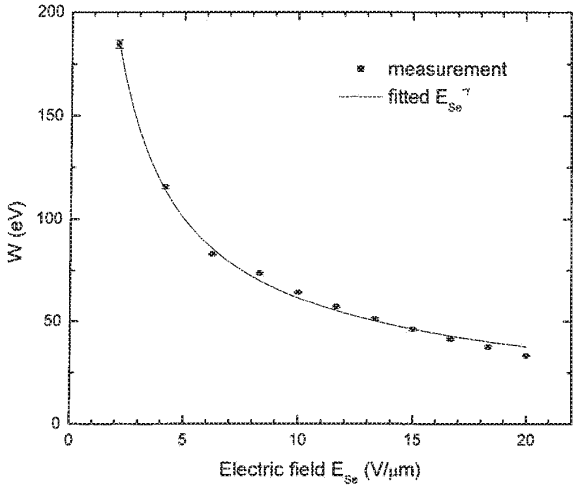


FIG. 7. The energy required to create one electron-hole pair (EHP), W, of a-Se determined as a function of the electric field across a-Se, E_{Se}. The fitted curve used $W \sim E_{Se}^{-\gamma}$.

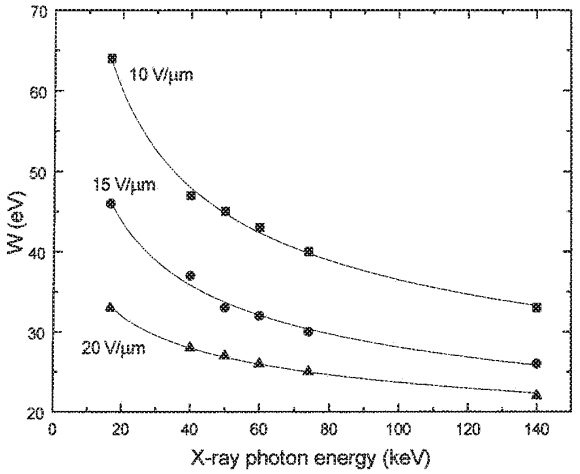


FIG. 8. Measured W at $E_{Se}=10$, 15, and 20 V/μm plotted with previously published measurement of W as a function of incident x-ray energy E. The W values for $E=40$ to 140 keV were extracted from Ref. 25. The solid lines are fitted curves using $W \sim E^{-\gamma}$.

for the spectrum used in our experiment was 16.6 keV, which is lower than the x-ray energy used in previous studies. The dependence of W on the incident photon energy E was investigated experimentally by Blevis *et al.*[25] for photon energies ranging from 40 to 140 keV (monoenergetic x rays). It was found that W increases as E decreases, and the dependence can be best fitted by a power law. Figure 8 shows the W measurement published by Blevis *et al.* as a function of incident photon energy E for three E_{Se} bias of 10, 15, and 20 V/μm. Plotted in the same graph are our measurements of W for mammographic x-ray energy (mean energy of 16.6 keV) under the same E_{Se}, and the data were fitted to the power law of $E^{-\gamma}$. From Fig. 8, it is plausible that the higher W value obtained in our experiment is due to the lower x-ray energy. However, we cannot rule out the possibility that it is due to the difference between the properties of our a-Se samples and those used in previous studies.

IV. CONCLUSIONS

We have investigated the x-ray sensitivity of a-Se at mammographic x-ray energies. The energy required to generate a EHP, W, was measured as a function of electric field E_{Se} with a 27 kVp x-ray spectrum (Mo target with 30 μm of Mo filtration). It was found that the dependence of W on E_{Se} can be best fitted to the empirical expression of $W \sim E_{Se}^{-\gamma}$, with γ determined to be 0.70 ± 0.01. This is within the range of possible values found with previous studies. Compared to previous measurement of W for higher x-ray photon energies, our measurement of W at mammographic energies yielded values that are ~25% higher. This is consistent with the photon energy dependence of W discovered previously for the photon energy range of 40–140 keV. This investigation provides a measurement of W of a-Se at mammographic energies that is independent from any operation of digital

SIONYX1403000042.0057

SAMSUNG EX. 1002 - 592/4148

detectors, and the results can aid the investigation of imaging performance of a-Se-based digital mammography detectors, such as the flat-panel detectors.

ACKNOWLEDGMENTS

We would like to thank Dr. Ziad Shukri from Anrad Corporation for providing the a-Se samples used for this investigation. We acknowledge financial support from SUNY at Stony Brook (USB) through a seed grant for USB-BNL (Brookhaven National Laboratory) Research Initiatives, and from the US Army Breast Cancer Research Program (DAMD17-0110347).

[a)]Author to whom correspondence should be addressed. Electronic mail: wei.zhao@sunysb.edu

[1] M. J. Yaffe, "Digital mammography," in *Categorical Course in Diagnostic Radiology Physics: Physical Aspects of Breast Imaging—Current and Future Considerations*, edited by A. G. Haus and M. J. Yaffe (RSNA, Oak Brook, 1999), pp. 229–238.

[2] G. Lubberts, "Random noise produced by x-ray fluorescent screens," J. Opt. Soc. Am. **58**, 1475–1483 (1968).

[3] R. Nishikawa and M. J. Yaffe, "Effects of finite phosphor thickness on detective quantum efficiency," Med. Phys. **16**, 773–780 (1989).

[4] J. A. Rowlands, D. M. Hunter, and N. Araj, "X-ray imaging using amorphous selenium: A photoinduced discharge readout method for digital mammography," Med. Phys. **18**, 421–431 (1991).

[5] J. G. Mainprize, N. L. Ford, S. Yin, T. Tumer, and M. J. Yaffe, "Image quality of a prototype direct conversion detector for digital mammography," Proc. SPIE **3659**, 398–406 (1999).

[6] W. Zhao and J. A. Rowlands, "X-ray imaging using amorphous selenium: Feasibility of a flat panel self-scanned detector for digital radiology," Med. Phys. **22**, 1595–1604 (1995).

[7] D. L. Lee, L. K. Cheung, B. G. Rodricks, and G. F. Powell, "Improved imaging performance of a 14× 17-in. Direct Radiography system using a Se/TFT detector," Proc. SPIE **3336**, 14–23 (1998).

[8] A. Tsukamoto, S. Yamada, T. Tomisaki, M. Tanaka, T. Sakaguchi, H. Asahina, K. Suzuki, and M. Ikeda, "Development and evaluation of a large-area selenium-based flat-panel detector for real-time radiography and fluoroscopy," Proc. SPIE **3659**, 14–23 (1999).

[9] R. A. Street, J. T. Rahn, S. E. Ready, K. S. Shah, P. R. Bennett, Y. N. Dmitriyev, P. Mei, J. P. Lu, R. B. Apte, J. Ho, K. van Schuylenbergh, F. Lemmi, J. B. Boyce, and P. Nylen, "X-ray imaging using lead iodide as a semiconductor detector," Proc. SPIE **3659**, 36–47 (1999).

[10] L. E. Antonuk, J. Boudry, W. Huang, D. L. McShan, E. J. Morton, J. Yorkston, M. J. Longo, and R. A. Street, "Demonstration of megavoltage and diagnostic x-ray imaging with hydrogenated amorphous silicon arrays," Med. Phys. **19**, 1455–1466 (1992).

[11] C. Chaussat, J. Chabbal, T. Ducourant, V. Spinnler, G. Vieux, and R. Neyret, "New CsI/a-Si 17×17-in. x-ray flat-panel detector provides superior detectivity and immediate direct digital output for general radiography systems," Proc. SPIE **3336**, 45–56 (1998).

[12] T. Kameshima, N. Kaifu, E. Takami, M. Morishita, and T. Yamazaki, "Novel large-area MIS-type x-ray image sensor for digital radiography," Proc. SPIE **3336**, 453–462 (1998).

[13] J. M. Boudry, "Operation of amorphous silicon detectors for chest radiography within system latency requirements," Proc. SPIE **3659**, 336–344 (1999).

[14] L. Cheung, R. Bird, A. Chitkara, A. Rego, C. Rodriguez, and J. Yuen, "Initial operating and clinical results of a full field digital mammography system," in *Digital Mammography*, edited by N. Karssemeijer, M. Thijssen, J. Hendriks, and L. van Erning (Kluwer Academic, Dordrecht, 1998), pp. 11–18.

[15] S. Muller, "Full-field digital mammography designed as a complete system," Eur. J. Radiol. **31**, 25–34 (1999).

[16] B. Polischuk, H. Rougeot, K. Wong, A. Debrie, E. Poliquin, M. Hansroul, J. P. Martin, T. T. Truong, M. Choquette, L. Laperriere, and Z. Shukri, "Direct conversion detector for digital mammography," Proc. SPIE **3659**, 417–425 (1999).

[17] E. L. Gingold, D. L. Y. Lee, L. S. Jeromin, B. Rodricks, M. G. Hoffberg, and C. L. Williams, "Development of a novel high-resolution direct conversion x-ray detector," Proc. SPIE **3977**, 185–193 (2000).

[18] M. P. Andre, B. A. Spivey, P. J. Martin, L. Morsell, E. Atlas, and T. Pellegrino, "Integrated CMOS-selenium x-ray detector for digital mammography," Proc. SPIE **3336**, 204–209 (1998).

[19] J. A. Rowlands, G. DeCrescenzo, and N. Araj, "X-ray imaging using amorphous selenium: Determination of x-ray sensitivity by pulse height spectroscopy," Med. Phys. **19**, 1065–1070 (1992).

[20] J. A. Rowlands, "Digital X-ray systems based on amorphous selenium," AJR, Am. J. Roentgenol. **167**, 409–411 (1996).

[21] J. A. Rowlands and J. Yorkston, "Flat panel detectors for digital radiography," in *Medical Imaging. Volume 1 Physics and Psychophysics. Psychophysics*, edited by J. Beutel, H. L. Kundel, and R. L. Van Metter (SPIE, Bellingham, 2000), pp. 223–328.

[22] V. Aiyah, A. Baillie, B. Polischuk, A. Bekirov, and S. Kasap, "X-ray sensitivity of halogenated a-Se:As photoreceptors for electroradiography," J. Non-Cryst. Solids **137&138**, 1337–1340 (1991).

[23] S. O. Kasap, V. Aiyah, B. Polischuk, and A. Baillie, "X-ray sensitivity of a-Se for x-ray imaging with electrostatic readout," J. Appl. Phys. **83**, 2879–2887 (1998).

[24] C. Haugen, S. O. Kasap, and J. Rowlands, "Charge transport and electron-hole-pair creation energy in stabilized a-Se x-ray photoconductors," J. Phys. D **32**, 200–207 (1999).

[25] I. M. Blevis, D. C. Hunt, and J. A. Rowlands, "Measurement of x-ray photogeneration in amorphous selenium," J. Appl. Phys. **85**, 7958–7963 (1999).

[26] J. M. Boone, T. R. Fewell, and R. J. Jennings, "Molybdenum, rhodium, and tungsten anode spectral models using interpolating polynomials with application to mammography," Med. Phys. **24**, 1863–1874 (1997).

[27] H. P. Chan and K. Doi, "Energy and angular dependence of x-ray absorption and its effect on radiographic response in screen-film systems," Phys. Med. Biol. **28**, 565–579 (1983).

[28] R. Fahrig, J. A. Rowlands, and M. J. Yaffe, "X-ray imaging with amorphous selenium: Detective quantum efficiency of photoconductive receptors for digital mammography," Med. Phys. **22**, 153–160 (1995).

[29] R. Bevington and D. K. Robinson, *Data Reduction and Error Analysis for the Physical Sciences*, 2nd ed. (McGraw-Hill, New York, 1992), p. 55.

[30] J. L. Donovan, "X-ray sensitivity of selenium," J. Appl. Phys. **50**, 6500–6504 (1979).

SIONYX1403000042.0058

SAMSUNG EX. 1002 - 593/4148

AIP Applied Physics Letters

Simple integral screenprinting process for selective emitter polycrystalline silicon solar cells

J. Szlufcik, H. E. Elgamel, M. Ghannam, J. Nijs, and R. Mertens

Citation: Applied Physics Letters **59**, 1583 (1991); doi: 10.1063/1.106291
View online: http://dx.doi.org/10.1063/1.106291
View Table of Contents: http://scitation.aip.org/content/aip/journal/apl/59/13?ver=pdfcov
Published by the AIP Publishing

Articles you may be interested in

Evaluation of determination methods of the Si/Al contact resistance of screen-printed passivated emitter and rear solar cells
J. Appl. Phys. **115**, 084505 (2014); 10.1063/1.4867188

Optimization of oxidation processes to improve crystalline silicon solar cell emitters
AIP Advances **4**, 027127 (2014); 10.1063/1.4866981

Characterization and modeling of screen-printed metal insulator semiconductor tunnel junctions for integrated bypass functionality in crystalline silicon solar cells
J. Appl. Phys. **113**, 214502 (2013); 10.1063/1.4807931

High-efficiency screen-printed silicon ribbon solar cells by effective defect passivation and rapid thermal processing
Appl. Phys. Lett. **82**, 224 (2003); 10.1063/1.1536027

Rapid thermal processing and screen-printing for low cost silicon solar cells
AIP Conf. Proc. **462**, 354 (1999); 10.1063/1.57909



This article is copyrighted as indicated in the article. Reuse of AIP content is subject to the terms at: http://scitation.aip.org/termsconditions. Downloaded to IP: 128.141.1.149 On: Thu, 24 Oct 2014 08:40:24

SIONYX1403000042.0059

SAMSUNG EX. 1002 - 594/4148

Simple integral screenprinting process for selective emitter polycrystalline silicon solar cells

J. Szlufcik, H. E. Elgamel, M. Ghannam, J. Nijs, and R. Mertens
Interuniversity Micro-Electronics Center, IMEC, Kapeldreef 75, B-3001 Leuven, Belgium

(Received 20 May 1991; accepted for publication 27 June 1991)

This letter describes a new simple fabrication process, developed recently for "blue response" improvement in low-cost polycrystalline silicon solar cells. A selective emitter is created by heavily doping the emitter, followed by a wet etching-back of the cell area between the fingers. An improvement up to 17 mV in V_{oc}, 1.5 mA/cm^2 in J_{sc}, and 1% (absolute value) in η is obtained. Effective phosphorus gettering, self-alignment, and application in a low-cost full screenprinting technology are the main advantages of the proposed process.

Screenprinting is considered as the most economical technique for the large-scale solar cell production. Screenprinted silver contacts penetrate about 0.3 μm in the Si wafer during firing due to an etching action of the glass frit contained in the silver paste. Therefore, a junction about 0.6 μm deep is made to impede the silver from reaching the junction region. At the same time a phosphorous surface concentration of 10^{20}–10^{21}at/cm^3 is necessary in order to obtain a low contact resistance and a high fill factor.[1] These two requirements are the cause of the very poor blue response of solar cells with screenprinted contacts.

Typical emitter sheet resistances of industrially produced solar cells lie between 30–45 Ω/sq. Higher sheet resistances result in a fill factor below 70% mainly due to the high contact resistance at the interface between the screenprinted contact and the emitter surface. However, since a high-efficiency emitter has a relatively high sheet resistance,[2] an effective design for increasing the blue response of solar cells with screenprinted contacts would divide the emitter in two distinct regions. In this selective emitter design[3–6] a low sheet resistance occurs under the fingers and a high sheet resistance occurs in the emitter areas between the fingers.

Many selective emitter solar cell fabrication processes involve two diffusion steps to form a grid-shaped emitter.[4,5] The main problem associated with the two-step diffusion processes when screenprinting is used is the accuracy of alignment of the front side metal grid with the highly doped emitter areas. Any misalignment results in shunting through the shallow junction between the fingers.[5]

In this work, a simple, fully screenprinting fabrication process excluding the necessity of two diffusion steps for the formation of a selective emitter structure and avoiding top contact misalignment is presented for the first time. As depicted in Fig. 1, this process starts by screenprinting a phosphorus-containing paste on the surface of a p-type polycrystalline silicon wafer. This is followed by phosphorous diffusion from the paste source into the substrate at 930 °C in a belt furnace to form a deep $n^{+}{}^{+}$ emitter with a sheet resistance of 16–20 Ω/sq [Fig. 1(a)]. It has been proven that this heavy phosphorus diffusion might be very effective in gettering of the substrate.[7] The back-side metal contact is made by screenprinting a silver-aluminum paste followed by firing at 720 °C. The front side metal pattern is obtained by screenprinting a silver paste on top of the $n^{+}{}^{+}$ emitter surface and firing at 645 °C [Fig. 1(b)]. In order to avoid any attack on the different metal layers by the etching solution, a polymeric protective paste is screenprinted over the metal fingers and on the back-side metal layer and dried at 150 °C. An HF/HNO_3 solution is used to etch-back the areas between the metal fingers. The etching-back is carried on until the sheet resistance of the free emitter surface reaches 60–70 Ω/sq. Finally a TiO_2 antireflective coating is screenprinted on the front surface and fired at 450 °C. During this step the protective polymeric layers are burned out.

The cross section of the selective emitter solar cell obtained by the integral screenprinting process described here is shown in Fig. 1(d). In Table I a comparison between the

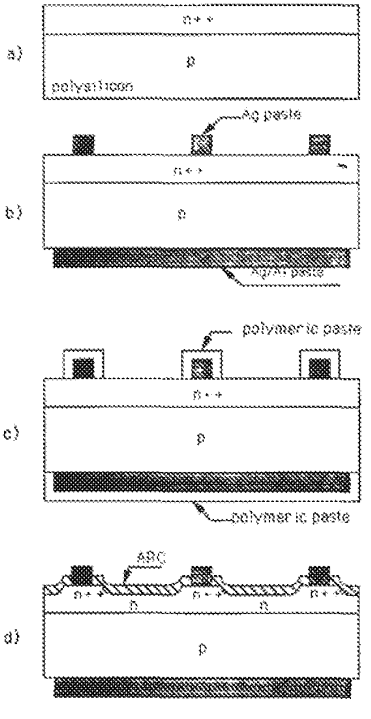


FIG. 1. Fabrication steps of the integral screenprinting process for a selective emitter solar cell.

 0003-6951/91/381583-02$02.00 © 1991 American Institute of Physics

SIONYX1403000042.0060

SAMSUNG EX. 1002 - 595/4148

TABLE I. Parameters of selective and homogeneous emitter solar cells processed following an integral screenprinting process.

Supplier	Type of emitter	Sheet resist. [Ω/sq]	V_{oc} [mV]	J_{sc} [mA/cm^2]	FF [%]	η [%]
Suppl. A	Homogen.	40	556	27	75.3	11.3
Suppl. A	Selective	60	573	28.5	75.3	12.3
Suppl. B	Homogen.	40	582	28.9	73	12.3
Suppl. B	Selective	60	587	29.7	73.6	12.8

parameters of solar cells with different types of emitters is given. From this comparison the improvement obtained by the selective emitter structure is clearly seen especially for the cell with the lower starting performance (supplier A). It should be mentioned that apart from the selective/nonselective emitter difference the cells of Table I followed an identical processing scheme with no additional intentional improvement steps such as surface passivation, texturization, or gettering.

The integral screenprinting selective emitter process leads to an improvement (1) in the open circuit voltage $\Delta V_{oc} \approx 17$ mV, (2) in the short circuit current density $\Delta J_{sc} \approx 1.5$ mA/cm^2, and (3) in the absolute value of the conversion efficiency $\Delta\eta \approx 1\%$. Note that the increase in V_{oc} is larger than what is expected to be associated with the increase in J_{sc}. Hence, one can conclude that this is due to a lower recombination velocity at the surface of the relatively lowly doped emitter areas between the metal fingers of the selective emitter solar cell. Finally, it should be mentioned that the width of the metal fingers for the cells processed here is 200 μm. Further improvements in the cell performance are expected when the screenprinted top contact finger width is made finer. A simple calculation shows that with a finger width of 80 μm the emitter area between the fingers can be etched-back until a sheet resistance of 100 Ω/sq or more is reached while keeping a fill factor over 70%.

In Fig. 2 the measured spectral response of solar cells (a) with an optimized homogeneous emitter, and (b) with a selective emitter is presented. As expected the cell with the selective emitter shows a higher response in the short wavelength region (blue response).

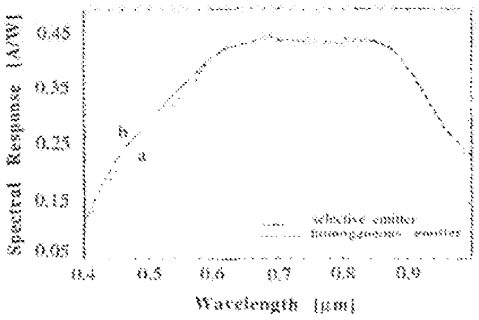


FIG. 2. Spectral response of supplier A solar cells: (a) with a homogeneous emitter (40 Ω/sq), and (b) with a selective emitter (20 Ω/sq under contacts and 60 Ω/sq between fingers).

The advantages of the selective emitter process presented here are numerous. First, only one phosphorus diffusion step is required for the emitter. At the same time, this heavy diffusion step getters the silicon substrate. Second, the critical alignment of the silver grid with the highly doped n^{++} regions is avoided and replaced by an easy alignment of the protective paste to the silver fingers. Finally, such a low-cost integral screenprinting process can be directly applied to the industrial production of solar cells.

[1] L. Frisson, G. Cheek, R. Mertens, and R. Van Overstraeten, Proc. of 5th European Community Photovoltaic Solar Energy Conference, Athens, Greece, 1002 (1983).
[2] E. Demesmaeker, M. Ghannam, E. G. Moreno, J. Nijs, and R. Mertens, 22nd IEEE Photovoltaics Specialist Conference, Las Vegas (1991) (unpublished).
[3] S. Tanaka, S. Okamoto, K. Nakajima, N. Shibuya, K. Okamoto, T. Namori, T. Nunoi, and T. Tsuji, Tech. Dig. Int. PVSEC-5, Kyoto, Japan, 315 (1990).
[4] M. Takayama, H. Yamashita, K. Fukui, K. Masuri, K. Shirisawa, and H. Watanbe, Tech. Dig. of Int. PVSEC-5, Kyoto, Japan, 319 (1990).
[5] M. Eyckmans, Proc. of 9th EPVSEC, Freiburg, Germany, (Kluwer-Academics, Dordrecht, 1989), p. 414.
[6] S. R. Wenham, M. R. Willison, S. Narayanam, and M. A. Green, 18th IEEE Photovoltaic Specialists Conference, Las Vegas, 1008 (Institute of Electrical and Electronics Engineers, New York, 1985).
[7] S. Martinuzzi, H. El Ghitani, D. Sarti, and P. Torchio, Proc. of 20th IEEE Photovoltaic Specialists Conference, Las Vegas, 1575 Institute of Electrical and Electronics Engineers, New York, 1988).

This article is copyrighted as indicated in the article. Reuse of AIP content is subject to the terms at: http://scitation.aip.org/termsconditions. Downloaded to IP: 128.141.1.140 On: Thu, 23 Oct 2014 08:40:26

SIONYX1403000042.0061

SAMSUNG EX. 1002 - 596/4148

C28

Formation of single crystal sulfur supersaturated silicon based junctions by pulsed laser melting

Malek Tabbal,[a] Taegon Kim, Jeffrey M. Warrender,[b] and Michael J. Aziz
Harvard School of Engineering and Applied Sciences, Cambridge, Massachusetts 02138

B. L. Cardozo and R. S. Goldman
Department of Materials Science and Engineering, University of Michigan, Ann Arbor, Michigan 48109-2136

(Received 26 June 2007; accepted 18 September 2007; published 18 October 2007)

The authors demonstrate the formation of *pn* and nn^+ junctions based on silicon supersaturated with sulfur (up to 0.46 at. %) using a combination of ion implantation and pulsed laser melting. Silicon wafers were implanted at 200 keV $^{32}S^+$ to doses ranging from 1×10^{15} to 1×10^{16} ions/cm^2 and subsequently melted and resolidified by using a homogenized excimer laser pulse. Above a threshold laser fluence of $\sim$1.4 J/cm^2, the process produces a single crystal supersaturated alloy, free of extended defects, with a sharp junction between the laser melted layer and the underlying substrate, located near the maximum penetration of the melt front. Hall effect measurements indicate that the laser melted layers are *n* doped with a free carrier density up to 8×10^{18}/cm^3 that decreases by one-third upon postirradiation furnace annealing at 550 °C. Dark current-voltage measurements performed on these structures show good rectifying behavior. The photovoltaic characteristics of the junctions were enhanced by postirradiation annealing at 550–800 °C. These effects are attributed to the evolution of a population of point defects that survive the laser treatment. The influence of ion implantation dose, laser fluence, and annealing temperature on the properties of the junctions is also presented and discussed. © *2007 American Vacuum Society.* [DOI: 10.1116/1.2796184]

I. INTRODUCTION

Recently, there has been significant interest in the optical and electronic properties of laser-microstructured chalcogen-laden silicon, a form of Si that shows enhanced optical absorption at wavelengths above and below the band gap.[1,2] For example, laser-microstructured chalcogen-laden silicon was recently used for the fabrication of Si-based electronic and optoelectronic devices including IR photodiodes,[3] photodetectors,[4] and electron emitters.[5] Typically, the material is synthesized by repeated femtosecond or nanosecond laser irradiation of Si wafers in SF_6, leading to sulfur-laden disordered silicon layers with about 10 μm tall spikes.[1,6,7] We recently demonstrated significant enhancement of the subband gap absorption,[8] with little surface damage or roughening, via the irradiation of sulfur-implanted silicon with a few spatially uniform nanosecond excimer laser pulses. Because excimer lasers are widely utilized for industrial processes, and smooth surfaces are well suited to many device architectures, this approach is very promising for a wide range of novel applications. However, to date, little is known about the structure and electronic properties of laser-microstructured chalcogen-laden silicon. In this article, we investigate the structural and electrical properties of excimer laser-crystallized Si ion implanted with sulfur at levels of several orders of magnitude above the solid solubility limit. The article focuses on the evaluation of the crystalline quality of the laser melted layers using channeling Rutherford backscattering spectrometry (C-RBS) and transmission electron microscopy (TEM), and on their electrical properties assessed using Hall effect and current-voltage (*I-V*) characterization performed in the dark and under simulated solar irradiation. The effect of implantation dose, laser fluence, and postirradiation thermal annealing on the properties of the junctions is also presented and discussed.

II. EXPERIMENT

300 μm thick, single-side polished *n*-Si(111) (*P* doped, 1.2 kΩ cm, and $\sim10^{12}$ cm^{-3}), *n*-Si(001) (*P* doped and $\sim$5 Ω cm), and *p*-Si(001) (*B* doped, 5 Ω cm, and $\sim10^{15}$ cm^{-3}) were ion implanted at room temperature with 200 keV $^{32}S^+$ to doses ranging from 1×10^{15} to 1×10^{16} ions/cm^2. The ion implanted samples were then irradiated in ambient, using a spatially homogenized pulsed $XeCl^+$ excimer laser beam (308 nm, 25 ns full width at half maximum, and 50 ns total duration) with fluences of 1.0, 1.4, and 1.8 J/cm^2. In order to process a sufficiently large area (1.5×1.5 cm^2), the samples were mounted on an *X-Y* stage and the $\sim3\times3$ mm^2 excimer laser spot was tiled across the area; consequently, the average point on the surface was irradiated by four to five pulses. Time-resolved reflectivity (TRR) of a low-power Ar^+ ion laser (488 nm) confirmed an optically flat surface and allowed us to monitor the duration over which the surface was molten. The Ar^+ ion laser beam

[a]On research leave from the Department of Physics, American University of Beirut, Beirut, 1107 2020, Lebanon; electronic mail: malek.tabbal@aub.edu.lb
[b]Present address: Fatigue and Fracture Analysis Branch, Benet Laboratories, Watervliet, NY 12189.

SIONYX1403000042.0062

SAMSUNG EX. 1002 - 597/4148

is incident near the grazing angle on the Si surface and its reflected beam is detected by a fast photodiode that is connected to a digital oscilloscope in order to record the temporal variation of the reflected intensity. TRR was also used to calibrate the laser fluence by measuring the melt duration for a virgin crystalline Si wafer and to compare predictions of the melt depth versus fluence by a numerical solution of the one-dimensional heat equation using the well-established optical and thermophysical properties of crystalline, amorphous, and liquid silicon.[9,10] After the laser melting experiments, some samples were furnace annealed in flowing 99.999% Ar gas or in forming gas (10% H_2 and 90% N_2) for 30 min at temperatures ranging from 400 to 1000 °C.

The crystalline quality of the laser melted layers was quantified by Rutherford backscattering spectrometry in channeling mode (C-RBS) performed using 2 MeV He^+ ions down the [111] and [001] axes for the *n*-Si(111) and *p*-Si(001) substrates, respectively. Cross-sectional TEM (XTEM) examination was also carried out at 200 kV using a JEOL 2010F electron microscope, with lattice imaging obtained along the Si [110] direction. The surface morphology and roughness were investigated by *ex situ* atomic force microscopy using a MultiMode™ scanning probe microscope (NanoScope III) from Digital Instruments in tapping mode. The S concentration-depth profile in the laser melted layers were determined by secondary ion mass spectrometry (SIMS), as described elsewhere.[8] The carrier concentrations and carrier mobilities of the laser melted layers were determined using room-temperature resistivity and Hall measurements, both in the van der Pauw configuration.[11] In all cases, samples were cleaved into 0.6×0.6 cm^2 squares, and 99.99% indium solder contacts were applied. To determine the free carrier concentration n_e, the sheet carrier density (electrons/cm^2) is divided by the thickness of the S-incorporated layer determined from SIMS. To facilitate *I-V* measurements, electron beam evaporation was used to deposit, through a mask, narrow Cr–Au strips and metallic contact pads on top of the melted layers and on the back surface of the wafers, respectively. Current-voltage (*I-V*) measurements on the nn^+ and pn junctions were performed, at room temperature, in the dark and under an AM 1.5 solar simulator,[12] with 100 mW/cm^2 power density.

III. RESULTS AND DISCUSSION

A. Microstructural characterization

In Fig. 1, we present C-RBS spectra of S-implanted (1×10^{16} ions/cm^2) Si (111) substrates that were laser melted at different laser fluences. We also present the random and channeling spectra of the unimplanted virgin substrate and the channeling spectrum for the as-implanted wafers. In the latter spectrum, two distinct dechanneling peaks are observed, the first (~1130 keV) corresponds to the surface silicon atoms and the larger second peak (~1035 keV) arises from a heavily damaged crystalline or partly amorphous layer (~100 nm thick) buried beneath a more lightly damaged crystalline surface layer. The absence of a fully amorphous topmost damaged layer is indicative of surface heating by the incident ion beam during implantation. The peak of the damage is found to be at 210 nm, very close to the peak of the sulfur implant profile, which is located at 230 nm from the top surface, as measured by SIMS.[8] From the channeling spectra of the laser irradiated samples, it is clear that the crystallinity of the laser melted ion implanted layers is very sensitive to laser fluence. The strong dechanneling peak attributed to the buried amorphous/defective layer disappears for the sample irradiated at a laser fluence of 1.4 J/cm^2, as the C-RBS spectrum reveals a near-surface minimum backscattered yield χ_{min} —the ratio of the aligned to random yields—of about 4%, which is quite close to the value of 2.5% determined for the virgin single crystal Si substrate. Beyond a fluence threshold, pulsed laser melting of ion implanted silicon is known to melt the material to a depth greater than the defective region; the material then solidifies rapidly into highly supersaturated single crystalline material free of extended defects.[9,10] The channeling RBS spectrum from a sample irradiated at 1.8 J/cm^2 is nearly indistinguishable from the spectrum for a sample irradiated at 1.4 J/cm^2. These results were reproduced for *p*-Si(001) substrates and for different ion implantation doses. In addition, it was found that the χ_{min} measured from the C-RBS spectra of the laser melted samples (at 1.4 J/cm^2 and above) could be reduced to that of the virgin Si substrate upon annealing at 550 °C, which we attribute to point defect elimination by postirradiation anneals.

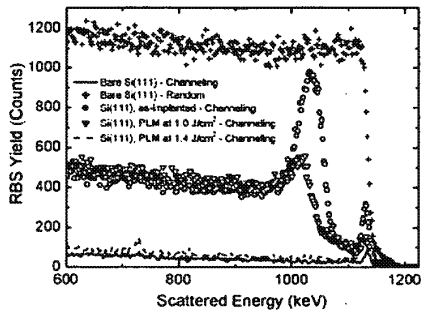
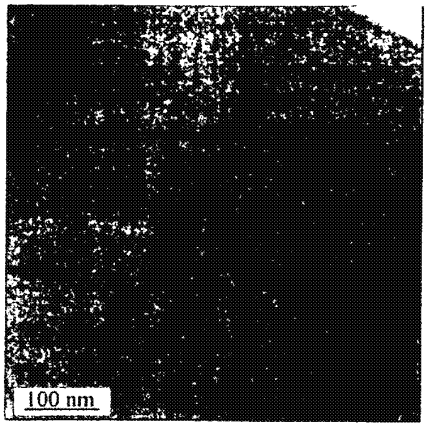


FIG. 1. Channeling RBS spectra of the following Si (111) substrates: unimplanted virgin (—), as implanted (○), implanted and pulsed laser melted (PLM) at 1.0 J/cm^2 (▽), and implanted and PLM at 1.4 J/cm^2 (---). The random spectrum of the virgin Si (111) wafer is also shown (+). The ion dose for the implanted spectra is 1×10^{16} ions/cm^2. The peak at ~730 keV is from surface oxygen.

The high crystalline quality of the samples was further confirmed by XTEM, as shown in Fig. 2. No extended defects are observed and the transition between the implanted/laser melted layers and the underlying crystal is not distinguishable. In addition, atomic force microscopy (AFM) measurements indicate the occurrence of very little roughening of the surface of the wafers after laser melting. The surface roughness in 2×2 μm^2 AFM topographs was found to slightly increase from 0.21 nm, for layers implanted to a dose of 1×10^{16} ions/cm^2, to 0.36 nm, following laser melting with 1.8 J/cm^2.

SIONYX1403000042.0063

SAMSUNG EX. 1002 - 598/4148



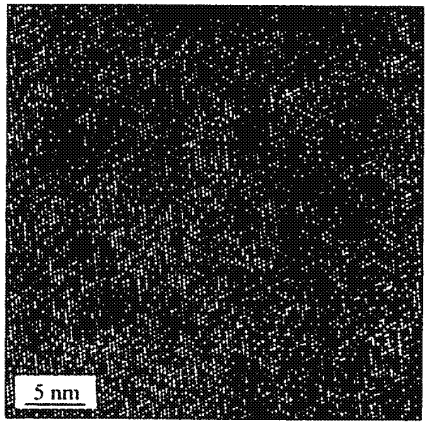


FIG. 2. (a) XTEM image of n-Si(111) sample implanted to a dose of 1×10^{16} ions/cm^2 and irradiated at 1.8 J/cm^2, sample surface is in upper right. (b) Lattice resolution XTEM image of the same sample.

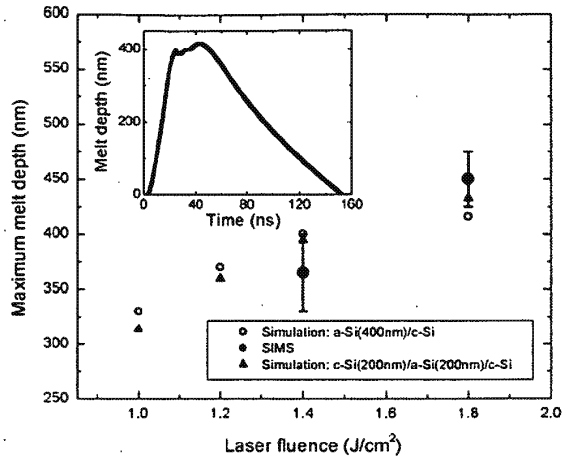


FIG. 3. Plot of the calculated maximum melt depth vs laser fluence for a structure consisting of a 200 nm thick a-Si layer buried at a depth of 200 nm in crystalline silicon (▲) and another consisting of 400 nm thick a-Si on top of the crystalline silicon substrate (○). Values inferred from SIMS (●) measurements are also shown with error bars.

Because estimating the melt depth induced by the laser is important for process control, heat flow simulations of melting and solidification were performed so the melt depth could be deduced from melt duration measurements. The calculated value of the maximum melt depth versus laser fluence is plotted in Fig. 3 for a structure consisting of a 200 nm thick amorphous Si (a-Si) layer buried under 200 nm of crystalline silicon and another consisting of a 400 nm thick a-Si layer on top of the crystalline silicon substrate. An example of the melt depth versus time from a simulation at a laser fluence of 1.8 J/cm^2 on a 400 nm a-Si layer is presented in the inset. The simulated melt depth versus fluence is consistent with the maximum melt depth inferred from the SIMS measurements. The SIMS concentration-depth profiles[8] indicated an abrupt drop in sulfur concentration at the maximum melt depth. The SIMS profiles also indicated no loss of sulfur upon laser melting. The results are qualitatively consistent with rapid solidification-induced solute trapping scenarios that are well documented for single laser shots on silicon implanted with other dopants.[13,14] In the case of sulfur documented here, it appears that we obtain supersaturated sulfur concentrations, as listed in Table I, exceeding by four orders of magnitude the equilibrium solubility limit.[15]

B. Electrical characterization

The electrical properties of the samples are summarized in Table I. For all the laser melted S-implanted layers, the sign of the Hall coefficient indicates n-type conductivity. It is evident that n_e increases with S implantation dose, reaching a

TABLE I. Total sulfur concentration, Hall mobility, free carrier concentration, and carrier-to-donor ratio in the laser melted layers for several implantation doses and a laser fluence of 1.8 J/cm^2.

S dose (ions/cm^2)	S concentration (atoms/cm^3)	Hall mobility (cm^2/V s)	Carrier density (e/cm^3)	Carrier-to-donor ratio (%)
1×10^{15}	2.3×10^{19}	200	7×10^{17}	3.0
3×10^{15}	7.7×10^{19}	69	3×10^{18}	3.9
1×10^{16}	2.3×10^{20}	61	8×10^{18}	3.5
1×10^{16} +550 °C anneal	2.3×10^{20}	184	5×10^{18}	2.1

SIONYX1403000042.0064

SAMSUNG EX. 1002 - 599/4148

maximum value of 8×10^{18} electrons/cm^3 for a dose of 1×10^{16} ions/cm^2. In contrast, the electron mobility decreases with S implantation dose, presumably due to increased ionized impurity scattering for higher doses.

For the unannealed laser melted samples, the ratio of free carrier density to total S concentration, which we termed as "carrier-to-donor" ratio, ranges from 3% to 4%. These low carrier-to-donor ratios may be due to the formation of S-induced midgap states in Si.[16]

SIMS measurements on laser melted samples subsequently annealed to temperatures as high as 900 °C reveal no change in retained S dose. In contrast to femtosecond laser microstructured Si:S, for which 40% of the sulfur could be lost upon annealing at a temperature of 450 °C,[6] there is no detectable loss and no detectable diffusion beyond the laser melt depth.[8] Therefore, the observed decrease in n_e from 8×10^{18} to 5×10^{18} electrons/cm^3 for the annealed laser melted samples is due to a reduction in the carrier-to-donor ratio of the S dopants, rather than to a decrease in the total S incorporation in the layers. This drop in carrier-to-donor ratio upon annealing could be a consequence of the formation of precipitates or clusters with S or with native point defects at the expense of the total number of isolated S atoms in substitutional sites. The energetically favored form of isolated S atoms, substitutional sulfur,[17] forms electrically active dopants. Upon annealing, a clustering-induced decrease in electrically active substitutional S could occur. The formation of S clusters or precipitates could also explain the very limited diffusion of sulfur observed upon annealing to 900 °C. Their presence could not be confirmed by C-RBS or XTEM because of the very low S concentration in the layers,[8] namely, 0.46 at. %, for the highest implantation dose used in this work.

In contrast to the carrier-to-donor ratio, the mobility was significantly enhanced upon annealing, reaching 184 cm^2/V s for the sample implanted at 1×10^{16}/cm^2. This value is thrice that of the unannealed sample implanted at the same dose and is close to that of the unannealed sample implanted at the much lower dose of 1×10^{15}/cm^2. Because the ionized impurity concentration for the latter is nearly an order of magnitude less than that of the annealed sample, the annealing-induced electron mobility enhancement is not primarily due to a decrease in ionized impurity scattering. Post-laser melting annealing may lead to the removal or modification of other point defects, thereby reducing the scattering probability of the free carriers. For example, annealing may lead to the removal of vacancies known to be present in laser-crystallized implanted regions.[18,19] Additionally, annealing may enable the evolution of inactive point defects from a charged to a neutral configuration, thereby reducing the scattering probability of the free carriers.[20]

In Fig. 4, we present the dark current versus voltage (I-V) characteristics of the pn junctions formed by laser melting at 1.8 J/cm^2 of p-doped Si substrates implanted to a dose of 1×10^{16} S/cm^2 and annealed at various temperatures up to 1000 °C. All curves show good rectifying behavior except for the one corresponding to the highest annealing temperature, which has poor forward current characteristics and a significantly high leakage current, I_L (0.85 mA/cm^2 at −0.5 V). The lowest value of I_L at −0.5 V was 0.064 mA/cm^2, obtained for the nonannealed layers. The ideality factor n was determined by fitting the forward current I_F to the relationship[21]

$$I_F \sim \exp(qV/nkT),$$

where q is the charge of the electron, kT is the thermal energy, and V is the applied voltage. An ideality factor of 2.06 was determined for the junctions annealed at 550 °C, a value that is very close to the value of 2 which is an indication of bulk recombination of the charge carriers occurring in the depletion region.[21]

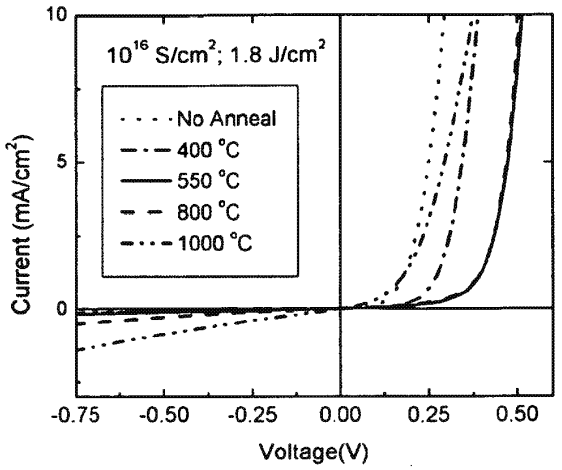


FIG. 4. Dark I-V curves measured for p-Si(001) samples implanted at a dose 1×10^{16}/cm^2, irradiated at 1.8 J/cm^2, and furnace annealed at different temperatures.

In Fig. 5, we present the I-V curves of the same pn junc-

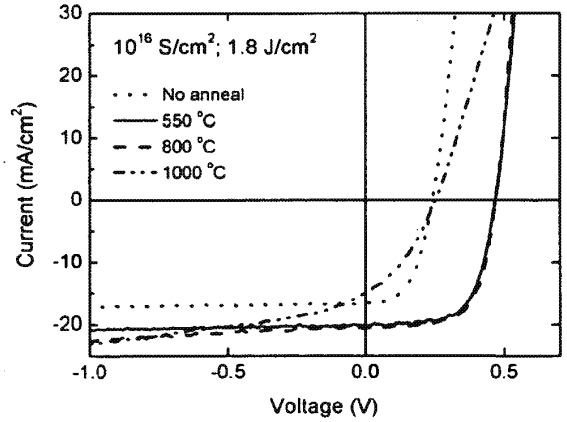


FIG. 5. I-V curves measured under one sun for p-Si(001) samples implanted to a dose of 1×10^{16}/cm^2, irradiated at 1.8 J/cm^2, and furnace annealed at different temperatures.

SIONYX1403000042.0065

SAMSUNG EX. 1002 - 600/4148

tions measured under one sun (AM 1.5 and 100 mW/cm^2) for different annealing temperatures. In agreement with the dark current measurements reported in Fig. 4, annealing at 550 or 800 °C leads to an increased short circuit current, I_{sc}, and open circuit voltage, V_{oc}, but a further increase in annealing temperature to 1000 °C results in a significant reduction. With the 550 °C annealed samples, values of 20 mA/cm^2 and 470 mV were measured for the I_{sc} and V_{oc}, respectively, leading to a fill factor >65% and an energy conversion efficiency >6%. It should be noted that these latter values were obtained without any solar cell device engineering such as the application of an antireflection coating on the top surface, the formation of a back-surface field, base doping, or top electrode geometry optimization. With device engineering, the short absorption length[2,8] of these structures might present an opportunity for advances in thin film silicon photovoltaics.

We attribute the increase in the values of V_{oc} and $|I_{sc}|$ upon annealing at 550 °C to a decrease in the density of point defects, which was proposed as one of the two mechanisms that lead to the observed increase in mobility reported in Table I. Indeed, point defects that survive the laser melting process can act as recombination centers for photogenerated carriers; their subsequent annealing would improve the photovoltaic characteristics of the junctions. This does not exclude the presence of the other mechanism—namely, the neutralization of ionized dopants—as deduced from the measured drop in the value of n_e from 8×10^{18} to 5×10^{18} electrons/cm^3 upon annealing (see Table I). However, the effect of this drop in n_e on the value of V_{oc} would be a decrease of a few percent, which is likely to be masked by the enhancement of V_{oc} due to point defect annealing. Although the C-RBS spectra and the XTEM micrographs (Figs. 1 and 2, respectively) indicate that laser irradiation at 1.8 J/cm^2 results in the formation of a single crystal supersaturated with S and free of extended defects, the presence of point defects that are undetectable by C-RBS and XTEM cannot be ruled out. They could be located either within the melted layers during solidification or they could be generated by the ion implantation process in the channeled tail beneath the amorphous layer. In the latter case, this ion implantation damage region would extend beyond the laser melt depth (~450 nm at 1.8 J/cm^2) and, therefore, postirradiation annealing would be necessary to reduce the density of these defects. It is also noteworthy that the enhancement of the electrical characteristics of the junctions was found to be independent of the ambient gas flowing during the annealing process, as the use of Ar or forming gas led to similar *I-V* characteristics of the junctions. Therefore, any hydrogen passivation mechanism of point defects (such as dangling bonds) plays only a minor role in improving the electrical properties of the junctions. For anneals at the very high temperature of 1000 °C, excessive clustering or precipitation of the S dopants is expected to occur,[17] thereby degrading the electrical properties of the junctions. These two competing

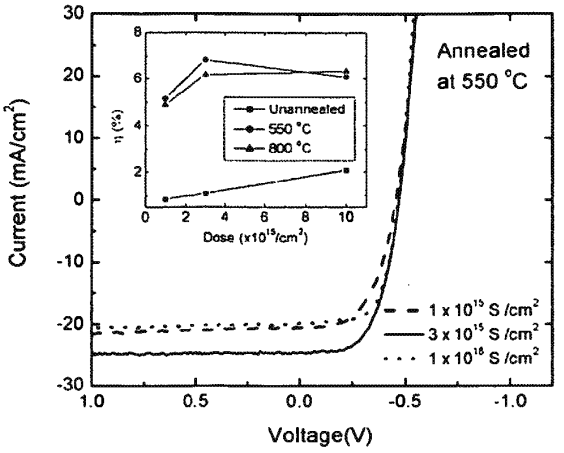


FIG. 6. *I-V* curves measured under one sun for samples implanted with different ion doses in *p*-Si(001), irradiated at 1.8 J/cm^2, and furnace annealed at 550 °C. The inset shows the variation of the efficiency η vs ion implantation dose for different annealing temperatures.

phenomena would explain the occurrence of a window of annealing temperatures for good rectifying and photovoltaic behaviors of the junctions.

The effect of annealing on the *I-V* characteristics of the samples implanted for various doses is presented in Fig. 6. The value of V_{oc} is nearly independent of implantation dose at (470±10) mV. The value of I_{sc} is significantly higher (~25 mA/cm^2) for the medium dose of 3×10^{15} S/cm^2. However, the increase in photocurrent measured for the medium dose sample is accompanied by a loss in fill factor, resulting in almost no change in efficiency, as is seen in the inset. The trend is consistent with the effects of annealing shown in Figs. 4 and 5.

Finally, preliminary electrical characterizations were also carried out on laser melted S implanted *n*-Si(001) substrates. Because sulfur acts as a donor, nn^+ homojunctions were thus formed, with the n^+ region being the implanted/laser irradiated top layers. Dark *I-V* curves from two such homojunctions are presented in Fig. 7. Both curves show a good rectifying behavior with a built-in voltage V_{bi} lower than those observed for the *pn* junction. This is justified by observing that, for a nn^+ junction, the V_{bi} is given by the following expression:

$$V_{bi} = (kT/q)\ln(n^+/n),$$

where n^+ and n are the free charge carrier concentrations in the highly doped region and underlying substrate, respectively. In our case, the ratio n^+/n is of the order of 1000 ($\sim10^{18}/10^{15}$), thereby leading to a V_{bi} of 0.17 eV. The junction annealed at 550 °C shows better *I-V* characteristics than the one annealed at 1000 °C, as inferred from a lower leakage current and a lower ideality factor in forward bias (~2.1 vs 3, respectively). These observations are consistent with the results presented above for the *pn* junctions, where an

SIONYX1403000042.0066

SAMSUNG EX. 1002 - 601/4148

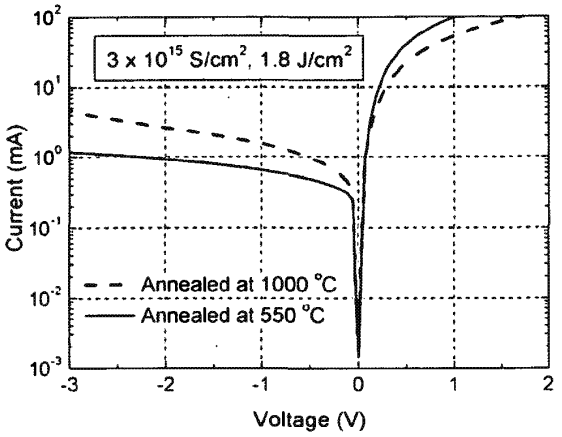


FIG. 7. Dark *I-V* curves corresponding to *n*-Si(001) substrates implanted to a dose of 3×10^{15}/cm^2, laser irradiated at 1.8 J/cm^2, and subsequently annealed at 550 or 1000 °C.

annealing temperature window appears to enhance the electrical characteristics of the junctions.

IV. SUMMARY

We have investigated the crystalline and electrical properties of silicon with 0.46 at. % of sulfur in supersaturated solid solution. This novel material was synthesized by ion implantation of sulfur into Si wafers followed by pulsed laser melting–induced rapid solidification using an excimer laser. The low number of laser pulses used in this work ensures little irradiation-induced surface damage or roughening of the wafers. The crystalline quality of the layers after laser irradiation was evaluated by channeling RBS and TEM. It was shown that laser fluences of 1.4 J/cm^2 and above are necessary to melt through the amorphous implanted region leaving, after solidification, a perfect single crystal free from extended defects. By performing experiments on *p*-doped and *n*-doped substrates, *pn* and *nn*$^+$ junctions were formed and showed good rectifying and photovoltaic behaviors. The properties of the junctions were enhanced by postirradiation furnace anneals, with samples annealed within a window of 550–800 °C exhibiting good properties. We attribute the improvement in properties upon annealing to the annihilation of point defects that survive the laser melting and rapid solidification process. We attribute the deterioration upon annealing at 1000 °C to clustering or precipitation of the sulfur atoms. The junctions could be further optimized by applying the appropriate device engineering processes. The short absorption length of these structures might present an opportunity for advances in thin film silicon photovoltaics, but there remain many unanswered questions regarding, e.g., band structure and minority carrier diffusion lengths.

Excimer laser melting combined with ion implantation is shown to be a controllable and well characterized technique that enables the production of unusual compositions in stable, supersaturated solid solution, making it potentially attractive for the fabrication of electronic and optoelectronic devices based on chalcogen-laden Si.

ACKNOWLEDGMENTS

The authors thank E. Mazur, J. E. Carey, E. Kaxiras, Y. Mo, F. Capasso, and J. Bao for helpful discussions. This work was supported by National Science Foundation Grant No. DMR-0306997. One of the authors (M.T.) acknowledges the financial support of the Arab Fund and Fulbright programs and another author (R.S.G.) a Radcliffe Institute Fellowship. T.G.K. was supported by the Korea Research Foundation Grant funded by the Korean Government (MOEHRD, Basic Research Promotion Fund), Grant No. KRF-2004-214-C00156. B.L.C. and R.S.G. were supported by the U.S. Department of Defense through the Intelligence Community Postdoctoral Fellowship under Grant No. HM1582-05-1-2027. Central facilities were used within the Harvard Center for Nanoscale Systems.

[1]C. H. Crouch, J. E. Carey, J. M. Warrender, E. Mazur, M. J. Aziz, and F. Genin, Appl. Phys. Lett. **84**, 1850 (2004).
[2]C. Wu *et al.*, Appl. Phys. Lett. **78**, 1850 (2001).
[3]J. E. Carey, C. H. Crouch, M. A. Sheehy, M. Shen, C. M. Friend, and E. Mazur, Opt. Lett. **30**, 1773 (2005).
[4]Z. Huang, J. E. Carey, M. Liu, X. Guo, E. Mazur, and J. C. Campbell, Appl. Phys. Lett. **89**, 033506 (2006).
[5]V. Zorba, P. Tzanetakis, C. Fotakis, E. Spanakis, E. Stratakis, D. G. Papazoglou, and I. Zergioti, Appl. Phys. Lett. **88**, 081103 (2006).
[6]C. H. Crouch, J. E. Carey, M. Shen, E. Mazur, and F. Y. Genin, Appl. Phys. A: Mater. Sci. Process. **79**, 1635 (2004).
[7]A. J. Pedraza, J. D. Fowlkes, and D. H. Lowndes, Appl. Phys. Lett. **74**, 2322 (1999).
[8]T. G. Kim, J. M. Warrender, and M. J. Aziz, Appl. Phys. Lett. **88**, 241902 (2006).
[9]M. J. Aziz, C. W. White, J. Narayan, and B. Stritzker, in *Energy Beam-Solid Interactions and Transient Thermal Processing*, edited by V. T. Nguyen and A. G. Cullis (Editions de Physique, Paris, 1985), p. 231.
[10]R. Reitano, P. M. Smith, and M. J. Aziz, J. Appl. Phys. **76**, 1518 (1994).
[11]L. J. van der Pauw, Philips Res. Rep. **13**, 1 (1958).
[12]ThermalOriel model 66902 sun simulator.
[13]M. J. Aziz, Metall. Mater. Trans. A **27**, 671 (1996).
[14]J. A. Kittl, P. G. Sanders, M. J. Aziz, D. P. Brunco, and M. O. Thompson, Acta Mater. **48**, 4797 (2000).
[15]R. G. Wilson, J. Appl. Phys. **55**, 3490 (1984).
[16]E. Janzen, R. Stedman, G. Grossmann, and H. G. Grimmeiss, Phys. Rev. B **29**, 1907 (1984).
[17]Y. Mo, M. Z. Bazant, and E. Kaxiras, Phys. Rev. B **70**, 205210 (2004).
[18]G. Mannino, V. Privitera, A. La Magna, E. Rimini, E. Napolitani, G. Fortunato, and L. Mariucci, Appl. Phys. Lett. **86**, 051909 (2005).
[19]L. Romano, A. M. Piro, V. Privitera, E. Rimini, G. Fortunato, B. G. Svensson, M. Foad, and M. G. Grimaldi, Nucl. Instrum. Methods Phys. Res. B **253**, 50 (2006).
[20]Y. Takamura, S. H. Jain, P. B. Griffin, and J. D. Plummer, J. Appl. Phys. **92**, 230 (2002).
[21]S. M. Sze, *Physics of Semiconductor Devices* (Wiley, New York, 1981), p. 68.

SIONYX1403000042.0067

SAMSUNG EX. 1002 - 602/4148

A 600×600 Pixel, 500 fps CMOS Image Sensor with a 4.4μm Pinned Photodiode 5-Transistor Global Shutter Pixel

I. Takayanagi, Y. Mo*, H. Ando, K. Kawamura, N. Yoshimura, K. Kimura,
T. Otaka, S. Matsuo, T. Suzuki, F. Brady**, and J. Nakamura
Micron Japan, Ltd. 4-2-8 Shibaura, Minato-ku, Tokyo 108-0023, Japan
* Micron Technology, Inc. 251 South Lake Avenue, Suite 600, Pasadena, CA 91101-1101, USA
** Micron Technology, Inc. 8000 S. Federal Way, Boise, ID 83707-0006, USA
Contact: Isao Takayanagi: tel: +81-3-5439-3300, fax: +81-3-5439-3311, email: istakayanagi@micron.com

Abstract

To realize a low cost image sensor, while maintaining a 500 fps-class high frame rate, we have developed a prototype image sensor where a 600×600 imaging array with a 4.4μm global shutter pixel and multiple pipeline analog-to-digital converters (ADCs) are implemented. In this paper, its image sensor architecture, pixel configuration and operation are described and characterization results are reported.

I. Introduction

Machine vision and high frame rate applications usually require the global shutter operation to "freeze" the image. In global shutter pixels, an in-pixel signal memory, an additional global reset gate and a global transfer gate should be equipped, which results in a larger pixel size than that of general purpose CMOS imagers. In previously reported high speed CMOS image sensors with the global shutter functionality, relatively large pixels, ranging from 7μm to 16 μm, have been used [1-3]. However, the large pixel size results in a large die size and thus high image sensor cost. Therefore, pixel size reduction has been strongly requested for low cost applications and/or small module applications.

In this paper we present a 600×600 pixel prototype imager with a 4.4μm pitch 5-transistor global shutter pixel. The imager can operates at a high frame rate of 500fps.

II. Sensor Design

a. Chip specifications and structure

Figure 1 shows a block diagram of the image sensor. The pixel signals from a 600×600 imaging array are read out through top and bottom circuit blocks and transferred to analog signal chain / analog-to-digital converter (ASC/ADC) blocks. The column block consists of column gain amplifiers, sample-and-hold capacitors and a column decoder with column select switches.

The ASC/ADC block consists of second gain amplifiers and 8bit low power pipeline ADCs. A DAC/Buffer block contains bias generators and reference voltage generators that are controlled by two-wire serial I/F, thus yielding a fully digital interface. All internal pulses are generated by an internal timing generator (TG) so that external control/trigger inputs are minimized.

The chip handles pixel readout and signal processing at 200Mpixel/s with a 50MHz master clock and operates at 500fps with 600×600 full pixel resolution.

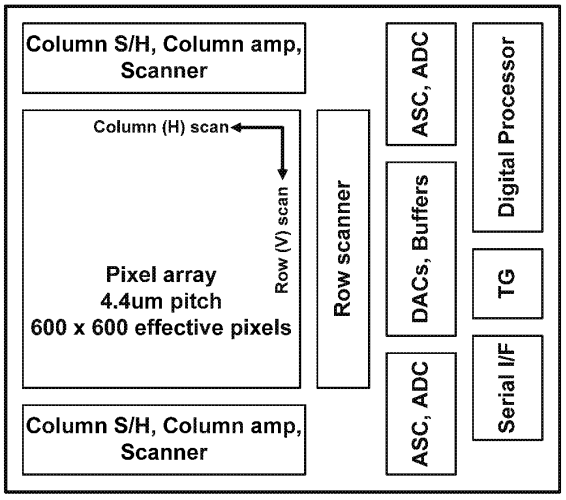


Figure 1. Block diagram of the chip.

b. Pixel configuration

The pixel consists of a pinned photodiode (PD), pixel memory (storage node M) and five transistors for pixel reset and readout as shown in Figure 2. The AB gate controls reset of the photodiode. This reset is global, i.e., all the pixels are reset simultaneously. The TX gate controls the charge transfer from PD to M. The complete charge transfer is required for both AB and TX operations to eliminate image lag and pixel-wise FPN.

SIONYX1403000042.0068

SAMSUNG EX. 1002 - 603/4148

In a global shutter mode, signal charge is transferred to node M, then the charge is read out in a similar manner to that of the conventional 3T pixel operation. Since a signal charge integration part and a readout part are separated by TX, the pixel allows simultaneous operations of charge integration and signal readout.

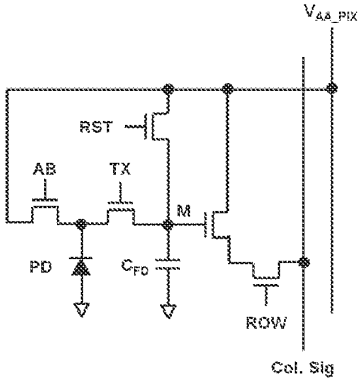


Figure 2. 5T global shutter pixel configuration

c. Signal chain

A schematic diagram of the signal chain is shown in Figure 3. The imager has two gain stages; one is in the column block and another in the video ASC block, as a primary gain stage and a secondary supplemental gain stage, respectively.

Pixel signal is amplified up to 8x by the column amplifier simultaneously to the pixel readout then stored on SH capacitors. Through a column select switch addressed by the column address decoder, stored signal in the SH capacitor is serially transferred to the ASC block followed by a low power 8bit ADC. Four ADC's, each operates at 50Msps, are integrated. Thus a total data rate reaches 200Msps.

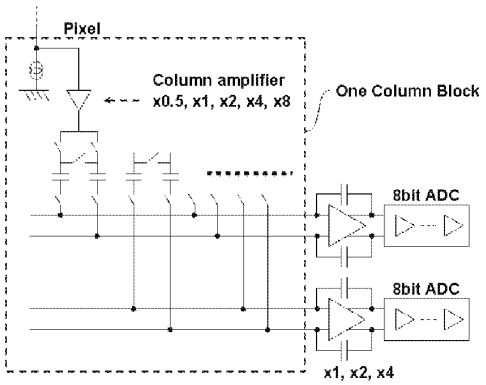


Figure 3. Signal chain of one column block

d. Global control and internal operation

A timing diagram for a frame operation is shown in Fig. 4. The sensor receives three external control pulses, 'START_EXPOSURE', 'END_EXPOSURE', and 'READ_START', each triggering the start of the exposure, the end of the exposure and the signal readout sequence. When 'START_EXPOSURE' is asserted, all photodiodes are reset by the global AB pulse that sweeps the charge out of the photodiode. Next, 'END_EXPOSURE' determines time for global TX that forces the charge to transfer from a photodiode to a memory node M. Readout of the charge in the memory node M starts when 'READ_START' pulse is asserted.

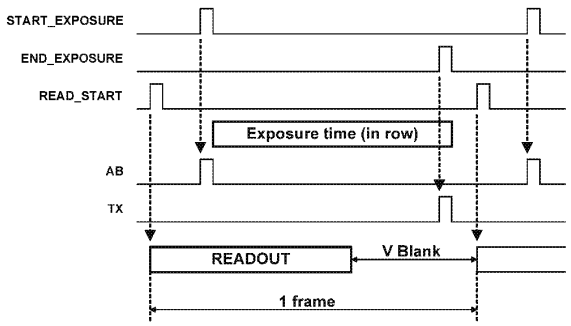


Figure 4. Operation timing

I2C interface is used for detail imager control. Also, two register banks are implemented, thus enabling instantaneous switching between two registered operation modes. This functionality helps enhance usability of high-speed imaging. For example, one register is set for a high-frame rate operation with reduced number of readout rows, and the other is set for reading out full resolution images. In this case, when an object is detected while the imager is operating in the high-frame rate mode, the system requests the imager to capture an full resolution image, thereby the imager immediately changes its operation mode for the full resolution snapshot readout. When the snapshot mode is chosen, the signal memory M should be reset to clean up noise charge or lag charge on the node during the charge integration period before the global TX is asserted.

III. Fabrication and Characterization

a. Fabrication

The 600×600 pixel image sensor was fabricated in 0.13μm 2P4M CMOS image sensor process. The prototype is a monochrome sensor with an on-chip

SIONYX1403000042.0069

SAMSUNG EX. 1002 - 604/4148

microlens array.

Figure 5 shows the top layout of the imager. An imager core including a pixel array and the rest of the analog blocks, together with integrated logic circuits, are implemented for prototyping. Video output is read out through 8bit × 4 parallel output ports, each handling a 50MHz data rate. Thus, a total output data rate of 200Mpix/sec is achieved. Imager core size is approximately 4.0mm × 4.0mm.

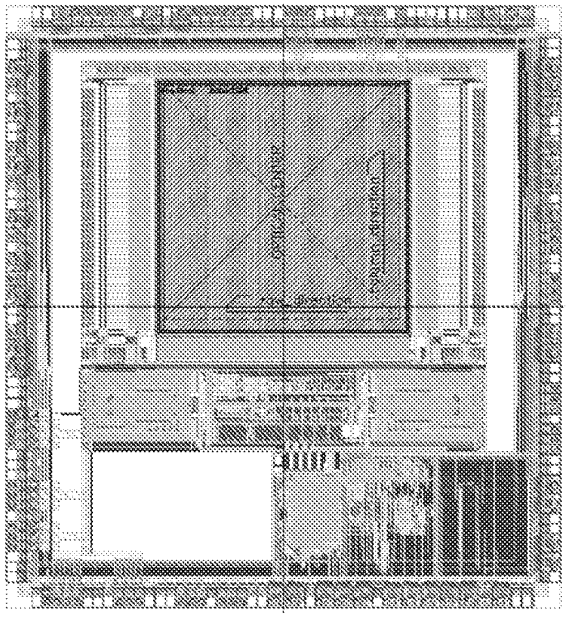


Figure 5 Prototype chip layout

b. Operation sequence for characterization

Besides the external trigger mode, the imager operation can be programmed with combinations of two registered modes. To perform characterization, we use a following operation sequence as shown in Figure 6; One cycle includes 8 fast readout frames and 8 full resolution readout frames. 32 effective rows are read out at 5000fps in the fast readout period then full resolution readouts at 500fps follow.

A full resolution image is evaluated from the first full resolution image. Also, image lag can be characterized with consecutive 8 frames in the full resolution readout period. Characterization was done under the 500fps full resolution condition.

c. Characterization results

Fig. 7 shows a spectral response. With an on-chip microlens, peak quantum efficiency reaches 63% at 500nm. Also the result shows good sensitivity against a wide wavelength range from near ultraviolet to near infrared. Quantum efficiency exceeds 20% within a range from 380nm to 830nm.

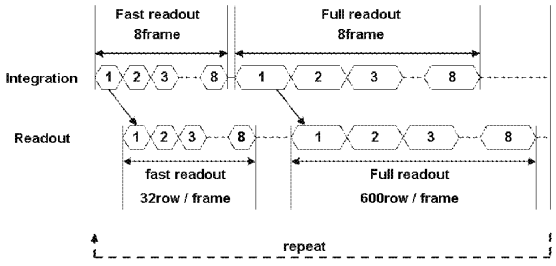


Figure 6. Operation cycle for characterization

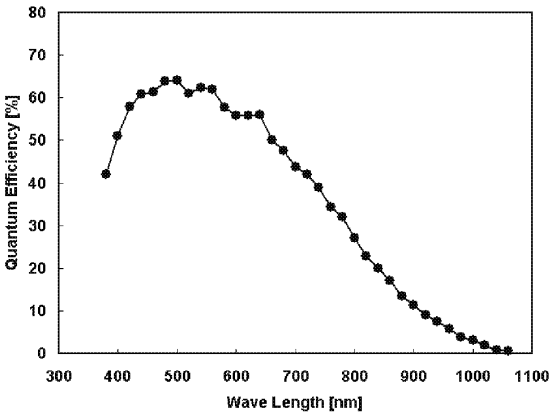


Figure 7. Spectral response

Image lag was negligibly small, which demonstrates the signal charge transfer from the pinned photodiode to both the memory node and the AB drain is almost complete.

Noise performance versus analog gain is plotted in Figure 8 with pixel-wise noise, temporal noise and structural noise. The data was obtained from one output port of 4, therefore offset variation between output ports are ignored. Total noise is very close to pixel random temporal noise and the result suggests main noise source is the pixel temporal noise that is caused by a reset operation of a floating node M in Figure 2. Capacitance of the floating node is estimated to be 3.4fF and it causes noise of 27 electrons-rms per reset operation. FPN including structural noise is smaller than 1/5 the pixel temporal noise when gain is larger than 2 and it is mostly invisible.

On the other hand, offset variation between signal chains was measured to be approximately 1.2LSBs at 4x gain, which corresponds to 17 electrons-rms. Although this noise level is smaller than 1/2 the total

SIONYX1403000042.0070

SAMSUNG EX. 1002 - 605/4148

noise at 4x gain, we can reduce the noise by offset adjustment in the backend process.
An image obtained from a snapshot and summary of imager specifications are shown in Figure 9 and Table 1, respectively.

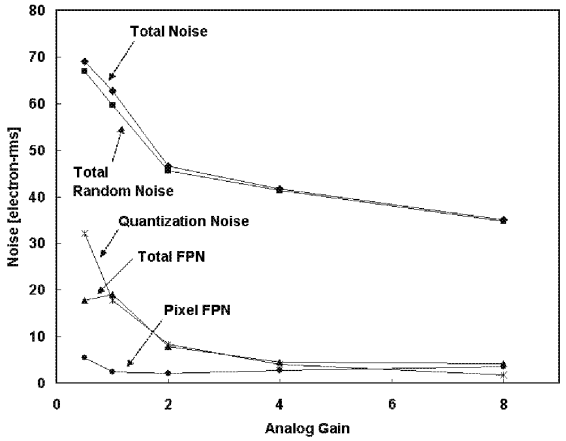


Figure 8. Noise measurement result

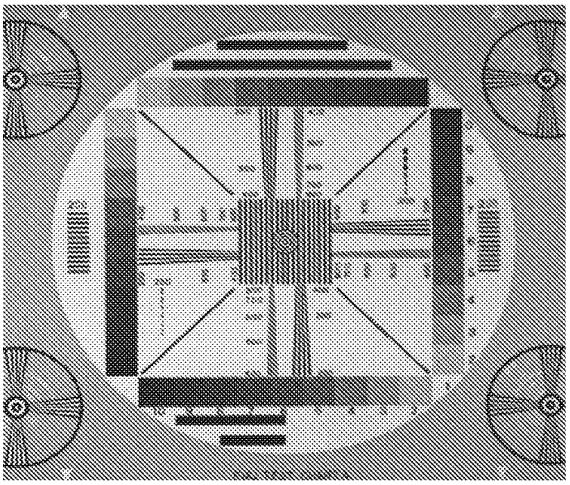


Figure 9. An output image from the first frame in a full resolution readout period in Figure 6 operating at 500fps. No correction of channel offset variations.

Table I. Specifications and Performance

Resolution	600 x 600
Pixel size	4.4 μm
Optical format	1/5 inch
Shutter scheme	Global shutter
Master clock	50 MHz
ADC resolution	8 bit
Full resolution frame rate	500 fps
Power consumption	248 mW
Peak quantum efficiency	63% at 500nm
Total noise	42 electrons at 4x gain
Linear full well capacity	12k electrons

IV. Conclusion

We have developed a prototype 600×600 pixel, 500 fps CMOS image sensor with a 4.4μm 5T pinned PD global shutter pixel for low-cost, high-frame rate imaging applications. It features a quick operation mode switching (ex. from a 5000fps windowing mode to a 500fps full resolution mode, and vice versa), while no degradation in image quality of the first frame after the switching is observed. High quantum efficiency of 63% at 500nm is obtained. The kTC noise associated with the in-pixel memory reset is a dominant noise source. Both FPN and image lag are reasonably suppressed.

Acknowledgment

The authors acknowledge R. Panicacci, J. Solhusvik, T. Gilton, G. Agranov, R. Mauritzson, N Bock and P. Gallagher for their guidance and valuable discussions. The authors would also like to thank H. Wang for developing a characterization system.

References

1]http://www.micron.com/products/partdetail?part=MT9M413C36STM

2] A. I. Krymski and N. Tu, "A 9-V/lux-s 5000-frames/s 512 ×512 CMOS sensor," IEEE Trans. ED., vol. 50, no. 1, pp. 136-143, January 2003.

3] N. Bock, et al., "A CMOS image sensor with global shutter and extended dynamic range, " in Final Program and Proceedings of ICIS '06 Int'l Congress of Imaging Science, pp. 571-574, 2006.

SIONYX1403000042.0071

SAMSUNG EX. 1002 - 606/4148

SAMSUNG EX. 1002 - 607/4148

Large Format Backside Illuminated CCD Imager for Space Surveillance

John R. Tower, *Senior Member, IEEE*, Pradyumna K. Swain, *Member, IEEE*, Fu-Lung Hsueh, *Member, IEEE*, Robin M. Dawson, *Member, IEEE*, Peter A. Levine, *Member, IEEE*, Grazyna M. Meray, James T. Andrews, *Member, IEEE*, Verne L. Frantz, Mark S. Grygon, Michael A. Reale, *Member, IEEE*, and Thomas M. Sudol

***Abstract*—The key features and performance data of a 2568×1960-pixel split-frame-transfer imager developed for space surveillance is described. The eight-port, backside illuminated charge coupled device (CCD) features 24 μm pixels with buried blooming drains to provide 180% optical fill-factor and >1000× overload protection from blooming. The imaging and storage registers are strapped with metal to achieve vertical transfer clock rates >400 KHz for the 61 mm long imaging register gates. The 5 million pixel array operates at 2.7 frames/s. The monolithic focal plane includes a 32×32-pixel frame-transfer imager, with a single output, which operates at 1000 frames/s. The output ports employ a floating diffusion output circuit with responsivity of 10.5 μV/e and noise of 7e RMS at a 1.25 MHz clock rate. The imager is photocomposed employing a combination of 5× and 1× lithography. The photocomposition approach is described.**

***Index Terms*—Backside illuminated CCD, charge coupled device, floating diffusion amplifier.**

I. Introduction

A large format charge coupled device (CCD) has been developed as the visible light sensor to support ground-based, deep space surveillance. This solid state device will replace Ebsicon imaging tubes in the current operational system. The CCD technology provides superior low light level signal-to-noise performance, geometric accuracy, and dynamic range compared to the tube technology. High broad-band quantum efficiency is achieved by thinning the CCD for backside illumination and applying a high performance backside treatment with antireflection coating.

The large format CCD design is very similar to that of the MIT Lincoln Laboratory CCID-16 [1]. The CCID-16 was developed by Lincoln Laboratory to demonstrate its applicability for space surveillance. Both devices have imaging formats of 2560×1960-pixels, readout in a split-frame-transfer architecture. The new design incorporates pixel antiblooming and metal strapping of the gates for improved vertical transfer rate. The Sarnoff device is produced employing a novel photocomposition approach incorporating both 5× and 1× lithography.

Manuscript received April 9, 2002; revised August 23, 2002. The review of this paper was arranged by Editor J. Hynecek.

The authors are with the Sarnoff Corporation, Princeton, NJ 08543-5300 USA (e-mail: jtower@sarnoff.com).

Digital Object Identifier 10.1109/TED.2002.807715

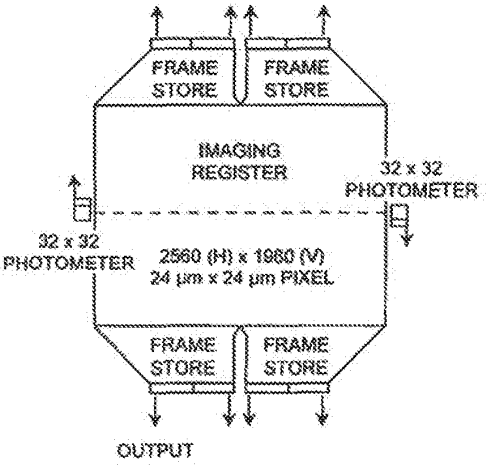


Fig. 1. Architecture of 5M pixel main array indicating split-frame-transfer architecture with eight output ports.

II. Device Design

A. Architecture and Process Overview

The architecture of the large format device is shown in Fig. 1. The 5 million pixel imaging register has a pixel size of 24 μm × 24 μm, providing an imaging format of 61 mm × 47 mm. The active imaging diagonal is 77 mm. The imaging register is split into a top and bottom half. The top portion is clocked up to four frame storage registers and the bottom portion is clocked down to four frame storage registers. There are eight horizontal registers servicing the frame storage registers. Each of the eight horizontal registers employs a floating diffusion amplifier to produce the signal output. The overall device just fits within an 85-mm-diameter circle. This is the limit of the processing region for the 100 mm wafers when employing whole wafer thinning. To make this device fit, the storage registers employ a smaller vertical pitch and fan-in on the outside edges to bring the output amplifiers away from the wafer rim, as depicted in Fig. 1.

There are also two small photometer arrays incorporated into the design adjacent to the main array. These 32 × 32-pixel frame transfer arrays are employed for high frame rate imaging. Each has a single horizontal register and one output port. In the

0018-9383/03$17.00 © 2003 IEEE

SIONYX1403000042.0072

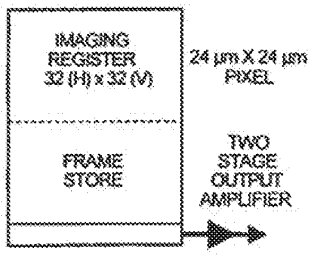


Fig. 2. Architecture of 32 × 32 photometer indicating frame transfer architecture.

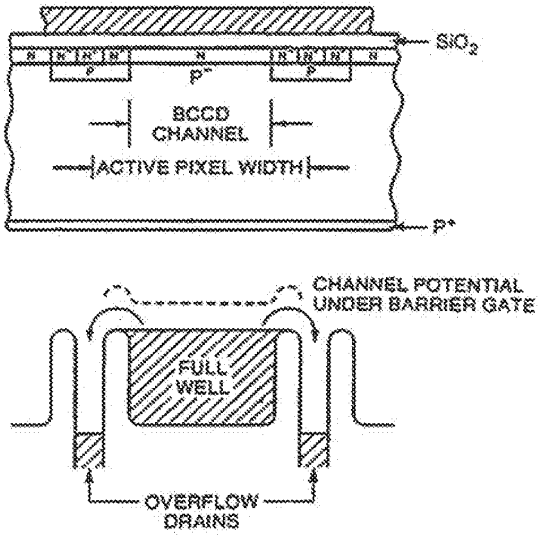


Fig. 3. Buried blooming drain cross section showing structure and potential profile of pixel.

imaging system only one of the two photometers is operational. The architecture for the photometer is shown in Fig. 2.

The wafer scale CCD is fabricated in a three-phase, triple-polysilicon process technology. A single level of metal is employed. The device is thinned employing the RCA/Sarnoff whole wafer thinning process [2]–[4]. The backside is implanted and given a high temperature furnace anneal. An antireflection coating is then applied. The wafer is then laminated to a glass support on the backside. The process provides high, stable quantum efficiency in the visible region and a flat imaging surface protected by the laminating glass.

B. Imaging Register and Pixel Design

The large array and the photometer both have 24 μm × 24 μm pixels. The pixels employ a buried blooming drain to ensure freedom from blooming [5]. The structure is illustrated in Fig. 3. A lateral overflow drain is formed by implanting a phosphorous N+ drain surrounded by a boron barrier region on both sides of the drain. The barrier implant is chosen to assure that charge levels exceeding full well will spill over the barrier and into the drain rather than spilling down the CCD column. For this design the blooming drain structure occupies 8 μm of the 24 μm column width. Structures as narrow as 4μm have been demonstrated, but for this large area device a conservative design was employed.

The blooming drain is buried to maintain a 100% optical fill-factor for backside illumination. This is done by creating a deep P region beneath the N+ drain and barrier regions. The P region is higher concentration than the substrate doping, creating an electric field barrier large enough to keep the majority of the photoelectrons from being captured by the N+ drain. Typical performance for this buried blooming drain structure across a variety of imagers has been antiblooming up to >1000× saturation, with a signal loss to the blooming drain of <5% for broadband illumination (400–900 nm), and a drain occupying 30% of the pixel area [6].

C. Storage and Horizontal Registers Design

A split-frame-transfer architecture is employed in this design to achieve a reduced loading time from the imaging register to the storage registers. This permits higher frame rate operation and reduces transfer smear. The frame storage is configured as eight frame stores with 640 (H) × 980 (V) storage elements each. Each frame store has a three-phase horizontal register with a two stage floating diffusion output amplifier.

The frame storage registers have a 24 μm vertical stage length for the first few rows, followed by a reduced vertical stage length of 11.1 μm. The horizontal pitch varies from 24 μm at the top of each frame store to 15 μm at the bottom, matching the 15 μm stage length of the horizontal register. The blooming drains extend into the first few rows of the frame storage register. In these rows the charge capacity is gradually reduced to assure that the minimum charge capacity of the frame storage registers and the floating diffusion outputs exceeds the charge level allowed to pass through these 'clipper' rows. The large >500 000 e charge capacity of the imaging pixel is thus transitioned to the 140 000 e charge capacity of the clippers. This clipper level is considerably below the minimum frame store capacity of 350 000 e. This approach maintains the antiblooming performance of the imaging register pixel.

III. High Speed Vertical Transfer

The imaging register and the frame storage registers have a requirement for relatively high vertical transfer speeds given the size of the device. The standard process achieves a vertical transfer clock rate of 100 KHz with the 61 mm long gates driven from both ends. Above this clock rate antiblooming performance is degraded in the central portion of the imaging register.

Higher vertical transfer clock rates are achieved employing a metal strapping option. Here metal bussing and strapping contacts are added within the active CCD imaging and storage registers to reduce the RC time constant of the gates. A completed CCD with metal strapping is shown in Fig. 4. The imaging register design contacts each gate in the middle of the 61 mm gate length and maintains the connections at the two ends of each

SIONYX1403000042.0073

SAMSUNG EX. 1002 - 608/4148

SAMSUNG EX. 1002 - 609/4148

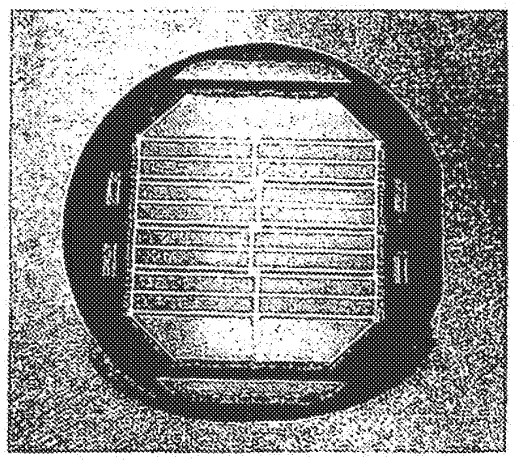


Fig. 4. Photography of backside illuminated imager, metal strapping is apparent.

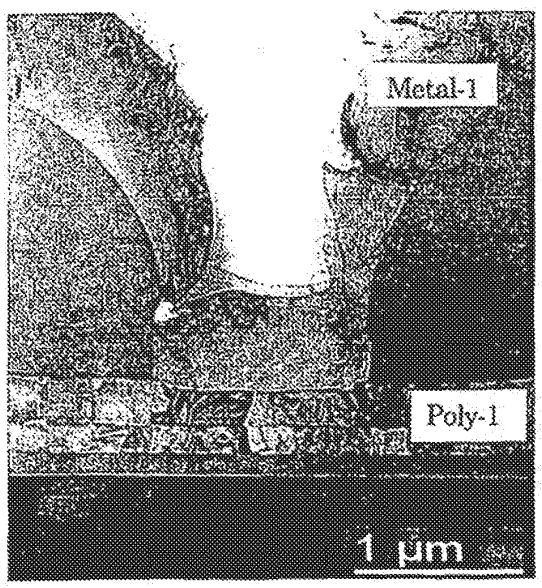


Fig. 5. TEM cross section of strapping contact to poly-1 gate.

gate. The storage registers achieve an equivalent RC time constant employing metal strapping. This optional strapping approach increases the vertical transfer clock rate to >400 KHz.

The connections from the metal strapping busses to the polysilicon gates employ specially designed strapping contacts [7]. The lithography and contact etching profile have been tailored to achieve high yield in the triple polysilicon topology of the CCD process. A storage register strapping contact to a first polysilicon gate is shown by high resolution transmission electron microscopy (TEM) in Fig. 5. The contact size is 1.1 μm × 3.0 μm, resulting in a nominal 1.0 μm spacing between the metal contact and the adjacent poly 2 and poly 3 gates of this 11.1 μm storage register pixel.

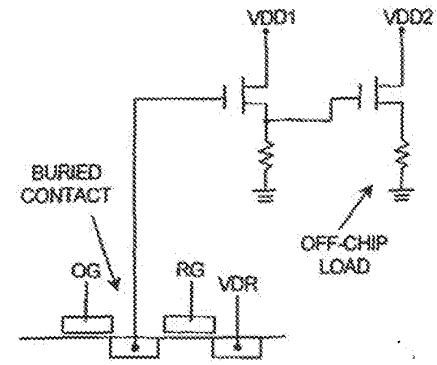


Fig. 6. Two stage floating diffusion output amplifier schematic.

IV. High Sensitivity Output Amplifier

The eight output ports on the main array are clocked at a 2-MHz rate to support the baselined 2.7 frames/s operation. The photometer output is clocked at a 1.25 MHz rate when the photometer is operating at a 1000 frames/s rate. All of the outputs employ the same design.

To achieve operation at >1 MHz clock rates the two stage output amplifier shown in Fig. 6 is employed. The first stage has a depletion mode source follower with a diffused resistor load. The second stage has an enhancement mode source follower with an off-chip load. The power supplies to the first and second stage are separately biased for optimum performance.

The output structures employ a buried contact to connect the floating diffusion to the first stage source follower gate. This design approach increases the output sensitivity and reduces the output noise compared to a more conventional metal contact design [8]. The linear full well requirement for the output is 140 000 e. The output sensitivity is chosen to be 10.5 μV/e, producing a 1.5 V signal at the linear full well requirement of 140 000 e.

A low resolution TEM cross section of the buried contact connection to the floating diffusion is shown in Fig. 7. The buried contact is formed by etching a 1.2 μm × 1.2 μm contact hole, depositing/doping of first level polysilicon, and then defining the polysilicon. The polysilicon dopant creates the N+ diffusion in the silicon and creates a low resistance connection from the N+ diffusion to the floating diffusion first polysilicon gate. The polysilicon gate thus extends from the N+ diffusion into the first stage source follower active region. The buried contact obviates the need to employ the more conventional floating diffusion metallization. The total capacitance of the floating diffusion node for this design is 7.6 fF.

A high resolution TEM cross section of the buried contact connection is shown in Fig. 8. Here it is evident that the polysilicon gate has made intimate connection to the silicon substrate, establishing a local alignment of the polysilicon material with the bulk silicon lattice. Electrical measurements on test structures have confirmed an ohmic connection of approximately 150 ohms with as small as a 1 mV test voltage.

SIONYX1403000042.0074

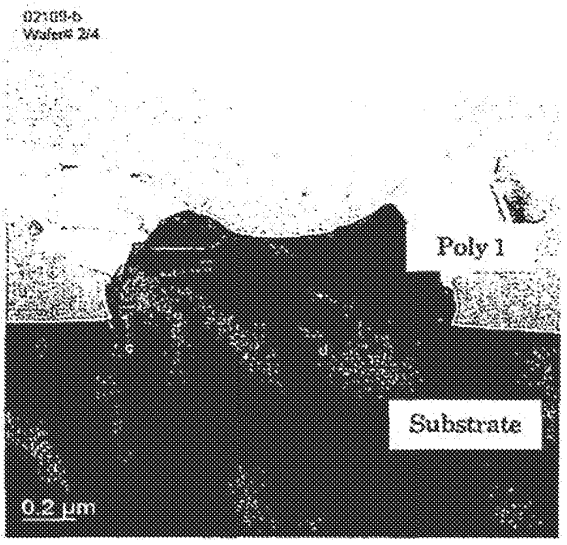


Fig. 7. Low resolution TEM of output amplifier buried contact.

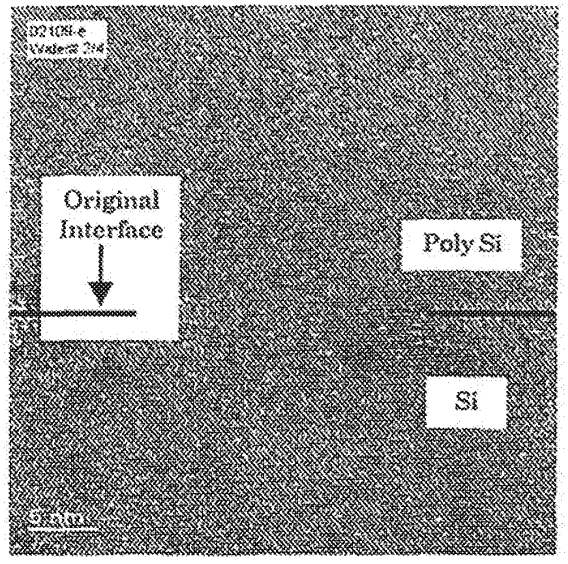


Fig. 8. High resolution TEM of output amplifier buried contact showing local alignment of polysilicon structure to silicon lattice.

V. Photocomposition

The layout of the metal strapping of the storage register polysilicon gates, the blooming drains, and the floating diffusion require 5× lithography to achieve the desired feature sizes and mask-to-mask alignment. Certain aspects of the design benefit from employing 1× lithography. Thus, a mix-and-match combination of 5× and 1× lithography is employed.

Prior to designing the CCD a test array was developed to evaluate the dimensional fidelity of the lithography approach over the required 85 mm diagonal field. It was found that with adequate 5× alignment marks placed just outside of the 85 mm diagonal, and with the 1× tool properly calibrated, that the 5×-to-1× run-out was an acceptable $+/-0.4$ μm across this field.

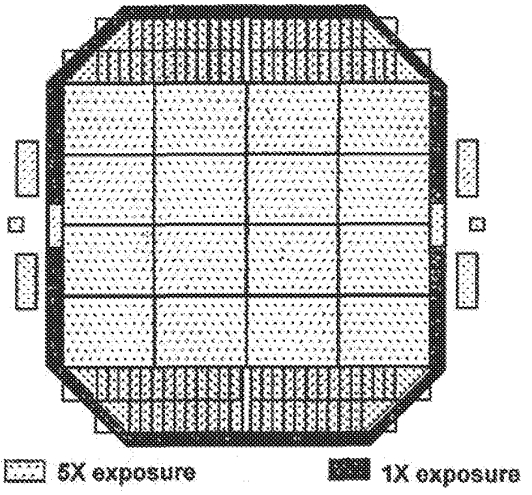


Fig. 9. Photocomposition approach for the poly-1 level employing 119 reticle patterns.

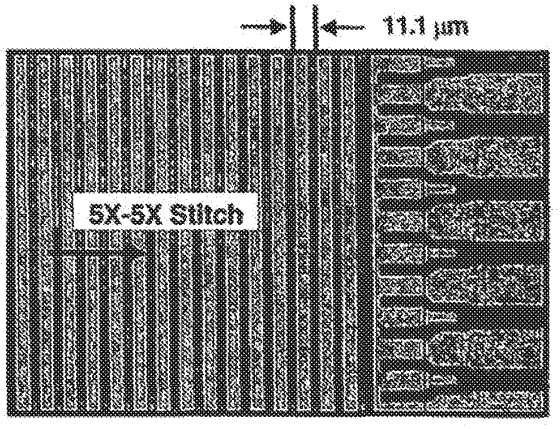


Fig. 10. Photomicrograph of stitching boundary (poly-1 photoresist pattern in frame store).

One of the most complicated mask levels is the first polysilicon level (poly 1). To photocompose this level three 5× masks and one 1× mask are employed. Each of the poly 1 reticle exposures is indicated in Fig. 9. There are 119 reticle patterns being combined to define the 77 mm×75 mm active area of the poly 1 field.

Care was taken in designing the overlap regions at the stitch boundaries to maintain the feature size across the reticle boundaries. Fig. 10 shows a poly 1 photoresist pattern across a 5×-to-5× stitch boundary in a frame store register with an 11.1 μm gate pitch. This photograph indicates typical reticle-to-reticle pattern alignment. The measured misalignment at the stitch boundaries is $< +/-0.15$ μm.

SIONYX1403000042.0075

SAMSUNG EX. 1002 - 610/4148

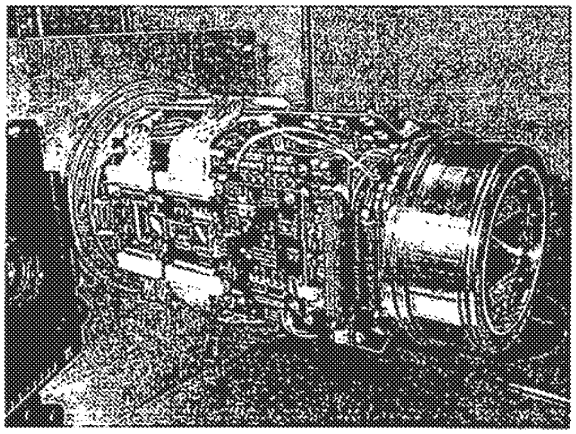


Fig. 11. Photograph of Deep STARE multiport camera.

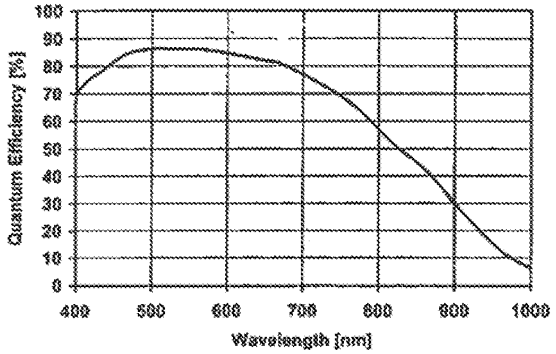


Fig. 12. Quantum efficiency of backside illuminated CCD with buried blooming drains.

VI. Performance

The data taken on the CCD comes from testing of the first two wafer lots. The production wafer lots, as of this writing, are not completed. The data was taken in the Deep STARE multiport camera system shown in Fig. 11. The data was taken on the main array at a frame rate of 2.7 frames/s, with the output ports running at a 2 MHz clock rate. The data taken on the photometer was taken at a frame rate of 1000 frames/s, with the output port running at a 1.25 MHz clock rate. Data was taken at the nominal operating temperature of −50 °C.

The typical quantum efficiency of the backside illuminated CCD with buried blooming drains and an antireflection coating on the silicon is shown in Fig. 12. Fig. 13 shows the typical percentage loss of photocharge into the blooming drain as a function of wavelength. This measurement is done by simultaneously measuring the blooming drain current and the output reset drain current in response to a monochromatic light source. The results verify the effectiveness of the buried, shielding layer beneath the blooming drain. Testing has verified that the pixel antiblooming can contain charge from spilling at illumination levels well beyond the requirement of 150× the saturation level.

The furthest pixel in the array is 7800 transfers from the output port for this three phase design. The imaging register gates are

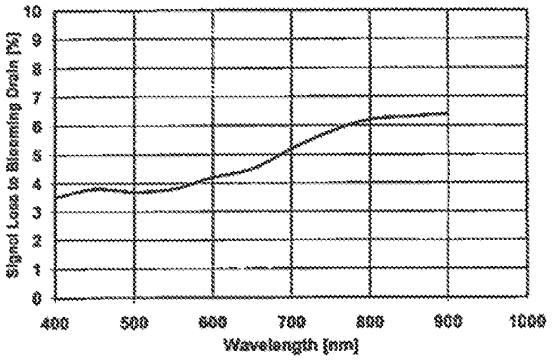


Fig. 13. Signal charge loss to blooming drain as a function of wavelength.

TABLE I
Performance Summary

Characteristic	Measured Performance (-50 C)
Main Array	
Image Size	2560 x 1960
Architecture	Split-Frame-Transfer
Output Ports	8
Frame Rate	2.7 fps
Pixel Size	24 micron x 24 micron
Peak QE	> 80 %
Anti-blooming	> 1,000X
Array Full Well	> 140,000 e
Noise Floor (2 MHz)	< 12 e RMS
Dynamic Range	13 bits
Average Dark Current	< 6 e/pixel/sec
Vertical CTI	$< 1.0 \times 10^{-6}$/transfer
Horizontal CTI	$< 2.4 \times 10^{-6}$/transfer
Photometer	
Image Size	32 x 32
Architecture	Frame-transfer
Output Ports	1
Frame Rate	1,000 fps
Pixel Size	24 micron x 24 micron
Peak QE	> 80 %
Anti-blooming	> 1,000X
Array Full Well	> 140,000 e
Noise Floor (1.25 MHz)	7 e RMS
Dynamic Range	13 bits

8 μm in gate length and the array is run at −50 °C. With these design parameters the charge transfer inefficiency was measured to be $< 1.0 \times 10^{-6}$ per transfer in the vertical direction and $< 2.4 \times 10^{-6}$ per transfer in the horizontal direction employing extended edge response measuring the overscan trailer.

The noise characteristics of the output amplifier were measured. The measured sensitivity at the output of the floating diffusion amplifiers is 10.5 μV/e. The noise level of the photometer array running at 1.25 MHz clock rate in the camera

SIONYX1403000042.0076

SAMSUNG EX. 1002 - 611/4148

SAMSUNG EX. 1002 - 612/4148

SIONYX140300004 2.0077

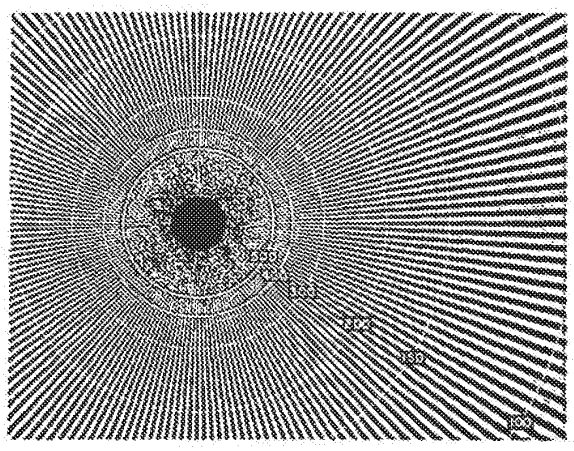


Fig. 14. Imagery from 5M-pixel main array (Lot 2 CCD).

system is typically 7 e RMS. The measured full well (limited by the frame store charge clippers) is 140 000 e. The dynamic range is thus >13 bits (the camera employs a 14 bit analog-to-digital converter).

A summary of the main array and photometer measured performance at −50 °C is given in Table I. Imagery from the eight port main array is shown in Fig. 14. Gain and offset corrections have been applied to the imagery.

VII. Summary

A backside illuminated 5M pixel imager has been developed to support ground-based deep space surveillance. The main array provides a large 61 mm×44 mm active imaging area, operating at 2.7 frames/s. An integrated high speed photometer operates at 1000 frames/s. Both arrays employ 24 μm pixels with lateral overflow, buried blooming drains.

Charge "clipper" structures are employed between the large pixel imaging register and the smaller pixel frame stores to maintain antiblooming. Full system noise performance of 7 e RMS at a 1.25 MHz clock rate (−50 °C) has been measured. A buried contact output design has been implemented for the eight port main array and single port photometer. The camera system dynamic range of both imagers is >13 bits.

The wafer scale design employs 5× and 1× reticles to photocompose the 18 mask levels. The layout just fits within an 85 mm diagonal circle. Excellent intra-level and level-to-level registration has been achieved.

Acknowledgment

The authors wish to acknowledge the many contributors to this imager and camera development effort. In particular, they thank S. Perna at Sarnoff for overall management of the development. Their appreciation is extended to B. Burke and J. Gregory of MIT Lincoln Laboratory for their consulting role on the CCD development. Significant CCD processing contributions were made by D. Furst, M. Bhaskaran, and N. Oldfield. Low noise camera electronics contributors were S. Gershtein, M. O'Neal, and J. Carroll. Testing contributors were M. Bhaskaran and M. McCollum.

References

[1] B. E. Burke, J. A. Gregory, R. W. Mountain, B. B. Kosicki, H. C. Clark, P. J. Daniels, V. S. Dolat, T. L. Lind, A. H. Loomis, and D. J. Young, "Back-illuminated wafer-scale CCD imager," in *1995 IEEE Workshop on Charge-Coupled Devices and Advanced Image Sensors*.

[2] P. A. Levine, W. F. Kosonocky, E. D. Savoye, and D. F. Battson, "High-performance frame transfer CCD imager for television applications," in *Proc. Int. Electronic Imaging Conf.*, Sept. 1984, pp. 46–50.

[3] P. A. Levine, D. J. Sauer, F.-L. Hsueh, F. V. Shallcross, G. C. Taylor, G. M. Meray, and J. R. Tower, "Multi-port backside illuminated CCD imagers for moderate to high frame rate camera applications," *Proc. SPIE*, vol. 2172, pp. 100–114, Feb. 1994.

[4] J. R. Tower, "Advancements in small-pixel, video-rate, backside illuminated charge coupled devices," in *Fourth Int. Conf. Scientific Optical Imaging*, Dec. 1998, pp. 1–6.

[5] J. Ambrose, B. King, J. Tower, G. Hughes, P. Levine, T. Villani, B. Esposito, T. Davis, K. O'Mara, W. Sjursen, N. McCaffrey, and F. Pantuso, "High frame rate infrared and visible cameras for test range instrumentation," *Proc. SPIE*, vol. 2552, pp. 364–383, July 1995.

[6] P. A. Levine, D. J. Sauer, F.-L. Hsueh, F. V. Shallcross, G. M. Meray, G. C. Taylor, G. W. Hughes, J. Pellegrino, D. Simon, L. Harrison, and W. Lawler, "Performance of a high frame rate CCD imager," *Proc. SPIE*, vol. 1693, pp. 65–74, April 1992.

[7] J. R. Tower, T. M. Sudol, V. K. Patel, P. K. Swain, P. A. Levine, F.-L. Hsueh, R. M. Dawson, G. M. Meray, J. T. Andrews, and S. Goldfarb, "High speed, backside illuminated, time delay integration (TDI) CCDs," *Proc. SPIE*, vol. 3794, pp. 148–156, July 1999.

[8] B. E. Burke, J. A. Gregory, M. W. Bautz, G. Y. Prigozhin, S. E. Kissel, B. B. Kosicki, A. H. Loomis, and D. J. Young, "Soft-x-ray CCD imagers for AXAF," *IEEE Trans. Electron Devices*, vol. 44, pp. 1633–1642, Oct. 1997.



John R. Tower (SM'81) received the B.S., M.S., and Ph.D. degrees in electrical engineering from the University of Pennsylvania, Philadelphia, in 1976, 1980, and 1993, respectively.

He joined the RCA Advanced Technology Laboratories, Camden, NJ, in 1976. He was responsible for the design of a number of CCD correlators in both NMOS/CCD and CMOS/CCD process technologies. In 1981, he was promoted to Unit Manager in the Advanced Technology Laboratories, responsible for developing system applications for Schottky barrier IRCCD technology and backside illuminated CCD technology. He joined Sarnoff Corporation (formerly RCA Laboratories), Princeton, NJ, in 1989 as Group Head, Advanced Imaging. He is presently the Senior Technical Director of the Imaging Technology and Products business at Sarnoff, focusing on UV, visible, and infrared imaging technologies in both CCD and CMOS APS process technologies. He has published 38 papers and has received eight patents.

Dr. Tower is a member of Eta Kappa Nu.



Pradyumna K. Swain (M'96) received the Ph.D. degree in physics from Indian Institute of Technology, Delhi, India, in 1995.

He subsequently joined New Jersey Institute of Technology, Newark, as a Post-doctoral Research Fellow, where he worked on strained SiGe devices. Since 1997, he has been with Sarnoff Corporation, Princeton, NJ, where he is engaged in research and manufacturing of various CCD and CMOS image sensors, process integration and device modeling for various MEMS devices.

Dr. Swain has published 23 papers.



Fu-Lang Hsueh (M'82) received the B.S. and M.S. in electrical engineering from National Chiao-Tung University, Hsinchu, Taiwan, R.O.C., in 1972 and 1974, respectively, and the Ph.D. degree in electrical engineering from Lehigh University, Bethelem, PA, in 1982.

He was with ERSO/ITRI, Hsinchu, during 1976-1979. He was involved in the successful CMOS technology transfer from RCA to ERSO/ITRI during 1976-1977. He joined Sarnoff Research Center, Princeton, NJ, in 1981 and is a Senior Member of Technical Staff. His circuit design experiences include: SRAM, high speed 6–12 bits 20–200 MHz CMOS SSA and flash ADCs, PLL, DAC, CMOS, VGA PtSi IR imager, high density high frame rate BCCD FPA and TDI imagers, high density VLSI active matrix EL displays, CMOS APS imagers, and SiGe ADC. He has published over 40 technical papers and has seven issued patents. He published two textbooks for electrical engineers in Taiwan in 1973.



Robin M. Dawson (M'86) received the Ph.D. degree in electrical engineering from the Pennsylvania State University, University Park, in 1993.

He joined Sarnoff Corporation, Princeton, NJ, in 1993 where his initial assignments included design of active matrix displays in polysilicon, SOI, and a-Si:H, ESD protection circuits in silicon, and back illuminated CCD's. He is currently Group Head, Solid State Imaging, responsible for the development of UV and visible CCD imagers and cameras. He has published more than 30 papers and has received two patents.



Peter A. Levine (M'82) received the B.S.E.E and M.S.E.E. degrees from Cornell University, Ithaca, NY, in 1967 and 1968, respectively.

He has over 30 years of experience in CCD and CMOS imaging technology at RCA Laboratories (now Sarnoff Corporation), Princeton, NJ. He was a contributor to the development of RCA's CCD comb filter for television receivers, the first broadcast CCD camera, and a number of other successful consumer and government products. He is a Distinguished Member of Technical Staff within the Imaging Technology and Products business area at Sarnoff. He has authored or co-authored over 49 papers. He has 52 issued U.S. patents.



Grazyna M. Meray received the M.S.E.E degree from Warsaw University of Technology, Warsaw, Poland.

She joined RCA Laboratories, Princeton, NJ, in 1969. She continued her work at the David Sarnoff Research Center and now Sarnoff Corporation, Princeton, in the field of IC design and layout. She worked on layout, mask design and verification of a succession of CCD and CMOS imagers of various sizes for visible, ultraviolet, infrared and signal processing applications.



James T. Andrews (M'87) received the B.S.E.E. degree from Cornell University, Ithaca, NY, in 1976, and the M.S.E.E. degree from the University of Colorado, Boulder, in 1981.

He joined the Laser and Optoelectronics Laboratory, RCA Laboratories (now Sarnoff Corporation), Princeton, NJ, in 1981. For the past eight years, he has been with the Imaging Technology and Products Group, working on the design and layout of CCD imagers. Recently, his work on imaging devices has expanded to CMOS APS and MEMS devices.



Verne L. Frantz, Jr. attended Embry-Riddle Aeronautical University, Daytona Beach, FL, in 1971, where he majored in aeronautical engineering. He was trained in electronics in the U.S. Navy.

In 1983, he joined the David Sarnoff Research Center, RCA Corporation, Princeton, NJ, where he is currently the Photolithography Engineer in the Integrated Circuit Center within Sarnoff Corporation. He is the engineer responsible for advanced stepper projects, including the 1995 development of Sarnoff's current stitching capability used for several successful imager products.



Mark S. Grygon received the B.S. degree in electrical engineering in 1989 from Virginia Polytechnic Institute and State University, Blacksburg.

Since 2000, he has been an Associate Member of the Technical Staff at Sarnoff Corporation, Princeton, NJ. While at Sarnoff, he has been involved in the imager characterization, test, and design verification of multiple CCD programs ranging in application from spectroscopy to high performance digital cameras.



Michael A. Reale (M'82) received the B.S. degree in chemistry from Brooklyn College, City University of New York, in 1975, and the B.S. degree in electrical engineering from Pratt Institute, Brooklyn, in 1983.

He was a Member of the Technical Staff for the Department of Astrophysics, Princeton University, Princeton, NJ, from 1983 to 1999. At Princeton, he designed the camera electronics for a far UV high-resolution spectrometer that flew on two space shuttle missions. He joined Sarnoff Corporation, Princeton, in 2002. His most recent hardware design work includes a large area CCD camera for space surveillance (visible spectrum), and a high speed CCD camera for semiconductor inspection (ultraviolet spectrum).



Thomas M. Sudol received the B.S. degree in electrical engineering in 1989 and the B.S. degree in engineering physics in 1990, (both??) from Lehigh University, Bethlehem, PA. He then received the M.S. degree in electrical engineering in 1991 from the University of Pennsylvania, Philadelphia.

Since 1998, he has been a Member of Technical Staff at Sarnoff Corporation, Princeton, NJ, where he has been involved with solid-state imager characterization and test, and he has been performing electronic system design of high-performance digital imaging systems. He has authored three papers.

SIONYX1403000042.0078

SAMSUNG EX. 1002 - 613/4148

Femtosecond Laser Ablation of Silicon: Nanoparticles, Doping and Photovoltaics

A thesis presented

by

Brian Robert Tull

to

The School of Engineering and Applied Sciences

in partial fulfillment of the requirements

for the degree of

Doctor of Philosophy

in the subject of

Applied Physics

Harvard University

Cambridge, Massachusetts

June 2007

SIONYX1403000042.0079

SAMSUNG EX. 1002 - 614/4148

©2007 by Brian Robert Tull

All rights reserved.

SIONYX1403000042.0080

SAMSUNG EX. 1002 - 615/4148

Femtosecond Laser Ablation of Silicon: Nanoparticles, Doping and Photovoltaics

Eric Mazur Brian R. Tull

Abstract

In this thesis, we investigate the irradiation of silicon, in a background gas of near atmospheric pressure, with intense femtosecond laser pulses at energy densities exceeding the threshold for ablation (the macroscopic removal of material). We study the resulting structure and properties of the material ejected in the ablation plume as well as the laser irradiated surface itself.

The material collected from the ablation plume is a mixture of single crystal silicon nanoparticles and a highly porous network of amorphous silicon. The crystalline nanoparticles form by nucleation and growth; the amorphous material has smaller features and forms at a higher cooling rate than the crystalline particles. The size distribution of the crystalline particles suggests that particle formation after ablation is fundamentally different in a background gas than in vacuum. We also observe interesting structures of coagulated particles such as straight lines and bridges.

The laser irradiated surface exhibits enhanced visible and infrared absorption of light when laser ablation is performed in the presence of certain elements—either in the background gas or in a film on the silicon surface. To determine the origin of this enhanced absorption, we perform a comprehensive annealing study of silicon samples irradiated in the presence of three different elements (sulfur, selenium and tellurium). Our results support that the enhanced infrared absorption is caused by a high concentration of dopants dissolved in the lattice. Thermal annealing reduces the infrared absorptance of each doped sample at the same rate that dopants diffuse from within the polycrystalline grains in the laser irradiated surface layer to the grain boundaries.

SIONYX1403000042.0081

SAMSUNG EX. 1002 - 616/4148

Lastly, we measure the photovoltaic properties of the laser irradiated silicon as a function of several parameters: annealing temperature, laser fluence, background gas, surface morphology and chemical etching. We explore the concept of using thin silicon films as the irradiation substrate and successfully enhance the visible and infrared absorption of films ≤ 2 μm thick. Our results suggest that the incorporation of a femtosecond laser modified region into a thin film silicon device could greatly enhance its photovoltaic efficiency.

SIONYX1403000042.0082

SAMSUNG EX. 1002 - 617/4148

Table of Contents

Abstract *iii*

Table of Contents *v*

List of Figures *viii*

List of Tables *xi*

Acknowledgements *xii*

Citations to Published Work *xv*

1 Introduction **1**
- 1.1 Femtosecond laser irradiation of silicon . . . 2
  - 1.1.1 Absorption of the pulse . . . 2
  - 1.1.2 Melting and ablation: thermal regime . . . 6
  - 1.1.3 Melting and ablation: non-thermal regime . . . 6
  - 1.1.4 Resolidification of the surface . . . 7
  - 1.1.5 Comparison to this thesis . . . 8
- 1.2 Organization of the dissertation . . . 9

2 Background **11**
- 2.1 Previous work on femtosecond laser irradiation of silicon in a background gas 12
- 2.2 Experimental methods: femtosecond laser system . . . 20
  - 2.2.1 Creating the femtosecond laser pulses . . . 20
  - 2.2.2 Amplifying the femtosecond laser pulses . . . 22
  - 2.2.3 Controlling the injection and ejection of the seed pulse . . . 23
  - 2.2.4 The amplified femtosecond laser pulses . . . 25
  - 2.2.5 Aligning the amplifier cavity . . . 25
- 2.3 Experimental methods: irradiation process and vacuum chamber . . . 27

3 Formation of silicon nanoparticles by femtosecond laser ablation in a background gas **29**
- 3.1 Chapter abstract . . . 29

SIONYX1403000042.0083

SAMSUNG EX. 1002 - 618/4148

3.2 Introduction 30
3.3 Experimental setup 31
3.4 Results 32
3.5 Discussion 39
3.6 Conclusion 43

4 Mechanism of broadband infrared absorption in chalcogen-doped silicon 45
4.1 Chapter abstract 45
4.2 Introduction 46
4.3 Experimental setup 48
4.4 Results 50
4.5 Discussion 53
4.5.1 Diffusion theory 57
4.5.2 Comparison to diffusion theory 59
4.5.3 Diffusion theory using a lognormal distribution of grains 62
4.5.4 Diffusion theory with grain growth 64
4.6 Conclusion 70
4.7 Supplemental information 70
4.7.1 Using an evaporated film as the dopant source 70
4.7.2 Diffusion coefficients for sulfur, selenium and tellurium in silicon . . 74
4.7.3 Absorptance spectra of chalcogen-doped silicon after annealing . . . 75
4.7.4 Alternate graphs of optical data versus diffusion length 75
4.7.5 Absorptance spectra of samples irradiated in N_2 after annealing . . . 78

5 The photovoltaic potential of femtosecond laser irradiated silicon 79
5.1 Photovoltaic research 79
5.2 Laser irradiated silicon solar cells 82
5.2.1 Thin film silicon 85
5.2.2 Combining femtosecond laser irradiation and thin film silicon 86
5.3 The electrical characteristics of a solar cell 88
5.4 Photovoltaic experimental results and discussion 92
5.4.1 Measuring current-voltage (I-V) curves 92
5.4.2 The effect of annealing on the photovoltaic properties of sulfur-doped femtosecond laser irradiated silicon 94
5.4.3 The effect of HF acid etching on photovoltaic results 102
5.4.4 The effect of H_2 gas and resulting surface morphology on photovoltaic results 103
5.4.5 Creating a lower roughness laser-irradiated surface 109
5.4.6 Irradiating thin film silicon 115
5.5 Summary discussion 120

6 Summary and future directions 123

SIONYX1403000042.0084

SAMSUNG EX. 1002 - 619/4148

A Operation of a solar cell **126**
A.1 The photovoltaic cell in an electrical circuit 126
A.2 Satisfying the two conditions required for a photovoltaic response 130
A.3 Creating the internal electric field 132
A.4 The *I-V* characteristics of the *p-n* junction 137
A.5 The ideal material 145

References **147**

SIONYX1403000042.0085

SAMSUNG EX. 1002 - 620/4148

List of Figures

1.1 Direct and indirect electron transitions in the electronic band diagram of silicon 3
1.2 Absorption coefficient and absorption length of silicon as a function of wavelength 4

2.1 Images of femtosecond laser irradiated silicon during irradiation and after . 12
2.2 SEM images of femtosecond laser irradiated silicon 13
2.3 Absorptance spectra of silicon irradiated in different environments 14
2.4 Cross-sectional TEM analysis of femtosecond laser irradiated silicon 14
2.5 The effect of annealing on femtosecond laser irradiated silicon 16
2.6 The effect of annealing on the electrical properties of femtosecond laser irradiated silicon 17
2.7 Light detection and photovoltaic response of femtosecond laser irradiated silicon 18
2.8 Apsorptance spectra of chalcogen-doped femtosecond laser irradiated silicon using a powder source 19
2.9 Layout of amplifier cavity 23
2.10 Schematic diagram of the irradiation process and vacuum chamber 27

3.1 Experimental setup for collecting silicon nanoparticles. 32
3.2 TEM bright field image of particles formed in the ablation plume. 33
3.3 Selected area diffraction of particles formed in the ablation plume. 34
3.4 Analysis of diffraction pattern indicates diamond cubic. 35
3.5 Diffraction of single nanoparticles shows they are single crystals 36
3.6 TEM bright field and dark field imaging of particles formed in the ablation plume. 36
3.7 TEM image showing that particles aggregate in straight lines. 38
3.8 TEM image showing that particles form bridges. 39
3.9 Size distribution of crystalline nanoparticles formed in the ablation plume. . 40

4.1 Absorptance spectra of chalcogen-doped silicon before and after annealing . 51
4.2 Average absorptance from 1250–2500 nm of chalcogen-doped silicon versus annealing temperature at $T \leq 975$ K 51

SIONYX1403000042.0086

SAMSUNG EX. 1002 - 621/4148

4.3 Average absorptance from 1250–2500 nm of chalcogen-doped silicon versus annealing temperature at $T \geq 875$ K 52
4.4 Normalized absorptance of chalcogen-doped silicon versus diffusion length of the respective dopant 56
4.5 Fraction of dopant atoms remaining inside a sphere of radius, R_0, versus diffusion length. 60
4.6 The effect of a lognormal distribution of grains sizes on the fraction of dopant atoms remaining inside grains. 63
4.7 The effect of adding an offset to the lognormal distribution of grains sizes. . 64
4.8 Fraction of dopant atoms remaining inside a sphere of radius, R_0, versus diffusion length using an imaginary grain boundary. 67
4.9 Comparison of normalized infrared absorptance for selenium-doped silicon to the theory modified for grain growth 69
4.10 Evolution of surface morphology when using a film as the dopant source . . 72
4.11 The effect of film thickness and laser fluence on optical properties 73
4.12 Absorptance spectra of chalcogen-doped silicon after annealing 76
4.13 Transmittance and reflectance versus difussion length 77
4.14 Normalized transmittance and reflectance versus difussion length 78
4.15 Absorptance spectra of samples irradiated in N_2 gas after annealing 78

5.1 Solar spectrum of the sun at the earth above the atmosphere 83
5.2 Schematic cross-section of a femtosecond laser irradiated thin film silicon solar cell 87
5.3 Illuminated and dark current-voltage curve of a commercial polycrystalline silicon solar cell 89
5.4 Solar simulator and probe station setup 93
5.5 Illuminated and dark current-voltage curves of sulfur-doped femtosecond laser irradiated silicon 95
5.6 Illuminated and dark current-voltage curves of sulfur-doped femtosecond laser irradiated silicon annealed between 575–1075 K 96
5.7 Illuminated and dark current-voltage curves of sulfur-doped femtosecond laser irradiated silicon annealed between 1075–1208 K 97
5.8 I_{sc}, V_{oc}, FF and η versus temperature for sulfur-doped samples 99
5.9 Schematic cross-section of the junction between femtosecond laser irradiated silicon and the underlying substrate 100
5.10 Illuminated and dark current-voltage curves of samples irradiated in a mixture of H_2 and SF_6 at a fluence of 5 kJ/m^2 104
5.11 Photocurrent versus voltage curves of samples irradiated in a mixture of H_2 and SF_6 at a fluence of 5 kJ/m^2 104
5.12 Illuminated and dark current-voltage curves of samples irradiated in a mixture of H_2 and SF_6 at a fluence of 4 kJ/m^2 105
5.13 Photocurrent versus voltage curves of samples irradiated in a mixture of H_2 and SF_6 at a fluence of 4 kJ/m^2 106
5.14 Surface morphology at 4 kJ/m^2 versus 5 kJ/m^2 107

SIONYX1403000042.0087

SAMSUNG EX. 1002 - 622/4148

5.15 Images of the contact area between our probe and the top electrode at 4 kJ/m^2 versus 5 kJ/m^2 108
5.16 Surface morphology of samples irradiated in a mixture of H_2 and SF_6 . . . 108
5.17 Surface morphology of samples irradiated with varied pulses/area at 4 kJ/m^2 110
5.18 Surface morphology of samples irradiated with varied fluence at 7 pulses/area 111
5.19 Absortance spectra of samples irradiated with varied fluence at a fixed pulses/area and varied pulses/area at fixed fluence 112
5.20 Absortance spectra of Se- and Te-coated samples irradiated with varied fluence 113
5.21 SEM images of Se- and Te-coated samples irradiated with varied fluence . . 114
5.22 Absorptance spectra of femtosecond laser irradiated silicon films grown by electron beam heating evaporation 116
5.23 Absorptance spectra of femtosecond laser irradiated silicon films grown by hot-wire chemical vapor deposition 119

A.1 A photovoltaic cell in an electrical circuit 127
A.2 Relationship between current and voltage in a photovoltaic cell 129
A.3 Solar spectrum 131
A.4 Schematic representation of the depletion region 135
A.5 Changes in the *p*-*n* junction with applied voltage 140
A.6 Current-voltage relationship in an ideal *p*-*n* junction 142
A.7 *I*-*V* curve of an illuminated solar cell 144
A.8 Maximum theoretical efficiency as a function of band gap energy 146

SIONYX1403000042.0088

SAMSUNG EX. 1002 - 623/4148

List of Tables

2.1 Summary of previous relevant RBS data on femtosecond laser irradiated silicon 15

4.1 Diffusivity constants for sulfur, selenium, and tellurium in silicon 57
4.2 Diffusion coefficients for sulfur, selenium, and tellurium in silicon 75

5.1 Photovoltaic properties of sulfur-doped femtosecond laser irradiated silicon annealed between 575–1075 K 98
5.2 Photovoltaic properties as a function of HF etching time 103
5.3 Summary of laser conditions used to create a laser modified surface layer on the CVD grown silicon film 118

SIONYX1403000042.0089

SAMSUNG EX. 1002 - 624/4148

Acknowledgements

"I don't know half of you half as well as I should like; and I like less than half of you half as well as you deserve."

Bilbo Baggins

Wait, what happened. Oh yeah, that's right, it's over. I defended my thesis two weeks ago; I will be leaving Boston four weeks from now. And that's it. A six year chapter of my thirty year life comes to an end. Oh, I'm not sad. How can I be sad? I could not ask for the past six years to have turned out better. I was able to live in an awesome city, get a great education and meet people who have become some of my best friends. Well ... maybe I'm a little sad.

This thesis, along with all that I have accomplished in graduate school and prior to, is the result of hundreds of people's patience, generosity, kindness, hard work and friendship. First, I would like to thank my family. My parents, Stephen and Margaret, always provided me with the opportunity to do anything I wanted (or in the early years, urged me to do anything I wanted). They taught me how to work hard through their own example and the importance of respecting myself, my family and others. My brother, Cliff, and sister, Sarah, are two of the most down-to-earth and intuitive people I know. I love spending time with them and look forward to seeing them more often when I move from Boston.

The Mazur group is the single greatest invention of our time: a fun, wildly engaging

SIONYX1403000042.0090

SAMSUNG EX. 1002 - 625/4148

and intellectual group of people performing advanced science while generally having a good time, all orchestrated by the international man of mystery himself, Eric Mazur. I truly want to thank Eric for giving me the opportunity to be in his group and the freedom to pursue the research of my choosing.

I would also like to thank the other faculty members who helped me a great deal with this thesis and my work at Harvard in general and each of whom gave me the opportunity to be a teaching assistant for them: Cyndy Friend, Mike Aziz, and Frans Spaepen.

I want to thank all of the Mazur group members I have served with both past: Jon, Chris, Jim, Michael, Maria, Iva and Loren and present: Rafael, Geoff, Sam, Mark, Eric, Tina, Jessica, Prakriti and Mustafa. I would like to particularly acknowledge Jim, Michael, Mark and Eric for assisting with the experiments presented here. In the Mazur group, we get to work with a wide array of excellent post docs and visiting scientists. I had the pleasure of working with Alex, Tommaso, Veronica, Cleber, Tobias, Meng-yan and Catherine.

Additionally, I would like to thank Squeaker; Brazilla; Gizmo; Eric "Patron"; Jim Bud Light; Mike the inventor of Tic Tac; Mr. Awesome; Sam's commissary; Tina Las Vegas; and Dr. Evil, who taught me the meaning of persistence. You guys do (and in some cases do not) know who you are.

And finally, but most of all, I would like to thank my wife, Ruby, for her constant love and friendship, for giving me the energy to do all that I do, and for making me a better, more well rounded person than I ever was before I met her.

SIONYX1403000042.0091

SAMSUNG EX. 1002 - 626/4148

They say that the definition of insanity is performing the same act repeatedly and expecting a different result. While one could argue that this definition may apply to grad school as a whole, it is most certainly a fitting description of attempting to mode lock a femtosecond laser.

In the immortal words of Douglas Adams, "So long and thanks for all the fish."

Brian R. Tull
Cambridge, Massachusetts
May, 2007

Acknowledgements of Financial Support

This thesis is based on work supported by the Department of Energy under contract DOE DE-FC36-01G011051, the Army Research Office under contract ARO W911NF-05-1-0341, and the Center for Nanoscale Science at Harvard University.

SIONYX1403000042.0092

SAMSUNG EX. 1002 - 627/4148

Citations to Published Work

Parts of this dissertation cover research reported in the following articles:

[1] B. R. Tull, J. E. Carey, M. A. Sheehy, C. Friend, and E. Mazur, "Formation of silicon nanoparticles and web-like aggregates by femtosecond laser ablation in a background gas," *Applied Physics A-Materials Science and Processing*, vol. 83, no. 3, pp. 341–346, 2006.

[2] B. R. Tull, M. T. Winkler, and E. Mazur, "Mechanism of broadband infrared absorption in chalcogen-doped silicon," *submitted for publication in Physical Review B.*

[3] M. A. Sheehy, B. R. Tull, C. M. Friend, and E. Mazur, "Chalcogen doping of silicon via femtosecond laser irradiation," *Materials Science and Engineering B-Solid State Materials for Advanced Technology*, vol. 137, pp. 289–294, 2006.

[4] B. R. Tull, J. E. Carey, E. Mazur, J. McDonald, and S. M. Yalisove, "Surface morphologies of silicon surfaces after femtosecond laser irradiation," *Materials Research Society Bulletin*, vol. 31, pp. 626–633, 2006.

SIONYX1403000042.0093

SAMSUNG EX. 1002 - 628/4148

To my wife, RUBY, *for your love*

and friendship

SIONYX1403000042.0094

SAMSUNG EX. 1002 - 629/4148

We are an intelligent species and the use of our intelligence quite properly gives us pleasure. In this respect the brain is like a muscle. When we think well, we feel good. Understanding is a kind of ecstasy.

Carl Sagan – Broca's Brain

SAMSUNG EX. 1002 - 630/4148

Chapter 1

Introduction

Over the past several decades ultrashort pulsed laser irradiation of silicon surfaces has been an active area of materials science research [1–21]. The ultrashort duration of the laser pulses leads to extremely high energy densities in the material. A 100 femtosecond (1 fs = 10^{-15} s) laser pulse with a pulse energy of 100 μJ, focused to a 100-μm diameter area results in a peak energy density on the order of 10^4 J/m^2 and a peak intensity of 10^{17} W/m^2. Under these conditions, silicon is estimated to reach temperatures of $\sim 10^4$–10^5 K [22], equivalent to the surface temperature of the nearest star, while still retaining the density of a solid. This high energy density is achieved because the laser energy is deposited before any thermal diffusion or mechanical removal of material occurs. The evolution of this superheated and superpressurized material as the initial energy redistributes can lead to non-equilibrium processes as well as the formation of new materials [1–3, 6–8].

Numerous studies exploring the interaction of ultrashort pulses with silicon have been performed since the 1980's [1–21]. Picosecond laser pulses were used to induce phase transformations in silicon [1–7] resulting in the formation of non-equilibrium phases, including amorphous silicon [1–3, 6, 7] and Nb-Si solid solutions [8]. Pump-probe experiments

SIONYX1403000042.0096

SAMSUNG EX. 1002 - 631/4148

using picosecond [9–15] and femtosecond [16–21] laser pulses have explored the time evolution of the material processes that occur during ultrashort laser irradiation. An initial pump pulse excites the material and a delayed, weaker probe pulse measures the time-resolved reflectivity or second harmonic generation [17, 18] to identify the structural state of the material. Using this technique, many processes, including, electron-hole plasma formation [9, 10, 13, 14], melting [5, 9, 10, 12], ablation [19–21], and ultrafast melting [16–18], were studied in detail. These examples are a small subset of a much larger field of research. Section 1.1 discusses specific research from the literature that are relevant to the work performed in this thesis. Section 1.2 summarizes the organization of this dissertation.

1.1 Femtosecond laser irradiation of silicon

In this section, we review the processes involved in the absorption of the femtosecond laser pulse, and the subsequent heating, melting and ablation of the material.

1.1.1 Absorption of the pulse

When a femtosecond laser pulse is incident on the silicon surface the electrons are the first to respond. Absorption of visible and near infrared wavelengths occurs through the promotion of electrons from the valence band (where the electrons reside in spatially localized "bonding" states) to the conduction band (where they are mobile and more "free" like in a metal). A minimum amount of energy is required to excite the electron from the valence to the conduction band; this energy is known as the band gap energy. In the case of silicon, if this energy were to come solely from the incident light and no other source, 3.43 eV would be required; as a consequence, only wavelengths of light $\leq$ 362 nm would be absorbed in this way. Excitation of an electron in this manner is known as a direct band transition. At a nonzero temperature, silicon has a distribution of phonons which

SIONYX1403000042.0097

SAMSUNG EX. 1002 - 632/4148

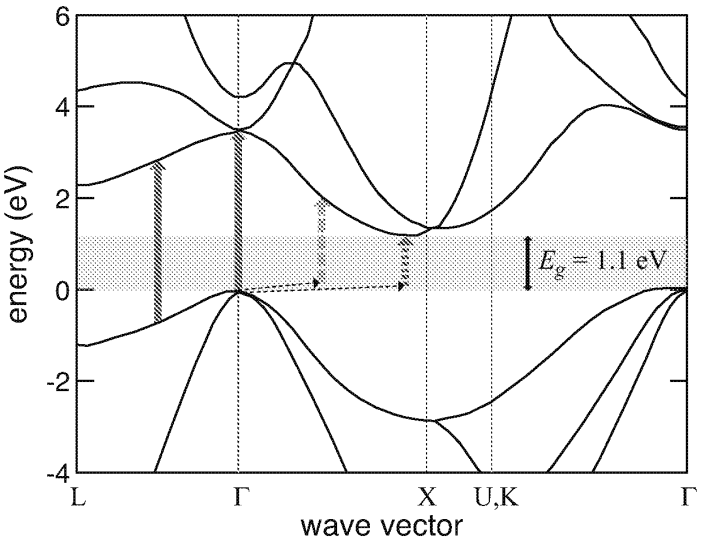


Figure 1.1: Direct (solid arrows) and indirect (dashed arrows) electron transitions across the band gap of silicon during absorption of a photon. For the indirect transitions shown, phonons of similar energy but two different momenta are needed. Band diagram obtained from [23].

can participate in the absorption of photons. For a photon absorption process in silicon that is mediated by a phonon, the minimum energy required is 1.1 eV, which extends the absorption spectrum of light to wavelengths as large as 1.1 μm. This process is known as an indirect band transition. Figure 1.1 shows direct and indirect band gap transitions of electrons with respect to the electronic band diagram of silicon.

The indirect band transition of an electron requires the simultaneous annihilation of a photon and a phonon and therefore has a far lower probability of occurring than the direct band transition. As the energy of the absorbed photon approaches the minimum energy needed for absorption in silicon (1.1 eV) a phonon with a larger and larger momentum is needed. As a result, the closer the photon energy is to 1.1 eV, the lower the probability of absorption. A measure of the probability of absorption is the absorption depth, which

SIONYX1403000042.0098

SAMSUNG EX. 1002 - 633/4148

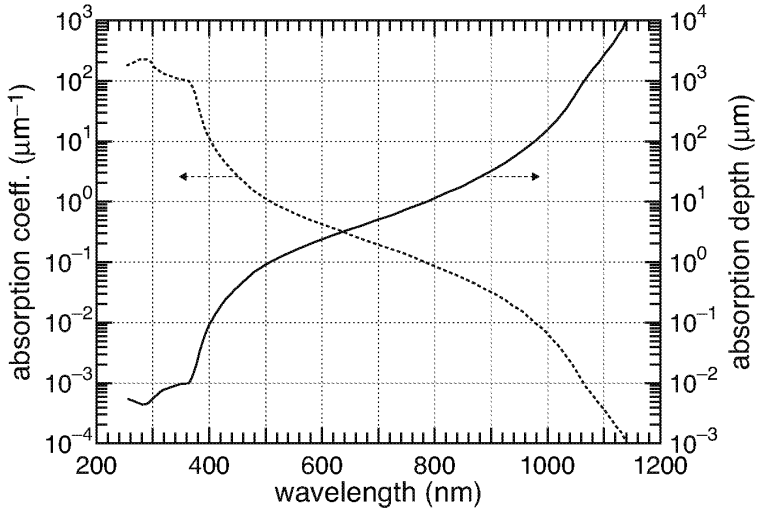


Figure 1.2: Absorption coefficient and absorption length of intrinsic silicon at 300 K as a function of wavelength of the absorbed photon. Data obtained from [24].

is the depth in the material where the intensity of the light has been reduced to $1/e$ of its original value. Due to the low probability of indirect band transitions in silicon, the absorption depth of 800 nm light is 13 μm while the absorption depth of 300 nm light is 6 nm. In Figure 1.2, absorption depth is plotted as a function of the wavelength of the incident light for intrinsic silicon at 300 K.

The above description of light absorption is valid in most cases. However, for ultrashort laser pulses, absorption is observed to occur at much shallower depths than is indicated by Figure 1.2. In a study using 532-nm, 25-ps laser pulses, absorption was determined to occur in a depth much less than 1 μm [5]. In pump-probe studies using femtosecond laser pulses (620-nm, 90-fs), surface melting was observed for energy densities that were too small if standard linear absorption depths were assumed [16, 17]. In another study using 620-nm, 100-fs laser pulses, researchers observe the reflectivity of the incident pulse increases to metallic (liquid) values within the duration of the pulse. They propose a

SIONYX1403000042.0099

SAMSUNG EX. 1002 - 634/4148

model where the initial edge of the laser pulse is absorbed deep into the material, but the rest of the pulse is absorbed at depths on the order of $\sim$ 10 nm when sufficient electrons are promoted to the conduction band to allow for free-carrier absorption [25]. This level of electron excitation is described as an electron-hole plasma [26–28].

Various absorption mechanisms have been proposed to account for the creation of an electron-hole plasma at shallow depths in the material. For 620-nm, 100-fs laser pulses, researchers found that two-photon absorption (the simultaneous absorption of two photons to promote an electron in a direct band transition) is the dominant mechanism [29], while for 800-nm, 100-fs laser pulses, absorption is found to be governed by avalanche ionization [30]. Avalanche ionization is a process where a conduction band electron directly absorbs additional photons, and then collides with a valence electron resulting in two electrons at the bottom of the conduction band which begin the process again [30]. Two-photon absorption and avalanche ionization are non-linear absorption mechanisms that become relevant at large intensities of light. For non-linear absorption, absorption no longer increases linearly with intensity of the light but rather intensity raised to a power. Regardless of the specific nonlinear process controlling absorption, an electron-hole plasma forms early in the absorption of the pulse [26–28] and absorbs the rest of the laser light in an absorption depth of $\sim$ 100 nm [22] (like a metal).

So far, the processes discussed above all take place within one pulse duration ($\sim$ 100 fs) after irradiation. At this point, we have a highly energetic electron-hole plasma and a relatively cold lattice of ions. Subsequent processes are highly dependent on intensity, or for a constant pulse duration of 100 fs, the processes are highly dependent on fluence. We can separate the subsequent processes as the energy redistributes and dissipates into two regimes: thermal and non-thermal.

SIONYX1403000042.0100

SAMSUNG EX. 1002 - 635/4148

1.1.2 Melting and ablation: thermal regime

In the thermal regime, melting (loss of long range order) and ablation (macroscopic material removal) occur after the excited electrons redistribute energy to the lattice and the entire material reaches a common temperature. The excited electrons redistribute their energy to the lattice through electron-phonon interactions. The time scale for the material to reach a common temperature is determined by the electron-phonon coupling constant (in silicon this is 1 ps [21]). Depending on the laser fluence, the resulting temperature of the material may exceed the melting point and melting will begin at the surface and move inward. At a higher fluence, the boiling point is exceeded and the gas phase will nucleate homogeneously in the superheated liquid. If the rate of gas bubble formation is high in comparison to the cooling rate of the liquid, material will be explosively ejected from the surface resulting in ablation.

In the thermal regime, ablation occurs on the order of 1 ns [19, 21]. The fluence thresholds for thermal melting and thermal ablation of silicon in a vacuum for 620-nm, 120-fs laser light have been determined as 1.5 kJ/m^2 and 3 kJ/m^2, respectively [19, 21]. The fluence regime for thermal melting and ablation ranges from the point of their onset (1.5 kJ/m^2 and 3 kJ/m^2) to less than the threshold for ionic plasma formation (10 kJ/m^2), where electrons are ionized from the lattice and material removal is governed by coulomb repulsion [21].

1.1.3 Melting and ablation: non-thermal regime

At higher fluences than those required for thermal melting, non-thermal melting of the lattice was observed by pump-probe studies [16, 17, 25]. Non-thermal melting is a term used to describe the loss of long range order in the lattice well before 1 ps (typically a few 100 fs) and, therefore, before the material has come to a common temperature. Theoretical

SIONYX1403000042.0101

SAMSUNG EX. 1002 - 636/4148

studies support that melting can occur in this manner. Disordering of the lattice is predicted to occur after 100 fs due to covalent bond weakening upon excitation of more than 15% of the valence electrons [31–34]. The lattice disorders within the period of one atomic vibration [34].

At extremely large fluences (40–120 kJ/m^2), particle formation after femtosecond laser ablation of silicon (800-nm, 200-fs) in vaccum has also been reported to occur in a manner that is not consistent with thermal processes [35, 36]. Solid particles were found to form within the ablation plume after only 50 ps [36], much faster than the typical time required for thermal ablation ($\sim$ 1 ns, [21]). In addition, the size of the particles was determined to be set by a mechanical fragmentation process and not through condensation from the vapor phase [36].

1.1.4 Resolidification of the surface

After melting and ablation, the thin molten layer cools quickly through thermal conduction into the cold bulk. Cooling rates are predicted to be as high as 10^{13}–10^{15} K/s [22]. The molten layer resolidifies on the order of nanoseconds [12]. As a result of the high cooling rate of ultrashort pulsed laser irradiation, the formation of amorphous silicon has been observed [1–3, 6, 7].

In addition to new phases, unusual surface morphologies can develop during resolidification. Picosecond laser irradiation of silicon near the melting threshold revealed that ripples formed on the surface with a wavelength related to the wavelength of the laser [4,37]. These features have been named Laser Induced Periodic Surface Structures (LIPSS) [38–41] and have been observed on a variety of materials after irradiation with one or more pulses from a wide range of laser systems (including femtosecond, picosecond and nanosecond pulses) [38]. When the laser pulse is energetic enough to fully melt the surface, the latter-

SIONYX1403000042.0102

SAMSUNG EX. 1002 - 637/4148

half of the incident pulse interferes with light scattered from defects at the surface, setting up a spatially non-uniform melt depth. The non-uniform melt depth induces standing capillary waves which can freeze in place if their lifetime is long compared to the resolidification time [41]. The phenomenon of LIPSS is the initiating process of spike formation on silicon after femtosecond laser irradiation [42].

After the molten silicon resolidifies, cooling continues as heat diffuses out of the irradiated region into the surrounding material and the silicon returns to room temperature.

1.1.5 Comparison to this thesis

The experiments in this thesis are performed with 800-nm, 100-fs laser pulses, focused onto a silicon surface at fluences ranging from 2–10 kJ/m^2. The two main experiments discussed in this thesis involve particle formation and elemental doping during solidification of molten silicon after irradiation of macroscopically large areas of the silicon on the order of 10 mm $\times$ 10 mm.

In contrast to a majority of the research discussed before, which deals with single shot experiments, we irradiate the silicon with greater than 100 pulses per area. After a few pulses, the surface is no longer flat due to the development of laser induced periodic surface structures. The surface structures continue to evolve into micrometer-size conical structures through material removal with each laser pulse.[1]

Due to the non-flat surface, the fluence is effectively increased in the valleys between the micrometer-sized cones due to reflection from the sides of the cones. Consequently, we see evidence for ionic plasma formation at any fluence greater than the ablation threshold (3 kJ/m^2, [21]) even though the threshold for ionic plasma formation is considerably

[1]The final surface morphology is a function of laser fluence and the chemistry and pressure of any background gas that is present. The physical mechanism behind its formation has been well documented elsewhere [42, 43] and will not be discussed in this thesis.

SIONYX1403000042.0103

SAMSUNG EX. 1002 - 638/4148

higher ($\sim$ 10 kJ/m^2). As a result, the physics of melting and ablation in our experiments may be dertermined by fluences greater than 10 kJ/m^2.

It is difficult to draw exact comparisons between the processes of melting and ablation discussed in the previous sections and those processes which govern melting and ablation in our experiments. All of the experiments in this thesis are performed in a background gas of near atmospheric pressure (500 Torr). The fundamental work determining the physics of melting and ablation after femtosecond laser ablation has been performed in vacuum. The extent to which the physics changes in a background gas of varying reactivity has yet to be determined.[2] A main result of Chapter 3 is that the mechanism of ablation in vacuum and a background gas at similar fluences is fundamentally different.

In this thesis, we hope to give the reader an impression of the exciting materials science processes (*e.g.* the formation of non-equilibrium phases and compositions) that are possible with femtosecond laser irradiation in a background gas.

1.2 Organization of the dissertation

Chapter 2 reviews the previous work on femtosecond laser irradiation of silicon in a background gas and describes the femtosecond laser system and the main experimental methods used in the thesis.

Chapter 3 presents the results of nanoparticle formation after femtosecond laser ablation of silicon in a background gas of H_2 and H_2S. Transmission electron microscopy shows the that both crystalline and amorphous material form in the ablation plume. The results indicate that the background gas affects the fundamental mechanism of particle formation.

[2]In addition, with each laser pulse the surface is changed structurally and chemically, and melting and ablation of this new material may be very different than pure single crystal silicon

SIONYX1403000042.0104

SAMSUNG EX. 1002 - 639/4148

Chapter 4 deals with the mechanism behind the near-unity absorptance of infrared wavelengths of chalcogen-doped femtosecond laser irradiated silicon. We show that the infrared absorptance decreases with thermal annealing at the same rate that the dopants diffuse from within the crystalline grains to the grain boundaries for all three chalcogen dopants.

Chapter 5 discusses using femtosecond laser irradiated silicon as a solar cell. We present results on the photovoltaic properties of sulfur-doped silicon wafers. In addition, we explore using Chemical Vapor Deposition (CVD) grown thin films of silicon as the femtosecond laser irradiated substrates.

Chapter 6 summarizes the main results obtained in this thesis and proposes future avenues of research to address several still unanswered questions regarding femtosecond laser irradiated silicon.

Appendix A offers a basic tutorial on the operation of a solar cell.

SIONYX1403000042.0105

SAMSUNG EX. 1002 - 640/4148

Chapter 2

Background

Nearly a decade ago, the Mazur group published the first report of femtosecond laser irradiation of silicon in a background gas of sulfur hexaflouride, SF_6, at near atmospheric pressure (500 Torr) [44]. Researchers found that the gray mirror finish of the silicon wafer changed to a deep matte black color wherever the laser irradiated the surface (see Figure 2.1). As a result, this material is referred to as "black silicon." Since then, the surface morphology [42, 43, 45], structure [46, 47], composition [46, 48–50], optical properties [46, 49–51] and optoelectronic applications [52] of the laser modified surface have been extensively investigated. In Section 2.1, we summarize the major findings from the previous work and review those unanswered questions that this thesis aims to address. In Section 2.2, we discuss the experimental methods used in this thesis and most of the previous work as well.

SIONYX1403000042.0106

SAMSUNG EX. 1002 - 641/4148

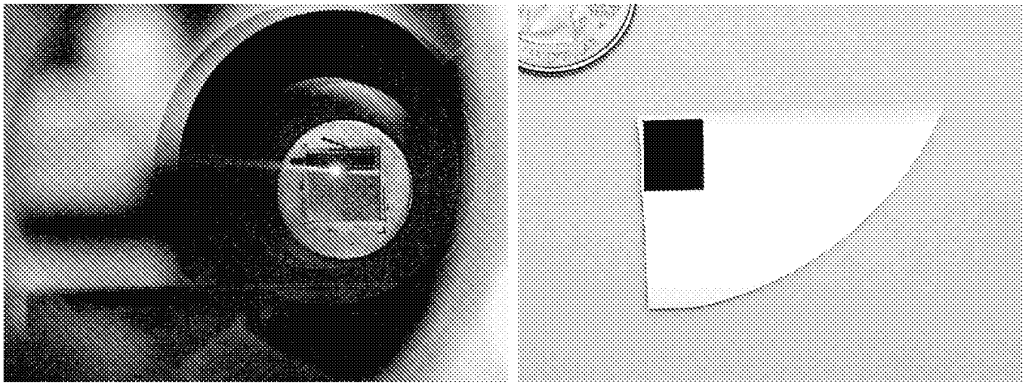


Figure 2.1: *Left:* Femtosecond laser irradiation of silicon inside a vacuum chamber filled with SF_6. *Right:* Visual appearance of the silicon after irradiation.

2.1 Previous work on femtosecond laser irradiation of silicon in a background gas

Closer inspection of the irradiated surface using a scanning electron microscope reveals that the flat silicon surface has been transformed into a forest of micrometer-sized spikes (see Figure 2.2). This surface morphology evolves after irradiation of the silicon with several hundred laser pulses focused to a typical fluence of 8 kJ/m^2, well above the ablation threshold of silicon (3 kJ/m^2). The size and shape of the surface features is a function of the laser fluence, wavelength and pulse duration as well as the background gas chemistry and pressure. The initial surface morphology after a few pulses is a result of non-uniform absorption of the laser light due to interference of the incident beam with a surface diffracted beam. The non-uniform absorption sets up a dynamic molten silicon layer of varying depth that ripples with capillary waves. The interaction of this non-uniform molten silicon layer with the background gas and then with subsequent pulses after it freezes determines the final surface morphology. A detailed description of this formation mechanism is addressed elsewhere [42, 43].

SIONYX1403000042.0107

SAMSUNG EX. 1002 - 642/4148

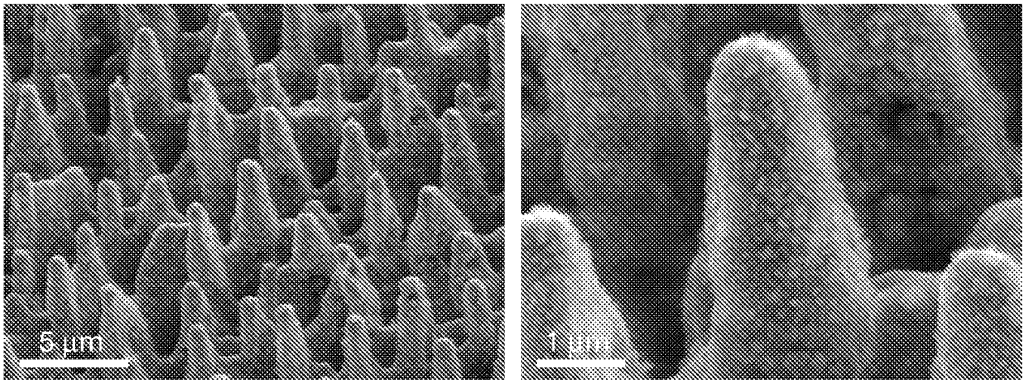


Figure 2.2: Scanning electron microscope images of the silicon surface after irradiation with 100 fs laser pulses focused to a fluence of 8 kJ/m^2 in a background gas of SF_6. Each area of the surface was irradiated by approximately 500 pulses. Images taken from reference [46].

Researchers in the Mazur group soon discovered that black silicon had unique optical properties. When the process is performed in a background gas of SF_6 [51] or H_2S [49], the surface absorbs nearly all incident light from 0.25–2.5 μm, which is the wavelength range of our spectrophotometer (see Figure 2.3. In contrast, irradiation was performed in a variety of other environments including H_2 [49], N_2, Cl_2, air [48] and vacuum [43] and broadband near-unity absorptance is not observed. What is most evident from Figure 2.3, is that sulfur appears to be a key ingredient in producing a surface that has near-unity infrared absorptance.

Enhanced absorptance at wavelengths less than 1 μm is exhibited by all samples in Figure 2.3. This increased absorptance is attributed to the natural linear absorption of silicon enhanced by multiple reflections due to the roughened surface.

The samples irradiated in N_2, H_2, Cl_2, and air exhibit a similar absorptance to samples irradiated in vacuum. Between 1.2–2.5 μm, the absorptance curve for these samples starts at near unity and then decreases with increasing wavelength. As all the samples resemble vacuum this absorptance spectrum is attributed to structural disorder in the laser

SIONYX1403000042.0108

SAMSUNG EX. 1002 - 643/4148

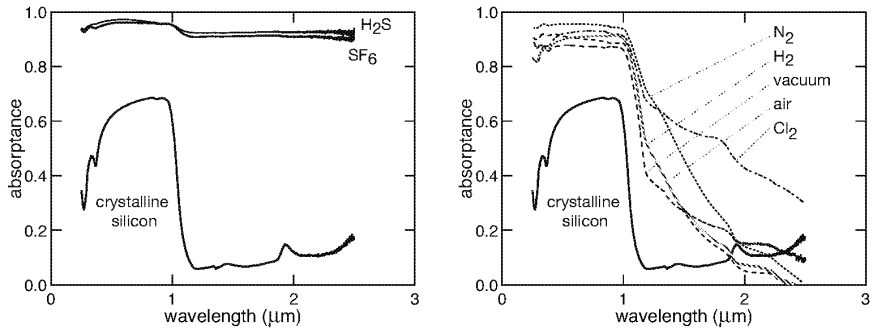


Figure 2.3: Absorptance spectra of silicon irradiated in different environments: SF_6 and H_2S (*left*) and N_2, H_2, Cl_2, air and vacuum (*right*).

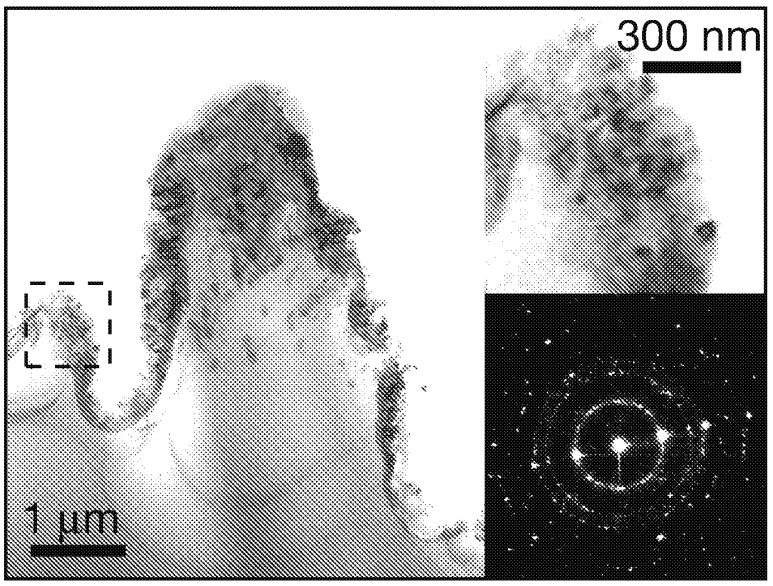


Figure 2.4: Cross-sectional transmission electron microscopy analysis of silicon irradiated with 100 fs laser pulses focused to a fluence of 8 kJ/m^2 in a background gas of SF_6. *Left and upper right:* bright field images showing the laser modified surface layer. *Lower right:* Selected area diffraction analysis of the laser modified surface layer. Images obtained from reference [46].

modified surface brought about by the trapping of defects during resolidification.

In order to understand the role sulfur plays in the infrared absorptance, the

SIONYX1403000043.0001

SAMSUNG EX. 1002 - 644/4148

structure and composition of the laser modified surface layer was investigated using cross-sectional transmission electron microscopy (TEM) and Rutherford backscattering spectrometry (RBS) respectively [46, 49, 50]. Figure 2.4 shows bright field TEM images and selected area diffraction of the laser modified surface layer. The diffraction pattern indicates that the single crystal substrate has a polycrystalline surface layer. Close inspection of the bright field images shows that the grains are extremely small, well less than 100 nm. The changes in contrast in the bright field image indicate changes in orientation of each grain of the polycrystalline material. Based on these observations the grain size of the polycrystalline material ranges from 10–50 nm [46].

Dopant source	Fluence	Pulses/area	Anneal T	Conc. of S, Se, or Te (at. %)
SF_6 gas [46]	8 kJ/m^2	500	–	0.7 ± 0.1
SF_6 gas [46]	8 kJ/m^2	500	725 K	0.5 ± 0.1
SF_6 gas [46]	8 kJ/m^2	500	875 K	0.5 ± 0.1
SF_6 gas [49]	10 kJ/m^2	600	–	1.0 ± 0.2
H_2S gas [49]	10 kJ/m^2	600	–	1.0 ± 0.2
H_2S gas [49]	10 kJ/m^2	600	900 K	1.0 ± 0.2
Ar + 1% SF_6 gas [49]	10 kJ/m^2	600	–	0.6 ± 0.2
sulfur powder [50]	10 kJ/m^2	600	–	1.0 ± 0.2
sulfur powder [50]	10 kJ/m^2	600	775 K	1.0 ± 0.2
selenium powder [50]	10 kJ/m^2	600	–	0.7 ± 0.2
selenium powder [50]	10 kJ/m^2	600	775 K	0.7 ± 0.2
tellurium powder [50]	10 kJ/m^2	600	–	1.5 ± 0.2
tellurium powder [50]	10 kJ/m^2	600	775 K	1.3 ± 0.2

Table 2.1: Summary of three previous RBS studies on femtosecond laser irradiated silicon.

Analysis of the surface with Rutherford backscattering spectrometry shows that the surfaces irradiated in SF_6 contain a large concentration of sulfur. Selected results are summarized in Table 2.1. These concentrations exceed the solid solubility by several orders

SIONYX1403000043.0002

SAMSUNG EX. 1002 - 645/4148

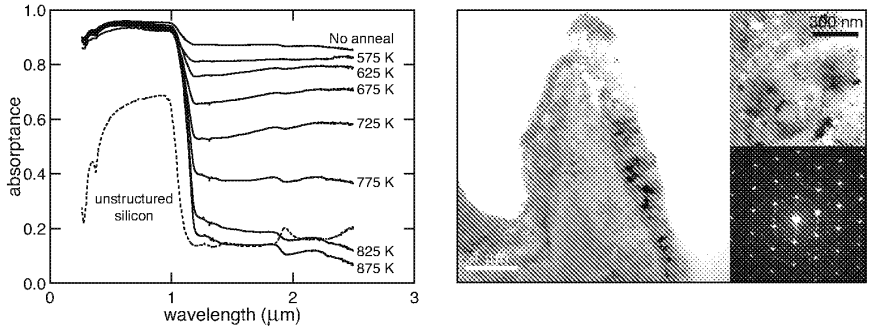


Figure 2.5: *Left:* Absorptance spectra of silicon irradiated in SF_6 after annealing at different temperatures for 30 minutes. *Right:* Selected area diffraction analysis of the laser modified surface layer after annealing at 875 K for 30 minutes. Spectra and images obtained from reference [46].

of magnitude. In one study, the percentage of sulfur atoms that are substitutional was estimated at 20–70% [46]. Based on these results researchers in the Mazur group proposed that the high concentration of sulfur atoms in the polycrystalline surface layer created a densely populated donor impurity band in the band gap of silicon. Promotion of electrons from this impurity band into the conduction band allows for the increased absorption of infrared light.

Along with exploring the structure and composition of the surface layer, researchers discovered that the absorption of infrared light decreases after thermal annealing [46]. Figure 2.5 shows how the infrared absorptance decreases with increasing annealing temperature. To explain this decrease, researchers investigated changes to the laser-modified polycrystalline surface layer with cross-sectional TEM and RBS analyses. Table 2.1 shows that annealing has only a small effect on sulfur concentration, and in some instances has no effect. Based on cross-sectional TEM analysis performed on annealed samples (Figure 2.5), there does not seem to be any structural change to explain the decrease in absorption of infrared light. The surface layer is still polycrystalline with an extremely small grain size.

SIONYX1403000043.0003

SAMSUNG EX. 1002 - 646/4148

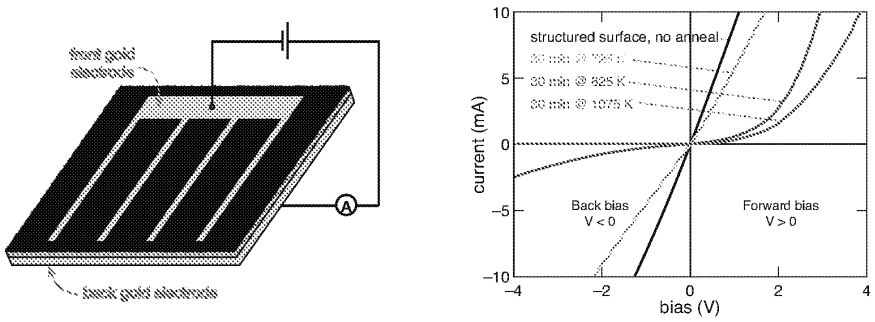


Figure 2.6: *Left:* Cartoon depicting the electrode configuration used to measure I–V curves of sulfur-doped femtosecond laser irradiated silicon. *Right:* Changes in I–V curves with annealing. Silicon substrate is Si(111), n-type (ρ = 800–1200 Ω-cm). Data obtained from reference [52].

At this point the most likely source of the infrared absorptance was thought to be sulfur atoms coordinated with the highly disordered silicon lattice in such a way that they were optically active immediately after irradiation [46, 49]. The sulfur atoms were not in the most energetically favorable equilibrium configuration; they were trapped in this configuration as a result of the extremely fast resolidifcation rate following ultrashort pulse laser irradiation [12]. Therefore, when annealing was performed, the sulfur-silicon network relaxed to a more favorable configuration where the sulfur atom was no longer optically active.

In addition to studying femtosecond laser irradiated silicon from a materials science viewpoint, various applications have been pursued including field emission [43], drug delivery, manipulation of biological species [53], photoluminescence [54], infrared light detection [52] and photovoltaics [43]. We will discuss the latter two as they are relevant to this thesis.

Annealing was discovered to have another effect on sulfur-doped femtosecond laser irradiated silicon. Figure 2.6 shows how current-voltage (I–V) measurements were made

SIONYX1403000043.0004

SAMSUNG EX. 1002 - 647/4148

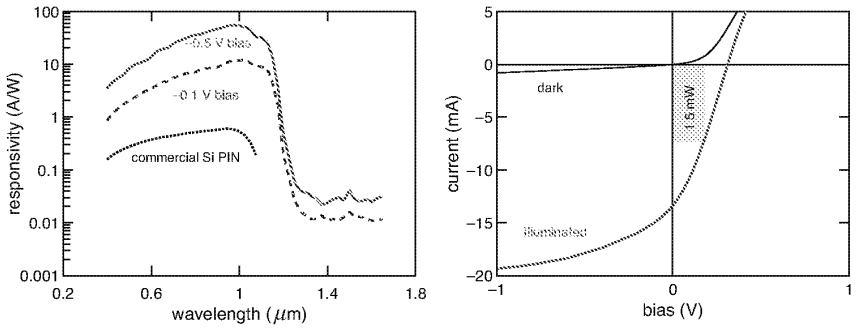


Figure 2.7: *Left:* Responsivity versus wavelength of incident light for sulfur-doped femtosecond laser irradiated silicon at different reverse bias voltages. *Right:* Current versus voltage graph showing the photovoltaic properties of sulfur-doped femtosecond laser irradiated silicon when illuminated with 100 mW/cm^2 of solar radiation (AM 1.0). The lower 4th quadrant shows a maximum power generation of 1.5 mW, resulting in a conversion efficiency of $\sim$ 1.5 %. Silicon substrate is Si(111), n-type (ρ =800–1200 Ω-cm) for the photodiode and p-type (ρ =1–10 Ω-cm) for the solar cell. Data obtained from references [43, 52].

through the plane of a sample. Immediately following irradiation, the entire wafer acts as a resistor; however with increasing annealing temperature a diodic junction is formed. Researchers proposed that after irradiation, the incorporated sulfur atoms did not contribute additional free carrier electrons and therefore the electrical response is determined by the substrate (Si(111), n-type, ρ = 800–1200 Ω-cm). However, after annealing, the coordination of the sulfur atoms changes and the extra valence electrons of sulfur increase the free carrier concentration in the surface layer. In addition, the annealing removes lattice defects that act as traps for charge carriers. The result is that the surface layer becomes heavily n-doped; this is supported by Hall measurements [52]. The gradient in free carrier concentration between the surface layer and the bulk sets up a static electric field that forms a diodic junction.

Under a reverse bias, this diodic junction was found to be highly responsive to visible and infrared light in comparison to commercial silicon photodetectors. Under zero

SIONYX1403000043.0005

SAMSUNG EX. 1002 - 648/4148

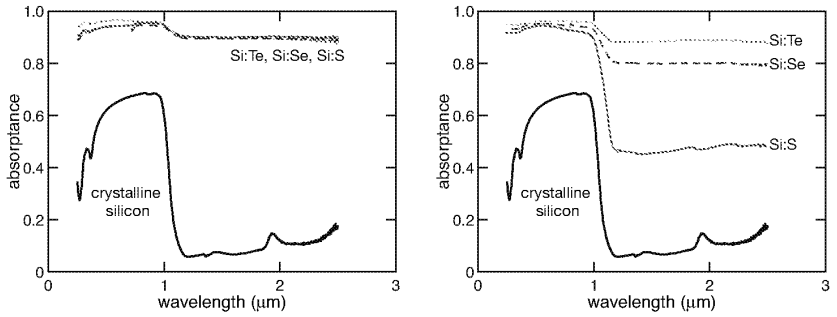


Figure 2.8: Absorptance spectra of silicon irradiated with 100 fs laser pulses focused to 10 kJ/m^2 in the presence of a powder dopant of sulfur, selenium or tellurium before *left* and after *right* annealing at 775 K for 30 minutes. Silicon substrate is Si(111), n-type (ρ = 800–1200 Ω-cm). Data obtained from reference [50].

bias, the junction behaved as a photovoltaic device with a maximum efficiency of ~ 1.5 % (see Figure 2.7).

Recently, several other elements have been incorporated into silicon during femtosecond laser irradiation resulting in near-unity absorptance of infrared light. Figure 2.8 shows the absorptance spectra obtained when silicon is coated with sulfur, selenium or tellurium powder prior to irradiation in N_2 gas. Based on the results obtained after annealing a new theory was proposed for the origin of the infrared absorptance [50]. The author of this thesis contributed to the development of that theory. We proposed that the absorptance was due to a supersaturated concentration of dopant atoms in the polycrystalline grains of the laser modified surface region forming a densely populated impurity band. This is similar to the previous theory, however, we proposed that the reduction of infrared absorptance is caused by diffusion of the supersaturated dopants from out of the bulk of the polycrystalline grains to the grain boundaries. This theory is consistent with the preliminary data in Figure 2.8 as sulfur diffuses the fastest in silicon, selenium diffuses less fast and tellurium diffuses the slowest.

SIONYX1403000043.0006

SAMSUNG EX. 1002 - 649/4148

This thesis covers several areas that add to the knowledge base of the previous work. Chapter 3 covers the formation of particles in the ablation plume during femtosecond laser irradiation of silicon in a near atmospheric pressure background gas which has not been explored before to the author's knowledge. The data and models presented in Chapter 4 provide strong evidence that the proposed mechanism for the infrared absorptance of femtosecond laser irradiated silicon is valid. Chapter 5 expands on the current understanding of the photovoltaic and light detection properties of femtosecond laser irradiated silicon.

2.2 Experimental methods: femtosecond laser system

The intense, high energy, untrashort laser pulses were produced by a home-built regeneratively amplified femtosecond laser system. Although the laser system evolved over the years, it was originally built in 1993 [55–57]. At that time it was one of the first of its kind.

Starting with the creation of the femtosecond laser pulses in the Ti:sapphire oscillator we will describe the journey that the pulses take as they travel through the various components of the laser system until they ultimately arrive at the silicon wafer for our experiment.

2.2.1 Creating the femtosecond laser pulses

The femtosecond laser pulses are initially created by pumping a titanium-doped sapphire crystal mounted in a Kapteyn-Murnane Labs oscillator kit using a Verdi solid state laser—532-nm, 5-W, CW (continuous wave, *i.e.* non-pulsed). The 532-nm pump laser produces 800-nm fluorescence in the Ti:sapphire crystal. The fluorescence wavelength is determined by the energy levels of the Ti:sapphire crystal. The 532-nm light excites electrons in the crystal to a high energy state. These electrons decay quickly to a slightly

SIONYX1403000043.0007

SAMSUNG EX. 1002 - 650/4148

lower metastable state where their lifetime is longer. Eventually they decay from this level to the ground level and a photon of wavelength ~ 800 nm is emitted for each electron that decays.

The end mirrors of the oscillator kit are aligned so that the fluorescence leaving both sides of the crystal are directed back through the crystal along the same path . By aligning the end mirrors in this fashion we can initiate lasing in the cavity. Lasing occurs when at any given instant a majority of the electrons available for excitation in the crystal are in the excited state (this is known as population inversion). Rather than these excited electrons decaying randomly, they are stimulated to decay by photons (which have already been created by fluorescence also called spontaneous emission) passing back through the crystal. This causes the stimulated photons to have the same phase as the photon which initiated their decay. The result is a self-perpetuating beam of photons that bounces back and forth in the cavity with the same phase. This is a continuous wave (CW) laser.

The oscillator is passively mode-locked to produce pulses of light rather than a CW laser. Passive mode-locking is achieved by aligning the pump laser and oscillator to produce the optimal spatial mode of the laser in the cavity and then introducing a disturbance. We accomplish this by moving one of the prisms in the oscillator kit in a step-wise fashion. The pulses leave the oscillator cavity through one of the end mirrors (called an output coupler), which allows a few percent of transmittance to escape. When mode-locked, and using a typical pump power of 3 W, the oscillator produces 100-fs laser pulses centered about a wavelength of 800 nm at 90 MHz with an average power of 350 mW at the exit of the output coupler. Each pulse contains only 4 nJ of energy. This energy alone is not sufficient to ablate silicon and we therefore amplify these pulses.

SIONYX1403000043.0008

SAMSUNG EX. 1002 - 651/4148

2.2.2 Amplifying the femtosecond laser pulses

The pulses are amplified inside a second laser cavity with a second Ti:sapphire crystal. This laser cavity is called the amplifier cavity. This crystal is pumped by a 1-kHz, 527-nm, 200-ns pulsed laser system. The nanosecond laser has a neodymium-doped yttrium lithium fluoride (Nd:YLF) crystal pumped by a flash lamp (as a result we refer to this laser as the "YLF", pronounced "yulf").

The pulses coming from the oscillator cavity cannot be amplified directly. Their short pulse duration would cause extreme intensities and would damage the optics in the amplifier cavity. The femtosecond pulses leaving the oscillator cavity are therefore stretched to picoseconds using a grating-based stretcher.

The amplifier cavity, pumped by the YLF, is a laser by itself that emits 200-ns pulses of 800-nm light at 1-kHz. One out of every 90,000 pulses from the oscillator cavity (this matches the pulse rate of the YLF, 1-kHz) is overlapped inside the amplifier crystal so that it occupies the same time and space as the 800-nm, 200-ns laser pulses. The timing can be adjusted so that the picosecond oscillator pulse arrives just before each 800-nm, 200-ns pulse forms. By doing this, the picosecond oscillator pulse causes stimulated emission of the electrons that were excited inside the amplifier crystal by the YLF pulse. The picosecond pulse in effect "steals" the energy that would have gone into the 800-nm, 200-ns pulse. In this scenario, the picosecond pulse is referred to as the seed pulse, because it seeds the stimulated emission of the amplifier cavity. The 200-ns pulse, which is not created, is referred to as the Amplified Stimulated Emission (ASE), since it would be the normal emission that would occur if the seed pulse was not present. When aligning an amplifier cavity the goal is always to reduce the magnitude of the ASE, as this is lost energy that cannot be added to the seed pulse.

In our system, the round trip time of light in the amplifier cavity is 11 ns. Therefore

SIONYX1403000043.0009

SAMSUNG EX. 1002 - 652/4148

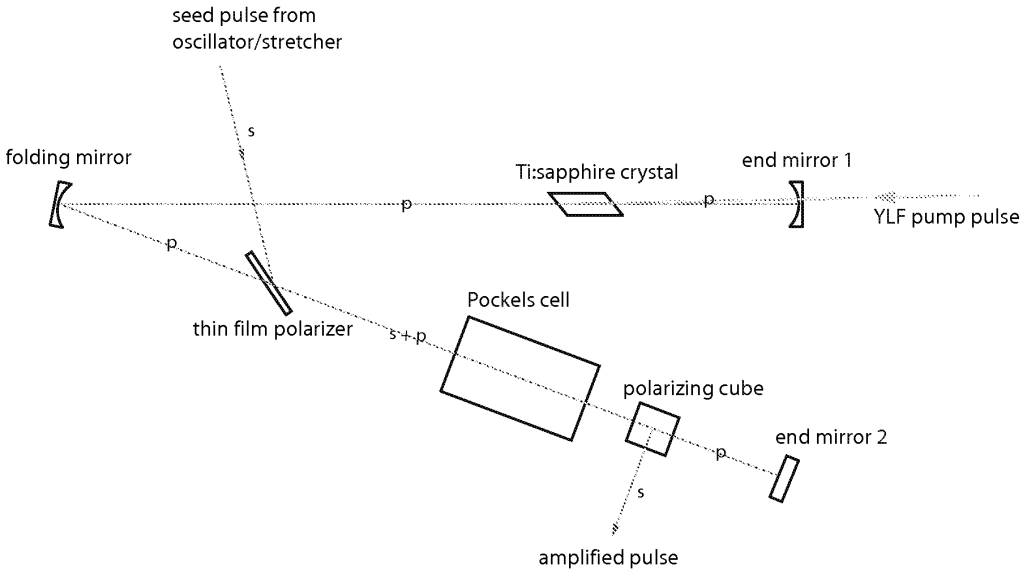


Figure 2.9: Layout of amplifier cavity. The polarization of the laser light in each section of the cavity is indicated by an "s" or "p."

every 11 ns, the seed pulse can gain in energy as it passes through the crystal. Each time the seed passes through the crystal it prevents the ASE from gaining in energy. The seed pulse grows to a maximum in energy after 20–23 round trips (depending on optimal alignment of all the optics). At this point there are no more excited electrons left in the amplifier crystal. When the seed has reached it's maximum energy, it is switched out of the amplifier cavity.

2.2.3 Controlling the injection and ejection of the seed pulse

Switching the seed pulse into and out of the amplifier cavity is accomplished by the following method. The seed pulse enters the amplifier cavity by reflecting off a thin film polarizer (TFP), which reflects s-polarized light and transmits p-polarized light. Figure 2.9, shows the relative positions of the optics in the amplifier cavity and necessary components for switching the seed pulse into and out of the cavity: the Pockels cell and polarizer cube.

SIONYX1403000043.0010

SAMSUNG EX. 1002 - 653/4148

The seed pulse is s-polarized so it reflects off the thin film polarizer and heads toward the Pockels cell. The Pockels cell contains a material which can rotate the polarization of light when an electric field is applied to the material. This is accomplished by applying a voltage to the Pockels cell. Our Pockels cell rotates polarization 90° from s to p or from p to s. When the Pockels cell is in a state so that it rotates the polarization of light, it is said to be "on" or "firing," when the Pockels cell passes the light unaffected it is said to be "off" or "not firing." The polarizer cube in our set up transmits p-polarized light and diffracts s-polarized light at a right angle out of the side of the cube. The Pockels cell and the polarizer cube together comprise an electro-optic switch.

When the Pockels cell is off, the s-polarized seed pulse passes through and remains s-polarized; it then diffracts off the polarizer cube and exits the amplifier cavity never having passed through the amplifier crystal. This happens to 89,999 pulses out of every 90,000 pulses coming from the oscillator. However for one out of 90,000 pulses the Pockels cell fires, resulting in an 8 ns window where the polarization of the seed pulse will be rotated from s to p. The seed pulse is then transmitted through the polarizer cube; back reflects off the amplifier cavity end mirror; passes through the polarizer cube and Pockels cell again; passes through the thin film polarizer (because it is now p-polarized); reflects off the folding mirror; passes through the Ti:sapphire crystal; back reflects off the second end mirror and repeats the same path for 20–23 round trips. Then after 210–240 ns (20–23 trips), the Pockels cell is fired again and the polarization of the now amplified seed pulse is rotated from p to s and it exits the cavity by diffracting off of the polarizer cube.

The timing of the Pockels cell is controlled by an SRS timing box. A small fraction of the initial seed pulse is reflected with a piece of glass into a photodiode. This 90 MHz signal is amplified and then sent to a countdown box that outputs 1 electrical pulse for every 90,000 pulses. This 1-kHz signal is split into two signals. One is used to trigger the

SIONYX1403000043.0011

SAMSUNG EX. 1002 - 654/4148

YLF and the second signal enters the SRS timing box where a delay can be added before being sent to trigger the firing of the Pockels cell. By performing the timing in this manner all of the electronics are controlled by the same original signal (so they all have the same clock) and the delay in the SRS timing box can be varied until the seed pulse arrives inside the amplifier crystal at the optimal time for amplification.

2.2.4 The amplified femtosecond laser pulses

For our system amplification works best when the YLF pumps the amplifier crystal at 6.75 W. Then, at the output of the polarizer cube, we obtain picosecond pulses at 1-kHz with a maximum average power of 1.1 W. The amplified pulses are then compressed to 100 fs by a grating-based compressor. As a result of grating losses, the maximum average power is reduced to 350 mW.

At this point each femtosecond laser pulse contains 350 μJ of energy, which is approximately 1000 times larger than the pulse energy at the output of the oscillator cavity and more than enough energy to ablate silicon.

2.2.5 Aligning the amplifier cavity

Two oscilloscopes are used to monitor the laser. One receives the signal from the photodiode that looks at the seed pulse and is used to help with mode-locking. A second one is used to monitor the seed pulse both inside and outside the amplifier cavity. To view the seed pulse while it is in the amplifier cavity, a photodiode is placed behind the second amplifier cavity end mirror. This end mirror is an output coupler allowing a small transmittance. This oscilloscope is used to help align the pointing of the seed pulse; align the amplifier cavity end mirrors; and adjust the Pockels cell timing to ensure that amplification is occurring as efficiently as possible. The second oscilloscope needs to be

SIONYX1403000043.0012

SAMSUNG EX. 1002 - 655/4148

triggered by the same common electrical signal that triggers all of the electronics.

The following procedure is used to obtain good amplification of the seed pulse. With the seed pulse blocked, we observe the YLF pulse and the ASE pulse on the same photodiode. This can be done essentially from anywhere on the optics table as both the YLF pulse and the ASE are quite bright and scatter light in all directions off of each of the optics. While viewing both pulses on the same photodiode, the amplifier cavity end mirrors are adjusted iteratively in order to shrink the time between the YLF pulse and the ASE pulse to the minimum value. A typical value for our system is 250 ns. The pointing of the YLF pulse may require adjusting as well in order to find the minimum time.

Next, we view the photodiode at the output coupler of the amplifier cavity and inject the seed while disabling the ejection of the seed. By blocking and unblocking the seed, we can watch the ASE appear and then dissappear (being replaced by the seed signal). The seed will look like a series of peaks that grow larger and larger. The peaks are separated by 11 ns (the round trip time of the amplifier cavity). The seed signal occurs earlier in time than the ASE. By monitoring the seed signal we adjust the mirrors that control the pointing of the seed pulse to cause amplification to happen at the earliest time possible. This ensures that the most efficient amplification is occurring. Next the timing of the injection is varied so that amplification occurs at the earliest time. We choose the latest injection time that results in the earliest amplification, meaning that if we move the injection time earlier and the amplification stays the same, we use the later injection time. Finally we then enable ejection of the seed pulse and monitor the power at output of the polarizer cube. We change the ejection timing in order to get the highest possible power (usually 1.1 W).

SIONYX1403000043.0013

SAMSUNG EX. 1002 - 656/4148

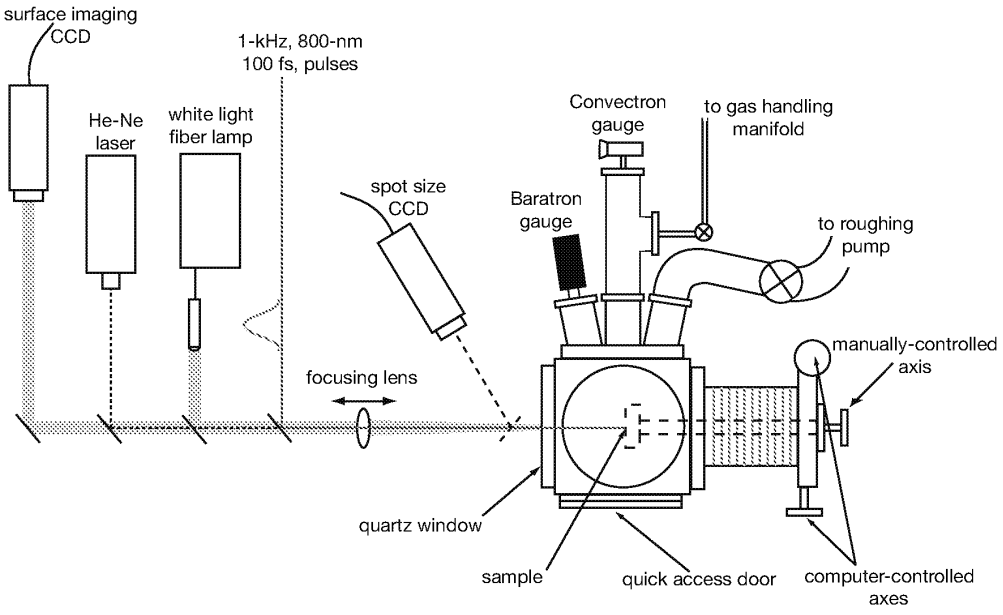


Figure 2.10: Schematic diagram of the system used for femtosecond laser irradiation of silicon in various environments.

2.3 Experimental methods: irradiation process and vacuum chamber

The experiments in this thesis were performed inside a stainless steel vacuum chamber anchored to the optics table on four legs (see Figure 2.10). The main chamber is an 8-inch welded stainless steel cube. A corrosion resistant roughing pump is used to evacuate to 10^{-3} Torr. A convectron gauge monitors the pressure between 10^{-3}–10^{-1} Torr; a baratron pressure gauge monitors pressure between 1 and 1000 torr.

Silicon wafers are mounted to a stainless steel magnetic disc with carbon tape. This disc is then placed inside the chamber on a permanent magnet that is anchored to a stainless steel arm connected to a 3-axis linear translation system on the back of the

SIONYX1403000043.0014

SAMSUNG EX. 1002 - 657/4148

cube. The two axes that are orthogonal to the laser beam (in the plane of the sample) are computer controlled; the third axis is manually controlled. The silicon wafer is centered on the translation stage using a CW Helium-Neon laser that is aligned to take the same path as the femtosecond laser pulses.

The femtosecond laser pulses are focused through the quartz window with a 25 cm focal length lens, anti-reflection coated for 800 nm light. The focus of the lens is behind the sample. The lens is mounted on a single axis linear translation stage with a 2-inch travel. Spot sizes ranging from 30–250 μm could be reliably achieved. The spot size is measured by raising a flipper mirror and directing the beam into a CCD camera at a calibrated distance from the flipper mirror.

Prior to irradiation the chamber is evacuated, and then filled with a specific background gas. During irradiation, white light shines on the silicon wafer and the reflected light is collected by a second CCD camera, which allows the reflectivity change of the silicon surface to be monitored live with a magnification of approximately 60 times.

The number of pulses that are incident on any one area is determined by the spot size, the repetition rate of the laser (1-kHz) and the translation speed of the wafer. The maximum translation speed for our motors is 1.5 mm/s. For a spot size of 150 μm, this equates to a minimum number of pulses/area of 100. A fast mechanical shutter triggered by the same electrical signal used to the trigger the electronics of the laser system allows the repetition rate of the laser to be varied from 1–100 Hz which allows for lower numbers of pulses/area.

SIONYX1403000043.0015

SAMSUNG EX. 1002 - 658/4148

Chapter 3

Formation of silicon nanoparticles by femtosecond laser ablation in a background gas

3.1 Chapter abstract

We show that the mechanism of nanoparticle formation during femtosecond laser ablation of silicon is affected by the presence of a background gas. Femtosecond laser ablation of silicon in a H_2 or H_2S background gas yields a mixture of crystalline and amorphous nanoparticles. The crystalline nanoparticles form via a thermal mechanism of nucleation and growth. The amorphous material has smaller features and forms at a higher cooling rate than the crystalline nanoparticles. The background gas also results in the suspension of plume material in the gas for extended periods, resulting in the formation (on a thin film carbon substrate) of unusual aggregated structures including nanoscale webs that span tears in the film. The presence of a background gas provides additional control of the structure

SIONYX1403000043.0016

SAMSUNG EX. 1002 - 659/4148

and composition of the nanoparticles during short pulse laser ablation.

3.2 Introduction

Femtosecond laser ablation is the explosive removal of material excited to extreme temperatures and pressures through absorption of a high-intensity laser pulse of subpicosecond duration. The femtosecond laser ablation of metals and semiconductors in a vacuum environment has been investigated extensively [20–22, 35, 36, 58]. Recent research has focused on the formation mechanism of silicon nanoparticles created by the irradiation of silicon in vacuum with 800-nm, laser pulses of 80 to 200-fs duration [22, 35, 36, 58]. Hydrodynamic models suggest that the nanoparticles form via mechanical fragmentation of a highly pressurized fluid undergoing rapid quenching during expansion in the vacuum [22]. Experimental studies of the evolution of the ablated silicon support this theoretical prediction and show that the ablated material is composed almost entirely of ejected liquid silicon with very little vapor [35, 36]. In addition, it was found that the nanoparticles form within 50 ps by a non-equilibrium, non-thermal phase transformation rather than by a thermal nucleation and growth process [36].

In this paper we present work on the irradiation of silicon with 800-nm, 100-fs laser pulses in a background gas of hydrogen (H_2) or hydrogen sulfide (H_2S). Our results indicate that the presence of the background gas during irradiation fundamentally changes the mechanism for nanoparticle formation. We observe two phases in the collected plume material: spherical particles of crystalline silicon ranging in diameter from 5–300 nm and a highly porous network of amorphous silicon with feature sizes ranging from 1–10 nm. We find that the crystalline nanoparticles form by thermal nucleation and growth; the amorphous phase forms from small droplets of liquid that are subjected to a high cooling rate.

SIONYX1403000043.0017

SAMSUNG EX. 1002 - 660/4148

The size distribution of the crystalline nanoparticles is log-normal—that is, the logarithm of the particle diameter has a Gaussian distribution—suggesting that the ejected material initially contains a vapor component instead of consisting of just liquid droplets as observed in vacuum [36]. The presence of the background gas also gives rise to the formation of unusual webs of nanoparticles on the collection substrate. Our results indicate that the background gas affords additional control of the structure and composition of the nanoparticles.

3.3 Experimental setup

The ablation plume was generated by irradiating a Si(111) wafer (n-type, ρ = 8–12 Ω-m) with a 1-kHz train of 100-fs, 800-nm laser pulses produced by a regeneratively amplified Ti:sapphire laser. The silicon wafer was placed in a stainless steel vacuum chamber, evacuated to about 6.7 Pa and then filled with either H_2 or H_2S to various pressures. The laser pulses were focused onto the silicon to a diameter of 150 μm yielding a peak fluence of 10 kJ/m^2 and a peak intensity of about 10^{17} W/m^2. The plume material was collected over the course of 1 hour as the silicon wafer was translated at a speed 250 μm/s to prevent degradation of the target. This translation speed resulted in an average of 600 pulses delivered to each spot on the surface.

We used transmission electron microscope specimen grids (3-mm diameter, 200 mesh copper grids, coated on one side with a 20-nm thick film of amorphous carbon) to collect material in the plume. The plane of the grids was perpendicular to the silicon surface and suspended above and in front of the silicon target with 18 gauge copper wire and carbon tape. The grids were positioned 10 mm from the target with the carbon-coated side facing down (see Figure 3.1).

SIONYX1403000043.0018

SAMSUNG EX. 1002 - 661/4148

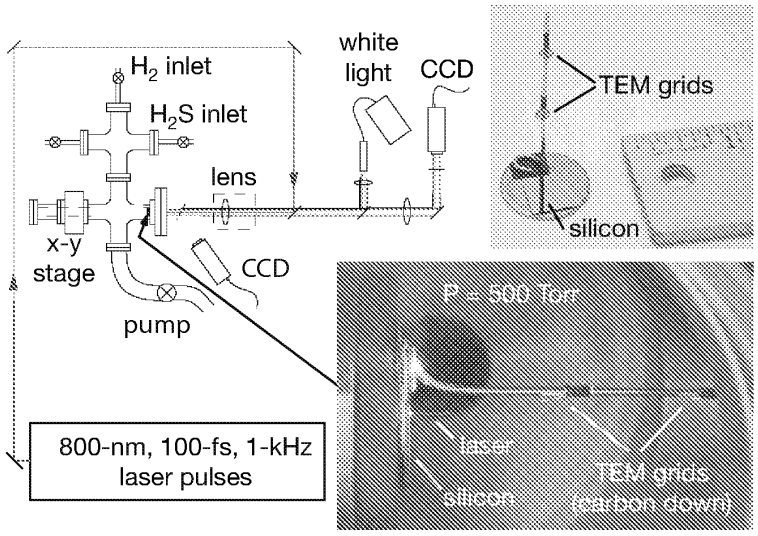


Figure 3.1: Experimental setup used for collecting nanoparticles.

3.4 Results

We visually observed the ablation plume and collected the ejected material on transmission electron microscope (TEM) specimen grids positioned 10 mm from the target. The size, structure and composition of the collected nanoparticles were determined using bright and dark field imaging, selected area diffraction, and energy dispersive spectroscopy in a transmission electron microscope.

The background gas influences the shape and trajectory of the ablation plume. At a 1-kHz pulse rate, the ablation plume appears as a constant stream of ejected material in the shape of a cone, which expands from the 150-μm diameter laser-irradiated spot to millimeter dimensions making it readily visible to the eye. In contrast to vacuum, where the ejected material retains most of its initial kinetic energy until it impacts a surface, the background gas reduces the kinetic energy of the ejected material to zero. The material

SIONYX1403000043.0019

SAMSUNG EX. 1002 - 662/4148

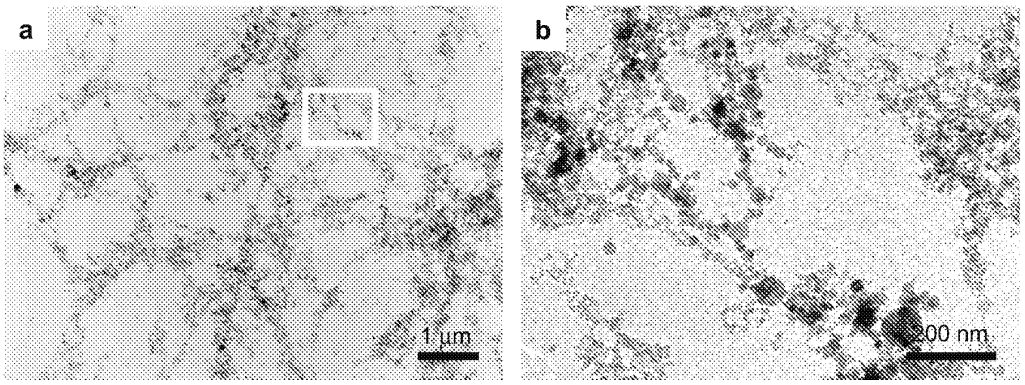


Figure 3.2: (a) Low magnification TEM bright field image showing particles formed in the ablation plume of silicon irradiated with trains of femtosecond laser pulses in H_2 at 67 kPa. (b) Higher magnification of the highlighted area in (a) reveals a network composed of spherical particles and porous material.

then remains suspended in the background gas for the duration of the experiment and travels around the chamber by convection. When H_2S is used as the background gas, the ablation plume is a narrow cone that initially travels perpendicular to the silicon surface and then curves upward until it comes to a stop and begins to fall back down. When H_2 is the background gas, the ablation plume is a wider cone that remains perpendicular to the silicon surface until it eventually slows to a stop and then travels around the chamber by convection.

Although the trajectory of the ablation plume is different for irradiation in both H_2S and H_2, the size and the structure of the collected material is the same. The TEM bright field image in Figure 3.2a shows that the collected material is composed of an extremely fine network of aggregated material. The network consists of clusters of spherical particles, ranging in diameter from 5–300 nm, dispersed in a highly porous material with feature sizes ranging from 1–10 nm (Figure 3.2b). In Figure 3.2b, the spherical particles vary in brightness from light gray to deep black. In bright field imaging, a low brightness indicates

SIONYX1403000043.0020

SAMSUNG EX. 1002 - 663/4148

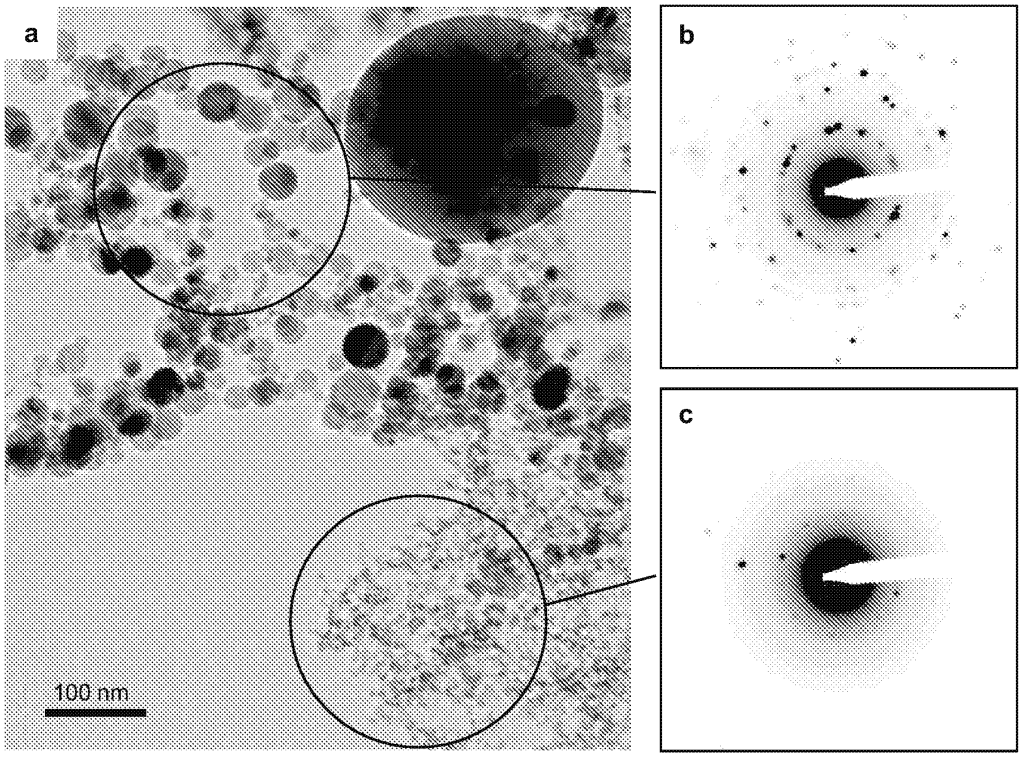


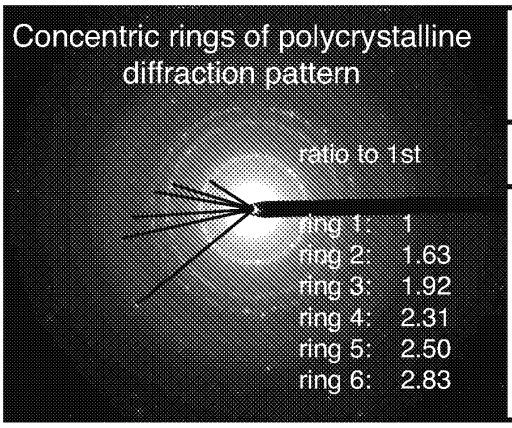
Figure 3.3: (a) TEM bright field image of particles generated in the ablation plume of silicon irradiated in H_2 at 67 kPa. Selected area diffraction reveals that (b) the spherical particles are crystalline and (c) the porous material is amorphous.

that the material is highly diffracting [59]. When imaging the spherical particles, they alternate between gray and black on the time scale of seconds. This observation supports that the particles are single crystals; the alternating brightness is caused by the particles tilting in and out of the diffraction condition when they collect charge in the electron microscope. In comparison, the brightness of the highly porous material does not vary with time and appears between light-gray and dark-gray depending on the thickness of accumulated material.

Figure 3.3a is a TEM bright field image showing the spherical particles on the left

SIONYX1403000043.0021

SAMSUNG EX. 1002 - 664/4148



Allowed reflections of diamond cubic structure		
hkl	$\sqrt{(h^2+k^2+l^2)}$	ratio to 1st
111	$\sqrt{3}$	1
220	$2\sqrt{2}$	1.633
311	$\sqrt{11}$	1.915
400	4	2.309
331	$\sqrt{19}$	2.517
422	$2\sqrt{6}$	2.829

Figure 3.4: Analysis of the polycrystalline diffraction pattern. The ratio of the size of each concentric ring in the diffraction pattern matches the allowed reflections of the diamond cubic crystal structure.

and the highly porous material on the right. Figures 3.3b and 3.3c are electron diffraction patterns obtained using the selected area diffraction apertures indicated by the corresponding circles in Figure 3.3a. The diffraction pattern in Figure 3.3b is characteristic of a polycrystalline material and the relative diameters of the rings confirm that the crystal structure of the spherical particles is diamond cubic (see Figure 3.4). By positioning the selected area diffraction aperture over an individual particle, we verified that each particle is actually a single crystal (see Figure 3.5) and that the diffraction pattern in Figure 3.3b is the result of an ensemble of single crystal particles each at a different orientation. In contrast, Figure 3.3c shows a diffraction pattern nearly absent of diffraction peaks, indicating an amorphous structure. The presence of a few diffraction peaks is due to crystalline particles mixed in with the amorphous material. Closer inspection of the image in Figure 3.3a confirms the presence of a few crystalline particles in the amorphous material.

The bright and dark field TEM images in Figure 3.6 confirm that the highly porous material is amorphous. Figure 3.6a is a bright field image showing a mixture of spherical

SIONYX1403000043.0022

SAMSUNG EX. 1002 - 665/4148

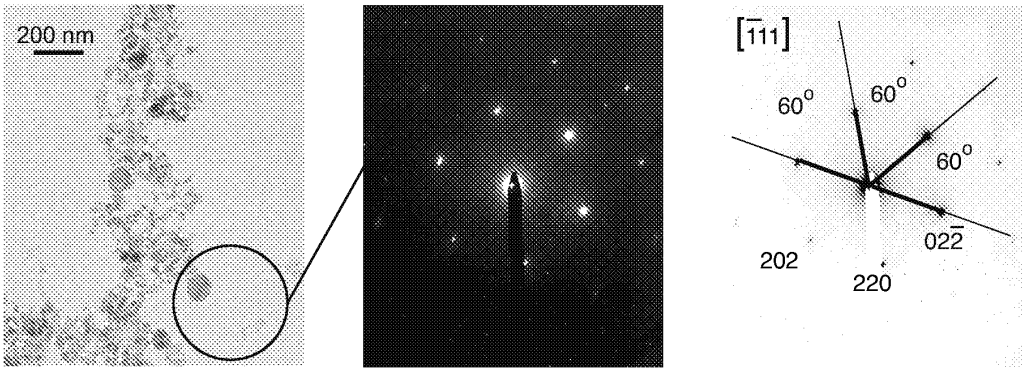


Figure 3.5: *Left:* TEM bright field image of nanoparticles. The circle indicates the approximate size and location of the selected area diffraction aperture. *Center:* Diffraction pattern from selected area diffraction aperture positioned over a single nanoparticle. *Right:* Inverse of the diffraction pattern. Analysis of the pattern shows the particle is a single crystal and oriented along a [111]-type axis.

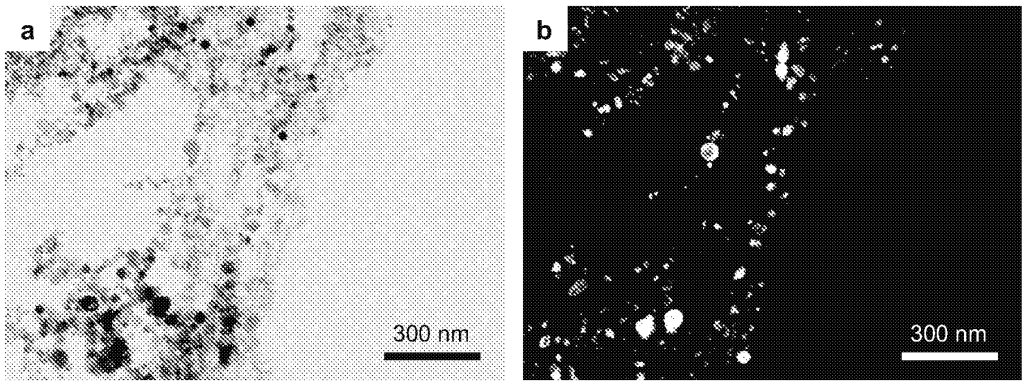


Figure 3.6: (a) TEM bright field image of particles generated in the ablation plume of silicon irradiated in H_2 at 67 kPa. (b) Compilation of eight dark field images acquired with the TEM C2 aperture positioned at eight different locations along the (111) diffraction ring. The bright areas indicate the locations of crystalline material.

particles and highly porous material. Figure 3.6b is a compilation of eight dark field images acquired with the TEM C2 aperture positioned at different locations around the first ring of the diffraction pattern in Figure 3.3b. The first diffraction ring is populated by crystalline reflections from (111) type planes. In each of the eight images, different spherical particles

SIONYX1403000043.0023

SAMSUNG EX. 1002 - 666/4148

appear bright depending on whether their crystalline orientation produces a (111) type reflection (e.g., each of the twelve [011] and twenty four [112] orientations in a diamond cubic crystal produce a (111) type reflection). Crystalline particles that do not appear bright in Figure 3.6b are likely oriented along a direction that does not produce a (111) reflection at any of eight locations. In contrast, the highly porous material is a uniform dark gray in all eight images, confirming that it is amorphous. If the highly porous material were crystalline, it would be unlikely that no part of that material produces a (111) reflection in any of the eight orientations.

The dark field images used to form Figure 3.6b were compiled in the following manner. In seven of the eight images, the lower fourth of the brightness scale was subtracted. This removed the dark gray amorphous material from each image and left the bright crystalline particles behind. These images were then summed together and then added to the eighth image (which was unaltered) to produce Figure 3.6b. By performing the sum in this manner, the relative brightness between the spherical particles and the amorphous phase in Figure 3.6b is representative of each of the eight dark field images.

Using energy dispersive spectroscopy we find that the main component of both the crystalline particles and the amorphous material is silicon. Trace amounts of oxygen, carbon, and sulfur are detected in the amorphous material, and to a lesser extent in the crystalline particles. Sulfur is only detected when H_2S is used as the background gas. The presence of oxygen and carbon can be attributed to oxidation and contamination during transportation of the TEM specimen grids from the vacuum chamber to the TEM.

Figures 3.7 and 3.8 show aggregated material on copper TEM specimen grids coated with a smooth continuous carbon film. Figure 3.7 shows several strands of particles over 30 μm in length. The strands also span 10-μm wide rips in the continuous carbon film like the strands of a web (Figure 3.8a). Higher magnification images show that these

SIONYX1403000043.0024

SAMSUNG EX. 1002 - 667/4148

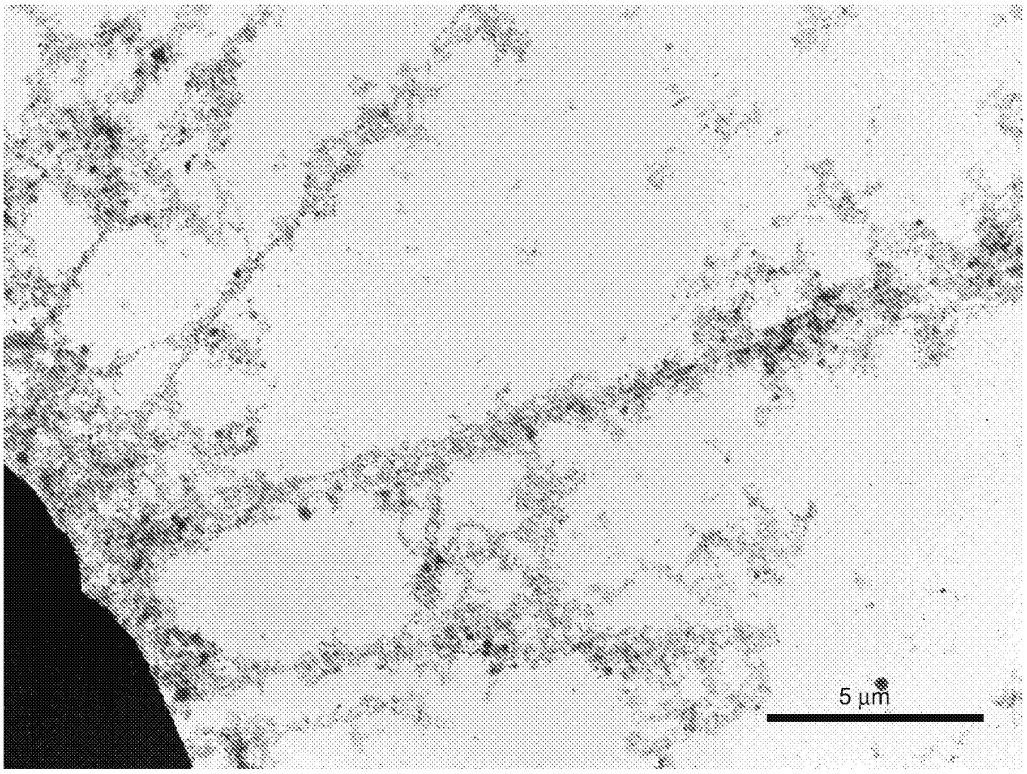


Figure 3.7: TEM bright field image showing that particles aggregate in straight lines measuring over 30 μm in length.

nanoscale webs are composed of both crystalline particles and amorphous material (Figure 3.8b). We find that the collection surface affects the aggregation of nanoparticles and amorphous material. For example, TEM specimen grids that are coated with an uneven, holey carbon film gives rise to small clusters instead of strands of particles. These observations suggest that it may be possible to control the self-assembly of nanoparticles through the morphology of the substrate.

We studied the dependence of the size and structure of the ablated material on pressure by collecting the ablated material at various H_2 background pressures. The amount of amorphous material collected on the TEM grids increases as the pressure decreases. At

SIONYX1403000043.0025

SAMSUNG EX. 1002 - 668/4148

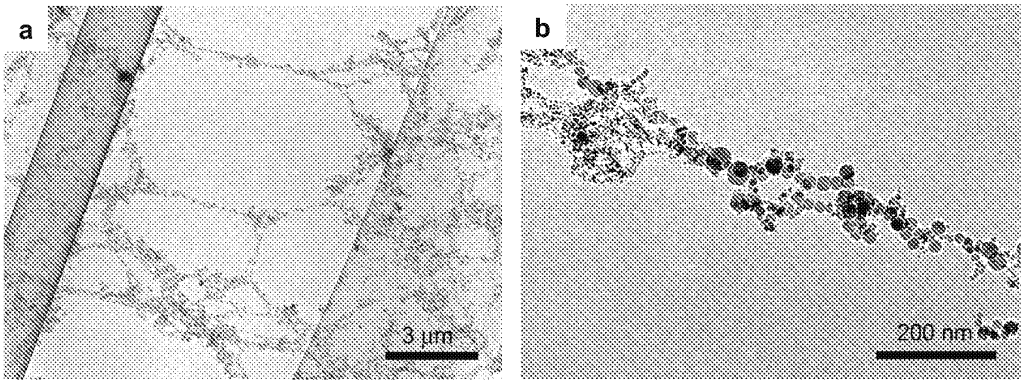


Figure 3.8: (a) Low magnification TEM bright field image showing particles forming nanoscale webs that span 10-μm wide gaps in the collection substrate. (b) Higher magnification TEM bright field image showing that the bridges are composed of both crystalline and amorphous particles.

13 kPa, there is approximately 3 times more amorphous material than at 67 kPa. At 0.27 kPa, the collected material is nearly completely amorphous, intermixed with a few crystalline particles. The crystalline material, too, changes with pressure. Figure 3.9 shows the crystalline particle size distribution at two different background pressures: 13 and 67 kPa. The average size of the crystalline particles increases as the pressure decreases. At both 13 and 67 kPa, the size of the crystalline particles fit a log-normal distribution. However, the geometric mean diameter is greater for particles produced at 13 kPa (18.8 $\pm$ 0.2 nm) than at 67 kPa (16.2 $\pm$ 0.2 nm). At 0.27 kPa, the crystalline particles are embedded in a continuous amorphous film preventing the determination of an accurate particle size distribution.

3.5 Discussion

Depending on the cooling rate, liquid silicon forms either the energetically favorable crystalline phase or a metastable amorphous phase upon cooling [60]. Amorphous

SIONYX1403000043.0026

SAMSUNG EX. 1002 - 669/4148

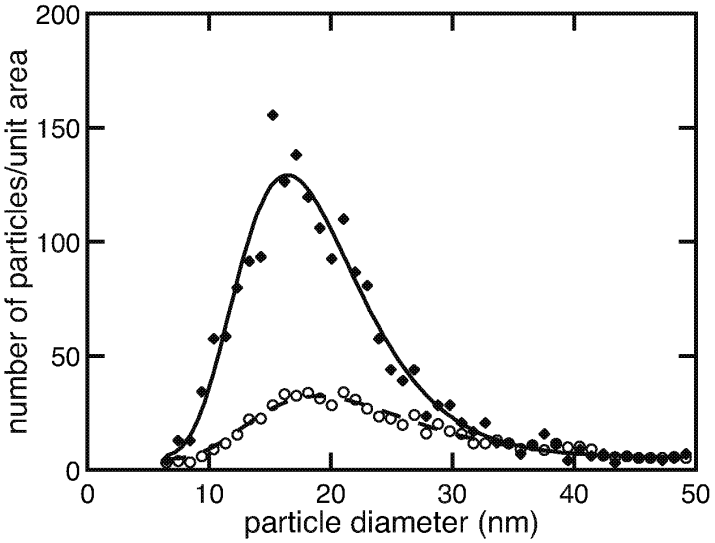


Figure 3.9: Size distribution of crystalline nanoparticles formed during femtosecond laser ablation of silicon in H_2 gas at 13 kPa (open circles) and 67 kPa (filled diamonds). The solid and dashed curves are log-normal fits with geometric means of 18.8 ± 0.2 nm and 16.2 ± 0.2 nm, and standard deviations of 0.50 ± 0.02 nm and 0.44 ± 0.02 nm for particles formed at 13 kPa and 67 kPa, respectively.

silicon is typically formed though vapor deposition processes, although, at high cooling rates, such as in electrohydrodynamic atomization of silicon in vacuum [61, 62] (10^6–10^7 K/s) or after irradiation of a silicon substrate with nanosecond [63] and picosecond [1, 12] laser pulses ($\geq 10^{10}$ K/s), a metastable amorphous phase can nucleate and grow from the liquid phase before crystallization occurs [60]. At lower cooling rates, there is sufficient time for the more stable crystalline phase to nucleate and grow. The presence of both amorphous and crystalline silicon in the collected material, indicates that the cooling rate in our experiment is near the threshold cooling rate for formation of the amorphous phase (10^6 K/s). This cooling rate is well below the estimated cooling rate for femtosecond laser ablation of silicon in vacuum (10^{12}–10^{18} K/s) [22], suggesting that the background gas lowers the

SIONYX1403000043.0027

SAMSUNG EX. 1002 - 670/4148

cooling rate of the ejected silicon. As the background pressure is increased, the amount of crystalline material increases (Figure 3.9) and the amount of amorphous material—which requires a higher cooling rate—decreases. The cooling rate within the ablation plume varies, because the mass of the silicon droplets is distributed over a range. Large liquid droplets cool by convection and radiation at a slower rate than smaller droplets. Indeed, nearly all of the crystalline particles we observe are larger in size than the amorphous particles (because of their larger size they cooled more slowly, providing enough time for crystallization).

The presence of a background gas fundamentally changes the mechanism of nanoparticle formation. In vacuum, the solid-liquid transformation is reported to be nonthermal and to take place within 50 ps [36]. This time period is too short for particles with crystalline order to form. The threshold speed for the crystalline-liquid interface above which the amorphous phase forms is reported to be 15 m/s [12]. At this speed 100-nm particles require 3 ns to form; 5-nm particles require 160 ps. We observe crystalline particles as large as 300 nm. Crystalline particles of this size can only form by a thermal process of crystal nucleation and growth.

The formation of single-crystal rather than polycrystalline particles is consistent with what is known about nucleation and growth of crystalline silicon. Multiplying the volume of the mean particle, 2×10^{-24} m^3, by the largest reported [64] value for the homogeneous nucleation rate, 2×10^{10} m^{-3}s^{-1}, and inverting the result, we find that the time between two nucleation events within the volume of the mean particle is at least 10^{13} s, which is far greater than the solidification time. In other words, the observed nanoparticles solidify completely before a second nucleation event can occur and therefore they must be a single crystal.

The log-normal nature of the size distribution of the crystalline particles allows us to draw conclusions about the process of ablation in a background gas. A log-normal size

SIONYX1403000043.0028

SAMSUNG EX. 1002 - 671/4148

distribution was first associated with the nucleation and growth of small particles during evaporation of metals in an inert gas [65]. It was recently shown that nucleation and growth of liquid droplets from the vapor phase produces a log-normal size distribution if the following four criteria are met [66,67]:

1. nucleus particles (or droplets) only grow in a finite active growth region
2. they travel through it by both drift and diffusion
3. they are collected at a fixed point outside the active zone
4. their size in the active region is a power function of time.

The ablation plume in our experiment meets all of the above criteria if we assume it is initially composed of vapor or a mixture of liquid and vapor. Liquid droplets in the ablation plume grow while new droplets nucleate and grow through vapor condensation until the vapor phase is depleted. The finite amount of vapor establishes a finite active growth region. The kinetic energy of the ablation plume provides a condition of strong drift, in addition to diffusion, which is always present. The liquid droplets then solidify as either crystalline or amorphous depending on their cooling rate and are collected on the TEM grid. The time dependence of the size of a droplet growing by vapor condensation is linear (i.e., it is a power function in time where the exponent is unity) [66].

As the background gas pressure is decreased, the peak in the lognormal size distribution of the crystalline particles shifts to a larger particle size (Figure 3.9). We can attribute this shift to an increase of the average cooling rate within the plume at lower pressures. As the cooling rate increases, more of the smaller liquid droplets become amorphous and the average size of the crystalline particles increases.

A key difference between femtosecond laser ablation in a background gas and in vacuum is the evolution of the kinetic energy of the ejected ablation plume. In a vacuum,

SIONYX1403000043.0029

SAMSUNG EX. 1002 - 672/4148

the ejected material retains much of its kinetic energy and is eventually deposited along a line-of-sight trajectory. Many evaporation-based thin film growth techniques, such as pulsed laser deposition, rely on this process. However, in a background gas, the kinetic energy of the ejected material is reduced significantly due to interaction with the background gas. The initial kinetic energy can be reduced to zero before any deposition occurs and the plume material moves about the chamber by convection. In H_2S, the ejected plume is observed to turn upward in the opposite direction of gravity. This upward turn is likely brought about by a density difference between the plume and the background gas resulting in a buoyancy effect. In H_2, the plume remains perpendicular to the target, indicating that the density of the plume is similar to H_2.

We attribute the formation of nanoscale webs to the aggregation of particles suspended in the background gas. As the plume material remains suspended in the chamber during the length of the experiment, the particles aggregate and form three-dimensional structures and clusters, which then come to rest on the TEM grids. The strands of the nanoscale webs are composed of individual aggregated nanoparticles (Figure 3.8b). A recent theoretical report on coagulation of particles suspended in a gas predicts that under certain conditions particles aggregate into web-like clusters similar in shape to the clusters we observe [68]. It may be possible to form more complex three-dimensional nanostructures by controlling the gas type and pressure as well as the morphology, structure and chemistry of the collection substrate.

3.6 Conclusion

The presence of a gas during femtosecond laser ablation of silicon changes the fundamental mechanism by which nanoparticles form. The background gas suppresses the

SIONYX1403000043.0030

SAMSUNG EX. 1002 - 673/4148

non-thermal phase transformation observed in vacuum allowing some particles to crystallize through a thermal nucleation and growth process. The log-normal size distribution of crystalline particles suggests that the ablation plume contains a vapor component. The presence of the background gas also results in the suspension of plume material in the chamber for extended periods of time resulting in the formation of long straight lines and webs of nanoparticles. The pressure and gas chemistry control the structure, composition and size distribution of the ejected material. Our results show that it may be possible to tailor the creation of nanoparticles and control their self-assembly on a collection surface.

SIONYX1403000043.0031

SAMSUNG EX. 1002 - 674/4148

Chapter 4

Mechanism of broadband infrared absorption in chalcogen-doped silicon

The organization of this chapter is as follows: Sections 4.1 through 4.6 very nearly represent the as-submitted journal article on the Mechanism of broadband infrared absorption in chalcogen-doped silicon. Section 4.7 provides supplemental information to the main arguments developed in Sections 4.1 through 4.6. The information in Section 4.7 is presented to provide more experimental details and more graphical representations of the data for future reference.

4.1 Chapter abstract

Sulfur doping of silicon beyond the solubility limit by femtosecond laser irradiation has lead to near-unity broadband absorption of visible and infrared light and the realization of silicon-based infrared photodetectors. The nature of the infrared absorption is not yet well

SIONYX1403000043.0032

SAMSUNG EX. 1002 - 675/4148

understood. Here we present a detailed study on the reduction of infrared absorptance after various anneals of different temperatures and times for three chalcogens (sulfur, selenium, and tellurium) dissolved into silicon by femtosecond laser irradiation. For sulfur doping, we irradiated silicon in SF_6 gas; for selenium and tellurium, we evaporated a film onto the silicon and irradiated in N_2 gas; lastly, as a control, we irradiated untreated silicon in N_2 gas. Our analysis shows that the deactivation of infrared absorption after thermal annealing is likely caused by dopant diffusion. We observe that a characteristic diffusion length—common to all three dopants—leads to the reduction of infrared absorption. Using diffusion theory, we show that the grain size of the re-solidified surface layer is a probable source of this characteristic diffusion length, indicating that deactivation of infrared absorptance could be caused by precipitation of the dopant at the grain boundaries.

4.2 Introduction

Silicon is often doped with chalcogens such as sulfur and selenium to obtain optoelectronic properties not typically available to silicon-based devices, such as detection of infrared light [52,69–71], and light emission (photoluminescence [72–75] and, more recently, electroluminescence [76,77]). In addition, the presence of the chalcogen atom in the silicon lattice is studied for its potential as a double donor [78,79].

Doping is typically done by vapor diffusion during furnace annealing [72,75,79–81] or ion implantation followed by furnace annealing [70,75,82–85]. These methods have been used to establish the bulk diffusivity and equilibrium solubility limit of sulfur [84,86,87], selenium [88–92], and tellurium [81,85,90] in crystalline silicon.

When doping is performed via thermal diffusion, the concentration is restricted to the solubility limit at the annealing temperature; however, when ion implantation is followed

SIONYX1403000043.0033

SAMSUNG EX. 1002 - 676/4148

by nanosecond pulsed laser irradiation [93–96], the doping concentration can exceed the solubility limit by several orders of magnitude through a process known as solute trapping [97–99]. This method has recently been used to create supersaturated concentrations of sulfur in silicon [95]. Recently, we created supersaturated concentrations of sulfur, selenium and tellurium, respectively, by femtosecond laser irradiation of silicon coated with a powder film [50]. We have also doped silicon in this manner using a background gas of sulfur hexaflouride (SF_6) or hydrogen sulfide (H_2S) [46, 49]. In these recent studies involving nanosecond and femtosecond laser pulses, the supersaturated solution of chalcogen dopants exhibits increased infrared absorptance [46, 49, 50, 95]. When femtosecond laser pulses are used, the infrared absorptance is near unity out to 2500 nm [46, 49, 50].

The mechanism by which chalcogen-doped silicon absorbs infrared light is not entirely understood. Two observations provide insight into how the dopant contributes to the enhanced infrared absorption. First, the infrared absorption decreases after thermal annealing, and this decrease becomes larger with increasing annealing temperature [46, 49, 50, 95]. Second, for the same thermal anneal, the infrared absorption decreases a different amount depending on the dopant [50]. Sulfur-doped samples show the largest decrease in infrared absorption, followed by selenium-doped samples and tellurium-doped samples, respectively [50]. Given that the bulk diffusivity of sulfur in silicon is roughly an order of magnitude larger than selenium and several orders of magnitude larger than tellurium,[1] the

[1]This large variation in diffusivity is related to the diffusion path of each dopant [100]. Fast diffusers in silicon, such as copper and iron [100], are dissolved interstitially and diffuse interstitially without the need for point defects in the lattice. Slow diffusers like the group III and V elements (boron and phosphorous [100]) are dissolved substitutionally and diffuse more slowly as substitutional diffusion relies on point defects such as vacancies and self-interstitials. The diffusivity of sulfur is closer to that of iron, while the diffusivity of tellurium is similar to the group III and V elements; selenium is in between. Research suggests that the large difference in diffusivity between sulfur, selenium and tellurium is due to the percentage of diffusion that occurs interstitially versus substitutionally [90]. Although, sulfur, selenium and tellurium dopants are predicted to occupy substitutional sites [101–103], diffusion can occur interstitially through either the Frank-Turnbull mechanism [104] (the substitutional dopant jumps into an interstitial site creating a vacancy) or the kick-out mechanism [105] (a silicon self-interstial takes the place of the substitutional dopant which jumps to an interstitial site).

SIONYX1403000043.0034

SAMSUNG EX. 1002 - 677/4148

two experimental observations seem to indicate that the reduction of infrared absorptance after annealing is related to diffusion of the dopant [50].

In this chapter, we further explore whether the deactivation of infrared absorption is a diffusion process by determining the optical properties of supersaturated chalcogen-doped silicon before and after numerous thermal vacuum anneals. The silicon is doped by irradiation with femtsecond laser pulses in the presence of a background gas (for sulfur doping) or coated with an evaporated film of the dopant (for selenium and tellurium doping). Our analysis shows that thermal annealing reduces the infrared absorptance in a manner that is consistent with diffusion of the dopant. In addition, the infrared absorption is observed to decrease the same amount after a similar diffusion length for all three dopants. Using diffusion theory, we show that a probable source of this characteristic diffusion length is the grain size of the re-solidified surface layer.

4.3 Experimental setup

For all experiments, we used boron-doped Si (100) wafers ($\rho = 1-20$ Ω-cm, dia. = 50 mm). Wafers were ultrasonically cleaned in methanol for 10 minutes. For sulfur doping, the wafers were placed on a translation stage in a stainless steel vacuum chamber that was evacuated to less than 1×10^{-2} Torr using a mechanical pump. The chamber was filled with 500 Torr of SF_6. For selenium and tellurium doping, the wafers were first placed into a resistive thermal evaporator that was evacuated to 1×10^{-6} Torr. A film thickness of 150 nm was deposited for both selenium and tellurium using solid selenium (99.95%) and tellurium (99.95%) pellets, respectively, in tungsten boat sources (for additional information on using an evaporated film as the dopant source see Section 4.7.1). The coated wafers were loaded into the stainless steel chamber, which was then evacuated to less than 1×10^{-2} Torr and

SIONYX1403000043.0035

SAMSUNG EX. 1002 - 678/4148

filled with 500 Torr of N_2. Femtosecond laser ablation in a gas of near-atmospheric pressure results in different hydrodynamics for melting and ablation than irradiation performed in a vacuum [106]. In order to keep the hydrodynamics of doping the same for all samples, we irradiated the selenium- and tellurium-coated samples in a background gas of N_2 at the same pressure as the samples irradiated in SF_6.

We irradiated the wafers with a 1-kHz train of 100-fs, 800-nm laser pulses with a fluence of 8 kJ/m^2 focused to a spot size of 150-μm full width half maximum, $FWHM$. Fluence equals the pulse energy/area, where the area (radius that intensity is 1/e of the peak value) is $\pi(FWHM)^2/(4\ln(2))$. The wafer's surface was perpendicular to the incident laser and translated in the plane of the surface with a velocity of 1.5 mm/s; each area received 100 shots. A 33 mm x 33 mm area was irradiated on each wafer by translating 33 mm vertically, stepping 75μm horizontally and repeating.

After irradiation, the wafers were removed and cut into 8 mm x 11 mm samples for annealing in a thermal vacuum oven evacuated to less than 1×10^{-6} Torr. We evaluated the optical properties of the samples before and after annealing by measuring the infrared absorptance with a UV-VIS-NIR spectrophotometer equipped with an integrating sphere detector. The diffuse and specular reflectance (R) and transmittance (T) were measured for the wavelength range of 0.9–2.5 μm, in 1-nm increments to determine the absorptance ($A = 1 - R - T$) at each wavelength.

Initially, we performed twenty-five thermal vacuum anneals covering a matrix of five temperatures (575 K, 675 K, 775 K, 875 K, 975 K) and five times (10 min, 30 min, 100 min, 6 hr, 24 hr) for each of the four types of samples: Si wafers irradiated in SF_6 (Type I); Si wafers coated with selenium (Type II) or tellurium (Type III) and irradiated in N_2; and Si wafers irradiated in N_2 (Type IV). To explore the high temperature behavior, the four types of samples were annealed to temperatures between 975 K and 1175 K for 100

SIONYX1403000043.0036

SAMSUNG EX. 1002 - 679/4148

minutes. Lastly, as a control, an untreated Si wafer was annealed to 1175 K for 100 min.

4.4 Results

After irradiation, the surface of each sample is transformed from a flat, mirror-finished, light gray wafer into a visibly matte black or dark gray surface. Closer inspection with a scanning electron microscope reveals that the surface is covered with a forest of micrometer-sized spikes. The formation of this surface morphology is a function of the laser wavelength, fluence, and pulse duration, as well as the gas chemistry and pressure; the mechanism behind its formation has been well documented elsewhere [42, 43].

Figure 4.1 shows the infrared absorptance (0.9–2.5 μm) of each of the four types of samples after laser irradiation compared to the absorptance of the initial silicon wafer. The initial silicon wafer is largely transparent to wavelengths of light greater than 1.07 μm due to the band gap energy of crystalline silicon (1.1 eV). The chalcogen-doped samples exhibit near unity absorptance of infrared light and samples irradiated in N_2 show some infrared absorptance, which decreases with increasing wavelength.

Figure 4.1 also shows the infrared absorptance of the chalcogen-doped samples after annealing at 775 K for the five lengths of time used in the annealing experiment. The infrared absorptance of all three samples is reduced after annealing; this reduction increases with annealing time. Sulfur-doped samples show the largest decrease in infrared absorptance, followed by selenium-doped samples; the absorptance of tellurium-doped samples changes the least.

Figure 4.2 displays the mean infrared absorptance (between 1.2–2.5 μm) after the initial twenty-five anneals performed at 575–975 K for each of the four types of samples: sulfur-doped (circles) selenium-doped (squares), tellurium-doped (triangles) and samples

SIONYX1403000043.0037

SAMSUNG EX. 1002 - 680/4148

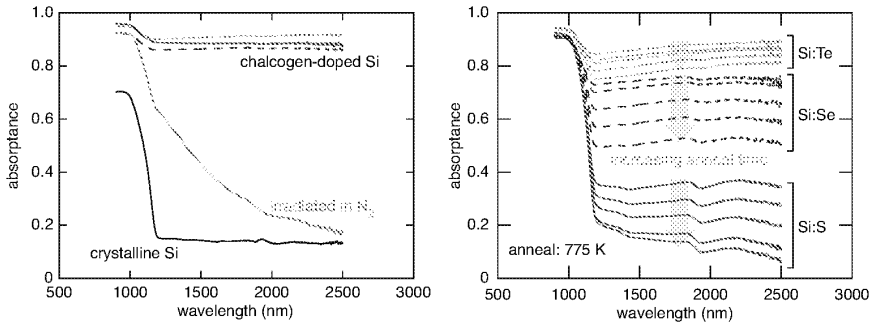


Figure 4.1: *Left:* Absorptance spectra for samples irradiated in the presence of sulfur hexaflouride (solid red line), selenium (dashed blue line), tellurium (dotted green line), and nitrogen gas (solid gray line) prior to thermal annealing. The absorptance of the untreated silicon wafer is included for comparison. *Right:* Absorptance spectra for sulfur-, selenium-, and tellurium-doped silicon after annealing to 775 K for increasing lengths of time (from top to bottom: 10 min, 30 min, 100 min, 6 hr, 24 hr).

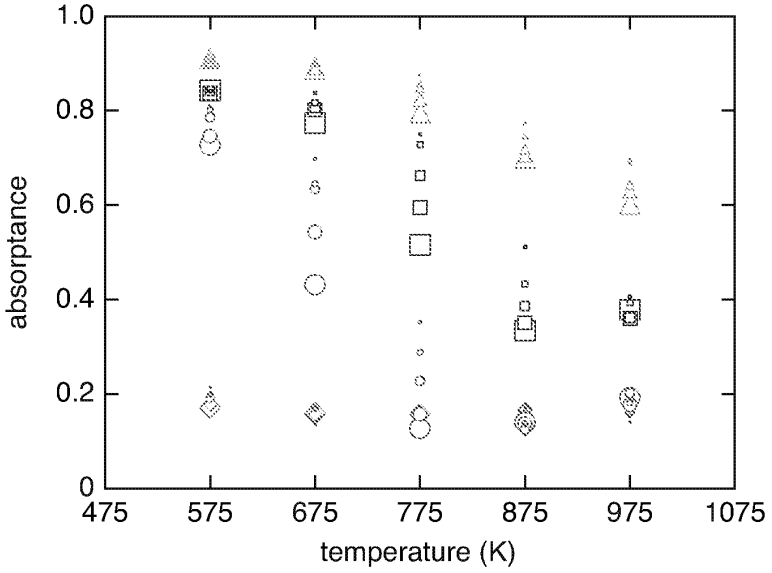


Figure 4.2: Average absorptance from 1250–2500 nm for sulfur-doped (circles), selenium-doped (squares), tellurium-doped (triangles) silicon and samples irradiated in N_2 (diamonds) after various thermal anneals at $T \leq 975$ K. A larger marker indicates a longer anneal (from smallest to largest: 10 min, 30 min, 100 min, 6 hr, 24 hr).

SIONYX1403000043.0038

SAMSUNG EX. 1002 - 681/4148

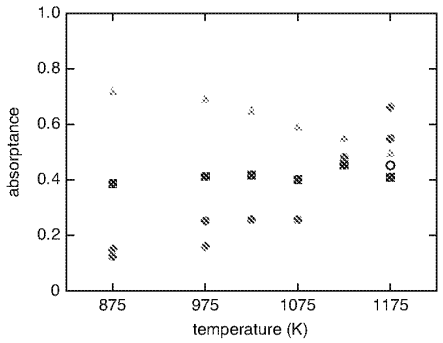


Figure 4.3: Average absorptance from 1250–2500 nm for sulfur-doped (circles), selenium-doped (squares), tellurium-doped (triangles) silicon and samples irradiated in N_2 (diamonds) after thermal anneals at $T \geq 875$ K for 100 min. The infrared absorptance of an unirradiated silicon wafer annealed to 1175 K for 100 minutes is also shown (open circle).

irradiated in N_2 (diamonds). The size of the marker indicates the length of each anneal, with the largest size equaling 24 hours and the smallest, 10 minutes. The results of the high temperature annealing study are shown in Figure 4.3. Between 575 K and 875 K (Figure 4.2), the change in absorptance has the same trend for all three chalcogen-doped samples; absorptance drops with increasing anneal temperature and at a given temperature, a longer annealing time results in a further decrease in absorptance. At 875 K, the absorptance of the sulfur-doped samples and the samples irradiated in N_2 have been reduced to the infrared absorptance of the original un-irradiated silicon substrate. Above 875 K (Figures 4.2 and 4.3), the change in absorptance of each sample has a different trend. The absorptance of sulfur-doped samples and those irradiated in N_2 begins to increase with increasing temperature. The absorptance of selenium-doped samples stays relatively the same as the value at 875 K and the absorptance of tellurium-doped samples continues to decrease.

SIONYX1403000043.0039

SAMSUNG EX. 1002 - 682/4148

4.5 Discussion

Crystalline silicon is mostly transparent to wavelengths of light longer than 1.07 μm due to its band gap. The absorptance of wavelengths of light shorter than 1 μm depends on the roughness of the silicon surface. Every sample [43, 46, 48, 49] that we irradiate exhibits enhanced absorption of wavelengths of light shorter than 1 μm (see Figure 1). This observation is also true of samples irradiatied in vacuum [43]; the enhanced absorption of wavelengths of light in this region is caused by multiple reflections on the textured surface.

If irradiation is performed in the presence of certain dopants, such as sulfur, selenium or tellurium, the absorptance of infrared light between 1.0–2.5 μm is enhanced to near-unity (see Figure 4.1). However, this behavior is not observed for all dopants, such as the samples irradiated in N_2 gas (see Figure 4.1). The N_2 samples exhibit a non-uniform absorptance of infrared light, which decreases with increasing wavelength. This same trace shape is seen when silicon is irradiated in many other gases [43, 46, 48, 49] (H_2, Cl_2, and air) as well as when irradiation is performed in a vacuum [43]. Because they are all similar to vacuum, we attribute this infrared absorptance to structural defects present in the nanocrystalline grains and not doping of the silicon with species in the background gas.

In order to understand the mechanism behind our samples' near-unity infrared absorptance (between 1.0–2.5 μm), we begin by reviewing what is known about their structure and composition. During irradiation of silicon with ultrashort laser pulses above the ablation threshold [21] (3 kJ/m^2) the top surface layer is ablated away and the next layer below melts. This thin molten layer resolidifies extremely quickly due to its contact with the cold bulk substrate. Cooling rates are estimated to be as high as 10^{15} K/s [22]. When a gas or surface dopant is present during irradiation it will be atomized by the high intensity of the ultra short laser pulse and mix with the molten silicon. Rutherford back

SIONYX1403000043.0040

SAMSUNG EX. 1002 - 683/4148

scattering measurements [46, 49, 50] show that these species are incorporated at a concentration on the order of 1 atomic percent and that 20–70% of the dopants are located on substitutional lattice sites [46]. This concentration is orders of magnitude above the equilibrium solubility limit and the dopants are therefore in a supersaturated solution [50]. The high concentration of dissolved atoms become trapped in the lattice during the extremely fast solidification in a process that is likely similar to the solute trapping that occurs after pulsed laser irradiation of ion implanted semiconductors [96]. Cross-sectional transmission electron microscopy reveals that the resolidified surface layer is an approximately 300-nm thick polycrystalline layer with nanometer-sized grains (10–50 nm) [46]. It is this surface layer that contains the supersaturated concentration of dopants and is responsible for the resulting optical properties.

We previously proposed that the broadband absorptance of infrared light is caused by the high concentration of chalcogen dopants in the nanometer sized grains of the polycrystalline surface layer [46, 49, 50]. An equilibrium concentration of sulfur, selenium or tellurium atoms each create deep level donors in the band gap of silicon [79, 80]. A supersaturated concentration of chalcogen atoms creates a densely populated impurity band around one or more of those deep levels. Below, we provide support for this mechanism by showing that the infrared absorptance decreases with annealing at the same rate that dissolved dopants diffuse out of the nanometer-sized grains to the grain boundaries. Diffusion of the dopants out of the grains reduces the number of impurity levels in the band gap and thus reduces the infrared absorption. Because the grains are on the order of nanometers in size, thermal anneals that result in diffusion lengths on the order of nanometers are required to decrease the absorptance. Below we show that this is the case for all three chalcogen dopants.

It is also possible that precipitation of the dopant within the crystalline grains (in

SIONYX1403000043.0041

SAMSUNG EX. 1002 - 684/4148

the form of clustering) could lead to deactivation of infrared absorption. This process will also involve diffusion of the dopant on the order of nanometers through the crystalline grains. With the current analysis, it will be difficult to distinguish whether clustering or diffusion to the grain boundaries is responsible. Here, we offer that it is plausible that diffusion of the dopants to the grain boundaries leads to deactivation of the infrared absorption.

For every thermal anneal, we can estimate the diffusion length, d, for each dopant (sulfur, selenium and tellurium) using the equation $d = \sqrt{Dt}$, where t is the annealing time; D is the bulk diffusivity for each dopant in silicon given by $D = D_0 \exp(-E_a/(kT))$; T is the annealing temperature; k is the Boltzmann constant; and D_0 and E_a are temperature independent constants obtained from the literature on the bulk diffusivity of sulfur, selenium and tellurium in silicon. For each anneal, the temperature and time is known; the diffusivity of the dopant can be calculated using the temperature and a diffusion length can be obtained for each anneal for sulfur, selenium and tellurium, respectively. Because diffusion length incorporates both time and temperature, it describes the amount of thermal energy each anneal imparts on the sample. For example, a very long low temperature anneal can impart the same thermal energy as a very short higher temperature anneal.

Slightly different values for D_0 and E_a for each dopant have been reported in the literature [81, 84–90, 90–92]. For our analysis, we chose diffusivity constants determined from studies that used the lowest temperature range and a similar silicon substrate (see Table I). For tellurium, the referenced study fit its data as the sum of two Arrhenius curves, giving high temperature and low temperature values for D_0 and E_a; in that case we used the low temperature values. Although the analysis below is carried out with one set of diffusion constants for each dopant, all reported diffusivities give similar results and do not change our conclusions.

In Figure 4.4, we re-plot the infrared absorptance graphed in Figures 4.2 and 4.3;

SIONYX1403000043.0042

SAMSUNG EX. 1002 - 685/4148

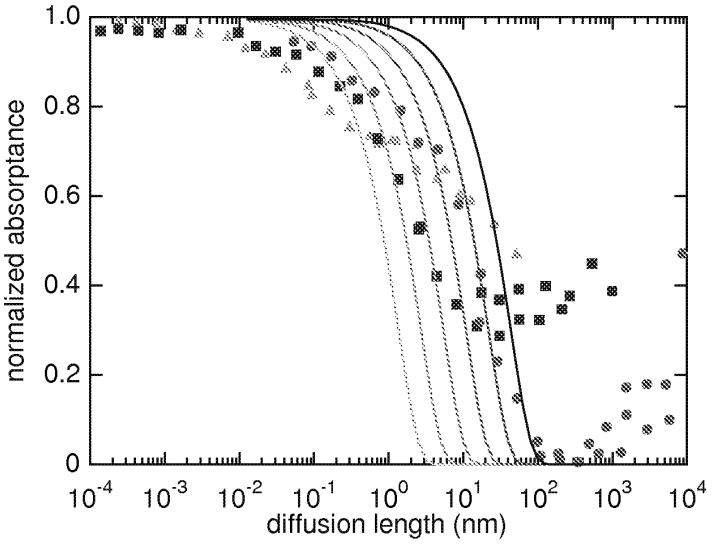


Figure 4.4: Normalized absorptance for sulfur-doped (circles), selenium-doped (squares), and tellurium-doped (triangles) silicon after various thermal anneals versus diffusion length of the respective dopant. The average infrared absorptance from Figures 4.2 and 4.3 has been renormalized so that the maximum is the preannealed value and the minumum is the infrared absorptance of the unirradiated silicon wafer (see Figure 4.1). The six solid curves are plots of Equation 4.4 for sphere radii from left to right of 5 nm, 10 nm, 20 nm, 40 nm, 80 nm, and 160 nm.

however, now the data for sulfur-doped (circles), selenium-doped (squares) and tellurium-doped (triangles) samples are plotted versus the diffusion lengths of sulfur, selenium and tellurium atoms, respectively (these diffusion lengths are calculated using the constants in Table I). In addition, the infrared absorptance is normalized so that the maximum value is the preannealed infrared absorptance from Figure 4.1 and the minimum value is the infrared absorptance of the unirradiated silicon wafer.

We can draw several conclusions from Figure 4.4. First, the data points—each representing a different sample and a different anneal condition—form a continuous curve when plotted versus the dopant's diffusion length. Second, the infrared curve for each chalcogen-

SIONYX1403000043.0043

SAMSUNG EX. 1002 - 686/4148

Dopant chemical	D_0 (cm^2/s)	E_a (eV)
S [87]	0.92	2.2
Se [89]	2.47	2.84
Te [85]	0.048	3.04

Table 4.1: Diffusivity constants used to determine the diffusion length of each dopant after a thermal anneal in order to create Figure 4.4.

doped sample decreases at diffusion lengths that are on the same order of magnitude as the observed grain size of femtosecond laser irradiated silicon. Third, longer lower temperature anneals which have roughly the same decrease in infrared absorptance as shorter higher temperature anneals result in roughly the same diffusion length for each dopant (*e.g.*, 24 hr at 575 K roughly equals 10 min at 675 K, 24 hr at 675 K roughly equals 10 min at 775 K, and 24 hr at 775 K roughly equals 10 min at 875 K, for all three dopants). Finally, when the data is normalized to the diffusion length of each samples' respective dopant, the infrared absorptance decreases at the same rate for all three samples; in other words, there appears to be a characteristic diffusion length associated with the deactivation of infrared absorptance. These observations are strong evidence that the reduction of absorptance is a diffusion related process.

4.5.1 Diffusion theory

If the decrease in infrared absorptance is caused by the diffusion of dopants out of the crystalline grains, we can use diffusion theory to estimate how the concentration of dopant atoms in the grains should decrease with thermal annealing and compare this to our data. To start, we make the following assumptions: the crystalline grains are spherical with a radius of R_0 and an initial dopant concentration of C_0 spread uniformly throughout; diffusion occurs radially out from the center; the grain boundaries are perfect sinks (*i.e.*,

SIONYX1403000043.0044

SAMSUNG EX. 1002 - 687/4148